Ga. 1155

ORNL-5275

FUSION ENERGY DIVISION

ANNUAL PROGRESS REPORT

Period Ending December 31, 1976

BLANK PAGE

Printed in the United States of America. Available from
National Technical Information Service
U.S. Department of Commerce
5285 Port Royal Road, Springfield, Virginia 22161
Price: Printed Copy $10.00; Microfiche $3.00

ORNL-5275
Dist. Category UC-20

Contract No. W-7405-eng-26

FUSION ENERGY DIVISION

ANNUAL PROGRESS REPORT
For Period Ending December 31, 1976

JUNE 1977

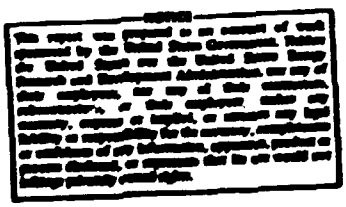

Prepared by the
OAK RIDGE NATIONAL LABORATORY
Oak Ridge, Tennessee 37830
operated by
UNION CARBIDE CORPORATION
for the
ENERGY RESEARCH AND DEVELOPMENT ADMINISTRATION

Reports previously issued in this series are as follow:

ORNL-2693	Period Ending January 30, 1959
ORNL-2802	Period Ending July 31, 1959
ORNL-2926	Period Ending January 31, 1960
ORNL-3011	Period Ending July 31, 1960
ORNL-3104	Period Ending January 31, 1961
ORNL-3239	Period Ending October 31, 1961
ORNL-3315	Period Ending April 30, 1962
ORNL-3392	Period Ending October 31, 1962
ORNL-3472	Period Ending April 30, 1963
ORNL-3564	Period Ending October 31, 1963
ORNL-3652	Period Ending April 30, 1964
ORNL-3760	Period Ending October 31, 1964
ORNL-3836	Period Ending April 30, 1965
ORNL-3908	Period Ending October 31, 1965
ORNL-3989	Period Ending April 30, 1966
ORNL-4063	Period Ending October 31, 1966
ORNL-4150	Period Ending April 30, 1967
ORNL-4238	Period Ending October 31, 1967
ORNL-4401	Period Ending December 31, 1968
ORNL-4545	Period Ending December 31, 1969
ORNL-4688	Period Ending December 31, 1970
ORNL-4793	Period Ending December 31, 1971
ORNL-4896	Period Ending December 31, 1972
ORNL-4982	Period Ending December 31, 1973
ORNL-5053	Period Ending December 31, 1974
ORNL-5154	Period Ending December 31, 1975

CONTENTS

BLANK PAGE

INTRODUCTION

During 1976, ORNL was a major contributor to the impressive progress of the international effort of many laboratories and many nations to harness fusion energy. The uniqueness of the ORNL program resides in the variety of its contributions, which lie in almost every area of fusion research and development. The breadth of our program provides a necessary counterpoint to our deliberate efforts to focus on the essential steps that must be taken to build a viable fusion reactor. In order to provide this focus, we have used the Demonstration Reactor study (Demo) to define our goal and the design of The Next Step (TNS) in the fusion program to guide our program planning. In order to work toward our goal, we have attempted to combine the technological disciplines of our program with industrial engineering expertise. Finally, we have attempted to leaven this activity by maintaining an environment of state-of-the-art experimental and theoretical plasma physics. I believe that these steps have multiplied the effectiveness of our resources in working toward practical fusion energy.

Our program continues to concentrate the bulk of its resources on the advanced design, plasma physics, and technological developments specific to tokamaks. However, these activities provide a fertile environment for the rapid development of alternate concepts. Increased electron cyclotron resonance heating power and diagnostic capability, especially the development of spatial potential measurements, on ELMO Bumpy Torus (EBT) have provided data which are in reasonable agreement with rapidly developed theoretical models partially derived from our tokamak program. In addition, a development program has been initiated to produce high power microwave tubes for future EBT experiments as well as for application to tokamaks. Thus, the EBT program is progressing rapidly in both plasma physics understanding and critical technological development, and EBT continues to be a very attractive fusion reactor alternative.

The most significant theoretical developments this past year have been the conception and initial investigations of the properties of high volume average beta ($\bar{\beta}$) "flux conserving tokamak" (FCT) equilibria. Equilibria with $\bar{\beta}$ of more than 20% have been found (both theoretically and from transport modeling) to be a natural consequence of auxiliary heating when the heating time is such that the poloidal and toroidal magnetic fluxes are frozen in during the heating. The marginal stability of FCT equilibria has been investigated in the ideal MHD limit. A nonoptimized case has been found to be stable for $\bar{\beta}$ up to 5% as long as the safety factor (q) at the plasma center is kept above about 1.2. Neutral injection, which has been pioneered at ORNL, is used for the auxiliary heating source; the beam deposition and transport effects for these high $\bar{\beta}$ FCT equilibria have also been considered. The net prospect is that the maximum $\bar{\beta}$ in tokamaks may readily reach — and perhaps even exceed — the 5-10% economic viability range, instead of being limited to less than 3%, as previously thought. This is a significant development for the entire tokamak-based fusion program.

One indication of the significance of the high $\bar{\beta}$ developments is the impact on the ORNL tokamak advanced design programs. Combining the high $\bar{\beta}$ concept and other plasma physics developments with advances in the materials, injector, and coil technology has made it possible to begin the design of an economically viable fusion reactor core for TNS. The minor radius of the TNS "core plasma" has been reduced to 1.25 m and the thermal power output increased to 2 MW. The Demo program has simultaneously produced a plan for utilizing the TNS plasma core in a series of logical steps to commercialize tokamak fusion power.

Based on the increased understanding of the behavior of modified stainless steels developed in the ORNL Fusion Reactor Technology Program, it is possible to expect first wall lifetimes in excess of 10 MW-yr/m^2 for TNS-type tokamak reactors. Simultaneously, increased theoretical understanding of the required heating profiles and advanced concepts in beam handling technology makes it possible

to achieve ignition in such a system with conventional positive ion technology, thus lessening the need for more efficient but more difficult negative ion technology. Relevant ignition experiments also require a pulse time on the order of tens of seconds, which implies that superconducting coils are an essential ingredient on both economic and technological bases. During this year, ORNL has taken a major step in the development program for these large, superconducting coils by the initiation of three design and fabrication contracts with industry.

This technological progress has been reinforced by a series of advances in tokamak plasma physics, both at ORNL and throughout the world. The ORNL experimental plasma physics program in 1976 was highlighted by the production of large increases in the plasma parameters in ORMAK through the use of neutral injection heating. This included increasing the ion temperature from 0.6 to 2.0 keV and demonstrating significant electron heating with neutral injection for the first time. We were also able to produce a peak β of 3% and an average β of 1% with neutral heating. Unfortunately, ORMAK operation terminated two months ahead of schedule, in December 1976, after a power supply accident which damaged some of the toroidal field coils. This final shutdown ended one of the most productive experimental programs in the history of fusion research. The ORMAK staff and many of the related facilities will now be concentrated on the Impurity Study Experiment (ISX), which begins operation in the spring of 1977. The scope of the ISX program has been expanded to utilize Princeton Large Torus (PLT) class ORMAK Upgrade neutral injectors to address high β plasmas after a year of important noninjected plasma impurity studies. Simultaneously, the ORMAK Upgrade experiment will be redesigned in order to include recent plasma physics developments and to carry on optimized high β experiments when ISX returns to its primary impurity study role.

The ORNL Plasma Heating and Fueling activities also completed a very productive year in 1976. The 150-keV test stand required for addressing high energy beam technology for the Tokamak Fusion Test Reactor (TFTR) and TNS was completed and successfully operated with a two-stage source. Initial operation was started with the first PLT beam line components. As expected, the quasi-steady-state ORNL ion sources were successfully scaled to the 60-A, 40-keV level required for PLT. Utilizing a hydrogen pellet fueling device developed at the University of Illinois, the first significant fueling experiments were conducted on ORMAK, and a good start was made on a more reactor-relevant mechanical pellet injector. These new beam and fueling facilities can be expected to produce many more developments in 1977.

These major achievements give us confidence that we are making progress toward our goal. However, we must recall that each successfully concluded project is made up of individual components, each based on painstaking research and craftsmanship. While we were completing the major projects mentioned above, the all-important components for future successes were being crafted in our laboratories. Consequently, the bulk of this annual report is devoted to those activities which lay the foundation for future progress.

We end the year with many achievements. More importantly, we have facilities and ideas to surpass these achievements in the new year. I can add only my gratitude to the men and women of the ORNL Fusion Energy Program who have made this possible.

John F. Clarke

John F. Clarke, Director
Fusion Energy Division
May 1977

PART I. PLASMA FUSION

ABSTRACTS
(Chapters 1-3)

1. HIGH BETA PLASMA SECTION

An increased understanding of the plasma properties in the ELMO Bumpy Torus has resulted from the experimental efforts in 1976. Ion and electron temperatures in the range of 100-300 eV have been measured using charge exchange and soft x-ray measurements respectively. Our confidence in the charge-exchange measurements has been increased by a separate experiment which has shown that the impurity component in the neutral flux is negligible.

Measurements in the ultraviolet spectral range have shown the absence of highly charged impurities. This observation, coupled with the electron temperature measurements, has led to the conclusion that the impurity density is very low in the plasma core – that the "natural divertor" action prevents impurity penetration. Further measurement and analysis of the Doppler width of neutral hydrogen light reaffirms the evidence that the hydrogen atoms in the plasma have a temperature of much less than 1 eV. A heavy ion beam probe has been installed with the excellent prospect of determining the spatial profile of the plasma potential. This information is of a great importance because of the large influence the radial electric field has on confinement properties in a bumpy torus. Measurements of the plasma diamagnetic field are under way; they will improve the knowledge of the hot electron volume.

The power capability at 18 GHz has been doubled, from 30 to 60 kW (cw). Higher powers at higher frequencies require that sources be developed; this development has begun.

2. TOKAMAK EXPERIMENTAL SECTION

The tokamak scheme of formation and containment of a toroidal plasma has shown considerable promise, because scaling laws, based on theory, are favorable to the achievement of controlled fusion by this means. In the program to formulate an extrapolation directly to a reactor, the Oak Ridge Tokamak (ORMAK) neutral beam heating experiments of this past year are key elements. There has been significant neutral beam heating of plasma electrons, and high toroidal beta values have been attained. The useful operating range for plasma studies has been extended: (1) by injection to approximately 500 kW neutral beam power, (2) with toroidal fields to 30 kG, and (3) with plasma currents to 230 kA. Values of Z_{eff} were reduced to 2.5 and the limiter safety factor to 2.5.

Neutral beam heating of the plasma attained a 1.8-keV central ion temperature at a density of 3×10^{13} cm^{-3} with 360 kW of injection power. The scaling of ion temperature with plasma density and injection power implied neoclassical ion-thermal conductivity and classical beam-plasma energy transfer.

ORMAK experiments with 150 kW of ohmic heating power and 360 kW of injection power have resulted in increases in the central electron temperature from 0.3-0.8 keV and in the average electron temperature from 0.2-0.45 keV at 70 kA plasma current. Similar electron temperature increases were also seen at higher plasma currents (175 kA). The scaling of electron temperature with power appeared to be the same for ohmic heating and neutral beam injection.

ORMAK measurements indicated that toroidal rotation velocities were limited to low values and were not substantially increased by unidirectional injection, so that coinjection may be sufficient for plasma heating. Impurities and radiation losses increased with injection, but the addition of 360 kW of injection power to 150 kW of ohmic heating power did not change Z_{eff} ($\approx$3) by more than one. This is in contrast to the observed linear scaling of Z_{eff} with ohmic heating power on ORMAK.

Some additional beneficial effects of injection were:

1) Attainment of higher maximum densites with gas puffing [$\bar{n}_e = 6 \times 10^{13}$ cm^{-3} and $n_e(0) = 9 \times 10^{13}$ cm^{-3} vs $\bar{n}_e < 4.5 \times 10^{13}$ cm^{-3} without injection],
2) operation at lower limiter safety factors [$q(a) = 2.5$ vs $q(a) > 3.5$ previously], and
3) attainment of higher toroidal beta [$\beta_T(0) = 1.4\%$ and average $\beta_T = 0.4\%$] and higher total toroidal beta [including stored beam energy ≈ plasma energy, $\beta_T(0) \approx 3\%$ and average $\beta_T \approx 0.8\%$].

Other contributions of interest are as follows.

1) Solid hydrogen pellets, 210 μm in diameter, injected with speed of 90 m/sec and path lengths in the plasma of 9 cm, approximately double the penetration distance obtained earlier.
2) Publications on the physics of surface mechanisms by which impurities are formed and the forces which cause the impurities to enter the plasma are abstracted.
3) A refined model for runaway electrons and some departures from the model are noted.
4) Internal mode structures and sawtooth oscillations are related to energy transport.
5) A new diagnostic tool, the fast soft x-ray analyzer, is described.
6) There are several improvements in the data handling system.
7) The status of ISX and ORMAK Upgrade is reviewed.

In the area of atomic physics, compilations and bulletins continue to be published and distributed to the fusion community. Cooperation with the International Atomic Energy Agency (IAEA) in the publication of a comprehensive bibliography is in progress. Utilization of the ORNL Tandem Van de Graaff accelerator and the development of a dedicated 10-100 keV accelerator have made new measurements of electron capture, ionization, and charge-exchange cross sections possible and have already given direction to the design of injectors for developing tokamaks.

In the area of diagnostic development, a 1-MW pulsed submillimeter laser system to be used for spatial ion temperature determinations using Thomson scattering techniques is described.

3. PLASMA THEORY SECTION

The most significant development this past year was the conception and initial investigation of high volume average $\bar{\beta}$ flux conserving tokamak (FCT) equilibria. These high-$\bar{\beta}$ (up to 20%) equilibria were found (both theoretically and from transport simulation modeling) to be a natural consequence of auxiliary heating when the heating time is much shorter than the magnetic diffusion time — so that the poloidal and toroidal magnetic fluxes are frozen in during the heating. The marginal stability of FCT equilibria was investigated in the ideal magnetohydrodynamic (MHD) limit; a nonoptimized case was found to be stable for $\bar{\beta}$ up to 5% as long as the safety factor (q) at the plasma center is kept above about 1.2. Neutral beam deposition and transport effects for these high-$\bar{\beta}$ FCT equilibria were also considered. The net prospect is that the maximum volume average $\bar{\beta}$ in tokamaks may readily attain and perhaps even exceed the 5-10% economic viability range instead of being limited to less than 3% as was previously thought. This is a significant development for the entire tokamak fusion program.

Other notable developments in tokamak theory this past year are as follows. First, a model for the sawtooth oscillations in which the slow rise is induced by ohmic heating and the abrupt drop is brought about by an $m = 1$ tearing mode that has an accelerating growth rate seems to be in very good agreement with sawtooth oscillation data from the Oak Ridge Tokamak (ORMAK). Second, significant improvements have been made in the Collisional Plasma Model, in which the drift-kinetic equation for tokamaks is solved numerically. Third, an improved understanding of the basic impurity transport processes in tokamaks has been reached. Fourth, an anomalous transport model based on strong turbulence theory and magnetic flutter effects of dissipative trapped electron instabilities has been hypothesized.

Instead of completely replacing neoclassical transport, these effects simply add to it.

The main thrust of the ELMO Bumpy Torus (EBT) theory efforts this past year was the evolution from zero-dimensional, radially averaged parametric studies to fully one-dimensional radial profile studies. This theory development parallels a similar one in the EBT experiment where the emphasis has been shifting over the past year from single point to radial profile measurements. The theoretical profiles for the plasma density and temperature agree reasonably well with those observed experimentally. A very important part of this work was the formulation of methods for determining the electrostatic potential in the plasma.

In the plasma engineering area, where applied plasma physics knowledge is developed into models for immediate use in the design of future tokamaks, the major developments this past year were in: (1) plasma start-up studies, where a zero-dimensional code has been developed to treat the initial breakdown and ionization of hydrogen gas with (for example, oxygen impurity atoms; and (2) investigation of poloidal field designs for the coil dispositions required to contain, center, and actively shape the intrinsically D-shaped, high-β FCT equilibria. In addition, the plasma physics characteristics of The Next Step (TNS) device were developed. Finally a first cut EBT reactor study, which confirms the initial promise of this concept, was completed.

In the computing support area, a major development this past year was the initiation of the high speed link with the National Magnetic Fusion Energy Computer Network (NMFECN) at Lawrence Livermore Laboratory. This development plus numerous software improvements resulted in a much higher level of reliability and functionality in our use of the NMFECN through our User Service Center. Finally, the data acquisition capabilities and use in the Division were improved substantially this past year.

BLANK PAGE

1. HIGH BETA PLASMA SECTION

R. A. Dandl, Section Head

F. W. Baity
M. C. Becker[1]
F. M. Bieniosek[2]
K. H. Carpenter[3]
J. A. Cobble
P. L. Colestock[2]
K. A. Connor[2]
H. O. Eason
M. Fujiwara[4]
G. R. Haste
R. L. Hickok[2]
H. Ikegami[4]
N. H. Lazar
G. F. Leichsenring[5]
R. L. Livesey
M. W. McGuffin
D. H. McNeill
H. W. Moos[6]
B. H. Quon
J. W. Reynolds[1]
W. J. Schill
E. S. Warden[6]
T. L. White
R. E. Wintenberg[1]
W. L. Wright[5]

1.1 INTRODUCTION

The principal modification to the ELMO Bumpy Torus (EBT) during 1976 has been the installation of additional microwave power at 18 GHz. Two new tubes with 15 kW each have been added; the total power at this frequency is now 60 kW. The power capability at 10.6 GHz remains 30 kW. Thus a total of 90 kW is available for electron cyclotron heating (ECH).

The operating characteristics of EBT are such that three distinct modes are evident. At high neutral pressure or low power, there is an unstable mode (C-mode) with low ion and electron temperatures. At lower neutral pressures, a transition to a quiet mode (T-mode) is observed; the bulk of the measurements is made in this mode. At still lower pressures, there is another transition to an unstable mode (M-mode) with large fluctuations in the stored energy. The experimental program has consisted of the addition of new diagnostic techniques and of further development of older techniques for determining the plasma characteristics in the various modes.

Sections 1.2.1 and 1.2.2 describe measurements of the charge-exchange flux leaving the plasma, with the result that the ion temperature can be measured with confidence. Sections 1.2.3 and 1.2.4 concern the evolution of previously described techniques in Thomson scattering and in the determination of the neutral hydrogen temperature by line broadening measurements. Section 1.2.5 describes the extension of the radial scanning technique into the ultraviolet (uv) spectral range, where both hydrogen light and light from the principal impurities can be scanned. X-ray measurements of the electron temperature are described in Sect. 1.2.6. In the same section a thick target bremsstrahlung calculation is applied to evaluate the response of an ionization probe. Section 1.2.7 reports the installation of an ion beam probe which will be used to determine the spatially resolved potential within the plasma, and Section 1.2.8 describes a program of measurement and calculation to determine the geometry of the hot electron confinement region. The recent increase in microwave power is discussed in Sect. 1.3, as

---

1. Instrumentation and Controls Division.
2. Consultant, Rensselaer Polytechnic Institute, Troy, New York.
3. Computer Sciences Division.
4. Consultant, Institute of Plasma Physics, Nagoya University, Nagoya, Japan.
5. General Engineering Division.
6. Consultant, Johns Hopkins University, Baltimore, Maryland.

is the development of sources at higher power and frequency for future application.

1.2 ION CHARGE-EXCHANGE MEASUREMENTS

The measurements of escaping neutrals from EBT have determined their energy spectrum and have shown a negligible impurity concentration.

1.2.1 Charge-Exchange Spectral Measurements

F. W. Baity B. K. Quon

The EBT charge-exchange neutral spectra usually contain several energy groups. It has been shown experimentally (see Sect. 1.2.2) that the neutral flux escaping the EBT plasma does not contain any significant fraction of impurities. The main problems which may affect the shapes of the neutral spectra are due to the suprathermal ion tail formation and the spatial profile effects. Thus, a local isotropic Maxwellian bulk ion distribution with a suprathermal tail and appropriate profiles has been adopted in analyzing the charge-exchange data. Our results are summarized as follows.

1) Figure 1.1 shows a typical spectrum. The shape of the charge-exchange neutral spectrum is Maxwellian over three to five orders of magnitude and has a well defined slope over a wide energy range, $2T_i < E \leq 10T_i$. The typical ion temperature measured from the slope of the spectrum corresponds to $T_i = 100$ eV within ~10% experimental error.
2) The value of $n_i n_o$, using the measured ion temperature and theoretical profiles, is in the range of $1\text{-}3 \times 10^{21}$ cm^{-6}, with errors estimated as ~50%. This result is comparable with a recent calibrated visible spectroscopy measurement. The corresponding ion confinement time is calculated to be
$$\tau \sim \frac{1}{n_o(\sigma_{\text{ionization}} v)} = 10\text{-}30 \text{ msec.}$$
3) Large suprathermal ion tails are measured near the high power T-M mode transition. The relative population of these hot ions (>200 eV) is observed to exceed 20% in some cases.

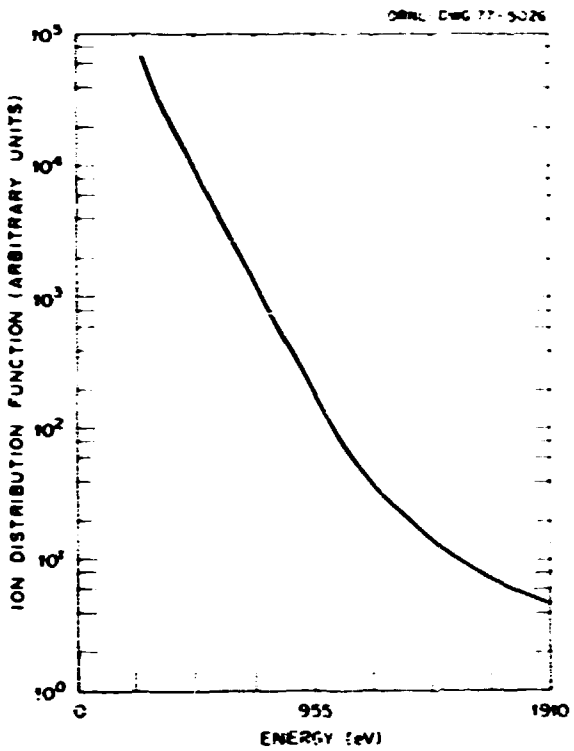

Fig. 1.1. Typical charge-exchange neutral spectrum escaping from EBT plasma. Plasma conditions: 18 GHz power ~ 32 kW, 10.6 GHz power ~ 6 kW, P ~ 5.8×10^{-6} torr, T-mode.

The results appear to be encouraging, even though detailed ion temperature and neutral density profiles are needed in order to pinpoint the relevant parameters so that precise scaling laws of EBT can be established. The four-beam charge-exchange analyzer under construction hopefully will help furnish this information before EBT-II is brought into operation.

The large (15-20%) suprathermal ion tail which was observed previously has been measured near the high power T-M mode transition. The formation of this fast ion group appears to be related to enhanced emission observed[1] near the lower hybrid or the ion acoustic frequencies under this operating condition.

1.2.2 Velocity Analysis of Charge-Exchange Neutrals on EBT

F. W. Baity B. H. Quon

Analysis of the mass of energetic neutrals escaping from EBT has now been made possible by the installation of a new charge-exchange neutral spectrometer employing an E × B velocity filter in addition to the parallel plate electrostatic energy analyzer. The main reason for the installation of this analyzer is to eliminate impurity particles whose presence may strongly influence the charge-exchange measurements.

The analysis has been performed under typical high power 2-mode conditions: 56 kW of 18-GHz (bulk plasma heating) and 8 kW of 10.6-GHz (profile heating) microwave power, plasma density $\sim 2 \times 10^{12}$ cm^{-3}, and bulk ion temperature 115 eV. The analyzer samples a thin cylindrical volume along a minor diameter of the plasma.

The electrostatic energy analyzer was set at 420 eV [420 eV lies in the middle of the energy range used to determine the central ion temperature in EBT (250 eV-1 keV)], the magnetic field of the velocity filter was set at 300 G, and the mass spectrum was taken by sweeping the electric field on the velocity filter.

Under these conditions, the mass resolution $\Delta m/m$ of the velocity filter is 0.22 (FWHM), sufficient to separate H and H_2. Figure 1.2 shows a spectrum taken under the conditions listed above. The signal-to-noise ratio of the peak is ~200. The single peak observed is identified as hydrogen atoms. The counting rate at the center of the peak is 94% of the total neutral counting rate with the velocity filter turned off (the width of the velocity filter "window" is comparable to the width of the energy analyzer "window" for hydrogen atoms). There is no evidence of any mass species other than hydrogen atoms in the spectrum at 420 eV. A mass spectrum taken at 830 eV also showed only a hydrogen atom peak (with a poorer signal-to-noise ratio). This extremely fortuitous result shows that the charge-exchange neutral particle flux leaving the EBT plasma does not contain a significant amount of impurity neutrals and that mass selection is not necessary in the analysis of charge-exchange neutrals.

1.2.3 Ruby Laser Scattering

J. A. Cobble

Following the advent of additional 18-GHz microwave tubes, a limitation on the existing Thomson scattering experiment was uncovered. An already poor signal-to-noise ratio worsened by increased plasma light under high power (30-60 kW) operating conditions. The difficulty apparently is attributable to increased radiation from molecular hydrogen and to a smaller extent from an aluminum ion multiplet, AlII 7049.[2]

Steps were taken for obtaining a ruby laser amplifier to boost pulse energy from 3 to over 14 J and faster integrators to cut sample times to below 30 msec. With the new equipment we anticipate a factor of fifteen enhancement in the signal-to-noise ratio.

1.2.4 Neutral Hydrogen Temperature

Fabry-Perot interferometer scans of intensity versus wavelength for H_α at 6563 A have been taken at a wide variety of pressure and microwave power operating points. It was found that H_α full width at half maximum intensity was 0.40 ± .02 A (1 standard deviation).

Possible line broadening mechanisms are Doppler effect, fine structure, and Zeeman effect. Instrument width at 0.04 A is negligible. The summed Doppler profiles of the seven H_α components in a field-free region may be used to find a maximum neutral temperature. Without detailed knowledge of radial magnetic field strength and particle densities, the influence of the Zeeman effect is uncertain; however, in a 5-kG field, some H_α components are split by over 0.10 A, and no components are undisplaced. The

maximum temperature, accounting for fine structure but ignoring magnetic field splitting, is ~1/2 eV.

1.2.5 Radial Scans of Impurity and Hydrogen Light

H. H. Lazar
H. W. Moos
E. S. Warden

The technique of scanning across the plasma using a rotating mirror to determine the spatial distribution of emitted light has been exploited into the far uv (1150 A-1850 A). For this development, cooperation with a group from Johns Hopkins University has been established. A spectrometer (originally designed by the Johns Hopkins group for satellite based astronomical studies) was used with a newly designed, anti-reflecting, cavity module in the EBT torus (see Fig. 1.3). Spectral line intensities from AlII and AlIII, CII, CIII, and CIV, and the Lyman H_2 line in hydrogen were measured with the calibrated spectrometer.

The asymmetry of the plasma prevents unambiguous unfolding of the plasma light profiles and therefore prevents the determination of the

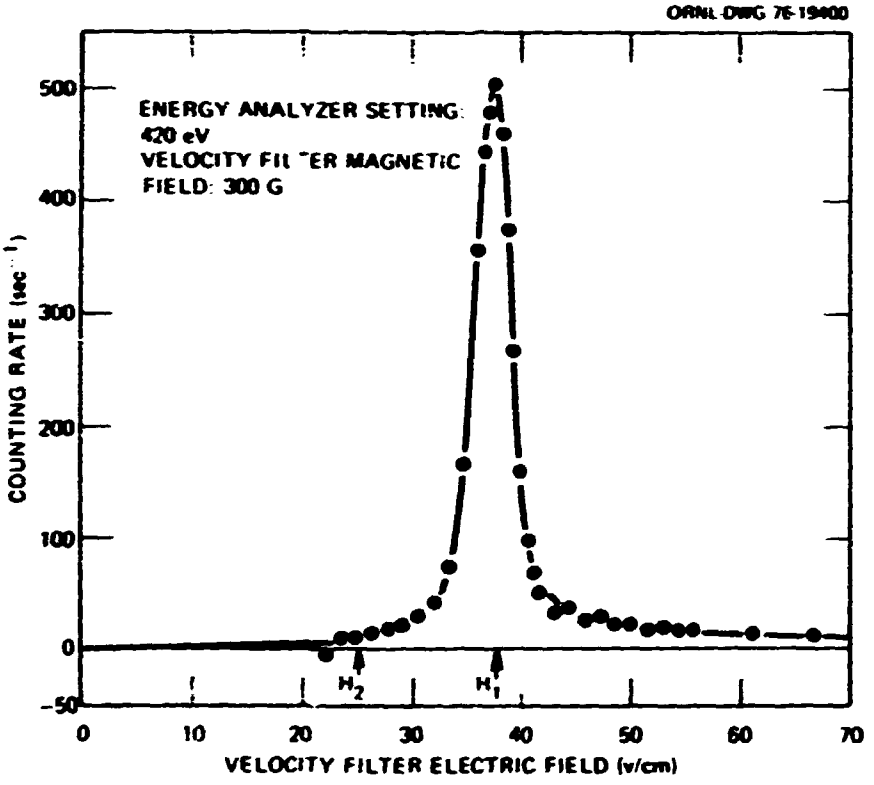

Fig. 1.2. Mass spectrum of 420-eV neutrals escaping from EBT under T-mode operating conditions after subtraction of background counting rate of 30 counts/sec. Plasma conditions: 56 kW at 18 GHz, 8 kW at 10.6 GHz; density 2×10^{12} cm^{-3}; ion temperature 115 eV.

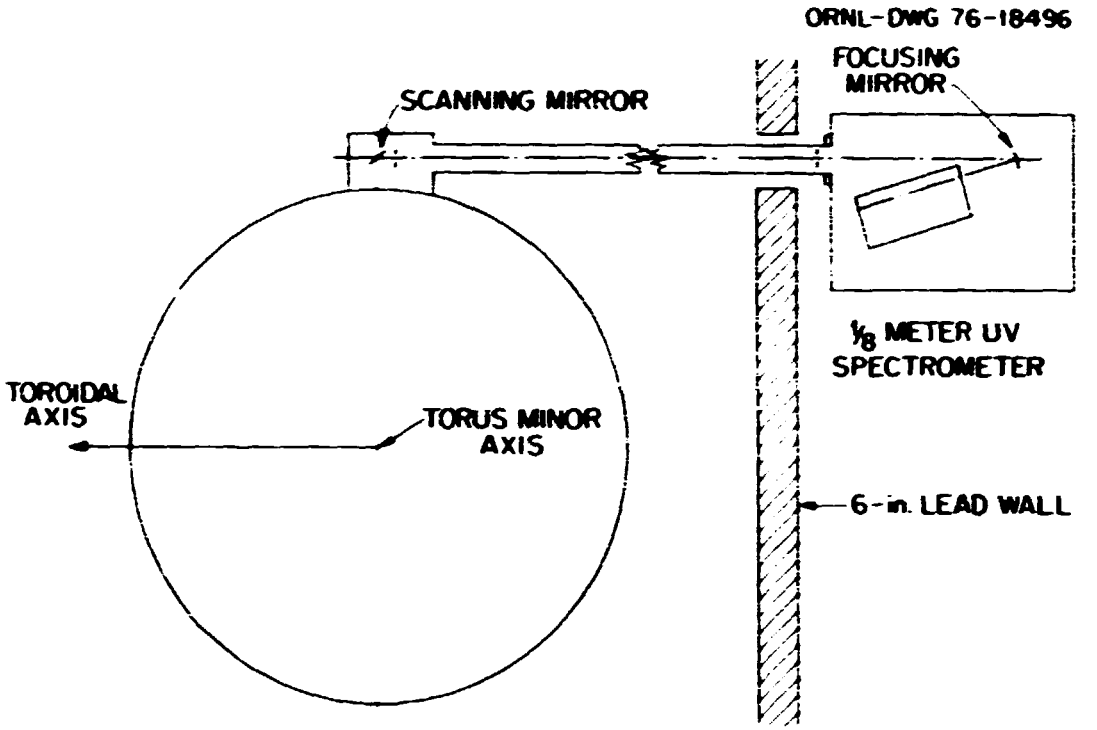

Fig. 1.3. Geometry for optical scans of EBT plasma.

spatial distribution of the product of electron and neutral hydrogen or impurity densities. If, however, a simple model is adopted in which a symmetric surface plasma surrounds but is displaced from the central toroidal core, then the light emission due to the central core can be determined by subtracting the light due to the surface plasma from the total signal. This is shown in Fig. 1.4. The light due to the central toroidal plasma may be compared with theoretical estimates as described in Sect. 3.1.1. The results appear to give good quantitative agreement even in this rough approximation.

The unknown asymmetries in the impurity distributions have prevented detailed, spatially resolved interpretations of the ionic densities, although an improved evaluation of the impurity lifetimes resulting from the ratio of carbon charge states could be obtained. These results are indicated in Table 1.1. In addition, a careful search was made for CV with

Table 1.1. Values of the product of electron density and impurity ion lifetimes at various viewing angles

Viewing angle	$N_e\tau$(CIII) (sec-cm^{-3})	$N_e\tau$(CIV) (sec-cm^{-3})	$N_e\tau$(AlIII) (sec-cm^{-3})
0°	1.4×10^8	0.64×10^8	2.2×10^8
10°	1.3	0.83	2.5
20°	1.1	0.55	0.78
30°	1.2	0.46	1.1

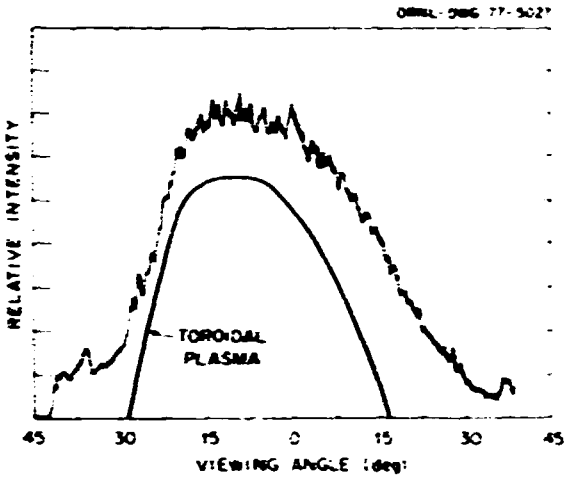

Fig. 1.4. Angular distribution of hydrogen Lyman α light. The upper curve is the experimentally measured quantity. The lower curve is the inferred contribution due to the central toroidal component.

The low energy spectrum, due to the low energy electron component, is superimposed on a high energy continuum. Separating the two spectra and calibrating the detector response at low energy are two essential tasks which allow the thermal spectrum to be determined. These tasks are accomplished by parametric variations which maximize or minimize the relative intensity of the low and high energy spectra.

EBT is operated with the high energy spectrum emphasized to calibrate the detector at low energy. Operation with the high energy spectrum minimized allows the combined spectrum to be measured. A graphical subtraction of the two gives the low energy spectrum. Figure 1.5 shows the results of this analysis. The peak in the spectrum at 1.5 keV is due to an aluminum impurity. The electron temperature shown in the

no success, with the result that upper limits on the density of CV in the toroidal core may be made. Further, the absence of CV light is consistent with the carbon ion lifetimes quoted in Table 1.1. These latter observations both point to the effectiveness of the plasma surface layer as a "built-in divertor" in the EBT geometry.

1.2.6 X-Ray Diagnostics

G. R. Haste

A new detector which has extended continuum measurements to the energy region below 1 keV has been installed. At the other end of the energy scale some calculations have been made which help in the analysis of thick target bremsstrahlung.

Soft x-ray diagnostics

A windowless Si(Li) detector has been installed on EBT. A thin aluminum foil (1000 Å) is used in front of the detector to attenuate the light from the plasma while transmitting the low energy x-rays. A vacuum path connects the detector to EBT.

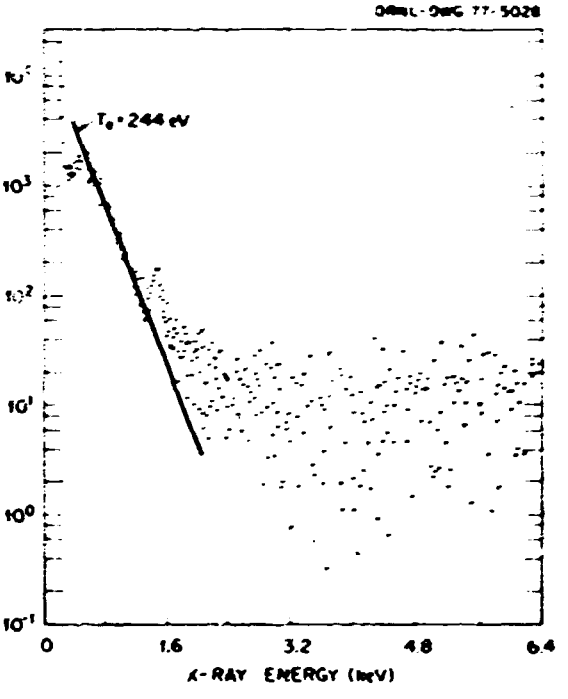

Fig. 1.5. Soft x-ray spectrum from EBT. This spectrum is the difference between the experimentally measured distribution (corrected for efficiency) and the calculated spectrum due to the high energy component. The points above 2.4 keV are due to the scatter in the data, with no net contribution. The points below 2.4 keV give the spectrum due to the toroidal electrons.

figure is 244 eV; depending on the experimental conditions this value can range from 200-300 eV.

Energetic x-ray diagnostics

As an aid in interpreting higher energy x-ray information, a computer code has been investigated to calculate the bremsstrahlung radiation due to monoenergetic electrons which strike a material surface. The calculated spectra have been compared with other spectra, both calculated and measured, with good agreement.

This code has been used to calculate the sensitivity of a probe used on EBT. This probe consists of an enclosed copper tube with an air space at the tip. Electrons striking the probe produce x-rays, and the x-rays, in turn, cause ionization in the air at the probe tip. A wire collects the ionization current. The calculated sensitivity of the probe is shown in Fig. 1.6.

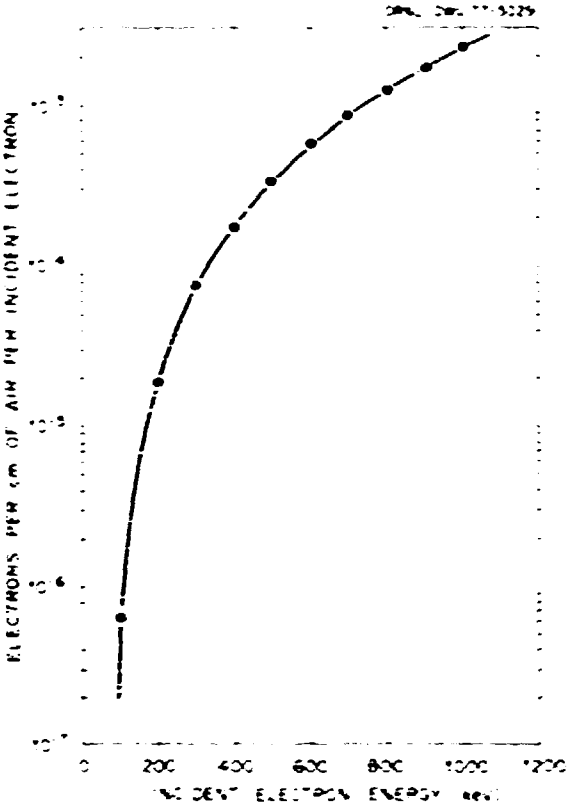

Fig. 1.6. Calculated response of ionization chamber probe. The incident electrons result in bremsstrahlung which in turn ionizes the air in the probe interior.

1.2.7 Heavy Ion Beam Probe

P. L. Colestock

In order to determine the ambipolar electric field in EBT, a heavy ion beam probing experiment has been installed. The system is designed to inject a heavy ion (singly charged) primary beam perpendicular to the magnetic field in the midplane. While traversing the plasma, a fraction of the primary ions undergoes electron impact ionization collisions given by

$$\frac{I_s}{I_p} = 2\, n_e\, \ell\, \sigma_{eff}, \qquad (1.1)$$

where I_s is the secondary ion (doubly charged) current, I_p is the primary current, n_e is the electron density, ℓ is the observed beam length, and σ_{eff} is the effective cross section for the interaction. Because such collisions involve little change in momentum, the secondary ions leave the plasma with the primary energy plus the space potential at which the interaction occurred. The space potential profile and hence the radial electric field are determined by detecting the energy difference between primaries and secondaries at a series of radial positions.

To date, the beam line (including rubidium ion gun, beam optics, and primary and secondary detection) has been installed and is operating (see Fig. 1.7). Secondary ion currents have been detected approximately consistent with values expected by Eq. (1.1). Measurements of space potential, however, have been hampered by the presence of uv and x-ray noise in the particle detectors and on the beam steering elements. Substantial reduction in the noise on the steering elements has been achieved through the use of uv shielding plates between the plasma and the beam optics. Further refinements in noise filtering have been accomplished through the use of a chopped beam with synchronous detection.

Initial measurements of the space potential within the toroidal plasma indicate a positive

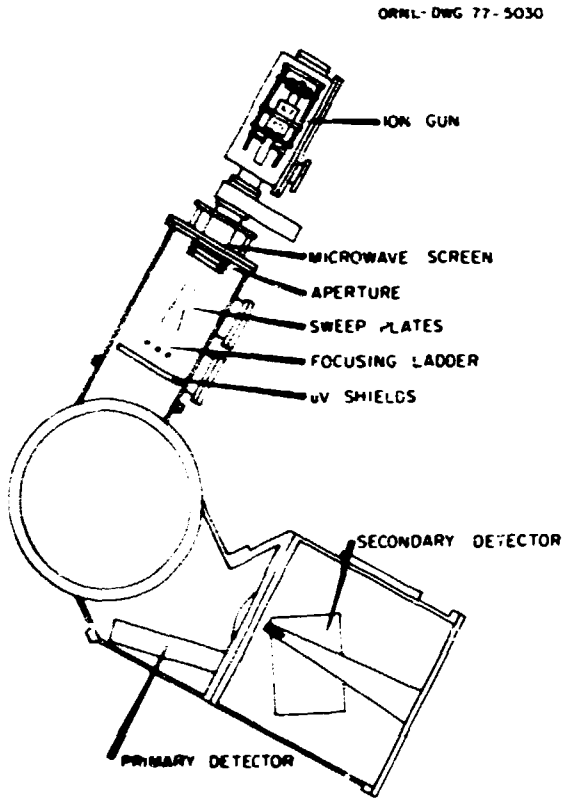

Fig. 1.7. EBT ion beam probe system.

body potential on the order of a few hundred volts. Calibration of the detection analysis is being carried out at the present time to allow radial potential profiles to be made.

1.2.8 Modeling the Electron Annulus in EBT from Diamagnetic Field and Flux Measurements

K. H. Carpenter

A simple model for the electron annulus in EBT has been developed to allow correlation between the values of diamagnetic fields and flux measured external to the plasma and the diamagnetic field within the annulus. Computer codes have been written to calculate the fields and flux values derived from the annulus model and to fit model parameters to experimental data. Preliminary experimental data have been taken, and examination of these data with the computer codes shows them to be compatible with the model – although additional data and analysis are needed to put definite values on the model parameters.

The annulus model needs to have as few parameters as possible while still retaining the essential magnetic effects due to the annulus. This restriction is necessary because the external fields do not depend strongly on the detailed structure of the model. The model chosen is that of two concentric, circular, cylindrical current sheets of radii R_1 and R_2, length L, and constant surface current densities J_1 and J_2. The surface current densities are in opposite directions, but the ratio of J_1 and J_2 is not specified. These cylinders are assumed to be centered in each EBT cavity (adjacent cavity effects are included in the calculations from the model), and limits on reasonable values of R_1, R_2, and L are determined by cavity geometry and skimmer probe sweep data. This model represents a constant density cylindrical shell of electrons with a drift velocity about the cylinder axis.

Calculation of the fields and flux at locations inside and outside the cylinders requires numerical integration over elliptic integrals. Analytic simplifications are not possible because the assumed geometry is not sufficiently short, long, thin, etc. Limiting geometrical cases have been used to check the computer codes written to do the numerical calculations on the PDP-10. The diamagnetic fields calculated for the current sheet model with a hypothetical set of parameters are shown in Fig. 1.8.

Measurements have been made of the axial components of the diamagnetic field at four points along the cavity length and at radii near the inside of the cavity outer wall. These measurements are compatible with the fields produced by the model, but taken alone, they do not provide enough information to fix the model parameters. The diamagnetic flux loops wound about the cavity provide an independent measurement, and preliminary analysis of flux data along with the axial field data

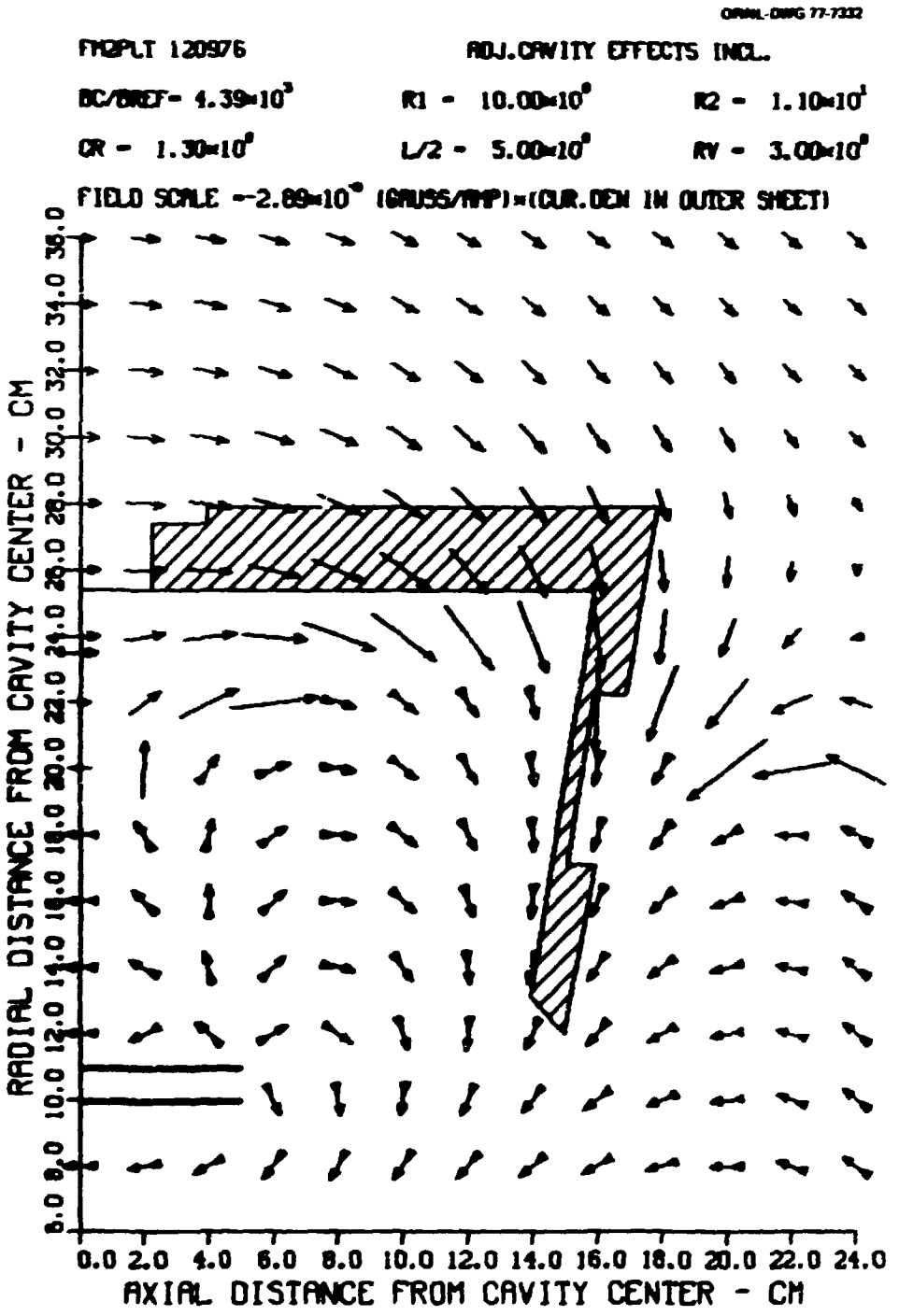

Fig. 1.8. Distribution of magnetic field due to an assumed current distribution for the hot electron annulus. The length of the single-ended arrows is proportional to the local field strength. The double-ended arrows represent field strengths greater than some reference value.

indicates that the model parameters can be fixed using diamagnetic flux loops combined with field measurements external to the plasma.

1.3 MICROWAVE TECHNOLOGY

M. C. Becker M. W. McGuffin
R. A. Dandl T. L. White
H. O. Eason R. E. Wintenberg

1.3.1 EBT Microwave Systems

Microwave power output capability of the EBT 18-GHz primary ECH system has been increased from 30 kW (cw) to 60 kW (cw) by incorporating additional klystron amplifier tubes in conjunction with appropriate modifications to the waveguide power distribution network. This increased heating capability, in addition to the existing 30-kW (cw), 10.6-GHz profile ECH system, has provided a much needed increase in the available range of EBT plasma parameter variation for diagnostic and scaling studies. Routine and reliable operation of the expanded system has been attained since completion of system modifications.

The manner in which the increased 18-GHz power capability was provided is indicated in the block diagram of Fig. 1.8. Two type VA-934 five cavity, liquid cooled klystron amplifiers, each having a power output capability of 15 kW (cw) at 18 GHz, were installed in addition to the two similar devices incorporated in the previously existing 30-kW (cw), 18-GHz source. The 60-kW source thus comprises a total of four output devices. The output of each device is fed through a ferrite circulator, connected as a load isolator, to a six-way power divider network from which six equal outputs are obtained. In this way the four klystron amplifiers provide the required 24 equal-level power inputs to the individual mirror regions of EBT. The four klystron amplifiers are driven by the output of a single reflex klystron oscillator augmented by a traveling wave tube (TWT) amplifier and divided by a passive network to provide four equal-level drive signals. A single master level control attenuator serves to control the output power of all klystron amplifiers simultaneously by adjustment of their drive power levels. A balance control attenuator at the input of each klystron amplifier compensates both for differences in power gain between tubes and for differences in attenuation due to unequal lengths of the input waveguides. The possibilities are readily apparent for further system expansion, if required, and for the similar attainment of much larger ECH systems at other frequencies.

1.3.2 Advanced Microwave Development

Multimegawatt continuous wave ECH systems operating at 120 GHz are required by the EBT Program.[3,4] Because this power generation capability is clearly beyond the present state of the art for microwave active devices (tubes), a program has been undertaken through subcontract with Varian Associates for development of the required devices. A simultaneous complementary program is under way at ORNL for development of complete ECH systems utilizing these devices. Such systems include microwave transmission and plasma coupling networks, power supplies, controls, monitors, and supporting equipment.

The Cyclotron Resonance Maser (CRM) has been identified as the approach holding the greatest promise for generation of 200 kW (cw) at 120 GHz from a single device. Multiple devices will be used to achieve megawatt systems. Encouragement for this device approach is provided by reported Soviet success in using the gyrotron, an oscillator form of CRM, for millimeter wave power generation. The Varian subcontract addresses development of the gyroklystron, an amplifier form of CRM, preferred because of simplified power output control in large systems. Initial gyroklystron development is being undertaken on a 200-kW (cw), 28-GHz device which

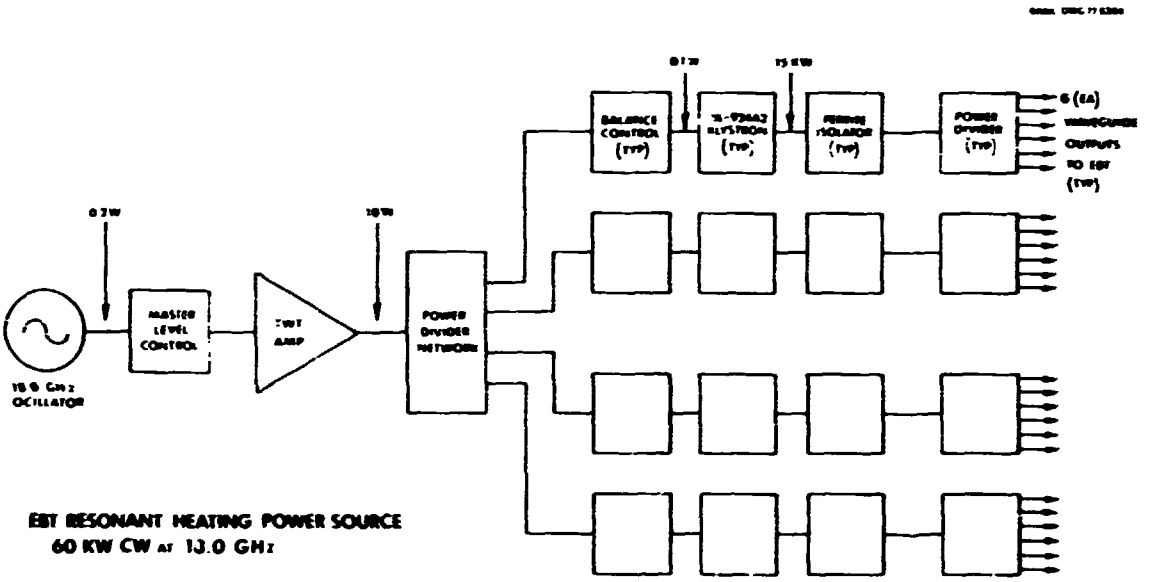

Fig. 1.9. Expanded EBT resonant heating power source, 60 kW (CW) at 18.0 GHz.

is a low frequency scale prototype for later 200-kW (CW), 120-GHz devices. Delivery of the first 28-GHz gyroklystron is scheduled for the summer of 1977.

Systems development has been initiated for employment of the 28-GHz gyroklystron in a plasma ECH system when it is received. This system will serve primary ECH requirements of the EBT-S facility (a modification of the present facility). Existing 60-kW, 18-GHz and 30-kW, 10.6-GHz systems will be retained in present form to provide profile ECH for EBT-S. The 28-GHz system includes a power supply subsystem consisting of a 100-kV, 10 A, dc beam supply with crowbar, electron gun supply with crowbar, and heater supply. Procurement of this subsystem has been initiated. The 28-GHz, oversized waveguide circuitry employing low loss, circular electric transmission modes is under development in the Fusion Energy Division, together with microwave structures for power division and plasma coupling. Equipment for control, monitoring, and other functions is also being developed with the overall objective of timely operation of the EBT-S 200-kW (CW), 28-GHz primary ECH system.

---

1. Work in progress; M. Fujiwara (Nagoya University, Nagoya, Japan), private communication, 1976.
2. D. H. McNeill, Bull. Am. Phys. Soc. 21, 1117 (1976).
3. R. A. Dandl et al., *The ELMO Bumpy Torus Program*, ORNL/TM-5451, Oak Ridge National Laboratory, Oak Ridge, Tennessee (April 1976).
4. R. A. Dandl et al., *Research Program for Plasma Confinement and Heating in ELMO Bumpy Torus Devices*, ORNL/TM-4941, Oak Ridge National Laboratory, Oak Ridge, Tennessee (June 1975).

BLANK PAGE

2. TOKAMAK EXPERIMENTAL SECTION

L. A. Berry, Section Head
J. L. Dunlap, Assistant Section Head

E. T. Arakawa[1]
C. F. Barnett[2]
D. D. Bates[3]
J. E. Bayfield[4]
M. A. Betz[5]
R. D. Birkhoff[1]
D. A. Brisson[6]
R. D. Burris[5]
C. E. Bush
J. D. Callen[7]
K. H. Carpenter[5]
B. A. Clark[5]
D. N. Clark[5]
R. E. Clausing[8]
R. J. Colchin
A. Cooper[9]
D. H. Crandall[2]
S. M. DeCamp
N. W. Durfee[10]
G. R. Dyer
P. H. Edmonds
O. C. Eldridge[11]
L. C. Emerson[8]
A. C. England
C. A. Foster[12]
R. H. Fowler[5]
J. E. Francis[7]
L. D. Gardner[4]
R. N. Hamm[1]
C. E. Hammons[7]
J. H. Harris[13]
L. Heatherly[8]
K. W. Hill
H. C. Howe
D. P. Hutchinson[2]
R. C. Isler
G. L. Jahns
T. C. Jernigan
C. O. Kemper[5]
M. E. Ketterer
H. J. Kim[2]
K. Kim[14]
P. W. King
H. E. Knoepfel[15]
D. C. Lousteau[16]
J. F. Lyon
F. B. Marcus[7]
L. A. Massengill
O. D. Matlock[16]
H. C. McCurdy
R. W. McGaffey[5]
R. H. McKnight[17]
D. H. McNeill
V. J. Meece
F. W. Meyer[2]
J. T. Mihalczo[3]
S. L. Milora[12]
E. C. Moore
T. J. Morgan[18]
M. Murakami
W. Namkung[19]
A. Navarro[20]
R. V. Neidigh
G. H. Neilson
D. R. Overbey[7]
V. K. Paré[3]
J. W. Pearce
R. A. Phaneuf[2]
J. A. Ray[2]
T. F. Rayburn
W. J. Redmond
M. J. Saltmarsh[2]
H. C. Sanderson
D. E. Schechter[12]
D. L. Shaeffer[21]
D. J. Sigmar[7]
J. E. Simpkins
D. L. Slagle
T. E. Smith[10]
J. C. Sprott[13]
P. A. Staats[2]
W. L. Stirling[12]
D. W. Swain
B. F. Thomas
D. M. Thomas[22]
D. M. Toodle[23]
R. J. Turnbull[14]
J. C. Twichell[24]
K. L. Vander Sluis[2]
B. V. Waddell[7]
C. C. Weaver
J. B. Wilgen
M. I. Wilker[2]
M. W. Williams[1]
W. R. Wing
J. W. Wooten[5]
O. C. Yonts[7]
S. J. Zweben[25]

---

1. Health Physics Division.
2. Physics Division.
3. Instrumentation and Controls Division.
4. Participant from University of Pittsburgh, Pittsburgh, Pennsylvania.
5. Computer Sciences Division.
6. Graduate Student, North Carolina State University, Raleigh, North Carolina.
7. Plasma Theory Section, Fusion Energy Division.
8. Metals and Ceramics Division.
9. University of Michigan, Ann Arbor, Michigan.
10. UCC-ND Engineering.
11. Consultant, University of Tennessee, Knoxville, Tennessee.
12. Plasma Heating and Fueling Section, Fusion Energy Division.
13. Present address: University of Wisconsin, Madison, Wisconsin.
14. University of Illinois, Urbana, Illinois.
15. Consultant, Laboratorio Gas Ionizzati, Frascati, Italy.
16. Engineering Services, Fusion Energy Division.
17. Summer employee, University of Virginia, Charlottesville, Virginia.
18. Consultant, Wesleyan University, Middletown, Connecticut.
19. Guest Assignee, University of Tennessee, Knoxville, Tennessee.

20. Visitor, Spanish Nuclear Energy Commission.
21. Environmental Sciences Division.
22. Summer Student, Emory University, Atlanta, Georgia.
23. Summer Student, University of Alabama, Birmingham, Alabama.
24. Consultant, University of Wisconsin, Madison, Wisconsin.
25. Oak Ridge Associated Universities (Cornell University).

2.1 STUDIES OF ORMAK-PRODUCED PLASMAS

D. D. Bates	R. C. Isler	V. K. Paré
L. A. Berry	G. L. Jahns	T. F. Rayburn
R. D. Burris	H. E. Ketterer	W. J. Redmond
C. E. Bush	P. W. King	H. C. Sanderson
J. D. Callen	J. F. Lyon	D. E. Schechter
S. M. DeCamp	R. W. McGaffey	D. L. Shaeffer
J. L. Dunlap	D. H. McNeill	D. J. Sigmar
G. R. Dyer	V. J. Meece	W. L. Stirling
P. H. Edmonds	J. T. Mihalczo	B. V. Waddell
A. C. England	M. Murakami	J. B. Wilgen
J. H. Harris	R. V. Neidigh	W. R. Wing
H. C. Howe	G. H. Neilson	

2.1.1 Introduction

During the past year, significant advances have been made in our study of plasmas produced by the Oak Ridge Tokamak (ORMAK) in three general areas: (1) extension of the basic plasma parameters ($\bar{n}_e$, T_i, β_T) through increased injection power and gas puffing, (2) increased understanding of the interaction of neutral beams with tokamak plasmas and the role of impurities, and (3) refinement of the basic diagnostic measurement and data analysis techniques.

The most significant progress this year has been in the application of neutral beam heating to tokamak plasmas, including ion heating to 1.8 keV, doubling of the electron temperature by neutral beam heating, achievement of total (plasma + beam) peak $\beta_T \sim 3\%$, grossly stable operation with $P_{inj} \sim 3 \times P_{OH}$, increase of maximum plasma density with gas puffing to $\bar{n}_e = 6 \times 10^{13}$ cm^{-3} [$n_e(0) = 9 \times 10^{13}$ cm^{-3}], and the observation that unidirectional injection does not lead to large toroidal rotation velocities. Some of these points are discussed in the following sections.

Extension of operating range

The useful operating range for plasma studies in ORMAK has been extended during this report period by injection of up to ~500 kW of neutral beam power, toroidal field operation up to 30 kG, plasma currents up to 230 kA, reduction of Z_{eff} to as low as 2, and reduction of the limiter safety factor to as low as 2.5. These parameter improvements underlie the physics studies discussed in the following sections. The experimental emphasis has been on hydrogen plasmas with high power H^0 injection and gas puffing conditioned by overnight discharge cleaning in oxygen (followed by an hour of hydrogen discharge cleaning). However, some of the most interesting results to be discussed (electron heating, high β_T, and low limiter q) were obtained using only hydrogen discharge cleaning.

General studies related to injection, gas puffing, and impurity behavior

Two general areas are discussed: extension of the plasma parameters with injection and gas puffing, and the role of impurities in these plasmas. Section 2.1.2 discusses the scaling of ion temperature with injection power and with plasma density and the effect of injection on the plasma power flows. A complementary discussion is given in Sect. 2.1.3 of experiments in which the injection power exceeds the ohmic heating (OH) power, resulting in significant electron heating. Section 2.1.4 describes attainment of high total (plasma + beam) toroidal beta [$\beta_T(0) \sim 3\%$] at low limiter safety factor ($q = 2.6$) obtained with injection for grossly stable plasma conditions. The dynamics of the plasma behavior when the density is increased with gas puffing is given in Sect. 2.1.5.

The advances made in determining the concentration of impurities in ORMAK and their role in the radiative power loss are discussed in Sect.

2.1.8. Section 2.1.16 discusses the total (radiation + charge exchange) wall power flux for gas puffing and electron heating experiments and the scaling of this power with total input power up to 1 MW. The effects of equal amounts of coinjection and counterinjection power on the plasma behavior including impurities are discussed in Sect. 2.1.7. Spectroscopic evidence for charge exchange of injected neutrals on oxygen ions and the effect of this impurity charge exchange on the injected power disposition is given in Sect. 2.1.6. Section 2.1.14 discusses other injection effects on the plasma equilibrium and the lack of a large beam-induced toroidal rotation.

Improvements in diagnostic measurements and data analysis

Other advances are generally related to plasma modeling and interpretation of specific diagnostic measurements. Section 2.1.12 describes improvements made in a time-independent data analysis code with impurity modeling and in a time-dependent one-dimensional transport code. Transport modeling of the gas puff experiments and the role of an inward transport mechanism are discussed in Sect. 2.1.15. Section 2.1.10 discusses the internal magnetohydrodynamic (MHD) mode structure obtained from correlation studies with magnetic probes and collimated soft x-ray detectors and the improvements made in both the data acquisition and analysis systems. The mechanism of the soft x-ray sawtooth oscillation is discussed in Sect. 2.1.11 with reference to a tearing mode instability model, along with the diffusive nature of the associated propagating heat pulse. Section 2.1.9 describes how the spectral line profile of the Balmer α line can be used to infer a toroidal ion rotation velocity. Section 2.1.13 describes a procedure which closely models the measured charge-exchange flux in ORMAK, along with a comparison of the ion temperature profiles obtained with neutron measurements and the H_α spectral line profiles. Finally, Sect. 2.1.17 discusses the neutron time behavior due to D^0 beam injection into a hydrogen plasma and compares it with Fokker-Planck calculations of the fast ion distribution.

2.1.2 Ion Heating Studies

P. H. Edmonds J. T. Mihalczo D. E. Schechter
R. C. Isler M. Murakami M. L. Stirling
J. F. Lyon G. H. Neilson J. B. Wilgen

The previous annual report discussed some preliminary experiments with high power, neutral beam injection (up to 366 kW) at high plasma currents (~175 kA). These experiments have been extended and the data analysis refined to give a clearer picture of ion heating and ion confinement in ORMAK. The themes of these studies are (1) the scaling of ion temperature with injection power and plasma density, (2) comparison with neoclassical calculations, and (3) the effect of injection on the plasma power flows.

For these studies the plasma current (I_p = 170 kA) and toroidal field (B_T = 25 kG) were held constant, giving a limiter safety factor $q \approx 5$. The start of the injected beam pulse was typically delayed for 15 msec until the discharge current reached the constant current phase. About 30 msec after beam turnon, the plasma parameters reached a quasi-steady state, and so the measurements reported were taken about 45 msec into the discharge. In these studies the injection dominates the ion power flow ($P_{inj,i} > P_{e,i}$), although the total injection power was less than the ohmic power input ($P_{inj} \sim 0.6\ P_{OH}$). In this regime the ion temperature is higher than the electron temperature, and the power flow between electrons and ions ($P_{e,i}$) is reversed from that for ohmic heating alone. In addition, injection has made it possible to attain higher plasma densities before disruption occurs, as discussed in Sect. 2.1.5. These observations underline the usefulness of injection in attaining plasma physics regimes not accessible by ohmic heating alone.

Scaling of ion temperature with injection power

Figure 2.1 shows the scaling of ion temperature with injection power for approximately constant density, current, and toroidal field. The measured central ion temperatures increase approximately linearly with injection power (≈3.5 eV/kW) and are in reasonable agreement with those calculated from a one-dimensional transport code using neoclassical ion thermal conductivity[1,2] and classical beam-ion energy transfer.[3] For the highest T_i point in Fig. 2.1, $\nu_i^* \approx 0.5$. Experimental profiles for $n_e(r)$ and $T_e(r)$ were used in calculating the theoretical $T_i(0)$ values shown in Fig. 2.1. Uncertainties in these profiles and in the values for n_+/n_e and $P_{inj,i}$ calculated from them produce uncertainties that are not indicated in the calculated $T_i(0)$ values.

The effect of the injection power on the ion and electron temperatures and on the plasma power flows can be illustrated by comparing the two extreme cases in Fig. 2.1. Figure 2.2 shows the no injection case and Fig. 2.3 the 360-kW H^0 injection case. The injected power transferred to the ions is 2.5 times the collisional heating by electrons without injection. The central and density-averaged ion temperatures essentially triple, indicating approximately constant ion energy confinement time. Because the electron temperature does not increase, $T_i > T_e$ over most of the plasma radius. One-third of the injected power transferred to the ions is lost to the electrons by collisional cooling. Thus, the role

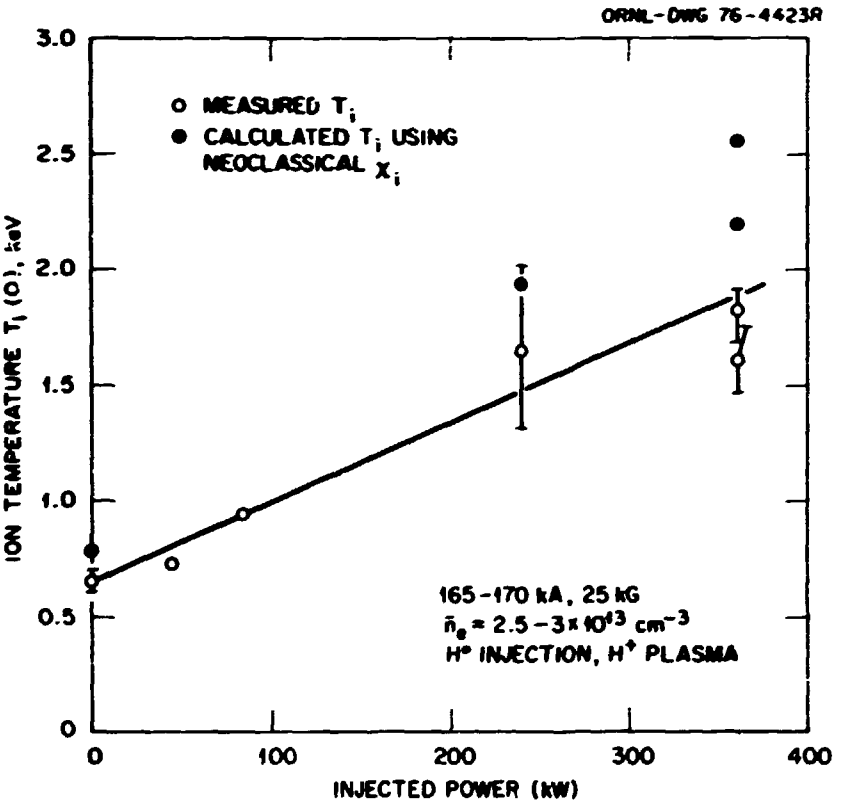

Fig. 2.1. Scaling of central ion temperature with injection power for fixed plasma density ($\bar{n}_e \sim 2.8 \times 10^{13}$ cm^{-3}) and comparison with neoclassical calculations.

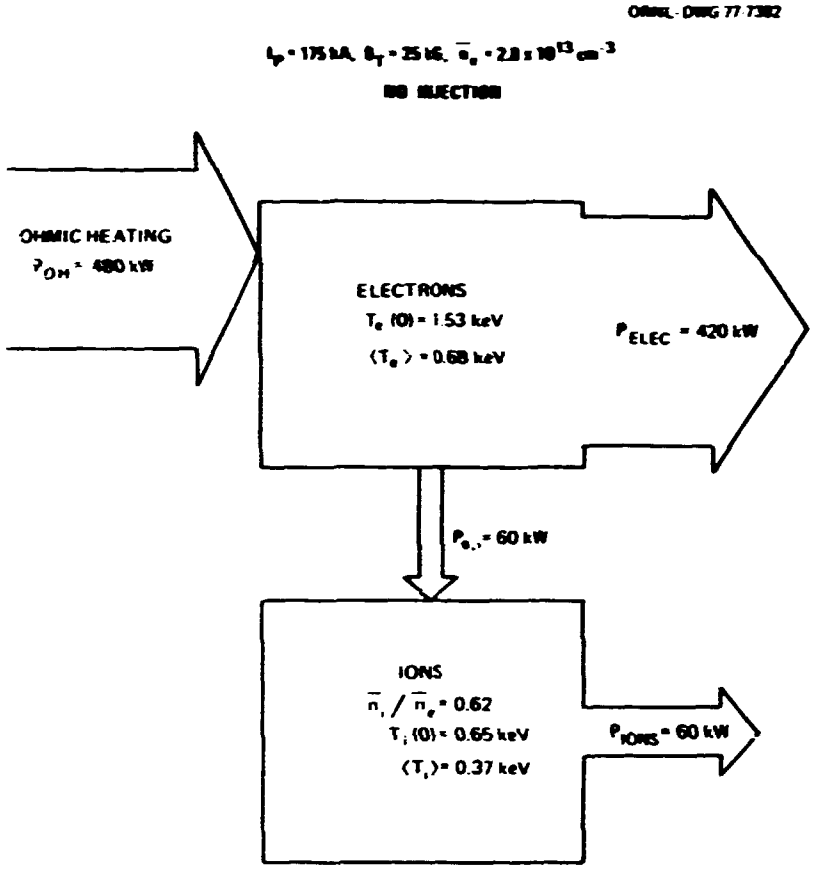

Fig. 2.2. Power flow diagram for ohmic heating and for the ion and electron plasma components for a base case with no injection (I = 175 kA, B_T = 25 kG, and $\bar{n}_e = 2.8 \times 10^{13}$ cm^{-3}).

of electrons is reversed, and the electrons become a major power loss for the ions and limit the ion temperature obtained with injection heating.

The density-averaged electron temperature $\langle T_e \rangle$ remains unchanged although the total electron input power has increased by 75%. This implies a reduced overall electron energy confinement time. In addition, for the central half of the plasma the total electron input power has also increased (by 40%), but the central electron temperature has fallen by a factor of two and $T_e(r)$ shows a tendency towards a hollow profile. The hollow electron temperature profile is apparently associated with impurity influx due to the counterinjected beam component, as discussed in Sect. 2.1.7.

Ion temperature scaling with density

Figure 2.4 shows the scaling of central ion temperature with line-averaged electron density as injection power and other plasma parameters are held approximately constant. The error bars on the ion temperature are larger than those in Fig. 2.1 because the charge-exchange data cover a smaller range of energies. The decrease in ion temperature with increasing density is primarily due to the rough constancy of the ion energy confinement time and hence the same input power being shared among an increasing number

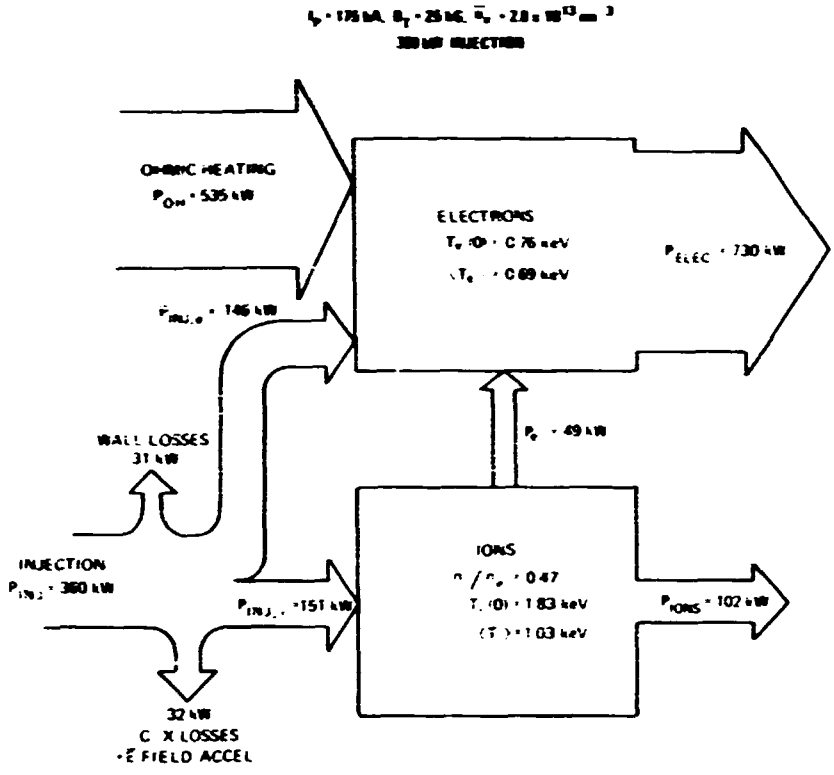

Fig. 2.3. Power flow diagram for ohmic heating, neutral beams, and the ion and electron plasma components with 360 kW of injection added to the base case.

of ions. Again, reasonable agreement is obtained between measured values for $T_i(0)$ and those calculated from the one-dimensional transport code assuming neoclassical ion thermal conductivity. However, the evaluation of the theoretical value for $T_i(0)$ may be less certain than that in Fig. 2.1 because of the greater uncertainty in the n_+/n_e values and in the beam deposition profiles for the higher density, high Z_{eff} cases.

Figure 2.5 shows the plasma power flows for the highest density case shown in Fig. 2.4, $\bar{n}_e = 5.9 \times 10^{13}$ cm^{-3}, obtained with gas puffing and equal amounts of coinjection and counterinjection power. Injection power is necessary in addition to gas puffing to reach densities of $\bar{n}_e > 4.5 \times 10^{13}$ cm^{-3}. The ion and electron temperatures are approximately the same ($\sim$1.3 keV), and $\tau_E = 15$ msec, $\beta_p = 0.93$, $\beta_T(0) = 1.2\%$, and $n_e(0)\,\tau_E = 1.3 \times 10^{12}$ cm^{-3} sec. Compared with the no injection base case at $\bar{n}_e = 2.8 \times 10^{13}$ cm^{-3} shown in Fig. 2.2, the total plasma energy content and β_p have increased by a factor of three. In addition, a larger fraction of the beam energy goes to the ions than in Fig. 2.3 because of the higher electron temperature.

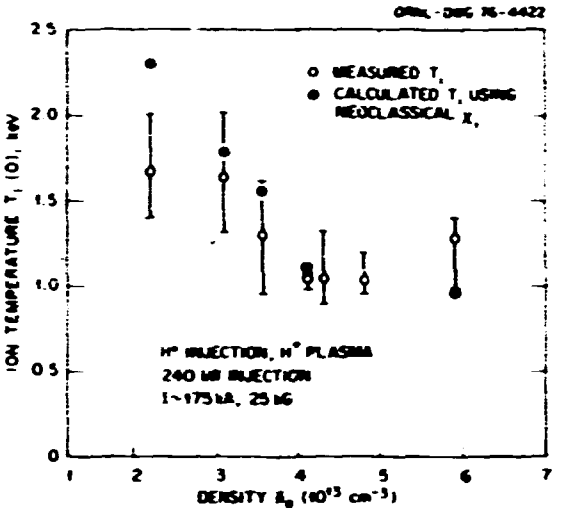

Fig. 2.4. Scaling of central temperature with plasma density for fixed injection power (P_{inj} ≈ 240 kW) and comparison with neoclassical calculations.

2.1.3 Electron Heating Experiments

L. A. Berry, C. E. Bush, J. L. Dunlap, G. R. Dyer, P. H. Edmonds, H. C. Howe, R. C. Isler, S. L. Jahns, H. E. Ketterer, P. W. King, J. F. Lyon, D. H. McNeill, J. T. Mihalczo, M. Murakami, A. Navarro, R. V. Neidigh, G. H. Neilson, V. K. Paré, J. B. Wilgen

Large increases in the temperature of ions have been observed during injection of high energy neutral beams into tokamaks, but little, if any, heating of electrons has been detected. A factor which contributes to the inability to measure definite increases in electron temperature is the conditions under which experiments have been performed. In all cases, the ohmic heating power has been considerably larger than the power which could be delivered to the electrons by the neutral beam sources that are presently available; as a consequence, the expected changes of temperature have been within the experimental uncertainties of the absolute measurements.

In a recent experiment we attempted to obtain definitive results concerning the heating of electrons through the use of neutral beams by operating at low plasma currents, so that the ohmic heating power is comparable to or less than the power provided to the electrons by injection (~180 kW). The outcome of this successful experiment revealed a significant rise in the temperature of the electrons, which increases as the injected power increases. In this section we discuss these results, including evaluations of the major mechanisms for energy losses, radiation by impurities, and anomalous heat conduction.

Figure 2.6(a) illustrates the typical operating conditions employed in the electron heating studies. The discharge is sustained for 130 msec at a current of 70 kA [q(a) = 7] during the steady-state portion of the pulse. At 20 msec after breakdown, a puff of hydrogen is put into the machine in order to keep the concentration of protons large enough to trap most of the energetic hydrogen atoms which are subsequently injected into the plasma. Injection begins at 40 msec. The beams begin to turn off at 75 msec, and the neutral particle current is effectively zero by 80 msec. Plots of the power input as a function of time are shown in Fig. 2.6(b) for cases where two injectors are employed. These sources supply a total power of 340 kW, and the beam current is in the same direction as the ohmic heating current. Calculations indicate that this power should be divided between electrons and ions in the amounts illustrated by the curves labeled $P_{inj,e}$ and $P_{inj,i}$ respectively. The rise of the electron temperature during injection is reflected in the decrease of the loop voltage.

Figure 2.7 illustrates the evolution of the electron temperature, $T_e(r)$, and density, $n_e(r)$, as functions of the minor radius of the machine. These measurements are performed by analyzing the Thomson scattering of ruby laser light. The standard deviation of $T_e(r)$ is 10-15%. Prior to initiation of the neutral

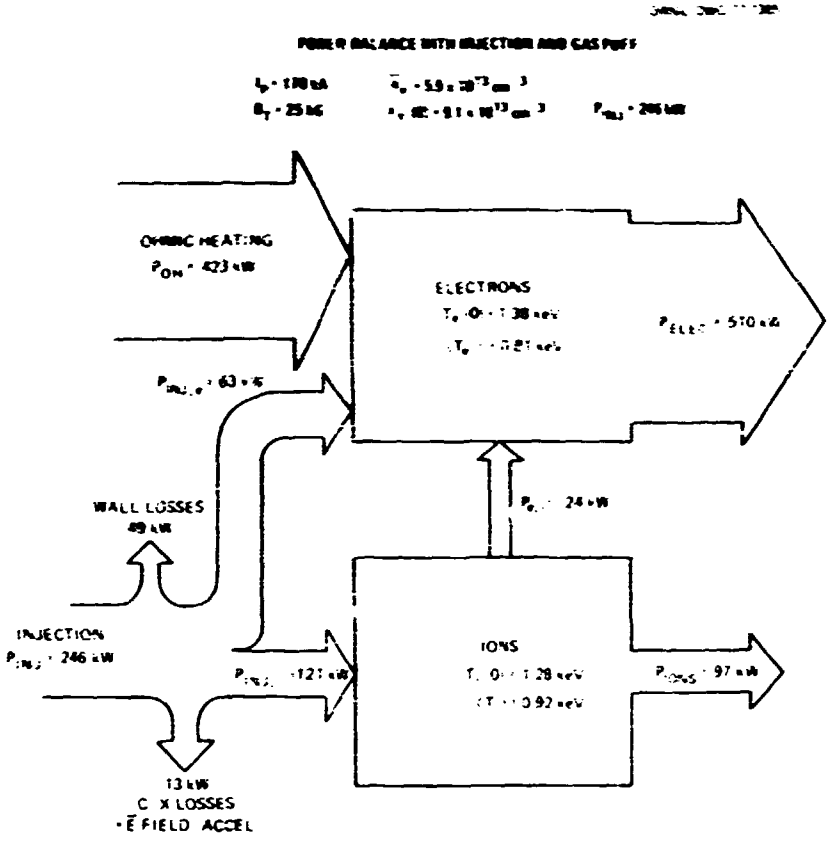

Fig. 2.5. Power flow diagram for ohmic heating, neutral beams, and the ion and electron plasma components for the highest density case ($\bar{n}_e = 5.9 \times 10^{13}$ cm^{-3}).

beam pulse, a slightly hollow profile of $T_e(r)$ is observed. Similar profiles would probably be observed over most of the discharge in the absence of injection. During injection the electron temperature and density appear to rise throughout the plasma. Also evident is a significant outward shift of the peaks of the profiles, despite the use of feedback control of the center of the plasma column (i.e., the last magnetic flux surface). After the beam is turned off, the temperature off axis decreases faster than the central temperature.

Various functions of temperature and density are plotted in Fig. 2.8. Figure 2.8(a) shows the evolution of the peak electron temperature, $(T_e)_{max}$, the density-averaged electron temperature, $\langle T_e \rangle$, and the kinetic energy of the electrons in the plasma, W_e. The open circles indicate $(T_e)_{max}$ derived from Thomson scattering, while the squares are from soft x-ray energy spectra [using an Si(Li) detector] averaged over each 10-msec interval. The discrepancies seen in the early time of the discharge are primarily due to poor statistics of the soft x-ray signals. An important feature of $(T_e)_{max}$ is the slow decay observed after the beam is turned off. In fact, the continuous soft x ray intensity measurements from planar silicon PIN diodes exhibit a pronounced increase of signal [Fig. 2.9(a)] near the center of the plasma until about 10 msec

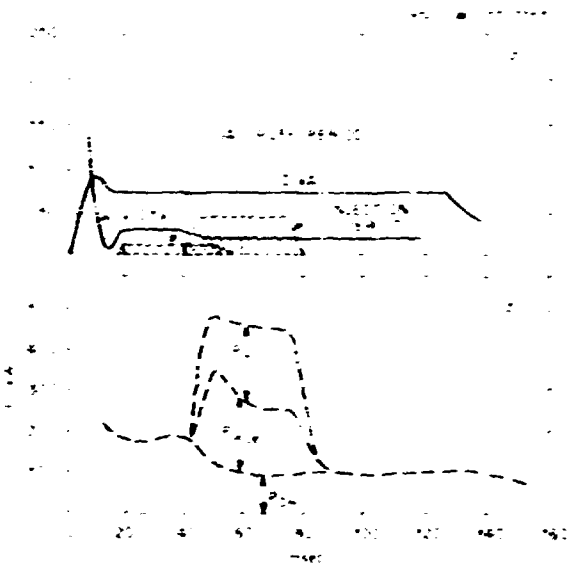

Fig. 2.6. Evolution of discharge parameters of the electron heating experiment with 340 kW of coinjection power: (a) toroidal current I, loop voltage V, and duration of the gas puff and injection periods; (b) ohmic heating power P_{OH}, neutral beam power transferred to electrons $P_{inj,e}$, and neutral beam power transferred to the ions $P_{inj,i}$.

after the beam is switched off. The maximum of this signal corresponds to a rise of 200 eV in T_e. Although $\langle T_e \rangle$ increases rather slowly during the neutral beam pulse, the growth of the electron energy content saturates after about 10 msec, a period which is consistent with expectations from the characteristic times involved (i.e. beam-plasma energy transfer time plus energy confinement time). However, the energy decay is much slower than expected from those times.

Previous failures to observe significant heating of electrons by neutral beam injection have often been blamed on concurrent influxes of impurities and enhanced radiative losses. It is known that emissions from ORMAK are dominated by lines of oxygen and by narrow band continua in the region from about 20-100 Å, and, as illustrated in Fig. 2.9, several of these features have been examined during the present experiments. The lower stages of oxygen such as O V and O VI [Fig. 2.9(b)] attain peak concentrations within 4 msec of breakdown, and the intensities of the lines are decreasing up until the gas puff is initiated at 20 msec. Thereafter, the intensity tends to follow the same pattern as does the average electron concentration, $\bar{n}_e$ [Fig. 2.8(b)]. The effects of the onset of injection are not obvious in lines from the low stages of ionization, and the intensity begins to decrease when the gas puff is terminated. The rate of excitation of the O VI line at 1032 Å should be relatively independent of temperature and should only reflect variations in the product of the concentrations of electrons and oxygen ions. Thus the injection does not appear to significantly increase the total number of oxygen ions in the outer 2-3 cm of the plasma.

The behavior of the O VII and O VIII lines, which originate inside a radius of 15 cm, differs markedly from the behavior of the lower stages. Figures 2.9(c) and 2.9(d) show the evolution of the first resonance lines of O VII and O VIII; Fig. 2.9(e) depicts the nearby continuum. These lines begin to appear above the background about 6 msec after breakdown, but the introduction of the gas puff quenches the signal, presumably by cooling the plasma. It is believed that most of the oxygen in the core of the plasma resides in the O VII and O VIII stages just before injection begins. When injection is initiated, the intensities of lines from these species increase as the temperature rises. However, the characteristic time for the ionization of O VII in particular is short enough that lines of this species should burn through if the concentrations remained constant; the observed increase throughout the period of injection appears indicative of an increasing concentration of oxygen in the center of the plasma. This contention is supported by the rapid decrease of intensity in a period of 10-15 msec after injection while the plasma settles to a new equilibrium; calculations of the intensity of the O VIII line from known rate coefficients and measured profiles of $T_e(r)$ and $n_e(r)$ indicate that the emission should increase slightly between 60 and 115 msec if the

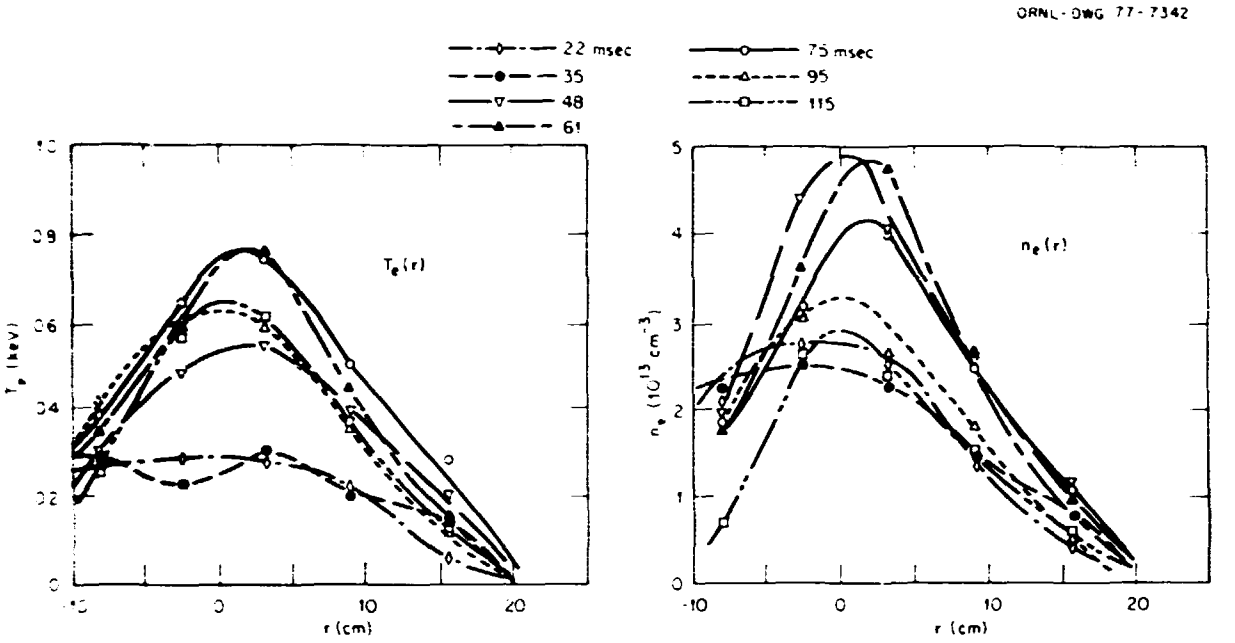

Fig. 2... Evolution of electron temperature and density profiles as measured from the Thomson scattering in the electron heating experiment. Times during the injection pulse are t = 48, 61, and 75 msec.

concentration of oxygen remains constant. The observed decrease of intensity in the O VIII line implies a drop of a factor of three to four in the concentration of this species. However, we find that the O VII and O VIII lines do not contribute more than 8 kW of radiated power, so that electron heating in the core of the plasma should not be seriously affected by the variations of the concentrations of oxygen.

Integration over the low wavelength region of the spectrum indicates that most of the radiated power appears in the narrow band continua. The strong correlation of signals from the region of 20-100 A with the temporal behavior of signals from the pyroelectric radiometer [Fig. 2.9(f)] confirms this result, and within the experimental uncertainty of a factor of two, the absolute intensity of radiated power from spectroscopic measurements agrees with the radiometer measurement of 110 kW. The radiometer signal, of course, includes a small contribution from the neutral particles which strike its surface.

There is a growing body of both experimental[4] and theoretical[5] evidence indicating that these features which appear as narrow band continua are actually groups of closely spaced lines of tungsten which result from $\Delta n = 0$ and $\Delta n = 1$ excitations of the N-shell electrons. The radiation from these features increases by a factor of one and one-half to two during injection, and then falls off rapidly when the injection stops. Theoretical calculations imply that this sudden drop cannot be caused solely by the modest decrease in temperature after injection, but that similar to oxygen, tungsten diffuses out of the machine rapidly after injection is terminated. A rapid efflux of impurities at this time is consistent with the maintenance of an elevated temperature once the beams are shut off; in view of the fact that radiated power comprises such a large fraction of the losses,

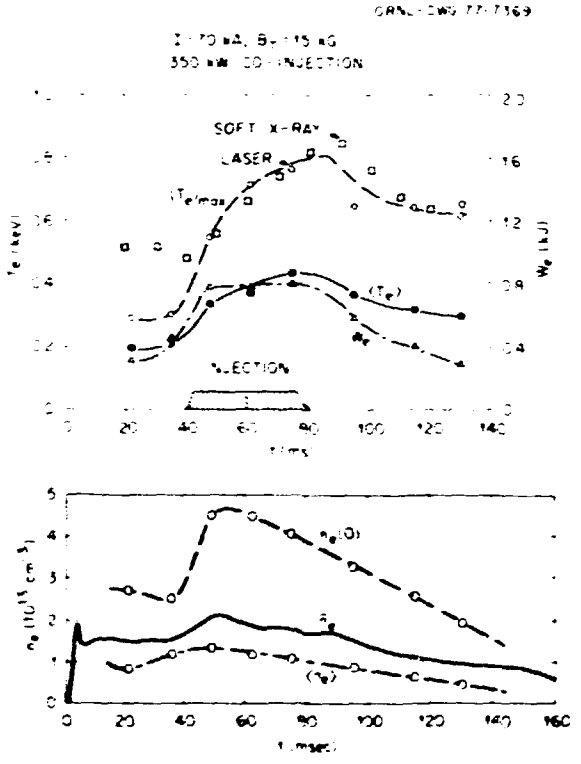

Fig. 2.8. Temperatures and densities measured as a function of time during electron heating experiments. (a) Peak temperature, $(T_e)_{max}$; density-weighted temperature $\langle T_e \rangle$; energy content of electron, W_e. The maximum temperatures were measured from the soft x-ray spectra (□) as well as from the laser Thomson scattering (o). (b) Central electron density, $n_e(0)$; line-averaged density, $\bar{n}_e$; volume-averaged density, $\langle n_e \rangle$.

this could explain why the PIN diodes seem to show that there is an upward excursion of the temperature in the center of the plasma before a new equilibrium is established.

Although the spectroscopic results indicate that the concentrations of impurities and the radiation increase during injection, the beam power is sufficient to overwhelm the loss mechanisms so that the electrons can be significantly heated.

The quantity Z_{eff} is often used as an indicator of the concentration of impurities,

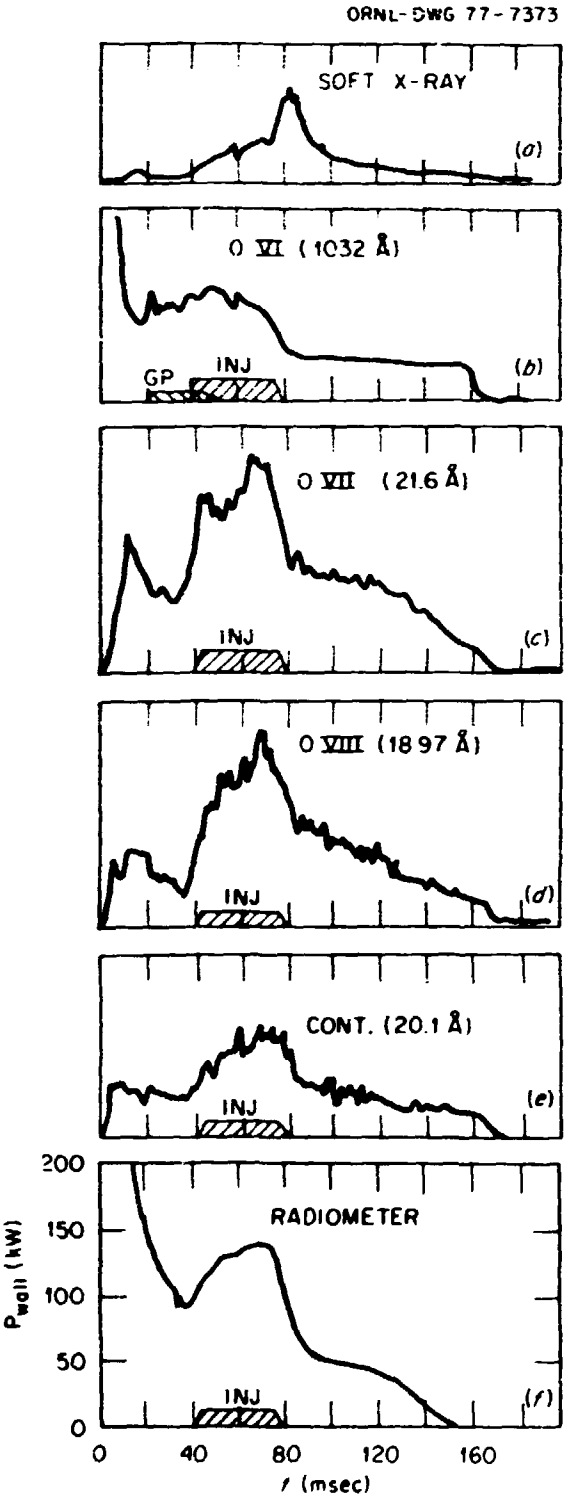

Fig. 2.9. Temporal dependence of: (a) a PIN diode signal from the central chord; (b)-(e) the intensities of oxygen lines and continuum; and (f) the pyroelectric radiometer signal.

and it is useful to examine its behavior as calculated from the resistance of the plasma (including neoclassical correction) under the assumption that the electric field is independent of radius. The experimental points are shown in Fig. 2.10. This calculation neglects effects of injection-induced current whose theoretical prediction amounts to ~20% of the total toroidal current with a significant peaking near the center over the average value. This nonresistive current raised $\bar{Z}_{eff}$ by ~20% and $Z_{eff}(0)$ to 5 under the assumption of $q(0) = 1$. Estimates of $Z_{eff}(0)$ from the absolute intensity of the soft x-ray PIN diode signals and from ultraviolet spectroscopy are consistent with a value of 5 during injection. It should be pointed out that most of the contribution to Z_{eff} is due to oxygen, which exists in concentrations of $1\text{-}4 \times 10^{12}/cm^3$, but that most of the radiated power is due to tungsten, which is present in much smaller amounts. An average concentration of tungsten of 2×10^{10} cm^3 with $\bar{n}_e = 2 \times 10^{13}/cm^3$ may indicate 110 kW at a temperature of 300 eV while contributing only 0.9 to Z_{eff}.[6]

Another concern which arises when studying energy losses during injection is that the heat conduction of electrons may be enhanced. In particular, when the stored fast ion energy becomes nearly equal to the bulk plasma energy (as estimated from the equilibrium measurement and the numerical computation of the slowing down process), excitation of plasma instabilities by the energetic ion population may further increase the anomalous heat conduction. Figure 2.11 shows the evolution of the gross energy confinement time,

$$\tau_{Ee} = \frac{W_e}{P_{OH} + P_{inj,e}} \quad . \tag{2.1}$$

The value of τ_{Ee} at 95 msec is significantly higher than the rest of the values. This sharp increase may reflect on the sudden increase of $(T_e)_{max}$ in the soft x-ray PIN diode measurement at the instant of the beam turnoff. Although the previously discussed rapid fall of the radiative power appears to be responsible for the discontinuity of $\tau_{Ee}(t)$, the possibility of plasma instabilities caused by the injection calls for a more refined definition of energy confinement time,

$$\tau_{Ee}' = \frac{W_e}{P_{OH} + P_{inj,e} - \dot{W}_e - P_{rad} - P_{ei}} \quad , \tag{2.2}$$

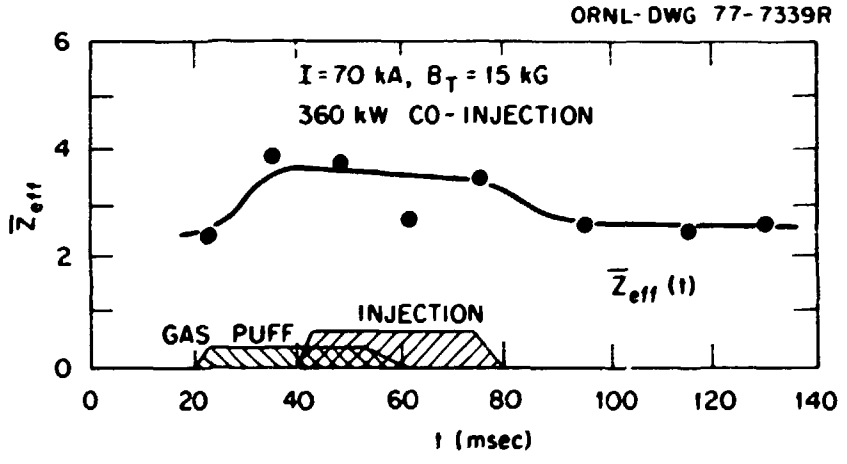

Fig. 2.10. Evolution of $\bar{Z}_{eff}$ estimated from the resistance in the electron heating experiment.

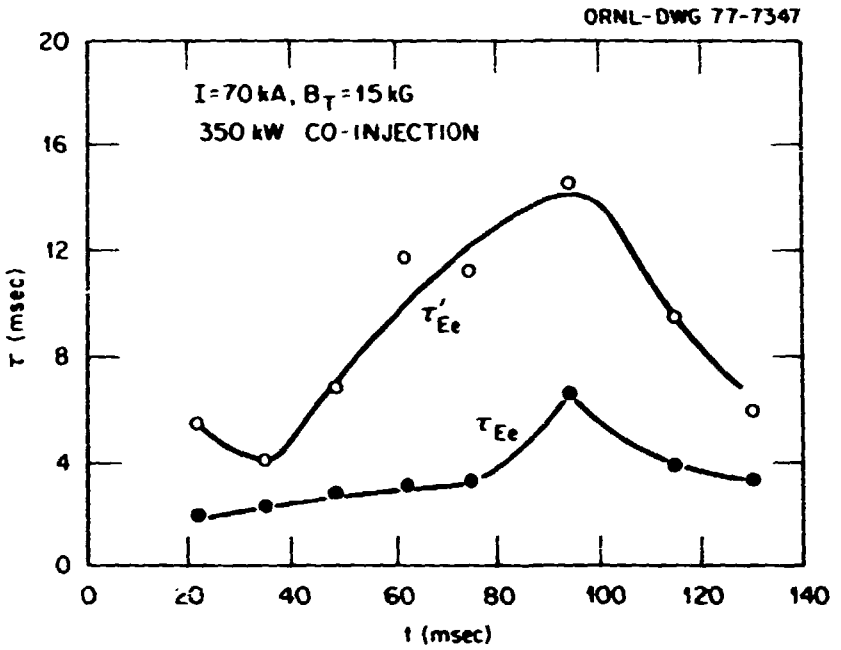

Fig. 2.11. Evolution of the gross electron energy confinement time, τ_{Ee} [Eq. (2.1)], and the electron energy confinement time, τ_{Ee}' [Eq. (2.2)], in the electron heating experiment.

where P_{ei} is the electron-ion heat transfer. The quantity τ_{Ee}' is an energy confinement time primarily related to electron heat conduction loss, because the other losses (convection and ionization) which are not explicitly specified in Eq. (2.2) are small. Using the radiometer values for P_{rad}, we show the evolution of τ_{Ee}' in Fig. 2.11. This indicates that there is no discrete jump such as seen in $\tau_{Ee}(t)$, implying that τ_{Ee}' during the injection pulse is no worse than that after the turnoff. We observe that τ_{Ee}' tends to increase with rising T_e. The last feature is generally observed in discharges with ohmic heating alone. In fact, when the injection pulse was simulated with ohmic heating pulsing ($I = 70 \rightarrow 110 \rightarrow 70$ kA), we observed a similar behavior of $\tau_{Ee}'(T_e)$.

We described above the temperature increase during the highest power injection pulse. In order to establish electron heating by neutral beam injection, it is equally important to show the scaling of the electron temperature with injection power. Figure 2.12 illustrates such a scaling. As in the previous case, the electron temperatures before the injection pulse of the intermediate powers were lower than those after the turnoff because of the change in radiation-dominated thermal equilibria. The effects of the change in equilibria without injection are indicated by the bound of the temperature before and after the injection pulses. Nonetheless, we observe that electron temperature increases monotonically with injection power.

Three other experiments related to electron heating are noteworthy.

1) Injection into a discharge at a higher density ($\bar{n}_e = 3.3 \times 10^{13}/cm^3$) with other conditions fixed produces an increase of $\langle T_e \rangle$ similar to the lower density case, implying that energy confinement improves with increased density during injection.
2) When the toroidal field is lowered to 10.5 kG [q(a) = 5 instead of 7], relatively weak sawtooth oscillations are present in the

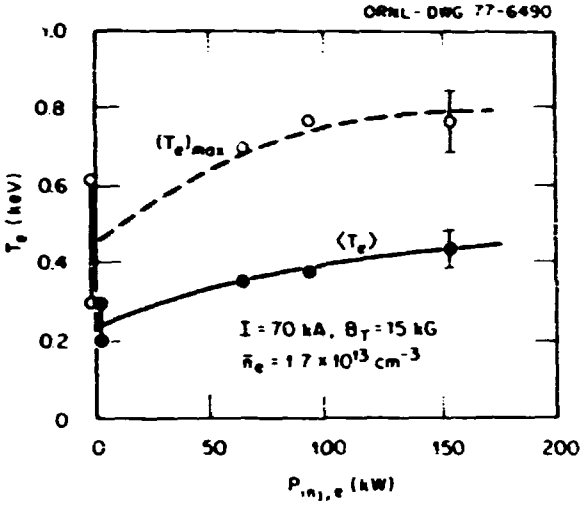

Fig. 2.12. Scaling of electron temperatures with injection power to electrons. Two electron temperatures are shown for no injection, corresponding to those before and after injection pulses.

soft x-ray signals throughout the discharges, but they do not reduce the increase in $\langle T_e \rangle$. Therefore, internal disruptions at $q(a) > 5$ do not seem to affect electron heating significantly.

3) Similar increases of electron temperature are observed with 310-kW injection into a higher current discharge [I = 175 kA, B_T = 26 kG, $\bar{n}_e = 2.2 \times 10^{13}$ /cm^3, $T_e(0) = 0.85 \rightarrow 1.3$ keV, $\langle T_e \rangle = 0.55 \rightarrow 0.7$ keV].

In conclusion, we observe that there is significant electron heating with the condition $P_{inj,e} > P_{OH}$ and that the electron temperature increases with injection power. The most significant power loss is caused by enhanced radiation due to a concurrent influx of high-Z impurities. The power loss due to other mechanisms (especially heat conduction) is not worse than the losses with ohmic heating alone.

2.1.4 High-β Experiments

L. A. Berry, J. L. Dunlap, P. H. Edmonds, G. L. Jahns, H. E. Ketterer, P. W. King, J. F. Lyon, D. H. McNeill, J. T. Mihalczo, M. Murakami, G. H. Neilson, V. K. Paré, J. B. Wilgen

Attainment of high toroidal beta ($\beta_T \sim 5$-10%) is vital for realizing an economical fusion reactor. Intensive theoretical efforts have recently focused on stability properties of plasmas based on the flux conserving tokamak (FCT) concept, which is a promising route to the achievement of such $\bar{\beta}_T$ values. Experimental observations of equilibrium and stability properties of plasmas with high β_T attainable on present tokamaks are useful for verifying theoretical results.

A recent ORMAK experiment with neutral beam injection at a low safety factor [$q(a_\ell) = 2.6$] achieved a relatively high β_T ($\bar{\beta}_T \sim 1\%$). The discharge was grossly stable, and the behavior of the internal MHD activities was normal.

Figure 2.13 shows time-dependent discharge parameters in the experiment. A mild gas puffing was used to sustain the density, which otherwise would have decayed in these discharges after prolonged hydrogen discharge cleaning. A stronger gas puffing would have increased the energy content to achieve an even higher β_T value. The H^0 injection power (~340 kW) from two coinjectors exceeded the ohmic heating power (~260 kW). The discharge was grossly stable and reproducible, which was not the case without beam injection. Figure 2.14 illustrates the electron temperature and density profiles measured from the Thomson scattering. The $T_e(r)$ profile is significantly broader than those obtained with higher $q(a_\ell)$ values. These profiles are reminiscent of those in the U.S.S.R.'s T-3A tokamak. A preliminary estimate of the central ion temperature from the

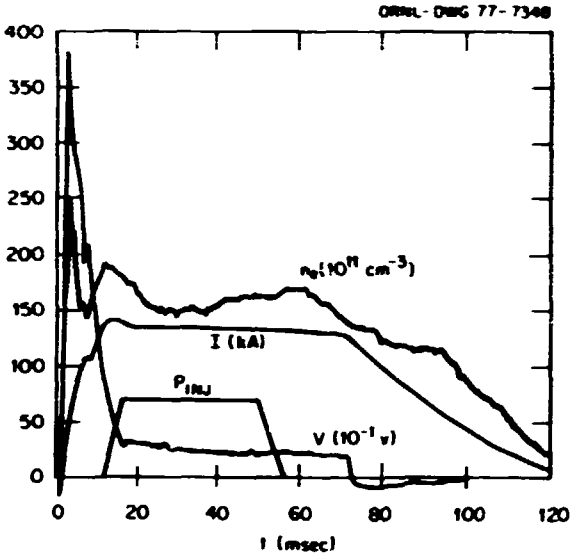

Fig. 2.13. Temporal evolution of discharge parameters in the high β experiment.

charge-exchange analysis is 550 eV, resulting in the central toroidal beta for the plasma energy alone, $[\beta_T(0)]_p$, being equal to 0.4. Using the electron density profile for the ion temperature profile, we calculate $(\bar{\beta}_p)_p = 0.30$ and $(\bar{\beta}_T)_p = 1.4\%$. Under these experimental conditions, the equilibrium measurement indicated that the stored fast ion energy is comparable to the bulk plasma energy, and the numerical computation of the slowing down process gives the ratio (Γ_f) equal to 1. Therefore, the total beta, $(\bar{\beta}_T)_{f+b}$, is estimated to be ~1%. Assuming the spatial distribution of the stored fast ion to be that of the bulk plasma energy, we estimate $\beta_T(0)_{p+b} \sim 3\%$.

These β values with the beam and plasma energies are not far from the β thresholds for MHD instabilities (of the ballooning mode) predicted by some numerical stability codes. Therefore, stability aspects of this discharge are of appreciable interest.

Most of the soft x-ray signals (Fig. 2.15) from the PIN diode system in this sequence exhibited strong sawtooth oscillations, and fewer shots showed strongly growing high frequency oscillations (presumably m = 1) superposed on the sawtooth oscillations. The high frequency oscillations appeared also in the $\tilde{B}_\theta$ and loop voltage signals at the instant of the internal disruptions. The m = 1 mode rational radius (q_1) as deduced from the soft x-ray signals is 9 ± 1 cm. The q(r) profile inferred from the $T_e(r)$ profile indicates that $r_1 = 11$ cm, $r_2 = 20$ cm, and $q(0) = 0.65$. Although r_1 is somewhat larger than a typical value, the overall behavior of the internal MHD activities is similar to that for discharges at a higher safety factor.

In conclusion, $\bar{\beta}_T \sim 1\%$ was obtained with injection at $q(a) = 2.6$. The discharge did not exhibit significantly abnormal behavior of MHD activities.

2.1.5. Gas Puff Experiments

C. E. Bush, P. H. Edmonds, C. A. Foster, H. C. Howe, P. W. King, J. F. Lyon, D. H. McNeill, M. Murakami, R. V. Neidigh, D. L. Shaeffer

The empirical scaling laws obtained from the previous series of scaling experiments[7] with steady filling conditions indicate significant improvement of overall plasma characteristics with increasing density. The technique of gas puffing has been used to study this interesting discharge regime. The objectives of this series of experiments are:

1) to verify the previous empirical scaling laws under gas puffing conditions,
2) to study particle transport in conjunction with a one-dimensional transport code simulation, and
3) to explore the limit of attainable densities in tokamak plasmas.[8]

Time evolution of plasma parameters in a typical gas puff experiment in ORMAK without neutral beam injection is shown in Fig. 2.16. Gas puffing with the throughput of 10 torr

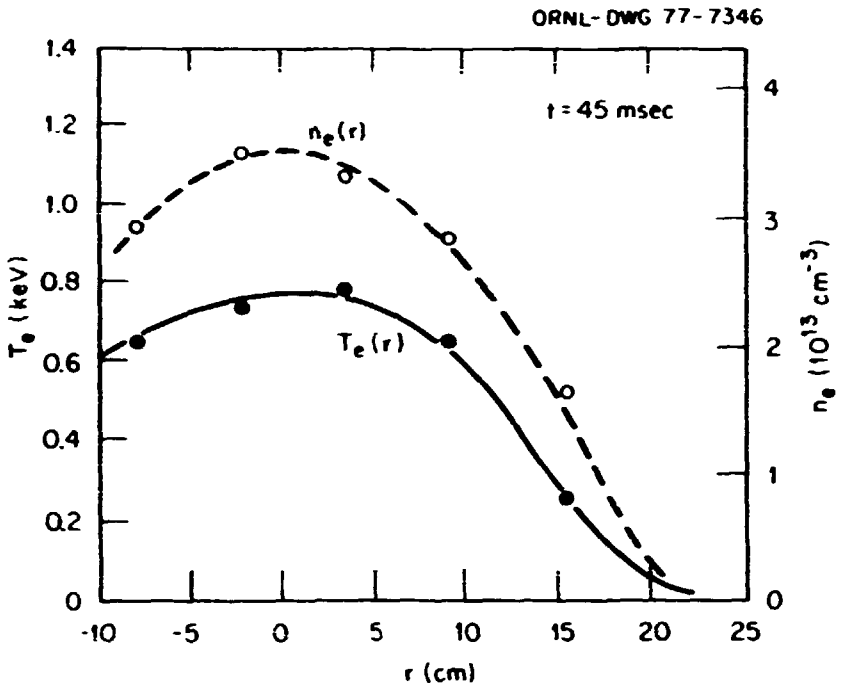

Fig. 2.14. Electron temperature and density profiles measured from the Thomson scattering.

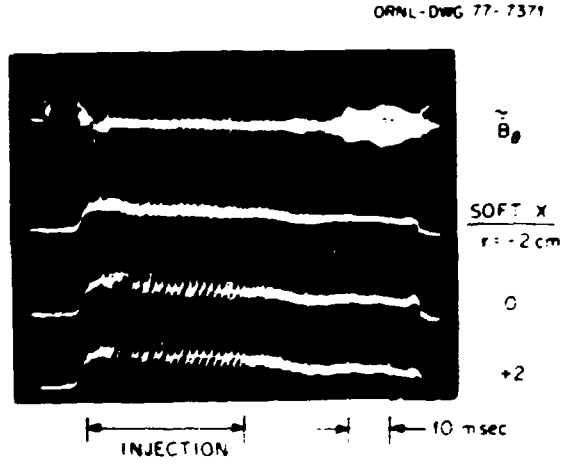

Fig. 2.15. External and internal MHD oscillations as measured by a magnetic loop and PIN diodes.

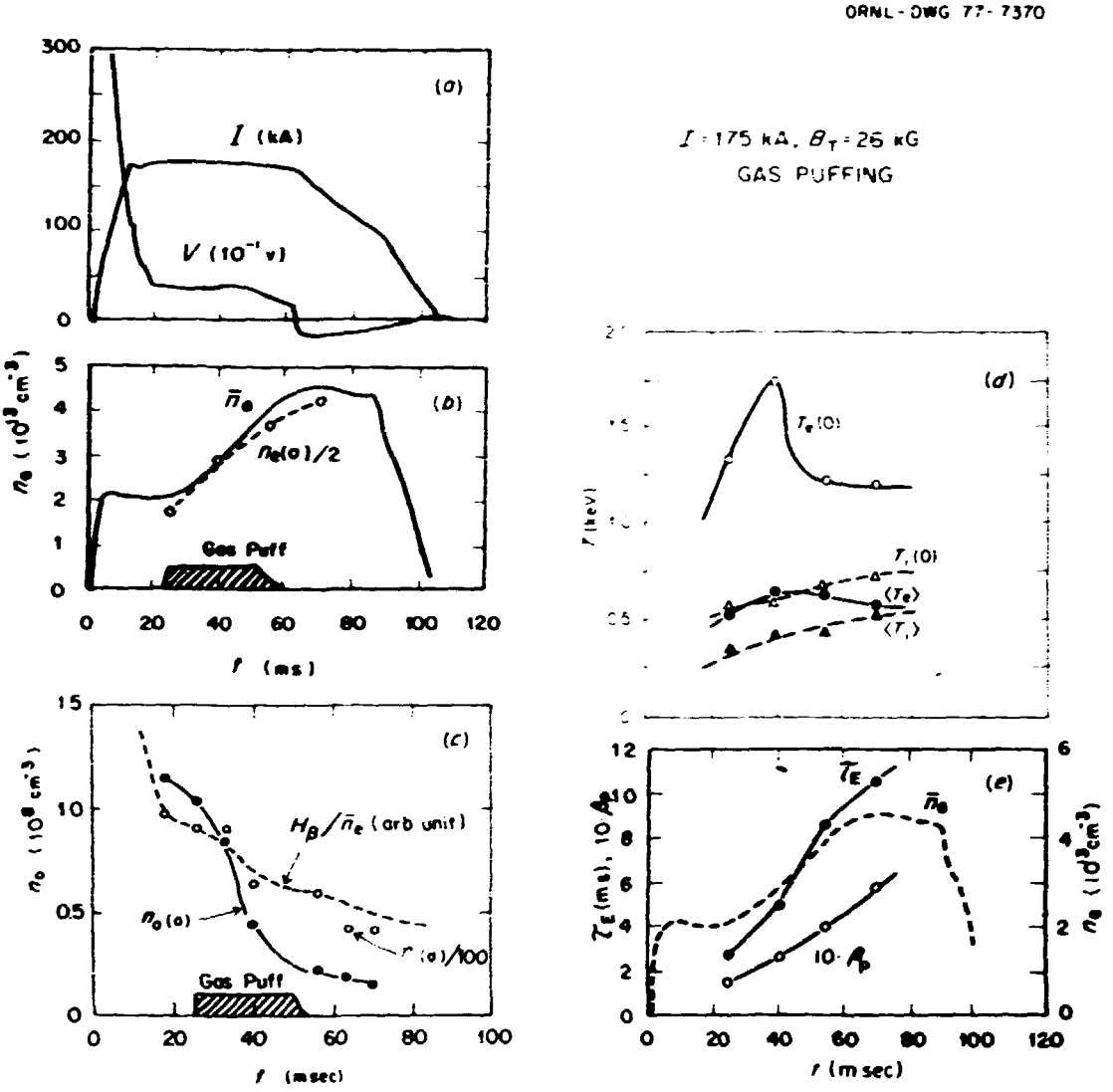

Fig. 2.16. Evolution of plasma parameters in a typical discharge with delayed gas puffing without neutral beam injection.

liters/sec was applied at 25 msec into the discharge, resulting in an increase of the line-averaged density, $\bar{n}_e$, from 2×10^{13} cm^{-3} to 4.5×10^{13} cm^{-3}. The increase in the total number of electrons at 60 msec corresponds to roughly 60% of the total number of injected atoms.

Figure 2.17(b) shows the evolution of the electron density profiles, $n_e(r)$. Although the wide time and space resolutions and uncertainties in the Thomson scattering measurements do not allow the observation of fine structures of $n_e(r, t)$, the electron density tends to increase uniformly without prolonged inverted density profiles. This is seen as the increase of the central density, $n_e(0)$, in parallel with that of $\bar{n}_e$, as shown in Fig. 2.16(b).

The rapid rise of $n_e(0)$ observed here and in other experiments is an intriguing phenomenon for the particle transport simulation, which will be discussed in Sect. 2.1.15. The charge-exchange analysis provides an estimate of the central neutral density, $n_0(0)$, [Fig. 2.16(c)] on the

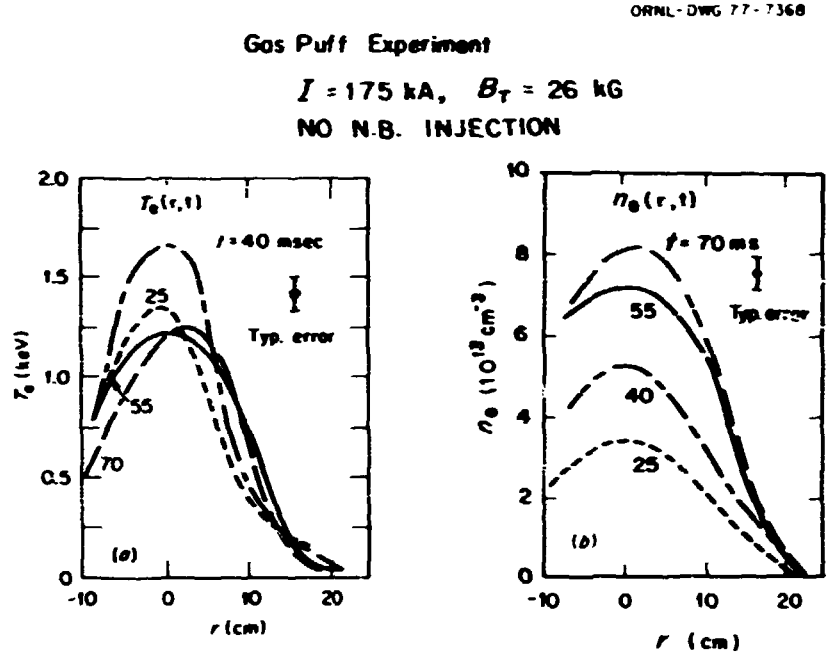

Fig. 2.17. Evolution of electron temperature and density profiles with gas puffing. Other experimental data are for the same discharges shown in Fig. 2.16.

basis of a model which is discussed in Sect. 2.1.12. The neutral density model used in the charge-exchange analysis compares favorably with the chordal integration of H_β line intensity in that the edge neutral density, $n_0(a)$, is parallel with the H_β intensity normalized to line-averaged density. The one-dimensional simulation of particle transport using such neutral density leads to prolonged inverted density profiles with no substantial increase in $n_e(0)$ — a contradiction with the experiment. Section 2.1.15 discusses the necessity of including a density pinch (such as the Ware pinch) in the particle balance equation.

The electron temperature distribution (Fig. 2.17) evolved from a peaked distribution at the early stage of the gas puffing to a broad one later. The transition coincides with a transition of the main features of MHD oscillation characteristics from the m = 2 modes to the m = 1 modes (with strong internal disruptions). In other discharges in which the m = 2 modes continued to dominate, $\bar{n}_e(t)$ started to decay during gas puffing, indicating poor particle containment. Further increases in gas throughput in the latter case caused disruptive instabilities, resulting in a lower maximum density than that for the former case. Therefore, the presence of internal disruptions apparently helps to obtain a higher density. This is probably due to heat transport associated with internal disruptions to prevent current channel shrinkage which otherwise would lead to disruptive instabilities.

The particle-averaged electron temperature did not change significantly, as shown in Fig. 2.16(d). On the other hand, central ion temperature increases with increasing density, as predicted by the Artsimovich scaling. At high density, electron- and ion-averaged temperatures become roughly equal. These temporal variations of plasma parameters agree with those expected from the scaling laws previously obtained under

quasi-stationary conditions. At constant I and B_T,

$$\tau_E \sim \bar{n}_e[q(a)/Z_{eff}]^{1/2} \sim (\bar{n}_e)^{3/2} \quad ,$$

$$\beta_p \sim \bar{n}_e/I^{4/3} \sim \bar{n}_e \quad ,$$

$$Z_{eff} \sim I/\bar{n}_e \sim 1/\bar{n}_e \quad ,$$

$$\langle T_e \rangle \sim I^{2/3} \sim \text{const.}, \text{ and}$$

$$T_i(0) \sim (\bar{n}_e I B_T)^{1/3} \sim (\bar{n}_e)^{1/3} \quad .$$

These scaling laws clearly indicate the advantages of high density operation in tokamaks. Previously, we established a scaling law of the maximum densities of ohmically heated tokamaks,

$$(\bar{n}_e)_{max} \sim B_T/R_0 \sim j(0) \quad .$$

We have noted that the maximum densities attained by gas puffing in the Alcator and Pulsator devices are higher than those obtained under steady filling conditions in other tokamaks. In Fig. 2.18 is plotted the maximum density (without disruptive instabilities) obtained with gas puffing at q(a) = 5 in ORMAK, superposed on the data from other tokamaks. The maximum density with gas puffing is about 1.6 times higher than that with steady filling, but the value is still lower than that scaled with B_T/R_0 from the Alcator and Pulsator values. This may be due to higher impurity influx from the wall. However, with added injection power of a modest (240 kW) level, the attained density does scale to the Alcator and Pulsator values.

With ohmic heating alone at I = 170 kA, densities up to 4.5×10^{13} cm^{-3} can be obtained with gas puffing. Added injection power is necessary to reach the maximum density, $\bar{n}_e = 6 \times 10^{13}$ cm^{-3}. In this discharge, a significant portion of the injected power was deposited in the outer portion of the plasma, as discussed in Sects. 2.1.2 and 2.1.6. In addition, strong internal disruptions were observed in the soft

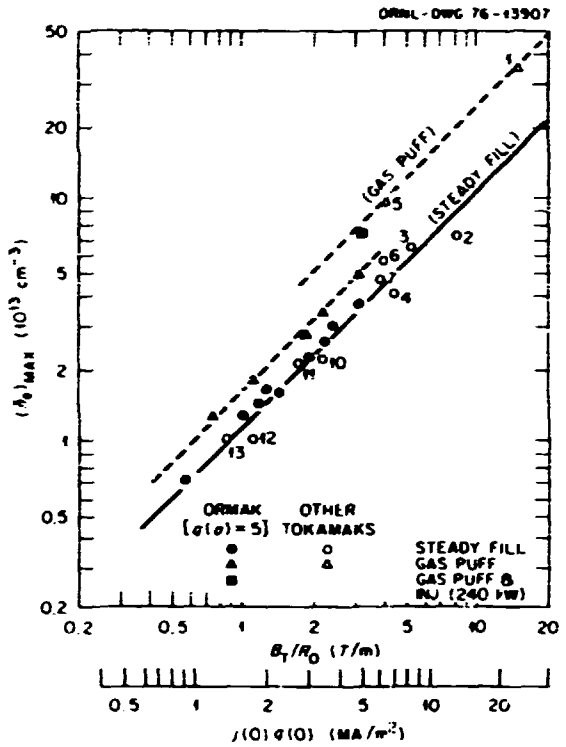

Fig. 2.18. Scalings of maximum line-averaged densities with and without gas puffing for ORMAK and other tokamaks (see Ref. 8). Neutral beam injection allows an increase of the density limit in ORMAK.

x-ray signal, indicating a significant energy transport to the plasma edge. The power deposited in the outer plasma region tends to counter the edge cooling and may prevent disruptive instabilities. The electron and ion temperatures are approximately equal (~1.3 keV), and their profiles are broad. These favorable features, in addition to good overall confinement (τ_E = 15 msec, $(\bar{\beta}_p)_\rho = 0.93$, $[\bar{\beta}_T(0)]_\rho = 1.2\%$, and $n_e(0)\tau_E = 1.3 \times 10^{12}$ cm^{-3} sec}, suggest that the combination of neutral beam injection and gas puffing is a viable operational mode of tokamak devices.

2.1.6 Beam Trapping by Impurities

During the past year the role of neutral beam trapping by charge transfer to impurities

has been recognized as being more significant than previously thought. This change is the result of measurements by Phaneuf et al. (see Sect. 2.10) of the cross sections for charge exchange between H^0 and various light (C,O) and heavy (Fe) ionized impurities present in tokamaks and of calculations and beam trapping measurements on the Tokamak Fontenay-aux-Roses (TFR) by Moriette.[9] We report two studies related to this impurity trapping: (1) spectroscopic evidence for this process in ORMAK, and (2) calculation of the effect of this process on the beam power distribution for the highest density case in ORMAK.

Spectroscopic evidence for impurity charge exchange

R. C. Isler

Direct evidence for the charge transfer reaction, $H^0 + O^{8+} \rightarrow H^+ + (O^{7+})^*$, has been observed during injection experiments on ORMAK. In these experiments the ohmic heating current is maintained at 70 kA until the plasma reaches a well established equilibrium; injection begins at 38 msec after breakdown. The sequence of shots analyzed here was obtained subsequent to discharge cleaning overnight with oxygen.

Both normal- and grazing-incidence monochromators are used to monitor radiation from the plasma. The acceptance cones of these instruments encompass sections of the plasma which lie along the axis of one of the beams.

Temporal dependences of various spectral lines are illustrated in Fig. 2.19. The upper two traces in all of the pictures result from the 1032-Å line of O VI which is detected at two different sensitivities, whereas the lower traces represent the behavior of various features in the soft x-ray region. Figures 2.19(a) and 2.19(b) are illustrative of the differences observed between shots that are taken with and without injection. Breakdown occurs at 4 msec after the oscilloscope is triggered. After 15 msec, the intensities of the lines remain constant or decrease slowly when there is no injection. However, when the injectors are activated, the trace due to the O VI line exhibits a sudden change in slope as the intensity

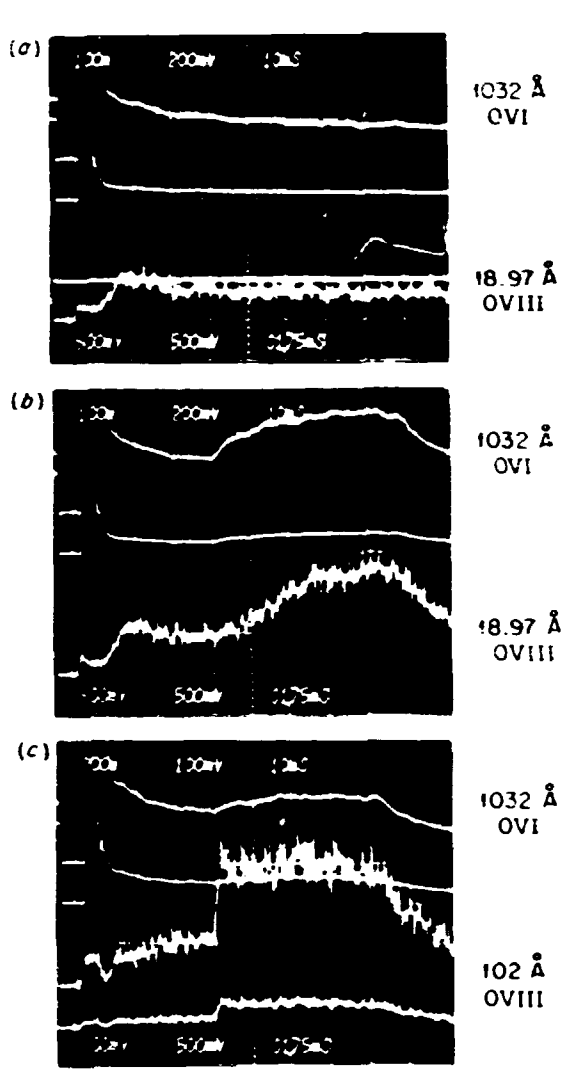

Fig. 2.19. Temporal dependences of the radiation of several spectral lines: (a) is characteristic of shots without injection; (b) and (c) are representative of the behavior obtained with neutral beam injection.

begins to increase. Similarly, the intensity of the Lyman α line of O VIII increases, but the initial rate is slower than the rate observed for the O VI line. These results are indicative of oxygen being ejected from the liner as a result of bombardment by energetic hydrogen atoms.

But in Fig. 2.19(c), which illustrates the temporal behavior of the radiation from the

Balmer α line, we see an evolution which differs markedly from that of the Lyman α line. There is a sudden, sharp increase in the intensity as soon as the injector is turned on. This prompt signal in the Balmer α line is reproducible, although it does not appear as dramatically in all of the shots as it does in Fig. 2.19(c). Nevertheless, after the contribution due to continuum radiation is subtracted, the data from six different shots all show that the intensity of the Balmer α of the O VIII line increases by a factor of four within 4 msec after injection begins, whereas the intensities of the Lyman α, β, and γ lines and of the Balmer β line all show increases of less than 20% in this interval.

It appears certain that the behavior observed in Fig. 2.19(c) is due to direct interaction between the particles of the beam and the plasma, and these data represent the first direct observation of beam trapping by impurities.

Effect of impurity charge exchange on beam power deposition

H. C. Howe J. F. Lyon M. Murakami

Attenuation of injected neutral beams by impurity ion collisions can prevent beam penetration to the plasma core at sufficiently high impurity densities. This effect was previously evaluated for ORMAK cases by neglecting impurity charge-exchange collisions, which were thought to be less important, and by assuming that the impurity ionization cross section for an ion of charge Z was $Z^2\sigma_{pi}$, where σ_{pi} is the proton ionization cross section. The additional neutral beam attenuation per unit length by both proton and impurity ionization was thus taken to be $n_e Z_{eff} \sigma_{pi}$. Because this term is less than that for resonant charge exchange on protons, impurity trapping of the injected beams was thought to be unimportant for typical ORMAK cases. Recently, impurity charge exchange was incorporated into the beam deposition calculations using the empirical fit $\sigma_{cx}(Z) = Z^2\sigma_{cx}(H^+)$ (E/67 keV) suggested by Sheffield.[10] The additional impurity charge-exchange contribution to the beam attenuation per unit length then becomes $n_e (Z_{eff} - 1) \sigma_{cx}$ (E/67 keV).

Figure 2.20 illustrates the importance of this term on the beam power deposition profile for the highest density ORMAK case. The ohmic heating power deposition profile is also given for reference. The power per unit volume P is peaked on axis for both ohmic heating and injection if impurity charge exchange is neglected. Taking this term into account shifts the injection peak out to 15-16 cm. Figure 2.20 shows instead the power deposited per unit radius, $2\pi rP$, so that the area under each curve represents the total power deposited. These powers are 425, 230, and 185 kW for ohmic heating, beam injection neglecting impurity charge-exchange

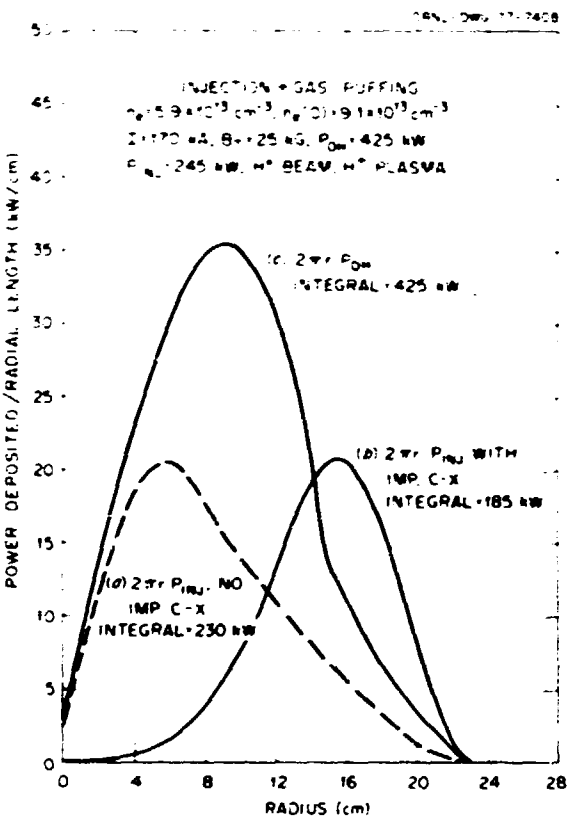

Fig. 2.20. Calculated radial power deposition profiles for: (a) injection neglecting impurity charge-exchange trapping, (b) injection including impurity charge-exchange trapping, and (c) ohmic heating. The power deposited per unit radius, $2\pi rp$, is plotted so that the area under each curve gives the total power deposition.

trapping, and injection including this term, respectively. The fraction of this power deposited within half the plasma radius ($r_{1/2}$ = 11 cm) is 62, 71, and 13%, respectively, for the three terms. For this highest density case ($\bar{n}_e = 5.9 \times 10^{13}$ cm^{-3}), the beam power deposition is greater than the ohmic power for $r \geq 14$ cm. This additional power input in the periphery of the plasma permits attainment of higher plasma density before disruption occurs, probably by heating the plasma edge and thus forestalling shrinkage of the current channel.

However, this beam power deposited at larger radius is more susceptible to being lost to the wall via unconfined orbits, especially with counterinjected beams. Figure 2.21 shows the calculated distribution of beam power for this highest density case for both the coinjected and counterinjected beam components and the effect of including the impurity charge-exchange term. The coinjected power deposition is relatively unaffected by this effect. However, the fraction of the counterinjected beam lost to the wall by initially bad orbits increases from 0.4 to 38% when impurity charge exchange is included. In addition, counterinjected ions, once trapped, can pitch-angle scatter into unconfined orbits and suffer additional losses. Of the total beam power input (coinjected plus counterinjected), the 93% that would have been deposited in the plasma if impurity charge exchange had not occurred becomes 75% when this term is included. The corresponding fractions are more dramatic for the plasma core ($r \leq 11$ cm), 66 vs 9.4%.

For the case discussed above, $\bar{n}_e Z_{eff} = 6.5 \times 10^{14}$ cm^{-3}. The impurity trapping effect is considerably reduced at lower Z_{eff} or lower plasma density and is not usually dominant for most ORMAK conditions. For example, for the highest ion temperature case [$T_i(0) = 1.8$ keV, $\bar{n}_e = 2.8 \times 10^{13}$ cm^{-3}, $Z_{eff} = 10$] discussed in Sect. 2.1.2, 81% of the beam power is trapped in the plasma if impurity charge exchange is ignored and 83% if it is included in the calculation. The corresponding fractions for $r \leq 11$ cm are 62 and 37%, respectively.

2.1.7 Counterinjection Studies

C. E. Bush, J. L. Dunlap, P. H. Edmonds, H. C. Howe, R. C. Isler, J. F. Lyon, J. T. Mihalczo, M. Murakami, G. H. Neilson, J. B. Wilgen

Injection antiparallel to the plasma current (counterinjection) is planned in future tokamak experiments in addition to injection parallel to the plasma current (coinjection), despite the reduced plasma heating efficiency with counterinjection and the presence of some deleterious effects on the plasma behavior. Counterinjection is planned in order to obtain additional injection access and because of the assumed need to balance the momentum input calculated for coinjection (see Sect. 2.1.14). Here we compare the effects of coinjection and counterinjection on plasma behavior for the same nominal plasma conditions ($\bar{I} = 170$ kA, $B_T = 25$ kG, and $\bar{n}_e = 2 \times 10^{13}$ cm^{-3}) for 125-kW H^0 injection into hydrogen plasmas conditioned by oxygen discharge cleaning.

Figure 2.22 shows the similarity of the basic gross discharge parameters obtained for the four cases studied: no injection, coinjection, counterinjection, and coinjection plus counterinjection. The main differences occur after the beam turnoff at 65 msec and the cases will be compared at 45 msec, the equilibrium portion of the discharge. Figure 2.23 shows the electron density and temperature profiles obtained from laser Thomson scattering measurements at 45 msec into the discharge for these cases. The density profiles are similar except for a slight inward shift for the coinjection and counterinjection cases. The main differences occur in the electron temperature profiles in Fig. 2.23, especially in the depressed central electron temperatures with counterinjection. Although there are large differences in the $T_e(r)$ profiles and the values for $T_e(0)$, the density-averaged electron temperatures, $\langle T_e \rangle$, are essentially identical for the four cases.

The addition of counterinjection produces increases in the impurity radiation losses and in the resulting total energy flux to the wall

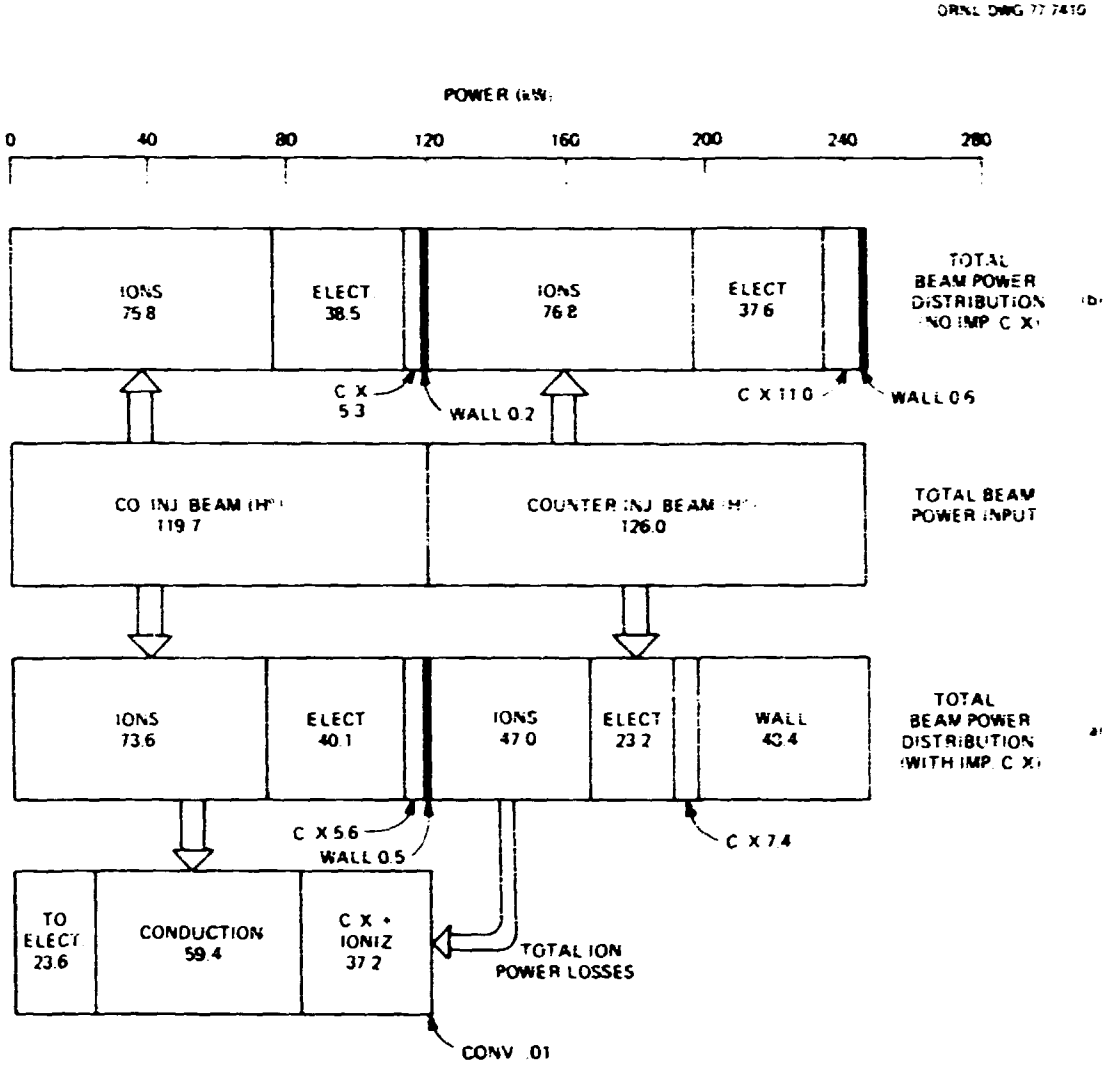

Fig. 2.21. Calculated beam power distribution for coinjected and counterinjected neutral beams for the highest density case in ORMAK, both (a) including and (b) excluding the beam trapping by impurity charge exchange.

(radiation + charge exchange). Relative to the no injection case, the fraction of the total power input to the plasma (ohmic plus beam heating) detected by the radiometer wall power measurements decreases by 20% for coinjection but increases by 40% with counterinjection. Figure 2.24(a) shows the time behavior of the radiometer signal for the four cases studied. For these oxygen discharge cleaned plasmas, more than half of the impurity radiation is thought to be due to oxygen ions outside the central core of the plasma (see Sect. 2.7).

However, the depression of the central electron temperature with counterinjection is thought to be more related to higher Z impurity radiation (believed to be due to tungsten from

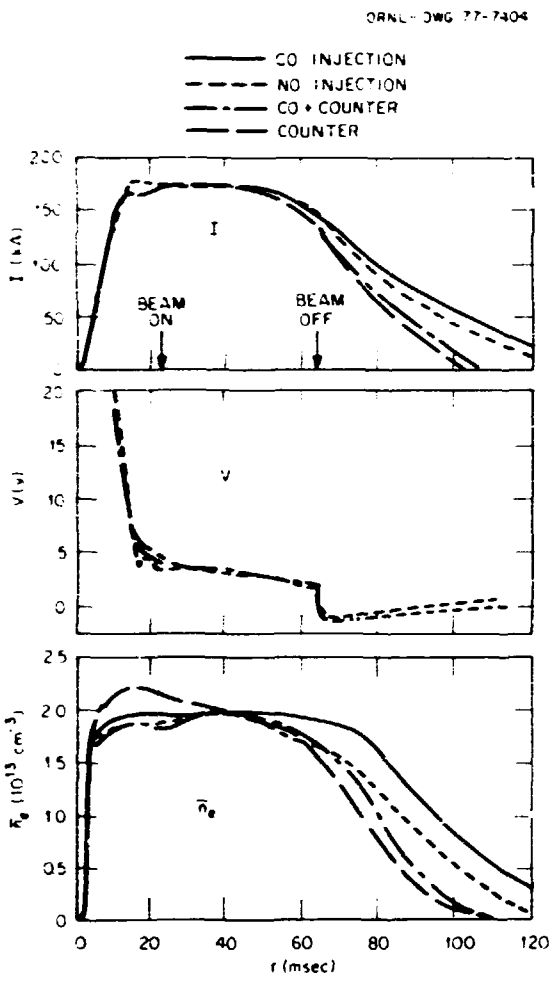

Fig. 2.22. Similarity of discharge parameters (current, voltage, and central chord-averaged density) for the cases compared: no injection, coinjection, counterinjection, and *coinjection plus counterinjection.*

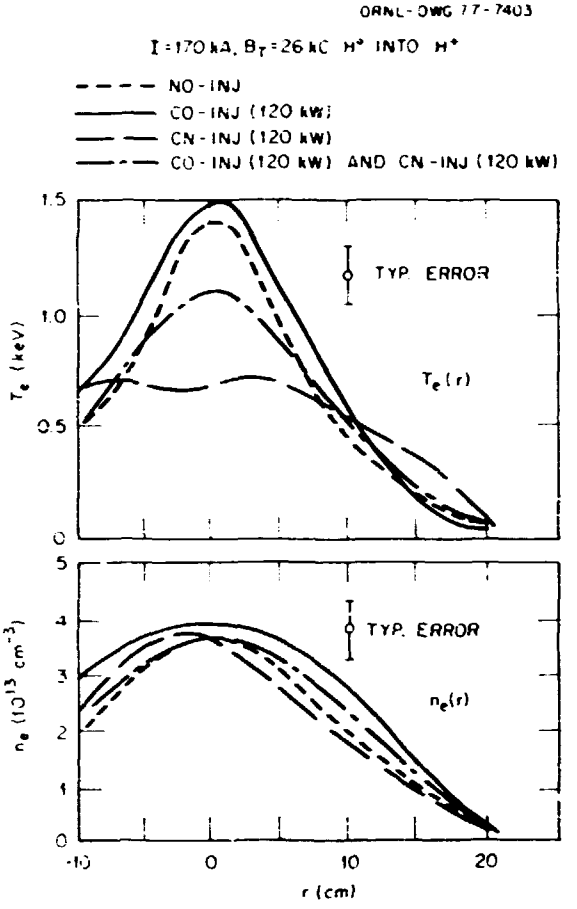

Fig. 2.23. Electron density and temperature profiles at 45 msec for the cases compared: no injection, coinjection, counterinjection, and coinjection plus counterinjection. The main difference occurs in the electron temperature profile for these 170-kA, 26-kG, $\bar{n}_e = 2 \times 10^{13}$ cm^{-3} hydrogen discharges with 120-kW H^0 beams.

the limiter). Figure 2.24(b) shows the correlation between the presence of counterinjection and a heavy impurity line, in this case Fe XVI (360.8 A). The top traces are for counterinjection alone and coinjection plus counterinjection, while the bottom traces are for no injection and coinjection alone. Heavy impurities released by *unconfined, counterinjected ions* can cause radiation cooling of the plasma. In fact, discharges without injection but with a contaminated wall produced even more pronounced hollow $T_e(r)$ profiles than that shown in Fig. 2.22. The only way we have been able to reproduce these hollow profiles in our one-dimensional transport simulation has been to include enough heavy impurities to cause substantial cooling near the center of the plasma. This deleterious effect of counterinjection should become less significant at higher discharge currents because the width of the unconfined, counterinjected banana orbit scales as the poloidal ion gyroradius. Previously,[11] similar deleterious effects with less counterinjection power were observed to improve rapidly with plasma current.

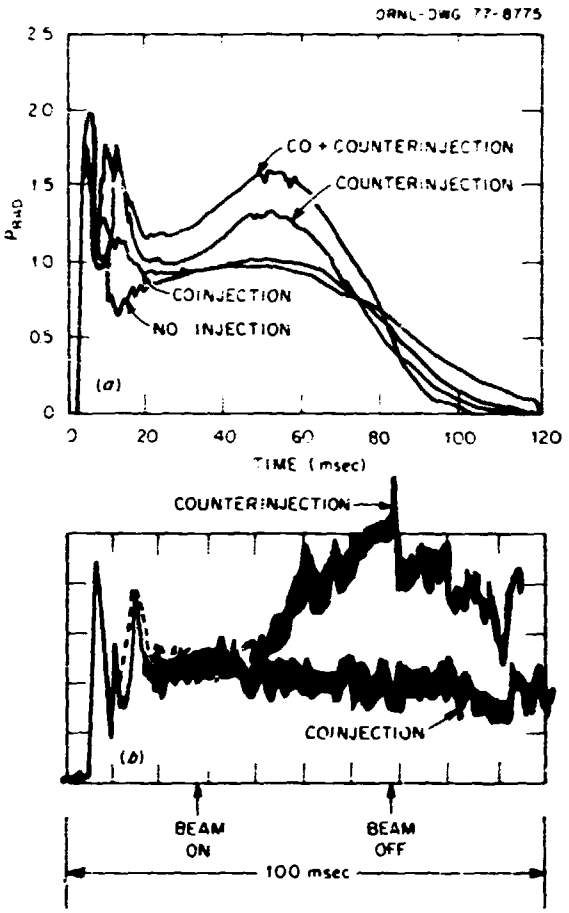

Fig. 2.24. Effect of injection on (a) total energy flux to the wall and (b) a specific heavy impurity line (FeXVI - 360.8 Å) for the four cases considered. The increased radiation loss is correlated with counterinjection.

Figures 2.25 and 2.26 contrast the power flows and plasma parameters obtained with coinjection vs counterinjection. For the coinjection case, roughly twice as much power goes to the ions as for counterinjection. The beam ion to plasma ion energy transfer is higher with coinjection because of the higher electron temperature, but then half of the ion power input is lost to the electrons for this same reason. More beam power is transferred to the plasma (ions + electrons) with coinjection because of the reduced wall losses due to bad orbits and the beam ion acceleration by the applied electric field (vs deceleration for counterinjection).

The ion temperatures obtained with counterinjection are considerably less than those obtained with coinjection. Transport modeling of ion heating indicates that the decreased central electron temperatures with counterinjection can explain these lower ion temperatures without the need for additional ion losses. The estimated ion energy confinement times for the plasma core are similar for the two cases. In the transport simulation, electric field effects and electron temperature profile shapes are much less important than the actual magnitude of the electron temperature.

We conclude that even at higher plasma current, counterinjection has deleterious effects on plasma behavior. Although in the above comparison oxygen discharge cleaning was used, similar behavior is seen with hydrogen discharge cleaning. The maximum plasma density attainable before disruption occurs is reduced if counterinjection is added to coinjection. As the plasma density increases still further, these deleterious effects will become more important. Counterinjected orbit losses at the plasma edge can increase the impurity influx, and the increased impurity trapping of the beam at the plasma edge moves the beam deposition profile still further out in radius. This then leads to increased counterinjected orbit losses and can limit beam penetration to the plasma core. In addition, at higher densities T_i and T_e approach each other, and an increased radiation loss limiting T_e also limits T_i both directly through electron-ion heat transfer and indirectly through reduced beam-ion energy transfer. The supposed need for counterinjection is examined in Sect. 2.1.14.

2.1.8 Impurity Measurements

Significant advances in determining the concentrations of impurities and their role in radiative losses were made during the past year.[12] Most progress resulted from improvements in instrumentation for the vacuum ultraviolet region of the spectrum. A 1-m normal-incidence monochromator has been added to ORMAK, and a

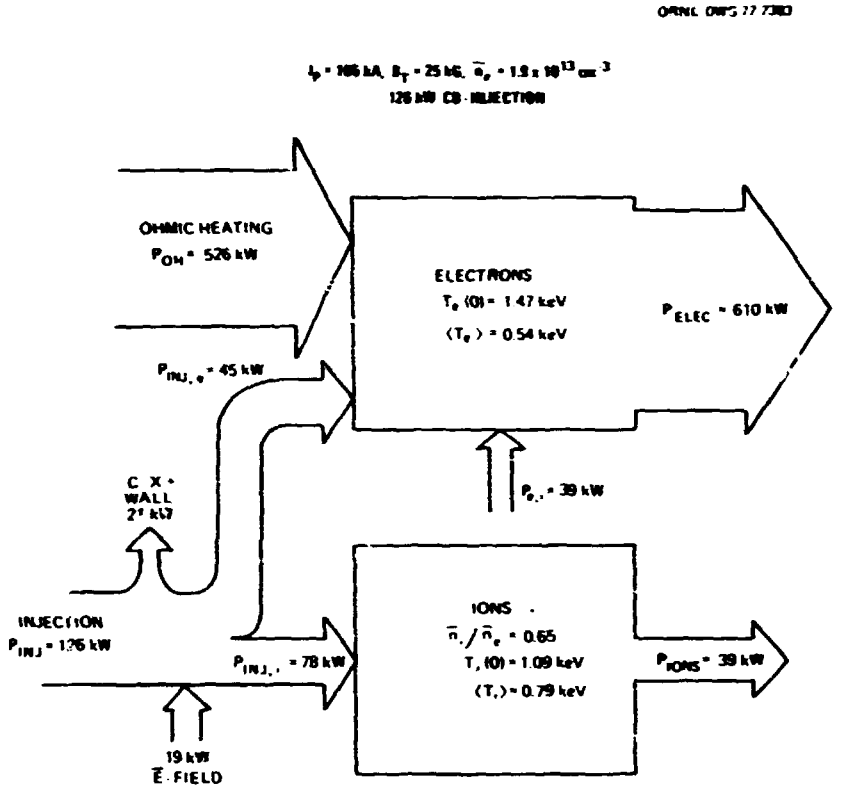

Fig. 2.25. Power flow diagram for ohmic heating, neutral beam, and ion and electron plasma components for the coinjection case.

holographically produced grating has been substituted for the ruled gratings used previously in the grazing-incidence instrument.

The efficiencies of the ruled gratings vary rapidly as a function of wavelength, particularly below 50 Å, and in the densitometer trace presented in last year's report the resonance lines of O VII and O VIII around 20 Å are barely distinguishable.[13] For contrast, a partial densitometer tracing of a plate taken with a holographic grating is shown in Fig. 2.27. Several lines from np → 1s transitions of O VII and O VIII are observed clearly, and many $\Delta n = 1$ transitions of iron are also apparent. Intense lines of $\Delta n = 0$ transitions of Fe XVIII-Fe XX also appear at longer wavelengths (~100 Å). The identification of these iron lines has enabled us for the first time to obtain quantitative estimates of the concentration of iron in the center of the plasma.

One of the most puzzling aspects of ORMAK-produced spectra has been the appearance of narrow band continua in the region from 20-70 Å. These continua account for most of the power radiated from the plasma except in circumstances in which the concentration of oxygen is large enough that the strong spectral lines of this element dominate. There is a growing body of evidence, both experimental and theoretical, that these features are actually many closely spaced lines of tungsten (Z = 74) which arise from the excitation of N-shell electrons. Calculations based on the assumption of coronal equilibrium[14] indicate that the stages W XIII through W XLVI should be present in a plasma in which the temperature ranges from 40-1000 eV and

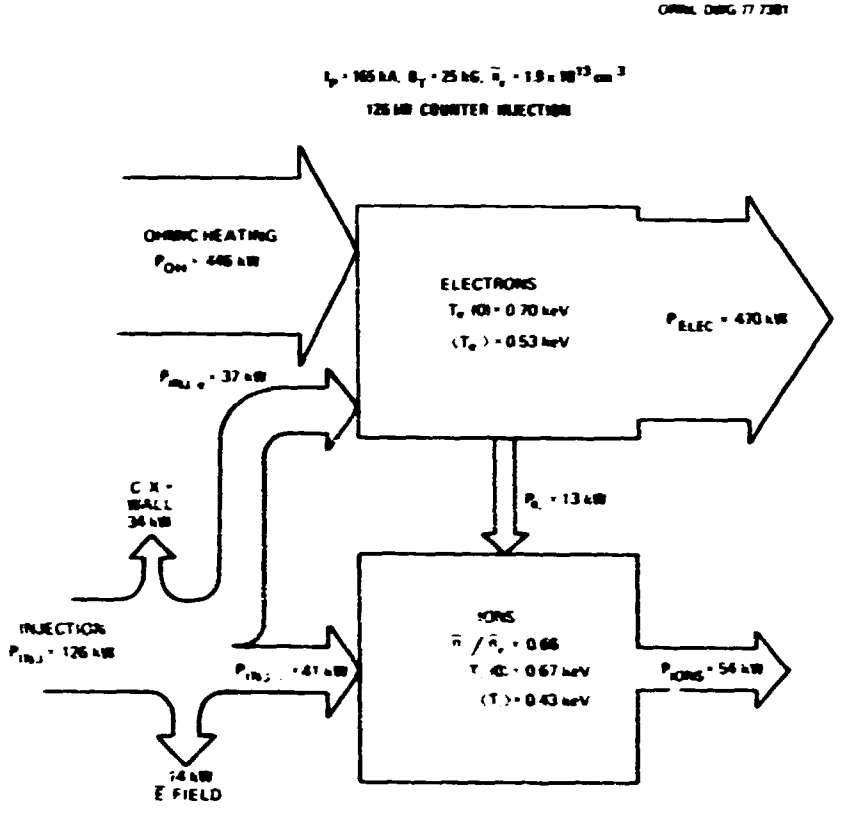

Fig. 2.26. Power flow diagram for ohmic heating, neutral beam, and ion and electron plasma components for the counterinjection case.

that many spectral lines may be excited in the region from 10–400 A. Elements having almost the same atomic number as tungsten should show similar spectral features, and indeed there is a striking resemblance between laser-produced spectra[14] from tantalum ($Z = 73$) and the narrow band continua from ORMAK. Some of the radiation may also be due to gold or platinum from the plating on the liner, but at the present time we assign all of it to tungsten because several discrete, unidentified lines in the region around 50 A correspond closely to wavelengths calculated for this impurity.[15]

As an example of our present understanding of impurities in ORMAK, we present an analysis from a sequence of shots taken after discharge cleaning in oxygen. The results have been obtained by correlating time-dependent signals of lines from O III-O VI with simultaneously acquired spectroscopic plates of the short wavelength region (15-100 A). The normal-incidence spectrometer is used to examine the behavior of the low stages of ionization of oxygen. It is calibrated by a modified branching ratio technique, and the uncertainty of absolute calibration below 1200 A is taken to be a factor of three. A separate apparatus for performing calibrations of gratings has been constructed, and it is anticipated that the uncertainty can be reduced to 30% in the near future.

The plates that are taken with the grazing incidence instrument are calibrated by first comparing the intensities of the np-2s transitions ($n > 3$) with the intensity of the 2p-2s transition and utilizing calculated excitation rates.[16] It is assumed that O VI ions have a

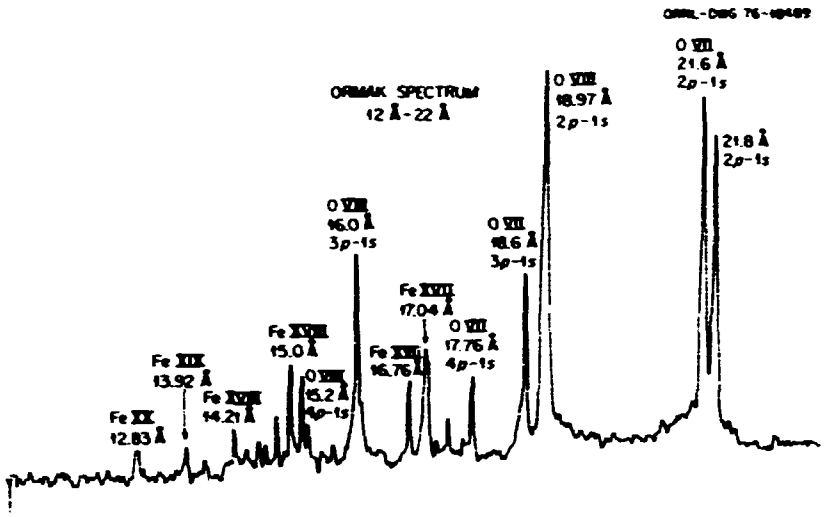

Fig. 2.27. Densitometer tracing of plate from about 10 Å to 22 Å.

maximum concentration at T_e = 40 eV; this temperature is slightly higher than that calculated by coronal models[17] (27 eV) in accordance with experimental measurements[18] and the knowledge that transport of impurities does not permit them to settle into complete coronal equilibrium. The absolute intensities around 20 Å are then determined by comparison of the Balmer and Lyman series of O VIII and the use of Jacob's cross sections for excitation.[19]

The power losses are shown in Table 2.1 for the dominant sources of vacuum ultraviolet radiation. Because both spectrometers accept radiation only from a chord along the minor radius of the plasma, it is necessary to multiply the detected signals by a factor which accounts for the distribution of radiators in order to calculate the total radiated power. A coronal equilibrium model has been used with a modeled profile of the temperature in order to obtain these factors for iron and the light elements. The distribution of continuum radiators (tungsten) has been assumed to be uniform throughout the plasma because a more detailed analysis is not possible at the present time.

Approximately 20% of the ohmic heating power is taken into account by the results shown in Table 2.1 in contrast to the data from the radiometer, which indicate that approximately 50% of the power appears at the liner. This difference may result from the large uncertainties in spectroscopic calibrations, or it may arise from the uncertainties in the modeling which is required to analyze the data.

Table 2.1. Power radiated by various impurities for an average ohmic heating power of 575 kW (data taken subsequent to discharge cleaning in oxygen)

Source	Radiated power Rate (kW)
O IV	4
O V	15
O VI	36
O VII	7
O VIII	5
N V-N VII	1
C IV-C VI	1
Fe XV-Fe XX	1
Continuum (tungsten) 24-70 Å	41
Total	111

The same set of data has been analyzed to obtain densities and an average value of Z_{eff}. The results are shown in Table 2.2. Several features concerning these results are worth noting. Oxygen has by far the largest concentration of the impurity ions and makes the dominant contribution to Z_{eff}. This concentration appears to decline only slowly towards the edge of the plasma and the outer regions may be almost all oxygen in experiments performed after discharge cleaning in oxygen. The proton defect of almost 80% at the center of the plasma is consistent with the data from the neutral particle detectors. The power radiated in the oxygen lines is reduced by a factor of about three if the discharge cleaning employs hydrogen rather than oxygen as the working gas.

Table 2.2. Contributions of impurities to Z_{eff} subsequent to oxygen discharge cleaning with $n_e(0) = 3 \times 10^{13}/cm^3$

Species	Concentrations	Contribution to $Z_{eff}(0)$
oxygen	$2.9 \times 10^{12}/cm^3$	6.21
iron	$3.0 \times 10^{9}/cm^3$	0.03
tungsten	$1.0 \times 10^{10}/cm^3$	0.41
hydrogen	$6.4 \times 10^{12}/cm^3$	0.22
	Total =	6.9

The concentrations of iron are very small, and this element appears to have little effect on radiated power or on Z_{eff}. Similarly, the concentrations of tungsten appear to be small, but the calculations of Jensen and Post[20] which were used to infer the concentrations imply that the power radiated could be as large as $68 \times 10^{-26} n_W n_e$ W/cm^3 in the temperature range from 300-1000 eV. Thus, even though the contribution to Z_{eff} is small, the radiative rates may be quite high. In fact, a concentration of tungsten of the order of $2\text{-}3 \times 10^{10}/cm^3$ could account for all of the power detected by the radiometer in most circumstances, yet make a contribution of less than two to Z_{eff}. As long as concentrations of iron and other elements of intermediate charge remain small, it should be unusual to produce values of Z_{eff} which are greater than 8 or 9.

2.1.9 Balmer α Line Profile Measurement

The suggestion that tokamak plasmas may execute toroidal rotation during the constant current portion of their ohmic heating cycle was first made by Rosenbluth et al.[21] The plasmas' toroidal rotational velocity was theoretically shown by Sigmar et al.[22] to be related to the existence of trapped particles. At that time we reported an experimental observation of an apparent linear relation between ion temperature and toroidal drift velocity. Since that report, we have examined the Balmer α (6563 A) spectral line profile of many ORMAK shots with an improved detection and collection system and substantiated that there is, indeed, a systematic distortion of the Balmer α line profile and that it appears to be related to ion temperature and Z_{eff}. This report describes the components in the improved detection system, unfolds the Balmer α line profile, and relates the line shape to ion temperature and Z_{eff}.

Our method incorporated a Czerny-Turner spectrometer with the associated optics for the selection of the radiation band; a time gated vidicon for detection, digitization, and accumulation of the radiation; and a computer for data storage and analysis. The apparatus is schematized in Fig. 2.28. Simply by positioning the entrance slit of the spectrometer, it was possible to see upstream or downstream with respect to plasma current. Spatial resolution is not obtained by this technique, but depending on the mean free path and observed energy of charge-exchanged neutrals, the Balmer α radiation in the wings of the line profile comes more or less from the plasma core.

A spectral line profile may be unfolded by force-fitting it to the sum of several Gaussians, each with a different width and shift. Usually three Gaussians will reduce the remaining misfit to less than the measurement errors. Or the

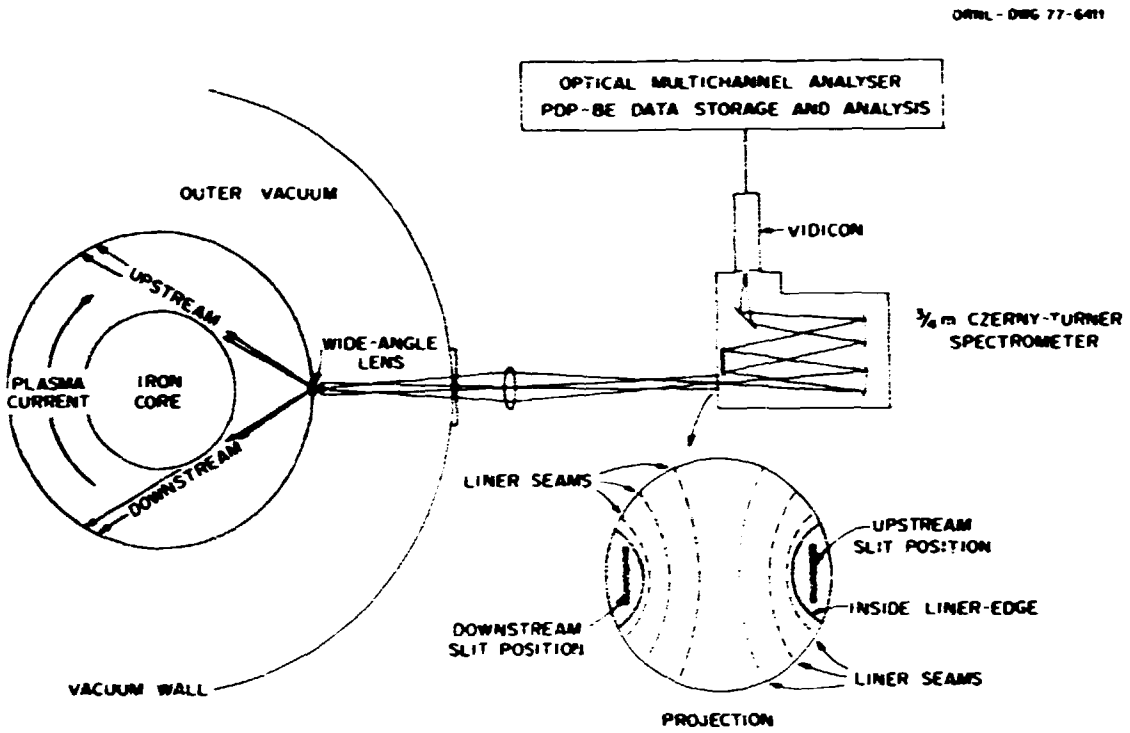

Fig. 2.28. Data collection system schematized. The insert depicts the projection of the ORMAK-produced plasma by the wide angle lens system. The spectrometer was positioned so that its entrance slit selected the desired portion of the projection.

line profile may be unfolded, as was done in the following examples, into the sum of its even and odd components. The even components can then be related to average ion energies and the odd components to an average drift velocity. (Note that the odd component may be caused by a pure shift and/or a distortion in the tail. We refer to the total effect as the average drift velocity.)

There is ample evidence for the distortion of the Balmer α (6563 Å) line shape. A contrast between observation upstream and downstream (with respect to the ohmic heating current) is shown in Fig. 2.29. Note that $(I_{\Delta\lambda} - I_{-\Delta\lambda})$ is negative (blue shift) if the view is upstream and positive (red shift) if the view is downstream. The line shape intensity ($I_{\Delta\lambda}$) is a direct image of the proton velocity distribution function.

The width of the Balmer α profile at a given intensity level is associated with an average ion energy and is related to the magnitude of the average drift velocity. It can be seen in Fig. 2.30 that the relationship appears to be small but consistent. All the data shown were collected during the constant current portion of many ORMAK shots at 30-60 msec. Z_{eff} was calculated from the plasma current and the line density at 45 msec. The distortion of the line seems to be altered by impurity levels and average ion energy. It appears that (1) the slope is related to Z_{eff}, (2) the drift velocity increases with power input from either ohmic heating or injection, (3) that impurity effects on the line shape are not changed by injection, and (4) hydrogen discharge cleaning permits a cleaner plasma than oxygen.

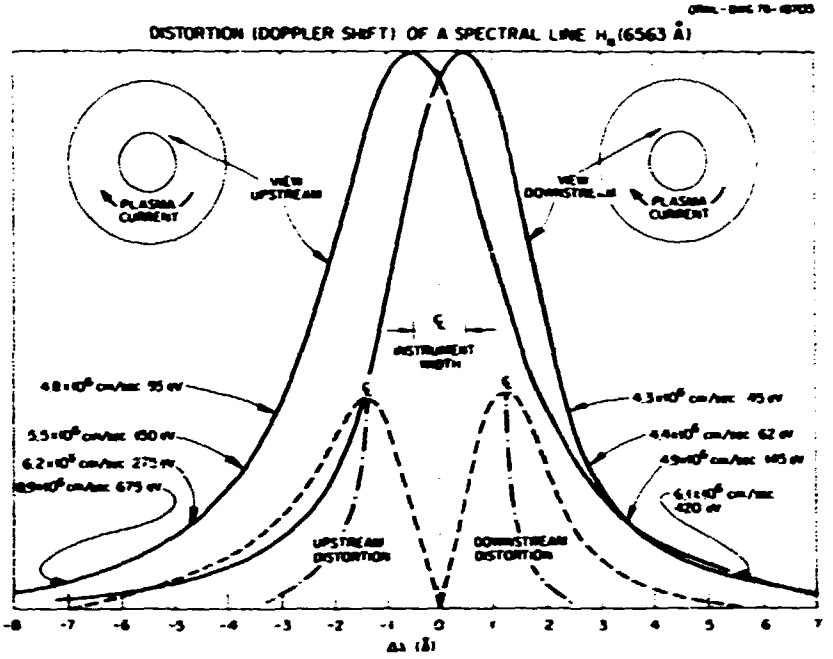

Fig. 2.29. Spectral line profiles of H_α (6563 A). The two large amplitude curves are profiles of H_α and show the total line shape. The smaller amplitude curves show only the odd components, the displacement of their centroids being a measure of the average drift velocity. The profiles are averages of up to 15 shots collected during the 30-60 msec period of each shot. The arrows indicate the intensity levels from which the average ion energy and drift velocity were obtained.

2.1.10 Internal Mode Structure from Correlation Studies

9. D. Burris J. L. Dunlap
J. H. Harris V. K. Paré

The previous annual report[23] described studies of internal mode structure in ORMAK using collimated soft x-ray detectors and magnetic probes as the principal diagnostics. Significant improvements in both the data acquisition and analysis systems were made during this present report period. These improvements are described below. Results from the study of one particular discharge are also presented.

1) Adding other x-ray detectors. Earlier work used a nine-detector array (the top one in Fig. 2.31) which limited m (the poloidal mode number) assignments to near the center of the plasma. Four additional detectors in a side-mounted array in the same toroidal section allow phase comparisons with the four corresponding detectors of the top array in order to define m values at r = 6, 8, 10, and 12 cm.
2) Replacing amplifiers for the x-ray signals. The newer ones have wider bandwidth and smaller phase shift.
3) Using 14-track magnetic tape for simultaneous recording of analog signals from selected x-ray and loop detectors for the full time of the discharges.
4) Using Fast Fourier Transform (FFT) processing to calculate the amplitudes, frequencies, and phases (relative to an arbitrarily chosen reference channel) of the signals. The poloidal and toroidal mode numbers can

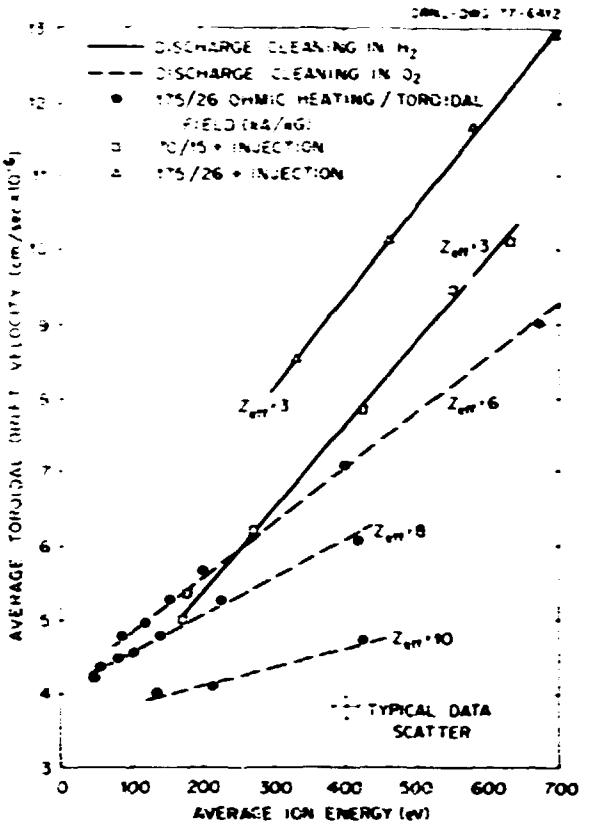

Fig. 2.30. Drift velocity dependence on energy impurities. Energy and velocity thresholds of 10 eV and 5 x 10^5 cm sec^{-1} are determined by the resolution, dispersion, and noise levels of the system.

then be determined from plots of electrical phase versus mechanical angle. This analysis was done by playing the analog tape at 1/64 the recording speed into a computer-based Fourier analyzer, which generated the auto- and cross-power spectra of the signals. Referenced to real (discharge) time the digitization rate was 128 kHz, and the spectra were developed through 32 kHz using time blocks of 4-msec duration.

5) Developing procedures for measuring the transfer functions of the x-ray detectors, the amplifiers, and the tape recorder itself. The Fourier analyzer was used to measure these transfer functions and to correct the spectra of the data appropriately.

6) Acquiring the ability to obtain plots of broadband, time domain data (waveforms) at arbitrary intervals in the discharge, either by playback of the taped signals or by recall of the digitized form.

As noted, the m values for the x-ray perturbation, $\tilde{X}$, derive from the detector arrays shown in Fig. 2.31. We have no corresponding detectors at other locations around the torus and thus do not determine n, the toroidal mode number, of $\tilde{X}$.

In systematic data acquisition, we deal with the 13 x-ray detectors and 20 $\tilde{B}_\theta$ magnetic loop probes. Eight of the latter are at the same poloidal angle but displaced at 45° intervals around the torus; these yield the n values of the current perturbation, $\tilde{I}$. The remaining 12 are at the same toroidal location but displaced at 30° intervals in poloidal angle; they yield the m value of $\tilde{I}$. Because the detectors total 33, we require three reproducible shots to determine the mode history of a particular discharge.

This diagnostic system became operational in October 1976, and the emphasis throughout the rest of the year was on data acquisition. As a result, a considerable amount is in hand, but most of it is not yet analyzed.

The capabilities of the system will be illustrated by data on the following ohmically heated discharge.

I_p = 175 kA $\quad B_T$ = 25.5 kG
No injection, no gas puffing
Parameters at 50 msec:

$T_e(0)$ = 1480 eV $\quad \langle T_e \rangle$ = 610 eV

$T_i(0)$ = 650 eV $\quad \langle T_i \rangle$ = 390 eV

$n_e(0) = 3.5 \times 10^{13}$ cm^{-3}

$\bar{n}_e(0) = 2.0 \times 10^{13}$ cm^{-3}

β_p = 19.4%

β_T = 0.07%

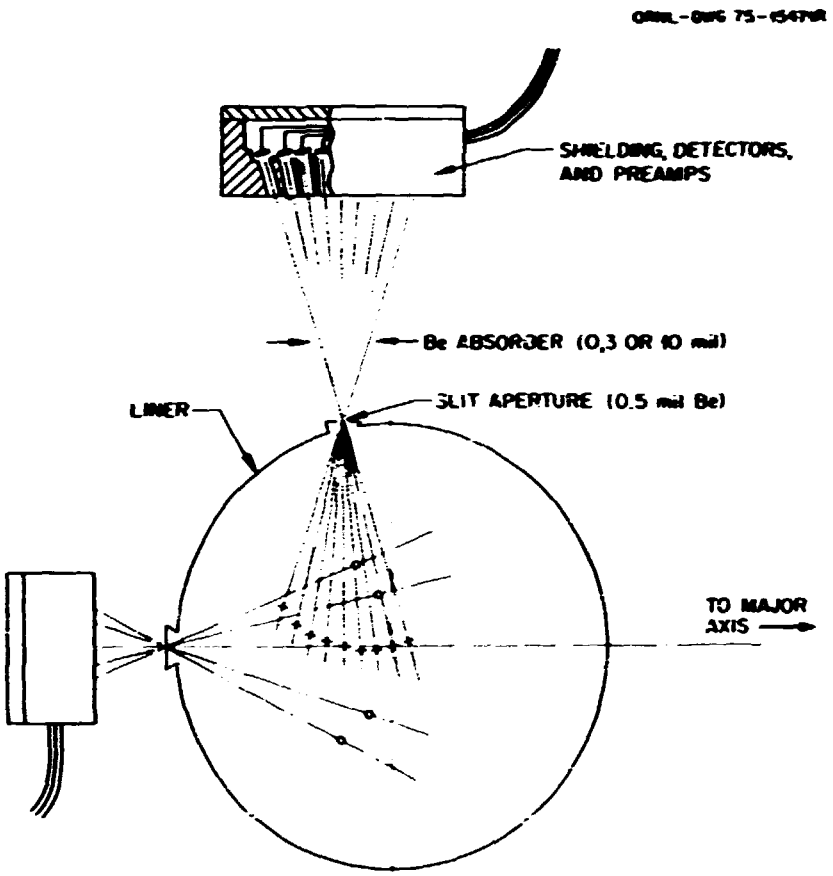

Fig. 2.31. The PIN diode soft x-ray diagnostic.

Figure 2.32 shows one of the magnetic loop signals and traces from several of the x-ray detectors. The detail available for computer analysis is illustrated in Fig. 2.33.

At any given time, the major oscillatory component in the x-ray signal (aside from sawteeth) is the same frequency as the $\tilde{B}_\theta$ signal. All of the phase measurements and comparisons we introduce below are for this dominant frequency component (approximately 5 kHz during the constant current phase of the discharge).

Periodic $\tilde{I}$ first appear at 5 msec into the discharge. The toroidal mode number, n, is 1 at this time and remains at that value (Fig. 2.34). The m number is initially 4 and progresses to 3 and then 2. An example of the poloidal phase plot for each m value is given in Fig. 2.35.

Periodic $\tilde{X}$ first appear at about 8 msec. The m values for these perturbations are deduced from the relative phases of the signals across the top array (Fig. 2.36) and from the relative phases between side and corresponding top detectors (Fig. 2.37).

In Fig. 2.36, the 180° phase shift at larger radius seems to represent the approximate location of the singular surface for $q = 2$. The sawtooth oscillation in these discharges begins at about 25 msec and persists well into the rundown. During that period, it is reasonable to associate the large phase shift at smaller radius with the center of an $m = 1$ mode. This

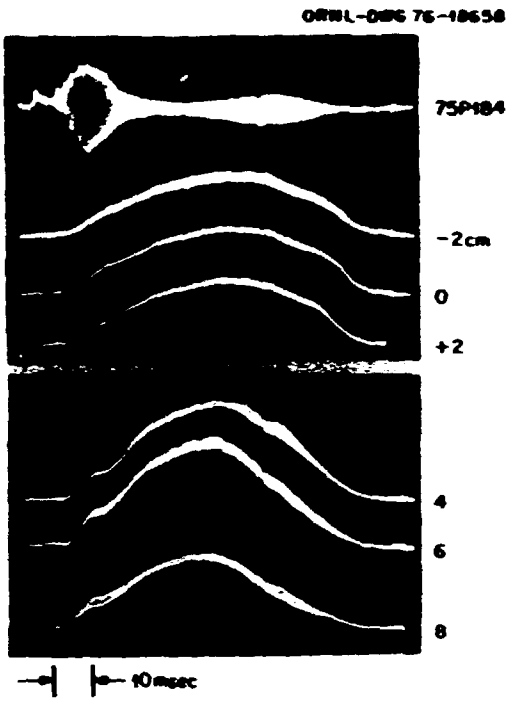

S-15454. LOOP AND x-RAY SIGNALS
(174 kA, 25.5 kG, $q(a) = 4.85$, $\bar{n}_e(C) \approx 2 \times 10^{13} cm^{-3}$)

Fig. 2.32. Magnetic loop and x-ray signals. The oscilloscope sweep is triggered 4 msec before the beginning of the discharge (t = 0). Rundown of the plasma current starts at t = 60 msec.

center is also the center of the discharge, as indicated by the plasma shift signals. At earlier times we make the same association, supported by shift signals which show the plasma initially forming somewhat outside the r = 0 equilibrium position and then drifting inward. This assignment of m = 1 at the earlier times is less certain. Because the detector array does not probe equally far toward negative minor radius, the possibility that the inner phase shift is the interior phase reversal associated with the m = 2 mode alone cannot be excluded.

The data in Fig. 2.37 show that the $\tilde{X}$ at r = 6, 8, and 10 cm are m = 2 throughout most of the discharge.

Table 2.3 details the time history of the mode structures observed in this discharge; different combinations of modes are present at different times.

Table 2.3. Mode structures

Time (msec)	$m_{\tilde{X}}$	$m_{\tilde{I}}$	$n_{\tilde{I}}$	q(a)
6-8	No signal	4	1	8.8-6.4
8-12	1,2	4	1	6.4-4.8
12-20	1,2	3	1	4.8
20-24	1,2	?	1	4.8
24-80	1,2	2	1	4.8-9.8

The measurements do not distinguish absolutely between poloidal as opposed to toroidal drift of the mode structures, but the fact that the frequencies are the same makes toroidal drift the simpler alternative. For toroidal drift, $\omega = n\, v_\phi/R$, and all the observed frequencies are the same if $v_\phi(r)$ is uniform and the n values are the same (n = 1 in agreement with the $\tilde{I}$ measurements). But with poloidal drift, $\omega = m\, v_\theta/r$, and a very precisely structured $v_\theta(r)$ profile is required to give the same ω for different m values.

An additional point is that frequency locking of the modes implies a phase locking. This phase locking is such that the perturbations observed ($\tilde{I}$ and $\tilde{X}$, the latter assumed to be $\tilde{T}_e$) have a constant phase along an outward directed minor radius. A reinforcing phase alignment along the outward directed radius results for harmonic structures even in the linear MHD theory.[24]

In summary, the frequency and phase relations observed can be reproduced by:

1) at one location around the torus arranging whatever m valued modes are present with perturbation phases aligned as indicated in Fig. 2.38,
2) assigning n = 1 to all modes, and
3) applying a uniform toroidal drift velocity. The magnitude required during the constant

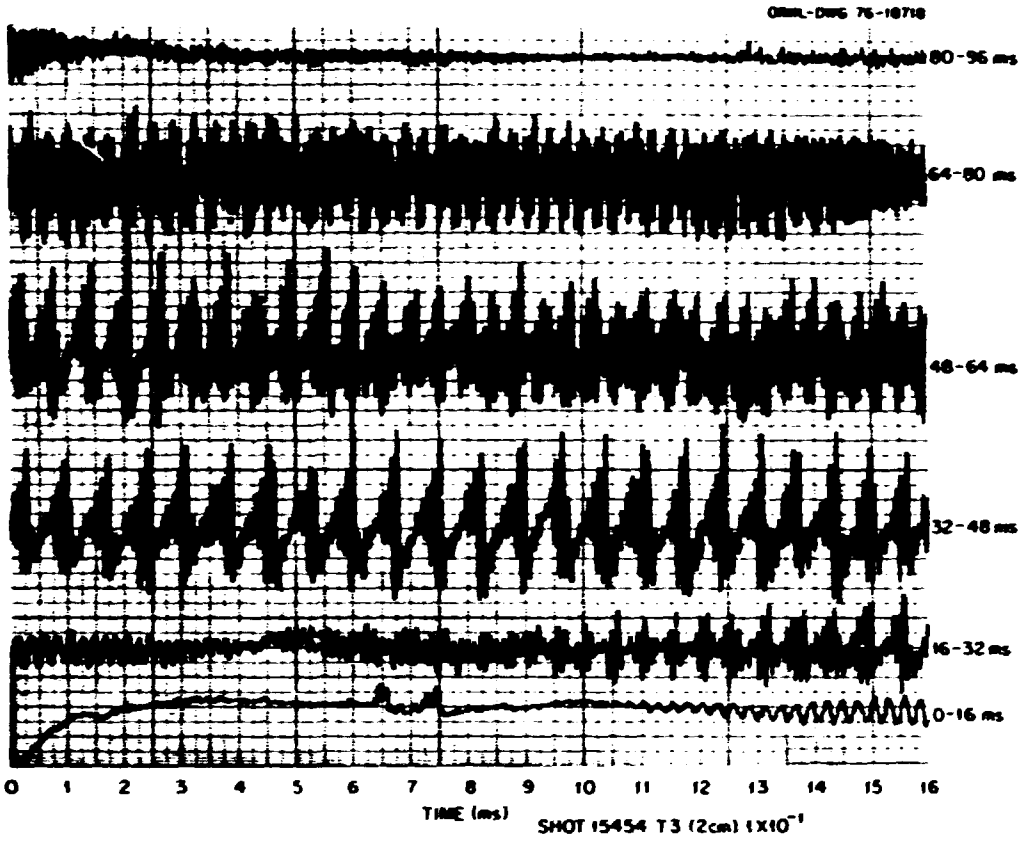

Fig. 2.33. This is the x-ray signal from the detector at +2 cm for the same shot shown in Fig. 2.32. The signal was passed through a 100-Hz high pass filter, recorded, and later digitized. The digitized form is shown here; there are 6.4 data points per smallest grid interval of the time scale.

current phase of the discharge is $v_\phi \approx 5 \times 10^6$ cm/sec, and the direction is that of the electron component of the plasma current.

Mode coupling such as we have described has been observed on the Pulsator[25] and TFR[26,27] experiments in the form of a coupling of m = 1 and m = 2 perturbations <u>after</u> the perturbations build up to critical amplitudes near thresholds for disruption. The Pulsator observations also included phase relations consistent with mode structure possessing the outward directed line of phase reinforcement and drifting toroidally in the direction of the electron component of plasma current.

In the ORMAK discharge illustrated, the coupling existed even though the perturbation levels were far below disruption. The coupling appears to have been a consistent feature of the ORMAK plasma throughout the parameter space investigated during the scaling studies reported last year.[28] The lower aspect ratio of ORMAK (3.5) should enhance the toroidal coupling and may account in part for the difference. Z_{eff} may also be involved. The discharge illustrated and those of the scaling studies were characterized by our typically high values of Z_{eff} (~6-10). In the very recent work after prolonged hydrogen discharge cleaning, Z_{eff} was significantly lower.[29] Under these conditions we observed some discharged with otherwise typical ORMAK parameters that showed $\tilde{I}$ frequencies distinctly higher than the $\tilde{X}$.

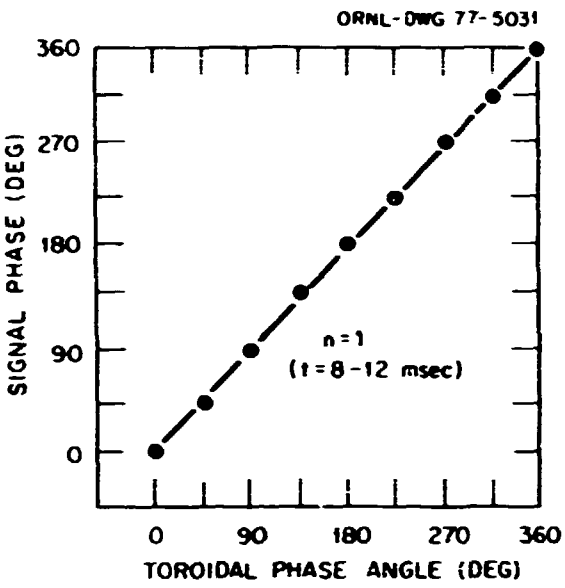

Fig. 2.34. Toroidal mode number determination from magnetic loop signals. The determination from data in the 4-msec time intervals centered at 6, 14, 18, 22, . . ., 86 msec are equally clear.

We are grateful for the cooperation of many of our colleagues in this work. G. R. Dyer and O. D. Matlock contributed in the areas of electronic and mechanical design. G. L. Jahns, M. Murakami, and A. Navarro assisted in data acquisition. Discussions with R. G. Bateman, Jr., Y-K. M. Peng, and B. V. Waddell have been helpful. That pure toroidal rotation might provide the simpler explanation of some features of early frequency observations was suggested to us by Bateman. The FFT processing was made possible by the equipment loaned to us by Instrumentation and Controls Division. Finally, as always, we are indebted to the members of the ORMAK operating crew.

2.1.11 Sawtooth Oscillations and Plasma Transport

G. L. Jahns J. D. Callen B. V. Waddell

Sawtooth mechanism

Since their discovery in 1974,[30] sawtooth oscillations, sometimes referred to as minor or

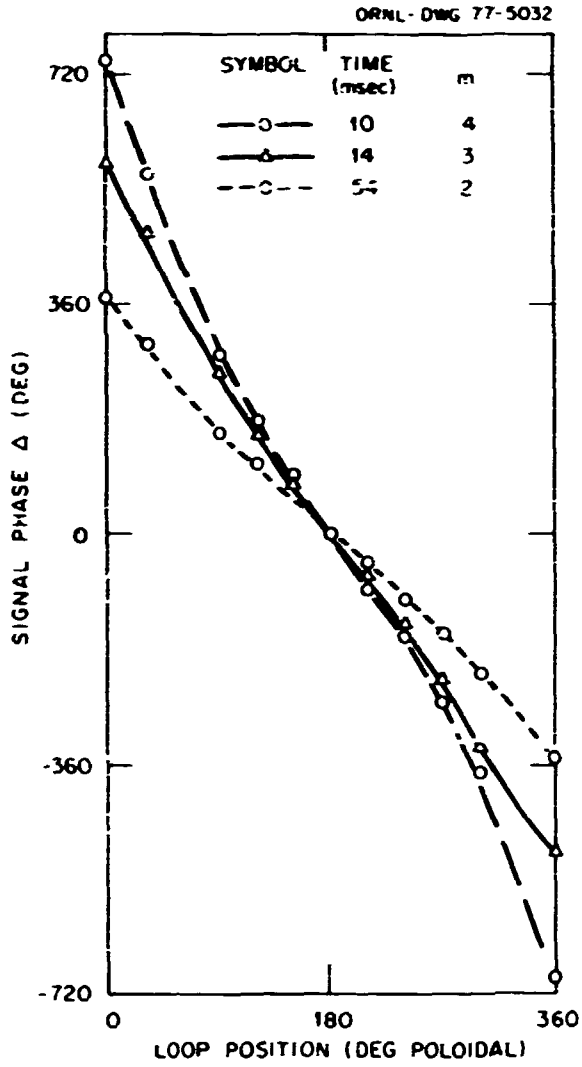

Fig. 2.35. Poloidal mode number determinations from magnetic loop signals.

internal disruptions, have remained one of the intriguing properties of tokamak discharges. Their occurrence in ORMAK was described in last year's annual report.[31] This year, sawtooth data from a large, representative set of discharges were compared with a tearing mode instability model,[32] briefly described in Sect. 3.2.4 of this report.

Soft x-ray intensities are temperature-dependent, and the sawtooth has been identified as principally an electron temperature fluctuation.[30,33] In our model, it is assumed that

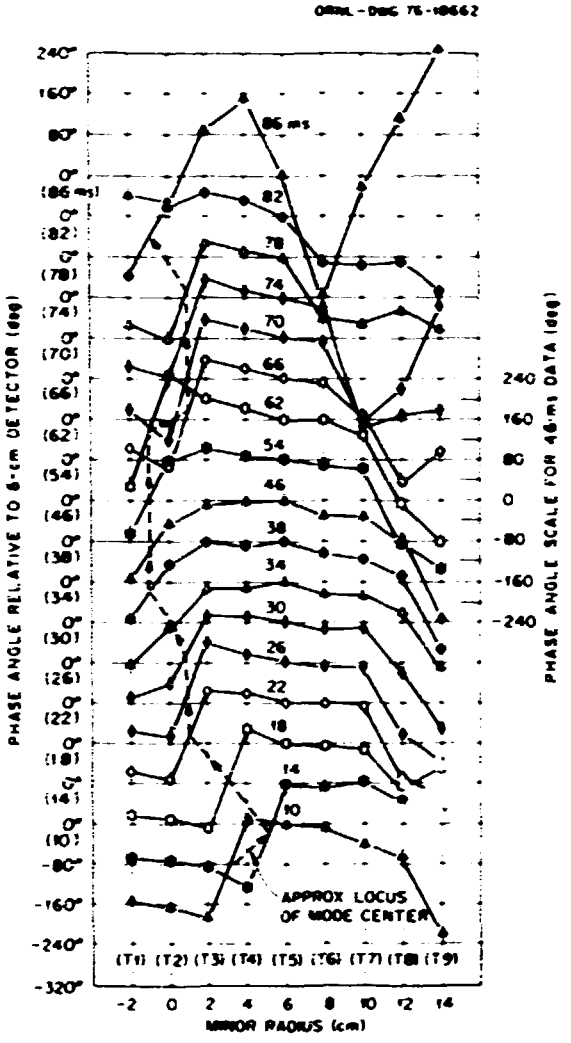

Fig. 2.36. Relative phases of the x-ray signals from the top detector array.

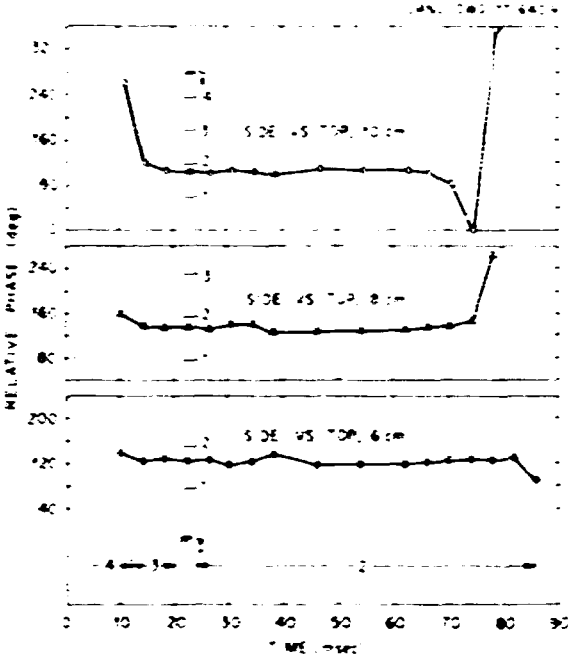

Fig. 2.37. Relative phases of x-ray signals to side and top detectors at minor radii of 6, 8, and 10 cm, and the poloidal mode number of the magnetic loop signal.

when a given sawtooth begins to rise, the temperature and safety factor profiles inside a radius, r_0, are nearly flat due to the preceding disruption; here r_0 is some radius greater than the radius r_s, of the $q = 1$ singular surface. Then, the excess heat between r_s and r_0 diffuses away, producing the heat pulse analyzed at the end of this section. Simultaneously, the electrons inside r_s begin to reheat resistively because the flat temperature profile has a very small gradient and hence little outward heat conduction.

As explained in Ref. 32, our comparisons with experiment show that the resistive heating and electron-ion equilibration terms are sufficient to explain the positive slope of the waveform.

As resistive heating continues, the increase in the electron temperature produces a decrease in resistivity; this leads to an increase in the current and a corresponding reduction in the safety factor (q) to a value less than unity at the origin. As q decreases, the shear ($\equiv dq/dr$) at the singular surface increases. Because the $m = 1$ tearing mode growth rate is proportional to the square of the shear,[32] the growth rate increases rapidly with time until the magnetic island produced by the mode becomes extensive enough to flatten the temperature, current density, and safety factor profiles as magnetic reconnection occurs. Then the process is repeated.

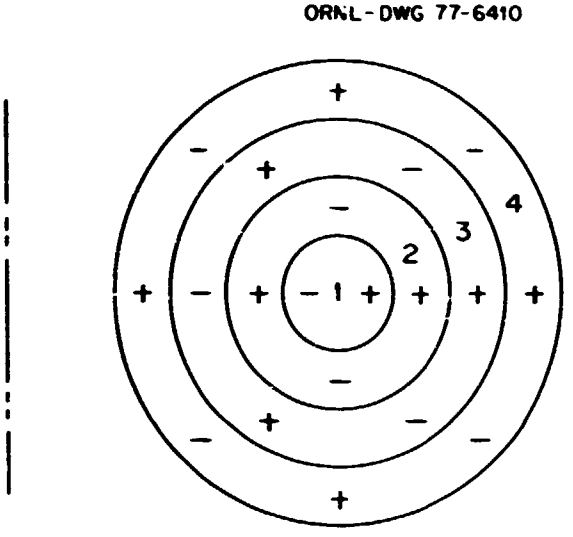

Fig. 2.38. A representation of the mode structure indicated by these studies. Note phase reinforcement along the outward directed radius.

The tearing mode in general is adequate to explain the radial dependence of fluctuation amplitudes. In Ref. 32 we have compared experimental x-ray amplitudes with recent numerical results that are an extension of the tearing mode calculation of Waddell et al.[34] The radial profile of the amplitude of the m = 1 precursor oscillations agrees well with the observed profile. Furthermore, once the temperature has become flat, the radial profile of the dominant m = 0 component of the temperature obtained numerically agrees well with the radial profile of the observed sawtooth amplitude, including the phase reversal at the q = 1 singular surface. However, if diamagnetic drifts were included in the numerical algorithm, the structure of the temperature perturbation near the singular surface might change somewhat.

To make further predictions, specific details must be added to the model. To evaluate the growth rate of the m = 1 oscillation, the time dependence of the shear at the singular surface (α) is estimated[32] to be $\alpha = \alpha_0 + \bar{\alpha}t^2$. The time-dependent linear growth rate (γ) of the tearing mode including diamagnetic drifts[32] is proportional to α^2, so the time dependence of the x-ray fluctuation amplitude is

$$\ln \tilde{A} \propto \int_0^t \gamma(t)dt \propto \alpha_0^2 t + \frac{2}{3}\alpha_0\bar{\alpha}t^3 + \frac{1}{5}\bar{\alpha}^2 t^5 \quad . \tag{2.3}$$

If α_0 dominates in Eq. (2.3), $\ln \tilde{A}$ is proportional to t; if $\bar{\alpha}$ dominates, $\ln \tilde{A}$ is proportional to t^5. As shown in Fig. 2.39, our measurements of the time dependence of the amplitude of the precursor oscillations show that some

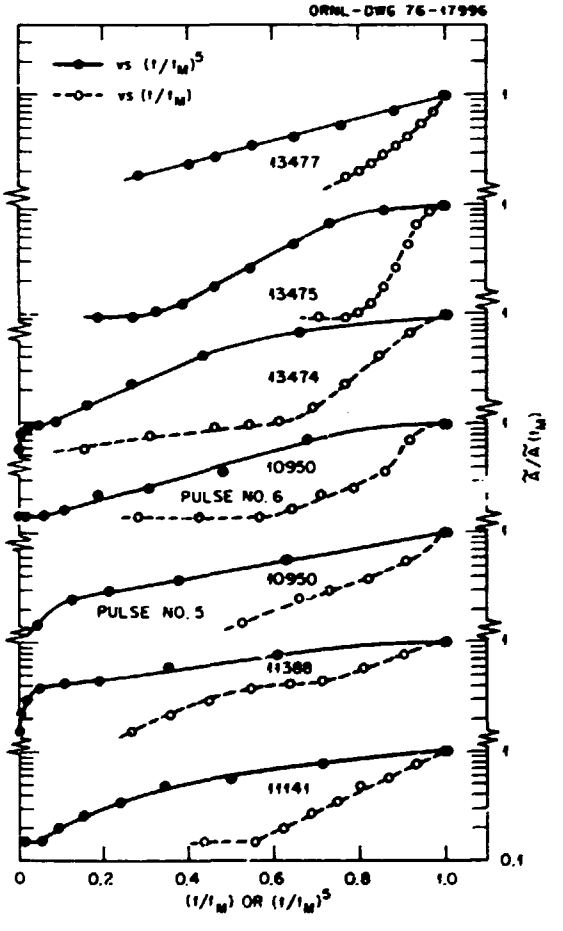

Fig. 2.39. Normalized amplitude of the m = 1 oscillations for the chord nearest the singular surface vs t/t_M and $(t/t_M)^5$, where t_M is the largest time for which the amplitude was measured.

discharges exhibit clearly either t or t^5 dependence while others show what can be interpreted as a transition from t to t^5. Furthermore, for the individual pulse examined in ORMAK discharge 11141, which clearly shows t dependence, the theoretical proportionality constant compares well with the experimental value (9 and 5 $msec^{-1}$, respectively). Similarly, for the example from discharge 13477, which clearly exhibits t^5 dependence, the theoretical proportionality constant is 0.09 $msec^{-1}$ compared to an experimental value of 0.06 $msec^{-1}$. No arbitrary parameters are adjusted in obtaining these proportionality constants.

An inspection of a large number of discharges heated by neutral beams yields t^5 dependence for the growth rate of the m = 1 oscillations. Furthermore, for purely resistively heated discharges the growth exhibits some t^5 dependence, at least for large t. Thus, we expect $\ln \tilde{A}$ to be always proportional to t^5 just before disruption.

Of fundamental interest is a prediction of the sawtooth repetition time (t_0) in terms of plasma parameters. Based on the above discussion, we use the t^5-dependent growth and calculate the time required for the island width to equal $2r_s$. The resulting expression is of the form

$$t_0 = D\bar{t} \quad , \tag{2.4}$$

where D and $\bar{t}$ are defined in Ref. 32. For the present discussion, we simply note that Eq. (2.4) provides a good estimate of t_0, as shown in Fig. 2.40.

In summary, the model described above unites a tearing mode instability calculation with specific plasma dynamics that are suggested by experimental observation. This model compares favorably with data from ORMAK in explaining: (1) the rate at which a sawtooth rises, (2) the radial dependence of the precursor and main sawtooth oscillation amplitudes, (3) the accelerating growth rate of the precursor oscillations, and (4) the repetition time of the sawteeth.

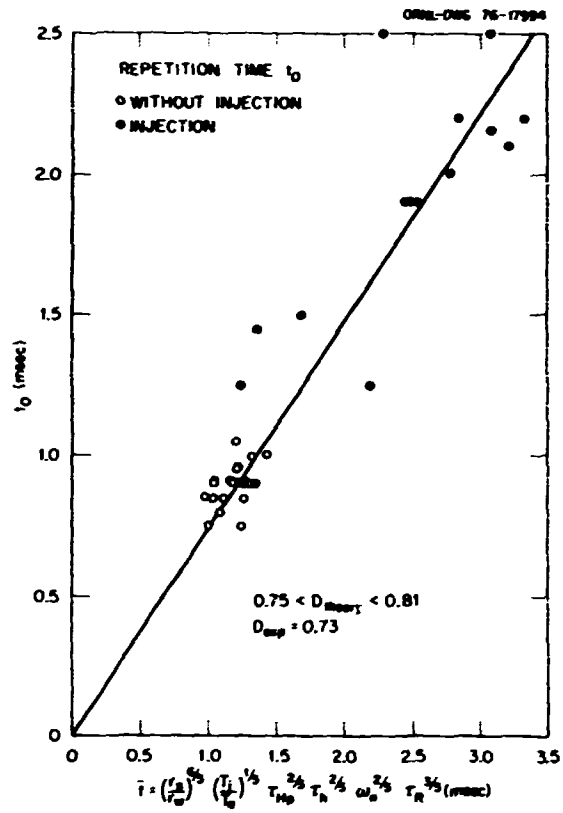

Fig. 2.40. Experimental sawtooth repetition time compared with the theoretical predictions given by Eq. (2.4).

Heat pulse propagation

We have also carefully examined the space-time evolution of the pulse of heat resulting from the internal disruption and have interpreted this evaluation in terms of electron energy transport in the bulk plasma. As has been described previously, the sawtooth shape changes at r_s: inside sawteeth have the slow, linear rise and sharp fall analyzed above; the outside sawtooth's sharp rise coincides with the sharp fall inside, followed by a slower decay. As seen in Fig. 2.41, the outside sawteeth peak later in time and broaden with increasing radius. Our interpretation of this behavior is that the heat lost from the central core due to disruption evolves in the outside region by local transport processes.

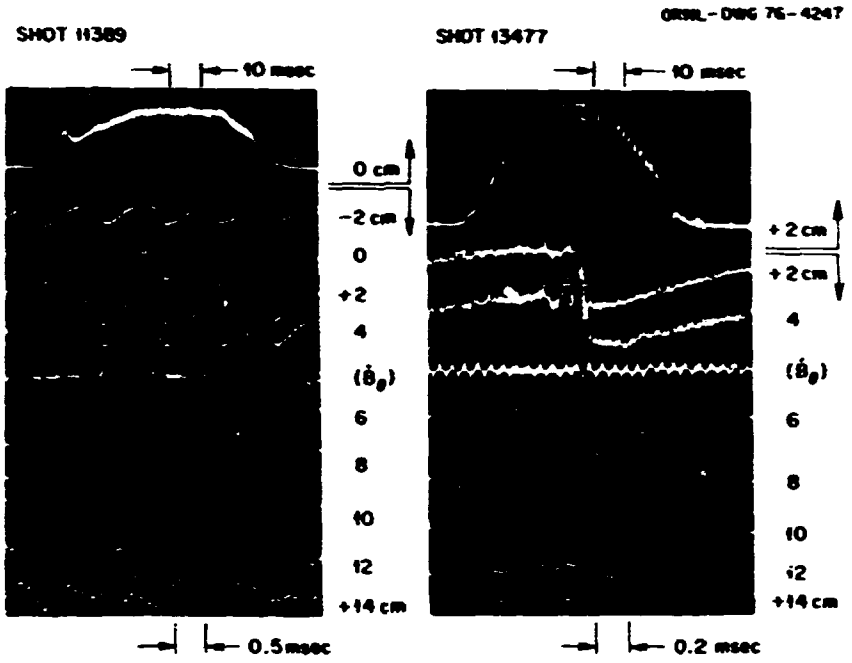

Fig. 2.41. Composite oscillograms of soft x-ray signals for two discharges. For both cases, the top trace gives the signal from one detector over the full time of the discharge; the rest of the signals are on an expanded timescale starting at 45 msec, which falls in the middle of the full-time trace. Amplification factors are different for purposes of display. The temporal variation in the signal (sharp fall inside, sharp rise outside) shows that r_s is 5 cm for shot 11389 and 8 cm for shot 13477. The signals labeled $\dot{B}_\theta$ are poloidal magnetic field fluctuations from pickup loops.

As detailed by Callen and Jahns,[35] the electron heat balance equation for the electron temperature perturbation (ΔT_e) of the heat pulse can be modeled as a simple diffusion equation:

$$\frac{\partial}{\partial t}\left(\frac{3}{2}\Delta T_e\right) = \frac{\chi_{ep}}{r}\frac{\partial}{\partial r} r \frac{\partial \Delta T_e}{\partial r} \quad , \qquad (2.5)$$

where χ_{ep}, assumed constant, is the conduction coefficient associated with the heat pulse. The pulse boundary condition suggested by observation gives, for a single isolated pulse ($t_o > 3r^2/8\chi_{ep}$), the solution

$$\Delta T_e = \frac{8 r_s \Delta Q}{3 n_e r^2}\left(\frac{t_p}{t}\right) e^{-t_p/t} \quad , \quad t_p \equiv \frac{3r^2}{8\chi_{ep}} \quad . \qquad (2.6)$$

The important points to note about this heat diffusion solution are: (1) the peak of ΔT_e occurs at $t = t_p$, which is proportional to r^2 and inversely proportional to χ_{ep}; (2) at a given r, $\Delta T_e(t)$ increases smoothly to its peak in a time (t_p) and then decays roughly as t_p/t thereafter; (3) the maxima of $\Delta T_e(t)$ vary inversely with r^2 – a manifestation of energy conservation in the cylindrical expansion of the heat pulse.

The experimental data are compared with the diffusive model in Fig. 2.42. The first point, demonstrated in Figs. 2.42(a) and 2.42(b), is that t_p agrees with the predicted asymptotic r^2 dependence. Second, the pulse shapes follow calculated curves [see Fig. 2.42(c)]. Finally, Fig. 2.42(d) shows that the maximum ΔT_e decreases

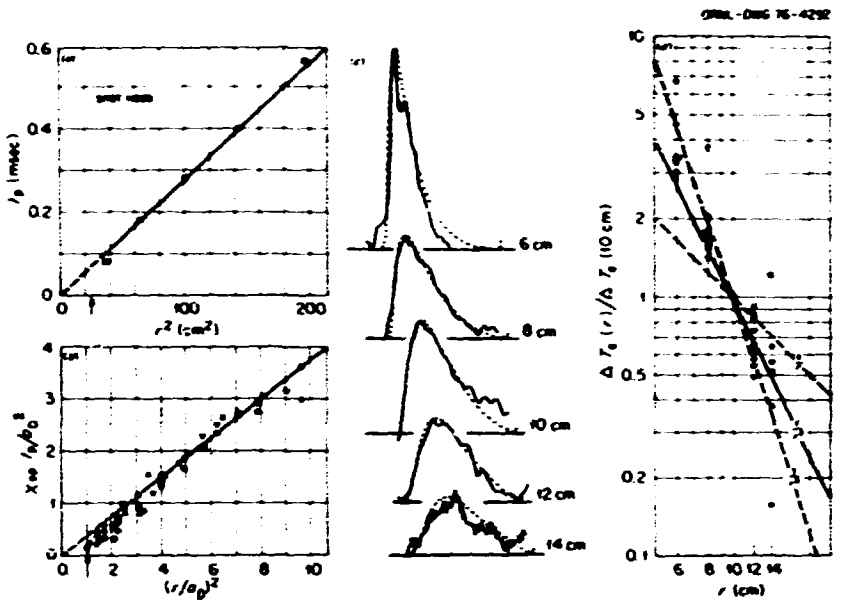

Fig. 2.42. Comparison of data with the diffusion model. (a) Peak arrival time vs radial position. The slope of the asymptote is $3/(8\chi_{ep})$ and thus gives a measurement of χ_{ep}. (b) t_p vs r^2 in normalized units for a representative set of discharges ($a_D \equiv r_s$). Each symbol corresponds to one discharge, for which χ_{ep} has been obtained from a plot such as Fig 2.42(a). Solid symbols are discharges with neutral beam injection, and open symbols are for no injection. (c) Graphical reconstruction of one set of pulses (third from left in Fig. 2.41, shot 11389) compared with normalized computer-generated pulse shapes. (d) Maximum ΔT_e (normalized) inferred from x-ray signal level as a function of radius.

roughly as $1/r^2$. The data show reasonable agreement with the heat conduction model. Thus, we conclude that the heat pulses produced by internal disruptions propagate out through the outside region of ORMAK by a diffusive process, at least on length scales longer than the spatial resolution of the detector array, which is about 2 cm.

Next, we compare the rate of this process with the gross electron energy transport. A conduction coefficient can be estimated from

$$\tau_{Ee} \approx a^2/4\chi_e \quad , \qquad (2.7)$$

where τ_{Ee} is the electron energy containment time obtained by the usual method of dividing the stored energy by the power input (ohmic, plus the fraction of injection power transferred to the electrons, minus the power to the ions). The χ_{ep} determined from heat pulse propagation is compared with the χ_e determined from Eq. (5) in Ref. 35. The comparison shows that: (1) there is little correlation between χ_{ep} and χ_e, and (2) χ_{ep} exceeds χ_e by factors ranging from 2.5 to 15. This disagreement between χ_{ep} and χ_e in both magnitude and scaling is significant and is surprising because one expects the heat pulse propagation to reflect the gross plasma behavior.

We do not yet understand the reason for this disagreement, but experimental correlations discussed in Ref. 35 suggest two hypotheses. First,

there is evidence that χ_{ep} depends on the energy of electrons producing the x-ray signal; these electrons are in the tail of the distribution. This suggests that χ_{ep} is characteristic of high energy electrons in a non-Maxwellian distribution. Second, we observe a correlation between χ_{ep} and r_s, the disruption radius. Empirically, the size of r_s is related to the strength of the internal disruption, so the suggestion here is that the pulse propagation is significantly affected by the driving force of the sawteeth – a feature not included in our model.

In conclusion, the electron temperature perturbations produced by internal disruptions are found to have a clearly diffusive space-time evolution. This heat conduction, however, is not related in a straightforward way to the transport determining the gross confinement of the device.

2.1.12 ORMAK Plasma Modeling

H. C. Howe M. Murakami D. L. Shaeffer

Modeling ORMAK plasmas is accomplished by two different codes: a time-independent code (data analysis code) used primarily to analyze experimental data, and a time-dependent code (transport code) to test various transport models against experiments. In this report period, significant improvements were made on each code.

Improvements of the data analysis code

The code (ZORDIC) used to analyze tokamak data with impurity modelings was upgraded in the following areas.

1) Two new methods of modeling impurities based on the plasma resistance were added to the original model.
2) Injected beam power deposition is calculated and included in the calculation of various transport coefficients. The injection routines used in the transport code were incorporated with this code.
3) Ion power balance is calculated in this code with the ion temperature profiles $T_i(r) = T_i(0) \cdot [1 - (r/a)^{p_i}]^{q_i} + T_o$ is determined from the charge-exchange analysis.

A number of examples of the calculation of the injection power deposition and the ion power balance are found in previous sections. Therefore, we only describe here the impurity modeling.

Three different models for the Z_{eff} of the plasma (and thus for the current density under the assumption of uniform electric field) are now available in this code. These are the Z_η model, the Z_Q model, and the Z_c model. The Z_η model is the original one developed by E. C. Crume and later modified by Shaeffer and Crume. In this model, the impurity density is taken to be a constant fraction of the plasma ion density. The Z_Q model utilizes the mode rational radii r_1^{sx} and r_2^{sx} for $q(r) = 1$ and 2, respectively, determined from the fluctuation mode structure in the soft x-ray signals. The model assumes a current density in the form

$$j(r) = j(0) \cdot [1 - (r/a)^{\alpha}]^{\beta} ,$$

where the free parameters, $j(0)$, α, and β are used to satisfy the constraints $q(r_1^{sx}) = 1$ and $q(r_2^{sx}) = 2$ with proper total current. This current density with the usual small neoclassical resistivity correction yields a space-dependent $Z_{eff}(r)$. The Z_c model assumes that Z_{eff} is constant across the plasma cross section. This model determines the Z_{eff} value by accounting for the total neoclassical resistance, whereas the Z_Q model obtains $Z_{eff}(r)$ by accounting for the neoclassical resistance anomaly at each point along the plasma radius.

Comparisons were made between these models.[36] Considering the accuracy of the measurements involved and the model dependence, determination of a specific Z_{eff} profile is beyond the present capability. However, the results of the comparisons do appear to eliminate the possibility of an extreme central peaking of the Z_{eff} profile. For consistency, we usually use $Z_{eff}(r)$ values resulting from the Z_c model. Knowing $Z_{eff}(r)$,

and assuming a single impurity species (usually iron), we infer impurity density, $n_z(r)$, based on the average ionization state, $Z(r)$, corresponding to the measured T_e profile with a coronal equilibrium. The proton density, $n_i(r)$, is obtained from charge neutrality. (In the Z_c model, the Z_{eff} very near the plasma edge is allowed to deviate from the constant Z_{eff} value in order not to violate charge neutrality.) The various quantities related to plasma energy (such as β_p and τ_E) are based on the ion energy content with $n_i(r)$ calculated in that fashion.

The Z_{eff} values determined from the resistance are generally in qualitative agreement with those estimated from other measurements. For example, as reported earlier,[37] the absolute intensity of the soft x-ray continuum gives an estimate of Z_{eff} which is consistent with the Z_{eff} inferred from the resistance measurements. Therefore, it is believed that most of the plasma resistance is accounted for by impurities in the plasma.

However, accuracies of each measurement and its interpretation are far from being satisfactory for quantitative comparison between the measurements. For instance, the resistance measurement needs a more complete theory of plasma resistance in the presence of impurities with multiple ionization states. Along this line, new theoretical efforts were made by Kirillov et al.[38] to include unstripped high-Z impurity in the resistance formula.

They attempted to explain the observed tokamak resistance anomalies, which lie in the range of 2-50 for U.S.S.R.'s TM 3, by the presence of ionized heavy impurities such as iron, molybdenum, and tungsten. However, the larger anomalies required impurity ion densities larger than might reasonably occur experimentally. In an attempt to reduce the required impurity ion densities, they considered the effect of the residual electron core on the momentum transfer cross section for electron-impurity collisions. This effect was evaluated for typical ORMAK discharge data by Shaeffer.[39] Results indicated that only elements of high atomic number (such as gold) will reduce Z_{eff} significantly (about 15%), whereas Z_{eff} for a species of an intermediate atomic number (such as iron) is reduced only about 5%. This is contrary to their analysis of TM-3 data, which were taken early in the discharge when the impurity stripping was still in progress. Because the core effect varies roughly as Z_j^{-2} (Z_j being the average charge state of the impurity), a more pronounced reduction in Z_{eff} occurs early in the discharge when the impurity stripping is incomplete.

Improvements of the transport code

The transport code used primarily to model ORMAK was improved this year. Major changes include the following.

1) The neutral particle routine calculates the neutral temperature and thus gives an improved estimate of the charge-exchange energy loss.
2) A new neutral routine includes the effect of wall reflection of fast neutrals.
3) The complete Fokker-Planck routine, written by Fowler et al., was incorporated into the transport code and used to study loss cone effects for counterinjection in ORMAK.
4) An interactive version of the transport code with real time graphics display was implemented on the Fusion Energy Division (FED) PDP-10. This code allows the user to interact with the code during execution and has proven valuable for studying a variety of problems including gas puffing and radiation-dominated transport models.
5) A routine to simulate electron-cyclotron resonance heating (ECRH) was added and used to predict the performance of the Impurity Study Experiment (ISX).
6) A wall refluxing model and a Ware pinch term were added and found to lead to more realistic reproduction of the density behavior in ORMAK.
7) More realistic impurity stripping and radiation models were added.
8) The beam penetration routine now includes impurity ionization by charge exchange.
9) Finally, the code was completely documented

internally, and several routines were fully modularized for export.

2.1.13 Interpretation of Charge-Exchange Measurements

A. C. England J. T. Mihalczo G. H. Neilson
J. F. Lyon R. V. Neidigh J. B. Wilgen
R. W. McGaffey

The previous annual report[40] discussed the difficulty of determining a central ion temperature from the energy distribution of charge-exchange neutrals leaving the plasma and indicated the need for a better solution than the approximate correction method outlined. A better procedure has been developed which closely models the measured charge-exchange energy distribution. It also permits evaluation of the uncertainty in the calculated $T_i(r)$ due to different assumptions in the calculation as well as statistical uncertainties in the data.

In addition, the comparison of charge-exchange estimates of the ion temperature with those inferred from absolute neutron measurements has been extended and a modeling of the measured H_α (6563 Å) spectral line profile is in progress.

The problem: interpretation of charge-exchange flux

The central ion temperature is usually inferred from the high energy slope of the ion distribution function determined from chordal measurements of the charge-exchange flux. Figure 2.43 shows two such ion distribution functions obtained for no injection and 360-kW H^0 injection into hydrogen plasmas with $I = 175$ kA, $B_T = 26$ kG, and $\bar{n}_e = 2.8 \times 10^{13}$ cm^{-3}. The slope is not constant with charge-exchange neutral energy primarily because of the chordal integration over temperature and density profiles and, to a lesser extent, because of the energy-dependent attenuation of the escaping charge-exchange neutrals. At low particle energies the charge-exchange flux is predominantly from the plasma edge, and only the higher energies are sensitive to the central region. Typically, determination of the slope at energies $E/T_i(0) > 7$ is needed to obtain a central temperature estimate within 10%

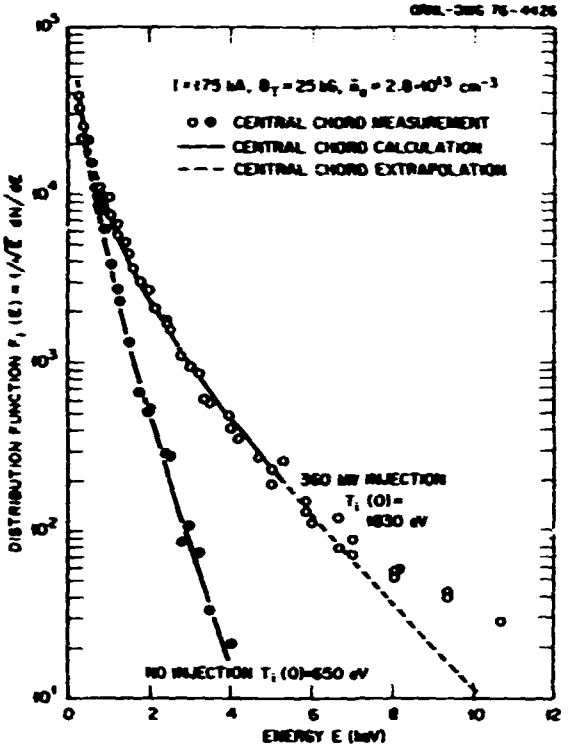

Fig. 2.43. Comparison of perpendicular charge-exchange data with the modeled ion energy distribution for no injection and 360 kW of injection into 175-kA, $\bar{n}_e = 2.8 \times 10^{13}$ cm^{-3} discharges.

accuracy. However, at these higher energies the charge-exchange distribution may be distorted by poor counting statistics and noise, by non-Maxwellian components of the ion distribution function, and (with injection) by beam ions which have lost most of their initial energy.

Procedure for interpretation of charge-exchange spectrum

Previously,[40] charge-exchange modeling studies indicated that the main effect of the plasma profiles was to produce a modified Maxwellian distribution $E^B e^{-E/T_i(0)}$ for charge-exchange neutral energies $E > T_i(0)$ where $B \approx 1/2$, the exact value depending on the plasma parameters. This rough correction has been replaced by another procedure in which $T_i(r)$ is obtained by minimizing the difference between the

measured charge-exchange flux and a model calculation of the flux utilizing data for energies up to ~3 $T_i(0)$ (with injection) and for different radial chords.

To determine the best fit for the charge-exchange data to that calculated, a form for $T_i(r)$ is assumed, usually $T_i(r) = [T_i(0) - T_i(a)] \times [1 - (r/a)^p]^q + T_i(a)$. An rms error ϵ_{rms} is defined, $\epsilon_{rms}^2 = 1/M \sum_i \epsilon_i^2$, where

$$\epsilon_i = \ln N_{i_{meas}} - \ln N_{i_{calc}} ,$$

and the sum i = 1 to M extends over the desired range of energies and radial chords.

The fitting parameters for $T_i(r)$ are then iterated [typically p = 2 is chosen and $T_i(0)$ and q are varied] to minimize ϵ_{rms}; this form for $T_i(r)$ is the nominal best fit to the data.

Figure 2.43 shows examples of the data and the best fit calculations for two cases — one for no injection and the other for 350-kW H^0 injection. Typically, ϵ_{rms} = 5-10% and q = 1.5-2 for a wide range of cases. If data above 7 keV in Fig. 2.43 are used in this procedure, much larger values for ϵ_{rms} are obtained. This is not unexpected because solution of the Fokker-Planck equation for the fast ion distribution in ORNAK indicates that this distribution should join the background ion distribution at an energy ratio $E/T_i(0) \sim 4$-5, or E ~ 8 keV for this case. Additionally, the fast ions interact preferentially with the faster ions in the background plasma, distorting the background ion distribution from a Maxwellian, as discussed by Cordey.[41] This effect becomes significant for this case for $E/T_i(0) \sim 3$-4, or E ~ 6.5 keV.

The effect of statistical errors on this fitting procedure is expressed in two ways: (1) the error bars on the fitting parameters [$T_i(0)$, q, etc.] due to counting statistics, and (2) the ϵ_{rms}^2 expected due to statistics alone if the exact temperature and density profiles were known.

The advantages of this procedure are that it allows use of the more representative intermediate energy range data [$E/T_i(0) \lesssim 3$] and permits evaluation of the effect of different assumptions and of statistics on the data analysis. In addition, the analysis gives an ion temperature profile, $T_i(r)$, that best fits data at all energies and radial chords analyzed and also gives an estimate of $n_0(0)$ $n_+(0)$ from the absolute count rate. The real test of the procedure is how the $T_i(r)$ determined compares with that calculated from other ion temperature diagnostics such as the neutron measurements and the H_α spectral line profiles discussed below.

Neutron measurements of ion temperature

In last year's annual report, we reported first comparisons between central deuteron temperatures obtained from charge-exchange analysis and neutron measurements. Further analysis of the data has shown good agreement between the temperatures over a wide range of experimental conditions.

The derived temperature is obtained from a calibrated neutron counting rate, assumed parabolic density and temperature profiles, a deuteron defect (n_D/n_e) obtained from laser scattering, interferometer measurements of $\bar{n}_e$, and an empirical fit for the D-D reaction cross section. There are no adjustable parameters. Figure 2.44 shows a comparison between the charge-exchange and neutron temperatures for two cases. The circles indicate temperatures obtained at 50 msec into the discharge from four different sets of runs where there were respectively zero, one, two, and three injectors. The squares indicate the points taken from one of these sets (the one-injector set) as a function of time during the discharge. The squares are at 5 msec intervals from 5 to 55 msec.

The line of 45° slope indicates the expected agreement and is not a fit to the data. In all cases, there are periods of good agreement between the two kinds of measurements.

Comparison with H_α spectral line profiles

Another measure of the ion temperature profile, especially near the plasma edge, is the Doppler broadening of the H_α (6563 A)

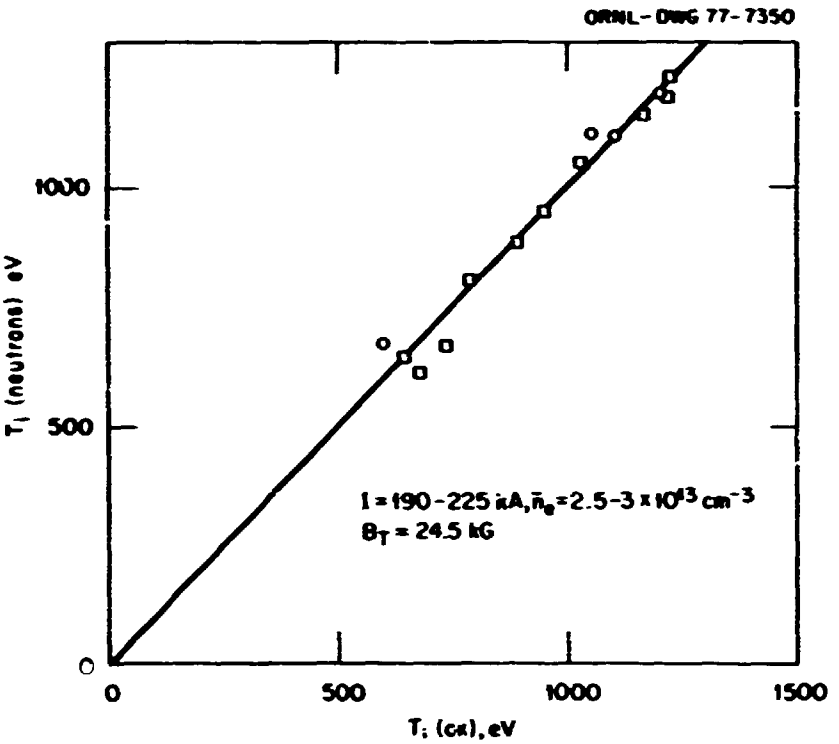

Fig. 2.44. Agreement between neutron estimates and charge-exchange estimates of the central ion temperature for deuterium plasmas with hydrogen beam injection.

spectral line profile, as discussed in Sect. 2.7. In a procedure similar to that described in the interpretation of the charge-exchange energy distribution, the profiles of neutral density, n_0, and temperature, T_0 (mean energy), are obtained from a one-dimensional neutral transport code using Thomson scattering data to obtain $n_e(r)$, $T_e(r)$, $n_i(r)$, and an assumed form for $T_i(r)$. From these quantities the spectral intensity, $I_{H_\alpha}(\lambda)$, is calculated by integrating over the viewing volume. The calculated intensity is given by the convolution of the spectrometer resolution function with the expected intensity

$$I'_{H_\alpha}(\lambda) = C \iint n_e(r)\, n_0(r)\, \frac{\langle \sigma_{ex} v_e \rangle}{\sqrt{T_0(r)}} \exp\left[-\left(\frac{\lambda}{\lambda_0}\right)^2 \frac{mc^2}{2kT}\right] ds \quad ,$$

where λ_0 = 6563 Å and the rate coefficient $\langle \sigma_{ex} v_e \rangle$ for electron excitation from the n = 1 to n = 3 level was taken to be constant in this preliminary calculation. The form for $T_i(r)$ is then iterated to get the best fit between the measured spectral intensity (squares) and the calculated intensity (circles), as shown in

Fig. 2.45. Although the agreement is good, further work needs to be done to refine the calculation and to further integrate it into the charge-exchange interpretation procedure.

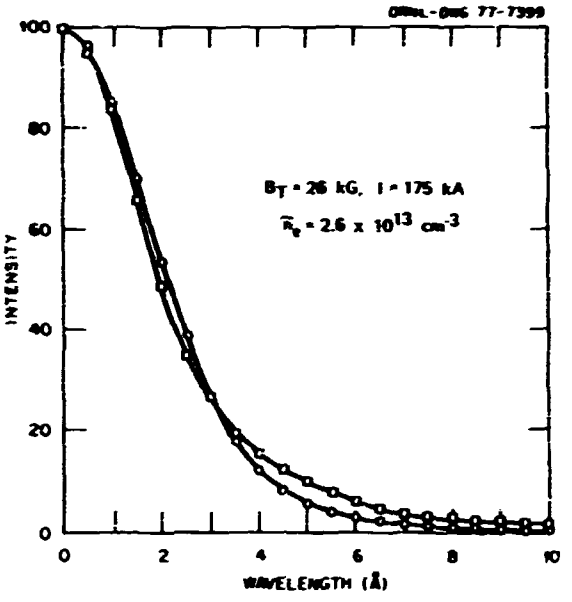

Fig. 2.45. Comparison between measured (solid curve) spectral line profile of H_α (6563 A) and that calculated (dashed curve normalized at line center) from the procedure described in the text.

2.1.14 Effects of Injection on Plasma Equilibrium

J. L. Dunlap M. Murakami
J. F. Lyon R. V. Neidigh

In the last three years, the effect of neutral beam injection on the Ohmic plasma has grown from a small perturbation ($P_{inj} \sim 45$ kW, $\Delta T_i/T_{io} \leq 0.25$) to a major modification of the plasma ($P_{inj} \sim 350$ kW, $\Delta T_i/T_{io} \sim 2$). In some cases injection has become the major power input to the plasma (for I = 75 kA, $P_{inj}/P_{OH} \sim 3$ and $\Delta T_e/T_{eo} \sim 1.5$). These higher power levels have led to extensive ion heating (Sect. 2.1.2), electron heating (Sect. 2.1.3), high β_T (Sect. 2.1.4), and higher attainable plasma densities with gas puffing (Sect. 2.1.5). In addition there are some deleterious effects, such as the impurity influx with counterinjection that depresses the central electron temperature (Sect. 2.1.7), as well as the beneficial effect of being able to have grossly stable discharges for lower limiter safety factors [q(a) = 2.5 vs q(a) > 3.5 without injection] as discussed in Sect. 2.1.4. Here we discuss two other effects of high power injection ($P_{inj} > P_{OH}$): changes in the plasma equilibrium (which are observed), and large bulk ion toroidal rotation (which does not occur).

Modification of plasma equilibrium by injection

For the high power ($P_{inj} > P_{OH}$), low density ($\bar{n}_e \sim 2 \times 10^{13}$ cm^{-3}) injection experiments, the beam slowing down time is considerably longer than the plasma energy confinement time, and we should expect the beam stored energy to be greater than the plasma energy. This modifies the plasma equilibrium and makes it necessary to feedback-control the vertical field with injection. In fact, the plasma position measurement provides an estimate of the stored fast ion energy through the equilibrium condition. The increase in the beam and plasma energies by injection is related to the additional vertical field provided by the feedback circuit to maintain the center of the plasma column at a prescribed position. Figure 2.46 illustrates the evolution of the quantity

$$\beta_\ell' = \beta_p + \frac{\ell_i}{2} + \frac{4}{\mu_0 R_0 I^2}\left(W_{\parallel b} + \frac{W_{\perp b}}{2}\right)$$

for plasmas with and without injection. Because the derivation of β_ℓ' involves several uncertain parameters (e.g., stray field from the iron core and the gap constant), the difference

$$\delta\beta_\ell' = (\delta\beta_\ell')_{inj} - (\delta\beta_\ell')_{no\ inj}$$

between the values for the injection and no injection cases is a more reliable quantity than are the individual values. Taking into

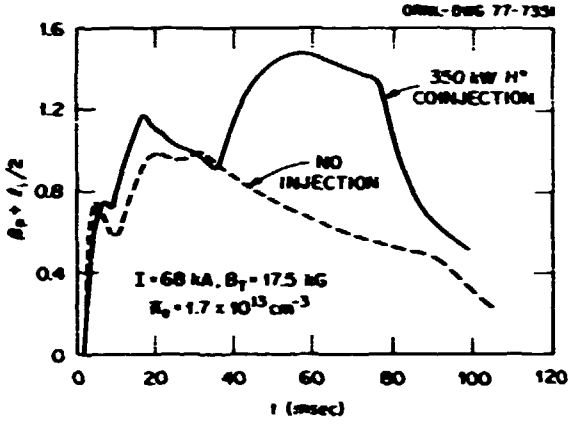

Fig. 2.46. Plasma equilibrium measurement indicates that the beam stored energy is approximately equal to the plasma stored energy for 360 kW of injection into a 68-kA, $\bar{n}_e$ = 1.7 x 10^{13} cm^{-3} hydrogen discharge.

account differences in β_p, and assuming $j \sim T_e^{3/2}$, we estimate

$$\frac{\delta W_f'}{\beta_p} = \frac{4}{\mu_0 R_0 I^2}\left(W_{\parallel b} + \frac{W_{\perp b}}{2}\right)\Big/\beta_p \sim 0.9 \quad .$$

In order to translate this ratio to the ratio (Γ_f) of the stored fast ion energy to the plasma energy, a multiplicative constant has to be determined, depending on the anisotropy of the fast ion distribution function. This multiplicative constant ranges between 1.5 and 1.2; therefore, the value of Γ_f from this measurement gives an estimate ranging from 1.3 to 1.1. This value is somewhat smaller than the value (1.9) calculated from the numerical calculation of the beam slowing down and pitch-angle scattering.

The internal modes explored by soft x-ray diagnostics are also affected by injection. Figure 2.47 illustrates the observations usually obtained with coinjection. The x-ray data are for a central chord. As indicated, the singular surface for q = 1 moves outward, and both sawtooth amplitude and period increase with injection. While the sawtooth amplitude and period start decreasing at beam turnoff and again at the start of plasma current rundown, the position of the q = 1 surface inferred from the sawtooth

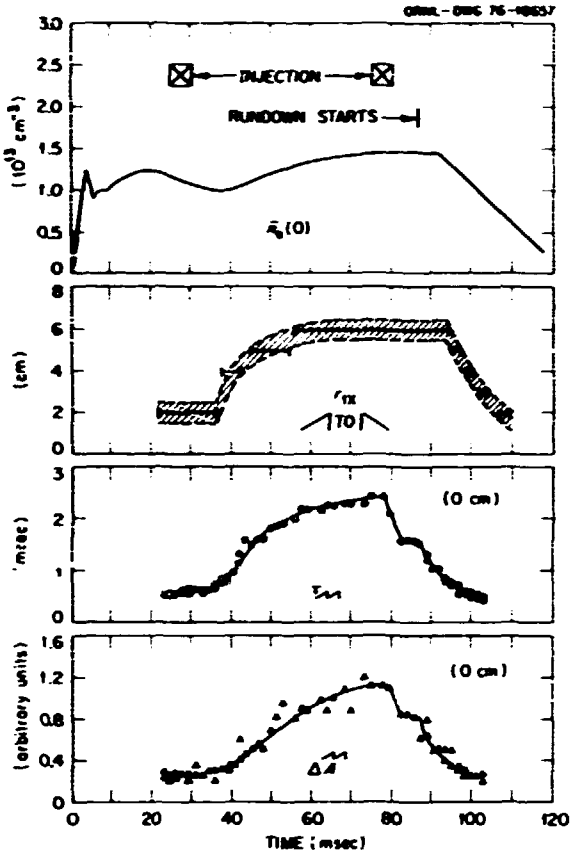

S-15494. $\Delta\tilde{A}$, τ_{sw}, r_{1X} AND $\bar{n}_e(0)$

(100 kA, 15 kG, $q(a)$=5.0, 2+3 CO-INJECTION)

Fig. 2.47. Time history of central chord-averaged density $\bar{n}_e$, radius r_{1X} for sawtooth phase reversal, sawtooth period τ, and sawtooth amplitude ΔA for 350 kW of H^0 coinjection into a 100-kA hydrogen discharge.

phase reversal remains constant and does not start to decrease until the density decay starts.

The behavior of the q = 1 location shown in Fig. 2.47 is probably not related to a nonresistive plasma current contribution from the slowing down beam ions, although the magnitude of this current is theoretically not small. For example, for the plasma parameters shown in Fig. 2.46, this calculated current perturbation is 21 kA, or 30% of the total plasma current. It could be an even larger fraction of the ohmic current density on the axis because of the calculated beam

peaking on axis. However, no direct evidence for this current has been obtained, and other effects expected – such as the large toroidal rotation discussed below – definitely do not occur.

Absence of beam-induced toroidal rotation

Despite the reduced ion heating efficiency and increased impurity radiation losses associated with counterinjection, there has been a supposed need for counterinjected beams to balance the toroidal momentum input expected from coinjected neutral beams. The average ion toroidal flow velocity, $V_{\parallel i}$, can be obtained from a toroidal momentum balance equation:[42]

$$m_i n_i \frac{dV_{\parallel i}}{dt} = \dot{n}_f m_b V_{bo} \cos\theta_o (K_e + K_i) - m_i n_i V_{\parallel i}/\tau \quad , \tag{2.8}$$

with the fast ion density input rate,

$$\dot{n}_f = \frac{(I_b/e)\, h(r)}{(2\pi R_o)(a^2)} \quad . \tag{2.9}$$

The first term on the right-hand side of Eq. (2.8) is the beam momentum input, where θ_o is the injection angle to the field and the beam momentum transfer fraction $K_i + K_e \approx 1$. In these equations $m_i = m_b$. V_{bo} is the initial beam velocity, τ is a toroidal momentum damping time, and $h(r)$ is the spatial shape factor[42] for the beam deposition. Solving Eq. (2.8) gives

$$V_{\parallel i} = \frac{(I_b/e)\, h(r)}{(2\pi R_o)(\pi a^2)} \frac{V_{bo}\cos\theta_o}{n_i} \times \tau\,(1 - e^{-t/\tau}) \quad . \tag{2.10}$$

Because the shortest classical damping time, $\tau = \tau_{cx} \geq 60$ msec, is longer than the beam pulse length, $\Delta t \leq 50$ msec, Eq. (2.10) gives

$$V_{\parallel i}/V_{bo} = \frac{2}{3} \frac{I_b(A) h(r) \Delta t}{n_i (10^{13}\ \mathrm{cm}^{-3})} \quad , \tag{2.11}$$

or

$$V_{\parallel i} \approx \frac{h(r)}{3} V_{bo} \approx 7 \times 10^7\, h(r)\ \mathrm{cm/sec}$$

for the parameters of Fig. 2.46. Since $h(0)$ is calculated to be ≈14 for this case, $V_{\parallel i}(0) \sim 5.5\, v_{bo} \approx 10^9$ cm/sec, an impossibly large value. Equation (2.10) is not correct for $V_{\parallel i} \geq V_{bo}$, and there is reason to believe that $V_{\parallel i}$ might be limited to much lower velocities ($\sim c_s$, the ion sound velocity) due to the onset of shocks in the plasma. Even this velocity, $V_{\parallel i} \sim \sqrt{kT_e/m_i} \sim 2.8 \times 10^7$ cm/sec, is quite large.

Estimates of the experimental values for $V_{\parallel i}$ come from two sources, the Doppler shift of the H_α line profile described in Sect. 2.1.9 and from comparison of the parallel and perpendicular charge-exchange energy distributions. The former measurement is weighted toward the plasma outside while the latter measurement is more representative of the plasma interior. H_α measurements similar to those discussed in Sect. 2.1.9 indicate that the toroidal velocity in the plasma interior is ≈6 × 10⁶ cm/sec with oxygen discharge conditioning, and moreover there is no significant change in this velocity with injection. Even the change from oxygen discharge cleaning with no injection to hydrogen discharge cleaning with injection produces a change in interior rotation velocity of ≤2 × 10⁶ cm/sec. The charge-exchange estimates are less certain, but they also give comparably small changes in interior rotation velocity.

Taking $\Delta V_{\parallel i} \sim 2 \times 10$ cm/sec gives [from Eq. (2.11)], a damping time $\tau = \Delta t \sim 1.4/h(r)$ msec or ≈100 μsec for the plasma interior, much faster than any classical process. It is also not plausible for this momentum to be transferred by collisions to plasma ions at the plasma edge where it is then lost either by charge exchange to the wall or directly to the limiter. Balancing the beam momentum input rate against the calculated ion loss rate requires each ion

to carry out much more additional momentum with injection than is observed. It is probably a field interaction rather than a direct particle loss that carries the momentum to the wall, but we do not yet understand the mechanism for this loss.

2.1.15 Transport Modeling of Gas Puff Experiments

H. C. Howe

The density in a tokamak discharge is sustained against diffusive loss by a flux of cold neutral hydrogen from the wall. In a gas puff experiment, the flux is increased 10 torr liters/sec by bleeding in gas from an external source. Because the cold wall flux penetrates only several centimeters into the plasma, most of the additional plasma source is near the wall. The subsequent evolution of the density is modeled using a transport code where the calculated neutral density includes neutrals generated by charge exchange within the plasma as well as wall-reflected neutrals. Because the plasma source is near the wall, the model density rapidly peaks off axis (Fig. 2.48). Experimentally, the central density increases rapidly due to gas puffing, indicating the presence of a mechanism to carry plasma inward.

One candidate for an inward transport force on the plasma density is the Ware pinch. When this effect is included in the transport model, the central density is governed by a balance between the pinch and diffusion. The density near the wall (in the bulk of the discharge) results from the usual equilibrium between the neutral source and diffusion. The gas puff increases the edge density and, by reducing the central gradient and hence the diffusive loss, allows the pinch to increase the central density (Fig. 2.48). The rapid increase of the central density is reproduced well by this model.

Two effects predicted by the gas puff model are not present experimentally. In the model, the density increase due to the puff cools the peripheral regions and shrinks the current channel. The resulting voltage increase which is predicted is not observed experimentally; current channel shrinkage is, therefore, probably

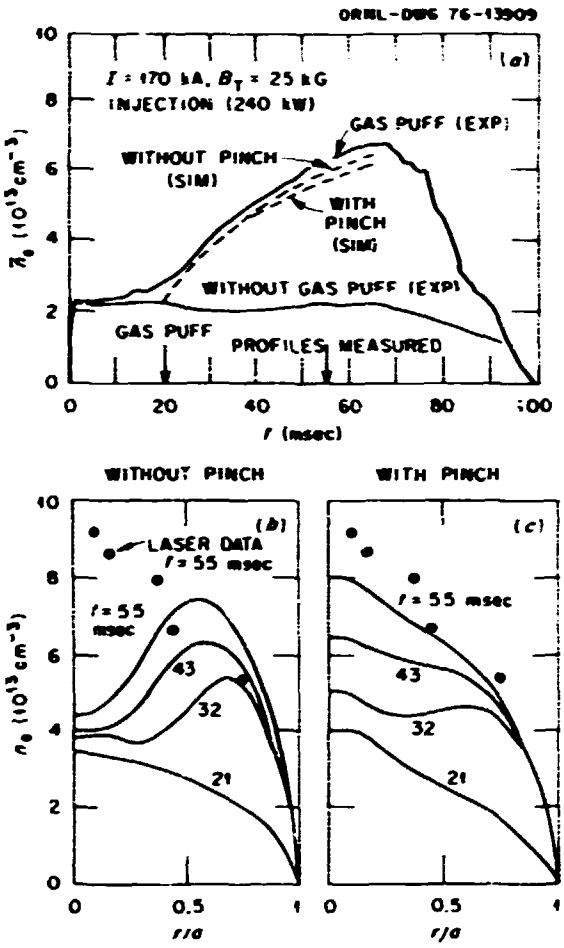

Fig. 2.48. The observed and modeled line density time behavior with and without a gas puff in ORMAK. The evolution of the profile is modeled without and with a pinch. Comparison with the measured profile shows the improvement in the model due to the Ware pinch.

not the cause of the disruption limit of density in gas puff experiments. Also, due to the pinch the density profile in the model becomes very narrow during the decay following a short puff. The case for the existence of the pinch would be much stronger if this profile narrowing were observed experimentally.

2.1.16 Wall Power Measurements

C. E. Bush J. F. Lyon

The preceding annual report[43] discussed time-resolved measurements of energy transport to

the ORMAK liner made using a radially movable pyroelectric detector. These measurements indicated that a large (~60-75%), relatively constant fraction of the input ohmic power was lost to the liner, rather than to the limiter, over a wide range of input powers and for most of the discharge duration. During the last year these studies were extended to higher density plasmas obtained with gas puffing and to injection-heated plasmas where the injected power exceeded the ohmic heating power. In addition, these data were correlated with vacuum ultraviolet spectroscopic observations which were not available during the preceding period. The result was a better understanding of the impurity radiation losses in ORMAK.

The use of gas puffing to increase the plasma density in ORMAK is discussed in Sect. 2.1.5. Two types of wall power behavior are observed for no injection plasma cases preceded by oxygen discharge cleaning. Figure 2.49(a) shows the plasma behavior obtained for the higher plasma densities ($\bar{n}_e \geq 4 \times 10^{13}$ cm^{-3}) obtained at higher plasma current ($I \sim 175$ kA). Except for the early discharge behavior ($t \leq 15$ msec) and for disruptions occurring late in the discharge ($t \geq 85$ msec), the radiometer (wall power) signal is nearly constant in time as the plasma density more than doubles. The power loss per plasma particle (almost entirely radiation in this ohmically heated discharge) decreases as the density increases, although the electron temperature remains relatively unchanged. This may indicate a reduction in the impurity density at the highest plasma densities.

For lower density ($\bar{n}_e \leq 4 \times 10^{13}$ cm^{-3}) discharges obtained with gas puffing, the plasma behavior is as shown in Fig. 2.49(b). After a delay of ~10 msec, the radiometer signal closely follows the plasma density behavior. In this case the plasma current and voltage are approximately constant (and hence the ohmic power input), as is the electron temperature. The proportionality of the radiometer signal (again essentially entirely due to impurity radiation) to the plasma density may indicate a relatively constant impurity density.

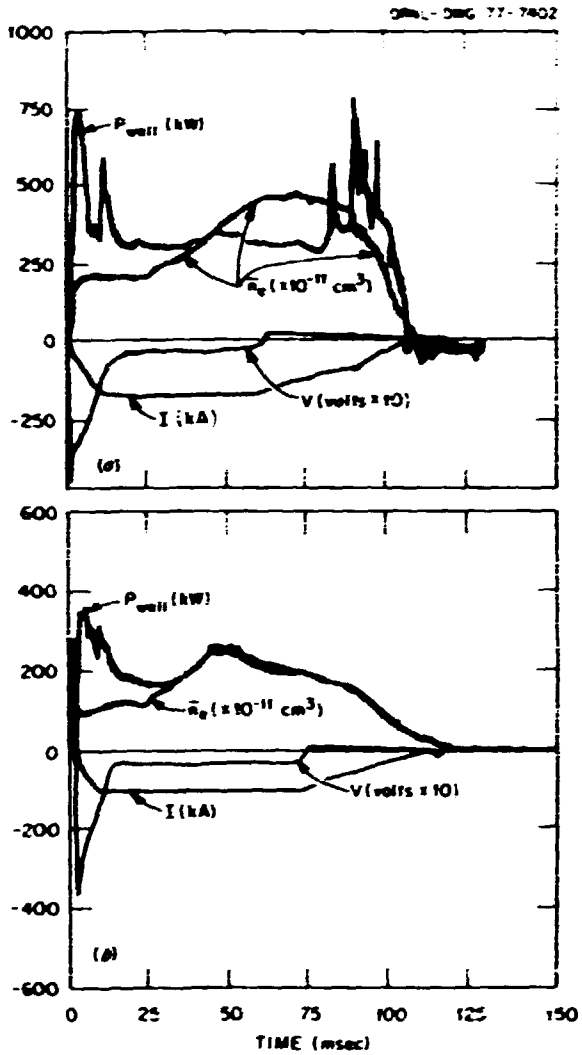

Fig. 2.49. Discharge time behavior (plasma current I, loop voltage V, central line-averaged density $\bar{n}_e$, and radiometer signal P) with gas puffing. A high density ($\bar{n}_e = 2.5 \times 10^{13}$ cm^{-3}), high current (I = 175 kA) case is shown in (a) and a lower density ($\bar{n}_e = 2.5 \times 10^{13}$ cm^{-3}), lower current (I = 100kA) case is shown in (b).

The variation of the wall power flux with total input power (ohmic plus beam heating) up to 1 MW is shown in Fig. 2.50 for plasmas with both hydrogen discharge cleaning and oxygen discharge cleaning preceding the experimental run and for no injection, coinjection, counterinjection, and coinjection plus counterinjection cases. There is a clear distinction between discharges

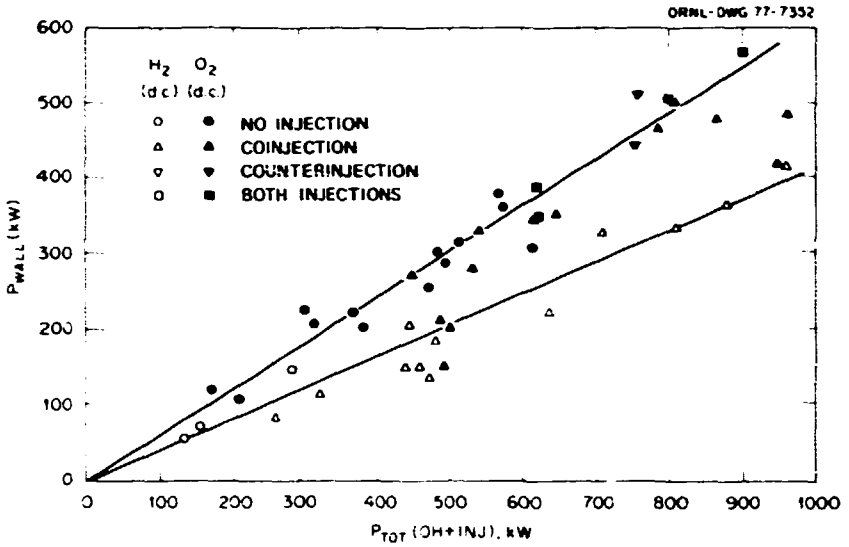

Fig. 2.50. Approximate linearity of radiometer power measurement with total input power for both hydrogen and oxygen discharge cleaned plasmas with different injection conditions.

preceded by hydrogen discharge cleaning and those preceded by oxygen discharge cleaning. Typically ~40% of the input power goes to the walls with hydrogen discharge cleaning and a much higher fraction (~60%) with oxygen discharge cleaning. There is also a tendency for the fraction of the input power going to the walls to be less with coinjection and more with counterinjection than for the no injection cases. The values for the wall power flux in Fig. 2.50 are obtained from the radiometer signal using the calculated detection geometry and the assumption of uniform wall power flux. While there may thus be some uncertainty in the absolute determination of the wall power flux, the relative variation shown in Fig. 2.50 is thought to be accurate. The remainder of the power presumably goes to the limiter.

The distinction between the results obtained for the two types of discharge cleaning does not hold for the coinjection cases plotted between 450- and 500-kW input power in Fig. 2.50. These low current (~75 kA) cases represent injection power (~350 kW) larger than ohmic heating power (~150 kW), as discussed in Sect. 2.1.3. The interpretation of the radiometer signal as being mainly due to impurity radiation may not hold for these cases, in which the ion power input is not small compared to the electron power input. Figure 2.51 shows the time behavior of the basic plasma parameters and some impurity radiation signals for such a discharge following hydrogen discharge cleaning. In this case $I = 75$ kA, $\bar{n}_e = 2 \times 10^{13}$ cm^{-3}, and significant electron heating occurs (doubling of the electron temperature). The radiometer signal rises rapidly in the 15 msec following beam turnon and then has a more gradual and often small increase for the beam duration, similar to the behavior seen in the plasma-stored energy (see Sect. 2.1.3). The radiometer signal falls quickly in the 15 msec following beam turnoff, unlike the plasma-stored energy, and by 95 msec (<20 msec after beam turnoff) has the same value as that obtained in cases without injection.

In all cases the radiometer signals are well correlated with the narrow band continua in the range of 20-70 Å, which account for most of the impurity radiation seen spectroscopically. Good

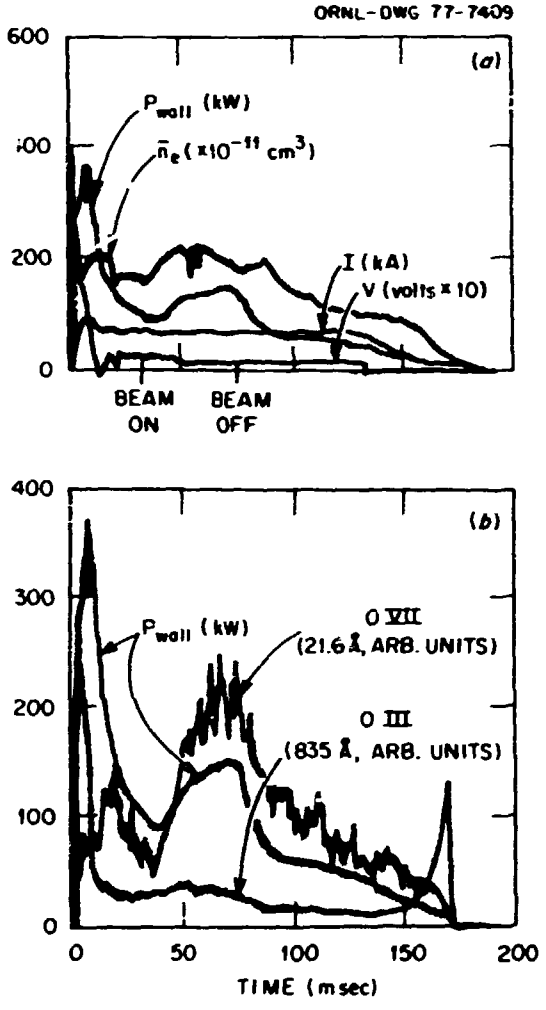

Fig. 2.51. Correlation of radiometer signal (a) with discharge parameters and (b) with specific impurity lines when the neutral beam injection power (~350 kW) exceeds the ohmic heating power (<150 kW).

correlation with the O VII and O VIII line intensities is also seen, as shown in Fig. 2.51(b), but the correlation is much weaker for the O VI line (150 A) originating at a larger radius (maximum for $T_e \sim 40$ eV). No correlation is seen with other impurity radiation, such as the O VI (1032 A), O V (629 A), O IV (790 A), and Fe XVI (360.8 A) lines.

2.1.17 Neutron Time Behavior Due to Deuterium Neutral Beam Injection into a Hydrogen Plasma

A. C. England H. C. Howe
R. H. Fowler J. T. Mihalczo

Neutrons were produced by D-D reactions when 28-keV deuterium beams were coinjected into a hydrogen plasma in ORMAK (I = 110 kA, B_t = 18 kG, $\bar{n}_e = 2 \times 10^{13}$, $T_e(0)$ = 1 keV, $Z_{eff} \sim 5$). Comparison of Fokker-Planck calculations (which followed the evolution of the fast ion distribution at the plasma center) with results of the measurements indicates that the majority of the neutrons are from the injected particles interacting with deuterons that have scattered through large angles before they have slowed down (beam-beam neutrons), as first suggested by Jassby.[44] The neutron flux was calculated by performing the appropriate integrals over the distribution function. There is also a contribution from deuterons that have slowed down to plasma temperature (beam-plasma neutrons). Both of these contributions, as well as the experimental data, are shown in Fig. 2.52 as a function of time — the beam-plasma contribution for two particle confinement times (10 and 100 msec). The beam-beam source rises much faster after beam turnon. The calculated and experimental values were normalized at their saturation levels because an absolute calibration of the neutron detectors was not available for these measurements. The delay of ~5 msec in the rise of the neutron production rate indicates that neutron production from beam interaction with deuterium already in the plasma is small. Saturation levels varying as the square of the beam current indicate that the beam is producing its own target. Quick saturation and agreement of the time dependence of the measured and calculated neutron flux from beam-beam reactions support the conclusion that almost all of the neutrons in these experiments were from beam-beam interactions.

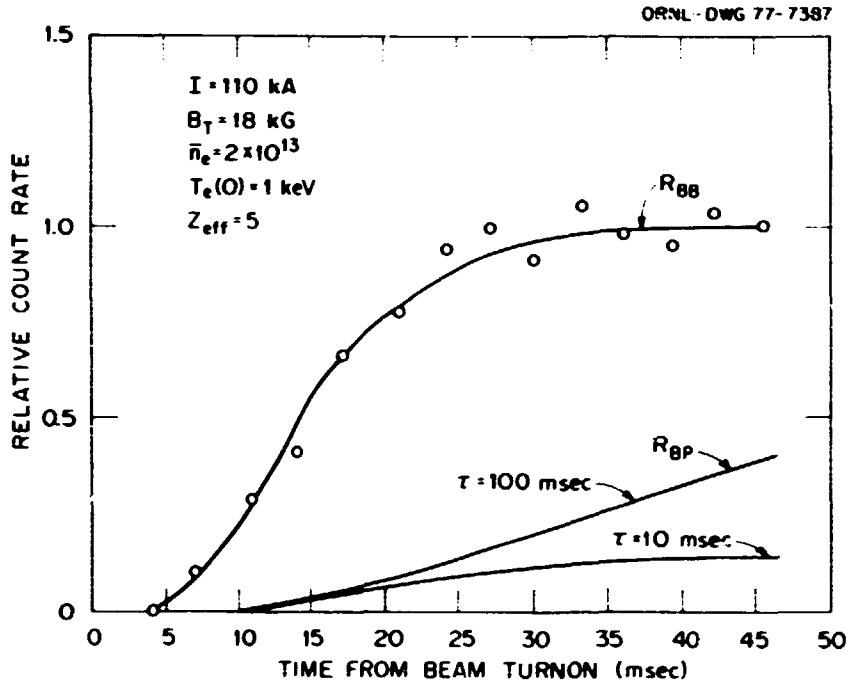

Fig. 2.52. Comparison of experimental neutron time behavior and the Fokker-Planck calculation of the neutron production from beam-beam (BB) and beam-plasma (BP) reactions. The parameter in the lower two curves (BP) is the deuteron particle containment in the plasma.

2.2 WALL IMPURITIES IN ORMAK

E. T. Arakawa
R. D. Birkhoff
C. E. Bush
R. E. Clausing
R. J. Colchin
L. C. Emerson
R. N. Hamm
L. Heatherly
R. C. Isler
G. L. Jahns
J. F. Lyon
M. Murakami
R. V. Neidigh
D. L. Shaeffer
J. C. Twichell
M. W. Williams

2.2.1 Introduction

It is generally acknowledged that tokamak plasma impurities originate on the walls and limiters. The mechanisms by which the impurities are formed are not well understood, nor are the forces which cause these impurities to enter the plasma. The results of efforts to resolve and remedy these problems are contained in the abstracts which follow.

2.2.2 Impurity and Surface Studies in ORMAK[45]

The ORMAK tokamak has been in operation since 1971, and surface impurities problems have been pursued from the beginning. Surface studies of materials removed from ORMAK have revealed the presence of C, O, and Fe. These are also the principal impurities observed spectroscopically in plasma discharges, although numerous other elements are present in lesser amounts. Spectroscopy, x-ray measurements, plasma resistance, and fast ion scattering have been used in an effort to determine Z_{eff}, the effective nuclear charge of plasma ions. All four measurements have practical difficulties leading to relatively large experimental error limits. Oxygen discharge pre-cleaning has allowed ORMAK discharges to reach higher currents and correspondingly

higher ion and electron temperature; spectroscopic studies reveal a lower level of contaminants, particularly C and N. Power measurements indicate that most of the input power strikes the walls, mostly as radiation. By varying operating parameters it is found that $Z_{eff} \sim I_p/\sqrt{n}_e$.

2.2.3 Surface and Impurity Studies in ORMAK and ISX[46]

The ORMAK vacuum liner is constructed of stainless steel, overcoated with a thin platinum diffusion barrier and a final layer of gold. Gold was selected as the vacuum surface because it is chemically inert to the adsorption of common gases. However, gold surfaces do adsorb hydrocarbons, and carbon (along with oxygen) was the principal plasma contaminant during the first two years of ORMAK operation. Upon switching discharge cleaning gases from hydrogen to oxygen, carbon levels dropped until carbon is no longer a significant contaminant. Residual hydrocarbons can now be controlled by either hydrogen or oxygen discharge cleaning. The principal measured plasma contaminant in ORMAK is now oxygen. Samples taken from the ORMAK liner and analyzed by Auger electron spectroscopy reveal the presence of iron and oxygen. There is evidence from a SXAPS (Soft X-ray Appearance Potential Spectroscopy) probe of iron and chromium diffusion from the stainless steel through the gold surface in spite of the platinum diffusion barrier. The Fe and Cr provide surface oxidation sites, and SXAPS analysis shows that these metals exist as oxides.

In order to investigate tokamak impurity problems further, the ISX (Impurity Study Experiment) tokamak is presently under construction. It will provide a cleaner and more flexible vacuum system in which to conduct studies of surfaces and plasma impurities. The operating characteristics will be much the same as those of ORMAK (with ohmic heating) in terms of size, plasma current, and plasma temperature.

2.2.4 Surface Impurities and "Clean-up" Techniques[47]

The detrimental role played by impurities in thermonuclear devices is now well-known. Experimental studies to identify those impurities residing on the liner, or first wall, of the Oak Ridge Tokamak (ORMAK) have been carried out in the laboratory using Auger Electron (AES) and X-ray Photoelectron (XPS) spectroscopic techniques. Additionally, liner measurements have been made in situ using a small soft x-ray appearance potential spectrometer (SXAPS). Oxygen, iron, and carbon were found to be the major surface impurities and, as confirmed by plasma diagnostics, also the major plasma impurities. Glow discharge cleaning of gold and stainless steel surfaces has been studied using various gases and gas mixtures. Oxygen discharges are very effective and hydrogen moderately effective in removing carbon and hydrocarbon deposits from both types of surfaces. Other parameters involved in the contamination-decontamination process, such as pressure and temperature, have been studied using techniques to controllably contaminate surfaces with hydrocarbons.

2.2.5 A Laser Reflection Technique for Studying Contamination Buildup on a Fusion Reactor Liner[48]

Calculations and measurements of optical reflectance of a gold substrate for various carbon overlayers suggested monitoring a tokamak liner optically for contamination. A He-Ne laser beam directed at the inner surface of the ORMAK liner reflected back several centimeters in diameter due to the optically rough and irregular surface. Gentle scouring of the liner greatly increased the reflected intensity. A beam splitter in the laser beam directed a portion through a chopper to a photomultiplier and oscilloscope, this acting as a reference signal. The remainder struck the liner and photomultiplier without being chopped. The reflectance

decreased during the first ~200 shots and returned to its original value at about shot 500. Separate reflectance curves were found after clockwise and counterclockwise discharge. Strong temperature effects were seen from liner expansion or gas condensation. Reflectances became erratic after neutral particle injection. We conclude the method is feasible and may have use in plasma diagnostics.

2.2.6 Wall Conditioning Studies for ORMAK and ISX[49]

Laboratory studies of various discharge cleaning techniques and the resulting surface trapping of hydrogen have been carried out in an attempt to explain conditions existing in the ORMAK tokamak. Gold and stainless steel samples have been both directly and indirectly exposed to oxygen and hydrogen glow discharges. Samples exposed either directly or indirectly to oxygen discharges experienced a more rapid removal of carbon (hydrocarbons) than samples exposed in a similar manner to hydrogen discharges, and similar results have been obtained during discharge cleaning in ORMAK. Samples directly bombarded as the cathode of a glow discharge were more rapidly cleaned than those indirectly exposed, i.e., facing away from and not immersed in the discharge. The oxygen concentration was found to increase on the surfaces of those samples which were oxygen discharge cleaned. Similarly, an increase in the oxygen impurity in ORMAK discharges is sometimes noted after oxygen discharge cleaning; however, the hydrogen discharge cleaning cycle which always precedes the initiation of normal tokamak plasmas tends to mask this effect. The presence of impurities (CH_4 and H_2O) in the cleaning discharge influences the composition of the surface in equilibrium with the discharge; thus it is important to remove impurities (reaction products) as efficiently as possible during the cleaning operation.

Direct hydrogen ion bombardment of stainless steel surfaces and subsequent thermal desorption demonstrated that 20-50 monolayers of H_2 were present in the surface oxide layer. Similar bombardment of nickel and gold surfaces showed little hydrogen loading. Hydrogen desorption from oxidized stainless steel surfaces is significant at room temperature and increases rapidly with even a few degrees rise in temperature, thus suggesting that thermal desorption may be an important mechanism of hydrogen release from tokamak walls.

2.3 SOLID HYDROGEN PELLET INJECTION IN THE ORMAK TOKAMAK[50]

R. J. Colchin K. Kim C. A. Foster
S. L. Milora R. J. Turnbull

Solid hydrogen spheres have been injected into the ORMAK tokamak as a test of pellet refueling for tokamak fusion reactors. Pellets 70 μm and 210 μm in diameter were injected with speeds of 91 m/sec and 100 m/sec, respectively. Each of the 210-μm pellets added about 1% to the number of particles contained in the plasma. Excited neutrals, ablated from these hydrogen spheres, emitted light which was monitored by either a photomultiplier or by a high speed framing camera. From these light signals it was possible to measure pellet lifetimes, ablation rates, and the spatial distribution of hydrogen atoms in the ablation clouds. The measured lifetime of the 70-μm pellets was 422 μsec, and the 210-μm spheres lasted 880 μsec under bombardment by the plasma. These lifetimes and the measured ablation rates are in good agreement with a theoretical model, which takes into account shielding of plasma electrons by neutrals ablated from spherical hydrogen ice.

2.4 RELATIVISTIC ELECTRON STUDIES

A. Cooper D. W. Swain S. J. Zweben

2.4.1 Introduction

The last annual report presented results indicating that the runaway electron confinement in ORMAK could be described by a simple orbit shift model, to lowest order. The work of the past year has been to refine the experimental measurements and to measure departures from this model. We have observed a small diffusion of runaway electrons in quiescent discharges, and

occasionally an increased radial transport of runaways associated with MHD activity and sawtooth oscillation. We have also observed a change in runaway loss rate correlated with rf and microwave emission from the plasma, apparently indicative of an instability involving the runaways.

More experiments have been performed on the runaway-dominated regime, in which the bulk of the toroidal current is carried by the electrons. Finally, theoretical calculations have been made of the equilibrium of a runaway-dominated discharge, and of the production of runaways in present and in future tokamaks.

2.4.2 Runaway Confinement Studies

The existence of runaways of 5-10 MeV in ORMAK implies that the particle confinement is very good. It has been our goal to find out under what circumstances the confinement is classical (i.e., given by the runaway orbit model described in last year's annual report). Any systematic deviation from this classical behavior can provide clues about the internal field structure of the plasma which would give rise to anomalous runaway-electron transport.

We have measured the movement of high energy runaways across a known distance and have inferred from the results that there is a small diffusion ($D \approx 100$ cm^2/sec) characteristic of runaways near the outside of a normal, low density ORMAK discharge. We have also observed in more unstable discharges that runaway loss can be correlated with MHD behavior or with the internal disruption. In general, however, we believe that the orbit model is necessary and usually sufficient to explain the confinement of the high energy runaways in ORMAK.[51]

The following experiment was done in order to test the confinement of the high energy runaways: during the steady state of a normal, low density ORMAK discharge the plasma was moved inward suddenly while the runaways striking the outer limiter were monitored in the usual way.[52] We expected, on the basis of the orbit model, that the runaway flux at the outer limiter would drop as the orbits were pulled inward by the shifting plasma current. Furthermore, we expected that as the runaways gained energy the orbits would move back outward until they reintersected the limiter, producing a gap in the hard x-ray flux which could be calculated from the measured rate of energy gain and the known inward shift.

The results of the experiment are shown in Fig. 2.53, where we see that the hard x-ray pattern does show a gap which roughly agrees

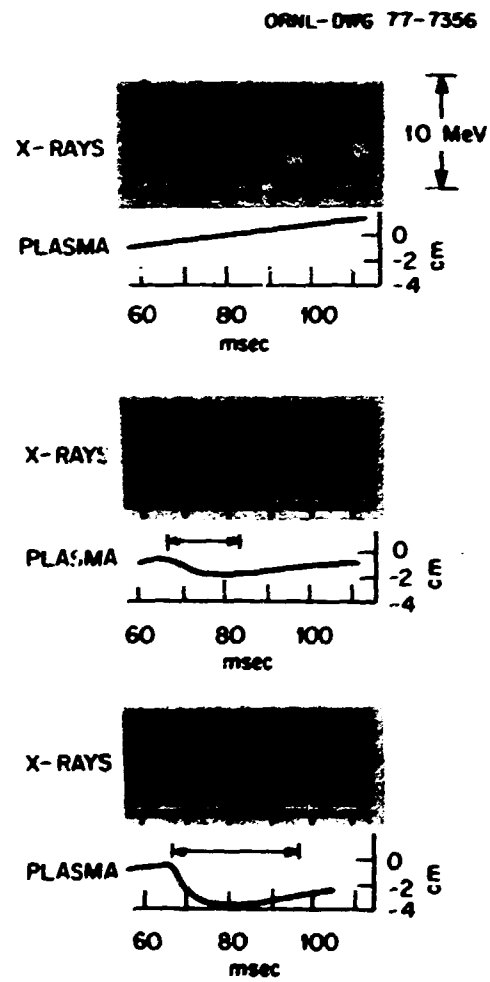

Fig. 2.53. Effect of shifting the plasma on the hard x-rays from the limiter. Top graph of each set shows pulses from NaI vs time; lower graph is plasma position vs time. (a) No shift; (b) 1.75-cm shift; (c) 3.5-cm shift. Arrows show hard x-ray gaps expected from theory.

with that calculated on the basis of the orbit model. In addition, however, we see that there are a few runaways which come out well before the time expected on the basis of the classical model.

This result has been analyzed in terms of a diffusion process which allows the orbit minor radius to change randomly due to some unknown mechanism. In Fig. 2.54 we show that the data can be fairly well fitted by assuming D ≈ 100 cm²/sec for these particles. We are presently attempting to understand this small but anomalous transport on the basis of possible field perturbations within the plasma.

In other circumstances we have seen evidence for larger diffusion rates apparently associated with an increased level of instability in the discharge. That such an influence is possible is clearly shown in several cases in which a correlation between runaway loss and plasma instability was observed.

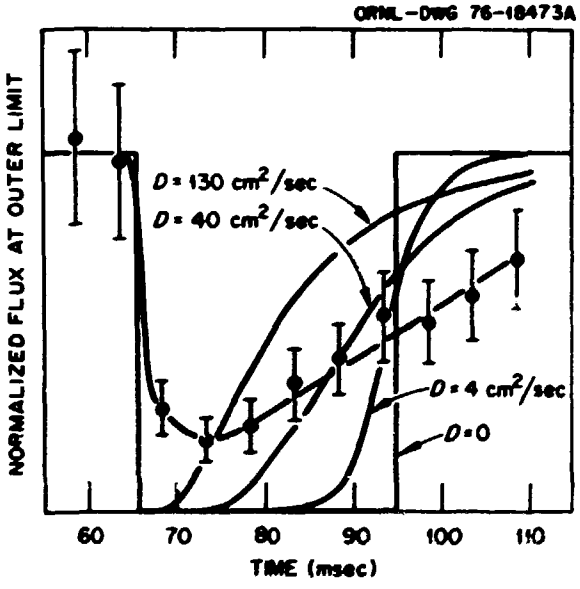

Fig. 2.54. X-ray flux to limiter vs time for 3.5-cm shift case, divided by the flux for the zero shift case. Points show experimental data, solid lines show predictions of the orbit shift plus diffusion model for different values of diffusion coefficient.

For example, in the presence of large amplitude m = 2 oscillations, there were occasionally corresponding oscillations in the hard x-ray flux. This correlation persisted over tens of milliseconds and can evidently produce an enhanced transport of runaways out from the plasma interior. This phenomenon is being investigated in terms of magnetic island structures which distort the runaway drift surfaces and, when rotating, can explain the periodic loss of runaways at the limiter.[53]

Also, when the q = 1 surface was at an unusually large radius we have seen a correlation between sawtooth oscillations and the runaway confinement; there is a modulation of the hard x-ray flux which follows the outer PIN diode signals. This behavior is being studied as a possible indication of changes in the current profile during these oscillations.

2.4.3 High Current Runaway Beam Experiments

We have performed experiments on ORMAK discharges in which a large fraction of the toroidal current was carried by runaway electrons of 1-5 MeV energy. The discharges were made to go into the runaway-dominated mode by doping the low pressure H_2 plasma with 5-20% Ar. Results of earlier work on this subject will be published shortly.[54]

In a recent set of experiments, the rf and microwave radiation was monitored during runaway beam discharges. Results are indicated in Fig. 2.55, which shows data for a shot with very few runaways (on the left) and for a runaway-dominated shot. In each case, the top trace is current, the third trace is hard x-ray intensity generated by electrons hitting the limiter, $I_x(t)$, and the second trace is the integral of the (inverted) x-ray intensity, $\int_0^t I_x(t)\,dt$. Characteristics of the runaway discharges are: (1) the large value of I_x compared to nonrunaway discharges; (2) the periodic x-rays bursts, which are associated with steps in the toroidal current (note the close similarity between $\int I_x$ and the toroidal current decay in the runaway shot); (3) the hump (or sometimes plateau) in the current at t = 2-3 msec from the start of the discharge;

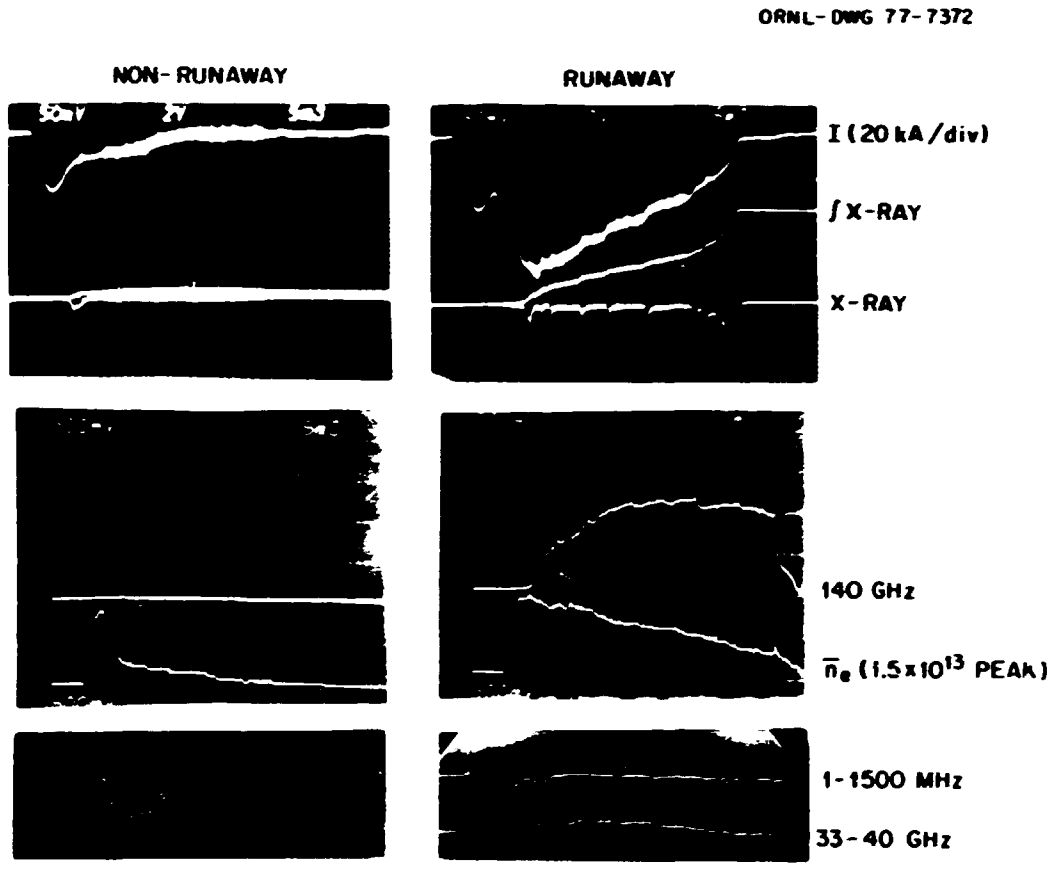

Fig. 2.55. Comparison of rf and microwave emission for runaway and nonrunaway cases. B_T = 10.5 kG, f_c = 30 GHz, $f_p < f_c$.

and (4) a large increase in β_p over a nonrunaway discharge (β_p is calculated from vertical field and plasma shift measurements).

The other traces of Fig. 2.55 are: (4) microwave emission at 140 GHz ($\sim 4.8\ f_{ce}$), (5) average electron density, (6) rf intensity in the range 1-1500 MHz (which contains the ion plasma and lower hybrid frequencies), and (7) microwave emission in the 33-40 GHz range (slightly larger than f_{ce} on the axis). As expected, the cyclotron harmonic radiation is much larger in the presence of runaways, but the low frequency radiation is much lower during the runaway-dominated current decay. Furthermore, the microwave emission shows no large steps or spikes during the decay, as has been observed in some normal discharges with a small but not negligible runaway component. This observation may imply that the runaway beam is stable to microinstabilities that change the distribution function (i.e., pitch-angle scattering). Furthermore, the beam is stable to macroinstabilities, as can be seen from the >20 msec decay time of the beam current.

Work is under way on the dynamics of the runaway beam discharge, including the production mechanisms and equilibrium of such a discharge. A theory of equilibrium has been developed in which the runaways drift on angular momentum surfaces, not constant ψ surfaces, which will then give agreement with the orbit model in the low runaway current limit. The studies of

production indicate that runaways may be created throughout the voltage pulse in substantial quantities due to the increase in the plasma resistance caused by the argon impurity.

2.4.4 Theory of Runaway Production and Confinement

Theoretical and numerical studies on the production of runaway electrons in ORMAK and the proposed next step (TNS) were carried out in the last year. For this purpose the tokamak start-up problem was addressed using a zero-dimensional model in which the circuit equations were modified to include a runaway current component. These equations were solved in conjunction with a simple set of coupled rate equations.

Under the assumption that runaways move at close to the speed of light, the rate of change of runaway current is proportional to the creation rate[55] minus the loss rate of runaways.

As runaways gain energy, their orbits shift outward according to the orbit shift model. The magnitude of the shift is proportional to the momentum of the runaway and inversely proportional to the total current. Because this treatment is zero-dimensional, it was assumed that on the average when the magnitude of the orbit shift of a runaway becomes equal to half the minor radius, it could be considered to be lost. Hence, an expression is obtained for the maximum momentum a runaway can have and still be contained, so that in essence the runaway loss rate at any given time is the runaway creation rate at some earlier time, starting from which any runaway created has free-fallen to the maximum allowable momentum it can have and still be contained.

The numerical solution of the coupled rate and circuit equations for ORMAK parameters and initial conditions yields a runaway discharge with virtually no plasma breakdown. In order to recreate experimental ORMAK discharges, an additional loss mechanism must be included. We have chosen to use one in which all runaways created early in the discharge may be lost on the limiter due to error fields. In Fig. 2.56, the calculated electron density is shown as a function of time. The $\tau = 0$ curve represents

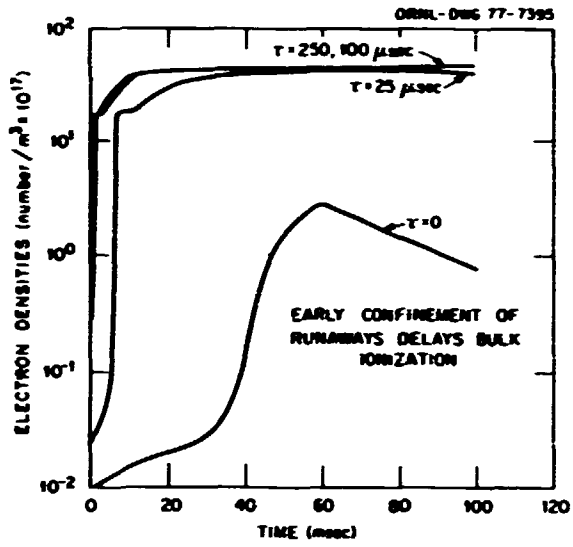

Fig. 2.56. Calculated electron density vs time from ORMAK modeling code.

the plasma evolution, assuming no runaways are lost other than by orbit shifts to the walls. The $\tau = 250$ μs curve represents the plasma evolution, assuming that all runaways created in the first 250 μs are instantaneously dumped on the walls. Figure 2.57 shows the runaway current in ORMAK (assuming that all runaways generated during the first 250 μs are lost instantaneously) for a set of different filling pressures and hence final electron densities. As in the experiments, most runaways in the low density case are generated after the plasma has been ionized, while in the high density case almost all runaways are generated prior to the plasma breakdown.

2.5 FAST X-RAY ENERGY ANALYZER FOR THE 1-10 keV RANGE

G. R. Dyer

2.5.1 Introduction

An energy-dispersive spectrometer for low energy x-rays has been built using a lithium-compensated silicon detector, electronics specifically designed for good performance at high count rates, and a fast multichannel analyzer.

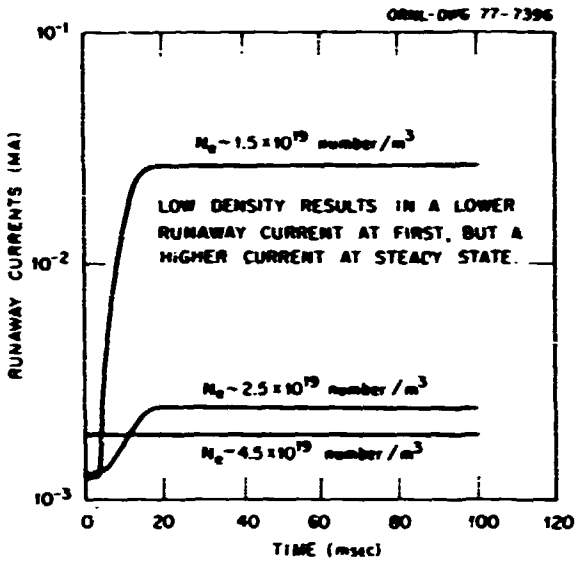

Fig. 2.57. Calculated runaway current.

The apparatus can acquire a usable bremsstrahlung spectrum in less than 10 msec, so an electron temperature vs time plot with 10-msec time resolution can be obtained for a single plasma shot. The device has been used on ORMAK, and data for several experimental sequences are available. Data are still being evaluated, but there appears to be reasonable agreement with Thomson scattering values for T_e.

2.5.2 Objectives

We proposed an x-ray diagnostic tool that could acquire a bremsstrahlung spectrum in a short time compared with an experimental shot time for ORMAK. Thus, several sequential bremsstrahlung spectra could be collected during a single shot; from these, an electron temperature, T_e, vs time plot could be derived. Because the spectra contain intensity information which is dependent on electron density and effective charge of the constituent ions as well as on electron temperature, other useful plasma parameters might also be obtained from them.

Evaluation of the available equipment and techniques for fast energy analysis led us to conclude that we could attain a count rate of the order of 10^5/sec with reasonable energy resolution and without excessive pulse pileup, system deadtime, or external interference. Under these conditions, a spectrum containing 10^3 counts could be acquired in 10 msec, allowing a plasma shot history to be resolved into 10-15 time segments.

2.5.3 System Requirements

A spectrometer with the capability of processing more than 10^5 events per second is required to meet the objectives outlined above. It should have better than 500-eV energy resolution, low deadtime, and freedom from jamming due to high count rates or overload pulses from high energy events. Stability over a long operating time, provision for pulse pileup rejection, ease of calibration, and reliable operation are also important. Finally, the amount of data to be collected requires an interface to a mass data storage system and access to computer data reduction.

2.5.4 Hardware

The spectrometer system comprises an ORTEC cryogenic x-ray detector and preamplifier, a linear pulse shaping amplifier, a pulse processor for peak detection and pileup rejection, a multichannel pulse height analyzer with buffered storage registers, and a data transfer interface to a PDP-8 computer.

The ORTEC detector is a lithium-compensated silicon diode 4 mm in diameter by 3 mm thick, mounted in a liquid-nitrogen-cooled cryostat with a 0.0125-mm-thick beryllium x-ray window. The associated charge-sensitive preamplifier incorporates resistive feedback to avoid latchup and deadtime problems inherent in optical feedback systems. The preamplifier remains functional at count rates exceeding 10^6/sec at 5-keV average photon energy. Energy resolution of the detector is 430 eV at 5.9 keV photon energy, using a delay-line-shaped linear amplifier with a 250-nsec shaping time constant.

The linear amplifier has been designed specifically for this application. It operates

at a fixed gain and with fixed time constants following initial calibration and uses a delay-line differentiator and two active integrators for pulse shaping. Pole-zero compensation and an active baseline stabilizer are incorporated for good performance at high count rate. A 250-nsec delay line, used for the data collected to date, gives a pulse width of approximately 1.1 μs. Count rates in excess of 2×10^5 can be tolerated without loss of baseline reference.

The pulse processor and multichannel pulse height analyzer have also been designed for this application. Pulse height analysis and data storage take place during the peak-to-baseline fall time of the linear amplifier output pulse. Thus, multichannel processing time is not a constraint on count rate capability. This has been accomplished by using a fast differentiator as a pulse peak detector and a stacked discriminator array as a pulse height analyzer. Twenty energy channels are sufficient for 500-eV resolution, so the multichannel circuitry is not unwieldy in spite of its straightforward design. Twenty buffered registers with 65,000-count storage capacity per register give the ability to accumulate one spectrum while the previous spectrum is being transferred to a mass storage file. Data transfer from accumulator to buffer takes less than a microsecond, so count rate is limited mainly to pulse pileup of the linear amplifier output. Trailing edge pileup rejection is incorporated in the pulse processor circuitry to minimize pileup effects on spectral shape.

The system hardware described so far can be used as a stand-alone instrument to collect two spectra per plasma shot, with data displayed on an oscilloscope. Preliminary evaluation was done in this way. However, the system potential is only fully realized when it is interfaced with a bulk data storage device. With the help of D. R. Overbey and R. V. Neidigh, we completed a PDP-8 interface capable of storing 20 x-ray spectra, each of 10-msec time duration, per plasma shot. The computer-interfaced system collected all the data of relevance to this report.

2.5.5 Machine Tests and Data Collection

With considerable encouragement from P. H. Edmonds and considerable help from S. M. DeCamp and Y-12 craftsmen, the fast x-ray analyzer was installed on ORMAK on November 5, 1976. The detector was mounted on port C-18 just over the personnel access door, looking horizontally through the central chord of the liner. Initial detector-to-plasma distance was approximately 124 cm. The initial count rate proved much too high, so it was necessary to increase the detector-to-plasma distance and decrease the solid angle of plasma seen by the detector. A couple of iterations led to the geometry used for all data collected so far: 217 cm from detector to centerline of the liner, viewing angle of 1×10^{-6} steradians, viewing along the central chord of the liner. In the future an adjustable geometry would definitely be an asset, because our geometry was certainly not optimum for the varying intensities encountered under various operating conditions.

The machine performed according to expectations. Overload recovery, baseline stability, gain stability, and pileup rejection functioned according to bench test data. We experienced no difficulty with ground loops or excessive noise pickup. The detector proved to be quite insensitive to hard x-ray flux. Preliminary data agreed within statistical uncertainties with T_e (peak) from laser data.

With D. R. Overbey's help the PDP-8 interface and data collection program was implemented, and by December 8, 1976, time-resolved (10 msec/spectrum) x-ray histories of ORMAK shots were being collected on magnetic tape. We have some data for most experimental sequences from December 8 until shutdown of ORMAK.

2.5.6 Preliminary Data Analysis

To the present time, data analysis has been directed towards T_e determinations by slope measurements of ln (intensity) vs energy.

Overbey has written FORTRAN codes for the PDP-8 which perform weighted and unweighted

straight line fits to ln I vs E data. These codes calculate integral intensity, T_e, I(E = 0), a deviation figure for the slope calculation, and provide for averaging $T_e(t)$ over several shots in a sequence. Data for injection heating experiments are included elsewhere in this report. Preliminary analysis indicates that x-ray plots of T_e vs time agree reasonably well with laser data. There are still some questions as to the best method for calculating T_e.

2.5.7 Future Plans

Analysis of ORMAK data will continue with the intention of obtaining plots of T_e vs time for all sequences with x-ray and laser data in common. In addition, we plan to try to correlate integral intensity from the fast x-ray analyzer with current traces from the PIN diode array. Finally, we want to try to extract information on effective Z vs time behavior from the fast x-ray (FXR) analyzer data, using profile and density information from other diagnostics.

Tests on ORMAK show that the basic hardware works. Preliminary data analysis is encouraging, and the machinery is available for installation when ISX begins operation. Arrangements for an adjustable x-ray aperture and chordal scanning will increase the usefulness of the diagnostic. Data reduction programming appears to be far enough along now to give an on-line diagnostic capability of T_e vs time measurements with 5- or 10-msec resolution as a routine operating instrument on ISX. Agreement with laser data is good enough to lend credibility to the x-ray measurement, and installation and operation of the FXR analyzer are quite straightforward.

2.6 ELECTRON CYCLOTRON HEATING

A. C. England F. B. Marcus J. B. Wilgen
O. C. Eldridge J. C. Sprott W. Namkung

2.6.1 High Power Electron Cyclotron Heating in ISX and ORMAK Upgrade

A phased program of the electron cyclotron heating (ECH) of tokamak-produced plasmas is proposed for ISX and ORMAK Upgrade. Past programs of ECH at ORNL in mirror geometry and in the ELMO Bumpy Torus have been successful. The physics of wave propagation and particle heating are fairly well understood. Recent experiments in the U.S.S.R. on small tokamaks have shown that ECH is a viable heating technique, and studies of breakdown and runaway electron production will provide useful information for larger machines. Further technological development of the high power, high frequency microwave tube looks promising at this time, and current engineering practice suggests that the new developments are adaptable to the heating technique.

2.7 ORMAK DATA SYSTEM

N. A. Betz J. E. Francis D. R. Overbey
K. H. Carpenter C. E. Hammons W. R. Wing
D. N. Clark C. O. Kemper J. W. Wooten
B. A. Clark R. W. McGaffey O. C. Yonts

Work during 1976 on the ORMAK data system progressed along two essentially independent paths: consolidating and improving the system by building on changes implemented in 1975,[56] and planning for and starting purchase of the components of the data system expansions necessary for ISX and ORMAK Upgrade.

Several of the improvements are worth noting. At level one, the spectroscopy PDP-8/e was extended to handle data from the fast soft x-ray pulse height analysis system developed by G. R. Dyer. The neutral particle PDP-8/e was likewise extended by the addition of an interface to handle the data from the pulse height analyzer purchased by the Runaway Electron project. The teletype on the laser PDP-8/e was replaced by a faster output device to remove a bottleneck, and it was in turn replaced by a Tektronix 4006 graphic display. This display unit was installed just before ORMAK was shut down, so work had barely started on providing a set of FORTRAN-callable graphic routines for the laser data analysis. A floppy disk drive was purchased for the spectroscopy PDP-8/e but also arrived too close to the end of the year to be utilized. For analysis at level two, an automatic spooler to keep a day file of

the 80 most recent shots was added to the PDP-11/45. Several of the level two data analysis routines from the PDP-10 were down-loaded to the 11/45 and were modified to run under its operating system. The modifications consisted of breaking the programs up so that they could overlay themselves. In every case it turned out that the programs were larger than Digital Equipment Company's operating system could handle. Finally, at level three, the OOOBALL program was cleaned up and distributed to Lawrence Livermore Laboratory, General Atomic Company, and Los Alamos Scientific Laboratory (at their request). In addition, work was started in earnest on a parameter-manipulating program which opens up the whole ORMAK data base for analysis.

At the same time that these improvements were being added to the ORMAK system, the conceptual design was completed on the system for ORMAK Upgrade. The system will be built around large (32-bit) minicomputers which acquire data via CAMAC modules and have sufficient power and flexibility to handle the whole level one, level two workload in the control room. A series of benchmark programs designed to simulate ORMAK data analysis was written and run on all the available 32-bit computers. Specifications based on the needs of ORMAK Upgrade were then written and purchase of the first machine initiated. Engineering samples of the highest priority CAMAC data acquisition modules were purchased for test and evaluation. Finally, software specifications were written for the major components of the ORMAK Upgrade software.

2.8 IMPURITY STUDY EXPERIMENT

R. J. Colchin T. C. Jernigan M. W. Durfee
D. C. Lousteau M. J. Saltmarsh

The Impurity Study Experiment is a new tokamak experiment[57,58] under construction at ORNL. Final assembly has begun, and completion of the tokamak itself is scheduled for February 1977. During 1976, design and major fabrication were completed. The only major change in the device during this year was the discovery that the plasma was in unstable equilibrium vertically. To overcome this apparently general effect in shell-less iron core tokamaks,[59] windings have been provided to produce a small (~20 G) radial magnetic field with active feedback for vertical positioning of the plasma.

2.9 ORMAK UPGRADE

L. A. Berry J. D. Callen M. W. Durfee
H. C. McCurdy T. E. Smith

2.9.1 Introduction

ORMAK Upgrade is a new research tokamak which is to replace the present ORMAK. It is designed specifically for neutral beam heating experiments but is also well suited for other physics investigations. The design emphasizes features that will permit the device to be built in a relatively short time using existing technology. Compared to ORMAK, ORMAK Upgrade is somewhat larger and will provide significant improvements in performance, access, and experimental flexibility.

A Request for Directive to construct ORMAK Upgrade with 2 MW of injection capability was submitted to ERDA February 4, 1976, and authorization to proceed was provided by ERDA Directive No. Y-12-528, dated March 10, 1976. The target date for completion is October 1978, and the estimated cost is $7.3 million.

2.9.2 Design Description

ORMAK Upgrade will be located near the Impurity Study Experiment in Building 9201-2 in the Y-12 area of Oak Ridge National Laboratory. It will be operated in conjunction with ISX and will time-share the 72-MW toroidal field power supply with that device.

Design features of ORMAK Upgrade include: major radius of 100 cm, minor radius of 30 cm, water-cooled copper coils, air-core ohmic heating transformer, toroidal magnetic field of 4.0 T, plasma currents up to 700 kA, and four large (15 × 25 cm) injection ports. Two Princeton Large Torus (PLT)-type beam lines in the initial installation give a capability for 2 MW or

injected power; later addition of two more beam lines can increase this to 4 MW. The general arrangement with four injectors is shown in Fig. 2.58. Physical characteristics, performance goals, and predicted physics parameters are given in Table 2.4.

2.9.3 Progress in 1976

Principal efforts were concerned with detailed design and initiating procurement of long-lead components.

Tokamak systems

Design of the toroidal field (TF) coils was completed. A purchase order for the CDC-102 copper conductor was placed with the Anaconda Company; delivery is scheduled for January 1977. Separate bids were received in December 1976 for fabricating the stainless steel coil cases and for winding and potting the coils into the stainless steel cases; the bids are being evaluated.

Several iterations were required to fix the size and locations of the ohmic heating and vertical field (VF) coils. Detailed analysis revealed that the volt-seconds capability provided by the conceptual design was significantly less than anticipated. Ultimately, an increase in plasma major radius from 92 to 100 cm permitted the required volt-seconds capability to be achieved. Detailed design of the poloidal coils was initiated. Magnetic Engineering

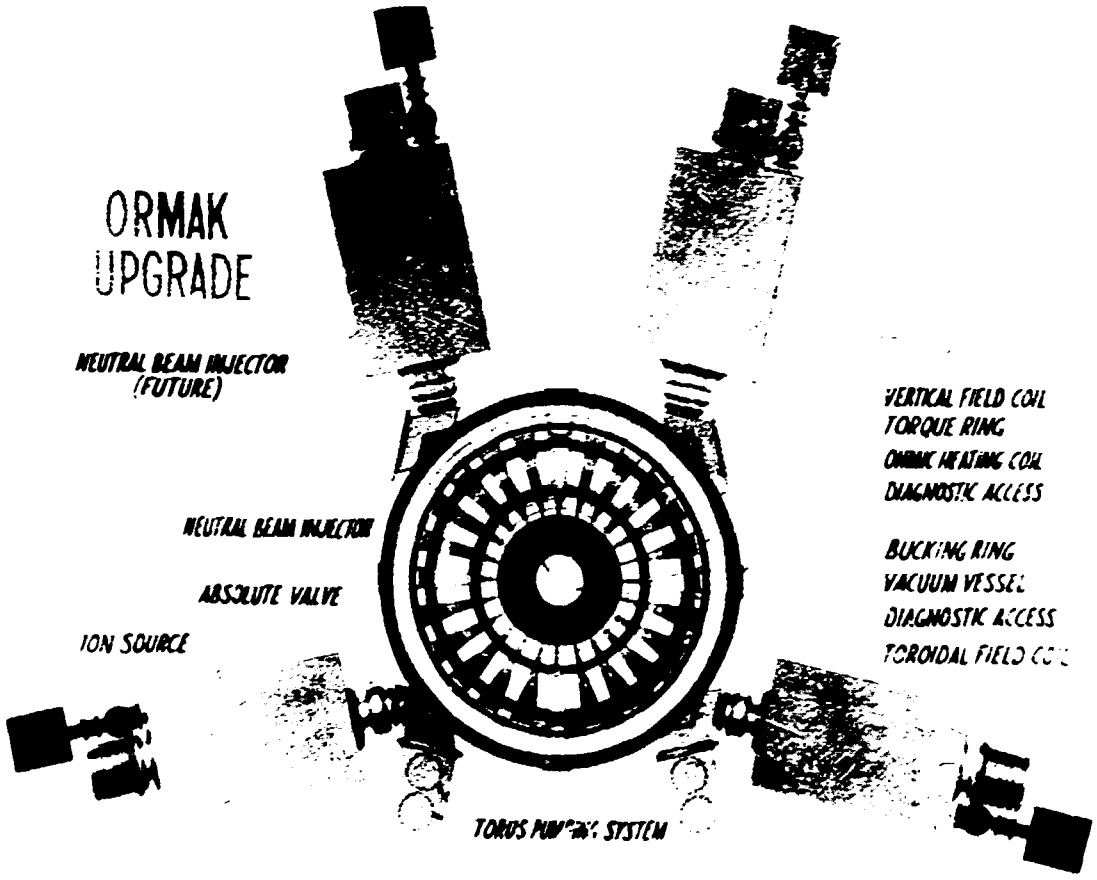

Fig. 2.58. General arrangement of ORMAK Upgrade with four neutral beam injectors.

Table 2.4. [illegible] Upgrade baseline reference design

PHYSICAL CHARACTERISTICS

Plasma	
Cross-section shape	Circular
Major radius (nominal)	100 cm
Minor radius (nominal)	30 cm
Plasma volume	1780 ℓ
Toroidal field system	
Number of coils	24
Coil shape	Circular
Conductor material	Copper
Coolant	Water
Ohmic heating system	
Conductor material	Copper
Coolant	Water
Transformer core	Air
Vertical field system	
Conductor material	Copper
Coolant	Water
Torus vacuum pumping	
Primary pump type	Cryosorption
Speed (each pump)	6000 ℓ/sec
Number	3
Supplementary pump type	Turbomolecular
Speed	500 ℓ/sec
Number	3
Primary vacuum vessel	
Material	Stainless steel
Cross section shape	Circular
Baking temperature	200°C
Injection or vacuum access ports	
Tangential	
Number	4
Size (elliptical)	15 × 25 cm
Perpendicular	
Number	4
Size (rectangular)	19 × 25 cm

Table 2.4 (continued)

Diagnostic access ports	
Standard (1-5 in. diam)	127
Special	15
Neutral beam injectors	
Injector design	PLT type, 20-cm-diam grid, 40-kV accel, 60-A drain
Number of injection lines	2
Number of injectors (total)	2
Electrical power systems	
Toroidal field	Existing ORMAK system
Vertical field (new system)	1000 V, 5000 A
Ohmic heating	Existing MG sets
Injector accel	New supplies – 60 kV, 60 A
Injector decel	Existing ORMAK system
Discharge cleaning (new system)	
Discharge voltage	60-40 kV
Pulse duration	1-5 msec
Pulse frequency	1 Hz

PERFORMANCE GOALS

Tokamak		Neutral beam heating	
Magnetic field at plasma axis	4.0 T	Injection energy	40 keV
Volt-seconds	1.9	Injected power (full plus half-energy neutrals)	2 MW
Plasma current (max)	700 kA	Injection pulse duration	100 msec
TF flat-top length		Design base pressure	$<2 \times 10^{-6}$ torr
at full field	200 msec	Gas loading to torus (per shot)	1 torr
at half field	TBD		
Ripple			
at plasma surface	4.5%		
at plasma center	0.16%		
Torus design base pressure	3×10^{-8} torr		

Table 2.4 (continued)

PHYSICS PARAMETERS

Ohmically heated plasma parameters (for I = 400 kA, $\bar{n}_e = 7 \times 10^{13}/cm^3$)

Electron temperature, $T_e(0)$	900 eV
Ion temperature, $T_i(0)$	800 eV
Beta poloidal, $\langle\beta_p\rangle$	0.3
Energy confinement time, τ_E	23 msec
Impurity charge, Z_{eff}	4

Maximum plasma parameters with 2-MW injection (at I = 200 kA)

Beta poloidal, $\langle\beta_p\rangle$	2.9
Injection power/OH power, P_{inj}/P_{OH}	24
Beam energy/plasma energy, Γ	0.39

Associates was engaged to perform the detailed design of the solenoid coil.

Detailed design of the vacuum vessel approached completion. The conceptual design and assembly procedure were modified to incorporate special sections with large diagnostic ports at four locations, and the total number of diagnostic ports was increased from approximately 50 to 142. The required baking temperature was evaluated and was reduced from 400 to 200°C. A remote welding machine developed by Culham Laboratory was selected for making the final closure welds on the vacuum vessel during tokamak assembly. Preliminary drawings and specifications of the vacuum vessel were provided to UCC-ND shops, which began planning and scheduling of the fabrication; the shop estimate of fabrication cost is approximately $400 K.

Continued study of torus vacuum pumping requirements and of commercially available pumping equipment led to selection of a combination of cryosorption pumps and oilless, air-bearing turbomolecular pumps for the torus vacuum pumping system. The turbomolecular pumps have desirable characteristics for pumping "trash" gases and can be used alone for vacuum maintenance during periods of standby operation, thereby reducing loading of the cryosorption pumps. Tentative plans based on estimates of gas loads from vacuum vessel walls, diagnostics, and injectors call for three 6000-ℓ/sec cryosorption pumps supplemented by three 500-ℓ/sec turbomolecular pumps.

Specifications were prepared for the VF power supply (5 MW, 1000-2000 V) and an order was placed with the Robicon Corporation. The purchase price is approximately $73 K and expected delivery date is July 1977. This power supply will be installed in the same enclosure as the existing 72-MW solid-state TF power supply.

An engineering study of the OH switch circuit was performed by Westinghouse under subcontract to ORNL. Westinghouse is also assisting in the design of this system. A reference circuit was selected, and tests were defined which will be performed at Los Alamos Scientific Laboratory to assist and confirm the design. A procurement specification was prepared for purchasing the vacuum circuit breaker.

Preliminary studies were performed to define instrumentation and control requirements for the Able-Ready-Go sequence of machine operation. Initial versions of an operational block diagram

and a timing diagram were developed, and a concept of the machine control console was proposed. Plans to use the existing IMP (Injection into Microwave Plasma) control room enclosure for ORMAK Upgrade were abandoned because the IMP control room does not meet current fire protection requirements; alternative control room locations are being investigated. An engineering study showed that the least costly method of controlling the TF and VF power supplies is to expand the PDP-11-based control system used for the existing TF supply.

Neutral beam systems

The PLT neutral beam line design is being modified to adapt it for ORMAK Upgrade. The principal modification is to shorten the beam line by relocating the calorimeter to the region between the bending magnet pole pieces. Other changes include use of inertial targets for beam dumps and modifications to simplify the beam-defining plates. Design studies were made of the interface duct between the beam line and the torus vessel, and a reference design was selected for detailing.

The neutral beam accel power supply that was planned in the conceptual design was based on installing an existing capacitor bank. While this power supply system would suffice for a 100-msec beam pulse at 2 MW, a change was made to high voltage power supplies because of strong interest in proceeding immediately to 4 MW of injection. A specification for the accel power supplies was prepared and a purchase request initiated. Each injector will have a 60-kV, 60-A power supply module. The modules will be stackable to 120 kV in order to provide a backup for the 150-kV beam development test stand and flexibility for future ORMAK Upgrade experiments. Proposals were requested for two supplies (for 2 MW of injection) with an option for two more.

Source and modulator tables for ORMAK Upgrade are to be essentially identical to those for the PLT beam test stand. However, the latter were built as a development effort, and documentation for reproducing them was not prepared. To facilitate documentation, one source table and one modulator table for ORMAK Upgrade are being built by the beam development team. Additional tables will be purchased or shop-fabricated.

2.10 ATOMIC PHYSICS, PLASMA DIAGNOSTICS, AND THE CONTROLLED FUSION ATOMIC DATA CENTER

C. F. Barnett J. E. Bayfield D. A. Brisson
D. H. Crandall L. D. Gardner D. P. Hutchinson
H. J. Kim R. K. McKnight F. W. Meyer
T. J. Morgan R. A. Phaneuf J. A. Ray
P. A. Staats D. M. Thomas D. M. Toodle
K. L. Vander Sluis M. I. Wilker

2.10.1 Introduction

During the past year electron capture collisions have been measured for C^{q+} ($1 < q < 4$), N^{q+} ($1 < q < 5$), and O^{q+} ($1 < q < 5$) ions incident on both atomic and molecular hydrogen gas targets over the energy range $5 < E_H < 150$ keV. Also, using the ORNL Tandem Van de Graaff, the electron capture cross sections of Fe^{q+} ($6 < q < 14$) over the energy range $30 < E_H < 290$ have been measured in atomic and molecular hydrogen. For the low mass ions in atomic H we have found that: (1) the electron capture cross sections are greater than 10^{-15} cm^2 for $E_H < 50$ keV; (2) for $E_H > 50$ keV the cross sections scale approximately as q^2; and (3) the energy at which the maximum cross section occurred shifts upward with increasing q. For Fe^{q+} the electron capture cross sections scaled as $q^{1.5}$ at low values of q and E up to $q^{3.0}$ for high values of q and E. Additional investigations included the electron capture cross section of He^+ and He^{++} in H, the study of high Rydberg H_2 states, and the blistering of stainless steel by energy-dispersed neutral He beams.

The main emphasis of the diagnostic developments has been on the design, fabrication, and testing of a 1-MW submillimeter laser to be used for spatial ion temperature measurements via Thomson scattering. An unstable resonator oscillator has produced approximately 10 kW of 447-μm power using CH_3I as the laser medium. Use of CH_3I rather than CH_3F or D_2O has resulted in large improvements in spectral line purity.

The system amplifier has been constructed utilizing beam-expanding optics to provide a large volume to absorb the 150-J CO_2 pump laser power. A 40-mW cw CH_3I laser has been operated successfully. This laser will be used to act both as a local oscillator for a heterodyne detector and as a source for multichannel electron density interferometer. Improvements have been made in neutral particle spectrometers by the development of an energy-velocity analyzer and the use of a Cs heat pipe to convert the H atoms to H^-, thereby increasing the spectrometer efficiency by two orders of magnitude.

Operation of the Controlled Fusion Atomic Data Center has continued with publication of the two-volume compilation *Atomic Data For Controlled Thermonuclear Research*; publication of a bimonthly bulletin "Atomic Data for Fusion"; and the searching, evaluating, and entering of bibliographical data into the computer file.

2.10.2 Charge Transfer Collisions of Multicharged Ions with Atomic and Molecular Hydrogen

The study of electron transfer in collisions between multiply charged ions and atomic hydrogen is fundamental to the understanding (due to the relatively small number of electrons comprising the ion-atom system) of charge transfer mechanisms. In addition, such studies are of practical interest because of potential applications in various areas of technology, such as the problem of neutral beam injection heating of fusion plasmas.

Experiments to measure charge transfer cross sections for multiply charged ions of helium, carbon, nitrogen, and oxygen incident on atomic and molecular hydrogen gas targets were initiated in June 1976 utilizing the 600-kV accelerator located in the Fusion Energy Division.[60]

Charge and mass analyzed beams of up to triply ionized C, N, and O, as well as $^4He^+$ and $^3He^{++}$ were produced in an electron impact ion source with a simple hot filament and accelerated through voltages ranging from 10-600 kV. Charge states greater than +3 were produced by stripping fast 2+ and 3+ ions on thin formvar foils or, in a few cases, on residual gas. The desired charge state was selected by electrostatic deflection and passed through a tungsten oven in which hydrogen could be thermally dissociated. The primary and charge transfer components in the emergent beam were separated by a second stage of electrostatic deflection and counted using a channel electron multiplier.

The directly heated tungsten hydrogen oven is essentially the same as that previously used and described by McClure.[61] The degree of dissociation of hydrogen was determined by monitoring the variation with oven temperature of double electron capture by 30-keV protons with H_2 and Ar flowing alternately through the oven.[62,63] For a heating current of 130 A, which resulted in an estimated oven temperature of 2350 K, the dissociation fraction was determined to be 95%. The target thicknesses were determined by normalizing to well-known cross sections for single electron capture by 20-keV protons incident on H and H_2 targets.

The results of the electron capture cross-section measurements for the various ions incident on both atomic and molecular hydrogen targets are presented in Figs. 2.59-2.63. At the lower velocities, where the relative particle motion is comparable to that of the outer atomic electrons ($v \sim 2 \times 10^8$ cm/sec), the collision cross sections are determined by the detailed behavior of the potential curves of the quasimolecule formed during the collision, which can differ considerably from system to system. At lower velocities no general trends are apparent in the data. The capture cross sections for C^{+3}, N^{+3}, and O^{+3} ions incident on H_2 are in very good agreement with the measurements of Crandall et al.[64] over the range of velocities where the measurements overlap ($5 \times 10^7 < v < 1 \times 10^8$ cm/sec).

At higher velocities ($v > \sim 2 \times 10^8$ cm/sec), however, momentum transfer becomes the dominant mechanism for charge transfer. In this velocity region, the cross sections for C^{q+}, N^{q+}, and O^{q+} projectiles are similar in magnitude for $q > 2$, fall off similarly with velocity, and scale

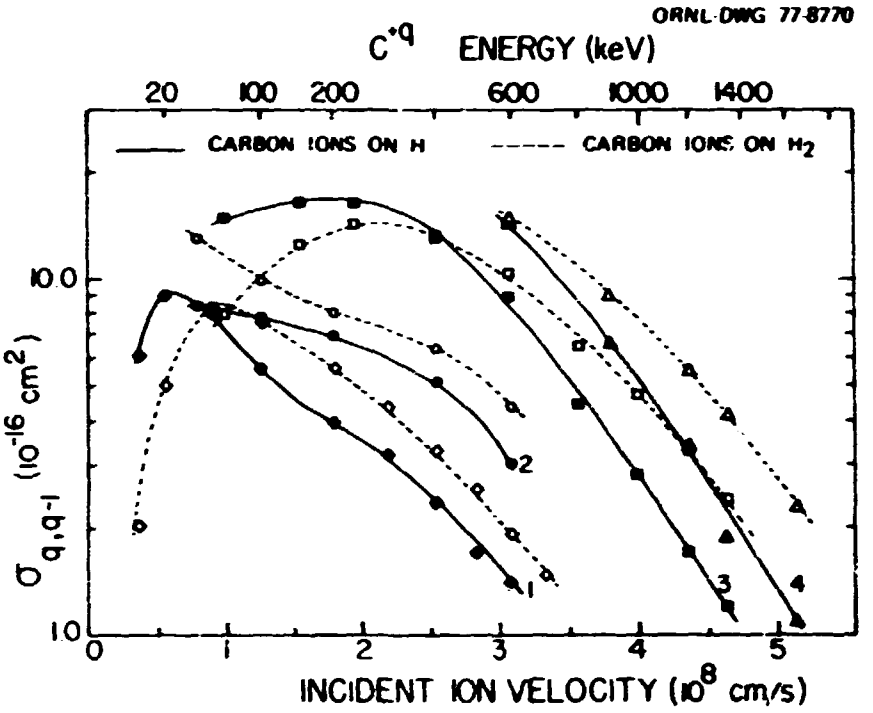

Fig. 2.59. Experimental electron capture cross sections for $C^{+q} + H \rightarrow C^{+q-1} + H^{+}$ (solid points and curves), and for $C^{+q} + H_2 \rightarrow C^{+q-1} + H_2^{+}$ (open points and dashed curves). The solid curves are labeled by the incident ionic charge "q". Diamonds, q = 1; circles, q = 2, squares, q = 3; triangles, q = 4.

approximately as q^2, as predicted by the Born approximation. At the highest velocities, the cross sections for electron capture from H_2 targets are roughly double those for atomic hydrogen targets in all cases.

Recent classical Monte Carlo calculations[65] of cross sections for electron capture at these velocities by multiply charged C, N, and O ions in atomic hydrogen are in very good quantitative agreement with the present data.

In the case of He^{++} ions incident on molecular hydrogen, our measurements of σ_{21} and σ_{20} are in good agreement with previous measurements.[66-69] For atomic hydrogen, the present data are in excellent agreement with the measurements of Shah and Gilbody,[66] and with those of Fite et al.[70] as renormalized by Shah and Gilbody,[66] but disagree substantially with those of Bayfield and Khayrallah.[67] For collisions of He^{+} ions with atomic hydrogen, the present σ_{10} cross sections are believed to be the first reported experimental values for total electron capture.

2.10.3 Electron Capture Cross Sections for $Fe^{q+} + H$

Utilizing energetic Fe ion beams from the Tandem Van de Graaff and a thermally dissociated atomic hydrogen target, we have measured the electron capture cross sections, $\sigma_{q,q-1}$, for Fe^{56} ions on a hydrogen target. The incident ion charge ranged from q = 4-13, and the energy ranged from 1.50-16.30 MeV. This energy range is equivalent to 27-291-keV hydrogen energy E_H (or incident energy per nucleon) and encompasses the Tokamak Fusion Test Reactor (TFTR) injection energy, E_H = 60 keV. The measured cross sections

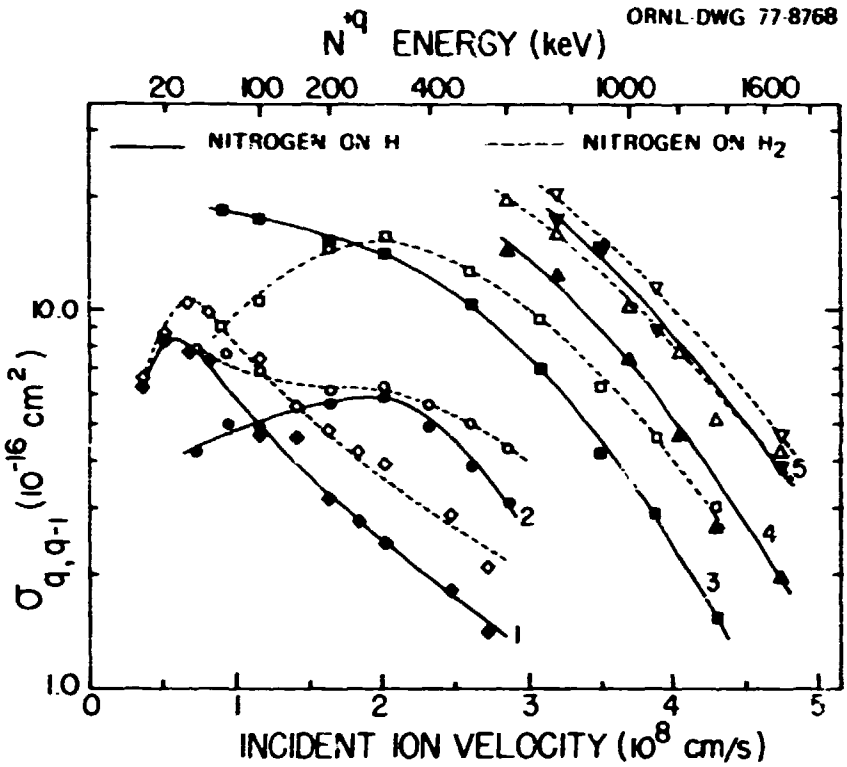

Fig. 2.60. Experimental electron capture cross sections for $N^{+q} + H \rightarrow N^{+q-1} + H^+$ (solid points and curves), and for $N^{+q} + H_2 \rightarrow N^{+q-1} + H_2^+$ (open points and dashed curves). The solid curves are labeled by the incident ionic charge "q". Diamonds, q = 1, circles, q = 2; squares, q = 3; triangles, q = 4; inverted triangles, q = 5.

are given in Fig. 2.64. The proton hydrogen atom charge transfer cross sections, σ_H, are given for comparison.

$\sigma_{q,q-1}$ decreases rapidly and monotonically with energy in a manner similar to σ_H, although its values are much greater and its discernible "knee" occurs at a higher energy than σ_H. A linear translation of the σ_H curve toward north-north-east direction in Fig. 2.64 would let σ_H represent the energy dependence of present results reasonably well. At a given incident energy the cross section increases with incident charge, q, for all energies: a simple expression

$$\sigma_{q,q-1(E)} \propto q^{\alpha(E)}$$

represents the data accurately. The values of α obtained by a least-square analysis as a function of incident velocity, v, are shown in Fig. 2.65. Classically, $\alpha = 2$, independent of v. Present results give $\alpha \sim 1.5$ for q = 4–10 near the TFTR injection energy.

2.10.4 Variable Energy Atomic Hydrogen Beam Apparatus

An apparatus which provides high quality atomic hydrogen beams suitable for the forthcoming experiments in which an H^0 beam is crossed with a multicharged beam has been designed, fabricated, assembled, and tested. A schematic diagram of the apparatus is shown in Fig. 2.66.

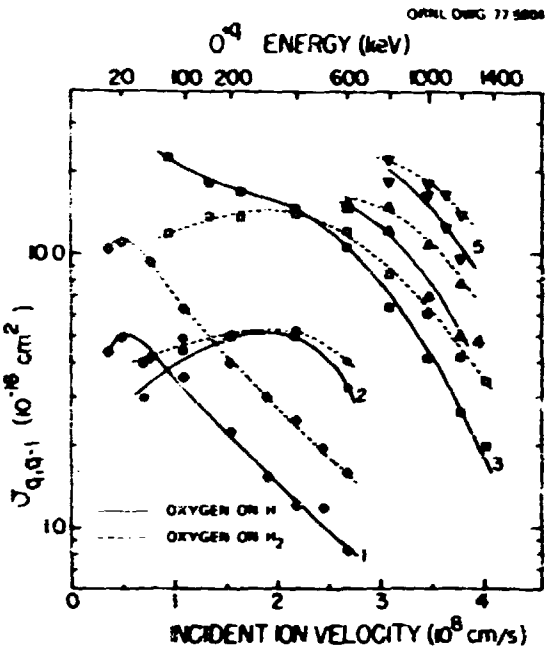

Fig. 2.61. Experimental electron capture cross sections for $O^{+q} + H \rightarrow O^{+q-1} + H^+$ (solid points and curves), and for $O^{+q} + H_2 \rightarrow O^{+q-1} + H_2^+$ (open points and dashed curves).[2] The solid curves are labeled by the incident ionic charge "q". Diamonds, q = 1; circles, q = 2; squares, q = 3; triangles, q = 4; inverted triangles, q = 5.

It consists of a proton accelerator comprised of a duoplasmatron ion source and extraction and acceleration gaps, a double focusing 45° analyzing magnet, and a 20-cm-long high pressure water vapor charge neutralization cell. The apparatus is constructed so that it may be readily transported to different experimental sites. Its relevant characteristics are: energy range 5-100 keV with 0.1% regulation, analyzed proton beam current in excess of 10 μA through a 1 × 3-mm beam defining aperture, good neutralization efficiency (<45% for 60-keV protons), and a vacuum of better than 3×10^{-8} torr at the end of the beam line. This apparatus will provide energy variable atomic hydrogen beams which will be crossed with heavy ion beams such as C^{3+} and O^{3+} to determine charge transfer and ionization cross sections of interest for controlled thermonuclear research.

2.10.5 Rydberg States of Hydrogen Molecules

Measurements have continued in an effort to understand the electron capture of H_2^+ into H_2 Rydberg states when passed through hydrogen gas. Theoretical predictions indicated that high Rydberg states ($n > 10$) of H_2 may be populated from lower valence levels ($n = 4$) by nonadiabatic coupling of the vibrational states. To confirm this prediction, an H_2^+ beam was passed through an electric field to remove or ionize all states of $n > 10$. During transit of the H_2 beam through a 30-cm drift region, the $n > 10$ levels should be repopulated by the nonadiabatic coupling. Passage through a second ionizing electric field indicated a repopulation of the higher levels by as much as 5%. Performing the same experiment with H atoms in which nonadiabatic coupling is absent gave essentially the same results, except that the fraction of repopulation was less for H atoms by a factor of two and the dependence of the fraction on the second ionizing electric field strength showed a sharp cutoff for H atoms. This behavior for H atoms is believed to result from Stark mixing of the n states in the ionizing field. Measurements with D_2^+ failed to confirm the expectation that the fraction of repopulated states would be greater than that for H_2^+ due to the increased number of vibrational levels ($x\sqrt{2}$) of D_2.

2.10.6 Blistering of Stainless Steel by Energy-Dispersed He Beams

Blistering of stainless steel by an energy-dispersed (0-40 keV) neutral beam has been studied. The energy-dispersed beam was formed by passing a 40-keV He^+ beam through an accelerator type structure gas cell in which a decelerating potential was placed across the electrodes. By knowing the electron capture and stripping cross sections of He^+ and He^0 in He gas, the computed He^0 energy distribution was a maximum at low energies (~00 eV) and decreased approximately 10%, reaching a sharp cutoff at 40 keV. Figure 2.67 shows two electron microscope photographs for two stainless steel specimens bombarded by

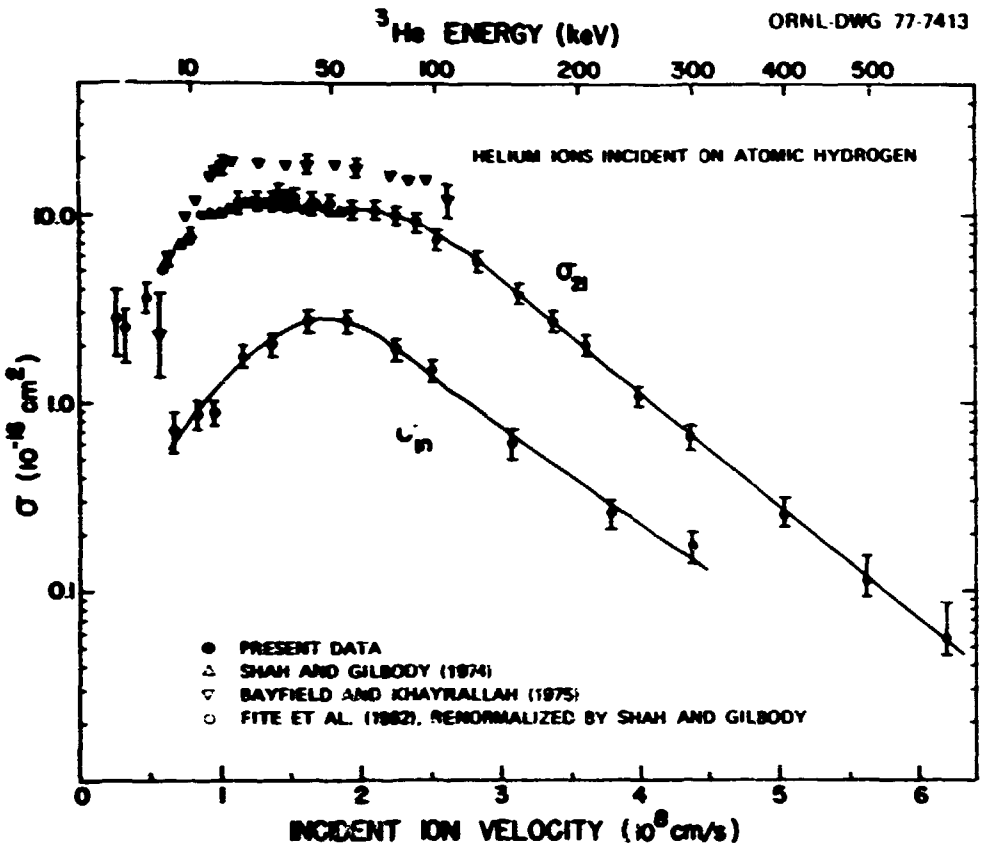

Fig. 2.62. Experimental electron capture cross sections σ_{10} for $^4He^+$ + H collisions, and σ_{21} for $^3He^{2+}$ + H collisions. Data of other investigators for σ_{21} are also plotted.

a monoenergetic, 40-keV He^+ beam and an energy-dispersed He beam of 0-40 keV to a dose of 1.9×10^{8} p/cm^2 and 2.6×10^{16} p/cm^2, respectively. The damage or density of surface blisters was less but clearly present for the energy-dispersed beam. However, on a second run no blistering from an energy-dispersed beam was found. Electron microscopic examination revealed evidence of surface oxidation. Work is continuing to try to understand this discrepancy.

2.10.7 Submillimeter Laser Plasma Diagnostics

During the past year, we have continued the development of a high power, submillimeter laser system to measure the ion temperature in thermonuclear plasmas via coherent Thomson scattering. In addition to the improvements in the CH_3F laser, we have developed both a cw and a pulsed submillimeter laser based on the 447-μm CH_3I line for use in this measurement. The cw CH_3I laser, optically pumped by the P(18) 10.6-μm-CO_2 line, exhibited better power conversion efficiency and amplitude stability than did the CH_3F operating in the same laser cavity. The amplitude stability is greater because the CH_3I molecule is pumped by a CO_2 laser operating at line center, as opposed to the CH_3F molecule which must be pumped approximately 20 MHz off line center, thus allowing greater drift and frequency jitter. Most lasers exhibit lower drift and less frequency jitter when operated at line center.

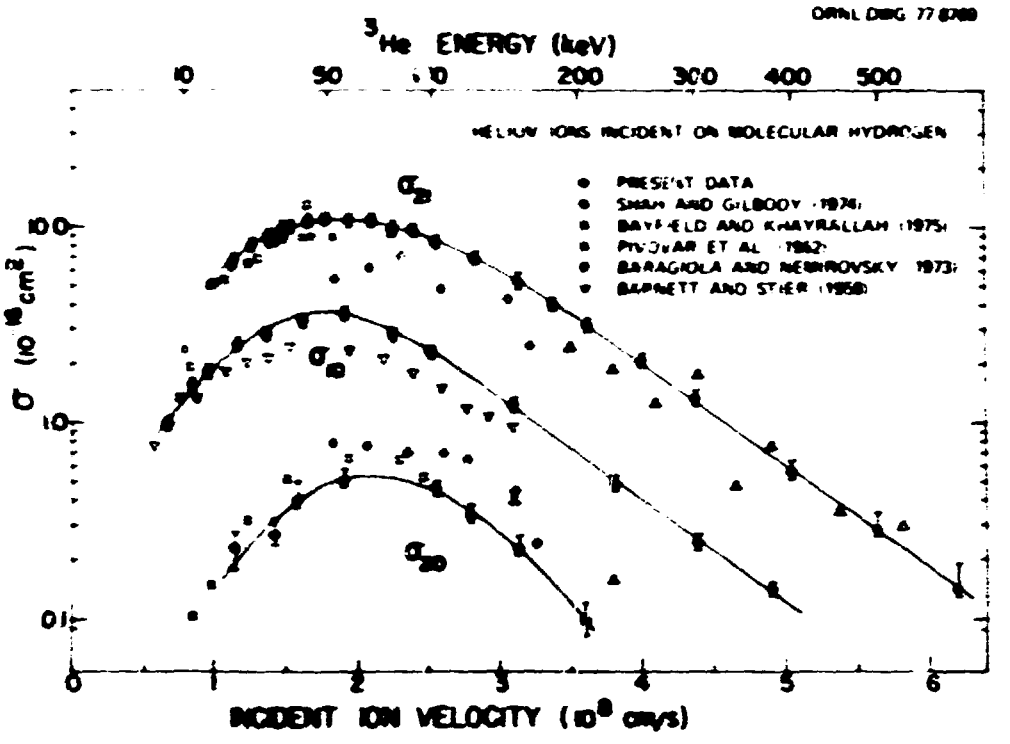

Fig. 2.63. Experimental electron capture cross sections, σ_{10}, for $^4He^+ + H_2$ collisions, as well as single electron capture cross sections, σ_{21}, and double electron capture cross sections, σ_{20}, for $^4He^{++} + H_2$ collisions. Data of other investigators for σ_{21} and σ_{20} are also plotted.

A new, pulsed, far-infrared oscillator based on an unstable resonator geometry has been operated using CH_3I (447 μm), CH_3F (496 μm) and D_2O (385 and 361 μm). Power output varied from approximately 10 kW with CH_3I and CH_3F to 20-30 kW for D_2O. Unlike CH_3F and D_2O, CH_3I shows little tendency for superradiance, while demonstrating conversion efficiency comparable to CH_3F. The longer wavelength of CH_3I compared to D_2O makes the detector problem easier for the scattering experiment. If the 447-μm CH_3I line continues to exhibit these attractive characteristics as the laser is scaled to higher power levels, this laser medium will become the gas for Thomson scattering.

The unstable resonator was developed to serve as an oscillator in a 1-MW oscillator-amplifier system for the ion temperature measurement experiment. A schematic diagram of the system is shown in Fig. 2.68. The oscillator will be excited by a TEA CO_2 laser at 15 J, while the amplifier will be driven by a TEA CO_2 laser at 150 J. The wavelength tuning of the CO_2 lasers will be achieved by an injection tuning technique which we developed last year.[71] The submillimeter amplifier utilizes parabolic beam-expanding optics, producing a large volume to absorb the 150-J pump pulse. At the same time it has a short length to inhibit superradiance: the overall length of the amplifier is 1 m, with a diameter of 0.64 m. This geometry yields an active volume of 230 liters.

Based on our work with CH_3I, a high power (40 MW), cw submillimeter laser, has been built to serve as a local oscillator for both the ion Thomson scattering receiver and a narrow band synchrotron emission detector.

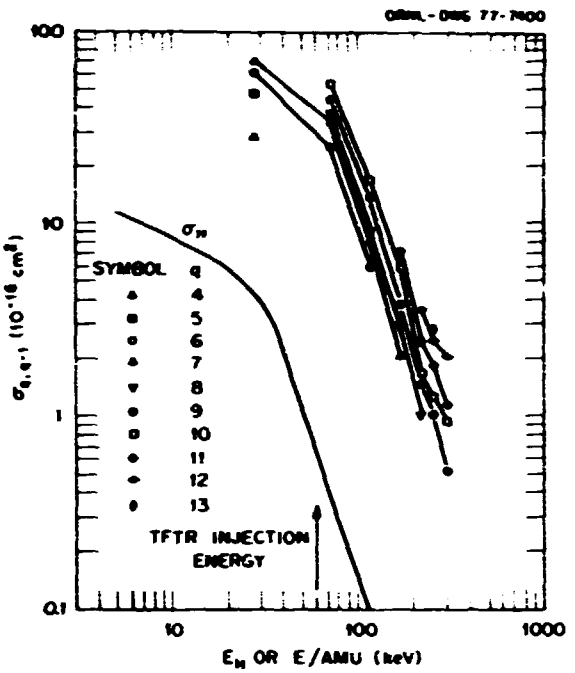

Fig. 2.64. Measured electron capture cross sections for $Fe^{q+} + H^0 \rightarrow Fe^{(q-1)+} + H^+$ as a function of incident energy per nucleon or equivalent hydrogen energy. Estimated uncertainties are less than 35%. The solid curve labeled σ_H indicates charge transfer cross sections for protons on hydrogen.

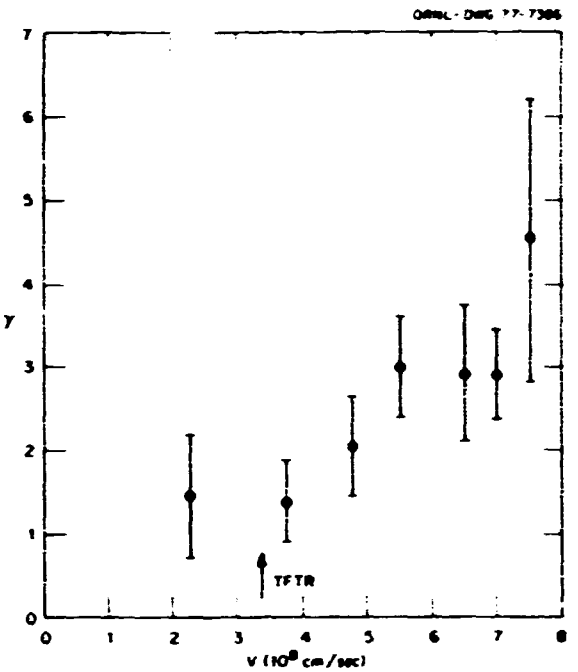

Fig. 2.65. Least square values of parameter α and standard deviations, where $\alpha_{q,q-1} \propto q^{\alpha}$.

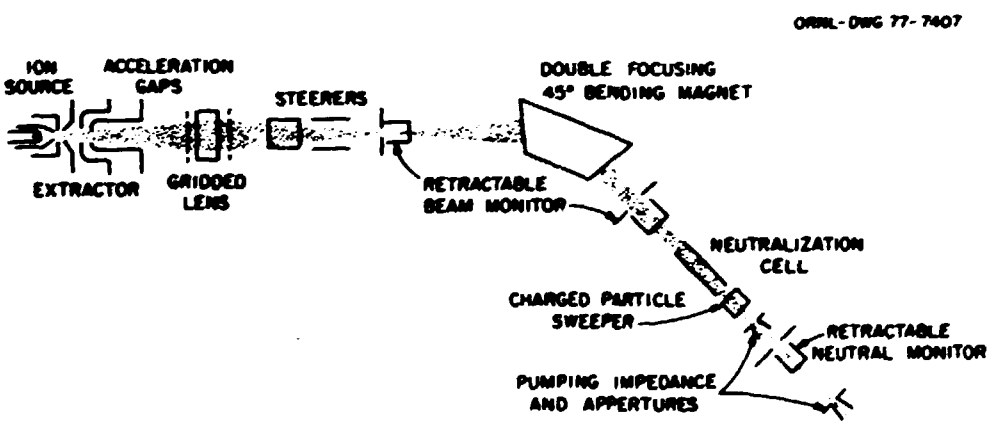

Fig. 2.66. Schematic layout of the atomic hydrogen beam apparatus.

ORNL-DWG 78-12605

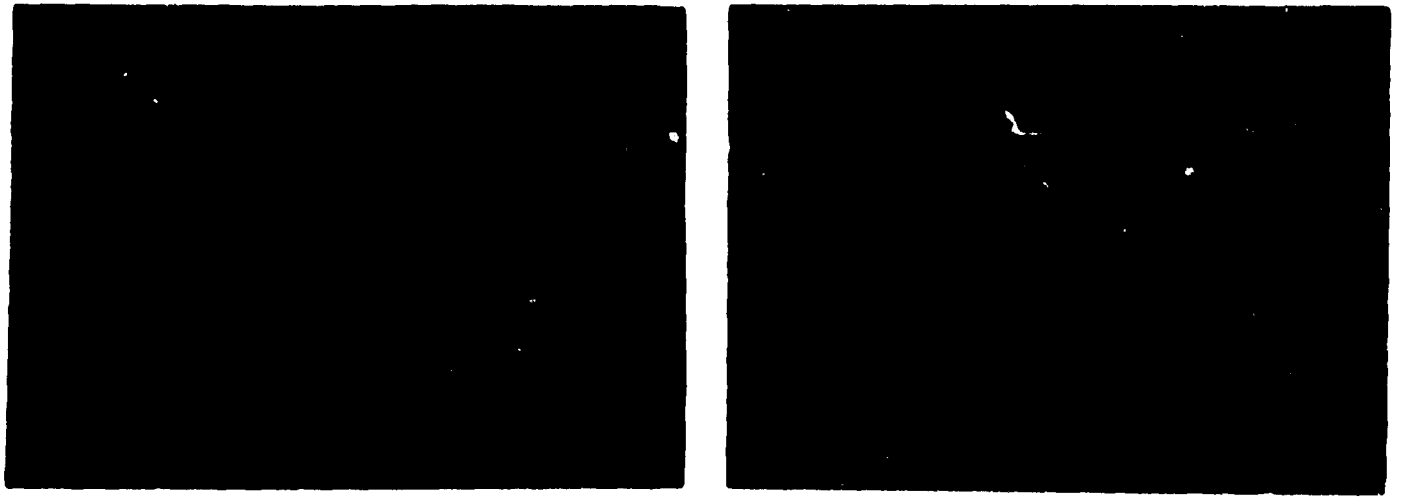

MAGNIFICATION - 875

40 keV He^+ ON SS
1.9×10^{18} p/cm^2

0-40 keV He^0 ON SS
2.6×10^{18} p/cm^2

Fig. 2.67. Electron microscope photographs of two stainless steel targets bombarded with a 40-keV He^+ beam and energy dispersed H^0 beam.

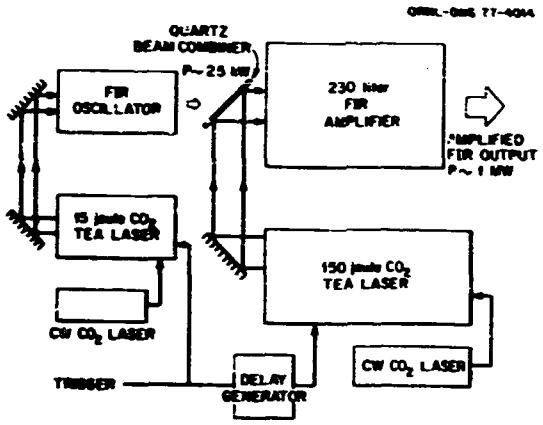

Fig. 2.68. Schematic diagram of the 1-MW CH_3I submillimeter laser system for ion temperature measurements.

Studies have been undertaken during the past year to develop: (1) a fast scanning Fourier transform spectrometer to measure the broadband synchrotron emission from high temperature plasmas and (2) a method of measuring the current density profile in a tokamak discharge by Faraday rotation.

2.10.8 Spark Measurements of Electric Fields in ORMAK

Previous analysis of line profile measurements of the Balmer α, β, γ, and δ radiation of hydrogen in ORMAK involved data averaging by a computer. In order to eliminate these computer routines as an influencing factor, several sets of data were analyzed directly from the Biomation recording with individual treatment. There were two weaknesses in the computer routines: (1) the averaging process, which tended to mask obvious noise, and (2) the sampling method, which ignored a slight variation in wavelength dispersion as a periodic function of time.

The Biomation recorded approximately 100 samples of the line intensity in 100 msec. Each data point represented a 10-μsec average of the photomultiplier current. In this time interval the rotating plate will change the wavelength by 0.032 A. This is 1/20 of the band pass of the slit of the spectrometer which, for the 40-μ slit used, is 0.65 K. This technique provided a distinguishing feature to separate qualitatively real wavelength variations from random time events. Examination of the raw Biomation data shows many single events which have a rise and decay time of over a few channels, typically three to five. A plasma current variation of this time characteristic cannot represent a wavelength character because the slit function of the spectrometer covers 20 channels. However, it is possible that the probability of observing a signal at that wavelength is low, and one is observing fluctuation in the signal level. In either case, the process of averaging over eleven channels erases this time feature and yields a broadened signal which is difficult to distinguish from the real 20-channel wavelength information.

This analysis provides evidence of why variations of the order of 0.25 A in the positions of real peaks occur. It also confirms that the signals are too close to the noise level to provide meaningful measurements of weak satellites. Finally, the major features of the profiles correspond to the basic Balmer emissions and to known impurity spectra.

2.10.9 H Neutral Particle Spectrometers

A parallel plate ion energy analyzer and a Wien type ion velocity filter analyzer using an N_2 gas cell to strip energetic H atoms have been fabricated, calibrated, and placed into operation on the ELMO Bumpy Torus (EBT) plasma to determine the plasma ion temperature. Measurements made by the EBT group have confirmed previously measured ion temperatures, indicating that previous measurements were not distorted by the presence of impurity neutrals escaping the plasma.

Using heat pipe techniques, a Cs oven has been fabricated and calibrated to convert H atoms to H^-. At 100 eV the spectrometer efficiency was two orders of magnitude greater than that obtained when using an N_2 gas cell to strip H to H^+. This cell will be placed on EBT

to measure both ion temperatures and density fluctuations.

2.10.10 Controlled Fusion Atomic Data Center

After numerous delays in editing and printing, the compilation *Atomic Data for Controlled Fusion Research* has been distributed to the fusion research community. Since parts of the compilation are two years out-of-date, data revisions are being made with emphasis on those atomic collisions involving impurities found in high temperature plasmas. To make the data more compatible with the needs of plasma modeling, a program has been completed to convert the cross section data to reaction rates and analytical expressions for the case of beam-Maxwellian distributions.

In cooperation with the Atomic Transition Probabilities Data Center at the National Bureau of Standards, the bimonthly publication of the "Atomic Data for Fusion" bulletin has continued. From an initial mailing of 57, the number has grown to 330 at the beginning of 1977. The bulletin has proven to be a very effective means of transferring recently acquired data to the fusion community several months before the data appear in laboratory records or open literature.

Searching, evaluating, and entering bibliographical data into the computer file have continued. Work is proceeding to evaluate critically the completeness of the file. After references that had been omitted have been added in, an index bibliography for specific collisional processes will be published.

During 1976 talks were continued with the International Atomic Energy Agency to determine the role the agency would undertake in their new program to provide the international fusion community with atomic data pertinent to fusion research. Their initial effort will be confined to the publication of a comprehensive bibliography compiled from inputs from the United States, the United Kingdom, the Federal Republic of Germany, the U.S.S.R., France, and Japan.

1. F. L. Hinton and M. N. Rosenbluth, Phys. Fluids 16, 836 (1973).
2. R. D. Hazeltine and F. L. Hinton, Phys. Fluids 16, 1883 (1973).
3. L. A. Berry et al., *Proc. 5th Intl. Conf. on Plasma Physics and Controlled Nuclear Fusion Research*, Vol. I, p. 101 (1975).
4. See Sect. 2.1.8, Ref. 14.
5. See Sect. 2.1.8, Ref. 15.
6. See Sect. 2.1.8, Ref. 20.
7. *Thermonuclear Division Annual Progress Report for Period Ending December 31, 1975*, ORNL-5154, Sect. 2.1.2, pp. 15-26, Oak Ridge National Laboratory, Oak Ridge, Tennessee (June 1976).
8. M. Murakami, J. D. Callen, and L. A. Berry, Nucl. Fusion 16, 347 (1976).
9. P. Moriette (representing the TFR Group), Bull. Am. Phys. Soc. 21, 1087 (1976).
10. J. Sheffield (JET, Culham Laboratory, UKAEA), private communication, 1976.
11. *Thermonuclear Division Annual Progress Report for Period Ending December 31, 1974*, ORNL-5053, pp. 15-18, Oak Ridge National Laboratory, Oak Ridge, Tennessee (July 1975).
12. R. C. Isler, R. V. Neidigh, and R. A. Phaneuf, Bull. Am. Phys. Soc. 21, 1051 (1976).
13. *Thermonuclear Division Annual Progress Report for Period Ending December 31, 1975*, ORNL-5154, Sect. 2.1.6, p. 39, Oak Ridge National Laboratory, Oak Ridge, Tennessee (June 1976).
14. P. G. Burkhalter and D. J. Nagel (Naval Research Laboratory), private communication, 1976.
15. R. D. Cowan (Los Alamos Scientific Laboratory), private communication, 1976.
16. R. Mewe, Sol. Phys. 22, 459-491 (1972).
17. C. Jordan, Mon. Not. R. Astron. Soc. 142, 501-521 (1969).
18. Equipe TFR, Nucl. Fusion 15, 1053-1065 (1975); TFR Groupe, Phys. Rev. Lett. 36, 1306-1309 (1976).
19. A. Jacobs, J. Quant. Spectrosc. Radiat. Transfer 11, 143-152 (1971).

20. R. Jensen and D. Post (Princeton Plasma Physics Laboratory), private communication, 1976.
21. M. N. Rosenbluth, R. D. Hazeltine, and F. L. Hinton, Phys. Fluids 15, 116 (1972). There should be a minus in front of the step function in Eq. (180).
22. D. J. Sigmar, J. F. Clarke, R. V. Neidigh, and K. L. Vander Sluis, Phys. Rev. Lett. 33, 1376 (1974).
23. *Thermonuclear Division Annual Progress Report for Period Ending December 31, 1975*, ORNL-5154, Sect. 2.1.4, pp. 27-33, Oak Ridge National Laboratory, Oak Ridge, Tennessee (June 1976).
24. R. G. Bateman, Jr. and Y-K. M. Peng, "MHD Stability of Flux Conserving Tokamak Equilibria," Phys. Rev. Lett. 38, 829-832 (1977).
25. F. Karger et al., "On the Origin of the Disruptive Instability in the Pulsator I Tokamak," paper presented at the 6th International Conference on Plasma Physics and Controlled Nuclear Fusion Research, Berchtesgaden, Federal Republic of Germany, October 6-13, 1976; proceedings to be published.
26. TFR group (presented by D. Launois), *Proc. 7th European Conf. on Controlled Fusion and Plasma Physics*, Vol. II, pp. 1-13 (1975).
27. TFR group, "Experimental Study of Instabilities in the TFR Tokamak," paper presented at the 6th International Conference on Plasma Physics and Controlled Nuclear Fusion Research, Berchtesgaden, October 6-13, 1976; proceedings to be published.
28. *Thermonuclear Division Annual Progress Report for Period Ending December 31, 1975*, ORNL-5154, Sect. 2.1.2, pp. 15-26, Oak Ridge National Laboratory, Oak Ridge, Tennessee (June 1976).
29. See Sect. 2.1.3 of this report.
30. S. Von Goeler, W. Stodiek, and N. Sauthoff, Phys. Rev. Lett. 33, 1201 (1974).
31. *Thermonuclear Division Annual Progress Report for Period Ending December 31, 1975*, ORNL-5154, Sect. 2.1.5, p. 28, Oak Ridge National Laboratory, Oak Ridge, Tennessee (June 1976).
32. B. V. Waddell, G. L. Jahns, J. D. Callen, and H. R. Hicks, "Interpretation of Tokamak Sawtooth Oscillations," submitted to Phys. Rev. Lett.
33. TFR Group (represented by R. Dei-Cas), Paper IAEA-CN-35/A8, presented at the 6th International Conference on Plasma Physics and Controlled Nuclear Fusion Research, Berchtesgaden, Federal Republic of Germany, October 6-13, 1976 (proceedings to be published); J. Hosea and V. Arunasalam, Bull. Am. Phys. Soc. II, 21, 1159 (1976).
34. B. V. Waddell, M. N. Rosenbluth, D. A. Monticello, and R. B. White, Nucl. Fusion 16, 528 (1976).
35. J. D. Callen and G. L. Jahns, Phys. Rev. Lett. 38, 491 (1977).
36. L. A. Berry et al., Paper IAEA-CN-35/A4-1, presented at the 6th International Conference on Plasma Physics and Controlled Nuclear Fusion Research, Berchtesgaden, Federal Republic of Germany, October 6-13, 1976; proceedings to be published.
37. *Thermonuclear Division Annual Progress Report for Period Ending December 31, 1975*, ORNL-5154, p. 25 and p. 34, Oak Ridge National Laboratory, Oak Ridge, Tennessee (June 1976).
38. V. D. Kirillov, B. A. Trubnikov, and S. A. Trushin, Sov. J. Plasma Phys. 1, 117 (1975).
39. D. L. Shaeffer, *Impurity Electron Core Effect in ORMAK*, ORNL/TM-5745, Oak Ridge National Laboratory, Oak Ridge, Tennessee (March 1977).
40. *Thermonuclear Division Annual Progress Report for Period Ending December 31, 1975*, ORNL-5154, pp. 41-44, Oak Ridge National Laboratory, Oak Ridge, Tennessee (June 1976).
41. J. G. Cordey, *Proc. 5th Intl. Conf. on Plasma Physics and Controlled Nuclear Fusion*

Research, Vol. I, p. 623 (1975).

42. J. D. Callen, R. J. Colchin, R. H. Fowler, D. G. McAlees, and J. A. Rome, *Proc. 5th Intl. Conf. on Plasma Physics and Controlled Nuclear Fusion Research*, Vol. I, p. 645 (1975).
43. *Thermonuclear Division Annual Progress Report for Period Ending December 31, 1975*, ORNL-5154, Sect. 2.1.5, pp. 33-37, Oak Ridge National Laboratory, Oak Ridge, Tennessee (June 1976).
44. D. L. Jassby, Phys. Rev. Lett. 55A, 225 (1975).
45. R. J. Colchin, C. E. Bush, G. L. Jahns, J. F. Lyon, M. Murakami, R. V. Neidigh, and D. L. Shaeffer, "Impurity and Surface Studies in ORMAK," paper presented at the International Conference on Surface Effects in Controlled Fusion Devices, San Francisco, California, February 16-20, 1976; published in J. Nucl. Mater. 63(1), 74 (December 1976).
46. R. J. Colchin, L. C. Emerson, L. Heatherly, R. E. Clausing, and R. C. Isler, "Surface and Impurity Studies in ORMAK and ISX," paper presented at the International Symposium on Plasma Wall Interaction, Julich, Federal Republic of Germany, October 18-22, 1976; proceedings to be published.
47. R. E. Clausing, L. C. Emerson, L. Heatherly, and R. J. Colchin, "Surface Impurities and Clean-up Techniques in ORMAK," paper presented at the International Symposium on Plasma Wall Interaction, Julich, Federal Republic of Germany, October, 18-22, 1976; published in J. Nucl. Mater. 63(1), 495 (December 1976).
48. R. D. Birkhoff, R. N. Hamm, M. W. Williams, E. T. Arakawa, R. J. Colchin, and R. V. Neidigh, "A Laser Reflection Technique for Studying Contamination Buildup on a Fusion Reactor Liner," J. Nucl. Mater. 63(1), 501 (December 1976).
49. R. E. Clausing, L. C. Emerson, L. Heatherly, and R. J. Colchin, "Wall Conditioning Studies for ORMAK and ISX," paper presented at the International Symposium on Plasma Wall Interaction, Julich, Federal Republic of Germany, October 18-22, 1976.
50. C. A. Foster, R. J. Colchin, S. L. Milora, J. Kim, and R. J. Turnbull, "Solid Hydrogen Pellet Injection into the ORMAK Tokamak," to be published in Nucl. Fusion.
51. H. E. Knoepfel and S. J. Zweben, "Dynamics of High Energy Electrons in the ORMAK Tokamak, submitted to Phys. Fluids.
52. H. E. Knoepfel and S. J. Zweben, High Energy Runaway Electrons in the Oak Ridge Tokamak," Phys. Rev. Lett. 35(20), 1340 (November 1975).
53. P. Cristman, J. F. Clarke, and J. A. Rome, *Magnetic Island Formation in a Tokamak Plasma from Helical Perturbations of the Plasma Current*, ORNL/TM-4501, Oak Ridge National Laboratory, Oak Ridge, Tennessee (1974).
54. H. E. Knoepfel, D. A. Spong, and S. J. Zweben, "Relativistic Runaway Electron Beams in the Oak Ridge Tokamak," to be published in Phys. Fluids.
55. J. W. Connor and R. J. Hastie, Nucl. Fusion 15, 415 (1975).
56. *Thermonuclear Division Annual Progress Report for Period Ending December 31, 1975*, ORNL-5154, Sect. 2.7, p. 53, Oak Ridge National Laboratory, Oak Ridge, Tennessee (June 1976).
57. *Thermonuclear Division Annual Progress Report for Period Ending December 31, 1975*, ORNL-5154, Sect. 2.8, pp. 55-59, Oak Ridge National Laboratory, Oak Ridge, Tennessee (June 1976).
58. R. J. Colchin et al., "ISX – Surface Interactions Studies," paper presented at the International Conference on Surface Effects in Controlled Fusion Devices, San Francisco, California, February 16-20, 1976; to be published in J. Nucl. Mater. 63.
59. G. L. Cardwell (University of Texas), private communication, 1976
60. R. A. Phaneuf and R. H. McKnight, Bull. Am. Phys. Soc. 21, 1266 (1976).
61. G. W. McClure, Phys. Rev. 148, 47 (1966).

62. J. E. Bayfield, Rev. Sci. Instrum. 40, 869 (1969).
63. G. J. Lockwood, H. F. Helbig, and E. Everhart, J. Chem. Phys. 41, 3820 (1964).
64. D. H. Crandall, D. C. Kocher, and M. L. Mallory, Phys. Rev. A 15, 61 (1977).
65. R. E. Olson (Stanford Research Institute), private communication, 1976.
66. M. B. Shah and H. B. Gilbody, J. Phys. B 7, 630 (1974).
67. J. E. Bayfield and G. A. Khayrallah, Phys. Rev. A 11, 920 (1974); Phys. Rev. A 12, 869 (1975).
68. L. I. Pivovar, M. T. Novikov, and V. M. Tubaev, Sov. Phys. – JETP 15, 1035 (1962).
69. R. A. Baragiola and I. B. Nemirovsky, Nucl. Instrum. Methods 110, 511 (1973).
70. W. L. Fite, A.C.H. Smith, and R. F. Stebbings, Proc. R. Soc. Lond. A 268, 527 (1962).
71. D. P. Hutchinson and K. L. Vander Sluis, "Injection Tuning of a Pulsed TEA CO_2 Laser," to be published in Appl. Opt.

3. PLASMA THEORY SECTION

J. D. Callen, Section Manager
R. A. Dory, Deputy Manager

R. Aghevli[1]	J. Denavit[11]	D. G. McAlees[15]	J. A. Rome
J. E. Akin[2]	O. C. Eldridge[12]	J. E. McCune[16]	K. E. Rothe[5]
T. Amano[3]	S. K. Fischer[5]	R. W. McGaffey[5]	R. T. Santoro[18]
C. H. An[4]	R. H. Fowler[5]	J. R. McNally, Jr.	R. O. Sayer[5]
D. E. Arnurius[5]	J. E. Francis, Jr.	H. K. Meier	R. D. Sharp[5]
S. E. Attenberger[5]	K. A. French	A. T. Mense	D. J. Sigmar[20]
D. B. Batchelor	R. C. Goldfinger[5]	J. R. Moore[17]	J. Smith[2,5]
R. G. Bateman, Jr.	R. K. Gryder	J. K. Munro[5]	M. Soler[8]
C. O. Beasley, Jr.	C. E. Hammons	W. Namkung[4]	D. A. Spong
D. J. Beckett[6]	E. G. Harris[2]	R. W. Napier[17]	D. J. Strickler[5]
E. S. Bettis[7]	C. L. Hedrick, Jr.	D. B. Nelson	K. T. Tsang
I. Burnett III	O. W. Hermann[5]	E. M. Oblow[18]	M. A. Uckan
R. D. Burris[5]	H. R. Hicks[5]	D. R. Overbey	T. Uckan[21]
B. Carreras[8]	J. T. Hogan	L. W. Owen[5]	W. I. van Rij[5]
M. F. Carver[9]	J. A. Holmes[5]	C. E. Parker	B. V. Waddell
P. J. Catto[10]	H. C. Howe[13]	Y-K. M. Peng	H. L. Watts[17]
D. W. Clark[5]	E. F. Jaeger	L. M. Petrie[5]	J. C. Whitson[5]
C. M. Copenhaver[4]	C. O. Kemper[5]	C. E. Rathmann[11]	J. W. Wooten[5]
E. C. Crume, Jr.	G. D. Kerbel[14]	J. W. Reynolds[19]	H. T. Yeh[22]
L. E. Deleanu[4]	F. B. Marcus	J. F. Roberts[5]	O. C. Yonts

1. Summer employee, on leave of absence from Tehran Polytechnic, Tehran, Iran.
2. Consultant, University of Tennessee, Knoxville, Tennessee.
3. Permanent address: Osaka University, Osaka, Japan.
4. Student, University of Tennessee, Knoxville, Tennessee.
5. Computer Sciences Division.
6. Computer Sciences Division: Summer student, University of Illinois, Urbana, Illinois.
7. Consultant, UCC-ND Engineering.
8. Visitor from Spanish Nuclear Energy Commission.
9. Summer student, Kalamazoo College, Kalamazoo, Michigan.
10. Consultant, University of Rochester, Rochester, New York.
11. Northwestern University, Evanston, Illinois.
12. Consultant, University of Tennessee, Knoxville, Tennessee, and Hunter College, New York, New York.
13. Formerly with the Tokamak Experimental Section, Fusion Energy Division.
14. Present address: Lawrence Livermore Laboratory, Livermore, California.
15. Present address: Exxon Nuclear Co., Inc., Richland, Washington.
16. Consultant, Massachusetts Institute of Technology, Cambridge, Massachusetts.
17. UCC-ND Engineering.
18. Neutron Physics Division.
19. Instrumentation and Controls Division.
20. On leave of absence from Massachusetts Institute of Technology, Cambridge, Massachusetts.
21. Postdoctoral Fellow, University of Michigan, Ann Arbor, Michigan.
22. Magnetics and Superconductivity Section, Fusion Energy Division.

INTRODUCTION

The principal goals of the Plasma Theory Section are to: (1) develop the theory of plasma equilibrium, stability (macroscopic and microscopic), transport, and heating to the level where it can be meaningfully applied to relevant fusion plasma experiments; and (2) apply this theory to understanding and improving present and future thermonuclear fusion experiments and devices. In addition, the computing support services provided within the Fusion Energy Division (FED) are administered by the Theory Section.

The progress during the past year, which is reported below, is organized by group efforts and divided into five major areas. The basic tokamak areas and the sections in which their work is summarized are: magnetohydrodynamic (MHD) theory (3.2), kinetic theory (3.3), and transport simulation (3.4). The ELMO Bumpy Torus (EBT) theory work (3.1) has its own research projects on MHD theory, kinetic theory, and transport simulation. In the plasma engineering area (3.5), relevant research work is further developed and synthesized into models that are used in the design of advanced fusion systems – The Next Step (TNS), demonstration fusion reactor (Demo), EBT ignition test, etc. Specific plasma engineering projects on providing the TNS physics basis and the development of the EBT reactor (EBTR) study are discussed in Sects. 3.6 and 3.7. Finally, in Sect. 3.8 the computing support activities during the past year are summarized.

3.1 EBT THEORY

D. B. Batchelor C. L. Hedrick, Jr. L. W. Owen
R. A. Dory* E. F. Jaeger J. F. Roberts
E. G. Harris D. B. Nelson D. A. Spong

EBT theory supports the EBT experimental program as well as the EBT reactor study program. The emphasis is on those elements of the theory which are critical and unique to EBT.

*Group Leader.

3.1.1 Neoclassical Transport Simulation for EBT

E. F. Jaeger

Two different approaches to the problem of particle and energy transport in EBT are currently being pursued. First, fluid models have been developed by taking velocity moments of the bounce-averaged, drift-kinetic equation. Given a knowledge of the transport rates, these moment equations can be solved for spatial profiles of velocity-space averaged quantities such as density and temperature. Alternatively, a kinetic model has been implemented to solve the bounce-averaged, drift-kinetic equation directly for the distribution of particles in phase space. Velocity integrals of this distribution lead to particle and energy fluxes, or equivalently, transport rates as a function of position.

Fluid models

Using analytic fits to neoclassical transport coefficients for ions and assuming equal rates for electrons with an ad hoc ambipolar field, a one-dimensional, radial fluid transport code has been developed[1,2] and the results compared to experiment. Results for spatial profiles of the product of charged and neutral particle density show good qualitative agreement with measurements of Lyman α radiation,[3] while ion temperatures[4] are typically 50% lower than temperatures indicated by charge-exchange measurements.

Next, assuming that electron and ion transport rates have different magnitudes, but the same functional form a one-dimensional, radial fluid transport code has been developed with a self-consistent ambipolar electric field. Preliminary calculations given in Fig. 3.1(a) show successive profiles of plasma density, electron temperature, ion temperature, and ambipolar field at 4-msec time intervals. At 40 msec an equilibrium is reached, as shown in Fig. 3.1(b). For this calculation, we assume an edge source of cold neutrals with density 3×10^9 cm^{-3} and energy 0.3 eV, and a fraction of microwave power absorbed by the bulk plasma electrons which is 20% of the total power

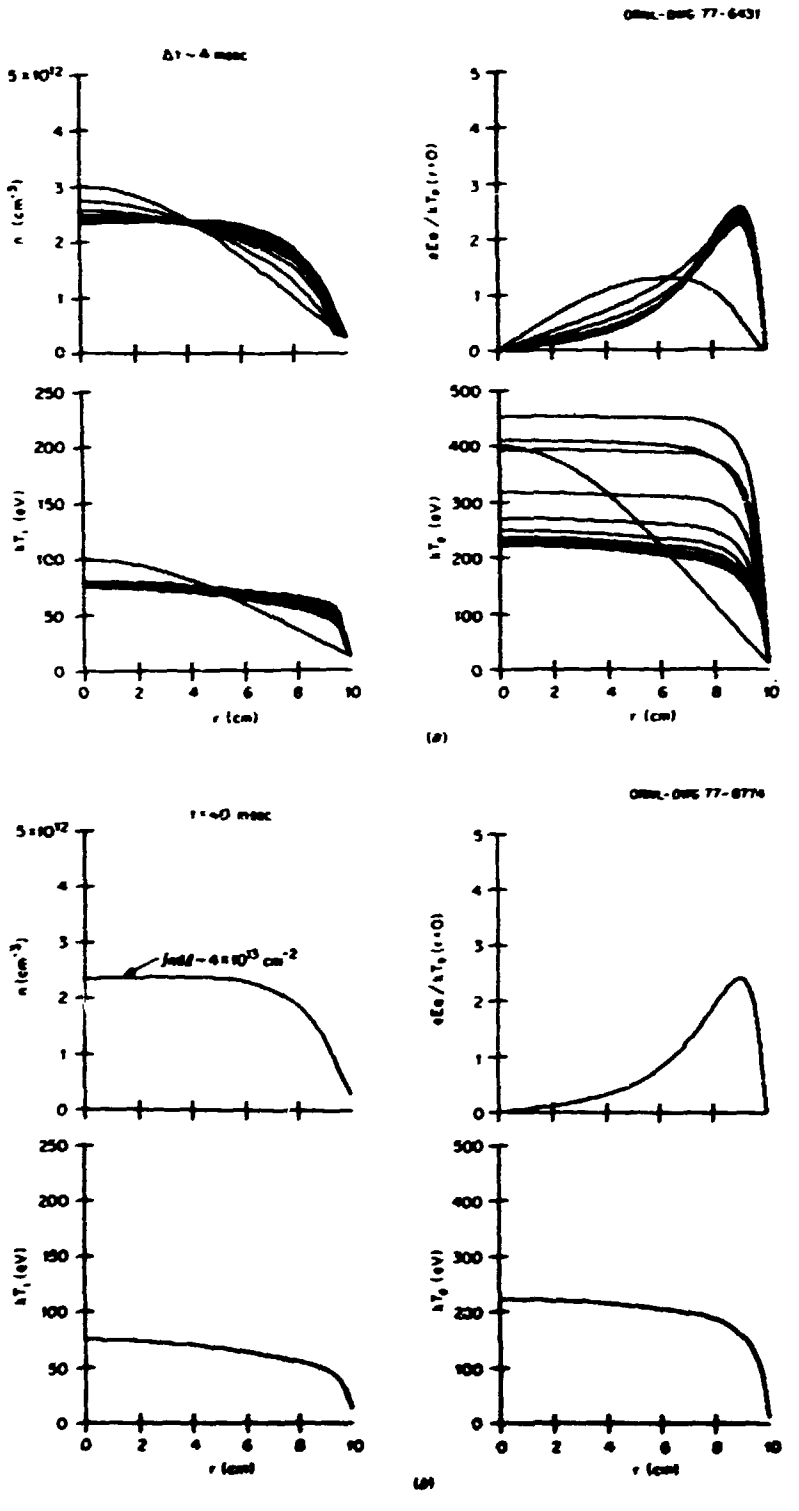

Fig. 3.1. (a) Time evolution and (b) equilibrium profiles for plasma density, electron temperature, ion temperature, and self-consistent ambipolar electric field.

available (60 kW). Equilibrium ion temperatures of 80 eV on axis are in better agreement with charge-exchange measurements than results of the simplified model with an ad hoc ambipolar field.

Kinetic model

Alternating-Direction Implicit (ADI) numerical techniques have been applied to solve the bounce-averaged, drift-kinetic equation directly in one velocity and one spatial coordinate. The method has so far been tested in the case of zero particle mobility and constant neutral density.[5] Transport rates for ions are in substantial agreement with results obtained from solutions in velocity space alone.[6] Such a kinetic transport model will be necessary to study effects of microwave heating terms, which produce a spatially localized high energy tail on the electron distribution function.

3.1.2 Neoclassical Transport Coefficients for EBT

D. A. Spong E. G. Harris

Estimates of ion neoclassical transport rates for energy and particles are an important ingredient in modeling the toroidal core plasma in the present EBT experiment as well as in larger future devices. In contrast to tokamaks, particle transport in a bumpy torus may occur as a result of like particle collisions, and loss rates for electrons and ions are not automatically equal. Earlier work by Kovrizhnykh[7] dealt only with the case where the ambipolar electric potential is large relative to the plasma thermal energy. Calculations done over the past year have extended this to the case where $e\phi/kT \sim 1$. Typical results are presented in Fig. 3.2 for the four transport coefficients. The particle and energy fluxes are related to these plots by:

$$S = \text{particle flux} = -\frac{nv_o^2}{2\Omega}\left[D_n\left(\frac{1}{n}\frac{dn}{dr} + \frac{e}{kT}\frac{d\phi}{dr}\right) + \frac{D_T}{T}\frac{dT}{dr}\right]$$

$$Q = \text{energy flux} = -\frac{nkTv_o^2}{2\Omega}\left[K_n\left(\frac{1}{n}\frac{dn}{dr} + \frac{e}{kT}\frac{d\phi}{dr}\right) + \frac{K_T}{T}\frac{dT}{dr}\right]$$

where $v_o = v_{th}(\rho_L/R)$

ρ_L = Larmor radius

R = major radius

Ω = poloidal drift frequency at mirror midplane

ν = ion-ion collision frequency.

These results were obtained by solving the linearized drift-kinetic equation with the full Landau collision operator. A bumpy cylinder approximation to the vacuum magnetic field was made to obtain a bounce-averaged poloidal drift frequency. An aspect ratio expansion was employed for the poloidal angle dependence in the distribution function, and a local approximation was made in the radius. The kinetic equation was solved by expanding the distribution function in a set of orthogonal polynomials (Laguerre polynomials in $|\vec{v}|$ and Legendre polynomials in pitch angle). This method is convergent as long as the $\vec{E} \times \vec{B}$ and drifts due to the bumpiness in the field do not cancel each other at velocities in the thermal range (such as is the case for electrons when $e\phi/kT < 0$). When this cancellation in the poloidal drifts occurs, there is a loss region which can affect a substantial fraction of the distribution; the functional expansion method breaks down because it cannot reflect the structure in the distribution function which forms near the loss region without going to a very large number of functions. In order to treat this case, a finite difference code has been developed for solving the kinetic equation using the ADI method. Besides providing transport rates for $e\phi/kT < 0$, this code is also being used as an independent check of the earlier results obtained for $e\phi/kT > 0$.

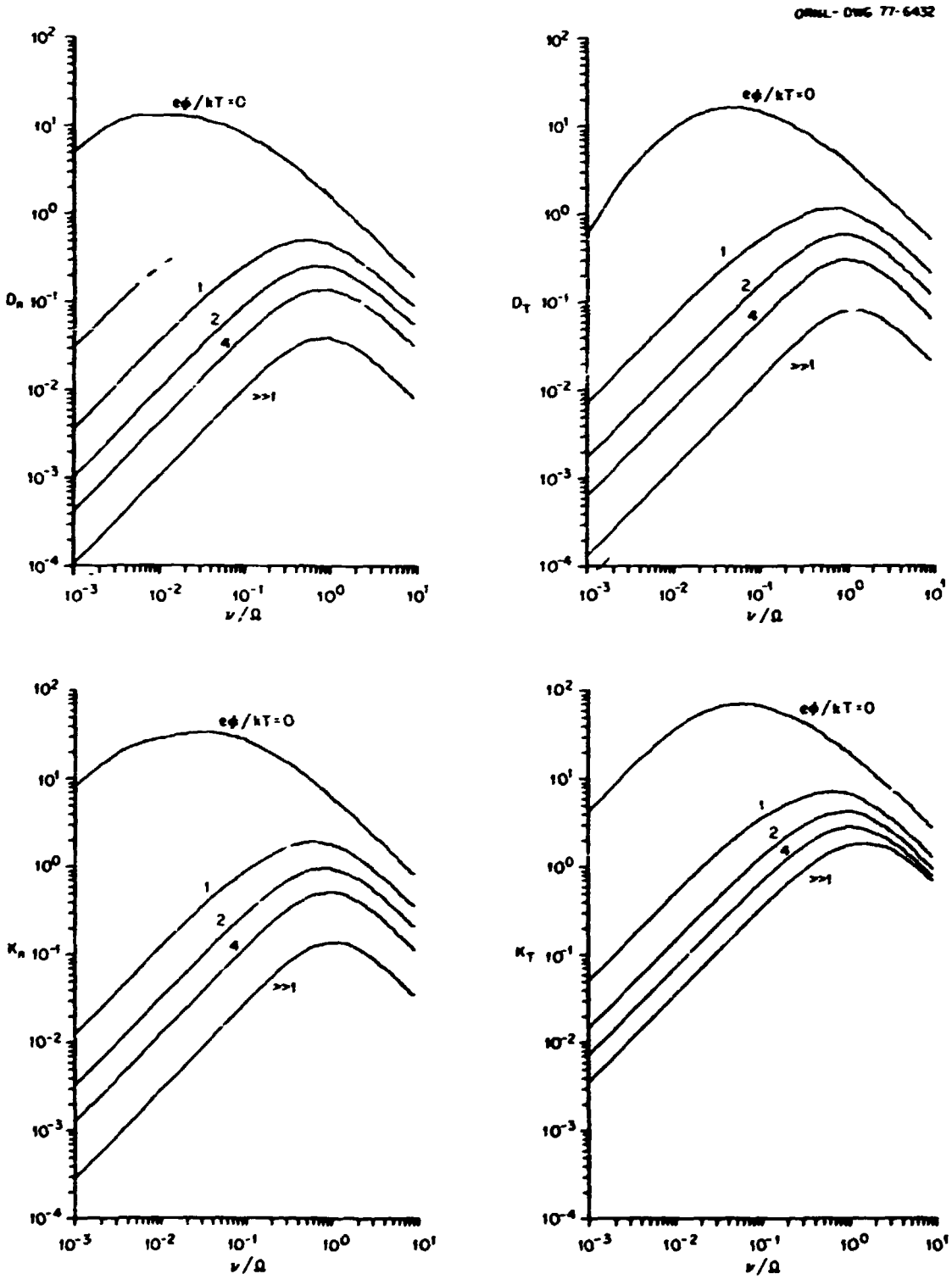

Fig. 3.2. Parametric dependence of neoclassical transport coefficients.

3.1.3 Magnetic Equilibria and Particle Orbits for EBT

C. L. Hedrick L. W. Owen J. F. Roberts

As part of the design studies for EBT and EBT-II we have examined single particle orbits in various finite β and ambipolar fields. From these calculations it became apparent that an alternate inner wall design was desirable for the reactor study. This suggested wall design[8] has been adopted for the following year's iteration in the EBT reactor study.

These numerical studies confirmed previous calculations with the three-dimensional equilibrium code[9] that high energy passing particles are the most poorly confined. We have examined several supplementary coil systems which can improve confinement of this class of particles and tentatively conclude that it is not possible to improve the orbits of high energy particles (without degrading the confinement of some other class of particles) with a coil system that is attractive from economic and engineering points of view. Because this lossy region of velocity space is expected to be sparsely populated even without these losses, it seems unlikely that such supplementary coil systems are warranted.

3.1.4 Microwave Heating in EBT

D. B. Batchelor

Because the plasma in EBT is produced and heated by microwaves and macrostability is dependent on microwaves through formation of the annuli, an understanding of microwave propagation and energy deposition is a crucial element in EBT theory. We have begun an investigation of microwave heating in EBT in which the propagation is treated by geometrical optics. The organization of the method we are developing is as follows.

1) The source microwave field (at the waveguide mouth) is expanded as a superposition of plane waves or rays.
2) The rays are traced through the plasma and allowed to reflect, split (by linear mode conversion), and be absorbed.
3) The rays (or trees of rays generated by mode conversion) are followed until all, or a certain fraction, of their energy is deposited in the plasma.
4) The energy deposition and microwave fields are coherently summed for a representative collection of rays in each region of plasma.

A central feature of the microwave heating study is the development of a ray-tracing code capable of operating in a wide variety of plasma equilibrium configurations. This code is now in a reasonably well developed state and has been extensively tested in one- and two-dimensional equilibria. Figure 3.3 shows ray trajectories and magnetic field lines (dotted curves) for extraordinary mode rays injected at the midplane of a simple mirror equilibrium. It can be seen that in this cold plasma model, rays do not penetrate to the cyclotron resonant surface. In order to explain the penetration of the extraordinary mode and the heating which is experimentally observed, it is necessary to include tunneling, linear mode conversion, and wall reflection within the model. Research is proceeding on techniques to handle these processes in the geometrical optics code.

We have also done a preliminary investigation on the effects of nonlinear processes such as parametric decay and filamentation due to the presence of a large-amplitude electromagnetic wave. The microwave energy density in EBT appears to be well below the threshold for most parametric decay processes.

3.1.5 Stabilizing Effects of Hot Electrons on MHD Modes in EBT

D. B. Nelson

Although the MHD or guiding center equations predict fast growing flutelike instabilities in the EBT for any plasma β, no such instabilities are observed in the presence of a sufficiently large (but not too large) hot electron population. The failure of the MHD equations is not surprising because the drift velocity and gyroradii of the hot electrons are too large for the assumed

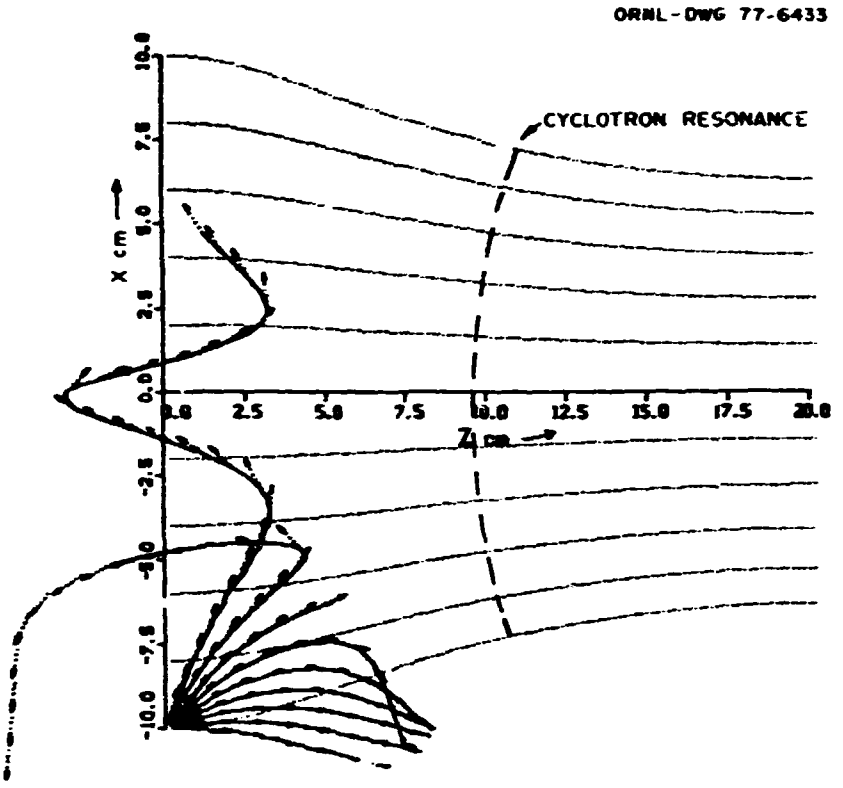

Fig. 3.3. Ray trajectories and magnetic field lines (dotted curves for extraordinary mode rays injected at the midplane of a simple mirror equilibrium.

scaling in MHD. To understand the stability of the three-component EBT plasma (composed of warm electrons, warm ions, and hot electrons), we have used the Vlasov equations, modeling the EBT geometry by an inhomogeneous, arbitrary β slab with gravity. Previous analyses of this geometry using the MHD equations showed that if $g\rho' < 0$ where g is acceleration due to gravity and ρ' is the derivative of density in the inhomogeneous direction, localized electromagnetic modes with $\underline{k} \cdot \underline{B} = 0$ are unstable (with a growth rate $\gamma \sim \sqrt{g\rho'/\rho}$).[10] For the Vlasov analysis we denote the ratio of hot electron density to ion density by δ and for $\delta = 0$ recover substantially the MHD growth rates. As δ increases the equilibrium is modified, but if $\delta < ka_i$ (a_i is the ion gyroradius) and $\delta < \beta_{ion}/\beta_{hot\ electron}$, the form of the dispersion relation is unchanged. The growth rates are modified because the coefficients depend on the equilibrium, and the plasma can be stabilized to these modes if $\beta_{hot} \geq 4r_p/r_c$, where r_p is the hot electron characteristic length and r_c is the average radius of curvature. In the annular plasma, $r_p \sim 1$ cm, whereas $r_c \sim 20$ cm, leading to a β_{hot} for stability of 20%. Given the simplifications of the model, this is in good agreement with the experimentally observed value of 10-15%.

In this range of δ, the hot electrons can be considered as rigid because they do not participate directly in the low frequency MHD instability. Their only effect is to modify the equilibrium magnetic fields through their plasma currents. This conclusion from the Vlasov equations provides considerable justification for our earlier ad hoc procedure using

the MHD variational principle to determine the β limits for stability of the ion plasma, considering the hot electrons as a rigid external current.

We have also considered the effect of increasing β beyond these limits and find that ω^2 then becomes complex, Reω approaches the hot electron drift frequency, and the MHD equations are no longer appropriate. This change of behavior may be reflected in the experiment by the transition from the T-mode of operation to the M-mode with increasing hot electron density.

3.1.6 MHD Analysis of Large-Scale Instabilities in the EBT Hot Electron Plasma

G. O. Spies* D. B. Nelson

Although the MHD equations are generally invalid for a plasma composed of particles with large gyroradii, for rigid displacements the finite gyroradius effects (due to the particle encountering a nonconstant perturbed field over its gyro-orbit) are eliminated. In a cylindrical geometry these displacements are the m = 1 modes, which in fact are observed in theta pinch experiments and are well described by the MHD equations. In contrast, m = 2 and higher modes are not observed, presumably stabilized by finite gyroradius effects.

No m = 1 instabilities are observed in EBT in its quiescent mode of operation. If this fact could be explained by the MHD equations on the bases of line tying, hollow pressure profile, wall proximity, or cold plasma effects, the much more difficult Vlasov theory of nonlocalized perturbations could be avoided. Accordingly, we have calculated the growth rates and eigenmode structure of m = 1 modes in a periodic bumpy cylinder modeling the EBT. Because qualitative information regarding stability mechanisms was desired, approximations were made to allow analytic solution of the linearized equations of motion. These include an expansion in the ratio of plasma width to coil spacing (long thin approximation) and the approximation of the continuous pressure gradient by a staircase pressure profile (constant pressure regions supported by sheet currents).

The resultant eigenvalue problem for the growth rates is purely algebraic. The validity of the staircase profile was tested by comparing with a diffuse profile in a bumpy theta pinch.[11] Three constant pressure regions were used, and very good agreement was found for the growth rates of modes having zero or one radial mode. (These are the fastest growing modes.)

When applied to hollow profiles typical of the EBT hot electron plasma, the model predicts an m = 1, radially nonlocalized instability with an e-folding time less than 0.1 μsec for any combination of wall proximity, external cold plasma, or line tying which is consistent with the experiment. We conclude that the behavior of the hot electron plasma in EBT cannot adequately be described by the MHD equations even for large-scale m = 1 modes.

3.2 MHD TOKAMAK THEORY

R. G. Bateman, Jr. B. Carreras D. N. Clark
R. A. Dory* H. R. Hicks J. A. Holmes
J. R. Moore D. B. Nelson Y-K. M. Peng
R. O. Sayer D. J. Strickler B. V. Waddell
J. W. Wooten

The year 1976 was an exciting one in this area because techniques and procedures begun over the past several years reached maturity and were available when needed. The equilibrium analysis methods (Sect. 3.2.1) made a very important contribution to the FED program in verifying t.. analytical calculations by Clarke and Sigmar[12] of equilibria at high β. The numerical procedures verified that flux conserving tokamak (FCT) equilibria were valid at a finite aspect ratio and that the equilibria existed even when the basic assumption (circular flux

*Max Planck Institute for Plasma Physics, Garching bei München, Federal Republic of Germany.

*Group Leader.

surfaces) of the analytical theory was badly violated. Related to this work were the timely contributions in the magnetic field design area to the Impurity Study Experiment (ISX) and Oak Ridge Tokamak (ORMAK) Upgrade machine designs and to the studies aimed toward tokamak experimental power reactors and TNS.

Codes for investigating (within a very simple model, of course) the ideal MHD instability regimes again were available after an extended developmental period for application to the new equilibrium conditions. These were used to show that the tokamak equilibria with a D-shaped cross section emphasized here at ORNL have significantly higher β limits than were found in an analogous study of the Tokamak Fusion Test Reactor (TFTR) device – at least for the internal kink or ballooning modes as in Sect. 3.2.3.

Significant advances were made in the understanding of what basic physics is required for realistic analysis of the fluid instability properties of tokamaks. Since nonideal (resistive) processes and nonlinear perturbations are known to be very important to serious assessment of specific configurations, the validation of calculations incorporating these features by direct comparison with ORMAK experimental data gives needed guidance to those attempting design of advanced MHD instability codes, as in Sect. 3.2.4.

3.2.1 High Pressure FCT Equilibria

R. A. Dory Y-K. M. Peng

MHD tokamak equilibria are found with values of β up to 20% and realistic MHD safety factor values [e.g., q(axis) = 1 and q(edge) = 4.8] for tokamaks with an aspect ratio A = 4 and a D-shaped cross section (Fig. 3.4). If such equilibria can be attained experimentally, they will be very attractive for decreasing the projected costs of tokamak power reactors. In the FCT model, where rapid heating is applied to an already relatively hot plasma, these high-β equilibria are achievable. We study the quasi-static evolution of FCT equilibria as β increases. An operating window is found in the pressure profile width, w_p, at the half-height: for high $\bar{\beta}$ the values of w_p lie between 0.40 and 0.55 times the plasma minor diameter. Within this window, plasma current and poloidal $\bar{\beta}$ increase with $\bar{\beta}$. For fixed plasma boundary, significant poloidal surface currents are induced, but these can be eliminated by small increases in the plasma minor radius, the pressure profile width, or the vacuum toroidal field. Detailed studies of other properties of high-β equilibria are in progress.

Free boundary FCT equilibria

Y-K. M. Peng R. A. Dory
D. J. Strickler J. R. Moore

High-$\bar{\beta}$ (~5-30%) tokamak equilibria have been found and the external magnetic field structures required to attain and hold them have been studied. The high-$\bar{\beta}$ equilibria can be a natural consequence of intense heating by an auxiliary power source such as neutral beams, if the heating is rapid compared to the magnetic diffusion time scale. Because magnetic fluxes are frozen in for such equilibria, they are called FCT equilibria. FCT equilibria are shown to exist and satisfy the local (Mercier) stability criterion with β values ranging up to 28%. For slightly D-shaped cross sections, we describe simple and efficient poloidal field (PF) systems which properly control and shape the plasma and admit poloidal divertors at the apexes of the natural D-shaped cross sections (Figs. 3.5 and 3.6). The PF system may also have the property (STATIC concept) of shielding (by a factor of about six).

Energy balance evaluation for D-shaped FCT

Y-K. M. Peng J. A. Holmes

Based on the peaked pressure profiles of the high-β equilibria in a D-shaped FCT,[13] the α power of deuterium-tritium (D-T) fusion from the TNS tokamak with B_T = 43 kG is calculated. Assuming that the averaged density, $\bar{n}$, increases linearly with $\bar{\beta}$ from 0.6×10^{14} cm^{-3} at $\bar{\beta}$ = 0.69%, the α power, P_α, is shown to be 200 MW (ignition)

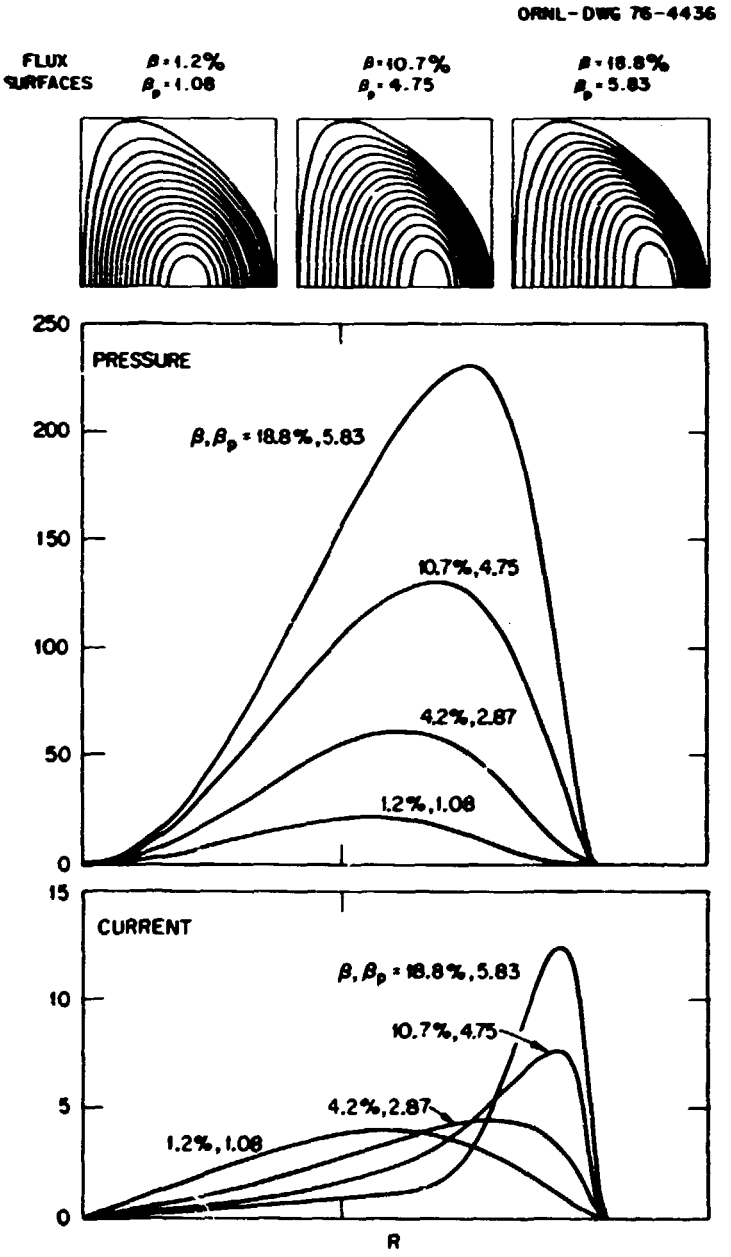

Fig. 3.4. Behavior of: (a) flux surfaces in R-Z plane, (b) pressure profiles, and (c) current density distribution vs R at Z = 0 for D-shaped FCT equilibria as they evolve from low to high β with q_a = 4.8.

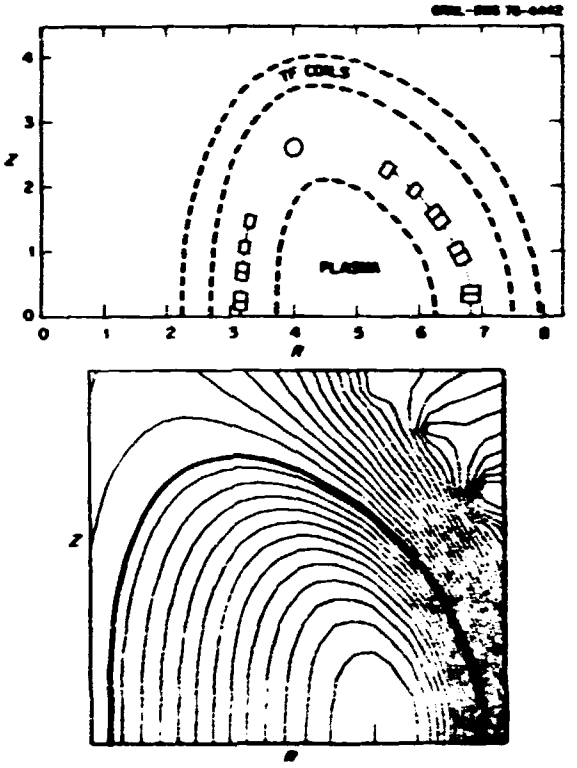

Fig. 3.5. (a) Optimized EF coil locations for a D-shaped FCT with A = 4. Coils connected with dots are in series; the " - " sign indicates current in the same direction as I_p. The distance between the coil centers and the nearest plasma edge is half the plasma horizontal minor radius. (b) Typical high-β (≈15%), high q_a (≈5), free-boundary FCT equilibrium confined by these coils.

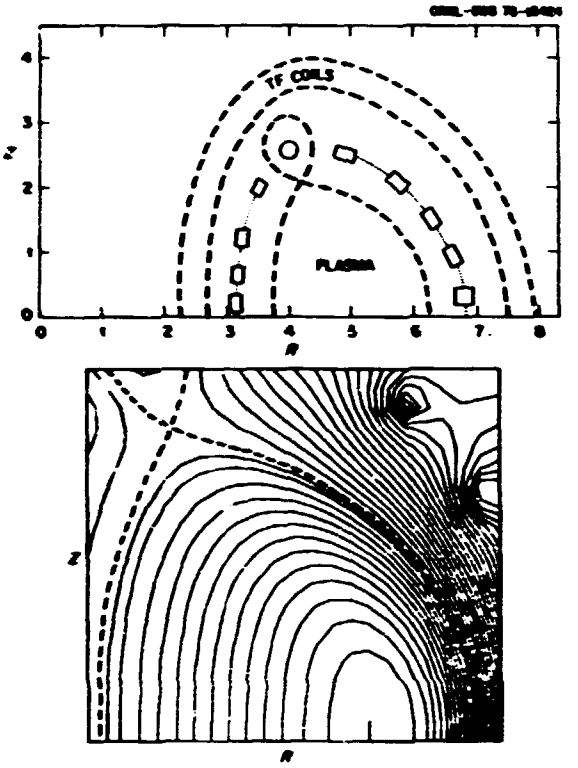

Fig. 3.6. (a) Optimized EF coil locations for a D-shaped FCT with A = 4 and a natural divertor. Coils connected with dots are in series; the " - " sign indicates current in the same direction as I_p. The centers of the coils are at a distance from the plasma edge of half the plasma horizontal minor radius. (b) A typical high-β (≈15%), free boundary FCT equilibrium using the same profile functions $p(\psi)$ and $F(\psi)$ as the equilibrium of Fig. 3.5 confined by these coils.

and 300 MW (burn) at $\bar{\beta}$ = 7.0% and 8.5% with $\bar{n}$ = 1.7×10^{14} cm^{-3} and 1.9×10^{14} cm^{-3}, respectively. These values are substantially lower than previous estimates of ignition ($\bar{\beta}$ = 11%) and burn ($\bar{\beta}$ = 14%).[14]

Peaked profiles also concentrate α-heating power near the plasma center. It is found that at $\bar{\beta}$ = 3.1% and $\bar{n}$ = 1.0×10^{14} cm^{-3}, P_α reaches 40 MW due to central ignition and becomes comparable to the net heating power, P_H, one expects from neutral injection. By assuming that $\tau_E \sim 1$ sec in a one-dimensional, one-fluid energy balance model, the value of P_H required to maintain $d\bar{\beta}/dt = 0.023$ sec^{-1} stays below 50 MW. By assuming a profile of heat conduction coefficient typical of present observations,[15] central ignition at $\bar{\beta}$ = 3.1% permits reduction in the required depth of neutral beam penetration by a factor of two to three. This indicates that with proper density buildup during heating, D^0 beams of 150 keV can be sufficient for heating a Z_{eff} = 1.8 ∿ 3.2-TNS plasma to ignition.

3.2.2 Analytic Approximation to Numerical Tokamak Equilibria Near the Magnetic Axis

D. B. Nelson R. O. Sayer

It is often desirable to have a detailed knowledge of the solution to the MHD equilibrium equation near the magnetic axis. For example, the Mercier criterion for local stability is

usually hardest to satisfy there, yet numerical evaluation of the contour integrals becomes inaccurate in this region because of the few grid points available. We have found it helpful to use a weighted least squares polynomial fit to the numerical equilibrium in the vicinity of the magnetic axis and then to evaluate analytically the relevant quantities. There are several equivalent polynomial expansions for ψ, the poloidal flux function, about the magnetic axis, r_0. If (r, z) are the cylindrical coordinates in which the equilibrium is determined numerically, then ψ can be expanded in $(r - r_0, z)$, or in $(r^2 - r_0^2, z)$, or after introducing the polar coordinates (ρ, θ) centered at the magnetic axis, in a polynomial in ρ and a Fourier series in θ. Because ψ satisfies an elliptic equation it is an analytic function; therefore, if the coefficients of one expansion are given, those of the others can be found algebraically. An example of such an equation is:

$$\psi = \sum_{i,k} \psi_{ik} (r - r_0)^i z^k \quad .$$

If r_0 is the magnetic axis (where $\nabla\psi = 0$), then ψ_{10} vanishes. If ψ is symmetric in z, then only even powers of z appear. We have generally used a fourth order polynomial ($i + k \leq 4$) and about ten percent of the grid points, with a weight function that emphasizes the points near the magnetic axis. The axis is found by iterating a first guess for r_0 until ψ_{10} vanishes. The relative error between the computed and the fitted ψ is typically less than 10^{-5}.

The coefficients ψ_{ik} are not all independent being constrained by the equilibrium equation and the source terms. The constraint equations can be used to check the consistency of the coefficients, or else they can be used to reduce the number of free parameters in the fit. For example, if ψ is symmetric in z, then only four coefficients (e.g., ψ_{00}, ψ_{20}, ψ_{30}, ψ_{40}) are computed in the fourth order least squares fit. Solov'ev[16] has previously shown this to the third order.

Lower order polynomials can also be used for some quantities. For example, the ellipticity, the safety factor (q), and $dV/d\psi$ (where V is the volume enclosed by a flux surface), are determined on axis from the second order terms. The triangularity, shift, and Mercier criterion on axis are third order,[17] whereas $d^2V/d\psi^2$ and $dq/d\psi$ on axis are fourth order.

Effects of energy deposition profile on the time evolution of a flux conserving tokamak

D. B. Nelson

A simple nondiffusive model has been used to study the effects of different energy deposition profiles on the time evolution of a flux conserving tokamak. The equations employed[18] are those of mass, energy, and poloidal flux conservation

$$\left.\begin{aligned} &\frac{\partial \rho}{\partial t} + \nabla \cdot (\rho u) = \sigma, \\ &\rho \frac{de}{dt} + p\nabla \cdot u = Q, \\ &\frac{\partial \psi}{\partial t} + u \cdot \nabla\psi = 0, \end{aligned}\right\} \qquad (3.1)$$

along with the equilibrium equation

$$j \times B = \nabla p \quad . \qquad (3.2)$$

Here σ and Q are mass and heat sources representing the neutral beam. We assume an adiabatic law for the equation of state, so that the internal energy, e, is given by

$$e = \frac{p}{(\gamma-1)\rho} \quad .$$

The calculation proceeds from an initial state with prescribed $p(\psi)$, $\rho(\psi)$, and safety factor $q(\psi)$. If the plasma adiabat, $\mu(\psi)$, is introduced through

$$p(\psi) = \mu(\psi) \left(\frac{d\psi}{dV}\right)^{\gamma} \quad ,$$

then flux surface averaging of Eq. (3.1) leads to an ordinary differential equation for the time

evolution of μ:

$$\frac{1}{\mu}\frac{D\mu}{Dt} = (\gamma-1)\langle Q\rangle/p + \langle\sigma\rangle/\rho \quad , \qquad (3.3)$$

where D/Dt is the time derivative at constant ψ and <...> denotes the flux surface average. The evolution of ψ is determined from Eq. (3.2). This is solved using the ISLAND code,[19] which computes the toroidal current directly from $\mu(\psi)$ and $q(\psi)$.

Figure 3.7 shows three cases representing different $Q(\psi)$ profiles for $\sigma = 0$. In case (b), Q is strongly peaked at the magnetic axis; in case (c), it is more uniform; whereas in case (d), it is peaked off axis. The resultant plasma shapes are quite different: the plasma axis shifts more outward for deposition strongly peaked on axis; for deposition peaked off axis the magnetic axis actually shifts inward. Figure 3.7(e) illustrates pressure and q profiles for cases (a)-(d).

3.2.3 Results from the ORNL Ideal MHD Instability Code

R. G. Bateman, Jr. D. N. Clark H. R. Hicks
Y-K. M. Peng J. W. Wooten

The ORNL MHD instability code[20] has been used to study the effects of toroidicity and high poloidal β on large-scale instabilities in realistic tokamak equilibria. Stable equilibria have been found with average β values up to 5% in FCT sequences of equilibria.[21] As β is increased from the stability limit in these equilibria, the observed instabilities take on a strong ballooning character, concentrating near the outer edge of the torus and showing a mix of poloidal harmonics, m, which reinforce each other at the outer edge.

In general ideal MHD theory studies of toroidal instabilities, it is found that the toroidal wavelength has the greatest effect on the growth rates of large-scale linear MHD instabilities (holding the q-values per wavelength, nq, fixed); the shortest wavelengths have the largest growth rate.[22] Bending a given wavelength into a successively lower aspect ratio torus decreases the growth rate by only a factor of two or three, compared to the orders of magnitude effect of changing the wavelength by a factor of two or four. When all wavelengths are considered for a given toroid, the m = 1, 2, 3, . . ., n = 1, 2, 3, . . . modes pile up below $q_{axis} = 1$ with less tendency to overlap at higher q-values. High shear suppresses the ideal MHD modes for $q_{axis} > 1$. The structure of the instabilities is clearly shifted outward in major radius, often leaving a dead space at the inner edge of the torus. For a predominantly m = 1 mode, the perturbed poloidal magnetic field has a clear m = 2 structure, even for n = 2, 3, ... The experimental observation of the $\tilde{B}_\theta$ signal could mistake an ideal internal m = 1 mode for an m = 2 mode.

3.2.4 Resistive MHD

B. V. Waddell B. Carreras
H. R. Hicks J. A. Holmes

In general terms, the purposes of the Resistive MHD Project are as follows:

1) to study numerically the nonlinear behavior of the resistive MHD equations in geometries appropriate to tokamak experiments,
2) to develop analytic models based on the results obtained numerically, and
3) to compare the results of the codes and the analytic models with experiment.

Nonlinear evolution of the m = 1 tearing mode[23]

H. R. Hicks B. V. Waddell

The nonlinear evolution of the m = 1 tearing mode was studied by employing a version of the helically symmetric resistive MHD code that incorporates the electron heat transport equation. It was found that the electron temperature profile inside the q = 1 singular surface, as well as the toroidal current density and safety factor profiles, became flat as the tearing mode saturated and magnetic reconnection occurred. With resistive heating included in the electron heat balance equation, a marginally successful simulation of tokamak sawtooth oscillations was carried out.

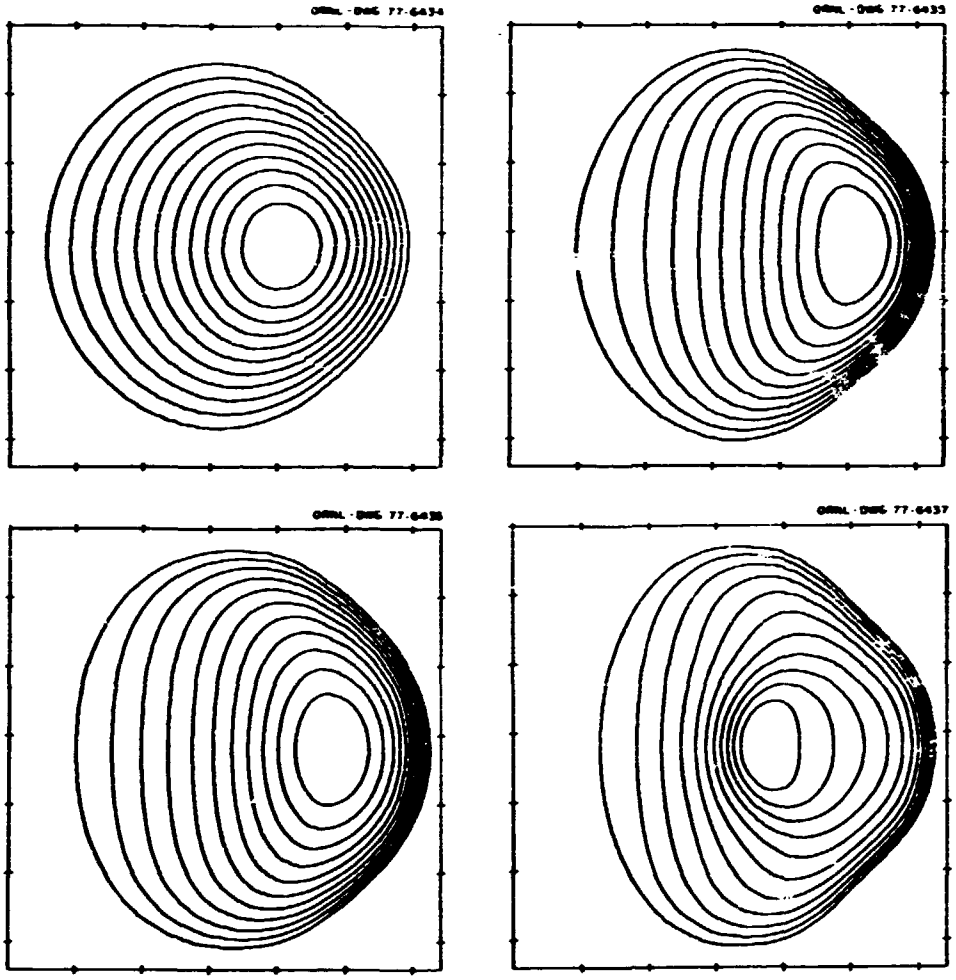

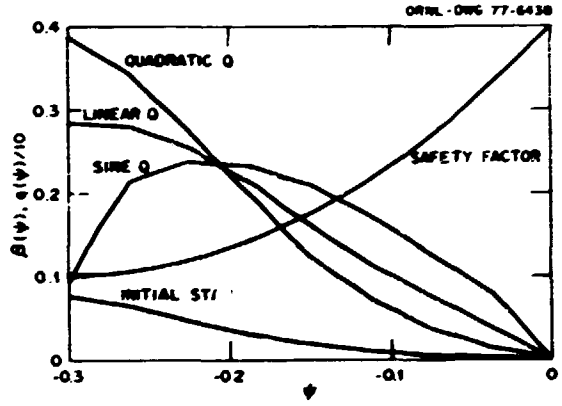

Fig. 3.7. (a) Flux contours of initial plasma state, $\bar{\beta}$ = 2%, aspect ratio 2:1, major axis is to left of figure; (b) flux contours of final state with heat deposition profile, quadratic in ψ, $\bar{\beta}$ = 13.4%; (c) flux contours of final state with heat deposition profile linear in ψ, $\bar{\beta}$ = 14%; (d) flux contours of final state with heat deposition profile varying as sin $\tilde{\psi}$, with $\tilde{\psi}$ normalized between zero and π, $\bar{\beta}$ = 15.5%; (e) pressure profiles for cases described above (pressure is normalized so scale gives local β) and safety factor [$q(\psi)$] profile (which is identical for all cases).

Interpretation of tokamak sawtooth oscillations[23,24]

B. V. Waddell G. L. Jahns
J. D. Callen H. R. Hicks

We hypothesize that sawtooth oscillations are the result of a cyclic process in which the plasma core is resistively heated until the safety factor drops below unity, causing the $m = 1$ tearing mode to become unstable, to grow with an accelerating growth rate, and ultimately to flatten the electron temperature and safety factor profiles. A model based on this hypothesis compares favorably with experimental data from ORMAK in explaining: (1) the rate at which a sawtooth rises, (2) the radial dependence of the precursor and main sawtooth oscillation amplitudes, (3) the accelerating growth rate of the precursor oscillations, and (4) the repetition time of the sawteeth. See Sect. 2.4.2 for more details on the comparisons with ORMAK data.

Reduced, three-dimensional, resistive MHD equations

B. V. Waddell H. R. Hicks
B. Carreras J. A. Holmes

A set of low-β, three-dimensional, reduced MHD equations was derived including the effects of resistivity and toroidicity. If the toroidal and poloidal magnetic fields are denoted by B_ζ and B_p respectively, the three basic assumptions are: (1) $\partial B_\zeta/\partial t = 0$, (2) $B_p/B_\zeta \sim \varepsilon$, and (3) $\beta \sim \varepsilon^2$. The first assumption eliminates fast time scale magnetosonic waves and should thereby greatly increase the efficiency of any numerical scheme based on these equations. It also allows the magnetic field to be expressed in terms of a flux function, thereby ensuring that $\nabla \cdot \underline{B} = 0$ numerically. The second and third assumptions imply that the toroidal velocity can be neglected and, consequently, permit the introduction of a stream function for the poloidal velocity. Equations correct to the first order in ε were obtained for the time evolution of the toroidal flux and the vorticity. A preliminary numerical scheme for solving these equations has been designed and is presently being implemented.

3.3 KINETIC THEORY

C. O. Beasley, Jr. J. E. McCune D. J. Sigmar
D. J. Beckett R. W. McGaffey J. Smith
J. D. Callen* H. K. Meier K. T. Tsang
P. J. Catto Y-K. M. Peng T. Uckan
E. C. Crume, Jr. C. E. Rathmann W. I. van Rij
J. Denavit J. A. Rome B. V. Waddell
R. H. Fowler K. E. Rothe J. C. Whitson
H. C. Howe

The activities in this group have been categorized as: 3.3.1, Neoclassical Transport; 3.3.2, Anomalous Transport; 3.3.3, Collisional Plasma Model; and 3.3.4, Particle Orbits and Injection Heating. Last year's work in each of these categories will be briefly summarized below, followed by short articles and/or abstracts of the individual published papers and reports.

To point out the highlights, progress in multispecies neoclassical transport theory is reflected in several papers in Physics of Fluids 19.

In anomalous transport, novel insights emerged concerning the nature of the Onsager transport coefficient matrix. (1) Anomalous (turbulent) processes affect only the transport coefficients perpendicular to the magnetic field, leaving the neoclassical parallel transport coefficients basically unchanged. (2) The magnetic perturbations ensuing from drift wave fluctuation levels $e\phi \sim 0.01$ kT can be shown to produce high mode number islation of the confining magnetic field, which leads to anomalous electron heat conduction not inconsistent with observations in tokamak experiments.

The Collisional Plasma Model (CPM) has found acceptance in the published literature. Significant advances in basic understanding and development of fast numerical techniques have been achieved.

Besides producing a set of codes for beam deposition, slowing down, and loss region effects, the orbit and injection project progressed in its

*Group Leader.

fundamental investigation of high energy guiding center orbit theory in flux coordinates (suitable for the new flux conserving, high-β equilibria) and of advanced (ripple) injection schemes.

3.3.1 Neoclassical and Neutral Particle Transport

D. J. Sigmar E. C. Crume, Jr.
H. C. Howe K. T. Tsang

The continued quantitative pursuit of neoclassical theory of multi-ion species tokamak plasmas is essential for the understanding of the direction of the impurity flow and its effect on the overall energy balance of the plasma. The neutral particle kinetics have become all the more important since the recent successes of gas puffing. Progress has been made (1) in the development of fundamental impurity theory and (2) in quantitative improvement and exploration of existing theories, including neutral kinetics.

Journal articles on fundamental neoclassical theory dealt with the smooth transition of transport coefficients from the banana to the Pfirsch-Schlüter regime by Tsang and Callen, multispecies impurity transport in the banana regime by Hirshman, Sigmar, and Clarke, and a systematic approximation to the Fokker-Planck operator by Hirshman and Sigmar. An ORNL report on temperature screening in a Pfirsch-Schlüter two-ion species plasma has been submitted for publication by Tsang and Crume, as has one by Tsang on banana drift diffusion due to field ripples.

Related to this subject, but rather in the vein of quantitative exploration of existing theory, Uckan, Tsang, and Callen evaluated the effect of the poloidal variation of magnetic field ripples on tokamak heat transport. A paper by Sigmar and Freidberg on transport in high β tokamaks appeared in a supplement to Plasma Physics. An ORNL report on neoclassical transport in all three regimes in an elliptic tokamak has been submitted for publication by Tsang. The motivation for the latter two papers derives from our orientation towards the next generation of experiments with high β and deformed cross section. In the area of neutral particle kinetics, a quantitative analytic-numerical study of inelastic wall reflection of warm neutrals incorporating the Robinson dynamic reflection model has been performed by Howe and Sigmar.

Smooth Transition of Neoclassical Diffusion from the Banana to Pfirsch-Schlüter Regime[25]

K. T. Tsang J. D. Callen

It is shown that neoclassical transport previously obtained by numerical evaluation of variational procedures can be reproduced analytically by taking account of the energy dependence of the collision and bounce frequencies through the separation of velocity space into banana, plateau, and Pfirsch-Schlüter regimes.

Neoclassical Transport Theory of a Multispecies Plasma in the Low Collision Frequency Regime[26]

S. P. Hirshman D. J. Sigmar J. F. Clarke

A comprehensive neoclassical transport theory for a multispecies plasma in the low collision frequency banana regime is developed. A recently developed approximate collision operator is used to calculate analytically the transport coefficients in a nonisothermal, finite β plasma for arbitrary mass ratios and all values of the aspect ratio. The physical effects of collisions in the large and small aspect ratio limits are discussed in detail. The bootstrap current is expressed in terms of the parallel friction forces, and an explicit calculation of the current is performed for the case of two ion species in which one is a heavy impurity ion.

Approximate Fokker-Planck Collision Operator for Transport Theory Applications[27]

S. P. Hirshman D. J. Sigmar

An analytically tractable approximation is developed for the linearized Fokker-Planck collision operator; it describes a plasma nearly in thermal equilibrium. This approximate operator preserves the symmetry properties of the exact collision integral which imply the physical conservation laws, self-adjointness, and the H

theorem. A renormalization procedure is developed for accurate treatment of collisions between particles of arbitrary masses. For large or small mass ratios, the approximate operator reduces to the standard expansions of the exact operator. In the case of identical particle collisions, the present approximation provides a significant improvement over the model operator previously given in the literature, yet retains the simplicity of former operators. The recalculation of the classical transport coefficients with this operator reduces to the solution of a coupled set of algebraic equations and indicates its reliability for use in complex neoclassical transport situations. The neoclassical electrical conductivity calculation demonstrates the new physical features of the approximate operator.

Temperature Screening Effect in Two-Ion Species Pfirsch-Schlüter Transport[28]

K. T. Tsang E. C. Crume, Jr.

We have solved the particle and heat flux problems in the collisional or Pfirsch-Schlüter regime for a two-ion species tokamak plasma using a kinetic approach with exact Fokker-Planck collision operators. These solutions are appropriate for analyzing the behavior of impurities in the low temperature plasma edge region, where impurities first enter the plasma from the outside. We find that low charge states of low mass impurities can be screened effectively from further penetration of the plasma.

Banana Drift Diffusion in a Tokamak Magnetic Field with Ripples[29]

K. T. Tsang

The drift motions of trapped particles in a tokamak field with ripples lead to a new transport process in large tokamaks in addition to the diffusion process due to particles trapped in the ripples. We study this problem by solving the bounce-averaged, drift-kinetic equation with a model collision operator. It is shown that the banana drift diffusion is proportional to the collision frequency when the poloidal banana drift frequency is smaller than the effective collision frequency. This result is contrary to earlier predictions, and in a reactor regime, this loss mechanism is shown to be unimportant.

Effects of the Poloidal Variation of the Magnetic Field Ripple on Enhanced Heat Transport in Tokamaks[30]

M. A. Uckan K. T. Tsang J. B. Callen

The use of a finite number of coils to generate the toroidal field of a tokamak introduces a magnetic field asymmetry and is responsible for an additional particle trapping that can affect the plasma confinement. The enhanced transport coefficients associated with the ripple-induced drifts have been calculated. The calculations include both the radial and poloidal variation in the magnitude of the field ripple. It is found that the consideration of poloidal variation significantly reduces the ripple-trapped transport but does not affect the banana drift diffusion. Results relevant to the ORNL Experimental Power Reactor (EPR) reference design are discussed.

Tokamak Transport at Large Poloidal Beta, Considering MHD Stability Limits[31]

B. J. Sigmar J. P. Freidberg

Operation of a reactor at the highest possible value of β is desirable from a power production standpoint. Moreover, there is experimental and theoretical evidence for reduced cross field transport with increasing β. Assuming the high β ordering $\beta \sim \epsilon$, $\beta_p \sim \epsilon^{-1}$ (where $\epsilon = a/R_0$ is the inverse aspect ratio), we study the effect of β on collisional and anomalous trapped particle diffusion for various equilibria under the constraint of MHD stability. (1) We demonstrate that at $\beta_p \sim \epsilon^{-1}$ the strong Shafranov shift results in a reduction of the banana width and thus of banana diffusion. (2) We investigate the maximum J properties of certain high-β equilibria with respect to their stabilizing influence on the interchange trapped particle mode.

Neoclassical Transport in an Elliptic Tokamak[32]

K. T. Tsang

Neoclassical transport for an elliptic tokamak in all collisional regimes is investigated by the technique of partitioning the

velocity space. It is found that in a tokamak of moderate elongation, particle and ion heat confinement times are increased by a factor of σ^2, where σ is the ratio of vertical minor radius to horizontal minor radius. Ripple diffusion in an elliptical tokamak is also studied. Ion heat conductivity due to ripples is reduced by a factor of approximately σ^2.

Neutral hydrogen kinetics in plasma including inelastic wall reflection

M. C. Nowe D. J. Sigmar D. Armurius

Recent advances in understanding the inelastic interaction between charge-exchange neutrals and the lattice dynamics of the wall by M. Robinson et al. have led us to reconsider the solution of the Boltzmann equation for the neutrals. A hybrid analytic-numerical method has been developed for solving the integral equation, with special care taken to conserve particles and energy in the neutral particle-wall interaction.

The warm neutral flux incident on the wall is due primarily to the first charge-exchange reactions between the Frank-Condon flux and the plasma. Thus the mean energy of this flux is characteristic of the plasma temperature at points corresponding to one Frank-Condon m.f.p. (several centimeters) into the plasma. The fraction of the cold wall-emanated flux which later returns to the wall as hot flux is approximately half the ratio λ_{cx}/λ_i of a cold neutral. (λ_{cx} and λ_i are the mean free paths against charge exchange and ionization.) When the hot neutrals are wall-reflected again, the total flux of neutrals incident on the plasma is therefore increased by up to 50%. Because it is more energetic the additional flux penetrates further and results in an increase of the central neutral density, which is inversely proportional to the energy lost in the wall during reflection. For elastic wall-reflection, the hot neutral density in the center of the plasma is increased by a factor <4.

3.3.2 Anomalous Transport

J. D. Callen K. T. Tsang J. C. Whitson
P. J. Catto B. V. Waddell

Radial transport processes (in particular the radial electron heat conduction) are anomalous in present tokamaks. Using primarily analytic methods, we are refining and further developing the theory of drift-dissipative, trapped-electron instabilities in order to determine if these modes, which seem to be the most likely candidates, are responsible for the anomalous transport currently encountered. In the following subsections we give brief descriptions of work in this regard carried out in the past year. In the first subsection we show in a model calculation that the destabilizing trapped-electron contribution is not strongly reduced when finite ion gyroradii effects and the attendant overlapping of mode-rational surfaces are taken into account. In the next two subsections we discuss our preliminary attempts to apply Dupree's strong turbulence theory to these modes. It seems plausible that the strong turbulence effects could cause mode saturation at roughly the amplitudes observed in the experiment ($e\tilde{\phi}/T_e \sim 10^{-2}$). Next, we discuss the transport induced by such turbulence. Following that we discuss a quasi-linear type of calculation in which we find that the anomalous transport only affects the perpendicular transport processes (i.e., electron heat conduction and particle diffusion, but not the resistivity, Ware pinch, etc.) and that the anomalous transport should be simply added to — but not replace — the irreducible neoclassical transport. Finally, in the last subsection we propose and briefly discuss a new hypothesis for the process by which drift wave fluctuations can cause anomalous transport — namely through radial magnetic flutter and consequent conversion of a portion of the very large parallel electron heat conduction into radial electron heat conduction. While the composite model being developed is not complete or specific

enough yet to make detailed comparisons with present experimental data, it is encouraging that a number of pieces of the model seem to agree with current experimental interpretations of anomalous transport processes in tokamaks.

Asymptotic behavior of trapped electron instability in the large $k_\theta \rho_i$ limit

K. T. Tsang J. D. Callen

In the large $k_\theta \rho_i$ limit, the distance between mode-rational surfaces (Δ) is much smaller than the turning point distance (χ_T) of the usual radial eigenmode. Thus, one can no longer solve for the radial eigenfunction by considering only an isolated mode-rational surface. We assume a radial mode structure that has a fast WKB function part and a slowly varying envelope. The fast radial variation has the same spatial periodicity as the mode-rational surfaces (Δ). The equation for the slowly varying part is derived. The trapped electron term is a localized source of free energy whose radial dependence is taken into account in the slowly varying part of the radial eigenmode equation through the standard perturbation technique. The effect on the dissipative trapped-electron instabilities is to decrease the trapped-electron contribution to the growth rate by a factor $(\Delta/\chi_T)\ell n(\chi_T/\Delta) \sim \sqrt{r_n/L_s}\,(k_\theta \rho_i)^{-\frac{1}{2}}$. Because this factor is not too different from unity at the $k_\theta \rho_i \geq 1$ limit of the calculation, we hypothesize that the radial eigenmode structure does not modify qualitatively the most unstable $k_\theta \rho_i \geq 1$ trapped electron modes.

Ion response due to nonisotropic turbulence produced by low frequency instabilities

K. T. Tsang

All strong turbulence calculations in the literature assume isotropic, linearly unstable waves in the background plasma. This is not true for low frequency drift waves. In toroidal geometry, we Fourier-expand all perturbed quantities in the toroidal and poloidal directions while keeping the radial structure unspecified. The nonlinear response for the ions is obtained from the Vlasov equation by Dupree's renormalization technique. This result is very useful in the strong turbulence theory of drift waves in tokamaks. The strong turbulence is found to affect the radial eigenmode structure and to introduce a k^2D damping decrement.

Strong turbulence effect on trapped electrons

K. T. Tsang

A bounce-averaged kinetic equation is used to investigate nonlinear effects on trapped electrons. Turbulence affects the trapped-electron response by introducing an ik_r^2D term in the resonant denominator, where k_r is an average wave number of the radial eigenfunction determined by the ion response. The relation between D and ϕ is derived by assuming a radial eigenfunction scaling as $\exp(i\mu x^2)$, as obtained in linear theory (even including certain nonlinear ion effects). A fluctuation level, $e\tilde{\phi}/T$, of about 1% is required to stabilize the mode for typical parameters. Figure 3.8 shows the nonlinear growth rate due to the trapped electrons for different levels of turbulence characterized by the parameter k_r^2D/ω_*. The case under study is low in collisionality ($\nu_* = 0.001$) and uses the following parameters: $\eta_i = \eta_e = 1$, $T_e/T_i = 1$, $r/R = L_n/R = 1/4$, and $q = 2$. Also shown is the shear damping contribution represented by the dash-dot line. The shear parameter, L_n/L_s, is 0.05. It is clear that the mode is stabilized when $k_r^2D/\omega_* = 0.2$, which gives a fluctuation level, $e\tilde{\phi}/T$, of about 1%.

A model for transport in tokamaks

J. D. Callen M. C. Howe K. T. Tsang

The original Kadomtsev and Pogutse development of the dissipative trapped-electron instability is invalid for present tokamak experiments. Recent generalizations of these modes to adapt the analysis of the mode to current experiments include curvature drifts, velocity-space partitioning to extend the analysis into the plateau regime, and finite ion gyroradius effects (cf. first subsection of Sect. 3.3.2). We hypothesize that the revised mode is a candidate for the fluctuations and transport observed in present experiments. A quasi-linear theory of the

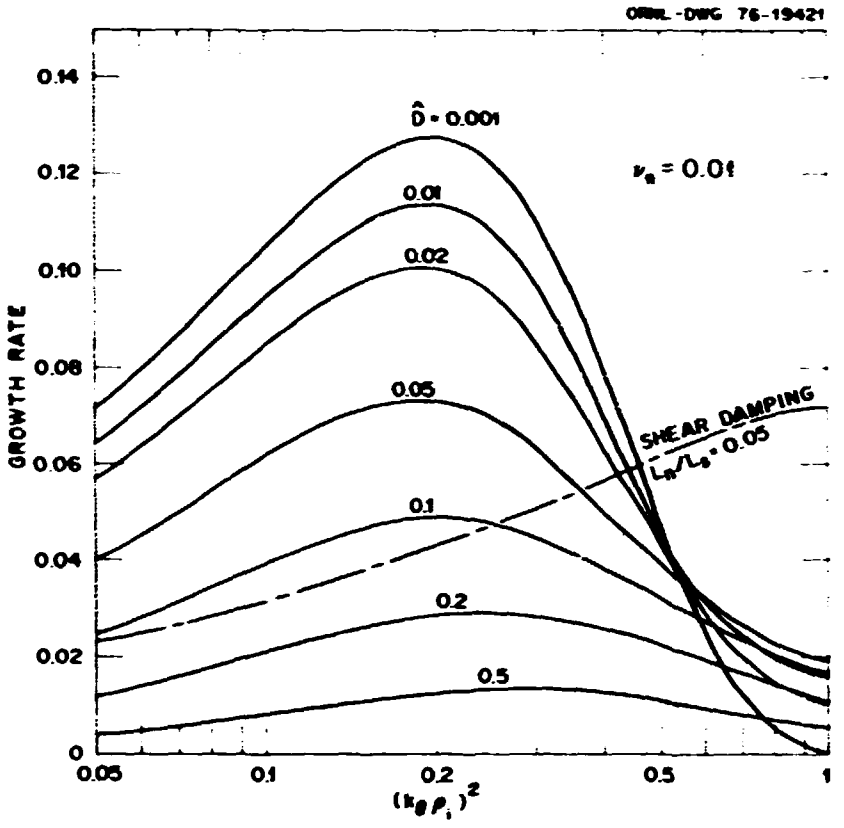

Fig. 3.8. Nonlinear growth rate due to trapped electrons for different turbulence levels.

generalized modes has been developed. The anomalous transport induced is in addition to neoclassical transport and affects only the cross-field processes of particle diffusion and electron heat conduction. The radial electron heat conduction induced by these modes seems to be a bit too small to explain the experimentally observed anomalous electron heat conduction. The particle density is determined by balancing the inward Ware pinch with the outward anomalous particle diffusion (cf. Sect. 2.1.15). Similarly, the impurity density results from balancing the inward classical diffusion against the outward anomalous diffusion.

The possible role of magnetic perturbations on anomalous transport in tokamaks

J. D. Callen

Small, resonant magnetic perturbations can easily tilt the magnetic field lines and modify the flux surface topology in a tokamak. Plasma transport is much faster parallel to the magnetic field lines than perpendicular to them. Thus, very small helically resonant magnetic perturbations (e.g., $\tilde{B}/B \geq 10^{-4}$) that cause field lines to wander radially can allow the very rapid parallel transport processes to enhance radial plasma transport over that produced by perpendicular transport processes alone. We hypothesize

that the magnetic perturbations induced[33] by the experimentally observed drift waves ($e\tilde{\phi}/T_e \sim 1$)[-2]) can cause this effect to be important in determining the radial electron heat transport in tokamaks. Preliminary estimates of the magnetic effects of unstable drift waves on electron and ion heat transport and on particle diffusion indicate that the radial electron heat conduction coefficient is the only transport coefficient significantly affected and that its magnitude is comparable to that observed in present tokamaks.

3.3.3 The CPM

C. O. Beasley, Jr. E. C. Crume, Jr J. Denavit
J. E. McCune R. W. McGaffey H. K. Meier
C. E. Rathmann K. E. Rothe T. Uckan
W. I. van Rij

Major emphasis during 1976 for the CPM project has been on development of new computational tools to treat theoretical problems within the scope of the CPM. The primary task was the completion of a new code, DKES (Drift Kinetic Equation Solver), described in the first subsection below. Not only was such a code needed to avoid major code modifications with each change in problem, but also the code made use of the advantages of the CPM described in detail below. Another major requirement was a vastly improved method of calculating the Fokker-Planck collision operator – one which permitted dynamic adjustment as species temperatures change as well as arbitrary mass-temperature ratios between species. Such a code is described in the second subsection. After completion and checkout of DKES, it was apparent that major code speedups would be needed in order for the code to be of practical use in most anticipated problems. While computational speedups have yet to be implemented, the most beneficial speedup was a more rapid determination of the lowest eigenmode (quasi-stationary for equilibrium or slowly growing for instability). A numerical method for doing this, called RELAX, is described in the third subsection. When it became apparent that existing theory for quasi-neutrality was inadequate for a complete description of the electric field in a drift-kinetic equilibrium and useless for nonlinear instabilities, a complete theory of quasi-neutrality in a drift-kinetic sense had to be derived. An abstract describes such a theory in the next subsection. Other reports discussed in the remaining sections deal with results from older CPM codes. The next four subsections deal with the use of the CPM in studies of impurity diffusion, comparisons with earlier results, use in a transport simulation code, and preliminary treatment of a bump-on tail relaxation. Finally, a preliminary report of work on the dissipative trapped-electron instability model of Denavit and Rathmann is given.

Drift-kinetic equation solver: DKES

C. O. Beasley, Jr. H. K. Meier
R. W. McGaffey W. I. van Rij

DKES is a multispecies collisional plasma computer program for toroidal devices. It solves the drift-kinetic equation in the form derived by Hazeltine[34,35] as an initial value problem, following in time the amplitudes obtained by expanding the distribution functions in the orthogonal velocity-space functions of the CPM[36] and toroidal and poloidal Fourier series. At this stage of its development, DKES treats the minor radius coordinate in a flux surface localization approximation.[37]

The drift-kinetic equation can be written in the form

$$\frac{\partial}{\partial t}\,\bar{f}(\vec{x},\vec{v},t) = -W(\vec{x},\vec{\nabla},\vec{v},\vec{\nabla}_v,t)\,\bar{f}(\vec{x},\vec{v},t) + \bar{C}(\vec{x},\vec{v},t), \tag{3.4}$$

with the Vlasov operator term, W, factorizing as follows:

$$W = \sum_{j=1}^{12} K_j(\sqrt{\rho}\,\vec{v},\frac{1}{\sqrt{\rho}}\vec{\nabla}_v)\,S_j(\vec{x},\vec{\nabla},t),$$

where

$$\rho = \frac{M}{T(r,t)} \tag{3.5}$$

An essential feature of DKES is its use of this factorization of M into velocity-space and physical-space operators. The velocity-space operators, K_j, are problem-independent, and their matrix elements in the CPM representation are pure numbers that can be calculated once and for all. Calculations of the CPM representation of the Coulomb collision operator,[36] $\bar{C}$, and a scheme for the rapid time-advancement of the drift-kinetic equation (Eq. 3.4) are described in the next two subsections.

DKES calculates the species and plasma number densities, temperatures, fluxes, mass-flow velocities, and heat fluxes. In particular, the Fourier amplitudes and flux-surface averages of these observables are calculated. The CPM representation for $\bar{f}$ is optimized when the temperature, $T(r,t)$, in Eq. (3.5) and the radial localization number density, $N(r,t)$,[37] are the flux-surface averaged species temperature and density, respectively; DKES has the capacity for updating $T(r,t)$ and $N(r,t)$ according to this prescription.

The workhorse part of DKES is a set of basic subroutines designed to perform operations such as addition, multiplication, division, square root, gradient, divergence, curl, dot product, and cross product.

A variety of problems can be studied with DKES, each problem being characterized by particular magnetic and electric fields. Examples are:

1) equilibria with vacuum toroidal magnetic field, equilibrium ring field, and poloidal magnetic field, and with or without self-consistent electrostatic field;
2) equilibria with self-consistent development of the poloidal magnetic field; and
3) self-consistent electrostatic instabilities.

Calculations involving the self-consistent electrostatic field have become a practical possibility because of the development of a prescription for this field in which the plasma oscillations have been eliminated.[38] The bulk of DKES is unchanged in going from one problem to another; only the module which calculates $\vec{E}$ and $\vec{B}$ is affected.

A stable recursive method for calculating matrix elements of the CPM collision operator

H. K. Meier

In the CPM, the full contribution to the time derivative of any amplitude, $f_{\ell n}^{(r)}$, of the rth species would be

$$\left[\frac{\partial f^{(r)}}{\partial t}\right]_{\text{Collis}} = \sum_{s=\text{species}} \sum_{\ell' n'} \sum_{\ell'' n''} \nu_{rs} C^{rs} \begin{bmatrix} \ell & \ell' & \ell'' \\ n & n' & n'' \end{bmatrix} f_{\ell' n'}^{(r)} f_{\ell'' n''}^{(s)} \quad . \tag{3.6}$$

In the linearized version this reduces to

$$\left[\frac{\partial f^{(r)}}{\partial t}\right]_{\text{Collis}} = \sum_{s=\text{species}} \sum_{n'} \nu_{rs} \left\{ C^{rs} \begin{bmatrix} \ell & \ell & 0 \\ n & n' & 0 \end{bmatrix} f_{\ell n'}^{(r)} f_{00}^{(s)} + C^{rs} \begin{bmatrix} i0\ell \\ non' \end{bmatrix} f_{00}^{(r)} f_{\ell n'}^{(s)} \right\} \quad . \tag{3.7}$$

The CPM derivation of Eqs. (3.6) and (3.7) has been covered in the past.[39] The method used to obtain numerically the matrix elements of C^{rs} involved recursive equations which were unstable; therefore, it was necessary to use a multiprecision computer program to calculate the element. Once calculated, the elements were stored on a disk; however, because the elements depend on mass-temperature ratio, the system was rather inflexible.

In the past year a stable method has been found to compute the elements as they are needed by means of a single precision program. Storage requirements are thereby greatly reduced, and flexibility of the program is increased. The method involves a replacement of the recursion relations for the R_m found in Ref. 39 by completely stable recursion relations. Derivation of these recursion relations will be elucidated in a forthcoming ORNL/TM report.

RELAX: A numerical procedure for the rapid determination of the lowest eigenmode of a time-dependent equilibrium problem

H. K. Meier

While the heretofore used Runge-Kutta procedure for following the time behavior of a tokamak plasma as it relaxed to a quasi-equilibrium was suitable for calculating neoclassical equilibria in the plateau regime, computation time was much too long when operating deep in the banana or Pfirsch-Schlüter regimes. This was particularly true in the banana regime, where there was an additional complication arising from storage of large arrays of amplitudes associated with the distribution function.

Recent work has shown that in mathematical terminology, the CPM calculation corresponds to a stiff differential system. In other words, the system of equations in the CPM representation has modes which are of very high (complex) frequency compared with the time dependence of physically interesting modes near the equilibrium. Because of these high frequency modes, a very short time step was necessary to maintain numerical stability; however, the short time step resulted in a large number of Runge-Kutta steps ($\geq 10^4$) in order to damp the low frequency modes.

Perhaps the simplest way to understand this effect is to consider a purely linear system (ours is almost linear) of the form

$$\frac{\partial \underline{f}}{\partial t} = \underline{\underline{M}}\, \underline{f} \quad .$$

If the operator $\underline{\underline{M}}$ has eigenvalues $-\lambda_i$ and corresponding eigenmode $\underline{g}_i$ such that

$$\underline{\underline{M}}\, \underline{g}_i = -\lambda_i \underline{g}_i \quad ,$$

then the time behavior of a vector consisting of a single eigenmode of the system will be

$$\underline{f}_i(t) = \underline{g}_i\, e^{-\lambda_i t} \quad ,$$

and hence,

$$\underline{f}_i(t + \Delta t) = e^{-\lambda_i \Delta t}\ \underline{f}_i(t) \quad .$$

Unfortunately an explicit scheme for advancing the functions in time (such as Runge-Kutta) results in

$$\underline{f}_i(t + \Delta t) = \left[1 - \lambda_i \Delta t + \frac{1}{2}(\lambda_i \Delta t)^2 + \ldots\right] \underline{f}_i(t) \quad .$$

This is a good approximation if $\lambda_i \Delta t$ is small; but for $\lambda_i \Delta t$ too large,

$$\left|1 - \lambda_i \Delta t + \frac{1}{2}(\lambda_i \Delta t)^2 + \ldots\right| > 0,$$

and the process is numerically unstable. For example, for a real eigenmode calculated by a fourth order Runge-Kutta procedure, it is required that

$$0 \leq \lambda_i \Delta t \leq z_0 = 2.7953 \quad .$$

Consequently, if a λ_i exists which is 10^n times the inverse collision time, it is necessary to use a Δt which is 10^n times smaller than would be required to calculate on a physical collision time scale in order to remain stable.

Figure 3.9 shows the stable region in the complex plane for the function D defined below:

$$D = \left|1 - \left(\frac{z}{z_0}\right) + \frac{1}{2}\left(\frac{z}{z_0}\right)^2 - \frac{1}{6}\left(\frac{z}{z_0}\right)^3 + \frac{1}{24}\left(\frac{z}{z_0}\right)^4\right| \quad ,$$

where $z = x + iy = \lambda \Delta t$, and z_0 is defined above. The outer solid line, corresponding to $D = 1$, marks the boundary of the stable region (i.e., $z < z_{D=1}$ is stable). The remaining contours show where eigenmodes will be damped by an order of magnitude within 200, 100, 50, 25, and 12.5 time steps respectively. By making Δt sufficiently small we can always be assured that any mode occurs within the stable regime.

However, there is nothing sacred about using the equation for D to find an equilibrium. Any sequency of the form

$$f^{(i+1)} = (1 + C_1 M + C_2 M^2 + C_3 M^3 + \ldots)\, f^{(i)}$$

$$= P(M)\, f^{(i)}$$

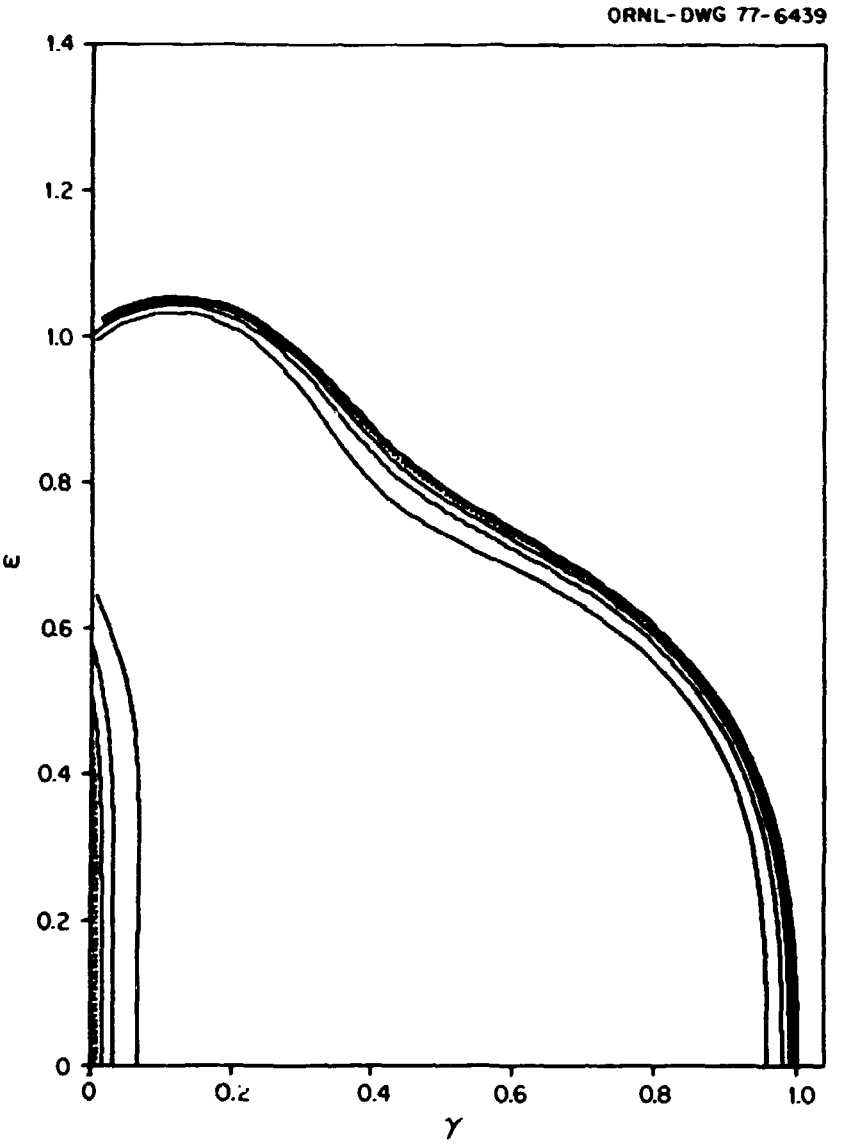

Fig. 3.9. Stable region for complex eigenmodes of a fourth order Runge-Kutta expansion.

(P is a polynomial in M, where $M^{(n)}f$ corresponds to applying the nth time-derivative operator) which serves to damp out all but the equilibrium will suffice. In particular, in the banana regime (where eigenmodes cluster up against the imaginary axis) or in the Pfirsch-Schlüter regime (where they cluster along the positive real axis) the D equation becomes extremely inefficient. A computer program has been written to generate sequences tailored to fit the modes present. Such a sequence for finding a banana regime equilibrium is shown in Fig. 3.10 for degree 20 in M. This particular sequence will damp by a factor of ten in the time required by 200 fourth order Runge-Kutta steps any mode that lies on the imaginary axis with

$$\frac{|\lambda|}{|\lambda_{max}|} > 3 \times 10^4.$$

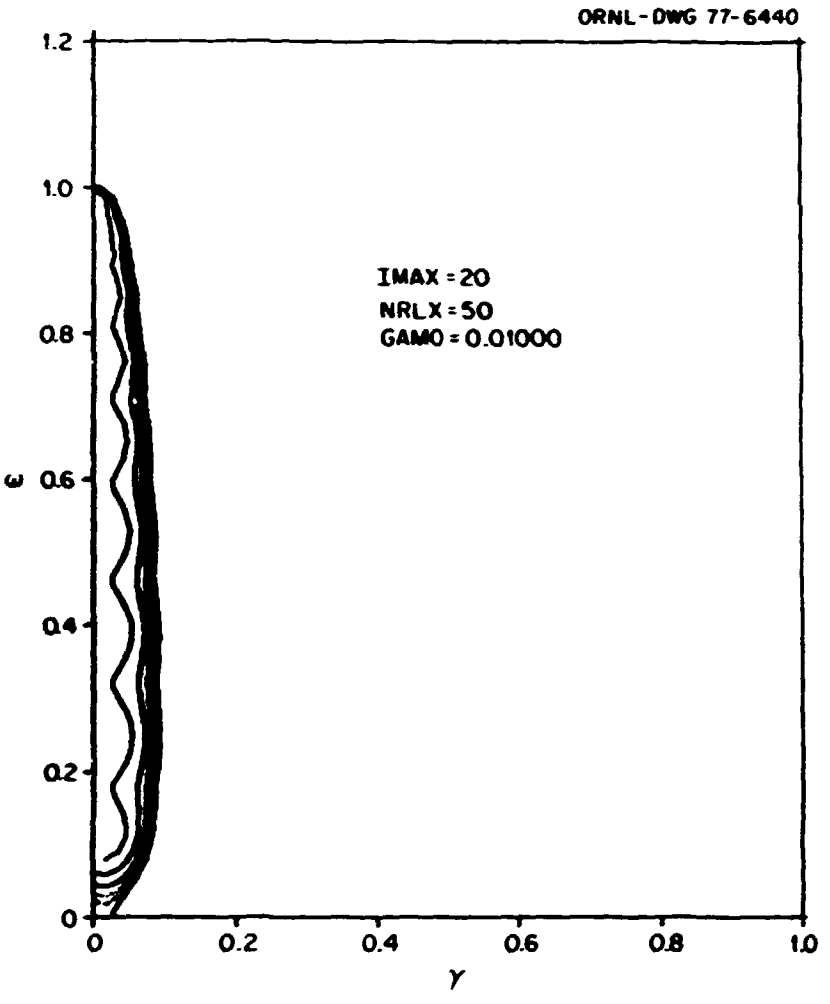

Fig. 3.10. Stable region for complex eigenmodes of a 20° relaxation polynomial.

This compares with about 5000 Runge-Kutta steps using the standard D sequence.

One can use the same method to follow the correct time development of a system. The difference here is that one uses the low order terms to improve stability. Such a sequence might be of the form

$$f(t + \Delta t) = \left[1 + M(\Delta t) + \frac{1}{2}M^2(\Delta t)^2 + \frac{1}{6}M^3(\Delta t)^2 + C_4M^4 + C_5M^5 + \ldots\right] f(t) \quad .$$

Calculation of a self-consistent, low frequency electrostatic field in toroidal geometry

C. O. Beasley, Jr. H. K. Meier
J. E. McCune W. I. van Rij

We derive an asymptotic series in ω_p^{-2}, the inverse square plasma frequency, for the self-consistent, curl free, low frequency electric field in tori. The derivation is consistent with the drift-kinetic ordering and may be used in either instability or equilibrium calculations. We find that in a time-dependent formalism, the

electric field is completely determined to the first order in a drift-kinetic expansion.

CPM calculations for two-ion species in the Pfirsch-Schlüter regime

E. C. Crume, Jr. K. E. Rothe
H. K. Meier W. I. van Rij

A version of the CPM was written to allow calculations involving two charged species. Although some preliminary investigations of an electron-ion plasma were made, most of the calculations were for two-ion species interacting in the Pfirsch-Schlüter regime. An analytic theory of transport in that regime, against which the CPM version could be calibrated, had recently been completed.[40] The results from two calculational cases involving hydrogen-oxygen plasmas are summarized and discussed below. These cases were chosen from a theoretical standpoint to demonstrate the presence or absence of temperature gradient screening[40] of impurities at the edge of a tokamak such as ORMAK, in the presence of a high edge concentration of an oxygen impurity. The plasma conditions that are the same for the two cases are given in Table 3.1.

Table 3.1. Plasma conditions for two-ion species calculations

Toroidal magnetic field, B_0	1.9 T
Plasma major radius, R	79.8 cm
Inverse aspect ratio δ at minor radius of flux surface of calculation	0.259
Electron density, n_e	5×10^{12} cm^{-3}
Electron temperature, T_e	10 eV
Proton density, n_p	9×10^{11} cm^{-3}
Common ion species temperature, T_p	10 eV
Common logarithmic gradient of density and temperature	0.106 cm^{-1}

The first case was selected to show temperature gradient screening of impurities (i.e., a reversal of the usual sense of the fluxes of the ion species so that the hydrogen flux is inward and the oxygen impurity flux is outward). Parameters and results for this case are given in Table 3.2. By comparing entries in Tables 3.1 and 3.2, it is seen that the density of the oxygen impurity ion O^{2+} is about twice that of the hydrogen ions or protons. This assumption is not unreasonable for edge conditions in ORMAK plasmas after oxygen discharge cleaning.[41]

Comparison of the collisionalities, ν_*, with $\delta^{-3/2}$ shows that both species are deep in the Pfirsch-Schlüter regime. The CPM calculations were run until the calculated particle and heat fluxes had stabilized, as indicated by slow rates of change, in order to compare them with the theoretical equilibrium fluxes. The particle fluxes are seen to be in reasonable agreement in both magnitude and sense with the theoretical fluxes, although ambipolarity, as evidenced by the ratio $\Gamma_{O^{2+}}/\Gamma_p$, is only satisfied to within about 25%. The conduction heat fluxes disagree by larger factors with theory, although the ratio of fluxes is within about 25% of the theoretical ratio.

The second case was chosen to illustrate the usual flux conditions (i.e., impurity flux inward and hydrogen flux outward). Parameters and results for this case are given in Table 3.3. The parameters are seen to be very similar to those of the first case, except that the impurity ion is O^{3+} rather than O^{2+}. Again the CPM particle fluxes are in reasonable agreement with the theoretical predictions, although the stabilization was not quite as good as in the first case. The fluxes also better approximate ambipolarity. While the proton heat flux agrees better with theory than in the first case, the O^{3+} heat flux is considerably in disagreement, and this latter fact accounts for most of the large discrepancy in the ratio of the fluxes.

The results of these preliminary calculations are encouraging, considering that the CPM model used in the code had significant approximations. It is expected that the newer code being developed will yield results in better agreement with theory.

Table 3.2. Summary for case with temperature gradient screening, H^+-O^{2+}

O^{2+} density	2.05×10^{12}
$\alpha = n_{O^{2+}} Z^2_{O^{2+}} / n_p$	9.11
ν_{*p-}	161.0
$\nu_{*O^{2+}}$	393.0
$\delta^{-3/2}$	7.57
τ_{pp}	6.22×10^{-5} s

	Theory	CPM (at $t = 200\tau_{pp}$)
Proton particle flux Γ_p	-3.44×10^{13} cm^{-2}s^{-1}	-3.4×10^{13} cm^{-2}s^{-1}
$(\Delta\Gamma_p/\Delta t)/\Gamma_p$	0	$0.00056\ \tau_{pp}^{-1}$
O^{2+} particle flux $\Gamma_{O^{2+}}$	1.72×10^{13} cm^{-2}s^{-1}	2.1×10^{13} cm^{-2}s^{-1}
$(\Delta\Gamma_{O^{2+}}/\Delta t)/\Gamma_{O^{2+}}$	0	$0.0011\ \tau_{pp}^{-1}$
Proton conduction heat flux $\tilde{Q}_p$	1.93×10^{15} eV cm^{-2}s^{-1}	3.5×10^{15} eV cm^{-2}s^{-1}
$(\Delta\tilde{Q}_p/\Delta t)\tilde{Q}_p$	0	$0.00016\ \tau_{pp}^{-1}$
O^{2+} conduction heat flux $\tilde{Q}_{O^{2+}}$	2.20×10^{15} eV cm^{-2}s^{-1}	3.2×10^{15} eV cm^{-2}s^{-1}
$(\Delta\tilde{Q}_{O^{2+}}/\Delta t)/\tilde{Q}_{O^{2+}}$	0	0
$\Gamma_{O^{2+}}/\Gamma_p$	$= -Z_p/Z_{O^{2+}} = -0.500$	-0.62
$\tilde{Q}_{O^{2+}}/\tilde{Q}_p$	$= \alpha(Z_p/Z_{O^{2+}})^3 = 1.14$	0.91

Table 3.3. Summary for case without temperature gradient screening, H^+-O^{3+}

O^{3+} density	1.37×10^{12}
$\alpha = n_{O^{3+}} Z^2_{O^{3+}} / n_p$	13.7
ν_{*p}	224.0
$\nu_{*O^{3+}}$	1.21×10^3
$\delta^{-3/2}$	7.57
τ_{pp}	6.29×10^{-5} s

	Theory	CPM (at $t = 200\tau_{pp}$)
Proton particle flux Γ_p	4.44×10^{13} cm^{-2}s^{-1}	4.0×10^{13} cm^{-2}s^{-1}
$(\Delta\Gamma_p/\Delta t)/\Gamma_p$	0	$-0.0012\ \tau_{pp}^{-1}$
O^{3+} particle flux $\Gamma_{O^{3+}}$	-1.48×10^{13} cm^{-2}s^{-1}	-1.2×10^{13} cm^{-2}s^{-1}
$(\Delta\Gamma_{O^{3+}}/\Delta t)/\Gamma_{O^{3+}}$	0	$-0.0018\ \tau_{pp}^{-1}$
Proton conduction heat flux $\tilde{Q}_p$	1.34×10^{15} eV cm^{-2}s^{-1}	9.7×10^{14} eV cm^{-2}s^{-1}
$(\Delta\tilde{Q}/\Delta t)\tilde{Q}$	0	$0.0026\ \tau_{pp}^{-1}$
O^{3+} conduction heat flux $\tilde{Q}_{O^{3+}}$	6.77×10^{14} eV cm^{-2}s^{-1}	1.5×10^{15} eV cm^{-2}s^{-1}
$(\Delta\tilde{Q}_{O^{3+}}/\Delta t)/\tilde{Q}_{O^{3+}}$	0	$-0.00051\ \tau_{pp}^{-1}$
$\Gamma_{O^{3+}}/\Gamma_p$	$= -Z_p/Z_{O^{3+}} = -0.333$	-0.30
$\tilde{Q}_{O^{3+}}/\tilde{Q}_p$	$= \alpha(Z_p/Z_{O^{3+}})^3 = 0.506$	1.5

Comparison of Model Distribution Functions with Collisional Plasma Model (CPM) Results in Various Collisionality Regimes[42]

T. Uckan C. O. Beasley, Jr.

The neoclassical electron distribution function derived by Rosenbluth, Hazeltine, and Hinton[43] is compared with CPM[36] results in the banana regime. Generally there is good agreement except for discrepancies at low energy, which may be attributed to lack of proper treatment of the collisional (low energy) particles by Rosenbluth et al.[43] Comparison of CPM results with those of Tsang and Callen[44] in the Pfirsch-Schlüter regime show good agreement, considering the approximations made by Tsang and Callen.

A tokamak transport code using self-consistent transport coefficients calculated by the CPM

C. O. Beasley, Jr. J. T. Hogan

In present transport codes describing the time evolution of toroidal plasmas, radial transport coefficients are generally modeled by some sort of scaling intended to approximate the correct functional dependence or parameters upon which the transport is physically dependent. Thus, for example, if one assumes that neoclassical transport is the dominant transport mechanism, the neoclassical transport coefficients are calculated on the basis of present neoclassical theory. In the case of neoclassical transport, a reasonably accurate result obtains. Unfortunately, experimental evidence indicates that not all transport coefficients in tokamaks behave classically, and no unique accurate means for calculating these coefficients exists at present.

Since the CPM promises to be a means of obtaining accurate transport coefficients, we have begun working on a code which incorporates the self-consistent calculation of the transport by the CPM with the determination of the parameters needed by the CPM codes using the transport code.

Ultimately, all kinetic anomalous transports – such as that arising from trapped particle instabilities – will be calculated by the CPM. As a first attempt, however, we are using a form of the CPM code which evaluates neoclassical transport associated with electrons. The ability to use our particular calculation procedure depends on the following assumptions:

1) the radial transport is describable functionally by flux-surface average transport coefficients,
2) the change in transport with radius is a slow and smooth function of radius,
3) radial transport is governed by radial gradients and other parameters which vary slowly in time, and
4) the transport coefficients adjust rapidly (on a given flux surface) with changes in parameters.

Then we begin with a calculation of neoclassical equilibrium and transport at a small number of radial positions using plasma parameters representative of the start of the current plateau in a tokamak shot (i.e., at the end of the current-penetration stage of tokamak operation). Using these coefficients, the transport code then steps forward in time until parameters change by predetermined amounts. Then, beginning with the previous distribution function, a new quasi-equilibrium on a flux surface is calculated.

The hybrid code is now being checked out on the ORNL computer. Changes to newer versions of the CPM code will be straightforward because the individual components of the program logic have been found to be compatible and execution time and storage requirements have been found to be adequate for combined CPM/transport code operation.

The time evolution of a bump on the Maxwellian distribution function with self-collisions

T. Uckan

The time evolution of a bump-on tail perturbation of a Maxwellian plasma with self-collisions (electrons) is studied through the CPM.[36] The purpose of this study is two-fold: (1) it serves as a test case in preparation for

studying the behavior of arbitrary distributions in tokamaks, and (2) it serves as a test of a program to generate the CPM amplitudes for an arbitrary distribution.

The equation of interest is

$$\frac{\partial f}{\partial t} = Cf \quad ,$$

where f is the electron distribution function and C is the Coulomb collision operator for self-collisions. We choose the following form for the distribution function:

$$f = \delta_1 f_m + \delta_2 f_b \quad ,$$

where f_m is the Maxwellian background, f_b is the non-Maxwellian bump, and δ_1 and δ_2 are the fractions of the distribution in the two species. Because we are using only the linearized form of the collision operator in these calculations, $\delta_2 \ll \delta_1$. In the CPM representation, we expand

$$f_m = \sum_{\ell,n} F_{\ell,o,n}\, \psi_{\ell o n}\, (\sqrt{\rho}\, v) \quad ,$$

where the $\psi_{\ell,n}$ are the basic functions described elsewhere[36] and where the amplitudes are given by

$$F_{\ell o n} = \delta_1 + \delta_2 \frac{2\pi\ 3/2\ n!\, e^{-(v_o/v_T)^2}}{\Gamma(\ell + n + 3/2)}\ Y_{\ell o}(\cos \alpha_0)$$

$$I_{\ell n}\ (v_o/v_T) \quad .$$

Here v_o is the beam velocity, v_T the thermal velocity of the Maxwellian, $Y_{\ell o}$ are spherical harmonics,[45] and the $I_{\ell n}$ integrals are defined by

$$I_{\ell n}\ (v_o/v_T) = \int_0^\infty dx\, e^{-x} (\sqrt{x})^{\ell+1} \exp[\sqrt{2}x\ (v_o/v_T)]$$

$$L_n^{\ell+1/2}(x) \quad ,$$

where $L_n^{\ell+1/2}$ is a modified Laguerre polynomial.

We choose a case where $v_o = 3v_T$, $\delta_1 = 1$, and $\delta_2 = 0.01$. By truncating the sum over I appropriately, we have a bump only at a particular angle, $\alpha_o = 45°$. We then use the CPM code in these calculations without the kinetic terms to follow the behavior of this bump in time.

Results are presented in Figs. 3.11 and 3.12. We find that, as expected, the distribution is thermalized: (1) the peak spreads out in pitch angle (Fig. 3.11) and (2) the bump loses energy, merges with the Maxwellian, and depletes the Maxwellian of lower energy particles, thereby raising its temperature (Fig. 3.12).

A parallel approach to a simulation of wave phenomena in toroidal plasmas in the drift-kinetic approximations

C. O. Beasley, Jr. C. E. Rathmann J. Denavit

A simulation technique has been developed by Rathmann and Denavit at Northwestern University for studying long wavelength phenomena in toroidal plasmas in the local flux-surface approximation.[46] This effort, which employs a model basically similar to but simpler than the CPM approach, will provide an independent and necessary check on CPM results pertaining to the dissipative trapped-electron instability, as well as being able to obtain results more quickly than the CPM.

As with the CPM, the distribution function, g, is expanded in a set of orthogonal functions

$$g = \sum_{\ell n} g_{\ell n}\ (\theta,\zeta)\ \psi_{\ell n}\ (v,\alpha) \quad ,$$

where

$$\psi_{\ell n} = P_\ell(u)\ z^{\ell/2} L_n^{\ell+1/2}(z)\ \exp(-z) \quad ,$$

where $u = \cos\alpha$, $z = \rho v^2$, α is the pitch angle, v is the particle speed, P_ℓ are Legendre polynomials, and L_n^p are Laguerre polynomials. This expansion differs slightly from the CPM representation (the two are simply related) and has the advantage that it is easily interpreted in terms of moments of the distribution function. In this representation, the drift-kinetic equation for electrons may be written in the form

$$\frac{\partial g_{\ell n}}{\partial t} = G_{\ell n}\ [(g_{\ell n}),\ E,\ \theta,\ t] \quad .$$

Coupled with ion fluid equations and Poisson's equation, the last equation allows for modes of

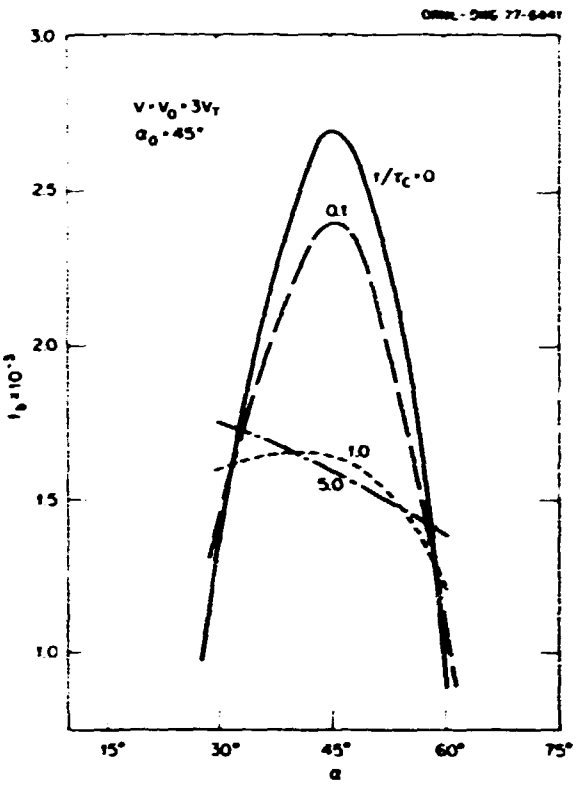

Fig. 3.11. The time evolution of the bump in pitch angle.

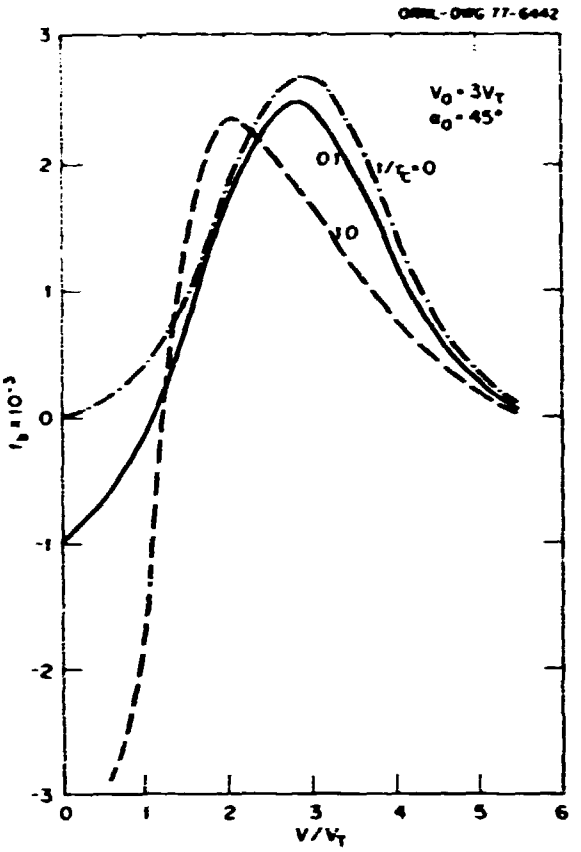

Fig. 3.12. The time evolution of the bump in velocity.

oscillation at both high frequencies near the plasma frequency, ω_p, and low frequencies, $\omega \ll \omega_p$. A slow time scale method for analysis of low frequency phenomena has been implemented by Rathmann and Denavit to study solution which are averaged over the electron plasma period $2\pi/\omega_p$. The following assumptions were made:

$$\frac{\partial g_{00}}{\partial t} \sim \varepsilon g_{00} \text{ and } \frac{\partial g_{10}}{\partial t} \sim \varepsilon g_{10} \quad ,$$

where

$$\varepsilon = (m_e/m_i)^{\frac{1}{2}}, \; g_{00} = n_e, \text{ and } g_{10} = n_e v_{e\parallel} \quad .$$

This leads to a solution of the $\frac{\partial g_{\ell n}}{\partial t}$ equation to the order ε:

$$G_{10}\,[(g_{\ell n}), E, \theta, t] = 0 \quad ,$$

which, along with the electron and ion continuity equations and the neutrality condition, $g_{00} = n_i$, yields

$$\vec{\nabla} \cdot (n_i \vec{v}_i) + G_{00} = 0 \quad .$$

These conditions can be shown to be analogous to the zeroth order solutions in ω_p^{-2} and Ω^{-1} discussed earlier.

Tests of the validity of their procedure were made by comparing the eigenvalues obtained by linearization of the fast time scale systems for basic plasma oscillation problems with parameters typically found in tokamak devices.

Ion acoustic waves

Parameters. $m_e/m_i = 1/2000$, $\Omega_e/\omega_e = 0.989$, $r/\lambda_D = 9.47$, $\varepsilon = 0.1$, $\nu/\omega_e = 0.5 \times 10^{-4}$, $k_\theta = 0$,

$k_\zeta \lambda_D = 1/947$, $\omega_A/\omega_e = 2.3612 \times 10^{-5}$, and $\ell_{max} = n_{max} = 3$. Here Ω_e is the electron cyclotron frequency, r is the flux surface minor radius, λ_D is the Debye length, ϵ is the aspect ratio, ν is the collision frequency, ω_A is the ion acoustic frequency, and k_θ and k_ζ are respectively the poloidal and toroidal wave numbers.

Note in Table 3.4 that the eigenvalues in both systems are in close agreement except for the absence of electron oscillations near $\pm\omega_e$ in the slow time scale system. We may therefore expect that the slow time scale model is applicable to computer simulations of long wavelength phenomena such as dissipative electron modes in toroidal plasmas. Additional comparisons of the eigenvalues of the fast and slow time scale systems for drift waves and a dissipative drift instability have also been calculated. These results also show good agreement between the two models for low frequency modes.

3.3.4 Particle Orbits and Injection Heating

J. A. Rome D. J. Beckett R. H. Fowler
J. Smith Y-K. M. Peng

This year has marked a change of emphasis in our work. Our fast ion Fokker-Planck code (FIFPC) has been refined, documented, and made available as an easily incorporated subroutine or as a stand alone code, as reported in Ref. 47. This completes a trio of codes which treat beam deposition,[48] slowing down, and loss regions[49] for circular concentric flux surfaces, assuming that the fast ions remain on a single flux surface.

With the advent of high-β, noncircular tokamaks as a viable option, our emphasis is changing in order to be able to treat these devices properly. Fundamental to this effort is the study of orbits in these machines. Beam deposition and slowing down codes can then be reworked in these more general cases and can be properly coupled to the one and one-half dimensional transport code.

We are also continuing our study of innovative injection schemes so that positive ion sources may still be used to heat large plasmas. This would allow use of deuteron energies of less than 200 keV.

An approach to solving the radially dependent Fokker-Planck equation

J. A. Rome

Because the collision time for injected ions in a tokamak is long compared to a bounce time,

Table 3.4. Complex eigenvalues of ion acoustic waves

Fast time scale		Slow time scale		Comments
ω/ω_e	γ/ω_e	ω/ω_e	γ/ω_e	
± 1.0003	2.4988×10^{-5}	----	----	electron oscillation
$\pm 3.1872 \times 10^{-3}$	1.9238×10^{-4}	$\pm 3.1872 \times 10^{-3}$	1.9238×10^{-4}	transit time frequencies
$\pm 1.7834 \times 10^{-3}$	1.9041×10^{-4}	$\pm 1.7834 \times 10^{-3}$	1.9041×10^{-4}	transit time frequencies
$\pm 1.1270 \times 10^{-3}$	1.4632×10^{-4}	$\pm 1.1270 \times 10^{-3}$	1.4632×10^{-4}	transit time frequencies
$\pm 4.9450 \times 10^{-4}$	1.0360×10^{-16}	$\pm 4.9450 \times 10^{-4}$	3.2315×10^{-17}	ion cyclotron
$\pm 2.3707 \times 10^{-5}$	9.9445×10^{-7}	$\pm 2.3713 \times 10^{-5}$	9.9495×10^{-7}	ion acoustic

the Fokker-Planck slowing down problem can be treated as a multiple time scale expansion. Accordingly, the fast particle distribution function and the individual orbits are regarded as functions of the three constants of motion which change slowly compared to the bounce time.

The choice of appropriate constants of motion and the topology of the resulting space was discussed last year.[50] By using the Massachusetts Institute of Technology (MIT) symbolic manipulation computer system, MACSYMA, we were able to finish setting up this problem for solution. We took the Fokker-Planck equation (which is valid at a fixed point in space) and changed variables to the three constants of motion, v, ζ, and r_{max}, keeping only the first term in $(r - r_{max})$. The equation was then averaged along the bounce orbit for each set of constants of motion. Finally, the boundary conditions in this space were derived.

The resulting three-dimensional, time-dependent diffusion equation can now be solved numerically to yield the desired correct slowing down distribution function; however, it was decided to delay doing this until the problem can be recast to apply to noncircular, high-β tokamaks.

Neutral beam deposition in the constants of motion space and in real space for arbitrary injection geometry

D. J. Beckett J. A. Rome R. H. Fowler

A new computer code has been developed to treat arbitrary injection geometry, but is restricted to tokamaks with circular concentric flux surfaces. The unique feature of this code is that it properly treats the finite width, fast ion orbits by depositing the fast ions as a distribution in the three-dimensional constants of motion space. Because in an axisymmetric tokamak the particle orbits are uniquely determined by three constants of motion, all orbit information is preserved with this method.

Figures 3.13-3.15 show beam deposition in TNS at a central density of 3×10^{14} cm^{-3}, $Z_{eff} = 1$, and a deuteron energy of 300 keV. The injection angle is 12° from perpendicular in the co-direction. Figure 3.13 shows the fast ion density in the constants of motion space, v, r_{max} (the maximum minor radius along an orbit), and ζ ($\equiv v_{\parallel}/v$ at $r = r_{max}$). Even at this high injection energy, most of the beam is deposited near the outside of the plasma. In Fig. 3.14, we have taken the orbits specified by the constants of motion and have properly distributed the fast ions along these orbits. For example, the density in real space will be peaked near the banana tips (where the particles slow down) and near the magnetic axis, due to the smaller volume occupied by the particles on these orbits. Finally, in Fig. 3.15, we have averaged the fast ion density over the flux surfaces to obtain the conventionally used beam deposition profile, H(r).

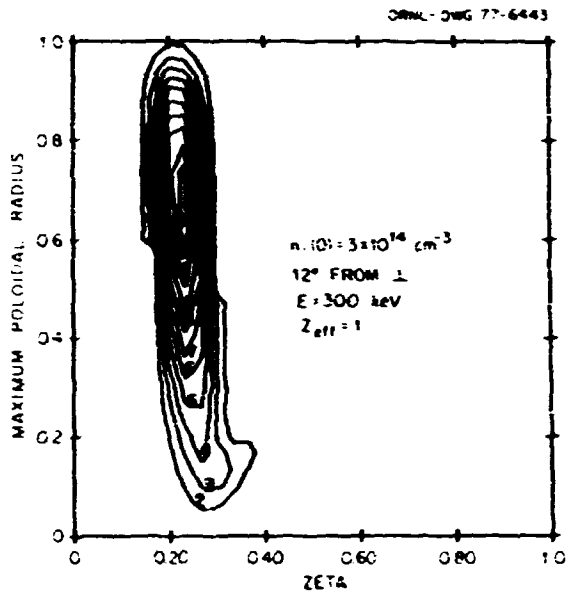

Fig. 3.13. Fast ion deposition in the constant of motion space.

Doing the beam deposition in the constants of motion space has several important advantages. It enables one to calculate any moment of the fast ion birth distribution function as opposed to only fast ion density; but more important, it can be used directly as the source function in a general, radially dependent treatment of the fast ion slowing down problem.

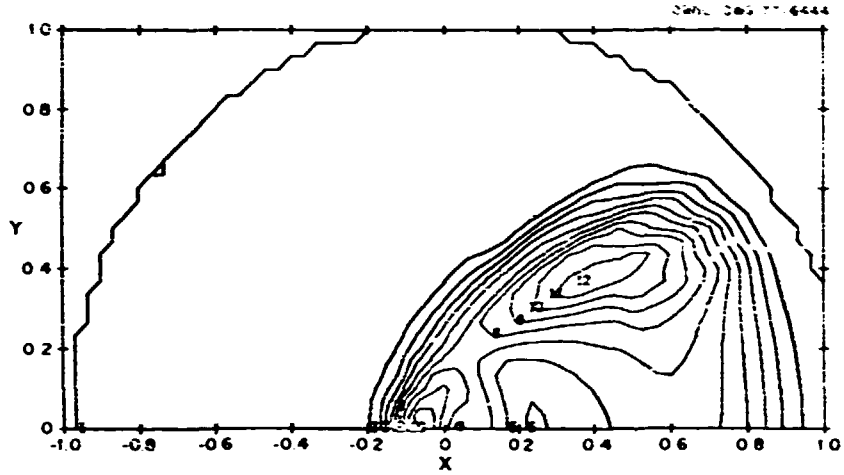

Fig. 3.14. Fast ion birth distribution in real space. Only the upper half of the cross section is shown.

Particle orbits in high-β D-shaped flux conserving tokamaks

J. A. Rome Y-K. M. Peng

High-β, flux-conserving equilibria are characterized by the appearance of an absolute minimum in $|\bar{B}|$ which occurs outside of the magnetic axis but inside the limiter. This causes a fundamental change which must be studied to occur in the orbit topology.

An appropriate set of constants of motion with which to characterize these orbits is v (the speed), ψ_m (the maximum value of poloidal flux along the orbit), and $\zeta(v_\parallel/v$ at $\psi = \psi_{max})$. If we use conservation of toroidal canonical angular momentum correct through the first order in gyroradius, we can solve explicitly for $B(\psi)$ along the orbit:

$$\frac{B}{B_m} = \frac{1}{\frac{1-\zeta^2}{2} + \sqrt{\left[\frac{1-\zeta^2}{2}\right]^2 + \left[\frac{\psi_m - \psi}{\frac{m}{e} Fc}\sqrt{\frac{c^2}{v^2} - 1}\, B_m - \frac{F_m \zeta}{F}\right]^2}}$$

where $F = RB_T$ (a function of ψ), and the subscript m indicates evaluation at ψ_{max}.

By studying these orbits, the following conclusions may be obtained.

1) The number of trapped particles decreases as β increases, due to the decreasing magnetic well depth.
2) The bounce time of trapped particles increases with increasing β.
3) A new class of counter-going orbits appears

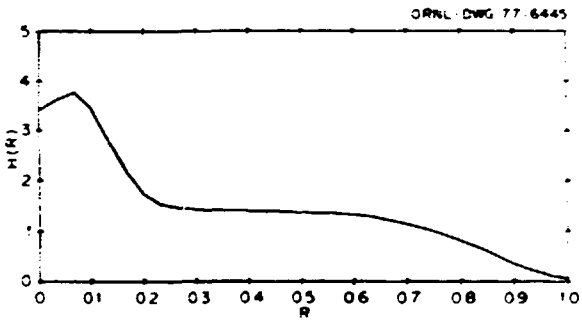

Fig. 3.15. Flux surface averaged beam deposition profile.

outside the magnetic axis as the minimum in $|B|$ deepens.

Computer codes for the guiding center motion of single particles

R. H. Fowler

Two computer codes have been developed to integrate the equations of motion of the guiding centers[51] of single particles. These codes have been used[52] primarily to study ripple injection into tokamak plasmas. One code uses the toroidal coordinates (r, θ, ϕ) and is restricted to zero electric field. The other code is written in generalized coordinates and treats both electric and magnetic forces. The execution time of the latter code is longer due to its generalization. Both codes assume that the fields are time independent. The Bulirsch and Stoer extrapolation method[53] is used to integrate the differential equations. The codes can be run either on a PDP-10 or on the CDC 7600 at the National Magnetic Fusion Energy Computer Network (NMFECN).

Comparative studies of numerical methods for the fast ion Fokker-Planck equation

R. H. Fowler

In an effort to increase the speed of FIFPC,[47] a comparison of three numerical methods is being made. The methods are successive over-relaxation (SOR), the strongly implicit procedure[54] (SIP), and alternating-direction implicit[55] (ADI). This study is being done only on the time-dependent calculation of the distribution function. The preliminary results of this study indicate that the SOR is not competitive with the other methods and that ADI yields results of comparable accuracy in about half the CPU time required by SIP.

Ripple injection studies

R. H. Fowler J. A. Rome

Ripple injection[56] was studied using the particle following code described earlier in Sect. 3.3.4. To make a local ripple, we used the field of a horizontal straight wire passing through the symmetry axis and above the plasma. We were able to penetrate to the center of the TNS plasma with a deuteron energy of only 45 keV with a wire current of 5×10^5 A; however, at this level, the plasma flux surfaces became ergodic and plasma confinement would be very poor. The disturbance to the flux surfaces could perhaps be reduced by using more than one local ripple to cancel out the lowest toroidal harmonic perturbations of the field lines.[57]

3.4 TRANSPORT SIMULATION

T. Amano E. C. Crume, Jr. J. K. Munro
D. E. Armurius J. T. Hogan E. M. Oblow
S. E. Attenberger H. C. Howe M. Soler
J. D. Callen* A. T. Mense T. Uckan

3.4.1 Physics Packages

T. Amano W. F. Carver T. Uckan
D. E. Armurius E. C. Crume, Jr.

Dynamic coronal model for impurities

D. E. Armurius E. C. Crume, Jr.

The dynamic coronal model computer code[58] has been upgraded to compute more efficiently the time-dependent charge state distribution of high-Z elements. This has been accomplished by providing internal checks so that only equations for the charge states needed to adequately describe the distribution, rather than equations for all the charge states, are integrated in any given time step. As necessary, the code automatically changes the number of equations being integrated by adding or deleting higher or lower charge states. For example, when calculating for iron, only six to eight charge state equations are necessary at any one time, rather than 26 (or 27 if neutral iron is included); thus there is a savings factor of three to four.

Pfirsch-Schlüter transport coefficients for impurities

W. F. Carver E. C. Crume, Jr. K. T. Tsang

Transport coefficients for a number of interacting ion pairs have been calculated to supplement the hydrogen-oxygen values given in

*Group Leader.

Ref. 59. The pairs include H-D, D-T, D(50)T(50)-a, D-O, H-C, H-Fe, O-Fe, and interactions among different ions of the same element. The coefficients are available as look-up tables for computer calculations; however, recent work by Hirschman[60] has led to analytic formulas that reproduce some of our numerical results, and such formulas are less bulky to use than look-up tables.

3.4.2 Tokamak Discharge Modeling

O. C. Eldridge H. C. Howe W. Namkung
M. Soler J. C. Whitson

Most of the tokamak discharge modeling specific to the understanding of ORMAK plasmas has been carried out this past year in close collaboration with and under the sponsorship of the Tokamak Experimental Section. Thus, most of these efforts are described in the ORMAK section of this report (Sect. 2.1). Particularly noteworthy in this regard is the gas puff modeling through use of the Ware pinch effect (Sect. 2.1.15). A more general effort concerning electron-cyclotron resonance heating (ECRH) in tokamaks is described in the following two brief accounts.

Electron-cyclotron resonance heating (profile) in tokamaks and numerical simulations on ISX

W. Namkung H. C. Howe

We calculate the radial distribution of energy absorption by electrons due to ECRH. The model adopts a simple spatial damping factor with a finite absorption width which removes singularities at the magnetic axis and at the tangency point of the resonant MOD-B surface. The results are plotted in Fig. 3.16. When the heating zone passes the magnetic axis, it is possible to give an analytic expression for the spatial shape factor, H(r), of the heating power deposition. This model could also be used for ion-cyclotron resonance heating (ICRH) in tokamaks. Using the ORNL one-dimensional transport code, numerical simulations for ISX are performed and the temporal and spatial behaviors of plasma parameters are obtained. The results are shown in

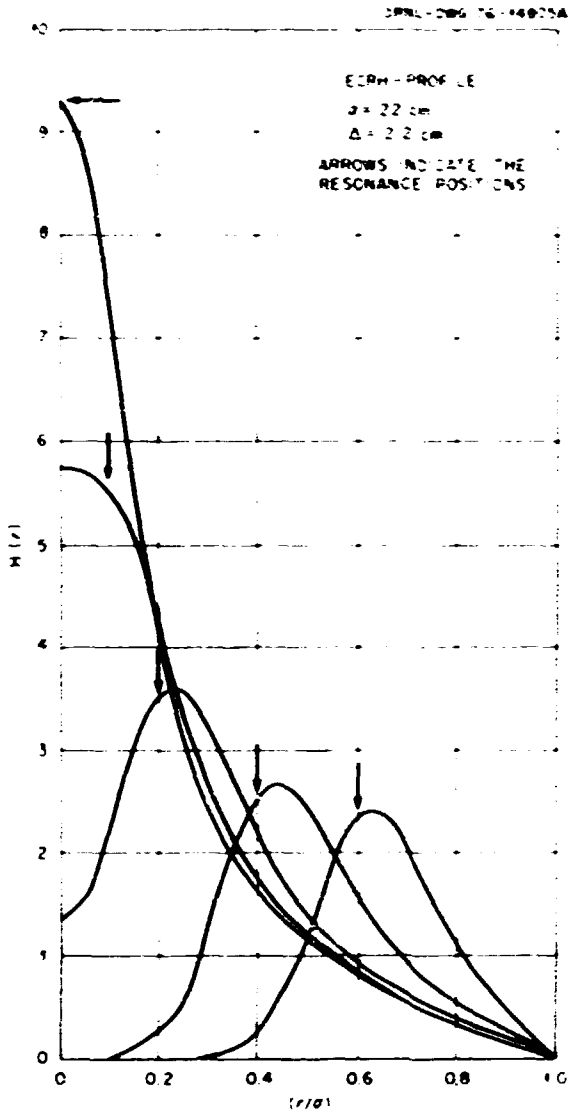

Fig. 3.16. The heating power deposition spatial shape factor, H(r), with different locations of the resonance zone. The arrows indicate the resonance positions; x_0 = 0, 2.2, 4.4, 8.8, and 13.2 cm. The minor radius of the torus, a, is 22 cm and Δ, the resonance width, is 2.2 cm.

Fig. 3.17. The 200 kW of heating proposed for ISX should double the electron temperature (assuming full absorption); the effect on sawtooth behavior due to ECRH profile modification may also be measured.

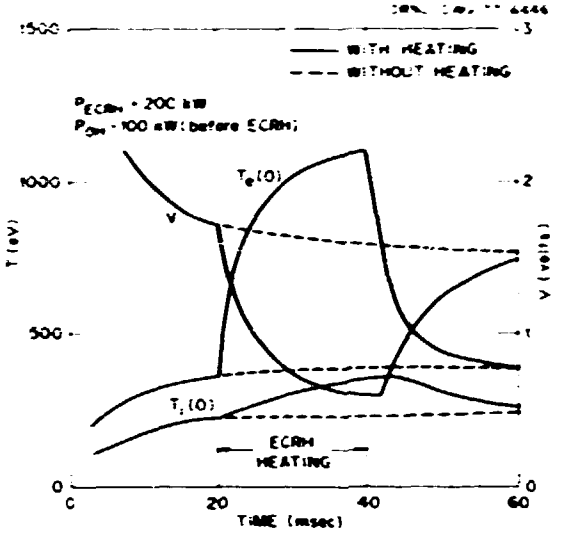

Fig. 3.17. Temporal behavior of $T_e(0)$, $T_i(0)$, and V for 200 kW of heating at $x_0 = 0$.

Electron-cyclotron heating in tokamaks

O. C. Eldridge W. Namkung

Electron-cyclotron heating can be shown to be an efficient process in tokamaks with densities below a critical point where the wave frequency equals the plasma frequency. The polarization of the electric fields at the cyclotron resonance is such that heating rates are proportional to electron temperature and inversely proportional to density. The slow wave launched from a waveguide aperture will be almost completely absorbed for current tokamak parameters. Absorption coefficients for the fast wave are smaller but still adequate. The perpendicular energy of the bulk of the plasma is increased for both polarizations.

3.4.3 Reacting Plasma Modeling

A. T. Mense S. E. Attenberger

We have developed a one-dimensional multifluid transport code which incorporates α heating and diffusion and divertor collection physics into the basic structure of the transport simulation codes already in existence at ORNL. A benchmark study was made of available neutral particle codes against each other and against the three-dimensional Monte Carlo code developed by G. G. Kelley. The neutral profiles determined by all the schemes agreed within a factor of two for the optically thick plasmas relevant to large fusion plasmas. Thermally stable, ignited, plasma equilibrium profiles have been generated for the TNS study assuming a perfectly collecting divertor and a uniform pellet injection profile. More detail is given in Sect. 3.6.5.

3.4.4 Tokamak Model Development

J. T. Hogan J. K. Munro E. M. Oblow

The Oak Ridge Tokamak Transport Code (ORTTC) has been improved in its description of several important areas. This section summarizes these developments, while the abstracts convey the results obtained through the use of the models.

Axisymmetric transport

J. T. Hogan D. C. Stevens* D. M. Nelson

It has been apparent for some time that a phenomenological treatment of the axisymmetric transport problem would yield valuable information. Indeed, quasi-static axisymmetric transport calculations (requiring <5 equilibrium calculations/problem) were performed some time ago.[5] With the availability of the MMFECN and the ISLAND Code module developed at the Courant Institute (New York University), it has become practical to do a fully axisymmetric treatment of transport, including the full variety of neutral gas, neutral beam, and impurity processes which play a role in tokamak dynamics. In particular, the code now has the capability to calculate the complementary processes of adiabatic toroidal compression [Fig. 3.18(a)] and rapid flux conserving heating [Fig. 3.18(b)]. No assumptions about instantaneous compression or instantaneous heating are required, and the code allows the testing of models for each of these

*Courant Institute, New York University.

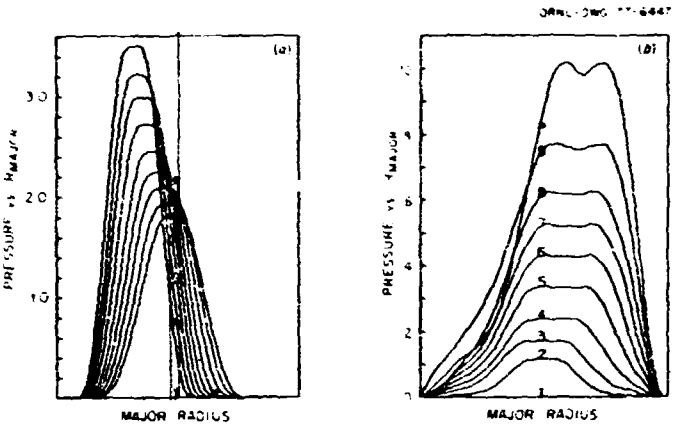

Fig. 3.18. (a) Pressure profiles as a function of time during adiabatic compression. (b) Pressure profiles as a function of time during rapid neutral beam heating.

processes. Two interesting results may illustrate the rationale.

1) For adiabatic compression, as in Fig. 3.18(a), the code follows the plasma evolution merely by increasing the applied external vertical field. We can then confirm the ideal scaling laws[62] except in one important aspect: as noted in the Adiabatic Toroidal Compressor (ATC) experiments,[63] electron heating fell below the expectations of the ideal adiabatic scaling laws. While the compression time in the experiments was comparable to the confinement time of the precompressed plasma, the subsequent compression should have raised τ_E by the compression factor, C, according to the empirical rule $\tau_E \propto na^2$. An alternate explanation is provided by the following calculation: we assume a small density of high-Z impurity is present (<0.05% n_e) in the precompressed plasma. In this illustration we choose tungsten instead of the molybdenum used in the ATC limiters. As shown in Fig. 3.19(a) the electron density rises as the plasma is compressed, while the electron temperature does not rise [Fig. .19(b)]. For these studies we have used radiative rates calculated by Tarter[64] and by Jensen, Post, et al.[65]
2) As discussed elsewhere in this report (cf. Sect. 3.2), flux conserving equilibria offer the prospect of enhanced economic performance for magnetic fusion. As an illustration we present code calculations of this concept which extend the original developments a step further. Figure 3.20 (a-d) shows the evolution of plasma parameters in a discharge isolated from the limiter and subject to intense neutral beam heating. We see that although the plasma parameters vary by wide margins, the $q(\psi)$ profile remains frozen and high pressures are attained. Although some impurity dynamics are included [e.g., Fig. 3.20(d)], we should stress that this is a rather optimistic depiction of the situation and is intended only to test the theoretical concept by relaxing some previous constraints.

Boundary model

J. T. Hogan F. B. Marcus S. E. Attenberger

The atomic and molecular physics package developed by F. B. Marcus and S. E. Attenberger for their start-up investigations (cf. Sect. 3.5.1) has been adapted for use in an internally consistent description of the plasma-wall interface in a conventional limiter bounded tokamak.

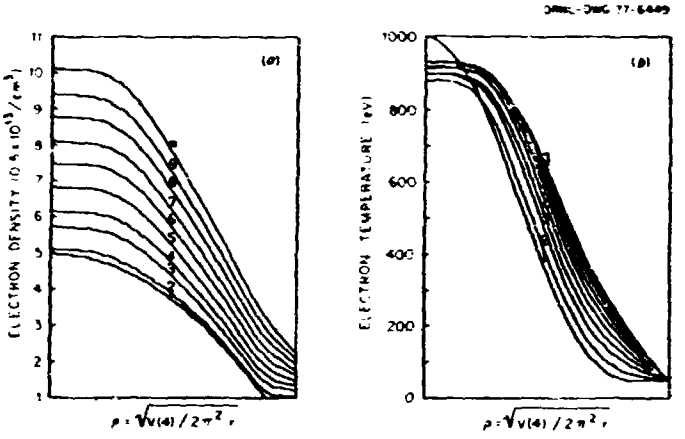

Fig. 3.19. (a) Electron density profiles during adiabatic compression. (b) Electron temperature profiles showing the effects of radiation during compression.

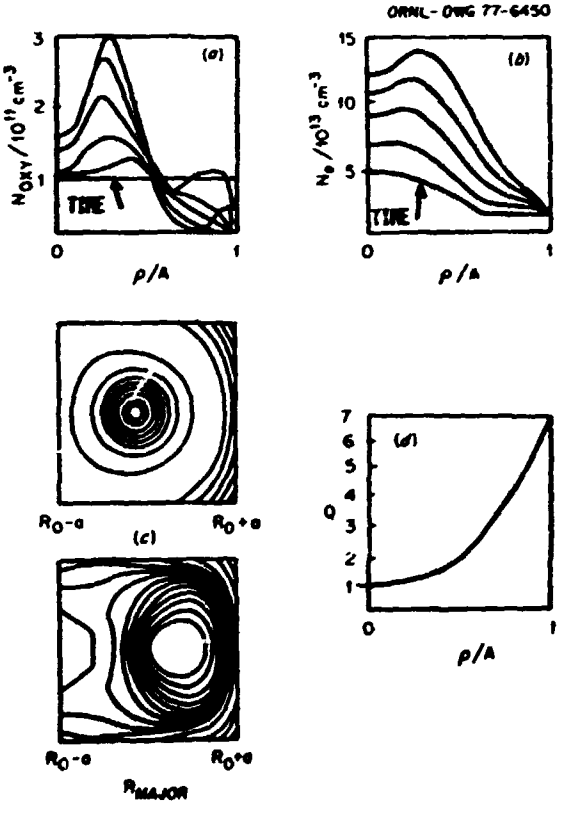

Fig. 3.20. (a) Evolution of oxygen density during the 300-msec neutral beam heating phase. (b) Electron density increases as the beam supplies particles. (c) Top: Initial configuration of pressure contours; Bottom: Final pressure configuration. (d) The q-profile during heating phase.

The model is specifically aimed at settling the question of how many wall-produced impurity ions survive to reach the tokamak discharge and incorporating the results of basic findings on the rates of impurity evolution. Such processes as photo-electron simulated and direct-electron simulated desorption, charge-exchange desorption, and sputtering have yet to be quantified for present tokamak devices, and further experimental results will be needed to validate the boundary model.[66]

Beam deposition module

J. T. Hogan J. A. Rome
D. J. Beckett R. H. Fowler

The impurity beam trapping instability described earlier (Sect. 3.3.4) can be ameliorated by more nearly perpendicular injection. Because previous studies of the beam deposition process have been limited by the restriction of drift orbits to be shifted circles, the inclusion of the new Rome, Beckett, and Fowler beam deposition module has expanded the scope of the code as the question of neutral beam penetration of large, dense, impure plasmas becomes crucial in the further development of neutral injection heating.[67]

Neutral transport

J. T. Hogan L. M. Petrie G. D. Kerbel
E. C. Crume, Jr. O. W. Hermann

The adaptation of the XSORN neutron and photon transport code into a neutral transport module has been described by Crume et al.[68] This neutral transport module has been incorporated in ORTTC (see Fig. 3.21) and can be used when its accuracy is needed.

3.5 PLASMA ENGINEERING

S. E. Attenberger J. D. Callen* G. D. Kerbel
F. B. Marcus D. G. McAlees† J. R. McNally, Jr.
A. T. Mense K. E. Rothe R. D. Sharp
D. J. Strickler N. A. Uckan

Plasma engineering applies and coordinates specialized theoretical plasma physics techniques and models to applied areas of fusion energy research, development, and engineering as needs arise or are anticipated.

3.5.1 Plasma Start-up[69,70]

F. B. Marcus S. E. Attenberger

The start-up phase of a tokamak plasma is modeled by coupled equations for the average density and temperature of H_1^0, H_2^0, H_1^+, H_2^+, e, and for current- and time-dependent oxygen ionization levels and radiation. The physical processes include ionization, dissociation, recombination, excitation, charge-exchange, energy-dependent neutral wall reflection, ohmic heating (OH) from elastic collisions, bremsstrahlung, Coulomb transfer, diffusion, refluxing, and runaway electrons. These equations are used to describe the current rise phase of ORMAK. In general, the temperature is nearly equal to 3 eV until the neutrals are ionized and then rises until limited by oxygen impurity line radiation if sufficient oxygen is present. This radiation power loss decreases when the O VII state is reached. In large tokamaks such as TNS, large loop voltages and much lower impurity levels than in present experiments are required to obtain breakdown.

An example of the result of insufficient voltage (50 V) applied to a large tokamak is shown in Fig. 3.22. The tokamak parameters are R_0 = 5 m, a = 1.25 m, b/a = 1.6/1, B_T = 4.3 T, initial H_2^0 density = 0.2×10^{20} m^{-3}, and no oxygen impurities. The H_2^0 density decreases, but levels at half its original value. The temperatures equilibrate at 0.002 keV, limited by H_1^0 excitation radiation. To achieve breakdown, especially if impurities are present, may require several hundred volts/turn.

3.5.2 Magnetic Field Ripple Effects

N. A. Uckan K. T. Tsang J. D. Callen

The ripple produced by the finite number of toroidal field (TF) coils destroys the ideal

*Group Leader, December.

†Group Leader, January-November.

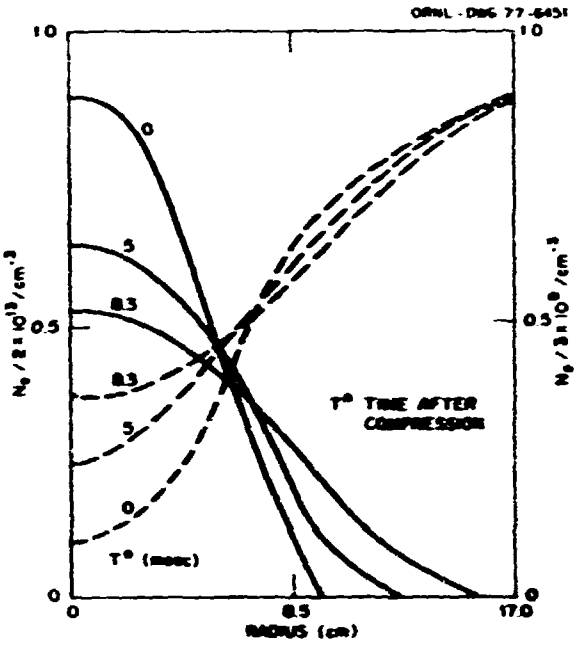

Fig. 3.21. Electron density and neutral profile evolving in an ATC free expansion plasma. The XSDRN module as coupled to the transport code calculates the neutral density behavior.

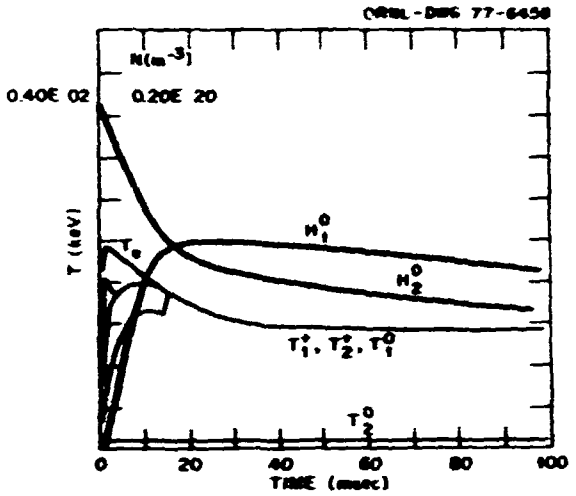

Fig. 3.22. Plasma startup in TNS (R_0 = 5 m). An applied voltage of 50 V/turn is insufficient for complete ionization. H_1^0 and H_2^0 are the densities of atomic and molecular hydrogen, and T_e, T_1^+, T_2^+, T_1^0, T_2^0 are temperatures of electrons, H_1^+, H_2^+, H_1^0, H_2^0.

axisymmetry of the magnetic field configuration and is responsible for additional particle trapping, loss regions, and plasma transport. The ripple can lead to enhanced plasma transport by two separate mechanisms. In the first, known as ripple trapping, particles can become trapped in the TF minima between the coils and experience a vertical guiding center drift which, in the presence of weak collisions, leads to ripple diffusion. The second mechanism of enhanced ion heat conduction is due to the ripple-induced radial drift of the banana drift orbit centers (cf. Sect. 3.3.1). The enhanced transport losses in circular and noncircular tokamaks due to field ripple, including radial and poloidal variation, as well as fast ion losses by ripple trapping, have been calculated.

Ripple-trapped diffusion[71]

N. A. Uckan K. T. Tsang J. D. Callen

Ripple trapping affects only a relatively small group of particles, namely those with $V_\parallel$ (parallel velocity) so small that they can be trapped in the ripple, i.e., $V_\parallel < \delta^{\frac{1}{2}}V$, where $\delta \equiv (B_{max} - B_{min})/(B_{max} + B_{min})$ is the ripple depth and V is the particle speed. The ripple depth varies with poloidal angle; thus, the induced ion heat transport varies as well. Because δ is usually maximum on the midplane at the outer edge of the torus, the flux-surface averaged ion heat transport due to ripples is less than that which is estimated when the poloidal variation is neglected.[72] The geometry-dependent factor (G) in the ion heat conduction coefficient characterizing this effect in a case with shaped TF coils is shown in Fig. 3.23 for various plasma cross sections and consequent magnetic field dependences on the poloidal angle (θ). The basic conclusion to be drawn from this figure is that, as long as the plasma and TF coils have roughly the same shape (so that the distance between them is roughly constant as a function of poloidal angle), the effect of poloidal variation is to decrease the induced ion heat

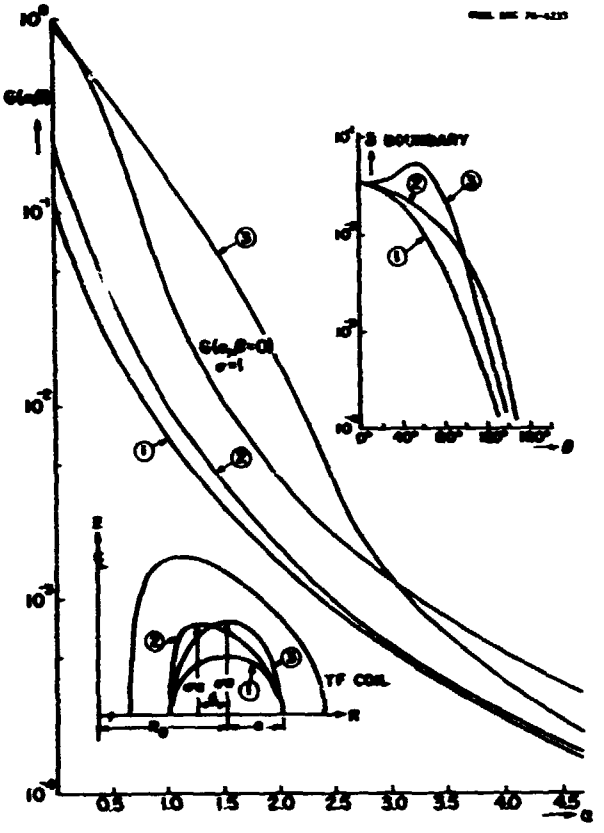

Fig. 3.23. The geometry dependent factor, G, in the ion heat conduction coefficient as a function of ripple well depth parameter $\alpha = r/NqR_0\delta$ (where q is the safety factor and N is the number of coils) for a given coil configuration and various plasma cross-sectional shapes: (1) circular, (2) D-shaped, and (3) elliptic. Insert (a) shows the toroidal field coil and plasma surface cross sections. Insert (b) shows the variation of ripple over the plasma cross section with poloidal angle θ.

conduction by a factor of three to ten. The ripple-induced ion heat conductivity in a non-circular cross-section plasma is slightly less by a factor of σ^2, where σ is the elongation, than that in a circular cross-section plasma.

Fast ion losses[73]

J. D. Callen K. T. Tsang N. A. Uckan

At the higher ion energies typical of neutral beam particles injected into large devices (≥100 keV) or α particles produced from D-T fusion (3.5 MeV), the ions can be lost directly or indirectly by ripple trapping effects. For an isotropic source of α particles, the fraction of these particles initially trapped in ripples ($\sim\delta^{\frac{1}{2}}$) will be lost directly. Those α particles that are not lost immediately after their production can be lost by diffusing into the ripple loss region during the slowing down process by pitch angle scattering. This problem has been investigated by solving the bounce-averaged equation governing fast ion slowing down and scattering processes for the approximate α particle distribution function in the presence of the ripple loss region. In defining E_* as the energy below which the particles are so collisional that they are detrapped before they can drift out of the machine and E_c as the critical energy below which the particle distribution becomes isotropic, it is found for α particles that E_* is lower than $E_c \sim 30\ T_e \sim 300$ keV. Thus, ripples will cause most of the α particles to become ripple-trapped and drift vertically out of the plasma; however, because its initial energy (3.5 MeV), E_0, is much greater than the typical energy at which it is lost, E_c, the average α particle will deposit most of its energy before drifting out.

For neutral beam heating, the injected ions have an $E_* > E_0$ (except near the outer edge of the plasma) for typical ion energies and coil designs.[71] Thus the vertical drift from ripple trapping of injected ions [parallel injection or perpendicular injection with an angle greater than $\sin^{-1}(\sqrt{2\delta})$] is not expected to cause appreciable loss.

Numerical calculation[74]

N. A. Uckan T. Uckan J. R. Moore

A computer model (RIPPLE) was developed to examine the magnetic field ripple effects on plasma transport and on scaling in circular and noncircular tokamaks. Calculations include the radial and poloidal variation in the magnitude of the field ripple. Two main magnetic field computer programs were used to calculate the magnetic field due to current flowing in a coil of finite rectangular cross section: BFULT for tori of circular coils, and BOVAL for tori of

noncircular coils. Results relevant to the ORMAK Upgrade, ORNL EPR, and TNS designs are obtained, and the criteria for the choice of the number of TF coils for a given tokamak configuration are discussed.

3.5.3 Poloidal Field Design

F. B. Marcus Y-K. M. Peng
J. R. Moore D. J. Strickler

Poloidal field design for D-shaped plasma in an ignition tokamak

Y-K. M. Peng D. J. Strickler J. R. Moore

Based on the equilibrium results in a flux conserving tokamak,[13] proper PF systems for a high-β, D-shaped plasma have been determined for an ignition tokamak. It is found that a relatively simple equilibrium field (EF) coil configuration (Figs. 3.5, 3.6) is sufficient and has the following characteristics.

1) It can shape and center plasma equilibria for a wide range of β values, both in FCT and non-FCT modes.
2) It retains the magnetic field shielding (STATIC) in that the volt-seconds and PF system power supplies are reduced and the EF currents are largely driven by inductive effects.
3) It admits a natural PF divertor configuration that requires only 0.4 I_p additional ampere turns at a distance from the plasma edge of half the plasma horizontal minor radius.

EPR with circular plasma cross sections

Y-K. M. Peng J. R. Moore
D. J. Strickler F. B. Marcus

A poloidal system with field shaping-shielding coils for future reactor-grade tokamaks that performs the following functions has been evaluated.[75-77]

1) It provides the necessary equilibrium field mostly by induction from the plasma.
2) It shields the superconducting TF coils from the pulsed fields and thus enhances their ability to reach higher toroidal fields (Fig. 3.24).

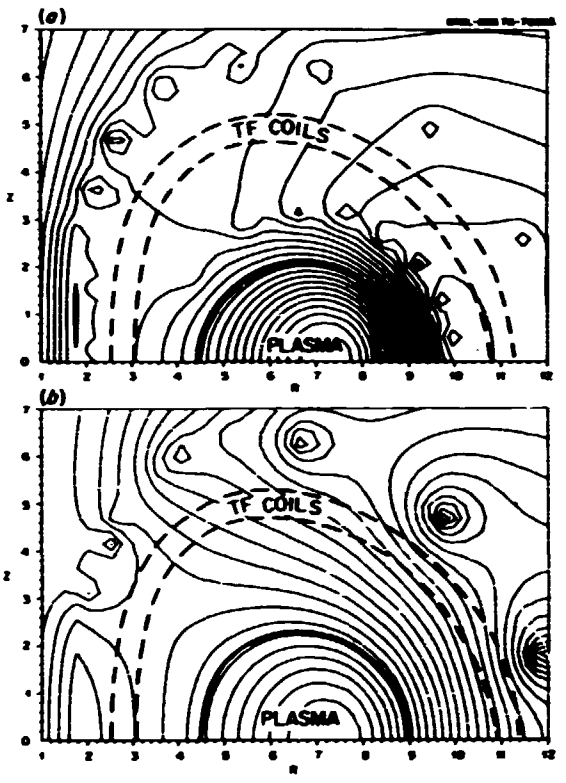

Fig. 3.24. Typical poloidal flux surfaces of: (a) a tokamak with magnetic field shielding (STATIC); and (b) a similar tokamak with VF coils external to the TF coils. The average poloidal field at the TF coils in (a) is 1/6 of that in (b).

3) It shapes the plasma cross section to a D-shaped plasma with elongation 1.6 for improved MHD stability against local modes and higher plasma current density.[78]

We have made some detailed comparisons of similar tokamak experimental power reactors with and without the shaping-shielding coils. These include comparisons of:

1) the time-dependent poloidal fields that intersect the TF coils,
2) the required amount of power and current supplies to the PF coils,
3) the forces experienced by these coils, and
4) the dependence of the self-consistent plasma shape on the plasma current profiles and β poloidal values.

It is shown from these comparisons that the shaping-shielding coils system effectively performs the first three of the four functions, is necessary for the fourth, and thus is considered exceedingly valuable for future tokamaks with D-shaped, high field, superconducting TF coils.

3.5.4 Particle Control

A. T. Mense

Much of the success of a fusion grade plasma in reaching an ignition condition is dependent upon particle control. By particle control we mean regulation of both input rate and egress of both neutrals and ions, Z = 1 particles, and impurities. Fueling in present plasmas is accomplished through a combination of recycling (plasma ions hitting limiter and wall and charge-exchange neutrals), gas puffing, and beam injection. Experimental progress in pellet fueling is just beginning, and its success may permit another control knob for future fusion devices. We have attempted in our particle control work to assess fueling problems, sputtering models, impurity deposition profiles, and plasma transport in both the central plasma core and divertor regions of a tokamak. Results as they pertain to TNS appear in Sect. 3.6.

3.5.5 Advanced Fuels

J. R. McNally Jr. R. D. Sharp K. E. Rothe

Advanced fusion reactors may permit the use of cleaner fusion fuels than the classical fuel, D-T. Studies are under way to evaluate the prospects and requirements of advanced fuels; such studies may be important to closed mirror reactor systems or other high-β systems.

Advanced fusion fuel symbiosis

J. R. McNally, Jr. R. D. Sharp

Ashworth[79] proposed breeding ^{3}He in large D-D advanced fuel reactors located on reservations while many locally sited advanced fuel reactor modules [150 MW(e)] burn D^{3}He in a clean mode. The factor by which a D^{3}He reactor is cleaner of 14-MeV neutrons compared to a D-T reactor of equal power is $F \sim 10\, n(^3He)/FBT\, n(D)$ at $T_i \sim 100$ keV. FBT = fractional burn-up of tritium. F can exceed 100 and tritium and P(neutrons)/P(total) can be down by over 100. D^{3}He high-β, ion-layer reactors also offer high thrust and direct conversion prospects. Prospects and requirements for such advanced fusion fuel symbiosis have been evaluated.[80]

Excitation heating of pellet fuels to ignition

J. R. McNally, Jr. R. D. Sharp

Metastable carbon ions (C^{2+*}), which have an inverted population at $T_e \sim 5$ eV, have been proposed as catalysts to produce runaway ion temperatures in long, dense, magnetically confined carbon arcs ($T_i \sim 500$ eV $\sim 100\, T_e$).[81] In very dense pellet fuels the runaway ion temperature is expected to be much higher and may lead to ignition of D-T fuel in the presence of such Be-like ions. Preliminary results on CD_2T_2 and $(CDT)_n$ pellets have been obtained. The $T_{ign}C$ condition is also less demanding for such systems than for pure D-T (C = required compression); $T_{ign} \leq 10$ keV. The microexplosion hazard should be carefully examined (1 mg D-T burn $\sim$ 0.1 ton TNT).

Advanced pellet fusion fuels[82]

J. R. McNally, Jr.

A survey has been made of D-T-enriched pellet fuels. The increased bremsstrahlung is offset in part by the much higher densities such that the product of ignition temperature and required compression favors some of these advanced fuels. T_{ign} is only about three to five times that for solid D-T because of the steepness of $\langle\sigma v\rangle$ vs T. For ignition breakeven one has

$$1 \leq Q_{ign} = \frac{n_D n_T \langle\sigma v\rangle Q_{DT}}{1.4 \times 10^{-27}\, n_e \Sigma n_i Z_i^2 \sqrt{T_e}} \propto KT^3$$

in the range of 3-10 keV and

$$K = \frac{n_i n_j}{n_e \Sigma n_i Z_i^2}$$

is given in Table 3.5. C is given by $(\rho R/\rho_0 R_0)^{3/2}$, where ρ_0 = liquid or solid density and R_0 = initial pellet core radius.

Ignition of a pellet fuel may permit the generation of a high-β, mirror-confined plasma for start-up; i.e., the pellet serves as a match to kindle a possibly steady-state, nuclear fusion burner.

Table 3.5. Macroscopic parameters of pellet fuels

Fuel	ρ (est.)	K
DT	0.21 g/cm³	0.25
$LiD_{0.5}T_{0.5}$	0.83	0.006
BeDT	0.97	0.009
$BD_{1.5}T_{1.5}$	0.77	0.010
CDT	1.16	0.003
CD_2T_2	0.57	0.010
$ND_{1.5}T_{1.5}$	1.03	0.004
ODT	1.16	0.0015

3.5.6 Pellet-Plasma Interaction Theory

G. D. Kerbel

The gas flow field, which arises around a pellet immersed in a tokamak plasma in the vicinity of the pellet surface, is strongly heated by incident plasma electrons. The interaction of the electrons with the gas serves to degrade the electron power flux responsible for the pellet ablation process. Electron energy and momentum deposition in the gas flow field have been calculated. The result is a refined self-consistent formulation of the ablation-induced shield.

The free boundary problem

Solution of the quasi-steady-state multifluid equations describing the pellet-plasma interaction requires the formulation of boundary conditions which are themselves determined by the solution of the equations. The physics which determines this free boundary aspect of the problem has been evaluated by means of an intuitive mathematical abstraction. The calculation involves the effect on the boundary conditions of the deposition of energy and momentum in the ablatant flow as well as the ionization and dissociation of the components of the ablatant.

The power transfer scheme

The processes by which the pellet ablatant absorbs energy from the plasma in which the pellet is immersed have been determined and categorized. The model relates the temperature of the components of the ablatant to the atomic, molecular, and plasma physics involved. Conduction, convection, and heat source terms have been formulated and associated in a coupled multifluid quasi-steady-state mathematical framework.

3.6 TNS PHYSICS

S. E. Attenberger F. B. Marcus* D. G. McAlees
J. R. McNally, Jr. A. T. Mense Y-K. M. Peng
J. A. Rome N. A. Uckan

3.6.1 Tokamak Plasma Systems Simulation[83,84]

S. E. Attenberger F. B. Marcus D. G. McAlees

Two tokamak system simulation models, one time dependent, the other time independent, have been used to model plasma behavior. Temperature and density profile effects have been included in the sputtering and radiation calculations.

Recent experimental and theoretical results indicate that high density and high-β plasmas can be achieved. It is found that high density permits ignition in a relatively small, moderately elongated plasma with a moderate magnetic field strength. Under these conditions, neutron wall loadings of 4 MW/m² must be tolerated. In Fig. 3.25 the plasma radius for ignition and β is plotted as a function of density at three axial toroidal field strengths for a fixed temperature of 13 keV and one-tenth trapped particle scaling. One possible ignition configuration is R_0 = 5 m, a = 1.25 m, b/a = 1.6/1, B_T = 4.3 T, I_p = 4 MA, $N_e = 2.2 \times 10^{20}$ m⁻³, T = 13 keV, β = 0.14, P_{fusion} = 1510 MW.

*Group Leader.

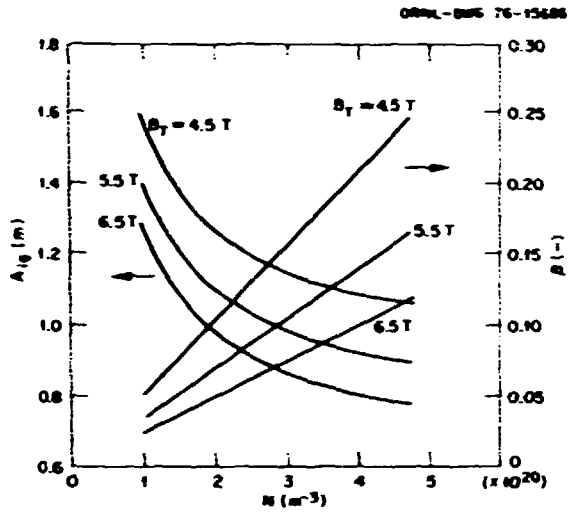

.Fig. 3.25. Plasma radius for ignition and β as a function of density.

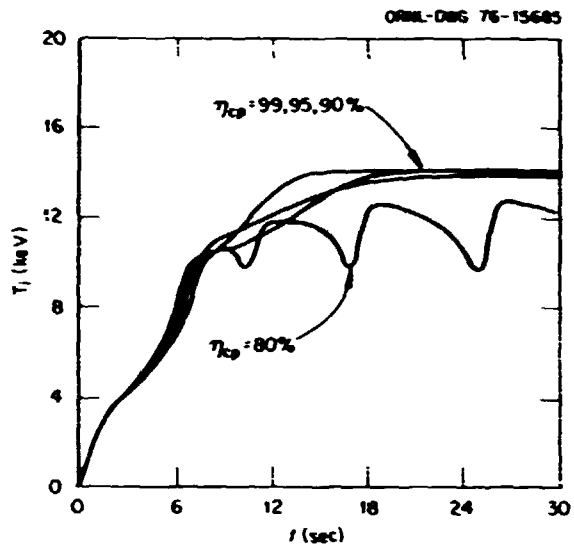

Fig. 3.26. Impurity buildup effects on the operating parameters for various impurity control efficiencies.

The sensitivity of the ignition and burning process to the level of impurity control has been investigated. In Fig. 3.26 the time-dependent plasma ion temperature is shown for various impurity control efficiencies. The charged particle screening efficiency η_{cp} equals $1 - \eta_1\eta_2$, where η_1 is the fraction of the outward plasma flux hitting the wall and η_2 is the fraction of sputtered impurities which diffuse into the plasma. For charged particle efficiencies of 99, 95, and 90%, a burning equilibrium is reached after 8-10 sec using 75 MW of neutral beam injection. When the efficiency is reduced to 80%, a steady burn is not achieved, and periodic beam heating is required.

If it is assumed that neutral beams will be used to heat the plasma to ignition, high energy injection is required (about 250 keV) when heating is attempted at full density. A more attractive scenario is illustrated in Fig. 3.27. Heating is initiated at low density with good beam penetration. The density is increased by fueling at a rate which does not cause a decrease in plasma temperature. Full density and ignition are achieved after four sec. The low density start-up ensures that significant heat will be deposited at the center ever with 150-keV D^0 beams.

3.6.2 Ripple Effects in TNS

R. A. Uckan

The theory of magnetic field ripple effects has been studied to include the effects of noncircular cross sections such as those encountered in high-β equilibria; Sect. 3.5.2 summarizes the findings of the study.

RIPPLE was developed to examine the field ripple effects on plasma transport and scaling in circular and noncircular tokamaks. A major question that arises in the design of tokamak devices is the choice of the number of TF coils; this number is determined by calculating the maximum TF ripple that can be tolerated from plasma physics considerations without seriously restricting the design of the mechanical support system for the blanket and shield and by the necessity for access to the neutral beam injection. From the plasma physics point of view: (1) the overall enhanced heat loss due to ripples

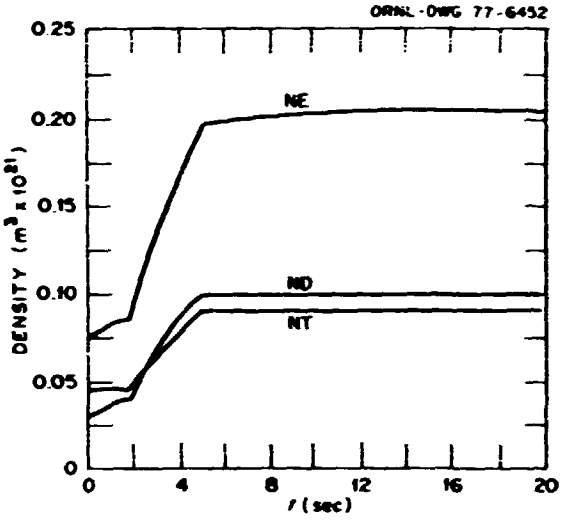

Fig. 3.27. Plasma density buildup during low density start-up procedure.

should be less than the total heat conduction loss due to neoclassical and trapped particle modes; and (2) fast ion losses due to ripple trapping should have no significant effect on power balance.

In order to optimize the design with tolerable field ripple, acceptable access space, and reasonable cost, it is possible to change: (1) the number of TF coils, (2) the coil bore dimensions, (3) the shape of the TF coils, or (4) the plasma location in the TF coils. Trade-offs among these alternatives have been studied for a given tokamak configuration (ORNL EPR, TNS, etc.) to provide information necessary for optimization.

3.6.3 Neutral Beam Penetration Strategies in Large, Dense Tokamaks

J. A. Rome Y-K. M. Peng

The new beam deposition code described in Sect. 3.3.4 was used to study beam penetration in large, dense tokamaks, and in particular, TNS. As a base case, we took R_0 = 5 m, a = 1.25 m, I = 4.3 MA, $J \propto [1-(r/a)^2]^2$, $n_e = n_p = 3 \times 10^{14} [1-(r/a)^2]$ cm^{-3}, and an injection angle of 16° from perpendicular. Brute force injection of deuterons at 300 keV seems to give marginal penetration with $Z_{eff} = 1$. If $Z_{eff} > 1.5$, the beam deposition is peaked towards the outside.

However, we feel that a more subtle approach will work at an injection energy of 150 keV. Suppose that the plasma starts at a full bore, but at low density [$n_e(0) = 5 \times 10^{13}$ cm^{-3}]. In this case, H(r) is strongly peaked [Fig. 3.28(a)]. In an FCT, as β increases, the magnetic axis moves out, and hence the beam penetration distance is decreased. By judicious use of fueling techniques such as pellet injection, density can be increased along with β so that the plasma arrives at the final flux conserving equilibrium (Fig. 3.29). In this state, the plasma is heated on the outside by the beams and near the center by the fusion produced α particles. Figure 3.28(b) shows the beam deposition in this final state where, at β = 15%, the magnetic axis is only 65 cm from the outer limiter.

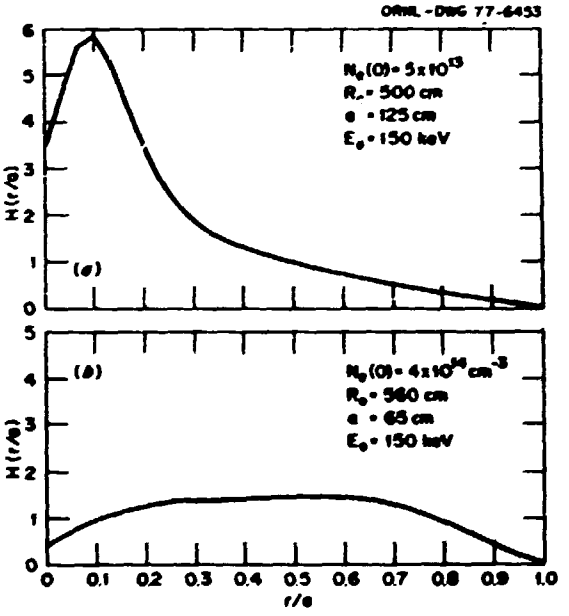

Fig. 3.28. (a) Injection into a full-bore but low density TNS plasma. (b) Injection into a β = 15% high density TNS plasma with strongly shifted flux surfaces.

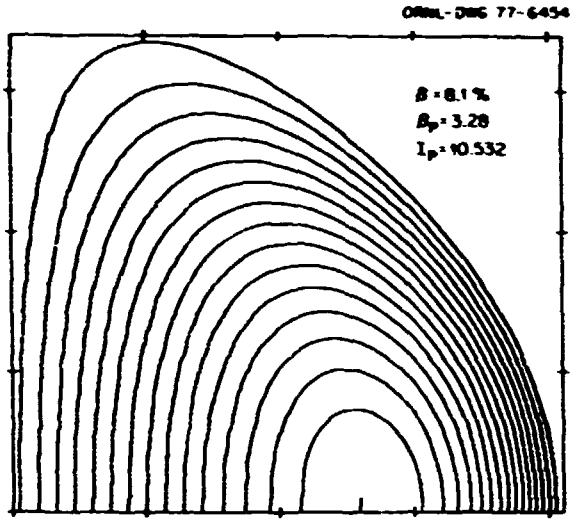

Fig. 3.29. ORNL FCT flux surfaces.

3.6.4 Dissipative Trapped Ion Loss Effects in TNS

J. R. McNally, Jr. K. E. Rothe

The advanced fuels reactivity code has been applied to TNS in order to evaluate the effects of various dissipative trapped ion mode fractions (FTIM) on steady-state, point equilibrium reactivity properties assuming cold fuel feed of D-T. The sensitivity of the degree of reactivity to FTIM, varying from 10^{-6} to 10^{0}, poses important operation problems (quench at FTIM = 10^{0} and over-reactive at $<10^{-1}$). TNS would burn only marginally at FTIM = 10^{-1}. Figures 3.30 and 3.31 show some parametric variations due to differing FTIM values. At FTIM = 10^{-2} the neutron power would exceed 12 MW/m^3 and the neutron wall loading would be about 9 MW/m^2. It should be noted that the dissipative trapped ion mode is yet to be observed experimentally; thus the seriousness with which one should take these conclusions with respect to TNS is not clear.

3.6.5 TNS Equilibrium Profiles

A. T. Mense S. E. Attenberger

Using a one-dimensional transport code (cylindrical geometry) we have found a set of (thermal) equilibrium profiles for TNS. These are found self-consistently and include the effects of divertor losses (both particle and energy), radiation (Z_{eff} = 1 assumed), particle correction, and thermal conduction. Production of α and energy deposition in the plasma are treated and a fusion D-T particle sink is kept in the continuity equation. Fresh fuel is supplied through the use of an assumed flat pellet deposition profile. More realistic models are now being investigated. The diffusion coefficient and thermal diffusivities are taken to be one-tenth trapped particle and are consistent with confinement times produced using empirical scaling at ignition. Due to the presence of the divertor, the edge density is low. This enhances the presence of the trapped ion mode, particularly when the α energy cannot be lost by radiation (Z_{eff} = 1 assumed, also $n_{high\ Z}/n_e$ = 0) and therefore temperatures are kept relatively high (>2 keV). It is not yet known whether or not one can achieve these high densities and temperatures using conventional techniques (e.g., gas puffing, neutral beam injection, small radius start-up). Work is currently under way to investigate the after breakdown to ignition phase using a one-dimensional transport/two-dimensional MHD code. Figure 3.32 illustrates the output.

3.7 ELMO BUMPY TORUS REACTOR STUDY

N. A. Uckan* E. S. Bettis D. A. Ehst†
C. L. Hedrick, Jr. J. S. Herring† E. F. Jaeger
D. L. Kaplan† L. M. Lidsky† D. G. McAlees
D. B. Nelson L. W. Owen A. Pant†
R. E. Potok J. F. Roberts R. T. Santoro
D. A. Spong H. L. Watts H. T. Yeh

The EBTR study was initiated in early 1976. Its objective is the evaluation of the potential for achieving a commercial fusion reactor based on the EBT confinement concept, which is an

*Group Leader.

†Massachusetts Institute of Technology.

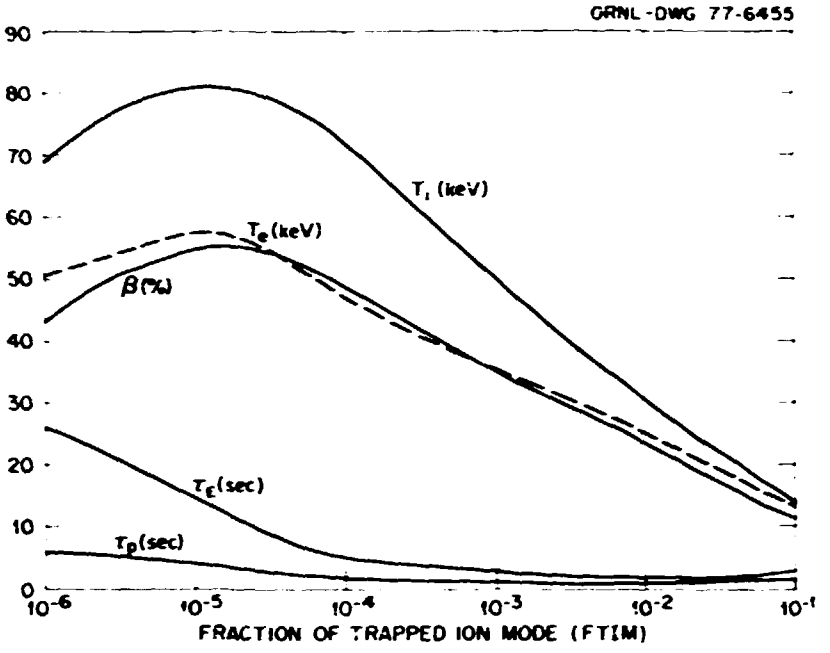

Fig. 3.30. Temperature, β, and confinement time variations for TMS vs fraction trapped ion mode (FTIM) for steady-state DT burn. R = 500 cm, a = 125 cm, b = 200 cm, B_T = 43.2 kg, I_p = 4.0 MA, n_e = 2 x 10^{14} cm^{-3}, DT fueling.

alternative to other mainline confinement systems. High β and steady-state operation distinguish an EBT system.

In 1976, the study was performed jointly with participants from MIT and Exxon Nuclear Co., Inc. A scoping and definitional study has been completed and is aimed at determining size, engineering physics, technology, and operating characteristics of a realizable plant. The results of the first year are in the form of a general feasibility study which includes such things as several plasma, blanket, and engineering options. In 1977, the effort will be devoted to continued and more detailed examination of specific subsystem options and the selection of a reference reactor.

A summary from ORNL/TM-5669, which describes the 1976 work on EBT, is given below.

3.7.1 The ELMO Bumpy Torus Reactor (EBTR) Reference Design[85]

The goal of the EBTR study is the evaluation of the EBT confinement concept as the basis for development of a commercial fusion power reactor. A multidisciplinary, self-consistent treatment of EBT reactor scaling and design has been completed and a reference design (EBTR-48) has been developed. This design, based on a realistic plasma model and relatively conservative engineering parameters (i.e., 1-MW/m^2 neutron wall loading and a 7.3-T maximum toroidal field), is a steady-state, ignited-mode system with high plasma power density and aspect ratio. The total thermal power of EBTR-48, exclusive of blanket multiplication, is 4000 MW; the design is based on a standard module, and the design power level for a particular plant is determined by the

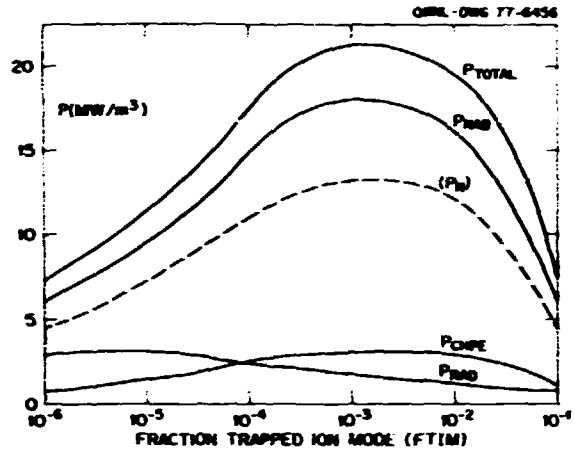

Fig. 3.31. Power variations for TNS vs fraction trapped ion mode (FTIM) for steady-state DT burn. P_{NAB} = neutron and blanket (4.8 MeV/n) power; P_N = neutron power; P_{CHPE} = charged particle escape power; P_{RAD} = bremsstrahlung and synchrotron radiation power, $P_{TOTAL} = P_{NAB} + P_{CHPE} + P_{RAD}$. Note: at FTIM = 10^{-6}, $n_\alpha/n_e = 0.23$, $n_p/n_e = 0.22$.

number of modules used. Several design variants have been investigated in detail to illustrate the effect of near-ter and advanced technologies and to illustrate the design freedom offered by devices with low field and high aspect ratio. The high aspect ratio simplifies many aspects of the design, most notably those associated with remote maintenance, accessibility, and repair. It appears that a commercially successful EBTR could be constructed with only slight advances in existing technology if the present understanding of the physics can be extrapolated to the reactor regime and does not differ markedly from the model developed for this study.

3.7.2 EBTR Reference Design Parameters[86]

A summary of the first reactor study based on the EBT confinement concept is presented here. An EBTR reference design has been developed and made consistent with the requirements of plasma engineering, plasma physics, magnetics, neutronics, and design engineering. Preliminary power balance calculations suggest that the toroidal plasma should be heated to ignition conditions using neutral beam injection and that the stabilizing relativistic electron rings should be sustained by microwaves. Figure 3.33 is a plan view of the system, and Table 3.6 shows the fundamental parameters for the system. The power output and neutron wall loading in the EBTR have been taken to be similar to the values assumed in low-β tokamak system studies in order to facilitate comparisons.

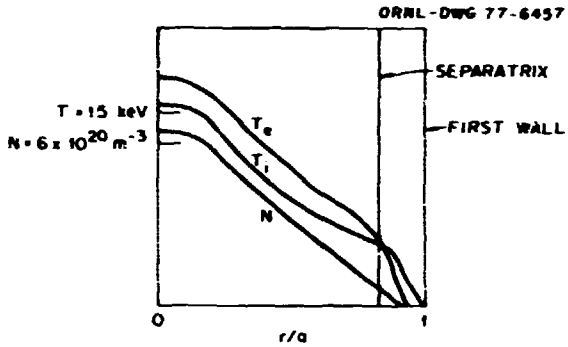

Fig. 3.32. Assuming spatially flat fueling, centrally peaked profiles of density and temperature are derived self-consistently.

The reactor is fueled by deuterium and tritium and operates in the ignited mode. It produces 4000 MW(th) exclusive of blanket multiplication. This is consistent with a source neutron wall loading of 1.1 MW/m^2 and a fusion power density of 3.4 MW/m^3. The confining magnetic field at the midplane is 2.5 T, which gives a β of 0.25. The magnetic field is produced by forty-eight 6-m-bore superconducting coils. The mirror ratio is 1.8 so that the field strength in a magnet throat is 4.5 T. The major radius of the device is 60 m, and the plasma radius is 1 m, so that the plasma aspect ratio is 60.

A final decision on the means of heating the EBTR plasma has not been made, but the frequency

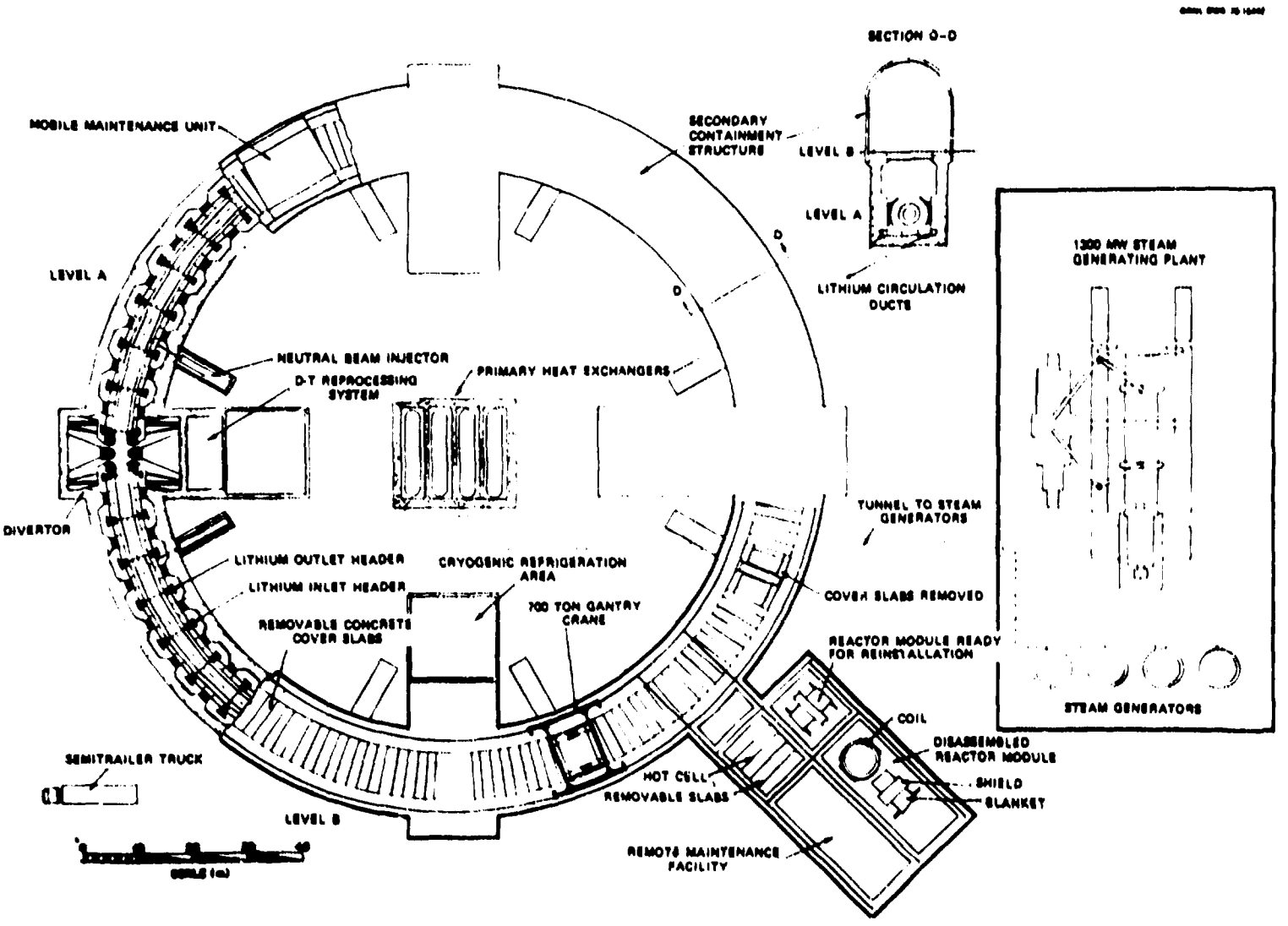

Fig. 3.33. EBTR plan view.

Table 3.6. EBTR reference parameters

	EBTR-48[a]	EBTR-24[b]
Plasma radius, a (m)	1.0	1.0
Aspect ratio, A	60	30
Major radius, R_o (m)	60	30
Mirror ratio, M	1.78	1.78
Ion temperature	15	15
Ion density, $N_i \times 10^{-20}$	1.2	1.25 2.13
Beta, β (%)	25	24 42
Magnetic field on axis, B_T (T)	2.5-4.5	2.5-4.5
Number of coils, N	48	24
Power, P_{th} (MW)	4000	1775 5300
Power density, P_{th}/V_p (MW/m^3)	3.37	3.0 9.0
Neutron wall loading, L_w (MW/m^2)	1.13	1 3
Cold zone, δ (m)	0.2	0.2
Blanket and shield thickness, t_{sb} (m)	1.75	1.75
Coil inner radius, r_c (m)	2.95	2.95
Current density, J_c (A/cm^2)	1500	1500
Coil radial thickness, t_c (m)	0.71	0.71
Coil half length, L/2 (m)	1.30	1.30

[a] Emphasis to date has been focused on EBTR-48.

[b] Alternative smaller size reactors with increased neutron wall loading are presently under study.

requirements, if microwaves are used, are compatible with those of components under development. A magnetic field of ~4.0-4.5 T exists near the magnet throat where the resonant frequency is ~120 GHz, suitable for background plasma heating. Because of the decreased density and field strength in the region of the stabilizing annuli, microwave frequencies less than this by a factor of two may be acceptable to sustain the annuli (~60 GHz, ~0.2 MW/sector) but use neutral beam injection (~150 keV, ~150-200 MW total) to heat the plasma to ignition.

The self-consistent relationships between the geometrical and power production parameters are obtained, and the major theoretical physics aspects of a reactor plasma are studied.

The high aspect ratio EBTR configuration affords several design options in the areas of materials, primary coolant, blanket and shield arrangements, superconducting magnets, and maintenance procedures. Two blanket and magnet shield concepts have been developed. The first blanket uses a stainless steel structure, natural lithium for breeding, and a eutectic nitrate salt for coolant. The associated shield materials are stainless steel and borated water. The shield is cooled by circulation of the borated water. The second design includes a Nb-1% Zr first wall, a stainless steel structure, and natural lithium both for breeding and as the coolant. Electromagnetic pumps are used to circulate the lithium. The magnet shield in this case is composed of concrete loaded with austenitic iron shot (40% by volume), and is cooled by CO_2.

Two superconducting magnet alternatives have been examined. In both cases the magnetic field and coil loading are nearly symmetrical. There is no need to use D- or oval-shaped coils to minimize bending moments, so coils with a circular shape are used. The first magnet system option has 48 NbTi superconducting magnets operated under pool-boiling conditions. The average current density in the windings is 1550 A/cm^2, which results in a peak field strength of 7.3 T in the winding and 4.5 T at the magnet throat. The second option has 48 NbTi-Nb_3Sn-composite superconducting coils cooled by supercritical helium under forced-flow conditions. The peak fields in the Nb_3Sn and NbTi windings are 10 T and 5.2 T respectively. The average current density in the high field windings is 2000 A/cm^2; in the lower field windings it is 4000 A/cm^2. Both options are fully stabilized and include current dump protection circuitry in case of a magnet failure.

Since impurity production and behavior in the reactor cannot reliably be predicted with certainty and since these will be critical to achieving ignition and steady-state operation, this area was treated conservatively. In one case a system with a toroidal divertor was studied. Energy and particle fluxes are accommodated by the divertor. Alternatively, a case was studied for which it was assumed that impurities are controlled, but the full energy flux from the plasma must be tolerated by the first wall. The latter system without divertor has significantly more stringent design criteria for the first wall thermal hydraulic system since it must handle 20% of the total thermal output power and ~8% of the neutron energy.

There are two structural arrangement options. In either, the torus is modular to facilitate assembly and remote maintenance, and both approaches allow standardization of the major EBTR components. That is, standard magnets and modules can be fabricated and assembled into toroidal configurations of different major radii. Forty-eight coils are needed when the major radius is 60 m. The minimum size device which is compatible with the standard module concept has a major radius of 30 m and requires 24 coils. The power output in the latter case is 1775 MW(th) for a neutron wall loading of 1 MW/m^2 and can be 5300 MW(th) if 3 MW/m^2 can be tolerated. Standardization has broad implications for commercialization.

Preliminary neutronics analyses of the blanket options discussed earlier have been carried out using the one-dimensional discrete

ordinates code ANISN to assess the nuclear performance of the two proposed blanket-shield designs. The ability of the blanket assemblies to recover the kinetic energy of the fusion neutrons and secondary gamma rays in the form of heat, to breed tritium, and to reduce the radiation which is incident on the toroidal magnet coils was used to evaluate the nuclear performance.

3.7.3 Principal Contributions

A multidisciplinary, self-consistent treatment of an EBTR includes participants and contributions from five basic disciplines: plasma engineering, plasma physics, magnetics, neutronics, and design engineering. The most important considerations in each of these areas are given below.

Plasma engineering

Plasma engineering uses the results from applied physics analyses to design fusion systems. The design process in EBTR is difficult because some of the critical aspects of the system and its behavior are not well understood at present. It is necessary to make plausible estimates of the parameters and to retain flexibility so the design can accommodate new results from theoretical and experimental programs. This approach generates design criteria which define the appropriate directions for engineering and technology development efforts.

The fundamental plasma and device characteristics, system economics, and technology considerations for a commercial reactor of about 4000 MW(th) have been studied. The neutron wall loading has been restricted to values near 1 MW/m^2. Although modest increases in wall loading improve system economics, loadings above 3 or 4 MW/m^2 will almost certainly be uneconomical due to reliability and pumping penalties.

The plasma size is determined by specifying power output, power density, and neutron wall loading. Plasma dynamics simulations, equilibrium, and drift orbit calculations show that a plasma radius of about 1 m is adequate to attain ignition, assuming neoclassical and/or classical scaling; however, no definitive basis for the size required for the reactor plasma has been developed. As in the other system studies, size and plasma parameters are determined self-consistently from theoretical models, but the ultimate values will be determined by experimental results which validate the assumptions used or provide the basis for changing them.

Plasma physics

The plasma physics areas which determine the EBTR operating characteristics are:
(1) particle orbits and their effects on efficient use of the plasma chamber volume;
(2) plasma stability and equilibrium; and
(3) scaling, transport, and modeling.

For a high-β, steady-state system, the plasma equilibrium, particle orbits, ambipolar electric field, and transport phenomena are closely coupled to one another, and an adequate treatment of any one requires consideration of the others. A self-consistent treatment of this coupled set of problems for a large-scale EBTR, while being vigorously pursued, is not yet available. Intermediate and/or partial answers have been used to proceed into the full self-consistent treatment.

Magnetics

The EBTR magnet system designs are determined by considerations of scaling, conductor design, coil design, cryogenics, and protection. Aside from the plasma constraints, the main goal is the design of coils which could be built with existing technology or with technology which is the immediate goal of existing development programs.

Independent of plasma physics considerations, the number of coils, mirror ratio, coil radius, and the reactor major radius can all be related by the geometry of the vacuum magnetic fields. Plasma physics considerations further relate the allowable mirror ratios to the aspect ratio, electron ring β, stable plasma volume, magnetic axis shift, and similar quantities.

An interesting possibility is that the magnets may be made modular and used in reactors of different sizes. As long as the ratio of

major radius to the number of coils is fixed, the field strengths produced by modular magnets of the same size are not sensitive to the size of the reactor.

Neutronics

Preliminary neutronics analyses for the EBTR designs have been carried out using the one-dimensional discrete ordinates code ANISN to assess the nuclear performance of proposed blanket-shield designs. The capability of the blanket assemblies to recover the kinetic energy of the fusion neutrons and secondary gamma rays in the form of heat, to breed tritium, and to reduce the radiation incident on the toroidal magnet coils was evaluated.

Design engineering

The EBT reactor study has considered the mechanical design of the following: (1) the first wall, (2) the nuclear blanket, (3) the radiation shield to protect the coils, (4) the superconducting coil support, and (5) the concrete enclosure and biological shield. The design was carried to sufficient detail to demonstrate fabrication and remote maintenance feasibility. The stresses will be within acceptable limits, and the required heat removal will be possible.

Because the EBTR has a high aspect ratio and relatively wide magnet spacing, it is possible to design one module that can be used in machines of various sizes. The module is composed of the first wall, blanket, shield, and coil. This concept of standardized modules is extremely favorable in the context of a fusion reactor economy.

3.7.4 Sensitivity of EBTR Burns to Catalyzed D-D

J. R. McNally, Jr. K. E. Rothe

A preliminary survey of steady-state T or ^{3}He-catalyzed D-D nuclear burns in EBTR-24 has revealed an extraordinary sensitivity to plasma density (for T-catalyzed burns they quench at $n_e = 10^{14}$ cm^{-3} but β exceeds 100% at $n_e = 1.25 \times 10^{14}$ cm^{-3}), indicating that an extremely tight burn control will have to be exercised. A ^{3}He-catalyzed burn at $n = 10^{14}$ cm^{-3} ran steady-state at $\beta \sim 62\%$; lower β operation may be feasible.

3.8 COMPUTING SUPPORT FOR FUSION ENERGY DIVISION

I. Burnett III R. D. Burris R. A. Dory*
J. E. Francis, Jr. K. A. French R. K. Gryder
C. E. Hammons C. O. Kemper R. W. Napier
D. R. Overbey C. E. Parker J. W. Reynolds
O. C. Yonts

Following the arrangement set up last year, computing support for FED is provided by three distinct entities.

1) Problem solving and programming are provided by the Computer Sciences Division (CSD) applied programming staff, under A. A. Brooks. Arrangements here are made primarily between the CSD staff and FED personnel who formulate the problems and watch over the solutions.
2) The User Service Center (USC) DECsystem-10 computer is administered by the USC Operations group, supervised by R. K. Gryder, and funded primarily directly from ERDA. The primary uses of the system are as a remote job entry terminal (RJET) into the MFECN and as a general purpose timesharing facility for small-scale, interactive computing jobs. Large-scale jobs, of course, are directed to the MFECN central computer at Lawrence Livermore Laboratory (LLL), to the extent available, and to the UCC-ND computing facility.
3) The data handling group is supported internally to provide coordination of the development of experimental data acquisition systems and (where appropriate) the interconnection or networking of the minicomputers to permit data transmission to the appropriate devices for analyses and storage of the data. The boundary between

*Group Leader.

this activity and the previous one is necessarily indistinct because the appropriate device often proves to be the PDP-10, the CDC 7600 at LLL, or the IBM 360's at ORNL. A Digital Equipment Corporation PDP-11/45 plays the part of central mode of the data network; interconnection of this machine to the USC DECsystem-10 represents a major factor in the work of 1976 and 1977.

3.8.1 User Service Center

I. Burnett III R. D. Burris R. A. Dory
K. A. French R. K. Gryder C. O. Kemper
C. E. Parker

The USC provides the research staff of FED with tools to use in solving problems. During the past year, these tools have been significantly improved.

A third RP04 disk drive was added to the USC PDP-10. The disk allocation is: one drive for active user file storage; one for swapping, systems storage infrequently accessed, on-line user file storage, and work space; and one drive for mounting user disks.

During 1976, an increase in memory size was obtained through complex procurement negotiations involving ERDA and LLL. An unusual temporary delivery of interim hardware resulted. The interim AMPEX ARM-10 memory was a constant source of trouble until an essential control band physically exploded. AMPEX sent a replacement which rectified all problems, and we had no more AMPEX memory failures. That unit, however, was returned to AMPEX when a new ARM-10 L memory was installed in accordance with the LLL arrangement. The new unit appears to be headed for an extended period of questionable performance similar to that experienced with the original ARM-10.

A communications front end consisting of a DN87 with 16 asynchronous lines and 1 synchronous line for interconnecting the USC with the PDP 11/45 has been purchased. Installation is scheduled for May 1977.

In the area of software, continuous effort has been devoted toward tuning the system for best performance. The 602 release of the TOPS-10 monitor had several problems which prevented it from working with the NMFECN configuration of hardware. These problems were fixed here at Oak Ridge, and the running monitor was shared with other sites in the NMFECN. The Virtual Memory option was purchased but was not used until January 1977 because of incompatibility with the NMFECN software. The 602A release was obtained in January 1977 and was installed with only minor problems. Its main virtue is improved handling of disk errors.

It is a pleasure to report that the NMFECN has attained a much higher level of reliability and functionality. The implementation of terminal traffic through the network has improved Oak Ridge's access to the point that we now can use the NMFECN A-machine productively. While credit for the development of this goes to NMFECN, a great deal of local effort was necessary in debugging and installing the software.

A major improvement in the usefulness of the USC has resulted from the acquisition and installation of the graphics software package, DISSPLA, on the Oak Ridge USC. DISSPLA integrated into the existing graphics software very nicely and has enabled many users to produce results in a fraction of the time which would have been required with any other graphics system.

Other software installed for specific projects or purposes includes APL, Setgo debugging compiler, and the IMSL library of mathematical and statistical routines. The DECUS library of programs is also available on a mountable disk.

Another development which will have major impact on the usefulness of the system is the Standardized Network Command Languages which has been developed for the USC. This consists of a command interpreter which will take a standard PDP-10 style command with the addition of a mode specification and initiate file transfer to either the NMFECN or the ORNL network. Full wild card specifications are possible, and any valid device or queue may be specified as the destination.

The adoption of a generalized communications philosophy has enabled considerable progress in the past year. File transfer between various computers in the two networks is possible, and the task of implementing additional capabilities has been well defined. The command may be entered in on any system in the network for which there exists a user interface. The file is then transmitted with the command through the network to the destination machine, and the destination specification is used to dispose of the file. The disposition may be storage on any valid device or submission into any valid queue including Batch input, printer output, graphical output, etc. User interfaces may be programmed for each computer in a form supported by that operating system. The specific implementation now in final debug stages is the NET command on the USC PDP-10.

The USC has had a very good uptime and reliability record due to the excellent maintenance service provided by Digital Equipment Corporation. The maintenance of terminals has been a major problem. We discovered that paper manufactured for the Texas Instruments terminals by one supplier caused excessive print head deterioration.

Operational procedures and an operator's guide are being formulated. Documentation is a continuing effort, and the assistance of a trained documentarian is being sought. A newsletter announcing improvements is planned.

A major new use of the USC promises to be the development of project managment tools and a comprehensive management information system (MIS). Several versions of PERT and CPM have been obtained and are being investigated. Graphics output is recognized as essential, but no adequate graphical output device is currently available within the Division. The MIS project has been initiated and currently has a procurement module operating. Plans include modules for cost accounting, cost projection, manpower allocation, and related project management tools. It is estimated that the new system will require a disk of its own for data storage and will use considerable core and CPU resources. In support of that project, an additional disk and data channel have been requested. The idea is that if we can separate the swapping to a dedicated channel, the MIS can operate without adverse impact on existing computing projects.

Work is under way to define a standard form of graphical data for interchange between various machines. It appears now that either (1) considerable inefficiency must be endured, or (2) different forms must be provided to take advantage of characteristics of specific types of devices. This is caused by the fundamental differences between vector and raster devices.

3.8.2 Experimental Data Handling Group

R. D. Burris J. E. Francis, Jr. C. E. Hammons
C. O. Kemper R. W. Napier D. R. Overbey
J. W. Reynolds O. C. Yonts

The primary activities during 1976 involved improvement of the ORMAK data handling system prior to the decommissioning of the experimental tokamak device to allow completion of the new ISX tokamak. The data handling system from ORMAK will be carried over, with improvements, so that a fully operational facility will be available when ISX is completed. New instrumentation added to the ORMAK/ISX system includes the Optical Multichannel Analyzer, a Multichannel Analyzer, and the Ultraviolet Spectrometer. Some data analyses have been transferred downstream to the PDP-11/45 coordinating computer.

An interim data handling system was set up for the Plasma Heating Department at the Princeton Large Torus beam test stand. Initially set up on a small PDP-11 supplied by Princeton Plasma Physics Laboratory for this purpose, this system has now been transferred over to an ORNL PDP-11. The group provided specifications and carried out the acquisition of the PDP-11, which will be used in the Medium Energy Beam Development Program.

A data acquisition system was provided for the Superconducting Magnet Development Program, using a PDP-12 previously assigned to the IMP (Injection into Microwave Plasma) experiment and later to ORMAK. Continued assistance was

provided for the design of a separate system for the Large Coil Project, although acquisition has so far been postponed because of programmatic and funding factors.

The EBT data handling system has undergone continuous improvement and refinement and now includes provision for transmitting data into the central computer network for analysis at the USC or X-10 PDP-10.

The group provides equipment backup support for the Division's USC DECsystem-10 and the PDP-11/45 coordinating computer, which permits communication from the data systems when required. Maintenance of the timesharing terminals is a major distraction and arrangements have been made to have the work done by the Y-12 Maintenance Division, but under strict supervision by the group.

Major improvements to the network communication software have been reported in the previous section of this report.

An important activity begun in 1976 is the monitoring of electrical interference from pulsed experiments in Building 9201-2. Variations in line voltages, ground potential, and radio frequency interference represent major impediments to making the Data Acquisition Systems and the USC DECsystem-10 reliable; in fact, there is a very real danger of doing serious harm to the computers or to the data. The problem is under study and a proposal for isolating the USC computers will be forthcoming.

---

1. C. L. Hedrick, R. A. Dory, E. G. Harris, E. F. Jaeger, D. G. McAlees, D. B. Nelson, L. W. Owen, D. A. Spong, and N. A. Uckan, "Transport and Scaling in the ELMO Bumpy Torus (EBT)," paper presented at the IAEA 6th International Conference on Plasma Physics and Controlled Nuclear Fusion Research, Berchtesgaden, Federal Republic of Germany, October 6-13, 1976.
2. E. F. Jaeger, D. A. Spong, C. L. Hedrick, and D. B. Batchelor, "One-Dimensional Fluid Theory for the ELMO Bumpy Torus," FED Plasma Theory Section Memo 75/76, Oak Ridge National Laboratory, Oak Ridge, Tennessee (June 1976).
3. N. H. Lazar and E. F. Jaeger, "Study of Neutral Hydrogen Spatial Distribution in EBT," Bull. Am. Phys. Soc. 21, 1070 (November 1976).
4. E. F. Jaeger, C. L. Hedrick, D. A. Spong, and D. B. Batchelor, "One-Dimensional Transport Simulation for the ELMO Bumpy Torus," Bull. Am. Phys. Soc. 21, 1069 (November 1976).
5. C. L. Hedrick and E. F. Jaeger, "Kinetic Transport Model for the ELMO Bumpy Torus," Bull. Am. Phys. Soc. 21, 1070 (November 1976).
6. D. A. Spong, E. G. Harris, and C. L. Hedrick, "Neoclassical Ion Transport Coefficients for the ELMO Bumpy Torus Device," Bull. Am. Phys. Soc. 21, 1069 (November 1976).
7. L. M. Kovrizhnykh, Zh. Eksp. Teor. Fiz. [Sov. Phys. – JETP] 29, 475 (1969).
8. D. G. McAlees et al., *The ELMO Bumpy Torus Reactor (EBTR) Reference Design*, ORNL/TM-5669, Oak Ridge National Laboratory, Oak Ridge, Tennessee (November 1976).
9. *Thermonuclear Division Annual Progress Report for Period Ending December 31, 1975*, ORNL-5154, Oak Ridge National Laboratory, Oak Ridge, Tennessee (June 1976).
10. W. A. Newcomb, Phys. Fluids 4, 391 (1961).
11. F. Freidberg, B. Marder, and H. Weitzner, Nucl. Fusion 14, 309 (1974).
12. J. F. Clarke and D. J. Sigmar, Phys. Rev. Lett. 38, 70 (1977).
13. R. A. Dory and Y-K. M. Peng, Nucl. Fusion 17(1), 21 (1977).
14. J. F. Clarke and D. G. McAlees, *High Beta Predemonstration Fusion Devices (Philosophy, Characteristics, and R&D Requirements)*, ORNL/TM-5692, Oak Ridge National Laboratory, Oak Ridge, Tennessee (November 1976).
15. Tokamak Experimental Section, "Confinement and Neutral Beam Injection Studies on ORMAK," IAEA-CN-35/A4-1, *Proc. 6th Intl. Conf. on Nucl. Fusion and Plasma Physics*, 1976.

16. L. Solov'ev, Zh. Eksp. Teor. Fiz. [Sov. Phys. — JETP] 26, 400 (1968).
17. D. Lortz and J. Nuhrenberg, Nucl. Fusion 13, 821 (1973).
18. H. Grad (New York University), private communication, 1976.
19. D. Stevens (New York University), private communication, 1976.
20. H. R. Hicks and J. W. Wooten, *MHD Linear Instability Code User's Manual*, ORNL/CSD/TM-3, Oak Ridge National Laboratory, Oak Ridge, Tennessee (June 1976).
21. Glenn Bateman and Y-K. M. Peng, "MHD Stability of Flux Conserving Tokamak Equilibria," submitted to Phys. Rev. Lett.
22. The modes with shorter wavelength appear at lower q-values and hence would not be observed experimentally.
23. B. V. Waddell, H. R. Hicks, G. L. Jahns, and J. D. Callen, "Comparison of Tearing Mode Theory with ORMAK Data," Bull. Am. Phys. Soc. 21, 1149 (1976).
24. B. V. Waddell, H. R. Hicks, G. L. Jahns, and J. D. Callen, "Interpretation of Tokamak Sawtooth Oscillations," to be issued as ORNL/TM-5712 and submitted to Phys. Rev. Lett.
25. Phys. Fluids 19, 667 (1976).
26. Phys. Fluids 19, 656 (1976).
27. Phys. Fluids 19, 1532 (1976).
28. ORNL/TM-5366, Oak Ridge National Laboratory, Oak Ridge, Tennessee (April 1976).
29. ORNL/TM-5630, Oak Ridge National Laboratory, Oak Ridge, Tennessee (November 1976).
30. ORNL/TM-5438, Oak Ridge National Laboratory, Oak Ridge, Tennessee (June 1976).
31. *Pulsed High β Plasmas*, ed. by D. E. Evans, Pergamon Press, Inc., Elmsford, New York, 1976.
32. ORNL/TM-5631, Oak Ridge National Laboratory, Oak Ridge, Tennessee (1977).
33. W. M. Tang, C. S. Liu, M. N. Rosenbluth, P. J. Catto, and J. D. Callen, Nucl. Fusion 16, 191 (1976).
34. R. D. Hazeltine, Plasma Phys. 15, 77 (1973).
35. W. I. van Rij, H. K. Meier, C. O. Beasley, Jr., and J. E. McCune, *Kinetic Equation for the Collisional Plasma Model*, ORNL/TM-5316, Oak Ridge National Laboratory, Oak Ridge, Tennessee (March 1976); to be published in Plasma Phys.
36. H. K. Meier, W. I. van Rij, C. O. Beasley, Jr., and J. E. McCune, *The Collisional Plasma Model: A Velocity-Space Orthogonal-Function Representation for the Distribution Function of a Collisional Plasma*, ORNL/TM-5314, Oak Ridge National Laboratory, Oak Ridge, Tennessee (March 1976); to be published in Plasma Phys.
37. C. O. Beasley, Jr., J. E. McCune, H. K. Meier, and W. I. van Rij, *Numerical Study of Drift-Kinetic Evolution of Collisional Plasmas in Tori*, ORNL/TM-5317, Oak Ridge National Laboratory, Oak Ridge, Tennessee (March 1976); to be published in Plasma Phys.
38. C. O. Beasley, Jr., H. K. Meier, W. I. van Rij, and J. E. McCune, ORNL/TM-5784, Oak Ridge National Laboratory, Oak Ridge, Tennessee (February 1977).
39. H. K. Meier, W. I. van Rij, and C. O. Beasley, Jr., *Techniques for Computing the Numerical Values of the Matrix Elements of the Collision Operator in the Collisional Plasma Model*, ORNL/TM-5315, Oak Ridge National Laboratory, Oak Ridge, Tennessee (March 1976).
40. K. T. Tsang and E. C. Crume, *Temperature Screening Effect in Two-Ion Species Pfirsch-Schlüter Transport*, ORNL/TM-5366, Oak Ridge National Laboratory, Oak Ridge, Tennessee (April 1976).
41. R. C. Isler (Oak Ridge National Laboratory), private communication, 1976.
42. ORNL/TM-5761, Oak Ridge National Laboratory, Oak Ridge, Tennessee (to be published).
43. M. N. Rosenbluth, R. D. Hazeltine, and F. L. Hinton, Phys. Fluids 15, 116 (1972).
44. K. T. Tsang and J. D. Callen, Phys. Fluids 19, 667 (1975).
45. M. E. Rose, *Elementary Theory of Angular Momentum*, John Wiley, New York, 1957.
46. C. E. Rathmann and J. Denavit, Bull. Am. Phys. Soc. 21(2), 1046 (1967).

47. R. H. Fowler, J. D. Callen, J. A. Rome, and J. Smith, FIFPC, *A Fast Ion Fokker-Planck Code*, ORNL/TM-5487, Oak Ridge National Laboratory, Oak Ridge, Tennessee (July 1976).

48. J. A. Rome, J. D. Callen, and J. F. Clarke, "Neutral Beam Injection into a Tokamak I: Fast-Ion Spatial Distribution for Tangential Injection," Nucl. Fusion 14, 141 (1974).

49. J. A. Rome, D. G. McAlees, J. D. Callen, and R. H. Fowler, "Particle Orbit Loss Regions and Their Effects on Neutral Injection Heating in Axisymmetric Tokamaks," Nucl. Fusion 16, 55 (1976).

50. J. A. Rome, "The Topology of Tokamak Orbits," p. 88 in *Thermonuclear Division Annual Report for Period Ending December 31, 1975*, ORNL-5154, Oak Ridge National Laboratory, Oak Ridge, Tennessee (June 1976).

51. T. G. Northrop, *The Adiabatic Motion of Charged Particles*, John Wiley, New York, 1963.

52. R. H. Fowler, D. J. Beckett, J. T. Hogan, and J. A. Rome, Bull. Am. Phys. Soc. 21, 1119 (1976).

53. R. Bulirsch and J. Stoer, Numer. Math. 8, 1 (1966).

54. Herbert J. Stone, SIAM J. Numer. Anal. 5, 530 (1968).

55. D. W. Peaceman and H. H. Rachford, Jr., J. Soc. Indust. Appl. Math. 3, 28 (1955).

56. D. L. Jassby and R. J. Goldston, *Enhanced Penetration of Neutral-Beam-Injected Ions by Vertically Asymmetric Toroidal Field Ripples*, MATT-1206, Princeton Plasma Physics Laboratory, Princeton, New Jersey (February 1976).

57. S. Matsuda, *Influence of the Minor Periodicity on Magnetic Island Formation in Tokamaks*, ORNL/TM-5114, Oak Ridge National Laboratory, Oak Ridge, Tennessee (February 1976).

58. *Thermonuclear Division Annual Progress Report for Period Ending December 31, 1975*, ORNL-5154, Oak Ridge National Laboratory, Oak Ridge, Tennessee (June 1976), p. 90.

59. K. T. Tsang and E. C. Crume, *Temperature Screening Effect in Two-Ion Species Pfirsch-Schlüter Transport*, ORNL/TM-5366, Oak Ridge National Laboratory, Oak Ridge, Tennessee (April 1976).

60. S. P. Hirschman, *Transport of a Multiple Ion Species Plasma in the Pfirsch-Schlüter Regime*, Princeton Plasma Physics Laboratory, Princeton, New Jersey (unpublished).

61. J. T. Hogan, R. H. Fowler, and R. A. Dory, Bull. Am. Phys. Soc. 17, 1055 (1972).

62. H. P. Furth and S. Yoshikawa, Phys. Fluids 13, 2593 (1970).

63. K. Bol, R. A. Ellis, H. Eubank, H. P. Furth, R. A. Jacobsen, L. C. Johnson, E. Mazzucato, W. Stodiek, and E. L. Tolnas, Phys. Rev. Lett. 29, 1495 (1972).

64. C. B. Tarter, *Radiative Losses from Impurity Ions*, UCRL-78119, Lawrence Livermore Laboratory, Livermore, California (1976).

65. R. Jensen and D. Post (Princeton Plasma Physics Laboratory), private communication, 1976.

66. J. T. Hogan, "Models for Impurity Production and Transport," paper presented at the International Symposium on Plasma Wall Interactions, Julich, Federal Republic of Germany, October 18-22, 1976.

67. R. H. Fowler, D. J. Beckett, J. T. Hogan, and J. A. Rome, "Neutral Beam Penetration in Large, Dense, Impure Tokamaks," Bull. Am. Phys. Soc. 21, 1119 (1976).

68. *Thermonuclear Division Annual Report for Period Ending December 31, 1975*, ORNL-5154, Oak Ridge National Laboratory, Oak Ridge, Tennessee (June 1976), p. 92.

69. D. G. McAlees, F. B. Marcus, S. E. Attenberger, R. N. Cherdack, G. D. Kerbel, J. R. McNally, Jr., Y-K. M. Peng, G. Schilling, D. J. Strickler, and N. A. Uckan, *Plasma Engineering in a Deuterium-Tritium Fueled Tokamak*, ORNL/TM-5573, Oak Ridge National Laboratory, Oak Ridge, Tennessee (1976).

70. F. B. Marcus and S. E. Attenberger, "Plasma Start-up in Tokamaks," Bull. Am. Phys. Soc. 21(9), 1125 (1976).

71. Summary of ORNL/TM-5438, Oak Ridge National Laboratory, Oak Ridge, Tennessee (June 1976).
72. T. E. Stringer, Nucl. Fusion 12, 689 (1972); J. W. Connor and R. J. Hastie, Nucl. Fusion 13, 221 (1973).
73. Summary of ORNL/TM-5573, Sect. 5.3, Oak Ridge National Laboratory, Oak Ridge, Tennessee (August 1976).
74. Abstract of ORNL/TM-5603, Oak Ridge National Laboratory, Oak Ridge, Tennessee (September 1976).
75. M. Roberts and E. S. Bettis, *Oak Ridge Tokamak Experimental Power Reactor Study Reference Design*, ORNL/TM-5042, Oak Ridge National Laboratory, Oak Ridge, Tennessee (November 1975).
76. F. B. Marcus, Y-K. M. Peng, R. A. Dory, and J. R. Moore, "A Magnetic Shielding System for the Tokamak Experimental Power Reactor," *Proc. 6th Symposium on Engineering Problems of Fusion Research*, p. 1110 (1975).
77. Y-K. M. Peng, F. B. Marcus, R. A. Dory, and J. R. Moore, "Magnetic Field Shielding in a Tokamak Experimental Power Reactor (EPR) – Concepts and Calculations," *Proc. 6th Symposium on Engineering Problems of Fusion Research*, p. 1114 (1975).
78. Y-K. M. Peng, R. A. Dory, D. B. Nelson, and R. O. Sayer, *MHD Stability of Axisymmetric Tokamak Equilibria*, ORNL/TM-5267, Oak Ridge National Laboratory, Oak Ridge, Tennessee (July 1976).
79. C. P. Ashworth (Pacific Gas & Electric), private communication, June 1976.
80. J. Rand McNally, Jr., "Advanced Fusion Fuels," in *Proc. 6th Symposium on Engineering Problems of Fusion Research*, p. 1012 (1975); J. Rand McNally, Jr. and R. D. Sharp, Bull. Am. Phys. Soc. 21, 1163 (1976).
81. J. Rand McNally, Jr., et al., Appl. Opt. 5, 187 (1966); Plasma Phys. 10, 903 (1968).
82. J. Rand McNally, Jr. and R. D. Sharp, Nucl. Fusion 16, 868 (1976).
83. S. E. Attenberger and D. G. McAlees, "Operation and Control of High Density Tokamak Reactors," paper presented at the 2nd ANS Topical Meeting, Richland, Washington, September 20-24, 1976.
84. S. E. Attenberger, F. B. Marcus, and D. G. McAlees, *Dynamics of Tokamak Plasma Experiments and Reactors*, ORNL/TM-5509, Oak Ridge National Laboratory, Oak Ridge, Tennessee (November 1976).
85. Abstract of ORNL/TM-5669, Oak Ridge National Laboratory, Oak Ridge, Tennessee (November 1976).
86. Summary of ORNL/TM-5669, Oak Ridge National Laboratory, Oak Ridge, Tennessee (November 1976).

BLANK PAGE

PART II. FUSION ENGINEERING

ABSTRACTS
(Chapters 4-8)

4. PLASMA HEATING AND FUELING SECTION

The Plasma Heating and Fueling Section has the responsibility for developing neutral beam injection heating and pellet fueling techniques, which are of vital importance to the ultimate success of tokamaks and other fusion machines. Progress in 1976 occurred on several fronts. The Medium Energy Systems Test Facility became operational in November with two Princeton Large Torus (PLT) beam line systems; it is expected that the first two beam lines will be installed on PLT in early 1977. The original conceptual design for the much larger Tokamak Fusion Test Reactor (TFTR) neutral beam systems was considerably revised, and an updated proposal was submitted to Princeton Plasma Physics Laboratory (PPPL) in December. The 150-keV Test Facility, a prototype for the TFTR systems, was completed in October and has been operated at 120 keV and 30 mA with a two-stage system. Operation at high currents will be possible after checkout of the power supply is complete. The 10-cm and 15-cm sources on the Oak Ridge Tokamak (ORMAK) operated throughout the year, and 500 kW of injected power was achieved. Frozen hydrogen pellets of 210-μm diam were also successfully injected into ORMAK.

These advances were made possible by a multifaceted program of experimental and theoretical studies. Better source plasma confinement was achieved through the addition of a multipole magnetic field around the arc chamber. The atomic ion fraction was increased by thermal predissociation of the hydrogen in a hot tungsten oven prior to arc discharge. Experiments with shaped apertures, insulating coating on the accelerating electrodes, application of precel, and optimization of decel voltages led to improved grid transparency and reduced beam divergence. These studies were supported by numerical and analytical calculations of beam trajectories and distributions. A new photodiode array diagnostic was developed to facilitate beam intensity distribution measurements. A solid hydrogen pellet extruder was constructed and successfully tested. A theoretical pellet ablation model was developed to predict the pellet velocity required for a given fractional penetration depth into a tokamak plasma, and various methods of attaining these velocities are under investigation.

In the future, work on the TFTR beam lines will continue as determined by the final decision of PPPL. Much higher power beams are envisioned for The Next Step (TNS). Ratings of 150 keV at 100 A with D^+ and 300 keV with D^- are projected. The two-stage source in the 150-keV test facility will be pushed to 150 keV at 50 A, and a charged fraction blowup scheme which magnetically confines free electrons in the neutralizer cell will be pursued. Neutral beam systems rated at 40 keV are being planned for ORMAK Upgrade and the Impurity Study Experiment (ISX). A new program to develop cryosorption pumping for high power neutral beam systems was instituted. Hydrogen pellet accelerators using the rotating arm and gas gun concepts will be developed.

5. MAGNETICS AND SUPERCONDUCTIVITY SECTION

The Magnetics and Superconductivity Section has the responsibility for developing superconducting magnet systems for tokamak fusion machines. This is being accomplished by carrying out those research and development needs which will provide the physics understanding and engineering data necessary to design, fabricate, and test large toroidal field (TF) and poloidal field (PF) coils. This information, in addition, supports the Large Coil Program (LCP).

A number of design projects have been performed, some in support of other programs and some of a continuing nature. These efforts support the goals and requirements for both the TF and PF magnet systems. Examples are the magnet designs for the EPR, Demo, EBTR, EBT-II,

and preliminary scoping for the TNS project. The principal effort was expended on the iteration of the EPR Reference Design. Three features of the original reference design – the honeycomb coil structure, the oval coil shape, and the forced-flow cooling of the conductor by supercritical helium – remain as key features of the TF coils. Considerable progress has been made in the theoretical understanding of forced-flow-cooled conductors, and optimized designs with maximum stability margin can be designed to meet specific applications. Experiments which will test the theory are in progress.

A number of projects consisting of laboratory scale experiments, primarily to characterize conductor, are performed as needed. A new pulsed parallel field apparatus has been constructed to determine the losses that a conductor exhibits in the environment characteristic of a tokamak TF conductor, i.e., pulsed longitudinal field superimposed on a transverse field. Both propagation and stability experiments were performed for pool-boiling conductors and compared with as complete a theory as can presently be constructed; it was concluded that transient heat transfer effects are very important. These experimental results and theoretical calculations, along with mechanical tests on a wide variety of conductors, resulted in new designs being prepared for 10-kA, 8-T conductors. At year's end two pool-boiling conductors had been ordered. Another series of small-scale experiments was directed at obtaining information relevant to the design of the PF coils. A pulse loss measurement system capable of providing the total energy loss and the loss voltage waveform for a pulsed (poloidal) coil was completed. The loss voltage was shown to be useful as a quench detection scheme for TF coils. Within the limits of the available power supplies, four small pulsed coils were tested and their losses characterized. All the pulse coil work to date is focused on obtaining an economical and reliable conductor design which will attain the maximum field at the anticipated field rate of change with acceptable losses in a scalable, stable magnet design.

Design, procurement, and fabrication development have been initiated for the Large Coil Segment (LCS) tests. A 3-m winding facility with some new refinements has been set up near the superconducting laboratories and the site selected for LCS, and an oval bobbin has been procured for practice winding. In addition some specialized instrumentation has been developed and a data acquisition system designed for use in the LCS tests.

The two disciplines that involve analytical calculations to a large extent, magnet protection and structural analysis, have contributed in a significant manner to all the large machine designs and the forthcoming large magnet tests. Examples of these developments are a new method for quench detection, complete analysis of the protection for a toroidal magnet system, development of a two-dimensional eddy current code applicable even if ferromagnetic material is present, and development of an analytical solution for the mechanical behavior of a transversely isotropic solenoid.

Procurement of facilities such as the large refrigerator, a liquid helium handling system, and power supplies for both the base research and development program and the LCP test facility has been initiated; these facilities will be procured and installed in the coming year.

6. THE NEXT STEP (TNS) PROGRAM

This ORNL study has resulted in an evaluated Reference Design that does satisfy the technical objectives set out for a Tokamak Experimental Power Reactor (EPR). Because of this design's large size, high cost, and poor extrapolation to a demonstration reactor, the basic physics and range of technical objectives have been reconsidered. This has led to an intermediate step and new design, The Next Step (TNS) after the Tokamak Fusion Test Reactor (TFTR), having a higher benefit/cost than EPR. The TNS Program, now in the early design phases, is focused on a device with smaller size and considerably higher power output than the EPR design. This device's improved performance is made possible by a

projection of operation at higher plasma density than that assumed for EPR. This more optimistic plasma performance projection is based on a re-examination of basic physics assumptions and of current plasma physics experiments; a focused experimental and theoretical effort will be required in the near future to validate this projection. With this improved performance, the TNS designs can be extrapolated to an economically viable fusion reactor.

Following the initial exploratory phase in which a succession of Reference Points was evolved and key engineering issues considered, a broad design space investigation was undertaken. The intent of this second phase of the TNS Program is to come to a well conceived and supported starting point for reference design studies by mid-FY 77. Achievement of this design basis is being pursued in an integrated program consisting of four main parts.

1) We are performing a trade study evaluation to support a plasma size and toroidal field coil technology decision.
2) We are specifically investigating the most critical scientific problems, especially impurity control and poloidal field winding locations, as well as determining the sensitivity of plasma performance to variations in key parameters.
3) We are evaluating R&D programs to identify available and required experimental support basis.
4) We will develop, early next year, a comprehensive construction schedule and plan to establish proper sequencing of design tasks, R&D tasks, and construction elements to support the orderly preparation for a TNS device.

The findings in each of these four areas will be synthesized into the reference design decision process.

7. FUSION REACTOR TECHNOLOGY PROGRAM

During the past year major accomplishments have been made in the following areas:

1) Materials compatibility studies, including corrosion studies of austenitic stainless steels in liquid lithium, corrosion studies of type 316 stainless steel in Li_2BeF_4, and the effects of helium impurities on super alloys.
2) The mechanical properties of structural materials in the first wall/blanket/shield system.
3) Radiation transport in fusion devices, including the spatial variation of neutron damage phenomena in an Li (D, n) facility, neutronics calculations for the Tokamak Fusion Test Reactor (TFTR) neutral beam line, and the development of an evaluated nuclear data file for fusion applications.
4) Radiation effects in blanket structural materials, including swelling and microstructural changes in type 316 stainless steel irradiated under simulated fusion conditions, the use of the Oak Ridge Research Reactor (ORR) in simulating fusion reactor irradiations, development of fatigue testing capabilities, and evaluation of nickel alloy response to simulated fusion reactor irradiations.
5) Surface studies including wall conditioning studies for the Oak Ridge Tokamak (ORMAK) and Impurity Study Experiment (ISX), hydrogen profiling for surface characterization, sputtering calculations using the discrete ordinates method, and hydrogen recycle.
6) System studies aimed at developing a plan for demonstrating, in this century, the commercial feasibility of fusion power based on the tokamak concept.
7) Tritium studies, including vacuum pumping studies, tritium sorption studies, and tritium chemistry studies.

8. LARGE COIL PROGRAM

The Large Coil Program (LCP) was organized early in 1976 to accomplish the national fusion program objectives of fabricating, testing, and demonstrating the reliable operation of superconducting coils large enough to prove the design

principles, materials, and fabrication techniques proposed for the toroidal magnet of a tokamak fusion reactor. A plan for accomplishing the LCP objectives has been formulated and documented (ORNL/TM-5824).

Based on a set of coil criteria extracted from the preliminary Experimental Power Reactor (EPR) Conceptual Studies done at Argonne National Laboratory, General Atomic, and Oak Ridge National Laboratory, contracts were made with suitable industrial concerns to produce conceptual designs of EPR toroidal field coils at two field levels. There was considerable difference in the design concepts of the three contractors, both in the high field and low field cases, reinforcing the ORNL opinion that no single concept can be shown to be clearly superior at the present time. The contractors did independently conclude that 12 T was the upper practicable limit and that testing of approximately half-size coils would be necessary to prove their design concepts. This size criterion for test coils agreed with ORNL work done earlier in the year.

During the year the long-range focus of the LCP shifted from the EPR to The Next Step (TNS), which probably will require an array of superconducting coils with bore approximately 5 × 7 m, and capable of producing a peak field in the winding of 8–12 T. The test coil size was therefore set at 2.5 × 3.5 m bore. Test facility, coil winding section, and current density were fixed to duplicate, approximate, or simulate all essential operating conditions of TNS. A detailed comparison of the benefits, costs, and risks of several possible test arrangements resulted in the choice of an 8-T compact torus of six coils with identical performance characteristics (but of three different design concepts) in which it is possible to fully test any coil even if all others perform only to 80% of their design currents. The LCP vacuum tank and facility structure are being designed such that they can be suitably modified for the later testing of 12-T coils.

4. PLASMA HEATING AND FUELING SECTION

L. D. Stewart, Section Head
G. Schilling, Associate Section Head

M. B. Baer[1]
G. C. Barber
C. W. Blue
E. H. Bryant[1]
D. D. Cannon[1]
J. S. Culver[1]
W. K. Dagenhart
R. C. Davis
W. H. Fletcher[1]
C. A. Foster
W. L. Gardner
D. H. Grey[1]
L. R. Grisham[2]
H. H. Haselton
R. E. Hill[1]
R. L. Johnson[1]
J. Kim
M. H. Kunselman[1]
G. Leichsenring[1]
K. Leung[3]
T. Mann[1]
M. Menon
S. L. Milora
N. S. Ponte
R. E. Potter
P. M. Ryan
J. D. Schaeffer[1]
D. E. Schechter
S. W. Schwenterly
D. O. Sparks
W. L. Stirling
P. B. Thompson[1]
C. C. Tsai
J. H. Whealton
J. C. Whitson[4]
R. E. Wright
W. L. Wright[1]

4.1 PLASMA SOURCE DEVELOPMENT PROGRAM

4.1.1 Introduction

A prime goal in this program is to develop a plasma source which fulfills the requirements of high power (MW) neutral beam injectors. These injectors are being developed for plasma heating of future fusion devices such as the Princeton Large Torus (PLT) and the Poloidal Divertor Experiment (PDX) at Princeton Plasma Physics Laboratory (PPPL) and the Oak Ridge Tokamak (ORMAK) Upgrade and Impurity Study Experiment (ISX) at ORNL. The basic requirement of the plasma source developed is the capability of providing positive ions for forming an ion beam of 60 A/40 keV. The desirable properties of such a plasma source (Table 4.1) are the production of a quiescent, uniform, and dense plasma; high gas and arc efficiency; operation reliability; and ion species selectivity. The duoPIGatron ion source[1-5] developed at ORNL fulfills most of these requirements and is a prime candidate for such injectors. The duoPIGatron has been scaled to larger versions with sources of 20 to 25-cm-grid diam now operating; initial operation of a 20-cm version has produced 60 A of hydrogen at 33 keV.

Another effort in this program is to develop alternative plasma sources for high power neutral beam injectors. A magnetic multipole plasma source developed for plasma confinement study by Mackenzie and his associates[6,7] can produce a large volume of uniform and quiescent plasma in argon with a density higher than 10^{12} cm^{-3}. To be useful as an ion source for neutral beam injectors, such a device must operate with hydrogen or deuterium and must be capable of delivering an ion beam of several tens of amperes. An experimental study to develop such a source for ion extraction has been undertaken.

4.1.2 Modified DuoPIGatron Ion Source

The scaled up duoPIGatron (Fig. 4.1), with a 20 to 25-cm-grid diam, uses 12-24 columns of permanent magnets to form a multipole line cusp field. As described elsewhere,[5] this multipole line cusp field is capable of confining ionizing

1. Engineering Division.
2. Princeton Plasma Physics Laboratory.
3. Consultant, Madison College, Harrisonburg, Virginia.
4. Computer Sciences Division.

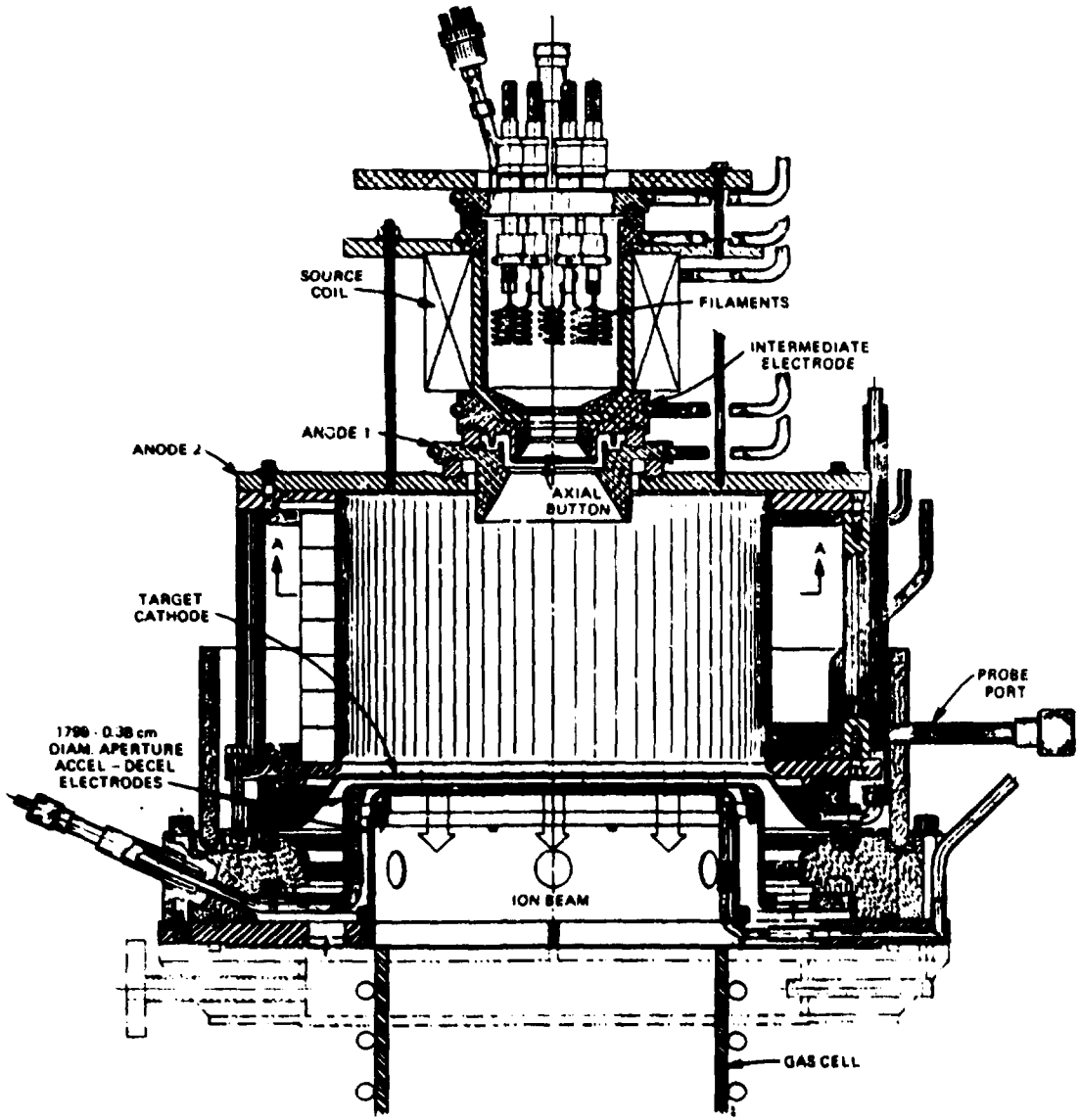

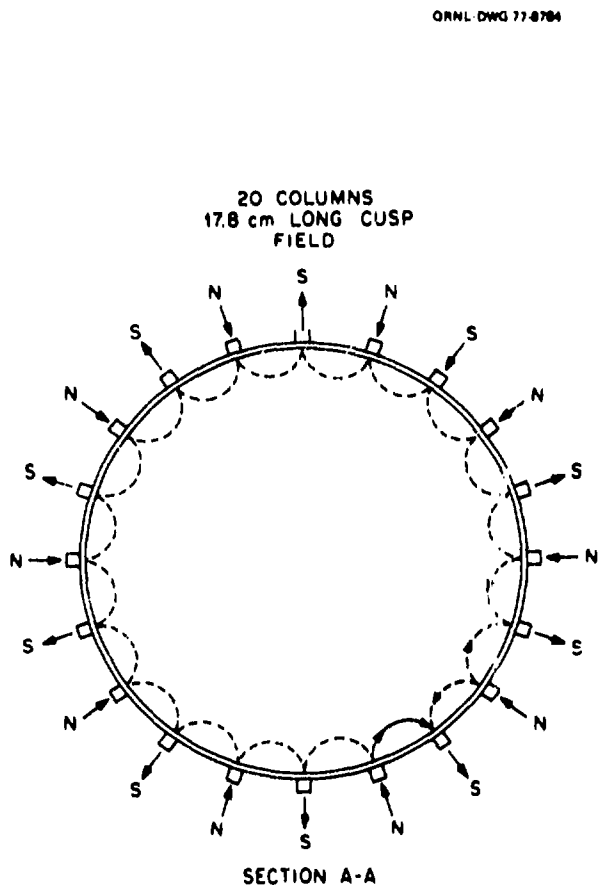

Fig. 4.1. Modified DuoPIGatron for PLT injectors.

Table 4.1. Desirable properties of a good plasma source

High plasma density	$\geq 2 \times 10^{12}$ cm^{-3}
Low nonuniformity	$\leq \pm 10\%$ over grid diam
Low noise level	$\leq 10\%$
Long pulse operation	≥ 0.5 sec
High gas efficiency	$\geq 50\%$
High arc efficiency	
Good source reliability	
Ion species selectivity	

electrons and to a lesser degree the plasma generated in the PIG region of the source. In the 20-cm-grid-diam source, which has a 30-cm-diam arc chamber, the created PIG plasma is characterized by spatial density variations within ±5% over a 23-cm diam at a density of about 2×10^{12} cm^{-3}. The source delivers a hydrogen ion beam of 60 A at 33 keV; the corresponding arc current is about 900 A and arc voltage about 90 V. The arc efficiency is good — 1.35 kW per ampere of beam. In the present source, the applied source magnetic field is inhomogeneous and axial, but the multipole line cusp field is transverse in the center plane of the magnet columns and is axial with alternate polarities at the ends of the columns. Consequently, there are loss areas (half of the column number) on the wall of the arc chamber (anode No. 2) adjacent to the intermediate electrode. This fact is consistent with the optimal column number of 20 found for this source. At such a condition the spatial uniformity is best, as shown in Fig. 4.2. Moreover, the plasma uniformity is usually found to be improved as the arc current is increased (Fig. 4.3). These two features can be explained by the diamagnetism of the dense plasma near the plasma electrode (or target cathode). That is, the PIG plasma expands close to the $\beta = 1$ surface. We also observed that the arc efficiency can be improved substantially by shortening the first anode, thus reducing the plasma loss to the anode surface and thereby improving the plasma uniformity. Figure 4.4 shows the plasma density variation with the dimension and configuration of anode No. 1 in the duoPIGatron.

4.1.3 Magnetic Multipole Plasma Source

This source (Fig. 4.5) has 12 magnet columns polarized radially with alternate polarities to form a continuous line cusp field on the anode surface. The hot cathode consists of several rows of tungsten filaments located within a 6-cm radius. For a typical case, the cathode is made of 72 tungsten filaments, 0.0127-cm diam and 7.5-cm length. The heating current for each filament is 2 A, the anode chamber has a 25-cm ID and is 36 cm long, and the plasma electrode is connected to the negative terminal of the hot cathode power supply. This source is capable of producing a noise-free, uniform, and dense plasma (Fig. 4.6). The arc efficiency is relatively high, at 1 kW arc power per ampere of beam current. These properties are desirable for neutral beam injector application. However, the use of tungsten filaments may cause some undesirable problems such as high heating power, short filament lifetime, and tungsten vapor-associated arc breakdown across the insulator surface in the source. Further study will be pursued continuously to develop this source for high power neutral beam injectors.

4.1.4 Enhancement of H^+ Fraction in Hydrogen Beams

Hydrogen ion sources typically produce multimomentum beams consisting of atomic ions

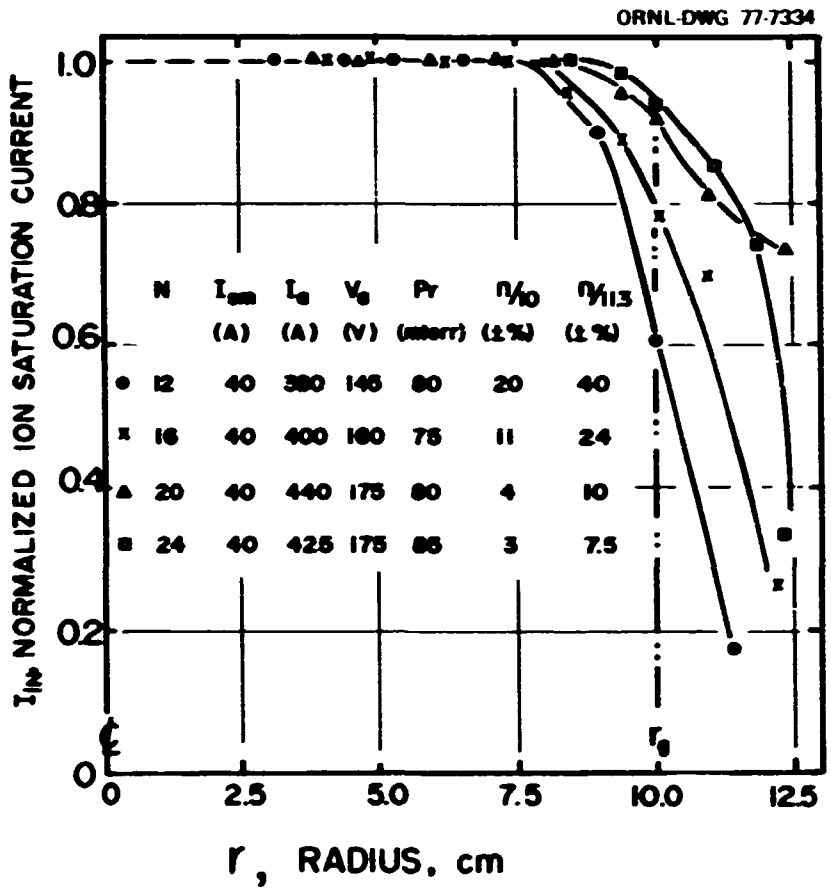

Fig. 4.2. Variations of plasma uniformity with number of magnet columns.

(H^+) and molecular ions (H_2^+ and H_3^+). Molecular ions passing through a charge-exchange gas cell break up into atoms with one-half (from H_2^+) or one-third (from H_3^+) of their accelerated energy. These lower energy components do not penetrate deeply into a plasma and may be of little use (or be unwanted) if the heating of the outside plasma yields an adverse effect. It is therefore desirable to enhance the atomic ion fraction in an ion source.

We have achieved a substantial enhancement of the H^+ fraction in a duoPIGatron by means of the thermal predissociation method.[8] The hydrogen gas is predissociated in a hot tungsten oven prior to arc discharge, while the recombination rate inside the ion source is simultaneously minimized by a hot wall environment. An increase in the H^+ fraction from 0.5 to 0.7 at the position of a detector has been obtained in a preliminary experiment with a single beamlet at an arc current of 40 A and a beam energy of 30 keV. This experiment is continuing with a full-scale source in pursuit of an expected H^+ fraction of 0.9.

4.2 ION ACCELERATION

4.2.1 Introduction

In addition to the plasma source, the ion accelerator is one of the crucial elements of MW neutral beam injectors. At ORNL the conventional ion beam is formed by hundreds to thousands of individual beamlets. The

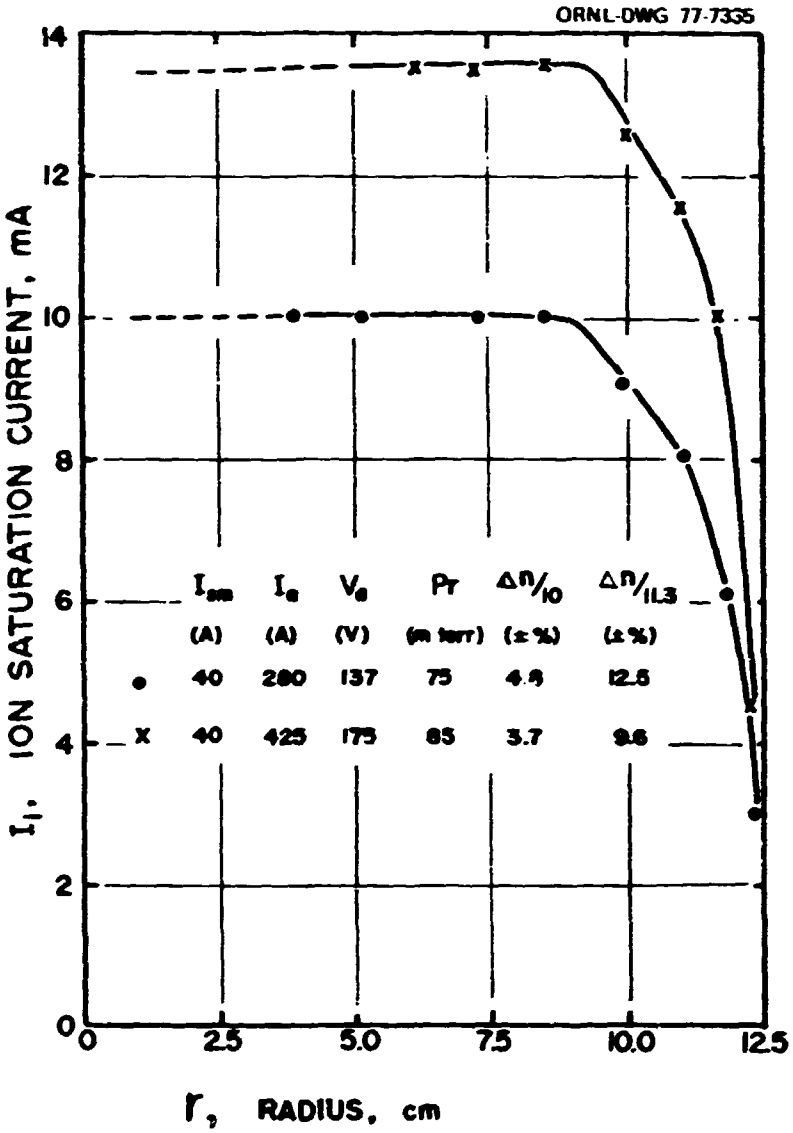

Fig. 4.3. Uniformity improvement with arc current in a 20-cm duoPIGatron ion source. Chamber diameter = 30 cm; grid diameter = 20 cm.

transmission efficiency of the neutral beam is determined by the optics of its original ion beam; the ion beam optics determines the divergence of each beamlet,[9] and each beamlet is steered to a common focal point. In the conventional accel-decel ion accelerator, the beam divergence of each beamlet is influenced essentially by the electrostatic lens effect (due to the configuration and dimensions of the aperture in the electrodes of the accelerator), particularly the plasma electrode (or target cathode) and the plasma properties of the source and the neutralizer plasmas. To examine the importance of the aperture shape on the beam divergence, a program including computer simulation and experimental study for a single beamlet has been initiated. One of the initial objectives of this program is to increase the percentage of

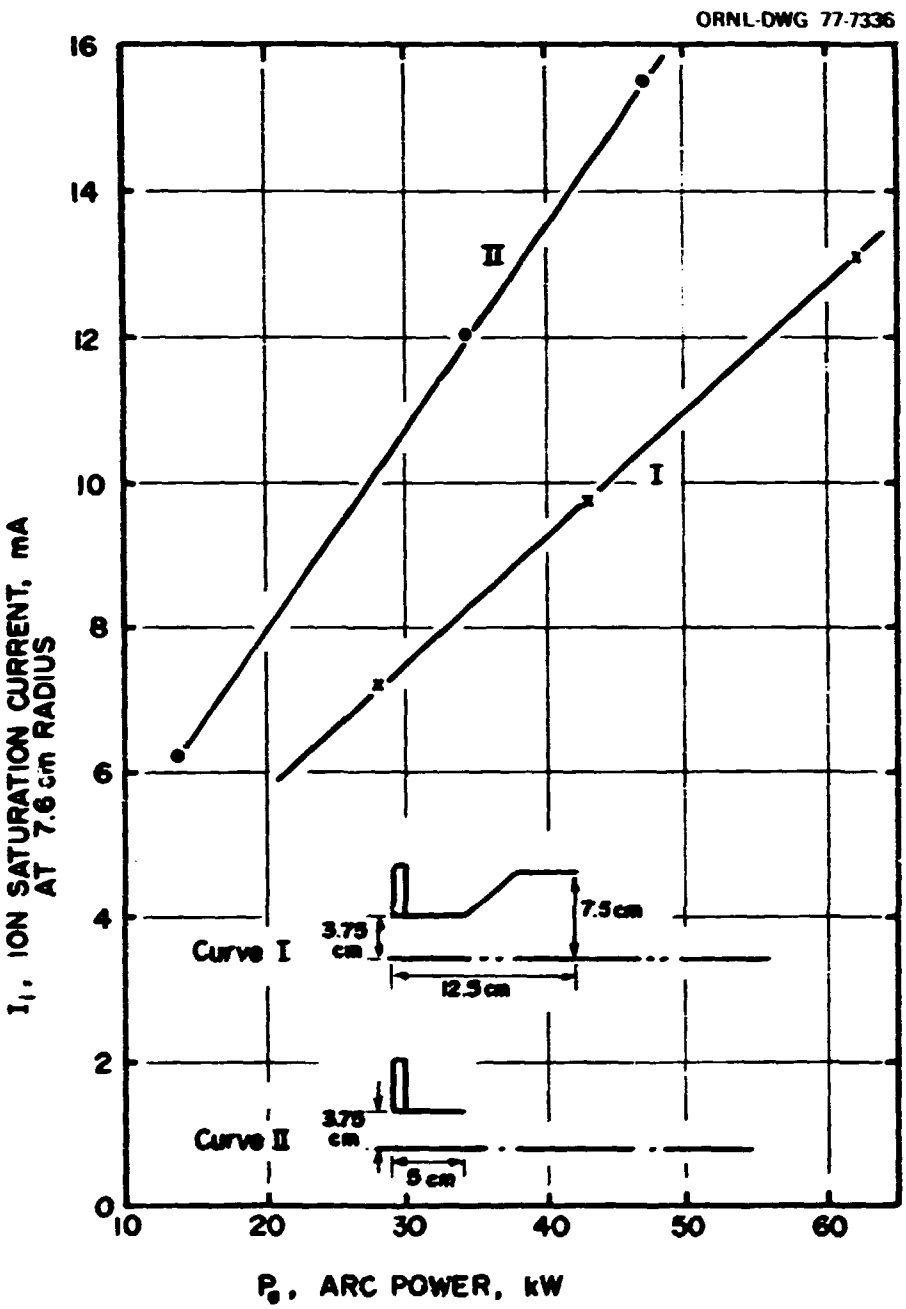

Fig. 4.4. Variations of ion saturation current with arc power for two types of anode 1.

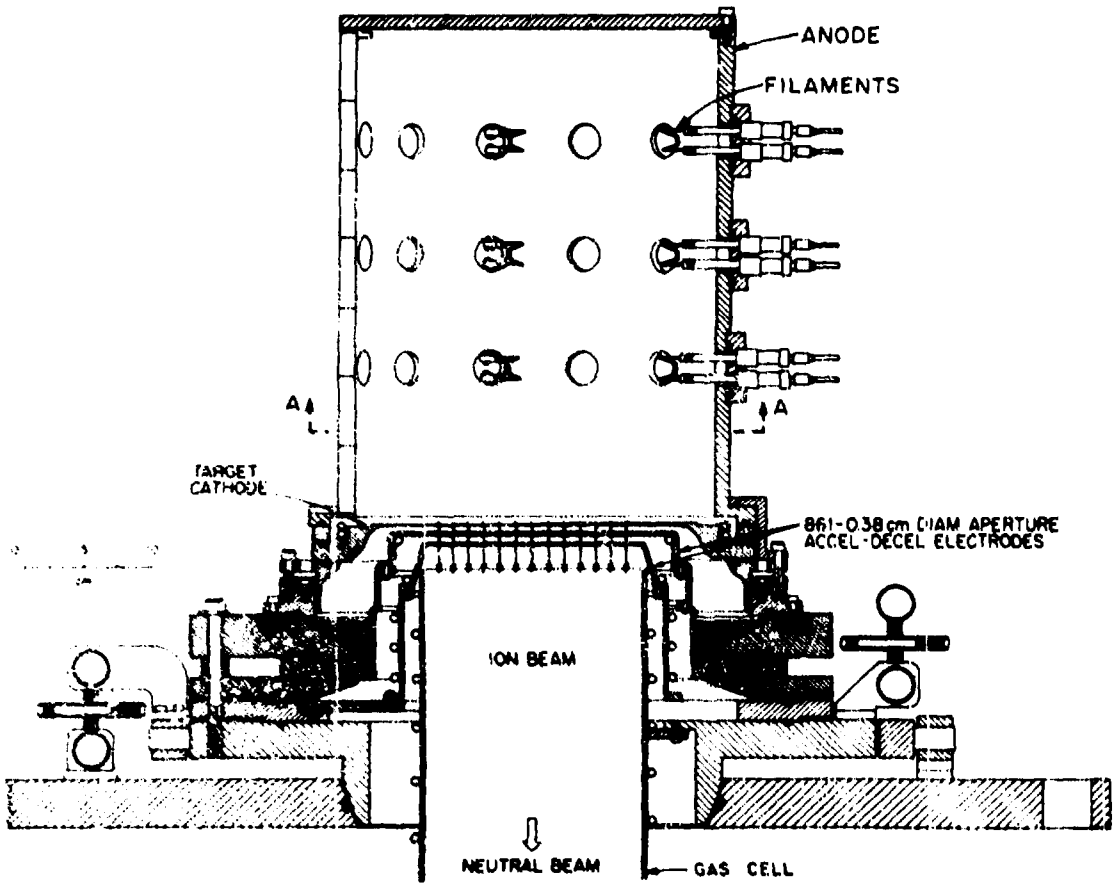

ORNL-DWG 77-8773

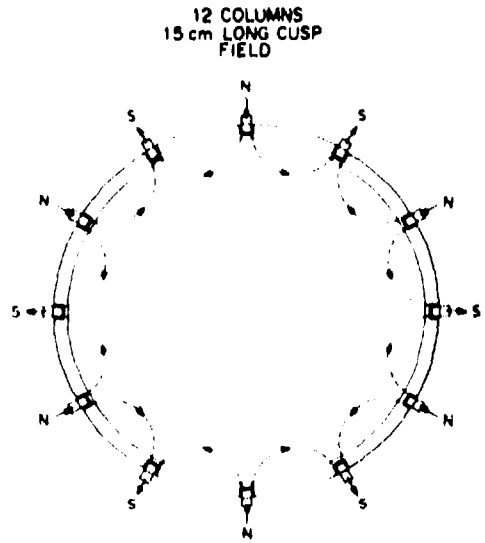

Fig. 4.5. Multipole plasma source.

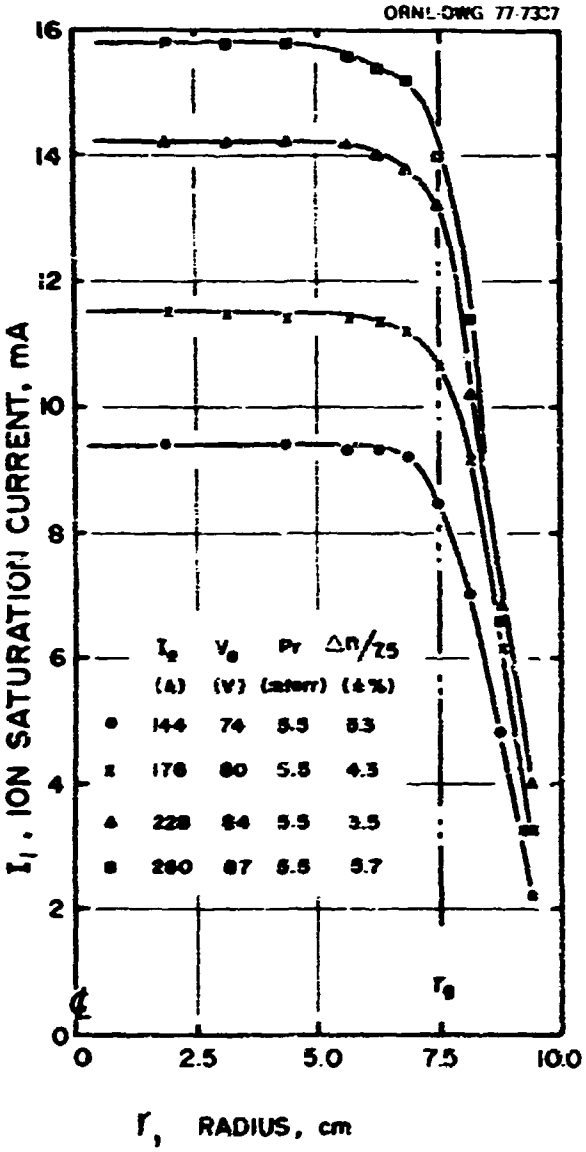

Fig. 4.6. Typical density profile of the plasma created in a magnetic multipole source.

available ions in the source plasma to be formed into the ion beam. In addition to the shaped aperture plasma electrode, we undertook a study of the effect of a thin insulator coating on the side of the plasma electrode facing the source plasma. Also, the effect of the decel voltage on the beam optics has been studied; as a result of these studies, a two-electrode ion beam formation system has been demonstrated. In addition, the effect of thermal deformation of the plasma electrode on beam optics during the beam pulse has been studied.

4.2.2 Shaped Aperture Plasma Electrode

Many conventional ion sources employ multi-aperture cylindrical bore electrodes. These electrodes introduce significant aberrations into the accelerating fields not entirely cancelled by the beam space charge; the residual aberrations in turn lead to degradation of the optical properties. We have carried out an experimental and theoretical study to explore two possible techniques to lessen the significance of the residual aberrations.

The first approach was to shape the aperture in the plasma grid to lessen the magnitude of the residual aberrations. We studied a single beamlet using an aperture in the plasma grid that was any of several shapes, and with conventional cylindrical (3.8-mm-diam) apertures in the extraction and ground grids. A spacing of 5.7 mm was used in the extraction gap and 2.0 mm in the decel gap. All three grids were the standard 1.5 mm in thickness. The shapes studied experimentally are shown in Fig. 4.7. Beamlet profiles were measured with a Faraday cup; as a consequence they are measures of the divergence of the unneutralized portion of the beamlet. However, it has been found that the profile is generally in good agreement with the power profile except that the power profile sometimes has a slightly smaller θ_{HWHM} than does the charge profile.[10] All shapes were found to yield approximately Gaussian beamlet profiles at optimum divergence.

Table 4.2 shows the minimum θ_{HWHM} obtained with the different apertures at various accel drain currents. The accel voltage in each case is that which was found to yield the optimum divergence angle at that drain current, and it is apparent that there are significant differences in the minimum divergence angles obtained. For instance, at V_{accel} = 26.8 kV, aperture type 8 produces a θ_{HWHM} which is only 0.58 that of type 1, the conventional cylindrical

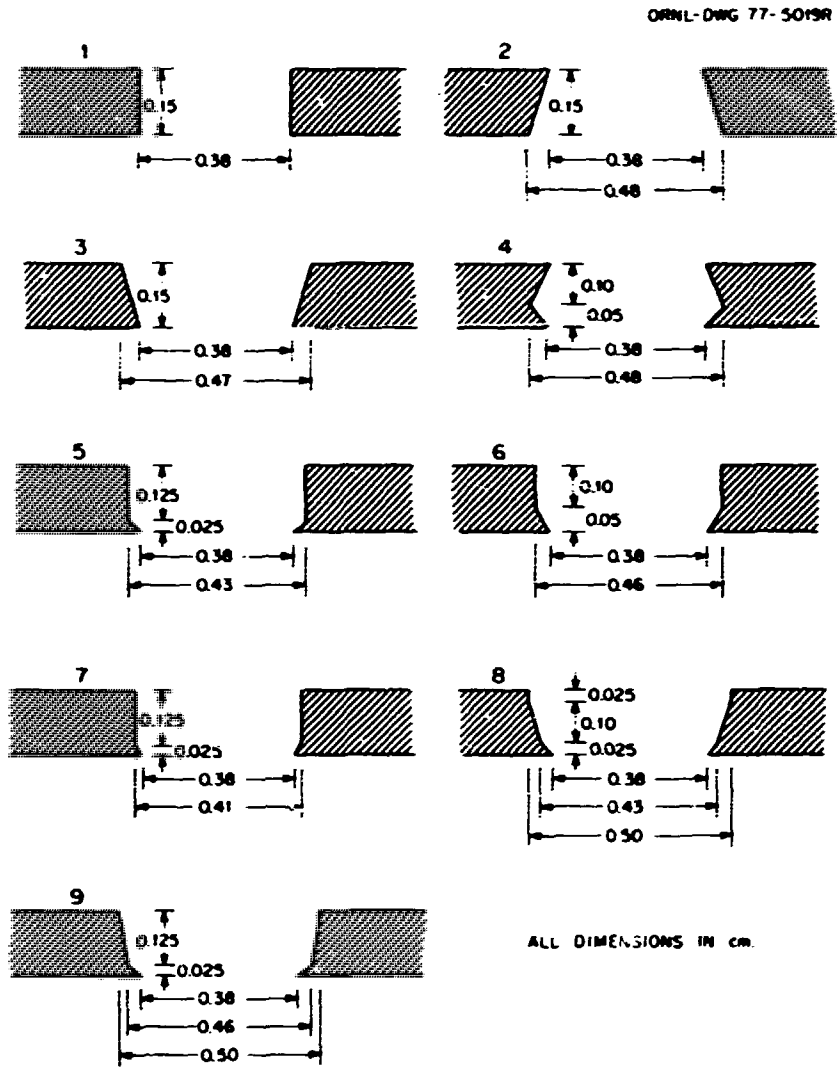

Fig. 4.7. Plasma grid shapes studied.

aperture. We note that aperture types 3, 5, 6, 7, 8, and 9 all yield significantly smaller optimum divergence angles than does type 1. These shapes share the characteristic of opening away from the source plasma. Neither shape 2, which opens toward the plasma, nor shape 4, which is reentrant, leads to smaller divergence than that obtained with the cylindrical aperture. The smallest divergence angles result with shapes 8 and 9, which are similar to the Pierce geometry used in electron optics.

A solution to the Poisson-Vlasov equation (as described in Sect. 4.6) was obtained for ions extracted through eight different shapes, shown in Fig. 4.8. Ion divergence angles ($\bar{\theta}$) and actual transparency (F), scaled by the geometric transparency, are shown in Fig. 4.8 as a function of source plasma density on a suitable scale, P/P_0 (the ratio of the actual perveance to the modified Child-Langmuir perveance), for each of the eight shapes. Results are that the divergence angles are about the same for shapes 1, B, 2B, and 4B, but the actual transparency progressively increases. Shapes 1, C, 2C, 3C, and 4C show progressively smaller beam divergence angles, larger actual transparency, and smaller optimum plasma

Table 4.2. Optimized single beamlet optics

Aperture type	I_{accel} (mA)	V_{accel} (kV)	HWHM angle (deg)
1	11	14.2	1.19
	14	16.9	1.17
	21	22.3	1.06
	28	26.8	0.99
2	11	13.8	1.45
	14	17.2	1.32
	21	20.8	1.12
	28	23.0	1.09
	34	26.6	1.09
3	11	14.8	0.79
	14	17.5	0.79
	21	22.4	0.78
	28	26.6	0.75
4	11	13.6	1.27
	14	17.8	1.23
	21	22.4	1.24
	28	26.6	1.14
5	11	15.5	0.85
	14	18.2	0.78
	21	22.3	0.75
	28	27.7	0.72
6	11	14.2	0.92
	14	16.4	0.92
	21	21.7	0.84
	28	25.4	0.79
7	11	12.7	0.87
	14	15.1	0.84
	21	20.2	0.77
	28	24.5	0.74
8	11	11.1	0.80
	14	13.6	0.73
	21	18.5	0.69
	28	23.5	0.61
	38	26.8	0.57
12	11	12.2	0.74
	14	13.9	0.71
	22	18.7	0.67
	28	23.2	0.63
	36	27.3	0.62

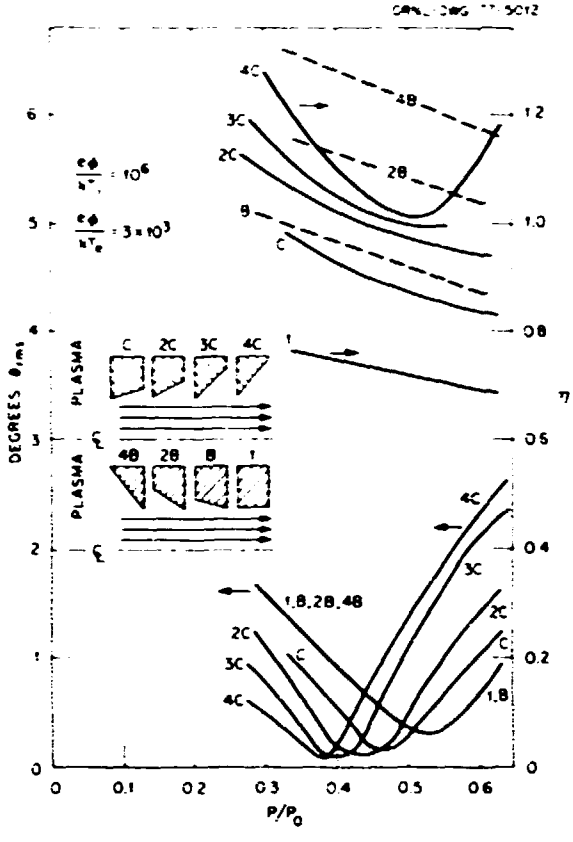

Fig. 4.8. Effect of plasma grid shape on ion optics and transmission.

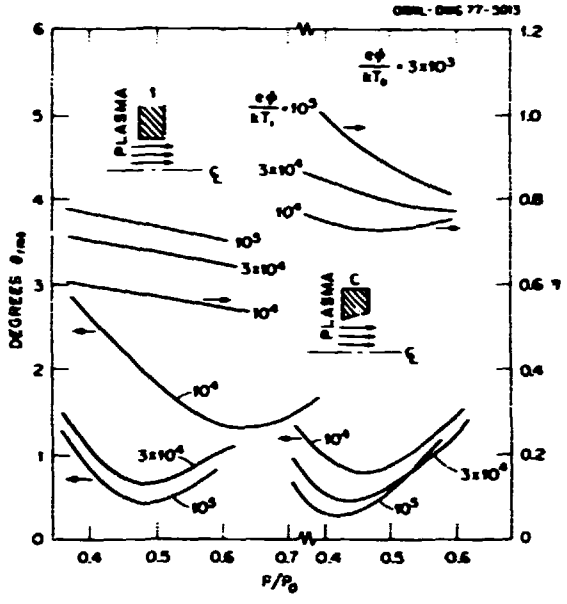

Fig. 4.9. Effect of ion temperature and plasma grid shape on ion optics and transmission.

density. In Fig. 4.9, ion divergence and transparency for two different shapes, 1 and C, are shown as functions of relative ion temperature as well as of relative perveance. The improvement of shape C does not diminish for higher relative ion temperature. Source emittance limited (EL) beam divergence angles are also shown in Fig. 4.9 for the three relative ion temperatures considered.

4.2.3 Insulator Coated Plasma Electrode

The second approach sought to maintain the high grid transparency obtainable with cylindrical apertures, but to lessen the deleterious effects of the attendant residual aberrations by accelerating the ions before they enter the aperture. Such a technique was suggested by the results of a numerical solution to the Poisson-Vlasov equation (Sect. 4.6). A thin layer (10 mils) of aluminum oxide was deposited by a plasma spray technique on the side of the extraction grid facing the source plasma. A ring insulator was installed to isolate the plasma grid from the rest of the source, and a power supply was connected across it to bias the grid negative with respect to the rest of the source. Because the plasma potential stays close to that of the anode, the plasma tends to assume a potential differing from that of the plasma grid by the applied voltage (which we will call the precel voltage) plus the usual sheath drop of 20-30 V. Consequently, an ion crossing the thin insulator encounters a sudden strong field which gives it a velocity parallel to the axis of extraction which is large compared to its value without a precel potential. The ions near the edge of the aperture thus spend less time in the aberrant regions of the field. By using an insulator with precel, we have observed a large decrease in beam divergence (see Table 4.3). With a larger accel gap, the change in the divergence was even more pronounced.

Table 4.3. Summary comparison of optics of all apertures at $V_{accel} \sim 14$ kV, $I_{accel} \sim 11$ mA

Aperture type	HWHM angle (deg)
1	1.19
2	1.45
3	0.79
4	1.27
5	0.85
6	0.92
7	0.87
8	0.80
12	0.74
Coated 3 (precel 330)	0.61
Coated 1 (precel 320)	0.53

With an accel gap of 11.43 mm and an accel voltage of 28.5 kV, an optimum θ_{HWHM} of 1.09° was obtained. With the addition of a precel voltage of 490 V, the θ_{HWHM} was 0.31°. Provided the precel technique can be successfully adapted to large multiaperture grids, this study indicates that it should be possible to obtain a beam with approximately the same current density and grid transparency as those obtained with the standard, high current density extraction systems in use on such machines as ORMAK, but with greatly improved divergence.

Solutions to the Poisson-Vlasov equation were obtained for ions extracted through an insulated plasma grid. The insulator was specified as a Dirichlet boundary on the plasma side with potential equal to the sheath drop from the plasma potential and a Neumann boundary condition on the cylindrical surface. Figure 4.10 shows (1) actual transparency (F), scaled by the geometric transparency, (2) rms beam divergence angles, shown by dashed curves, and (3) rms beam divergence angles of a truncated ion distribution, shown by solid curves as a function of relative sheath perveance for three different precel potentials, V, on the scale of the accel potential. Results are that for the

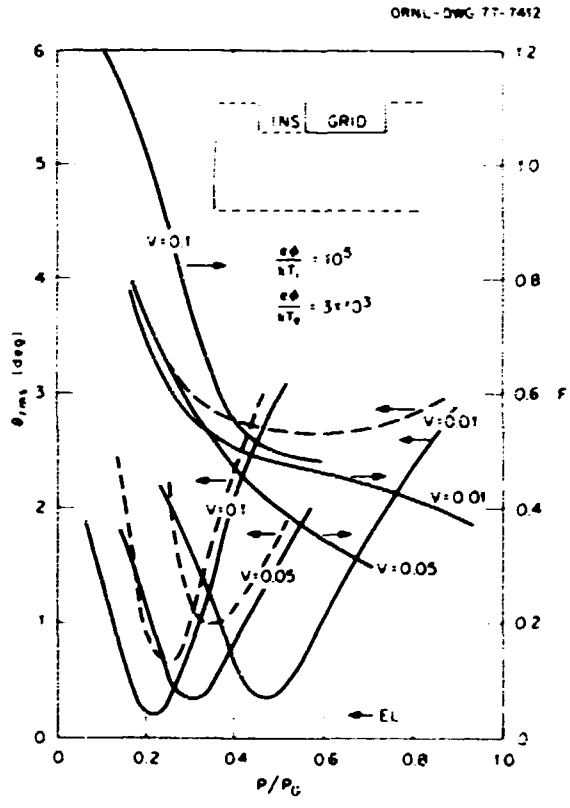

Fig. 4.10. Effect of precel on ion optics and transmission for various ratios V of precel voltage to accel voltage.

cases with progressively higher precel potential the minimum beam divergence decreases, the actual transparency increases, and the optimum plasma density decreases. One of the cases in Fig. 4.10 is considered for various relative ion temperatures in Fig. 4.11, along with the source emittance limited ion convergence showing that this limit is actually approached for insulated grids.

4.2.4 Effect of Decel Voltage

The accel-decel extraction system has been widely used for forming a high current and low divergence ion beam for neutral beam injectors. Such a system generally consists of at least three electrodes: plasma, extraction, and ground electrodes. A negative potential called the decel voltage is applied between the last two electrodes. It is utilized to prevent electrons created in the gas neutralization cell from leaking back to the plasma source and to ensure space-charge neutralization of the extracted beam. We have observed that for a given geometry and plasma condition, the beam divergence angle is reduced as the decel voltage is lowered toward a minimum value (V_c in Fig. 4.12). Further lowering of the decel voltage results in an abrupt deterioration of the beam optics due to leakage of electrons created in the neutralizer. When the decel voltage is below a value V_D, the divergence angle approaches a maximum angle, about 4° for this case.

A possible mechanism for the electron leakage has been proposed and developed by considering the potential distribution in the accel-decel region based on computer simulation and the boundary of the neutralizer plasma adjacent to the ground electrode. Apparently, the electron leakage occurs whenever the equipotential line, V_B (here, V_B is equal to the plasma potential in the neutralizer), penetrates from the accel gap into the decel gap and contacts the boundary of the neutralizer plasma. This electron leakage mechanism is also valid for explaining the observed beam optics variations with the decel voltage, as shown in

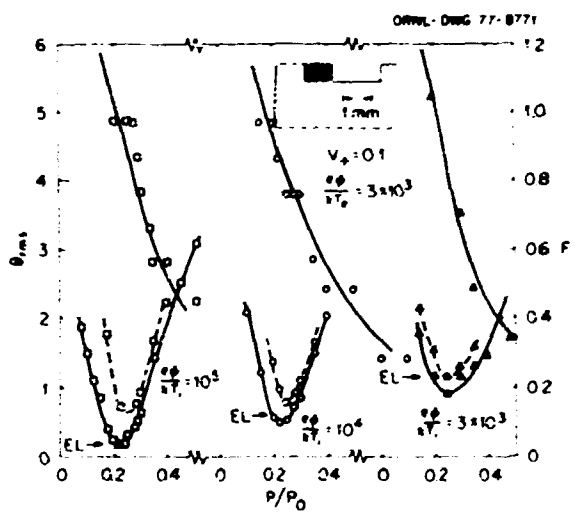

Fig. 4.11. Effect of ion temperature on ion optics and transmission.

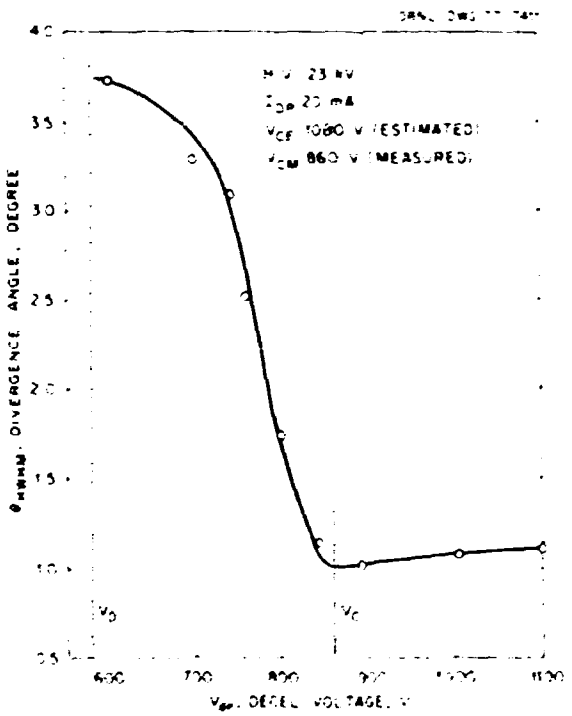

Fig. 4.12. Effect of decel voltage on beam optics.

Fig. 4.12. Based on the above considerations, an expression for estimating the minimum decel voltage, V_c, required for a given beam condition has been derived and is

$$V_c = \left[I_b n_o \sigma_i(E) D \cdot \frac{1}{3.9} \left(\frac{R + D}{R} \right)^2 \right]^{2/3} ,$$

where

V_c is the minimum decel voltage in kV,
I_b is the beam current in mA of a single beamlet,
n_o is the neutral gas density in cm^{-3},
$\sigma_i(E)$ is the cross section of cold ions generated by the energetic ions, at energy E, in cm^2,
D is the decel gap length in cm, and
R is the aperture diameter in cm.

The value of the minimum decel voltage can be estimated fairly accurately. For example, in Fig. 4.12 the measured value is 860 V and the estimated value is 1070 V. Hence, the minimum decel voltage is a function of the beam current and energy, gas density, length of the decel gap, and aperture diameter and electrode thickness in both the extraction and ground electrodes.

Because beam optics vary with the decel voltage, we can propose an explanation for the observed interelectrode high voltage breakdown or spitting based on the behavior of beamlets near the grid edge (which generally have poorer beam optics due to density falloff with radius). Ways to improve injector reliability will be pursued with the aid of computer simulation.

The injected beam power of the energetic neutrals must increase with the size of the tokamak. Often the peak power density of a MW neutral beam is well above 30 kW cm^{-2}, which exceeds the capability of the materials utilized for the present beam-stop calorimeter. Under such a situation, the total beam power may be measured without hurting the calorimeter by forcing the beam blowup through raising the decel voltage well above 3 kV. If the divergence angle is enlarged from below 1° to about 2°, the resulting extra power loading on the electrodes of the ion accelerator is expected to be below 5% of the beam power similar to that found in the present injectors. This forced beam blowup can be used to condition the electrodes of the ion accelerator, to measure the beam power of multimegawatt injectors without damaging the beam stop calorimeter, and to control the beam profile during the initial plasma buildup period of a fusion device should it be desirable.

4.2.5 Two-Electrode Ion Beam Formation System

The negative voltage across the decel gap in the conventional ion beam formation system is applied to ensure the space-charge neutralization of the extracted ion beam by preventing electrons in the neutralizer from leaking back to the plasma source. Our recent study with the insulator-coated plasma electrode (see Sect. 4.2.3) revealed that a precel potential of several hundred volts across the insulator layer can prevent the source plasma from entering the accel gap. From this it appeared that a similar function could be served by an insulator coating the side of the extraction electrode facing the neutralizer cell and applying the decel voltage across the insulator layer — i.e., between the extraction electrode and the neutralizer plasma — thus alleviating the need for a ground electrode.

We have designed, constructed, and tested such a two-electrode system (with insulator coating on both the plasma and extraction electrodes). The electrode thickness and aperture diameter of the extraction electrode were 0.3 cm and 0.25 cm, respectively, which were different from 0.15-cm thickness and 0.38-cm diam in the conventional aperture dimensions. Using a numerical solution to the Poisson equation, the required decel voltage is about 1000 V (as shown in Fig. 4.13). The viability of this system has been successfully demonstrated. A beamlet of hydrogen ions with a density of 100 mA/cm^2 at 38 keV has been formed with a beam divergence of about 0.35°. The corresponding precel voltage across the insulator on the plasma electrode was 300 V, and the

decel voltage was 80 V. As expected, optimum divergence angles were obtained with the decel voltage at the lowest value consistent with stable operation. It was also found that the beam optics improved as the decel voltage was raised to an optimum value. Hence, in this particular system, the beam profile can be controlled to have a divergence angle varying from 0.35° to about 1° without affecting beam operation. Another important observation is that the optimum beam divergence does not vary with ion beam energy over the range of parameters considered here. This feature is not attainable in the existing three-electrode system. Moreover, owing to its inherent ability to inhibit either the source or the neutralizer plasma from entering the accel gap, this system can improve source reliability with respect to high voltage breakdown in the accel gap and increase the flexibility of the injector operation because either the ion beam or the arc discharge can be turned on first. Additional advantages of this system are a simplified electrode arrangement of the ion accelerator and reduced fabrication costs. Considering the various advantages mentioned above, development of the two-electrode system will be pursued for the present and future high power neutral beam injectors.

4.2.6 Thermal Deformation of Plasma Electrode

Preliminary study on beam optics by electrical probes located on the beam stop target indicated that the beam divergence changes during the arc pulse. One possible explanation is thermal deformation of the plasma electrode. To understand the crucial role played by electrode deformation, an intensive analytical study has been conducted with a 15-cm electrode grid pattern. The anisotropy introduced by the presence of holes and cooling lines is included in the study. The steady-state temperature distribution for different heat loading distributions and different water cooling configurations has been calculated. Different electrode

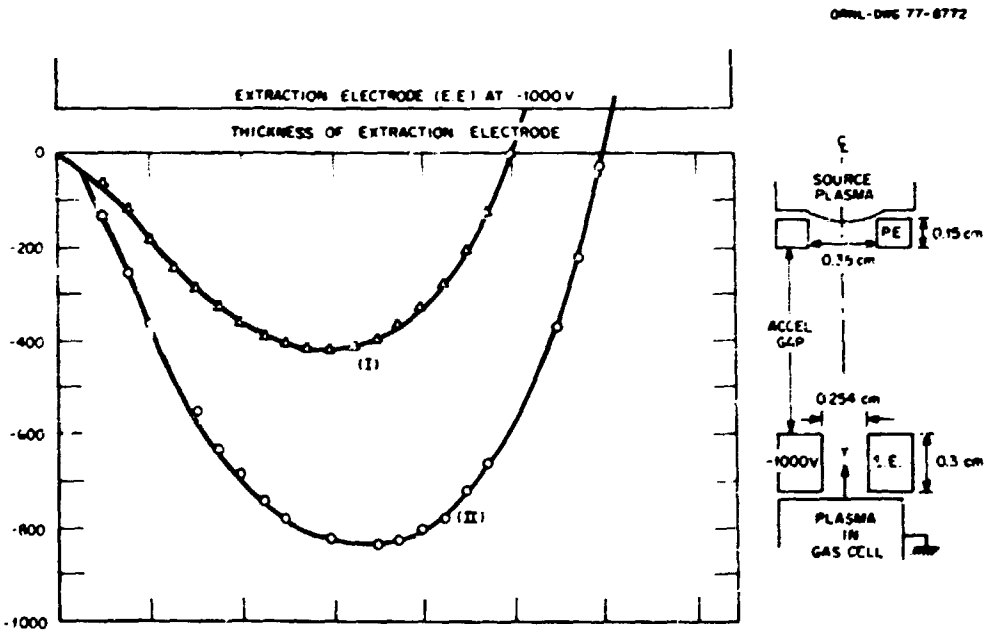

Fig. 4.13. Axial potential distribution within extraction electrode: (I) considering space charge of ion beam, (II) no ion space charge.

materials such as copper, tungsten, and molybdenum have also been considered. Thermal expansion of the electrode and the resulting effect on beam optics have also been analyzed. The results from this study are summarized below.

1) Alternating the water flow direction on successive tubes in the grid does not increase cooling efficiency.
2) Because of their lower heat conductivity, tungsten and molybdenum electrodes have a larger temperature rise than copper electrodes for the same power loading. However, due to a different expansion coefficient, tungsten and molybdenum electrodes experience less deformation than copper electrodes.
3) Increasing the water flow reduces the overall temperature rise, electrode deformation, and focusing angle change. This is a very important factor in avoiding defocusing in the ion accelerator.
4) A generalized model for various grid patterns has been suggested.

4.2.7 Photodiode Array for Beam Detection[11]

A linear array of individual PIN photodiodes which measures the excitation light from parallel chords of the beam cross section has been built and tested. In this prototype, twelve diodes are spaced 1.5 cm apart and are collimated to give an acceptance angle of 3°. The position of the beam center can be measured to within ±0.75 cm with one array. A second array perpendicular to this can provide an accurate two-dimensional determination of beam position.

In addition, a beam intensity profile can be obtained by unfolding the measured chordal values with an Abel inversion technique. Reasonable agreement with calorimetrically measured profiles has been achieved. Further refinement of the measurement technique and data reduction scheme is being pursued. A fast data acquisition system for immediate graphical display is also being investigated.

This indirect detection allows monitoring of the beam during actual injection shots and avoids the problems associated with the direct measurement of high power density beams. The detector assembly can be situated at various locations along the beam line, including the entrance port to a confinement device.

4.3 LOW ENERGY NEUTRAL BEAM SYSTEMS: 10-30 keV

4.3.1 Introduction

The 10-cm-diam duoPIGatron, operating typically at 30 keV and 10 A, has been the workhorse in this energy range. During the past year, the modified duoPIGatron principle, employing line cusp confinement of the source plasma, was applied to a 15-cm-diam ion source. Two such sources were fabricated and tested for use on the ORMAK experiment here at ORNL and on the Laser Initiated Target Experiment (LITE) at United Technologies.

4.3.2 ORMAK

The ORMAK 15-cm modified duoPIGatron utilized the latest fabrication techniques for mounting water cooling lines and headers on the grid structures. This new procedure is identified as gridded electrode. The ORMAK 15-cm source was designed to operate at the same voltage (30 kV) as the 10-cm source. However, the increased current capability should be 2.36, the ratio of the number of apertures in each system. Optimum focusing was achieved at 20-22 A. Test stand results with a simulated ORMAK beam line revealed that the 15-cm source focusing was about 86% as effective as the 10-cm source in terms of power transmission into the torus. This value was quite acceptable, considering that the entrance duct into ORMAK was not increased beyond 8-cm ID.

In the final experiments on ORMAK, three beam lines were employed: two with 10-cm sources and one with the 15-cm source. One of

the 10-cm source beam lines was a counterinjector. Approximately 500 kW of injected neutral power was achieved.

4.3.3 LITE

The Plasma Heating and Fueling Section agreed to supply the LITE experiment at United Technologies with a 15-cm modified duoPIGatron ion source. The source is to operate on hydrogen at 15 kV. The 256-cm beam line with a 10-cm-diam entrance aperture was simulated in the laboratory here at ORNL. Performance was well within expectation because the accelerating grid structure was the same as that used on the ORMAK source which was optimized at 30 kV. With careful tuning, the design goal of 15 A of extracted current at a 15-kV potential may be achieved. The equivalent neutral power on target in the ORNL simulated LITE beam line was 2.5-3 A at 15 keV.

There are two workable schemes to improve the injected neutral power of this source. One is to optimize the grid system for the 15-kV operation, in which case about 5 A of equivalent neutral power should be obtainable. The other is to operate the source at 30 kV, in which case the one-half energy component of the expected 25-30 A of extracted current would be utilized. The injected neutral current equivalent at 15 keV should be about 7.5 A. There is also a current of about 6.5 A of 30-keV H^0 which must be dissipated in the machine.

4.4 MEDIUM ENERGY SYSTEMS: 40-80 keV

4.4.1 Introduction

The transport system which must neutralize the ion beam, remove unneutralized ions, pump vast quantities of cold gas, and in general efficiently transport the neutral beam to the tokamak plasma has changed in scope and design as the demands for total neutral particle injection energy increase. The ion source must be upgraded to extract several MW of ions in the 40-80 keV range. Liquid helium cryocondensation panels have replaced the more conventional diffusion pumps. The length of the beam lines was increased to accommodate deflection magnet and ion removal systems and to remove the ion source from the strong residual magnetic fields of the tokamak. Magnetic shielding is required around the ion source and neutralizer. As the distance from the ion source to the tokamak increases the injection solid angle decreases, and so the ion optics must be improved. With this improvement in ion optics and beam power, much higher beam power density is realized, which places high demands on calorimeters and ion dumps. Several designs have evolved to comply with the particular details of the present generation of tokamaks: PLT, ORMAK Upgrade, ISX, PDX, and Doublet III.

4.4.2 Medium Energy Systems Test Facility

The ORNL Medium Energy Systems Test Facility (MESTF) has been operational since November 1976. It was constructed with the immediate purpose of providing a facility to develop and test PLT neutral beam lines. Sufficient space and flexibility are available so that the test facility can later accommodate beam lines for other projects such as ORMAK Upgrade, ISX, PDX, and Doublet III. Plasma generator studies and ion source development can also be carried out independently from beam line development.

The test facility, including PLT beam lines 1 and 2, is shown pictorially in Fig. 4.14. The test facility was designed to be double-ended, so that experimental work could be undertaken on one end while alterations or servicing were proceeding on the other. The test stand in Laboratory 263 shares the 60-kV, 60-A high voltage power supplies with this facility. Liquid helium cryocondensation vacuum pumps with a speed greater than 500,000 liters/sec provide the pumping for the target chamber. Cryogens are supplied by a CTI 1400 liquid helium cryostat. Individual controls are provided to operate a single beam line and both vacuum systems simultaneously.

A PDP-11/40 minicomputer is being interfaced to the test facility for data acquisition and

ORNL DWG 76-16833

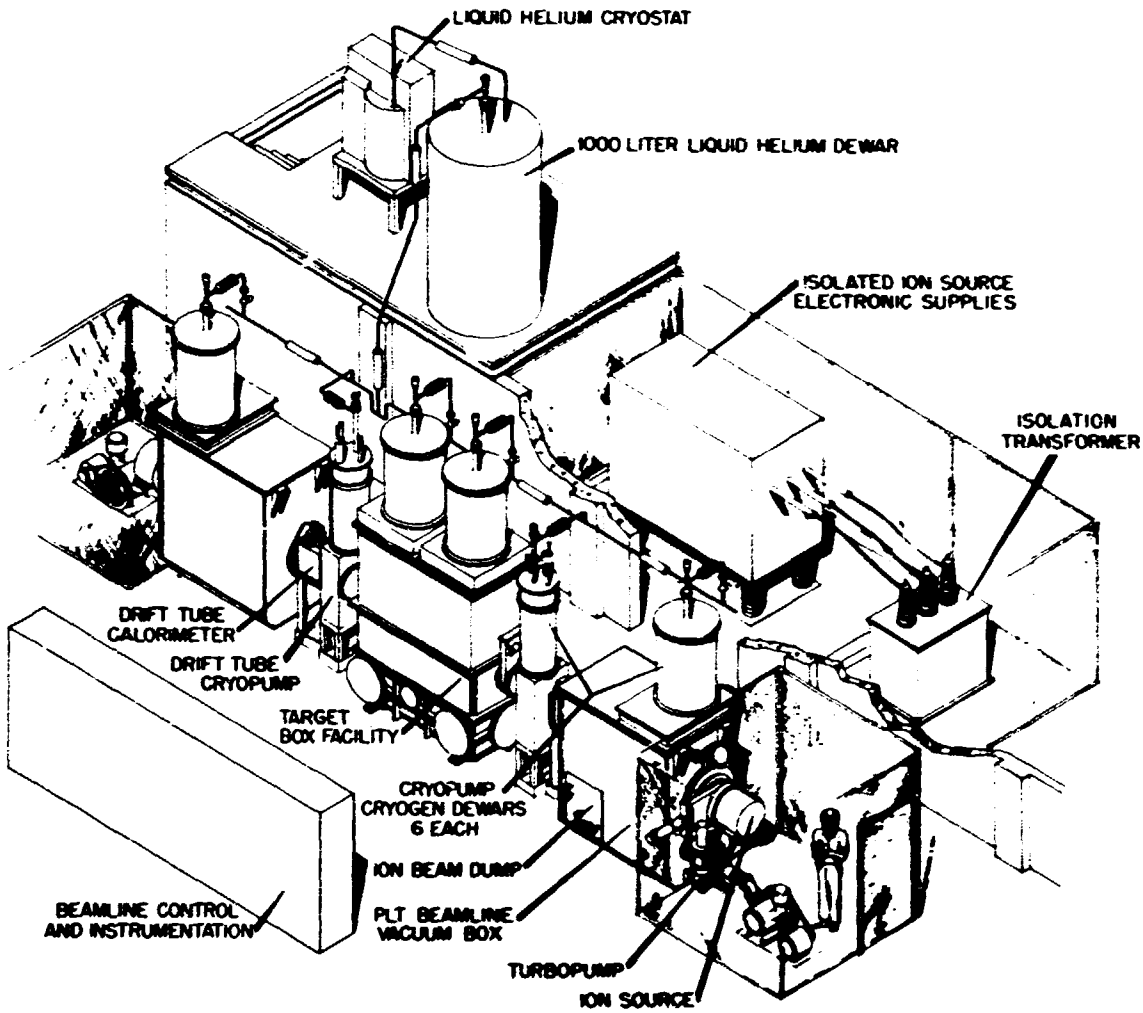

Fig. 4.14. ORNL medium energy systems test facility.

analysis. Rapid analysis of ion source parameters and calorimetric measurements of power deposition along the beam are essential for timely development of these large systems. Plans for computer control of the ion source and for daily monitoring of beam line systems have also been initiated.

4.4.3 PLT Neutral Beam Systems

Due to the critical integration of ion source and transport systems, responsibility for developing and fabricating neutral beam systems for the PLT was placed with ORNL. The first of

four PLT injection systems has been operating for approximately three months; shipment to PPPL is expected in April 1977. The second beam line is assembled and nearly operational and beam lines 3 and 4 will be assembled off test site with an expected shipment date of June 1977.

Each 3.6-m beam line (see Fig. 4.15) includes:

1) a modified duoPIGatron ion source which has been operated at 60 A of extracted ions for extraction potentials greater than 32 keV,
2) a close-coupled gas cell which produces sufficient line density for neutralization equilibrium with a minimum amount of gas throughput,
3) magnetic shielding which will reduce residual tokamak magnetic fields to a few gauss in the ion source region and to a few tens of gauss in the neutralizer,
4) an ion removal system consisting of deflection magnet and swirl tube ion dumps,
5) a diagnostic calorimeter capable of dissipating 2 MW of power,
6) a liquid helium cryopump which condenses hydrogen at a rate greater than 500,000 liters/sec for throughputs in excess of 20 torr-liters/sec,
7) a vacuum system to enclose the above hardware as well as a drift tube section

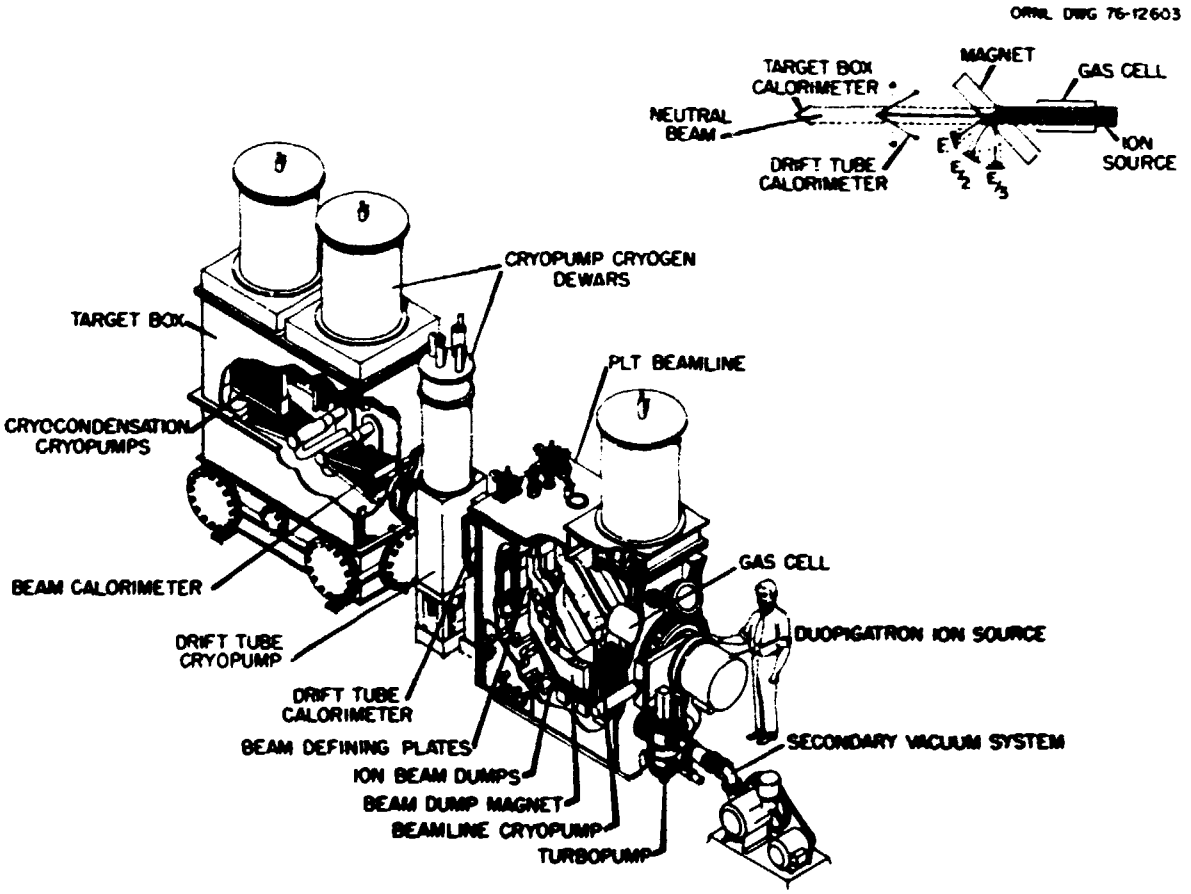

Fig. 4.15. ORNL/PLT beamline and ORNL test facility target box.

to transport the neutral beam from the main pumping chamber to the tokamak, and

8) a diagnostic system which will verify proper ion source and transport system operations.

4.4.4 ORMAK Upgrade and ISX

ORMAK Upgrade is in the planning and design stage, and ISX is in the fabrication stage. Both are considered to be prime candidates for intense neutral beam heating.

ORMAK Upgrade was initially approved to have two 40-keV neutral beam systems operating on the machine by October 1978. The objective at this time is uncertain, however. The beam line effort originally intended for ORMAK Upgrade has now been shifted to ISX. These neutral beam systems will also employ 40-keV injectors similar to the PLT system (Sect. 4.4.3). The principal differences between an ISX beam line and a PLT beam line are the length at the drift tube connecting the ion source vacuum chamber to the torus and the location of the diagnostic calorimeter. Perhaps the ISX beam line may be somewhat shorter than the 3.6-m PLT system. In addition, the entrance aperture on ISX will be circular, with an ID of 25-30 cm. Based on ORMAK performance (Sect. 4.3.1) it is projected that the injected neutral power should be about 40-45% of the total ion power extracted from the high voltage power supply, or about 1 MW (compared to about 860 kW for PLT). A rapid fabrication and assembly schedule for two ISX beam lines is now under way with the goal of installing them on the machine during December 1977.

4.4.5 Two-Stage Source

A multiaperture source with four electrodes and two acceleration stages is in fabrication. This source should be capable of about 40 A of extracted current at 120 keV. Two versions are being fabricated, differing primarily in the final energy desired. The beam divergence may be different in the two cases because the divergence is related to the beam energy through the electric field ratio in the two acceleration gaps.

The lower beam energy source is suitable for beam energies of 60-80 keV for use on ISX in high density, high beta experimentation. The optics of this source, though limited somewhat by the range of electric field ratios permitted, is still quite adequate for ISX beam line application.

The 120-150-keV source will have better optics (on the order of 0.5° HWHM) and will serve as a prototype for developing a two-stage source at 100 A and 150 keV for The Next Step (TNS) applications.

4.5 HIGH ENERGY SYSTEMS: >80 keV

4.5.1 150-keV Test Facility

Construction of the 150-keV Test Facility was carried out as scheduled. Figure 4.16 shows a view of the completed facility. The first pump-down of the facility was made in August, followed by the first running of an ion optics experiment beam (120 kV/30 mA) in October 1976. Five 89-cm oil diffusion pumps (two each on tanks 1 and 2 and one on tank 3) maintain the background pressure in the low 10^{-8} torr range.

The high voltage power supply (150 kV/50 A) and the decel power supply (20 kV/10 A) were delivered and are being tested. The modulator system is 90% finished as of this writing. The arc power supply system has been tested with a two-stage, single beamlet source up to ≈200 A. Currently a two-stage ion beam optics experiment is under way. The beam energy will be accelerated to 150 keV at a single beamlet current of ≤40 mA provided by power supplies of low current and high voltage until the main power supplies are ready for operation.

4.5.2. TFTR Neutral Beam Injection System Studies

Oak Ridge National Laboratory became involved in the neutral beam injection program for the

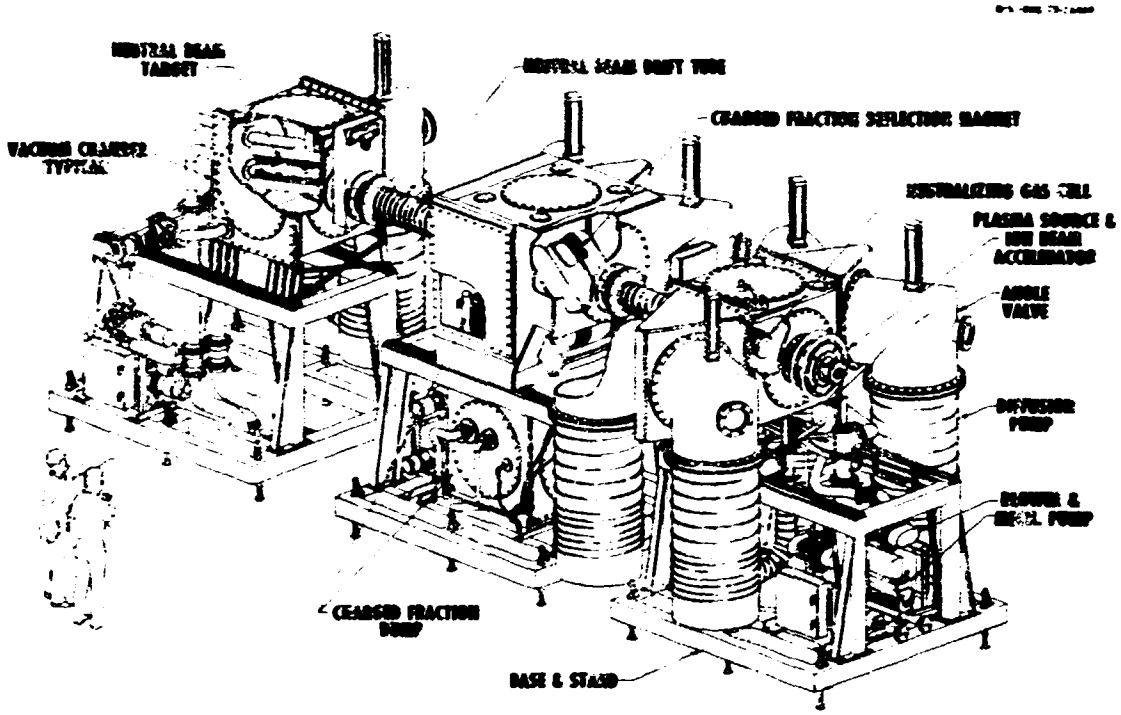

Fig. 4.16. View of completed 150-keV facility.

Tokamak Fusion Test Reactor (TFTR) in mid-1975 when the Division of Controlled Thermonuclear Research requested that ORNL and other developers of neutral beam injection systems participate in a conceptual design effort for TFTR beam systems. The resulting conceptual design report[12] was published in September 1975.

In March 1976 we started reassessing our conceptual design and at the request of the Energy Research and Development Administration (ERDA) started looking at designing some components that would be common for both our beam lines and that of Lawrence Berkeley and Lawrence Livermore Laboratories. After several iterations it was decided that it would be possible to use common technologies in many areas, but the only common component that could be agreed on was the vacuum enclosure.

Once a satisfactory vacuum vessel geometry was determined, we initiated Title I design of the beam lines for TFTR. This occurred in August 1976, at which time the design effort focused on the vacuum vessel, the calorimeter, a remote handling hard seal version of the ion source, and the cryopumping scheme. To augment our in-house design team, specialized outside contractors were called upon to provide preliminary design work on the components. In order to utilize the outside contractors efficiently, detailed task descriptions and criteria packages were prepared.

During this phase of design, a serious evaluation of our original concept was made; as a result of our evaluation several areas needing improvement emerged. An investigation of how these areas could be improved was started and covered such areas as:

1) means of generating fast ions with high atomic yield,
2) simplification of the neutralizer system,
3) a better way to remove and dissipate residual ions,

4) means of improving vacuum pumping, and
5) provision of adequate potential for upgrading the injection system with longer pulse length and for direct energy conversion of residual ions.

Out of this investigation evolved a new concept, which provides greater simplicity and reliability and produces higher atomic yield ions at the source through the incorporation of a thermal dissociator oven. The neutralization system was simplified by returning to the close-coupled gas cell concept used in previous ORNL beam lines.

To provide a more durable ion dump, the ion removal scheme was changed to spread over a larger area the power density of the residual ions being dumped. This was accomplished by replacing the ion beam deflection magnet with an electron trapping solenoid coil. The space-charge compensating electrons are reflected out of the ion beam, allowing it to blow up due to space-charge Coulomb forces; the ions are thus spread over an area which reduces the power density to the point that a thermal inertia target can reliably be used. This ion removal scheme could easily be adapted to incorporate a direct energy converter system.

Neutronic calculations were beginning to show that cryocondensation panels could be used instead of cryosorption. Appropriate design changes were made to use cryocondensation panels for vacuum pumping, simplifying the needed vacuum research and development because the PLT beam line cryopanels were working satisfactorily.

This new concept was described in a proposal[13] generated for PPPL on December 15, 1976. Considerable effort was made to take advantage of the experience gained through the fabrication of the PLT beam lines in the estimation of engineering costs as well as fabrication schedules included in this proposal.

Work on the R&D tasks identified during the TFTR beam line effort is continuing into CY 77. Development-size cryosorption panels are being designed and should be tested by late summer. The development of actively cooled targets and passive target material is continuing, both through in-house effort and industrial involvement. Component design to test the details of the new concept and feasibility studies are under way toward using an injection system concept as described above on future tokamak devices such as TNS.

4.5.3. TNS Neutral Beam Injection System Studies

The requirements for the deuterium neutral beams to be used for auxiliary heating on TNS presently lie in the range of 150-300 keV, with 75 MW of neutral beam power required in the plasma. The lower limit of 150 keV appears adequate if:

1) $Z_{eff} < 1.5$ and constant throughout the discharge,
2) the plasma magnetic axis shifts outward in the flux conserving mode, and
3) the plasma core is heated by the D-T reaction alpha particles generated by beam deposited farther out.

The upper limit of 300 keV appears adequate if these conditions are not met.

Our beam approach is therefore two-fold. We intend first to extend the positive ion approach developed for TFTR to the TNS requirements of higher power and pulse length per injector: 150 kV/100 A/20 sec D^+. Initial injector development may be carried out on the 150-keV Test Facility. We will use as a beam line base the residual ion blowup concept presented in the December 15, 1976 ORNL TFTR Neutral Beam Proposal. This concept will be extended to the power levels and pulse lengths of TNS, and direct ion energy recovery will be added in a natural fashion to the blow-up scheme. The second, parallel approach will be to develop a negative ion concept, which has the advantage of inherently higher efficiency. This will be essential for the 300-keV beam requirements, where the positive ion approach would give a neutral beam yield of less than 10%.

Both of these neutral beam generation approaches are being studied in increasingly greater detail, and experiments, R&D plans, and schedules are presently being initiated.

4.5.4 Two-Stage Ion Beam Optics[14,15]

For the next generation of neutral beam injectors with higher energies (>80 keV) the two-stage acceleration scheme (i.e., the extraction-accel-decel system) has been studied both experimentally and theoretically. The numerical solution to the two-stage ion optics was carried out for a 120-keV accelerator in terms of the extraction perveance (P) and the voltage ratio of the acceleration to the extraction gap (Γ). An analytic model has also been developed by summing up the lens effect of apertures and the space-charge effect to yield an expression for beam divergence as a function of perveance, voltage ratio, aspect ratio (i.e., aperture diameter divided by extraction gap), and spacing ratio of the accel to the extraction gap (Γ).

Figure 4.17 shows the comparison between the experimental results and corresponding numerical results of the two-stage ion beam divergence. The numerical model predicts the experimental results reasonably well. A parameter study is illustrated in Fig. 4.18, where the divergence angle is plotted as a function of the extraction perveance for different voltage distributions between the two stages at a fixed total acceleration voltage of 120 kV. The optimum perveance increases as Γ increases. There also exists a range of Γ for good optics; for example $3 < \Gamma < 7$ in the case of Fig. 4.18. Figure 4.19 shows the relationships between P and Γ at the best optics condition, obtained from the numerical solution (Fig. 4.17) and from the analytic model, respectively. The analytic model yields a reasonably good prediction of the more accurate numerical results.

It was shown both experimentally and theoretically that the two-stage acceleration scheme not only provides the beam energy boost but also improves the beam optics over

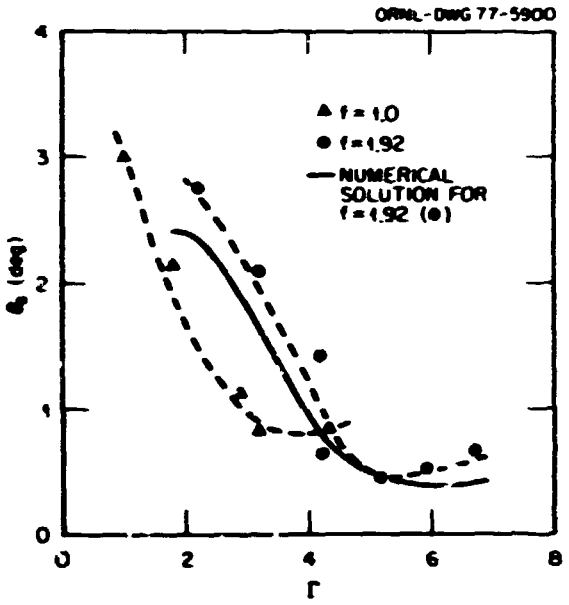

Fig. 4.17. The single beamlet divergence angle measured at V_{ext} = 10 kV, f = 2, and S = 0.81 as a function of Γ and the corresponding results from numerical calculation.

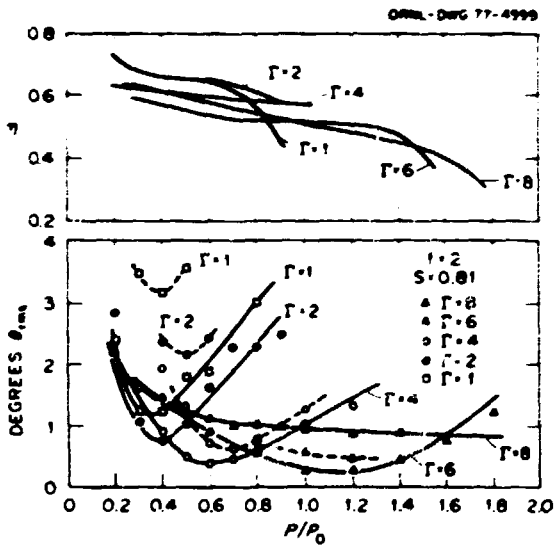

Fig. 4.18. The rms angle as a function of the extraction perveance and the voltage distribution obtained from the numerical computation, where P_0 is the Child-Langmuir perveance.

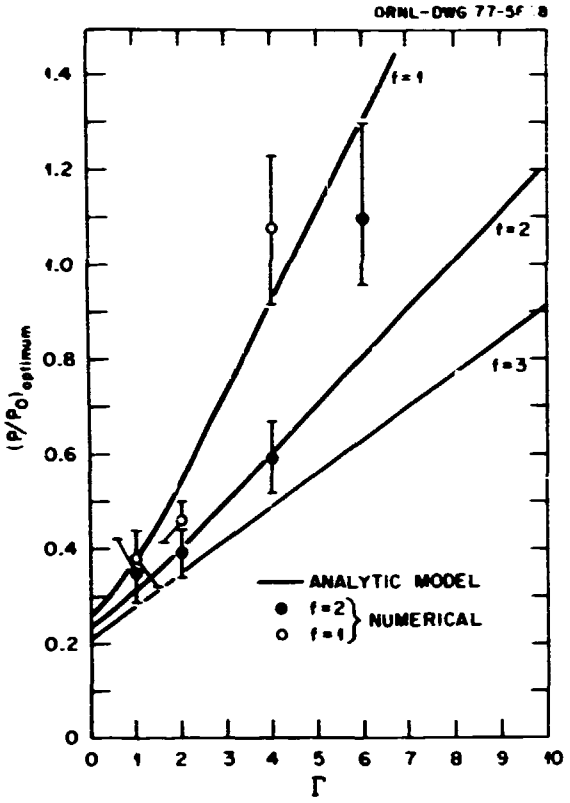

Fig. 4.19. The optimum extraction perveance vs the voltage distribution, obtained from the numerical simulation and from the analytical model.

the single-stage case. The two-stage beam optics is also less sensitive to the extraction perveance (and thus to the source plasma fluctuation) near the minimum divergence condition. The experimental investigation is continuing on the 150-keV Test Facility for energies up to 150 keV.

4.5.5 Separation of Charged Particles From A Neutral Beam by Means of Space-Charge Blowup

In a conventional neutral beam injection system, the unneutralized fraction of a ion beam is deflected away by a magnet from the neutralized fraction, which requires a large space for the magnet and the ion beam dump. We investigated a means of spreading the charged particles of a beam by preventing the background electrons in the neutralizing region from migrating into the expansion region by the use of a magnetic lens (either solenoidal or transverse). Generation of secondary electrons in the expansion region is minimized by maintaining a good vacuum. The blowup of the charged fraction into a large solid angle results in both the substantial separation of charged particles from neutral particles and the large reduction of the power density to a level easily handled by the ion beam stop. This concept simplifies the beam line design by the elimination of the magnet, reduces the target cooling problems which otherwise exist, and is the first step toward a direct recovery system. A magnetic lens strength of no more than a few kilogauss is typically required to balance the space-charge electric force on the electrons while producing a negligible focusing effect on the ions.

4.5.6 Beam Intensity Distributions in a Neutral Beam Injection System[16]

Analytic expressions for the beam intensity profile for focused multiaperture sources have been derived. These formulas are used to estimate the beam transmission, the effect of the single beamlet divergence on the beam evolution, and the beam power loading to various beam line components. The analysis is also extended to multisource beam line systems such as the TFTR beam line. As an example, Fig 4.20 shows a downstream evolution of the focused beam intensity profile in the PLT beam line system, where the beam target is situated approximately at $Z = 250$ cm.

4.5.7 Vacuum Components Development

Very high speed, clean pumping systems are required to remove the copious amounts of cold gas emitted by high power neutral beam injectors. The estimated cold gas load for a 120-keV injector with 5 MW of neutral power is 130 torr-liters/sec. This requires a total pumping speed of 1.3×10^6 liters/sec to maintain average

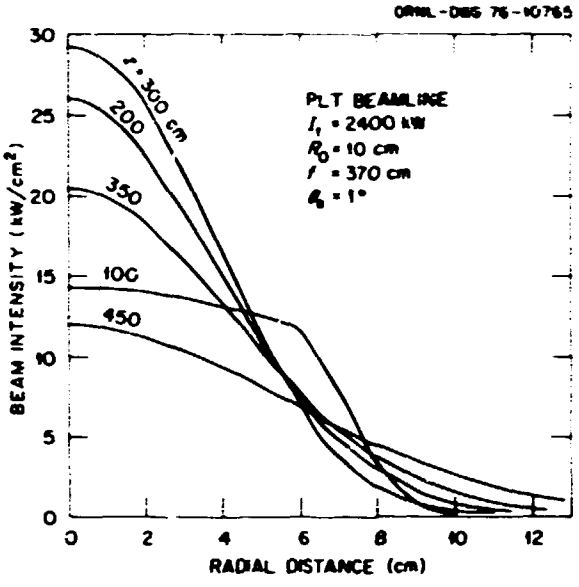

Fig. 4.20. Downstream evolution of the beam intensity profile in the PLT beamline.

chamber pressures at 10^{-4} torr.

Several techniques for achieving these speeds have been considered,[17] including diffusion pumps, getter pumps, cryocondensation, and cryosorption on molecular sieves or CO_2 frosts. Cryocondensation and cryosorption appear to offer the best prospects for attaining the required speed and cleanliness. Cryocondensation pumps are already in use on the PLT beam lines[18] as well as on fusion related projects in other laboratories. However, cryosorption pumps may be better able to hold accumulated deposits in the presence of high energy neutral beams and associated thermal radiation and neutron fluxes. Furthermore, cryosorption pumps offer the possibility of operation at temperatures of 15-20 K, leading to lower refrigeration costs and easier control of regeneration. Finally, with cryosorption at 4.2 K it is possible to pump helium produced in a thermonuclear burn out of the torus, an advantage not possessed by condensation pumping. However, present performance data on cryosorption are very sketchy and mostly limited to low pressures and throughputs.

With the above motivations, a new program to develop cryosorption pumping for fusion applications has been initiated. Two major activities are under way. First, small panels are being fabricated and tested in a variable temperature cryostat with the object of optimizing the pumping speed and total gas capacity. This work is being carried out in collaboration with the ORNL Chemical Technology Division, where a small commercial cryosorption pump is already being tested for tritium handling applications. Using design inputs from this program, a parallel effort to construct a large (~1 m² area) cryosorption panel for the 150-keV Test Facility is being carried out in order to verify satisfactory performance in the presence of high power hydrogen or deuterium beams and to determine requirements for future injection systems. A set of specifications has been written for this panel and submitted to the Arnold Research Organization in Tullahoma, Tennessee for development and construction under subcontract. A response is expected in January 1977.

Figure 4.21 shows a cross section of the commercial cryosorption pump under test in the Chemical Technology Division. The 320-cm² sorption surface consists of Linde 5A molecular sieve deposited on a cross milled stainless steel substrate. Chevron baffles at 77 K and 20 K intercept incoming thermal radiation and thermalize hot gas molecules. Long-term 4.2 K pumping speeds at 10^{-4} torr of about 3 liters-sec^{-1} cm^{-2} have been observed[19] for hydrogen and deuterium. At 4.2 K, the major pumping mechanism seems to be condensation. The performance with helium is more complex, with pressure oscillations between 10^{-4} and 10^{-1} torr occurring for gas loads greater than 2×10^{-3} torr-liters/sec. This appears to result from interaction between the sieve surface and the helium gas cooled first chevron via boiloff gas from the helium bath. Measurements of hydrogen pumping speed were also carried out with the sieve at temperatures up to 20 K. Preliminary analysis of the data

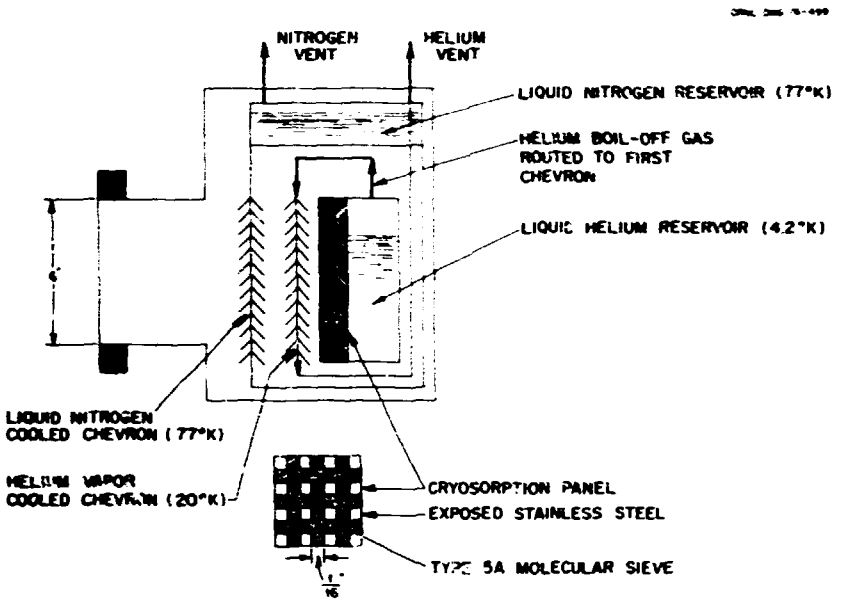

Fig. 4.21. Commercial cryosorption pump purchased from Excalibur, Inc.

indicates that the pumping speed does not decrease markedly at higher temperatures, although the total gas capacity is decreased. These experiments will be continued in the more versatile variable temperature cyrostat, which is scheduled for initial operation in January 1977. The effects of substrate material and geometry, sieve material and thickness, and baffle geometry on pumping performance will be investigated.

4.6 NUMERICAL SOLUTION OF POISSON-VLASOV EQUATIONS FOR IONS EXTRACTED FROM A PLASMA

The region considered in this two-dimensional solution is shown in Fig. 4.22, further described elsewhere.[20,21]

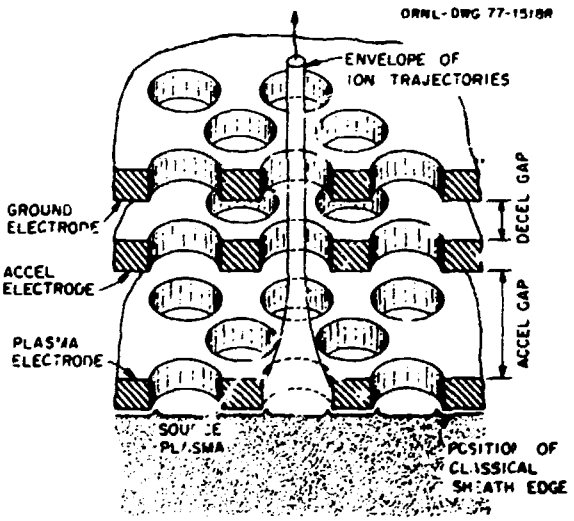

Fig. 4.22. Region in which the solution to the Poisson-Vlasov equation is found.

4.6.1 New Iteration Scheme

A new iterative scheme is proposed for the two-dimensional solution of the ion optics of high current ion beams extracted from a plasma, including the effect of plasma electrons. This is an accelerating electron under-relaxation, averaging, constrained potential, successive overrelaxation (SOR) scheme.[20] The range of perveance for which this scheme can be applied and its speed are shown in Fig. 4.23 (curve C)

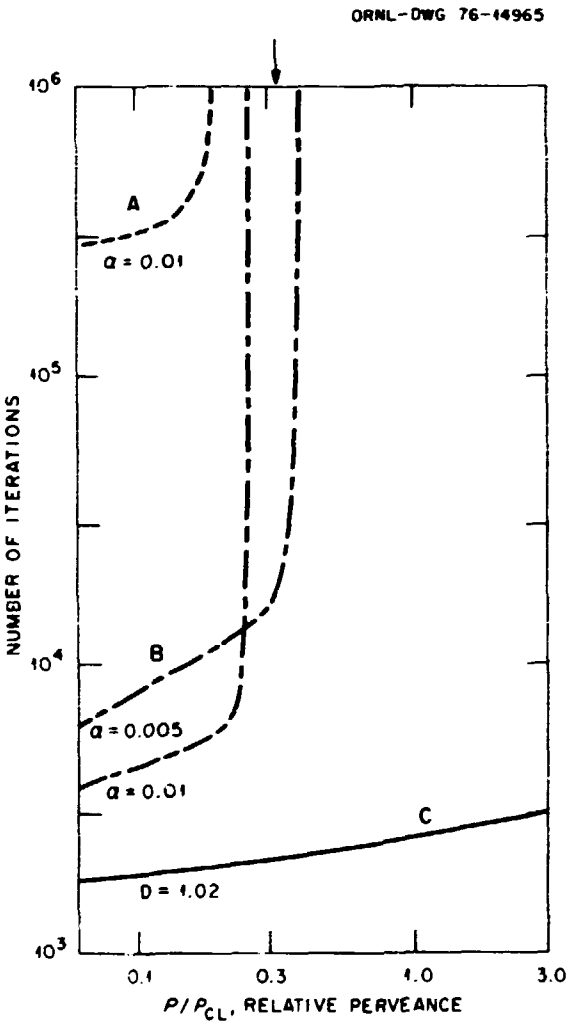

Fig. 4.23. Comparison of the number of SOR iterations necessary for convergence of three electron iteration schemes as a function of relative perveance.

where the total number of iterations required for convergence is plotted vs the perveance on the scale of the Child-Langmuir perveance. The Poisson-Vlasov equation is solved 100 debye lengths into the extraction plasma, which eliminates the need to stipulate anything about the sheath shape or position. Compared in Fig. 4.23 are two other schemes: the conventional sequential under-relaxation SOR scheme,[21] denoted by curve A in Fig. 4.23 and a simultaneous under-relaxation SOR scheme, shown by curve B, where the electron source term is reinserted during the SOR iterations. The properties of scheme C make possible the various calculations presented throughout Sect. 4.

4.6.2 Expeditious Exponential

The code speed was increased by about a factor of three when we taught the IBM 370/195 how to calculate the exponential 15 times faster.[22]

4.6.3 General Parameter Dependence of Ion Optics

For single-stage sources similar to that shown in Fig. 4.22, ion optics are always found to be aberration-dominated for any reasonably low value of the emittance.[23] The dependence of the ion divergence angle, B, and transparency, F, on the ion and electron temperature and the source plasma density, on a suitable scale P/P_0, is shown in Figs. 4.24 and 4.25. These results are valid for any accelerating potential, electron and ion temperature, ion mass, and source plasma density within the range of the three independent dimensionless parameters considered in Ref. 23. Figure 4.24 should be compared with Figs. 4.9, 4.11, and 4.13.

4.6.4 Comparison and Discussion of Three High Quality Ion Beam Optical Systems

The two-stage source[24] (Sect. 4.5.4) and single-stage source with a shaped,[25] (Sect. 4.2.2) or coated (Sect. 4.2.3) plasma electrode have both been shown experimentally and theoretically to yield considerably better optics than a single-stage, cylindrical bore, uncoated

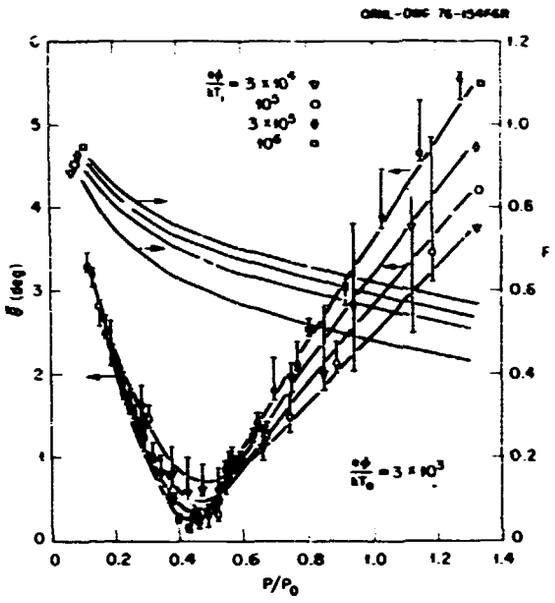

Fig. 4.24. Ion divergence angles and relative transparency as a function of relative perveance and ion temperatures.

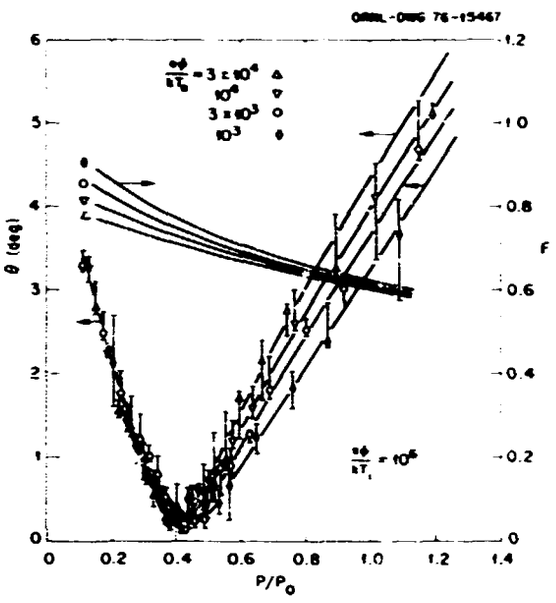

Fig. 4.25. Ion divergence angles and relative transparency as a function of relative perveance and electron temperature.

aperture. Here we compare the features of each and offer a physical explanation. Transparency: The transparency approaches the geometric transparency in the coated and some shaped single-stage sources. It is usually around 0.7 of the geometric transparency for a conventional cylindrical bore, uncoated single-stage source. For the operating region of the two-stage source,[24] it is usually around 0.6. The lower the transparency, the higher the source plasma density needed for a given beam current. Also the plasma grid becomes heated more. Optics: In all three systems the optics can be made to approach the source emittance limit (Figs. 4.3, 4.10, and 4.18) as opposed to the aberration-limited optimum optics (Figs. 4.24 and 4.25). The broad wings of the beam distribution which may be present in the conventional source can be eliminated in all three systems, meaning more power where it is needed and lower electrode loading due to secondaries, which tend to hit the source plasma and ions in the gas cell plasma instead of the electrodes. Explanation: The principal source of beam divergence in the conventional source as considered in Figs. 4.24 and 4.25 is the residual radial electric field due to the ion space charge and to incomplete cancellation of the aberration fields of the cylindrical bore plasma electrode. Each of these three high quality optical systems reduces or makes ineffective these residual radial electric fields. The shaped grid does it in the most direct fashion. It is possible to have a shaped-aperture plasma grid (described in Sect. 4.2.2) in which there are virtually no radial electric fields (Pierce-like geometry). The two-stage source (described in Sect. 4.5.4) can be made to operate at very high perveance in the first stage with the second electrode acting as a strong converging lens. Under these conditions, the source plasma sheath is much forward of its normal position in a single-stage source at optimum perveance. The space-charge

fields are able to cancel out more effectively the aberration fields of the plasma grid, thus reducing the residual fields and improving the optics. The coated grid with preacceleration of the ions (described in Sect. 4.2.3) makes the residual aberration fields ineffective in deflecting the ions because the ions travel in these fields for a much shorter time.

4.7 PELLET FUELING

4.7.1 ORMAK Pellet Injection Experiments

In collaboration with the University of Illinois and the ORNL Tokamak Experimental Section, experiments were performed on ORMAK[26] in which 210-mm-diam frozen hydrogen spheres were injected tangentially into the ORMAK edge plasma. The University of Illinois pellet injection apparatus[27] was used to inject the pellets at a speed of 100 m/sec. A schematic of the experiment is shown in Fig. 4.26.

Both temporal and spatial distribution of the light emanating from the pellet-plasma interaction were recorded. Figure 4.27 shows a record of the pellet ablation rate inferred from the observed luminosity as a function of time and radial distance in the plasma. The data were assembled from three separate but similar shots to form a composite of the ablation process. Pellets were observed to penetrate to the 19-cm position, where the plasma temperature is estimated to be 80 eV.

Also shown in Fig. 4.27 is the ablation rate predicted by a revised version of the neutral ablation model recently proposed by Parks et al.[28] The agreement obtained is good, and this model is now being used in our pellet accelerator development program as a guide to

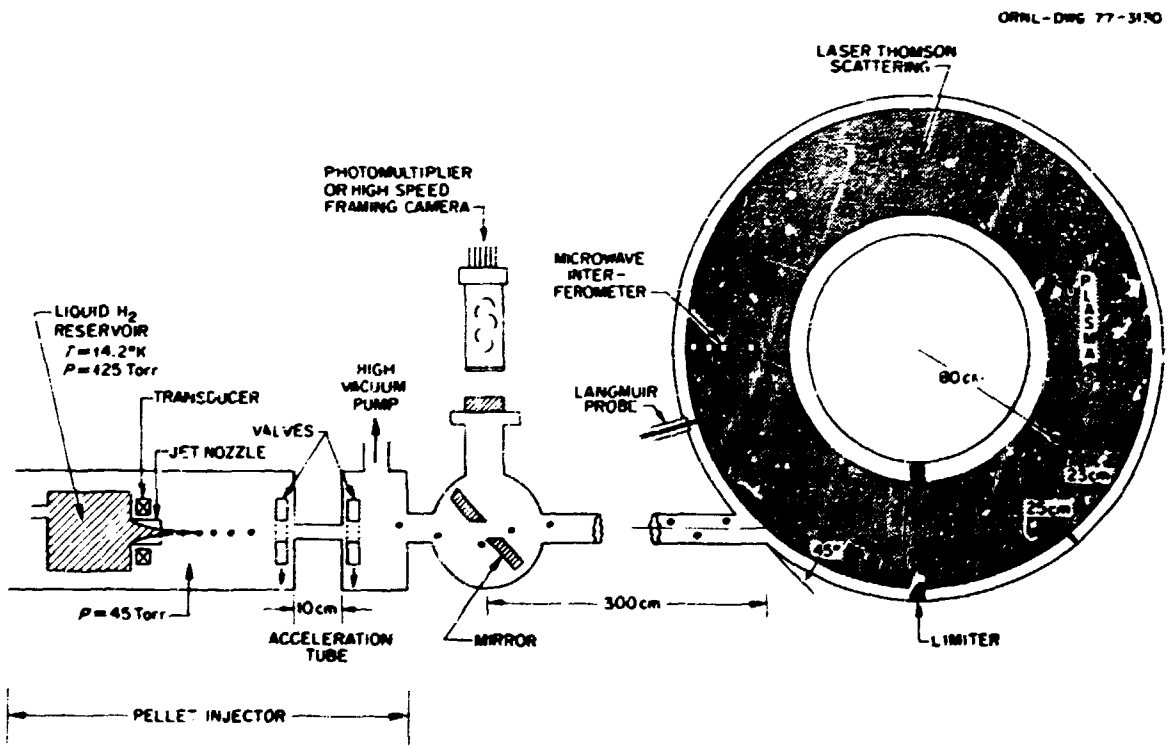

Fig. 4.26. Pellet injection apparatus shown mounted on ORMAK.

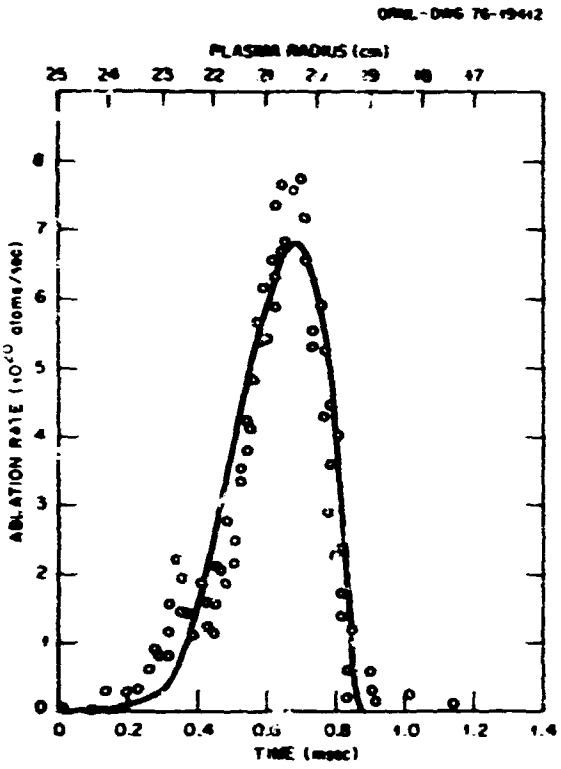

Fig. 4.27. Experimental pellet ablation rate as a function of time and position in plasma. Solid line represents neutral ablation model.

estimate injection device design parameters for the next generation of tokamaks.

4.7.2 Pellet Ablation Model Development

To describe the results of the ORMAK pellet injection experiment, a revised neutral ablation model was developed.[29] The approach taken was similar to that of Parks et al.[20] but differed by treating in more detail the hydrodynamic behavior of the cloud of molecular hydrogen that surrounds the pellet surface. Numerical solutions to the fluid dynamic equations, which include the effects of strong electron heating locally in the ablation cloud, reveal that the flow of material away from the pellet is initially retarded and then rapidly accelerated and rarefied. This behavior is more pronounced for higher temperature plasmas, and the net effect is that pellet lifetimes are prolonged slightly by including the heating effects in the analysis.

This model has been used to devise a simple pellet velocity scaling law. The velocity required to penetrate a given distance into a tokamak plasma varies as the cube of the fractional penetration depth to the plasma center. If this dependence is correct, injection of pellets to the central regions of a TNC-like plasma may require velocities on the order of several thousand meters per second.

4.7.3 Pellet Accelerator Development Program

An advanced pellet injector facility based on the rotating arm accelerator concept has been designed, and construction is proceeding. The key element of this device will be a 56-cm-diam, high strength aluminum arbor that rotates nominally at 500 Hz, resulting in rotor tip speeds approaching 1000 m/sec. A schematic of the facility is shown in Fig. 4.28. Solid hydrogen pellets introduced at the hub of the spinning arbor will be accelerated outward and will eventually leave the arbor tip with equal components of radial and tangential velocity. This prototype is expected to provide pellet velocities approaching 1400 m/sec.

The pellet feed mechanism for this device will utilize a solid hydrogen extruder capable of producing a continuous filament of frozen hydrogen. To test this concept, an extruder was constructed and initial tests demonstrated that a 400-μm filament of frozen hydrogen could be produced continuously. The design of this device will be modified for use with the prototype rotating arm accelerator. The projected initial applications for the complete injector system will be on ISX and PLT sometime in 1978.

Experiments to investigate the potential of other accelerating concepts such as the light gas gun and laser rocket[30] have begun.

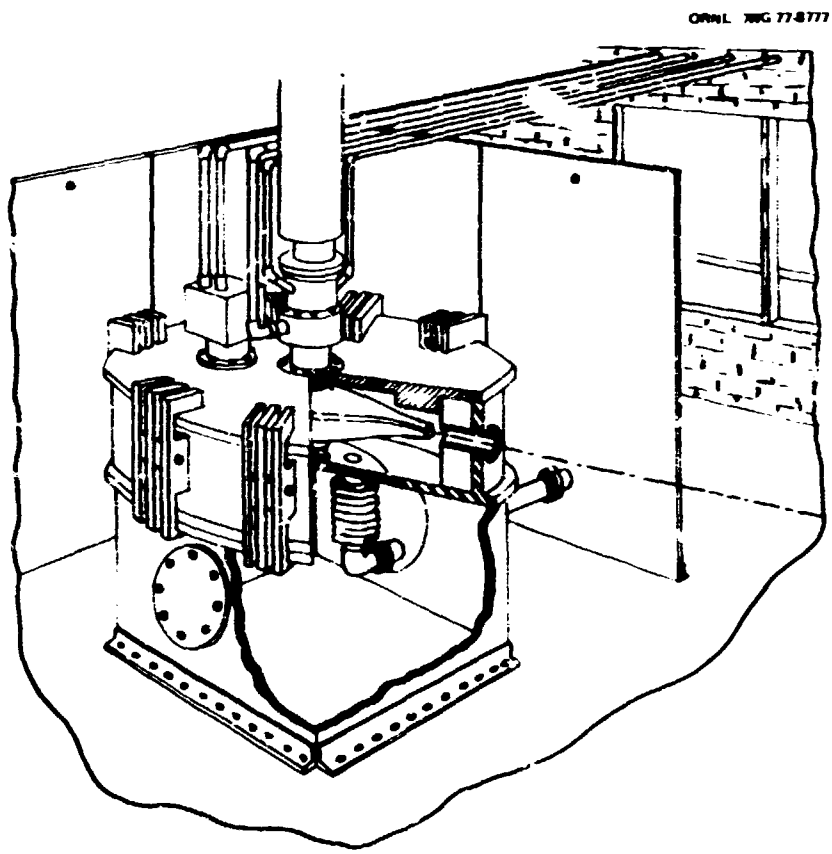

Fig. 4.28. Artist's concept of rotating arm pellet injection facility.

1. L. D. Stewart et al., "Neutral Beam Injection Research and Development Work at LBL/LLL and ORNL," IAEA-CN-35/15, *Proc. 6th Intl. Conf. on Nucl. Fusion and Plasma Physics*, 1976.
2. W. L. Stirling et al., "Plasma Properties and Performance of the 10 cm DuoPIGatron Ion Source," *Proc 2nd Symp. on Ion Sources and Formation of Ion Beams*, Berkeley, California (1974).
3. R. C. Davis et al., Rev. Sci. Instrum. 46, 576 (1975).
4. C. C. Tsai et al., *Plasma Studies on a DuoPIGatron Ion Source*, ORNL/TM-5292, Oak Ridge National Laboratory, Oak Ridge, Tennessee (January 1977).
5. W. L. Stirling et al., *15 cm DuoPIGatron Ion Source*, ORNL/TM-5662, Oak Ridge National Laboratory, Oak Ridge, Tennessee (November 1976).
6. K. R. Mackenzie et al., Rev. Sci. Instrum. 44, 726 (1973).
7. K. N. Leung et al., Phys. Lett. A 51, 490 (1975).
8. J. Kim and R. C. Davis, Appl. Phys. Lett. 30, 130 (1977).
9. L. D. Stewart et al., *Beam Focusing by Aperture Displacement in Multiampere Ion Sources*, ORNL/TM-4920, Oak Ridge National Laboratory, Oak Ridge, Tennessee (May 1975).
10. J. Kim (ORNL), private communication, 1976.

11. P. M. Ryan and Jinchoon Kim, "An On-line Optical Diagnostic for Neutral Beam Injectors," paper presented at the 18th Annual Meeting of the Division of Plasma Physics, San Francisco, California, November 15-19, 1976.
12. Plasma Heating Department, *TFTR Beam Systems Conceptual Design*, ORNL/TM-5227, Oak Ridge National Laboratory, Oak Ridge, Tennessee (March 1976).
13. G. Schilling et al. (ORNL), private communication with Princeton Plasma Physics Laboratory, December 15, 1976.
14. G. Schilling, J. Kim, and J. H. Whealton, Bull. Am. Phys. Soc. 21, 1065 (1976).
15. J. Kim, J. H. Whealton, and G. Schilling, "A Study of Two-Stage Ion Beam Optics," submitted to J. Appl. Phys.
16. J. Kim and J. H. Whealton, "Beam Intensity Distributions in Neutral Beam Injection Systems," Nucl. Instrum. Methods 141, 187 (1977).
17. W. K. Dagenhart, M. R. Busby, J. S. Culver, H. H. Haselton, R. L. Johnson, G. Schilling, W. L. Stirling, and S. A. Stern, "Cryopumping Techniques and Design for Neutral Beam Injection Systems," paper presented at the 6th Symposium on Engineering Problems of Fusion Research, San Diego, California, November 18-21, 1975.
18. S. W. Schwenterly, W. K. Dagenhart, H. H. Haselton, R. L. Johnson, G. Schilling, and W. L. Stirling, Bull. Am. Phys. Soc. 21, 1119 (1976).
19. P. W. Fisher, "Cryosorption Pumping of Deuterium, Helium, and Hydrogen at 4.2 K for CTR Applications," paper presented at the American Nuclear Society Winter Meeting, Remote Systems Section, Washington, D.C., November 14-19, 1976; proceedings to be published.
20. J. H. Whealton, J. C. Whitson, and E. F. Jaeger, Bull. Am. Phys. Soc. 21, 1066 (1976); submitted to J. Comput. Phys.
21. E. F. Jaeger and J. C. Whitson, *Numerical Simulation for Axially Symmetric Beamlets in the DuoPIGatron Ion Source*, ORNL/TM-4990, Oak Ridge National Laboratory, Oak Ridge, Tennessee (August 1975).
22. J. C. Whitson and J. H. Whealton, *A Fast Exponential Calculation for the IBM 370-195 at the Oak Ridge Gaseous Diffusion Plant*, ORNL/TM-5719, Oak Ridge National Laboratory, Oak Ridge, Tennessee (March 1977).
23. J. H. Whealton, E. F. Jaeger, and J. C. Whitson, submitted to Rev. Sci. Instrum.
24. J. Kim and G. Schilling, Bull. Am. Phys. Soc. 20, 1366 (1975); G. Schilling, J. Kim, and J. H. Whealton, Bull. Am. Phys. Soc. 21, 1065 (1976).
25. L. R. Grisham, W. L. Stirling, and C. C. Tsai, Bull. Am. Phys. Soc. 21, 1065 (1976).
26. C. A. Foster, J. J. Colchin, S. L. Milora, J. Kim, and R. J. Turnbull, "Solid Hydrogen Pellet Injection into the ORNAK Tokamak," submitted to Nucl. Fusion.
27. C. A. Foster, R. J. Turnbull, and C. D. Hendricks, "Apparatus for Producing Solid Hydrogen Pellets," to be published in Rev. Sci. Instrum.
28. P. B. Parks, R. J. Turnbull, and C. A. Foster, "A Model for the Ablation Rate of a Solid Hydrogen Pellet in a Plasma," to be published in Nucl. Fusion.
29. S. L. Milora and C. A. Foster, *ORNL Neutral Gas Shielding Model for Pellet-Plasma Interactions*, ORNL/TM-5776, Oak Ridge National Laboratory, Oak Ridge, Tennessee (April 1977).
30. S. L. Milora, G. D. Kerbel, and C. A. Foster "A Survey of Possible Pellet Injection Techniques for Refueling Tokamak Reactors," Bull. Am. Phys. Soc. 21, 1052 (1976).

5. MAGNETICS AND SUPERCONDUCTIVITY SECTION

M. S. Lubell, Section Head

J. E. Akin[1]
L. Alley
W. C. Anderson[2]
J. K. Ballou
R. L. Brown
P. B. Burn[2]
W. D. Cain[2]
K. H. Carpenter[3]
C. V. Jodd[4]
L. Dresner
R. B. Easter[2]
D. S. Easton[4]
J. F. Ellis
W. A. Fietz
C. M. Fitzpatrick
K. J. Froelich
W. F. Gauster[1]
J. C. Goddard[2]
W. H. Gray
C. C. Koch[2]
J. P. Kois[2]
M. H. Kunselman[2]
C. G. Lawson
D. L. Levine[5]
C. J. Long
H. M. Long[6]
J. K. Lovin
J. W. Lue
J. N. Luton
J. R. Miller
L. Nelms[2]
B. E. Nelson[2]
H. Pih[1]
J. P. Rudd
H. C. Sanderson[7]
R. E. Schwall
J. E. Simpkins
S. J. Sosnowski[2]
S. S. Shen
W.C.T. Stoddart[2]
P. B. Thompson[2]
L. M. Vinyard[2]
W. H. Wagner
P. L. Walstrom
H. T. Yeh

5.1 DESIGN PROJECTS

5.1.1 EPR

The previously designed Experimental Power Reactor (EPR) magnet systems (ORNL/TM-5042) were reevaluated and modified during this reporting period. Parametric studies, sensitivity checks, and detailed calculations were done for several selected subsystems. A revised design is reported in *Oak Ridge Tokamak Experimental Power Reactor Study – 1976, Part 3: Magnet Systems* (ORNL/TM-5574). This revised design resulted in a more economical and self-consistent design which is simpler in concept and easier to extrapolate to large demonstration and commercial power reactors. Some pertinent modifications are as follows.

1) The shape of the toroidal field (TF) coils was carefully reexamined. It appears that with a minor modification of the radius of curvature, the oval shape is a viable choice.
2) The fabrication of the coils was simplified by using L-shaped structural segments, each enclosing several conductor conduits. The number of welds has been greatly reduced, resulting in significant savings in both fabrication time and cost.

---

1. Consultant.
2. UCC-ND Engineering.
3. Computer Sciences Division.
4. Metals & Ceramics Division.
5. Graduate Summer Student.
6. Energy Division.
7. Fusion Energy Division.

3) The conductor cooling paths were shortened and the protection problem eased (discharge voltage lowered) by running four conductors in parallel. The series current is then increased from 20 to 78 kA.
4) The composition of the conductor cable was optimized with respect to stability using a new theory.
5) Improved theoretical understanding of the stability of forced-flow-cooled conductors allowed us to specify quantitatively allowable sudden and gradual heat inputs for a given conductor at a specified temperature and field.
6) The required pumping power was minimized with no sacrifice in stability margin. This was achieved by flowing the helium more slowly in layers where the field is lower so as to retain the same stability margin.
7) Evaluations were made of ac losses in the TF coils. Because the pulsed fields have components both perpendicular and parallel to the conductor, there is an optimum choice of filament twist pitch.
8) Extensive discussion on the position of the shield vertical field (S-VF) coils has resulted in their being left inside the TF coils.
9) The poloidal field (PF) coils have been moved to decrease further the stored energy and the ampere turns required.
10) Several possible schemes for connecting the ohmic heating (OH) coils were discussed in an attempt to find an acceptable compromise between the conflicting goals of low series current and low inductive voltage during the heating pulse.
11) Calculations of ac losses in the PF coils were made by taking into account the detailed behavior of the magnetic field inside the windings.
12) Flow paths of the helium through the OH coil central solenoids were determined and the pumping power calculated.
13) A protection scheme for the TF coil using external dump resistors and active switching was examined in detail. Satisfactory thermal excursions, terminal voltages, and mechanical loads can be achieved by connecting the TF coils in several parallel loops and isolating and discharging only the quenching coils. The protection problems associated with the PF coils were also examined.
14) The refrigeration cycle for forced flow includes a cold pump loop. Some experimental data on cooling of a cable by supercritical helium in forced flow are available to incorporate in updated estimates of refrigeration load.
15) Various schemes were studied for storing and transferring the energy of the OH coils; however, a satisfactory scheme has not been identified, and the matter requires more extensive study.

In short, the key features of the original reference design are judged to be satisfactory. The honeycomb coil structure and forced-flow-cooling by supercritical helium in a conduit remain as key features of the TF coils. It is worth noting that the modified structure can also be used with pool-boiling or convectively cooled conductors. Forced-flow-cooled conductor cable is recommended for both PF and TF coils. No insurmountable problems were identified in the magnet systems, including their protection, structural integrity, and long-term reliability.

Oak Ridge Tokamak Experimental Power Reactor Study – 1976.1 J. W. Lue (ed.), J. K. Ballou, R. L. Brown, R. B. Easter, C. G. Lawson, W.C.T. Stoddart, H. T. Yeh.

This part of the ORNL EPR composite report documents last year's design effort in the magnet systems. The discussion covers both the toroidal field (TF) coil system and the poloidal field (PF) coil system. Consideration of coil support structure, cryogenic requirements, and power supplies is included. Particular attention is also paid to the protection scheme of both TF and PF coils. The conductor design is based on

forced-flow supercritical helium-cooled cable in conduits. A hybrid system is proposed for the TF coil system; it uses Nb_3Sn in the high field region for a designed maximum field of 11 T, and NbTi in the low field region. Conductor stability analysis in the forced-flow scheme is discussed. Coil connection options to obtain desirable current and voltage rating in PF coils are described. The refined design of the magnet systems is more self-consistent in every respect.

Toroidal Field Coil System of the Oak Ridge EPR Reference Design.[2] J. W. Lue and J. N. Luton.

A refined design of the toroidal field (TF) coil system for the Oak Ridge Tokamak Experimental Power Reactor (EPR) study is presented. This design is based on cable conductor cooled by forced-flow supercritical helium. It uses superconducting multifilamentary Nb_3Sn for a maximum design field of 11 T at the coil windings. A hybrid system which uses NbTi at low field regions is recommended. The coil structure consists of stainless steel segments welded together to form a continuous stiff honeycomb. Conductor optimization and stability analyses specifically applicable to the forced-flow-cooled conductors are given.

5.1.2 Demo

A study has been made of the feasibility of using resistive coils to generate the toroidal magnetic field in a demonstration reactor. The design parameters used were: plasma major radius of 6 m, coil ID of 5 m, radial build of 2 m, and axial build of 1.4 m. The on-axis toroidal field was 4.2 T. The 18-member coil set, if resistive, would consume half the total electrical output of the plasma. When the power demands of other coils (such as OH and PF coils) and the power to drive the neutral beam injectors are considered, it becomes obvious that most of the coils will have to be superconducting. The cost of a resistive toroidal coil set was estimated to be about 350×10^6 dollars for about 8.75×10^6 kg (17.5×10^6 lbm) of copper. It appears that some advantage could be gained from optimized geometry and reallocation of space, but a totally resistive coil set still remains unattractive on a purely economic basis.

Future studies will center on interfacing resistive and superconducting coils as well as on designing the superconducting coils.

5.1.3 TNS

During the initial phase of The Next Step (TNS) TF magnet study, we supplied design criteria and machine parameters and identified feasible options for trade-off studies for the Westinghouse design team. We have reviewed and will continue to review their design and analysis studies. In these coordinated efforts, we have identified feasible designs for various TNS options which bracket physics uncertainties. Four different TF coil designs are being considered in the trade-off studies, namely: TNS-1, a water-cooled copper coil with $B_{max} = 12$ T; TNS-2, a superconducting NbTi coil with $B_{max} = 8$ T; TNS-3, a superconducting Nb_3Sn coil with $B_{max} = 12$ T; and TNS-4, a hybrid NbTi/copper coil with B_{max} between 8 and 12 T. A trade-off study model, which represents subsystems in detail with a consistent physics and engineering rationale, has been developed.

In order to ensure a firm engineering basis in the calculation, the design of the superconducting windings has been adapted to suit the TNS operation. For example, because of the low duty cycle and high nuclear heating pulse of the TNS machine, pulsed operation of the helium flow is proposed. The coil is to be pancake wound and the supercritical helium is to enter through the inner, high field turn and exit from the outer, low field turn. At the start of the plasma burn, the helium flow rate is increased so that the nuclear heat accumulated during the helium transit time through the first turn is kept below the superconductor stability margin. Additional stability margin is obtained when the helium reaches outer, lower field turns. As soon as the plasma burn stops, the helium flow can be reduced

to just maintain stable magnet operation. By operating in this manner one can use a thin shield and still consume relatively little pumping power.

It has also been found that by operating the helium at a lower temperature and higher pumping power, a magnet designed for a given field can be extended to higher fields while maintaining the same stability margin – assuming, of course, that the structure has been designed to withstand the higher mechanical load.

5.1.4 LCP

The Large Coil Program (LCP) is a separately funded project, the goals of which are to provide tested designs for the TF coils of future generations of tokamaks and to encourage development of an industrial base for the manufacture of such coils. The LCP is supported by the technical efforts of the Superconducting Magnet Development Program (SCMDP). This effort is supplied from any group of the SCMDP as the need arises; in 1976 it was equivalent to two men full time. The SCMDP support of the LCP occurred in four main areas: technical supervision of the ERDA contracts for EPR TF coil studies; drafting of a Program Plan for LCP; preparation of a Request for Proposal for the LCP test coils; and preparation of a major Project Proposal for the LCP test facility.

ERDA intended to fund three industrial contracts for conceptual studies of TF magnets for EPR, and more than three proposals were reviewed. The SCMDP helped evaluate the proposals, gave technical advice to the contractor selection committee, contributed to the orientation meeting held for potential contractors, and helped evaluate the three interim and final reports.

The SCMDP assisted in the preparation of the LCP Plan by proposing a testing configuration and size-scaling relations. The Program Plan, recommending testing at ORNL in a compact torus configuration, was approved by DMFE. SCMDP also participated in the LCP workshop in June.

To ensure wide industrial participation and a variety of candidate designs, the LCP requested proposals from industry for the conceptual design, detailed design, and construction of a test coil. The SCMDP assisted in preparing this Request for Proposal, particularly the section on required design and performance characteristics.

Work is under way to define the LCP test facility and to prepare a major Project Proposal for submission to ERDA. SCMDP personnel are participating in the effort, especially in setting the testing requirements and schedule and in matching the operation of the facility to the preexisting SCMDP helium refrigerator.

5.1.5 EBTR

In support of the EBTR Reference Design,[3,4] two versions of the magnet system were designed. One had 48 coils with a major radius of 60 m (EBTR-48), and the other had 24 coils with a major radius of 24 m (EBTR-24). Aside from the plasma constraints, the main goal was to design coils which could be built with existing technology. The main features of the design are as follows.

Conductor design

Monolithic NbTi superconductor was used. The average current density in the winding is 1500 A/cm^2; the peak field is 7.3 T. The conductor is cryostatically stabilized by soldering the NbTi-Cu composite to formed copper strips with punched slots that facilitate cooling.

Magnet design

The magnets are circular, pancake wound, and cooled by liquid helium in natural convection. As long as the ratio of major radius to the number of coils is fixed, the field strength produced by modular magnets of the same size is not sensitive to the size of the reactor. Thus, an important feature and advantage of an EBTR is that modular magnets may be used in reactors of different sizes and power ratings.

Protection

To ensure adequate protection by reducing the terminal voltage during discharge, a high operating current (25 kA) is used and four conductors (each carrying 6.25 kA) are connected in parallel. To avoid problems of uneven distribution of current, a spiral winding technique has been adopted. Voltage taps are used on each coil as the main quench detection device. Pickup coils on the current leads of the power supplies are used to compensate for the inductive voltage. External dump resistors are used as heat sinks.

5.1.6 EBT-II

Preliminary designs for a toroidal array of superconducting magnets for the proposed ELMO Bumpy Torus-II (EBT-II) plasma experiment have been developed to meet the following criteria provided by the High Beta Plasma Section:

- maximum field on torus minor axis 6.0 T
- minimum field on torus minor axis 3.0 T
- mirror ratio 2.0
- coil inner radius 15.2 cm (6 in.)
- x-ray heat load 1.0 W/coil.

The number of coils was to be maximized and the major radius minimized.

EBT-II has a very large aspect ratio and coil spacing compared to the TF coils of tokamaks, and the coils have only a small field asymmetry (about 2%). Therefore, in contrast to tokamak coils, the EBT-II coils can be axisymmetric and still have a favorable (i.e., nonbending) stress distribution without requiring special support precautions. The design effort also attempted to minimize the current density and the peak field in the windings. The following results evolved:

- winding outside radius 25.4 cm (10 in.)
- length 18.3 cm (7.2 in.)
- winding cavity current density 10 kA/cm^2
- maximum field 8 T
- number of coils 36
- torus major radius 3.05 m (10.ft).

Several analytic studies of the behavior of these magnets have been carried out, and it appears that the magnet system can be manufactured without encountering severe development problems. Some questions still remain about which design will yield the most reliable magnet system. Therefore, we intend to build four prototype coils, each of a different design, and test them to find the most reliable. The four magnets will be of the following types:

1) potted: NbTi in helium at subatmospheric pressure,
2) potted: hybrid NbTi-Nb_3Sn in helium at atmospheric pressure,
3) unpotted NbTi,
4) unpotted hybrid NbTi-Nb_3Sn.

The thermal studies indicate that the potted NbTi coils can operate at the estimated x-ray heat load; however, there is considerable doubt about the size of this heat load and about the thermal diffusivity of the coil, so the unpotted, ventilated prototypes are included. Potting was considered because of possible turn slippage due to (1) the 2% field asymmetry and (2) the possible addition of supplementary coils that would produce complicated stress patterns. The stress analysis systematically considered the problems of winding tension, bobbin thickness, and thermal contraction on cool-down, and it was concluded that the maximum hoop stress would be 90 MPa (13 ksi). The heat input to a coil due to superconductor hysteresis effects if its neighbor were to quench was calculated to be 11.7 J total, with a peak value of 980 mJ/cm^3. The maximum temperature reached in a quench was calculated to be 75 K, a safe value.

5.2 SMALL SCALE EXPERIMENTS

5.2.1 Pulsed Parallel Field

A series of experiments was carried out to examine losses in twisted multifilamentary composite superconductor when it is exposed to transient magnetic fields applied parallel to the longitudinal direction of the conductor. The usual practice of twisting the filaments of a composite conductor about its axis to decouple them from transient transverse magnetic fields enhances coupling (and thus the losses) in the presence of time-varying parallel fields. The TF coils of tokamak devices will be exposed to both transverse and parallel components of pulsed magnetic field over parts of their windings.

The most recent experimental results were reported by Miller and Shen at the 1976 Applied Superconductivity Conference in Palo Alto. This work demonstrated the difficulty of saturating the filaments of larger conductors when they carry no current and the ease of saturating the same conductors when they carry current near the critical value. Of course the latter case is the important one because any TF coil will be designed to operate at some large fraction of the critical current.

Because the interest of our program lies naturally with larger conductors, apparatus capable of examining larger conductors has been designed and is under construction. As in previous apparatus, the test conductor will be exposed to pulsed parallel fields by placing it inside a torus. Previously, however, the test conductor was wound into a thin solenoid and the torus was wound around it. In the apparatus being constructed, the torus is wound around a spool which can be rotated via a chain and sprocket to pull the test conductor in from the outside; thus, the torus need not be destroyed every time the sample is changed.

The torus windings of the new apparatus will be superconducting to allow a ramp and hold of the parallel field. The maximum parallel field component should be about 1.5 T and the maximum ramp rate should be about 3 T/sec if we use an available 30-V, 500-A motor-generator set to charge the torus. Controls for the set have already been designed and are ready for construction. The torus will initially be operated in a dewar inserted in a water-cooled copper solenoid that will provide a 6-T transverse field at the test conductor. Current to the test conductor will be provided through 5000-A, vapor-cooled leads.

5.2.2 Propagation and Stability Tests

Conductors cooled by boiling helium

Last year, calculations of propagation velocities that took into account current sharing and the temperature variation of the material properties of matrix and superconductor were carried out. These calculations were based on the restrictive assumption of a constant heat transfer coefficient. This year, this restriction was dropped, and full account is now taken of the temperature variation of the heat transfer at a copper-helium surface in the nucleate-boiling, transition, and film-boiling ranges. A new numerical method was developed to carry out the calculations. Comparison of the calculations with earlier measurements of Miller and Donaldson[5] indicates the need to include the effects of transient heat transfer in the calculations in order to achieve agreement between theory and experiment. An account of this work has been published in Cryogenics.

Measurements were undertaken to determine the stability of various composite conductors in realistic coil environments. The velocity of propagation or contraction of normal zones, the full recovery current, and the minimum propagating current were measured. The dependence of these quantities on background field, transport current, electrical insulation, cooling passage size and orientation, and proximity of other conductors was examined. The measured velocities of propagation were compared with those calculated with the theory mentioned above, and good agreement was achieved once an allowance was

made for transient heat transfer. This work was described in a paper given at the 1976 Applied Superconductivity Conference.

Propagation of Normal Zones in Composite Superconductors.[6] L. Dresner. This paper describes calculations of propagation velocities of normal zones in composite superconductors. Full account is taken of (1) current sharing, (2) the variation with temperature of the thermal conductivity of the copper matrix and the specific heats of the matrix and the superconductor, and (3) the variation with temperature of the steady-state heat transfer at a copper-helium interface in the nucleate-boiling, transition, and film-boiling ranges. The theory, which contains no adjustable parameters, is compared with experiments on bare (uninsulated) conductors. Agreement is not good. It is concluded that the effects of transient heat transfer may need to be included in the theory to improve agreement with experiment.

Investigation of Stability of Composite Superconductors in Typical Coil Configurations.[7] J. R. Miller, J. W. Lue, and L. Dresner. The stability of various composite conductor designs in realistic coil environments has been examined. We measure the velocity of propagation or contraction of a normal region, the full recovery current, and the minimum propagating current in a coil segment. We examine the dependence of these measurements on background field, transport current, electrical insulation, cooling passage size and orientation, and proximity of other conductors. Comparison of experiment and calculation provides indirect information about local heat transfer to the helium bath and direct information about safe operating current limits for particular coil designs.

Forced-cooled conductors

A computer program was written last year to calculate the temperature-time history of a uniformly pulse-heated NbTi-Cu conductor cooled by supercritical helium in forced convection. Using this program, one could find by trial and error the maximum sudden heat addition (ΔH) that still allowed recovery of the superconducting state. This year the program was improved by eliminating the trial and error feature, which resulted in an order of magnitude increase in the speed of the program. The faster running of the program allowed ΔH to be maximized by factorial search with respect to simultaneous variation of the helium volume fraction and the copper-to-superconductor ratio. Conductors with ΔH so maximized are called stability-optimized conductors; the use of these conductors in magnet design minimizes pumping power and pressure drop for a preassigned stability level ΔH. The design method based on these considerations was described in a paper given at the 1976 Applied Superconductivity Conference. Practical use of the method has already been made in aiding selection of forced-cooled conductors for purchase by the Magnetics and Superconductivity Section.

Stability-Optimized, Forced-Cooled, Multifilamentary Superconductors.[8] L. Dresner. A numerical program has been written to calculate the temperature-time history of a uniformly pulse-heated composite superconductor cooled by supercritical helium in forced convection. The program determines the maximum sudden temperature rise from which the conductor can still recover the superconducting state. The program includes the effects of (1) current sharing, (2) the temperature variation of the specific heat of both the matrix and the superconductor, and (3) the temperature variation of the heat transfer coefficient. Using this program, one may optimize forced-cooled conductors with respect to stability by simultaneously varying the copper-to-superconductor ratio and the metal-to-helium ratio. Use of stability-optimized conductors allows a given stability level to be maintained for a particular field and bath temperature and the pressure drop and pumping losses to be reduced.

5.2.3 Conductor Design and Tests

Conductor designs

NbTi conductor. Early this year a study of TF conductors was undertaken. A set of basic

criteria covering operating current, ac losses, stability, mechanical properties, and insulation requirements was established. Several conductor designs were proposed, and four of these – three pool-boiling and one forced-flow – were analyzed in detail and were shown to meet the projected needs of tokamak machines.

This study showed that the conductor geometry is strongly affected by ac loss requirements. They can be most easily met by using some form of cabling technique. The question of how this form of conductor construction affects stability was investigated by Fietz and Dresner, who examined current transfer between strands in a cable which were coupled either inductively or by a resistive matrix. Dresner studied the effect of the resistive matrix on stability in cables, some of the strands of which were composite superconductors and the remainder of which were pure copper.

As a result of these studies a specification (ORNL-7D-SP#192) detailing the performance expected of TF conductors was prepared. This specification formed the basis of a request for quotation (RFQ) that was submitted for competitive bidding. The RFQ did not specify conductor design, but asked the manufacturer to propose his own design, analyze it, and bid on a fixed price basis. In order to stimulate interest and innovative design, it was stated that ORNL might purchase other conductors in addition to the low bid if they were of sufficient interest. To guide the manufacturers, Fietz presented some conductor designs and analyses at the 1976 Applied Superconductivity Conference.

After receipt of conductor proposals in response to the RFQ, two pool-boiling conductors were ordered. Six hundred meters of each conductor (rated at 10,000 A in a perpendicular magnetic field of 8 T) were requested. Negotiations were also initiated for further development work on two forced-flow conductors and one additional pool-boiling conductor.

Nb_3Sn conductor. A mechanical testing program was carried out with the Metals and Ceramics (M&C) Division to characterize available multifilamentary Nb_3Sn. This program is described under the mechanical testing section.

Material which had previously been purchased in the form of a 7-strand cable was heat treated to optimize its performance, and a forced-flow Nb_3Sn conductor was designed on the basis of this cable. Initial experimental work necessary for its fabrication was performed.

A length of fine, unreacted multifilamentary Nb_3Sn wire was purchased for evaluation in pulsed coil operation. The preliminary design was completed for its use in a pool-boiling hybrid coil with NbTi cable in the low field regions and Nb_3Sn cable in the high field regions.

Discussions were begun with vendors for developmental work in the manufacture of Nb_3Sn forced-flow conductors for TF coils.

High Current Superconductors for Tokamak Toroidal Field Coils.[9] W. A. Fietz. Conductors rated at 10,000 A for 8 T and 4.2 K are being purchased for the first Large Coil Segment tests at ORNL. Requirements for these conductors, in addition to the high current rating, are low pulse losses, cryostatic stability, and acceptable mechanical properties. The conductors are required to have losses less than 0.4 W/m under pulsed fields of 0.5 T with a rise time of 1 sec in an ambient 8-T field. Methods of calculating these losses and techniques for verifying the performance by direct measurement are discussed. Conductors stabilized by two different cooling methods, pool-boiling and forced heli [illegible], have been proposed. Analyses of these conductors are presented, and proposed definitions and tests of stability are discussed. Mechanical property requirements (tensile and compressive) are defined, and test methods are discussed.

Mechanical tests

The studies of multifilament superconductors under mechanical load which were begun last year have continued through most of 1976. NbTi superconductors with both copper and aluminum matrixes have been studied, as well as a number of Nb_3Sn cables and monolithic conductors. The

results of this work have been reported in the literature.

Evidence has also been found for thermomechanical heat generation in NbTi composites. Preliminary results and calculations indicate that this heating may be comparable in magnitude to that due to magnetic hysteresis for a poloidal coil system.

The following are abstracts of papers published during the past year. (Other presentations were also given.[10-13])

Performance of Multifilamentary Nb_3Sn Under Mechanical Load.[14] D. S. Easton and R. E. Schwall. The critical current of a commercial multifilamentary Nb_3Sn conductor has been measured under the application of uniaxial tension at 4.2 K and following bending at room temperature. Significant reductions in J_c are observed under uniaxial loading. Results are presented for a monolithic conductor manufactured by the bronze-diffusion technique and for cable conductors formed by the tin-dip technique.

Thermomechanical Heat Generation in Copper and a Nb-Ti Superconducting Composite.[15] D. S. Easton, D. M. Kroeger, and A. Moazed. Heat generation via tensile stresses in both pure copper and a superconducting Nb-Ti composite was studied at 300 and 4.2 K. Linear thermoelastic behavior was found at room temperature but not at 4.2 K. At 4.2 K, stress levels on the order of 88 MPa and 0.1% strain produced energy losses of $1\text{-}2 \times 10^5$ J/m^3. When stress-cycled under adiabatic conditions, the composite showed a temperature increase with each cycle as a result of nonlinear (hysteretic) stress-strain behavior.

Stress-Induced Heating in Commercial Conductors and Its Possible Influence on Magnet Performance.[16] D. M. Kroeger, D. S. Easton, and A. Moazed. Calorimetric measurements show that significant amounts of heat are generated when a multifilamentary composite conductor is stressed in tension to levels expected to occur in large, high field magnet systems. When the stress on the conductor is repetitively cycled between zero and some maximum value, the amount of heat produced per cycle is constant after the first few cycles. Comparison is made between calorimetric determinations of heat injections and the work done on the specimen as indicated by stress-strain curves. Stress-strain curves for a number of commercial conductors indicate that the most important determinant of the magnitude of this effect is the choice of matrix material.

Measurement facilities

A short sample test facility comprising a 2000-A sample holder and a 7.9-T, 10-cm-bore, NbTi solenoid was put into operation for routine conductor testing. An additional 5000-A sample holder was constructed for testing conductor in the 8-T, 16-cm-bore, water-cooled copper solenoid. Conductor was purchased and tested and preliminary design completed for a 15-cm-bore, 5-cm-gap, split solenoid. The coil is designed to produce a central field of 7.8 T with the help of iron pole pieces. The maximum field in the windings will be 7.0 T. Clear access of 1-7/8 in. diam will be sufficient for testing of all conductors of LCS size.

5.2.4 Pulse (Poloidal) Coils

Poloidal field coil development by the SCMDP has been initially directed toward those aspects of the PF system which are device-independent, i.e., those areas in which work can be pursued independent of the detailed design of TNS. Given the limited resources available within the SCMDP for PF coil work, we feel that this approach has provided and will continue to provide the most usable information from the effort being expended.

Loss measurements

A pulse loss measurement system was completed. The system consists of fiberglass dewars, ramp power supply, Rogowski coils, and a PDP-12 computer. Test data are recorded and analyzed digitally. The method yields not only the total energy loss but also the loss voltage waveform.

Measurements have been performed on three different pulse coil systems.[17]

Discharging magnets may be a useful way of operating the poloidal coils in a tokamak fusion reactor. A discharge test has been performed on one pulse coil. The results have shown that the magnet can be discharged from 6.2 T at a rate of 10 T/sec without going normal. Filamentary hysteresis losses, coupling losses, eddy current losses in normal metal, and losses due to conductor motion have been individually identified and measured.

Pulse Loss and Voltage Measurements on Superconducting Magnets.[18] S. S. Shen and H. T. Yeh. This paper describes an electrical method for measuring pulse losses and compensated voltage in superconducting magnets. Test results from two pulsed solenoids were recorded and analyzed digitally by computer. Dependence of loss performance on B_{max} and $\dot{B}$ is studied. The effects of conductor motion and presence of normal metal on the loss performance are also discussed.

Experimental Simulation of Pulsed Field Losses in Tokamak Toroidal Field Coils.[19] J. R. Miller and S. S. Shen. Experiments have been carried out to measure loss in a twisted multifilamentary composite superconductor when exposed to a transient longitudinal field. We investigated the variation of losses both as a function of transverse applied field and of sample transport current. Losses are probed mainly by measurement of the dynamic resistivity of the sample during the longitudinal pulse. Experimental results are compared with theories for the zero transport current case. The extension of theory to include transport current is also discussed, and the impact on tokamak toroidal field coil design is considered.

Quench detection

A fault detection and protection scheme has been suggested, based on measurements of instantaneous loss voltages. Such a scheme has also been designed for the toroidal coil system of the EPR.[20]

Loss calculations in coils

A computer code named PLASS has been developed to calculate composite conductor losses in pulsed poloidal systems of tokamak machines.

A Computer Program to Calculate Composite Conductor Losses in Pulsed Poloidal Coil Systems.[21] W. H. Gray and J. K. Ballou. In the design of the cryogenic system and superconducting magnets for a poloidal field system in a tokamak fusion reactor, it is important to have an accurate estimate of the heat produced in the superconducting magnets as a result of the rapidly changing magnetic fields. Until recently, this estimate was obtained by assuming that the field and the time rate of change of the field were constant throughout the coil windings. A more accurate method of estimation involves integrating the losses over the coil windings, thus taking into account the spatial variation of the magnetic field. A computer code, PLASS (Pulsed Losses in Axisymmetric Superconducting Solenoids), has been written to perform this integration.

PLASS has been used to analyze the present design for the poloidal coil system of the ORNL Experimental Power Reactor (EPR). This design requires that superconductor hysteresis losses, superconductor coupling losses, stabilizing material eddy current losses, and structural material eddy current losses be taken into consideration in the calculation of conductor losses. A tabulation of individual losses vs variations in superconductor characteristics and coil current changes is presented to demonstrate the parameters which significantly affect the design. Results indicate that the total energy release into the cryogenic system is less than one-half of that predicted by the previously oversimplified calculation.

An Estimate of Thermoelastic Heat Production from Superconducting Composites in Pulsed Poloidal Coil Systems.[22] J. K. Ballou and W. H. Gray. In the design of the cryogenic system and superconducting magnets for the poloidal field

system in a tokamak, it is important to have an accurate estimate of the heat produced in superconducting magnets as a result of rapidly changing magnetic fields. A computer code, PLASS (Pulsed Losses in Axisymmetric Superconducting Solenoids), was written to estimate the contributions to the heat production from superconductor hysteresis losses, superconductor coupling losses, stabilizing material eddy current losses, and structural material eddy current losses.

Recently, it has been shown that thermoelastic dissipation in superconducting composites can contribute as much to heat production as the other loss mechanisms mentioned above. We discuss a modification of PLASS which takes into consideration thermoelastic dissipation in superconducting composites. A comparison between superconductor thermoelastic dissipation and the other superconductor loss mechanisms is presented in terms of the poloidal coil system of the ORNL Experimental Power Reactor Design.

Pulse coils

Two new coils were constructed to achieve maximum rate of rise in a design that would be scalable to large sizes.

ORPUS-1. ORPUS-1 (Oak Ridge Pulsed Solenoid), a reinforced, highly ventilated solenoid wound from copper-matrix, formvar-insulated, NbTi compacted cable, has been constructed and tested. The coil attained the design field of 4 T and can be charged at a rate of 2 T/sec (limited by the power supply only).

ORPUS-2. ORPUS-2, with the same structure as that of ORPUS-1, has been wound from solder-filled NbTi compacted cable. A number of heaters and voltage taps are embedded in the windings so that normal zone propagation can be studied and the recovery current determined.

ORPUS-1 — A Pulsed Superconducting Solenoid.[23] R. E. Schwall. The tokamak fusion reactors presently proposed require very large, pulsed, superconducting magnets for plasma breakdown and ohmic heating. These magnets are unique in their simultaneous requirements of high maximum field (B ≈ 7 T), high charging rate (B ≈ 7 T/sec), and bipolar operation. This paper describes the first of a series of magnets designed to develop the needed pulsed magnet technology.

ORPUS-1 is an 8-cm-bore, 25-cm-long solenoid wound of 11-strand, copper-matrix NbTi cable. The coil is designed to operate at 4.2 T at 2000 A and to be charged at 4 T/sec.

With the exception of compound stainless steel reinforcement, the structure is entirely nonmetallic. The coil is not potted and more than 50% of the conductor surface is exposed to helium. Data on dc and pulsed performance and on heat generation during pulsed operation are presented.

5.2.5 Instrumentation

Instrumentation work has been directed mostly toward mechanical and electrical measurements and data acquisition. Accomplishments include the development and evaluation of needed transducers that are not commercially available and the design of systems around data handling devices that are commercially available.

Mechanical measurements

Linear displacement transducers. Five moving coil differential transformers (MCDT) were fabricated and calibrated. Three of these units were installed and operated satisfactorily in the three-coil cluster test of the Princeton Large Torus TF coils at Princeton Plasma Physics Laboratory. As previously reported (period ending June 1, 1976) the MCDT exhibited a 1% increase in output when it was axially aligned parallel to a 6-T magnetic field and excited at 10 kHz by a commercial carrier amplifier-demodulator having a 4-Ω carrier output. This was due to vibrations of the transducer's windings caused by Lorentz forces. More recent experiments revealed that because of effective changes in the reactance of the primary winding, this error became larger and somewhat unpredictable when the transducer was excited by a 600-Ω source. The phase-angle dependence of this error signal was then determined, and a method was devised for reducing it to within ±0.3% for

any field up to 7.5 T at either ambient temperature or 4.2 K. A method was devised for correcting the transducer's temperature coefficient to within 1% for operation at either ambient temperature or 4.2 K.

Eddy current displacement transducer. An eddy current displacement transducer (ECDT) was developed to serve as a miniaturized comparison to the MCDT. Its intended uses are to measure small linear displacements in coils and to serve as a sensing device for bellows deflection in liquid helium pressure transducers. It differs from the MCDT in that the sensitive element is a copper (or other highly conductive nonmagnetic metal) slug, movable within two opposing coils operating at 2.7 MHz. The physical size of the first prototype is 0.95-cm diam by 5.1-cm length, the gaging range is 7.5 mm (±3.75 mm), linearity is ±2.5%, and sensitivity is 400 mV/mm. The device has not yet been tested in intense magnetic fields under liquid helium.

Expendable eddy current proximity transducer. An expendable eddy current proximity transducer has been developed for noncontacting measurements of small mechanical displacements in very high magnetic fields at ambient as well as cryogenic temperatures. It is intended for use in conductor motion studies and as a sensing element for diaphragm deflection in liquid helium pressure transducers. It is basically a modification of an earlier ORNL development (U.S. Patent No. 3-609-527) and differs from most of the commercial proximity transducers by containing no ferromagnetic material. It operates with the same electronic module used for the ECDT. The sensitivity (dc output) of the prototype was 150 mV/mm over a gaging range of 6.4 mm with a linearity of ±1.3%. It is suitable for use with any high conductivity metal surface such as copper or aluminum. It has not been tested in high magnetic fields under liquid helium.

Strain gages and cements. Platinum-tungsten gages were investigated for use in magnet testing and were found to have a considerably lower dR/dT at 4.2 K than Karma alloy gages. These gages need to be tested for low magnetoresistance and mechanical hysteresis before they are fully qualified for magnet use, however. Two strain gage cements, AE10 and AE15, obtained from Micro-Measurements Corporation, were found to be satisfactory for cryogenic use. They have the advantage of not requiring a high temperature cure, which is not feasible with large test pieces (e.g., large magnets).

Liquid helium pressure and flow. A product search for pressure and flow transducers suitable for use with liquid helium was conducted. While a few commercial devices appeared promising, none was found which clearly met all the requirements. Therefore, the development of a differential pressure transducer for use in intense magnetic fields was begun.

Electrical measurements

Coil current. A Rogowski coil with a novel coaxial bus arrangement for measuring dI/dT in a magnet coil was developed. The current flows through the center and back around the outside of the Rogowski coil in the coaxial bus to cancel the external field which would otherwise be induced. The entire device is enclosed in a heavy magnetic shield, the effectiveness of which is maximized by the cancellation of the induced external field. A prototype embodying the concept was fabricated and is in use in the pulsed coil program, where the amplified output of the Rogowski coil is subtracted from the magnet coil terminal voltage in order to yield the in-phase signal. The concept is also intended for use in toroidal coil tests where a similar subtraction will be made in order to detect the IR drop in normal zones.

Coil voltage. A voltage tap signal conditioning unit, quench detection circuit, and dump control unit were designed and fabricated. The voltage tap unit consists of a ten-channel, high-voltage isolation amplifier system with analog subtraction of dI/dT signals from Rogowski coils. The quench detection circuit produces a TTL logic signal when an IR signal

either instantaneously exceeds a preset high level or exceeds a preset lower level for a preset time. The dump control circuit takes the output of the quench detection circuit and the output of the comparators or other quench indicators (e.g., pressure transducers), and initiates a dump when given a TTL signal.

Data acquisition

A revised automatic data acquisition system was designed after an earlier proposed system was delayed by lack of capital funding. The revised system is designed to allow expansion to handle the LCP by addition of parallel processors with buffer memory. The parallel processors are microcomputers (LSI-11 or equivalent). An A/D unit on each of the outboard processors accesses the memory directly in order to achieve the necessary throughput.

A Moving-Coil Linear Variable Differential Transformer.[24] J. F. Ellis and P. L. Walstrom.

A moving coil linear variable differential transformer with no ferromagnetic components has been developed. The device retains all the advantages of the conventional moving coil linear variable differential transformer (high sensitivity and high output signal, infinite resolution, excellent linearity, and wide dynamic range) but is virtually unaffected by ambient magnetic fields up to 7.5 T. The sensitivity of the device was measured to be 18 mV/mm/V. Linearity was determined to be ±0.1% and 1% over 1-cm and 2-cm gaging ranges, respectively, when the transducer was excited by a commercial carrier amplifier unit at an excitation level of 5 V rms at 10 kHz.

Controlled Thermonuclear Fusion Reactors.[25] P. L. Walstrom.

Controlled production of energy by fusion of light nuclei has been the goal of a large portion of the physics community since the 1950's. In order for a fusion reaction to take place, the fuel must be heated to a temperature of 100 million °C. At this temperature, matter can exist only in the form of an almost fully ionized plasma. In order for the reaction to produce net power, the product of the density and energy confinement time must exceed a minimum value of 10^{20} sec m^{-3}, the so-called Lawson criterion. Basically, two approaches are being taken to meet this criterion: inertial confinement and magnetic confinement. Inertial confinement is the basis of the laser fusion approach; a fuel pellet, imploded by intense laser beams from all sides, ignites. Magnetic confinement devices, which exist in a variety of geometries, rely upon electromagnetic forces on the charged particles of the plasma to keep the hot plasma from expanding. Of these devices, the most encouraging results have been achieved with a class of devices known as tokamaks. Recent successes with these devices have given plasma physicists confidence that scientific feasibility will be demonstrated in the next generation of tokamaks; however, an even larger effort will be required to make fusion power commercially feasible. As a result, emphasis in the controlled thermonuclear research program is beginning to shift from plasma physics to a new branch of nuclear engineering which can be called fusion engineering, in which instrumentation and control engineers will play a major role. Among the new problem areas they will deal with are plasma diagnostics and superconducting coil instrumentation.

Cryogenic Instrumentation Needs in the Controlled Thermonuclear Research Program.[26] P. L. Walstrom.

The magnet development effort for the controlled thermonuclear research program will require extensive testing of superconducting coils at various sizes from small-scale models to full-size prototypes. Extensive use of diagnostic instrumentation will be necessary to make detailed comparisons of predicted and actual performance in magnet tests and to monitor the test facility for incipient failure modes. At later stages of the program, cryogenic instrumentation will be needed to monitor magnet system performance in fusion power reactors. Measured

quantities may include temperature, strain, deflection, coil resistance, helium coolant pressure and flow, current, voltages, etc. The test environment, which includes high magnetic fields (up to 8-10 T) and low temperature, makes many commercial measuring devices inoperative or at least inaccurate. In order to ensure reliable measurements, careful screening of commercial measuring devices for performance in the test environment will be required. A survey of potentially applicable instrumentation is presented, along with available information on operation in the test environment, based on experimental data or on analysis of the physical characteristics of the device. Areas where further development work is needed are delineated.

5.3 LARGE COIL EXPERIMENTS

5.3.1 Large Coil Segment Test

The Large Coil Segment test was conceived in 1976 as a test stand for the LCP-TNS generation of high current (10-20 kA) composite conductors and for winding designs using these conductors. It will provide essential data on the limits of cryostability of these conductors on a physically meaningful scale and thus will provide information which cannot be obtained by short sample or small magnet tests.

The facility is designed to accommodate test coils up to ∿3 m in diameter of either modified-D, oval, or circular shape, with a winding cross section of up to 12 × 20 cm with up to ∿60 turns. The test coil winding will be subjected to a total field of ∿7 T over a 0.6-m length, the background field being provided by a set of superconducting Nb_3Sn tape coils obtained from the old IMP plasma physics facility and rearranged in a new configuration. The coils were successfully tested in their old configuration to 95% of short sample critical current with no damage. A bell-jar vacuum will be provided by a vacuum tank salvaged from the ORMAK facility and modified by addition of a 1.22-m-diam cylindrical extension at the top hatch of the lid. The tank, along with test coil, background coils, and support structure, is shown in Fig. 5.1.

On October 1, 1976, a conceptual design and proposal were completed by Design Engineering and SCMDP personnel. The proposal was not submitted as a separate formal proposal because at that time it was decided to include the LCS facility in the overall LCP facility. The conceptual design included field and force calculations, mechanical structure design, cryogenic design, electrical system design, vacuum system design, a facility instrumentation design, and an overall layout.

On the basis of conductors which were ordered (see Sect. 5.2.3) or under consideration, winding schemes for five test coils were laid out. Detail design of the coils and bobbins was initiated.

5.4 PROJECTS BASED ON DISCIPLINES

5.4.1 Protection Analysis and Eddy Current Calculations

Protection analysis

Quench detection.[27] An electrical method for measurement of ac loss voltages has been developed to compensate for the large inductive voltages caused by charging and discharging of magnets. A pickup coil is placed at the current leads of each power supply. Loss voltages as small as 0.1% of the inductive voltage have been detected.

Coil interaction and protection. We have studied the mutual interaction between toroidal and poloidal coils during normal and fault conditions and the effect of plasma discharge on the first wall as a result of coil quenches. Temperature rise, induced voltage, and mechanical load on coils due to their mutual interaction have been computed. For the Oak Ridge EPR design, connecting symmetrically located TF coils in groups and isolating and discharging only the faulty coils result in satisfactory discharge voltages and temperature rises in the coil.

The Interaction and Protection of Superconducting Poloidal Field Coils and Toroidal Field Coils in a Tokamak Experimental Power Reactor.[28] H. T. Yeh and J. W. Lue. The

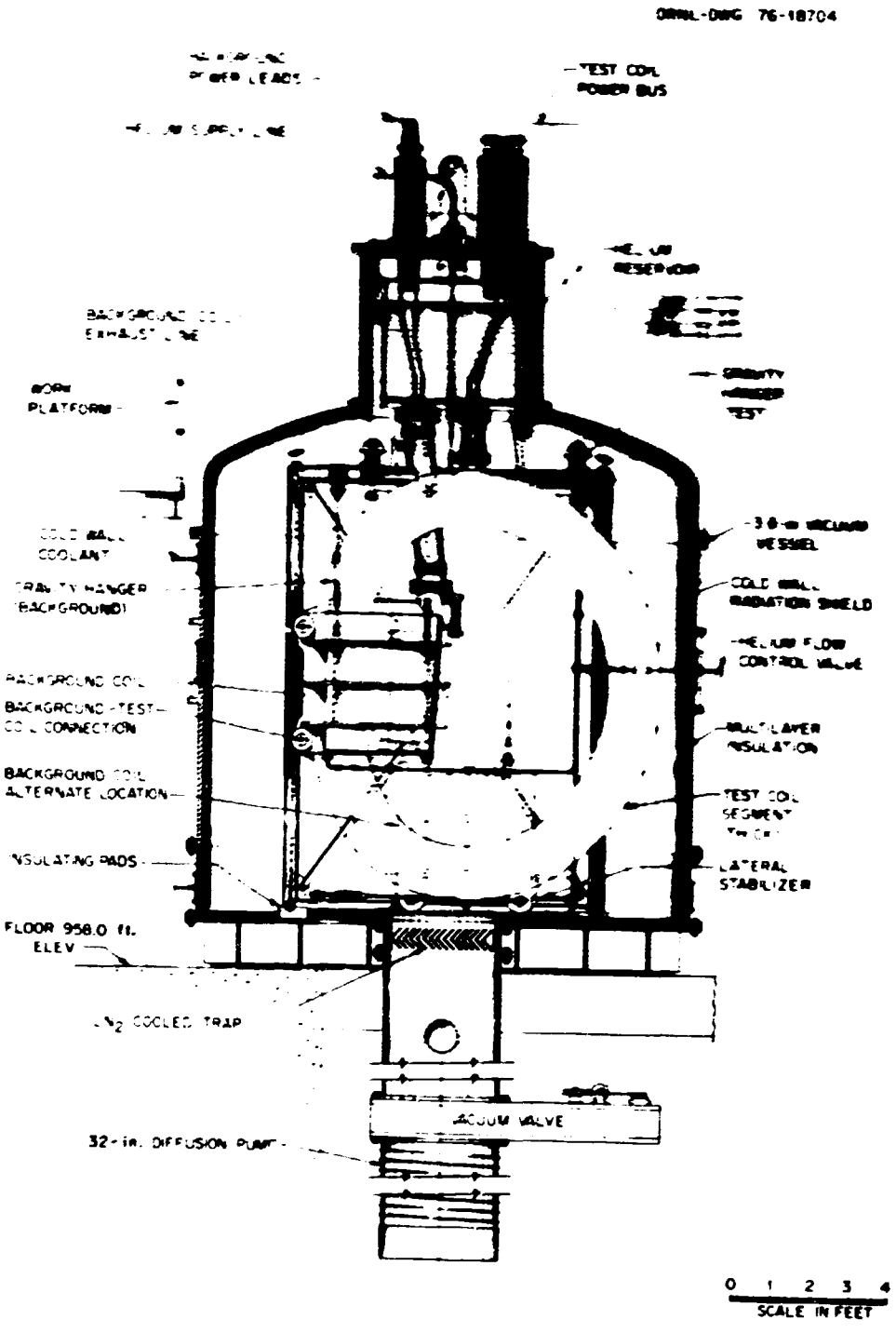

Fig. 5.1. Large Coil Segment test facility.

protection problems of superconducting coils in a large tokamak device are delineated. Effects of the plasma discharge on the first wall, the induced voltage, and the temperature rise during the quench of a superconducting coil, as well as the mechanical load on coils due to their mutual interaction under normal or fault conditions, are discussed. Various design choices and protection schemes are used to ensure the integrity of the coils during quench. For the Oak Ridge EPR design, a scheme of connecting symmetrically located toroidal field coils in groups and isolating and discharging the faulty coil only gives satisfactory results.

Eddy current calculations

A 2-D computer code has been developed to solve axially symmetrical eddy current problems, including those in which iron is present. Rapid relaxation is achieved by combining coarse and fine lattices in the transition region between air and iron. The program can be run interactively on a time sharing computer.

Eddy current codes have also been developed for thin, nonmagnetic rectangular plates and cylinders of finite length. The transient eddy current was found by solving the integro-differential equation in the form of a perturbation expansion with separated time dependence. No reference to field values outside the conductor is required. The time variation of the driving field is fitted by a polynomial in time. The effects of the boundary charges in modifying the eddy current pattern are taken into account.

A Two-Dimensional Relaxation Program for Systems with Inhomogeneous Permeability.[29] W. E. Deeds and C. V. Dodd. A computer program is presented and explained which will solve axially symmetric eddy current problems, including those with permeable media present. An unusual feature is the combination of coarse and fine lattices, which permits rapid relaxation of coarse lattices in homogeneous regions to be combined with more accurate calculations using a fine lattice in the transition regions where the permeability varies. Although the actual program listed is restricted to coils encircling a coaxial metal rod, the program can be modified to include any axially symmetric configuration.

A Perturbation Expansion with Separated Time Dependence for Eddy Current Calculations.[30] K. H. Carpenter and H. T. Yeh. A particular solution to the eddy current integro-differential equation is found in the form of a perturbation expansion with separated time dependence. No reference to field values outside the conductor is required and a full three-dimensional treatment is maintained. Transient behavior of the eddy currents is obtained by this method through a technique of fitting the time variation of the driving field with a polynomial in time. As an example, the case of a thin plate of constant conductivity is studied. The eddy current distribution is obtained as a function of time for the external magnetic field of a dipole having ramp time dependence and with the dipole axis perpendicular to the plate. The effects of the boundary charges in modifying the eddy current pattern are illustrated.

Eddy Current Calculations for Thin Cylinders of Finite Length with Driving Fields of Ramp Time Dependence.[31] K. H. Carpenter and H. T. Yeh. Eddy current density for a thin cylinder of finite length is calculated for the case of a driving field of ramp time dependence and dipole spatial dependence, the dipole being at the center of the cylinder. The calculations are made by using a perturbation expansion of the eddy current integral equations with a polynomial approximation to the time factor of the driving term. The steady-state solution, presented as an arrow plot, shows the effects of edge charges forcing currents to remain within the conductor. The transient solutions show that the entire geometrical pattern of the steady-state eddy currents is approached uniformly in the typical exponential manner of diffusion equations. Typical transient curves are given. All calculations are in normalized coordinates to allow maximum flexibility in applications.

FORTRAN Programs for Transient Eddy Current Calculations Using a Perturbation-Polynomial Expansion Technique.[32] K. H. Carpenter. A description is given of FORTRAN programs for transient eddy current calculations in thin, nonmagnetic conductors using a perturbation-polynomial expansion technique. Basic equations are presented as well as flow charts for the programs implementing them. The implementation is in two steps – a batch program to produce an intermediate data file and interactive programs to produce graphical output. FORTRAN source listings are included for all program elements, and sample inputs and outputs are given for the major programs.

5.4.2 Structural Analysis and Material Tests

Structural analysis

The structural analysis portion of the program concerns itself with analysis of magnetic fields, electromagnetic forces, and structural response of electromagnetic devices. Major accomplishments were achieved in five areas:

1) the development and refinement of an analytical solution for the mechanical response of a transversely isotropic solenoid;
2) the implementation of computer code GFUN-3D;
3) the completion of a photoelastic analysis of TF coils;
4) the numerical approximation of superconducting losses in solenoids of the ORNL EPR poloidal coil system by using the finite element method; and
5) the implementation of the GIFTS-IV computer code.

The details of these projects are discussed individually in the following sections.

W. H. Gray attended the GIFTS-IV workshop at the University of Arizona during the week of June 9, 1976. Subsequently, the GIFTS-IV computer program was implemented on the FED PDP-10. The GIFTS-IV system is a collection of program modules operating on a unified data base (UDB) designed to facilitate finite element analysis using modern data management techniques. It is a significant improvement over its predecessor, GIFTS-II.

ORNL participated in the meeting organized by Brookhaven National Laboratory on structural analysis needs in superconducting magnets. Five ORNL staff members from the Fusion Energy, Metals and Ceramics, and Engineering Divisions were present. W.C.T. Stoddart and W. H. Gray represented the Magnetics and Superconductivity Section. Sessions were chaired by C. R. Brinkman and W.C.T. Stoddart; Stoddart also presented an overview of the ORNL magnet structural analysis efforts.

The GFUN-3D computer program has been acquired from the Rutherford High Energy Laboratory in England. This computer program will perform a three-dimensional magnetostatic field analysis including the nonlinear effects due to ferromagnetic material. The code has been converted to account for the differences in the ORNL and Rutherford computational environment. C. W. Trowbridge and J. Simkin of Rutherford Laboratory assisted W. D. Cain in the implementation and check-out of this code. It is currently being used to calculate the influence of iron on the magnetic field of several electromechanical devices under design at ORNL.

D. L. Levine and W. H. Gray modified the STANSOL-II[33] computer program to augment the output with a sequence of computer plots which present the computed values in a concise form. The augmented version of the code is referred to as STANSOL-IIP (LOT). To facilitate the use of STANSOL-IIP (or -II), a preprocessor code, STNDAT, was also developed. This code interactively accepts input data about the geometry, material properties, and electrical characteristics of a solenoid and creates an input data file in a format acceptable to STANSOL-IIP.

These codes were extensively used during the EBT-II design studies discussed elsewhere in this report. Also, structural analysis and

design guidance were provided for the LCS, LCP, TMS, ISX, and ORMAK upgrade projects.

Our interest in graphical representation of the voluminous input and output data required and produced during magnetic and structural analysis has led to the modification of several graphic software libraries. These libraries, LSLTEK, LSLVEC, VECTEK, CALVEC, CALCO8, DISVEC, and DISCO8, are used routinely by users of the FED PDP-10. The last two programs represent the most important contribution, as they are the back end to the display graphics package.

Electromechanical Stress Analysis of Transversely Isotropic Solenoids.[34] W. H. Gray and J. K. Ballou. The mechanical behavior of superconducting magnets deviates from isotropy due to their construction techniques, which involve layering superconductor, insulation, and sometimes structural reinforcement within the windings. Previous mechanical analyses considered the windings of a magnet to behave isotropically. This paper describes an analytical solution for deflection, stress, and strain of axisymmetric, electromechanically loaded, and rotationally transversely isotropic solenoids. The results indicate that for magnets with a large radial build compared to inner radius, transverse isotropy has a dramatic effect; for magnets with a small radial build compared to inner radius, transverse isotropy has a negligible effect.

Photoelastic Analysis of Stresses in Toroidal Magnetic Field Coils.[35] H. Pih. Several two-dimensional photoelastic stress analyses were made on models of circular and oval toroidal magnetic field coils for fusion reactors. The circumferential variation of each coil's in-plane magnetic force has been simulated by applying different pressures to 15 segmented regions of the inner surface of the models. One special loading fixture was used for the model of each shape and size. Birefringence and isoclinic angles were measured in a transmission polariscope at selected points on the loaded model. Boundary stresses in the cases of known boundary conditions were determined directly from the isochromatics. Separate principal stresses were calculated using the combination of photoelastic information and isopachic data obtained by the electrical analogy method from the solution of Laplace's equation. Comparisons were made between experimental results and those computed using the finite element method. The theoretical and experimental stress distributions agree very well, although the finite element method yielded slightly higher stresses than the photoelastic method; further work is needed to resolve this difference. In this investigation several variations of coil geometry and several methods of support were evaluated. Based on experimental results, optimum structural designs of toroidal field coils were recommended.

Experience in the Use of Static SAP to Structurally Analyze Electromechanical Systems.[36] W. D. Cain and W.C.T. Stoddart. A large-scale effort is presently being undertaken to design and construct large electromechanical systems for use in controlled thermonuclear research machines, energy storage devices, and related systems. One of the major thrusts of this effort is directed toward the evaluation of stresses and deformations in toroidal field coils which are induced by electromagnetic body forces, differential temperatures, winding preloads, and other forces. The purpose of this paper is to describe some of the work which has transpired in the Fusion Energy and Engineering Divisions of Oak Ridge National Laboratory in the area of structural analysis of toroidal field coils. Basically, this paper describes the tools which have been developed to aid in the structural design analysis of electromechanical systems (in particular, TF coils) and relates some of the experiences encountered in the utilization and implementation of these tools.

Finite Element Calculation of Stress-Induced Heating of Superconductors.[37] J. E. Akin and A. Moazed. This research is concerned with the calculation of the amount of heat generated due to the development of mechanical stresses in superconducting composites. An empirical equation is used to define the amount of stress-induced heat generation per

unit volume. The equation relates the maximum applied stress and the experimentally measured hysteresis loop of the composite stress-strain diagram. It is utilized in a finite element program to calculate the total induced heat generation for the superconductor. An example analysis of a solenoid indicates that the stress-induced heating can be of the same order of magnitude as eddy current effects.

Materials evaluation

The materials evaluation portion of the SCMDP concerns itself with the properties of all materials except the conductor. The bulk of the effort has been directed at metallic primary structural materials (design studies) and at organics for both electrical insulation and potting applications (experimental work).

The primary structure work, which involved extensive liaison with other parts of the SCMDP, ORNL, and the ERDA fusion community, has been summarized in a technical memorandum.[38] C. J. Long was appointed secretary of an ERDA-DMFE Task Group on Special Purpose Materials for fusion reactors and continued as a member of ASTM-ASME-MPC Joint Committee J1.06, Low-Temperature Effects on Materials Properties.

During 1976 a series of tests of mechanical properties was conducted at room and cryogenic temperatures on potential insulation systems and potting compounds by K. J. Froelich (who left ORNL in September) and C. M. Fitzpatrick. A report on the results of tensile tests of insulators is in preparation.

A program to measure the radiation resistance of electrical insulators in liquid helium was formulated by C. J. Long (now Metals and Ceramics Division) and R. H. Kernohan (Solid State Division). This program, which will be conducted in the Low Temperature Irradiation Facility at the Oak Ridge Bulk Shielding Reactor, will measure degradation of both mechanical and electrical properties beginning in 1977.

A final report entitled "A Review of Electrical Insulation in Superconducting Magnets for Fusion Reactors" was prepared for ORNL by Magnetic Engineering Associates. The report concludes that significant radiation damage might be expected in organic insulators in a fusion reactor during its lifetime. No appreciable damage is expected in inorganic insulators.

Structural Materials for Large Superconducting Magnets for Tokamaks.[39] C. J. Long. The selection of structural materials for large superconducting magnets for tokamak fusion reactors is considered. The important criteria are working stress, radiation resistance, electromagnetic interaction, and general feasibility. The most advantageous materials appear to be face-centered-cubic alloys in the Fe-Ni-Cr system, but high-modulus composites may be necessary wher severe pulsed magnetic fields are present. Special purpose structural materials are considered briefly.

Lap Shear Strength of Selected Adhesives (Epoxy, Varnish, B-Stage Glass Cloth) in Liquid Nitrogen and at Room Temperature.[40] K. J. Froelich and C. M. Fitzpatrick. The lap shear strengths of several adhesives were measured in liquid nitrogen and at room temperature. The adhesives included several epoxy resins, a varnish, and a B-stage glass cloth (a partially cured resin in a fiberglass cloth matrix). Several parameters critical to bond strength were varied: adhesive and adherend differences, surface preparation, coupling agents, epoxy thickness, fillers, and bonding pressure and temperature. The highest lap shear strengths were obtained with B-stage glass cloth at both liquid nitrogen and room temperatures with values of approximately 20 MPa (3000 psi) and 25.5 MPa (3700 psi), respectively.

5.4.3 Fabrication Development

A large coil winding facility was constructed in the Y-12 Plant Electric Shop. Preliminary shakedown winding using a round bobbin was carried out and the operating characteristics of the winding equipment were evaluated. Some additions and refinements have since been made in the equipment. A variable speed motor drive and controls have

been procured for the winding table. Elevating mechanisms have been installed on both the tensioner and dereeler. Extensive alterations in the drive and controls of the dereeler have been made. Also, a prototype automatic winding clamp for keeping the windings compressed is in the shop and near completion. Before any practice winding could be done with the revised equipment it was necessary to relocate from the Y-12 Plant Electric Shop to Building 9201-4. An oval bobbin is now available for practical winding; it will help identify problem areas associated with fabricating LCP coils. The equipment will be used to wind the large coil segments.

The coil fabricating laboratory in Building 9204-1 now has equipment for winding coils up to 1.5 m in diameter. A very accurate tensioner (2%) has been developed for maintaining a conductor tension of up to 100 kg while winding. Several small superconducting coils for the pulsed poloidal coil project have been wound using this equipment.

A novel method of winding fat toroidal coils was develcped for the pulsed parallel field experiment. The winding is laced in and has no splices at all, a feature which is especially important in winding superconductors. Also, the major axis can be filled completely with conductors, thus obtaining the maximum possible number of ampere turns. These requirements cannot be met with industrial equipment. This method of lace winding may have applications in remote winding and unwinding (for example, of radiation damaged PF coils in fusion reactors). For the pulsed parallel field experiment, an inner spool inside the toroidal coil can be rotated for winding and unwinding conductor samples to be tested without disturbing the toroidal coil.

5.5 PROJECTS REQUIRING WORK BY SUBCONTRACTORS

5.5.1 Forced-Cooled Magnets*

A study[1,2] was conducted that concluded that economic cooling systems of forced-cooled superconducting magnets must employ efficient cold pump recirculators in which the flow to the magnets is confined to the cold end of the refrigeration column. This holds true if the liquid pump efficiency is 40% or greater.

Tests have been performed and results reported[3-5] measuring the stability of two types of forced-flow-cooled NbTi filament conductors. The tests were successful in that they demonstrated experimental results to be equal to or better than theoretically predicted conductor behavior during a recovery from a localized quench. Test measurements included voltage drop, helium discharge temperature, and pressure drop across the coil. Triplex wire conductor proved superior to grooved wire. Testing will continue with a modified version of the triplex wire cable.

A 1-m-scale test of a racetrack coil of NbTi filament superconductor has been designed for operation late in 1977. Five kilometers of NbTi superconductor wire have been received and a contract for fabrication of the coil is being negotiated. Construction of the installation site at the Francis Bitter National Magnet Laboratory has started and component parts of the test loop have been ordered. All components are expected for delivery by June 1977.

An additional contract to be supervised by ORNL has been signed with ERDA to evaluate the feasibility of Nb_3Sn forced-flow conductors.

5.5.2 Helium Refrigerator and Handling System

Helium refrigerator and reliquefier

A contract has been awarded to purchase a helium reliquefier and refrigerator from Cryogenic Technology, Incorporated, Waltham, Massachusetts. The refrigerator has the capacity to produce 0.0045 kg/sec of liquid helium and 866 W of refrigeration simultaneously at 3.56 K and 0.5 atm. This refrigerator and the liquid helium system connected with it should have the capacity to supply helium

*Subcontract with the Francis Bitter National Magnet Laboratory, MIT.

coolant to the first phase of operation of the Large Coil Project.

The refrigerator has a two-stage, oil-lubricated, rotary-screw compressor. The low pressure stage is rated at 400 hp and can operate with a 0.4-atm suction (0.5 atm at the return inlet to the coldbox). The high pressure stage has a 1000 hp motor. The overall compression ratio is about 35 to 1 for the two stages. Delivery is expected by July 1, 1977 and operation by January 1, 1978.

Liquid helium handling system

The liquid helium system associated with the refrigerator consists of an 18,000 liter (5000 gal) liquid helium storage dewar, a transfer line which will connect to the experiment and to the laboratory, helium gas storage capacity for an equivalent of 7200 liters of liquid, and gas lines to and from the compressor. Additional storage of gas, when required, will be supported by portable helium tanks. Detailed design of the liquid helium handling system is being carried out by the Engineering Division with the assistance of a subcontract architect-engineer chosen by ERDA.

---

1. Abstract of ORNL/TM-5574, Oak Ridge National Laboratory, Oak Ridge, Tennessee (1976).
2. Abstract of paper presented at the 1976 Applied Superconductivity Conference, Palo Alto, California, August 17-20, 1976.
3. D. G. McAlees, N. A. Uckan, E. S. Bettis, P. B. Burn, C. L. Hedrick, D. B. Nelson, R. T. Santoro, H. L. Watts, H. T. Yeh, L. M. Lidsky, D. A. Ehst, A. Pant, J. S. Herring, D. L. Kaplan, and R. E. Potok, "The ELMO Bumpy Torus Reactor," paper presented at the 2nd Topical Meeting on the Technology of Controlled Thermonuclear Fusion, Richland, Washington, September 21-23, 1976.
4. D. G. McAlees, N. A. Uckan, E. S. Bettis, P. B. Burn, C. L. Hedrick, D. B. Nelson, R. T. Santoro, H. L. Watts, H. T. Yeh, L. M. Lidsky, D. A. Ehst, A. Pant, J. S. Herring, D. L. Kaplan, and R. E. Potok, *The ELMO Bumpy Torus Reactor (EBTR): Reference Design*, ORNL/TM-5669, Oak Ridge National Laboratory, Oak Ridge, Tennessee (November 1976).
5. L. Dresner, J. R. Miller, and G. W. Donaldson, "Propagation of Normal Zones in Composite Superconductors," paper presented at the 6th Symposium on Engineering Problems of Fusion Research, San Diego, California, November 18-21, 1975.
6. Abstract of paper published in Cryogenics 16, 675 (1976); see also ORNL/TM-5543.
7. Abstract of paper presented at the 1976 Applied Superconductivity Conference, Palo Alto, California, August 17-20, 1976; see also ORNL/TM-5637.
8. Abstract of paper presented at the 1976 Applied Superconductivity Conference, Palo Alto, California, August 17-20, 1976; see also ORNL/TM-5637.
9. Abstract of paper presented at the 1976 Applied Superconductivity Conference, Palo Alto, California, August 17-20, 1976.
10. D. S. Easton and D. M. Kroeger, "Temperature Increases in Superconductivity Composites as a Result of Tensile Strain," Fall Meeting, AIME, Niagara Falls, New York, September 20-23, 1976.
11. D. S. Easton, "Stress Effects on the Current Densities of Commercial Conductors at 4.2 K in Magnetic Fields," paper presented at the 1976 Applied Superconductivity Conference, Palo Alto, California, August 17-20, 1976.
12. D. S. Easton, "Stress Effects on Mechanical and Superconducting Properties of Commercial Conductors at 4.2 K," paper presented at the 3rd NBS-ARPA Workshop, Vail, Colorado, April 5-6, 1976.
13. D. S. Easton, "The Effect on Critical Current of Tensile Stress in Nb_3Sn and NbTi Superconducting Composites," paper presented at the Spring Meeting, AIME, Las Vegas, Nevada, February 22-26, 1976.
14. Abstract of paper published in Appl. Phys. Lett. 29, 319 (September 1976).

15. Abstract of paper published in Appl. Phys. Lett. 29, 382 (September 1976).
16. Abstract of paper presented at the 1976 Applied Superconductivity Conference, Palo Alto, California, August 17-20, 1976.
17. W. H. Gray et al., *Papers on ac Losses and Pulsed Coils Submitted to the Applied Superconductivity Conference*, ORNL/TM-5635, Oak Ridge National Laboratory, Oak Ridge, Tennessee (August 1976).
18. Abstract of paper presented at the 1976 Applied Superconductivity Conference, Palo Alto, California, August 17-20, 1976; see also ORNL/TM-5635.
19. Abstract of paper presented at the 1976 Applied Superconductivity Conference, Palo Alto, California, August 17-20, 1976; see also ORNL/TM-5635.
20. H. T. Yeh and J. W. Lue, *The Interaction and Protection of Superconducting Poloidal Field Coils and Toroidal Field Coils in a Tokamak* EPR, ORNL/TM-5542, Oak Ridge National Laboratory, Oak Ridge, Tennessee (September 1976).
21. Abstract of paper presented at the 1976 Applied Superconductivity Conference, Palo Alto, California, August 17-20, 1976; see also ORNL/TM-5635.
22. Abstract of paper presented at the 2nd ANS Topical Meeting on the Technology of Controlled Thermonuclear Fusion, Richland, Washington, September 21-23, 1976; see also ORNL/TM-5661.
23. Abstract of paper presented at the 1976 Applied Superconductivity Conference, Palo Alto, California, August 17-20, 1976; see also ORNL/TM-5635.
24. Abstract of paper to be published in Rev. Sci. Instrum.
25. Paper submitted at the ISA International Conference and Exhibit, Houston, Texas, October 11-14, 1976.
26. Paper submitted at the ISA International Conference and Exhibit, Houston, Texas, October 11-14, 1976; see ORNL/TM-5596.
27. S. S. Shen and H. T. Yeh, "Pulse Loss and Voltage Measurements on Superconducting Magnets," paper presented at the 1976 Applied Superconductivity Conference, Palo Alto, California, August 17-20, 1976; see also ORNL/TM-5635, Oak Ridge National Laboratory, Oak Ridge, Tennessee (December 1976).
28. Abstract of ORNL/TM-5542, Oak Ridge National Laboratory, Oak Ridge, Tennessee (September 1976).
29. Abstract of ORNL/TM-5333, Oak Ridge National Laboratory, Oak Ridge, Tennessee (June 1976).
30. Abstract of ORNL/TM-5652, Oak Ridge National Laboratory, Oak Ridge, Tennessee (December 1976).
31. Abstract of ORNL/TM-5652, Oak Ridge National Laboratory, Oak Ridge, Tennessee (December 1976).
32. Abstract of ORNL/CSD/TM-18, Oak Ridge National Laboratory, Oak Ridge, Tennessee (November 1976).
33. N. E. Johnson, W. H. Gray, and R. A. Weed, "Stress Analysis of Non-Homogeneous, Transversely Isotropic Superconducting Solenoids," paper presented at the 6th Symposium on Engineering Problems of Fusion Research, San Diego, California, November 18-21, 1975.
34. Abstract of paper accepted for publication in J. Appl. Phys., 1976.
35. Abstract of ORNL/TM-5724, Oak Ridge National Laboratory, Oak Ridge, Tennessee (February 1977).
36. Abstract of paper presented at the 1st SAP User's Conference, University of Southern California, Los Angeles, California, June 9-11, 1976.
37. Abstract of paper presented at the 1976 Applied Superconductivity Conference, Palo Alto, California, August 17-20, 1976; see also ORNL/TM-5635.
38. C. J. Long, ORNL/TM-5632, Oak Ridge National Laboratory, Oak Ridge, Tennessee (December 1976).
39. Abstract of ORNL/TM-5632, Oak Ridge National Laboratory, Oak Ridge, Tennessee (December 1976).

40. Abstract of ORNL/TM-5658, Oak Ridge National Laboratory, Oak Ridge, Tennessee (1976).

41. Adrian Bejan, "Refrigeration for Forced-Cooled Large Superconducting Magnets," paper presented at the ASME National Meeting, New York, New York, December 12-15, 1976.

42. Adrain Bejan and M. O. Hoenig, "Refrigeration Costs for Forced-Cooled Superconducting Magnets," paper presented at the 1976 Applied Superconductivity Conference, Palo Alto, California, August 17-20, 1976.

43. M. O. Hoenig, Y. Iwasa, D. B. Montgomery, and A. Bejan, "Supercritical Helium Cooled, Cabled, Superconducting Hollow Conductors for Large High Field Magnets," Paper I-9, presented at the International Cryogenics Engineering Conference, Grenoble, France, April 1976.

44. Y. Iwasa, M. J. Lupold, J.E.C. Williams, "Stabilization of Large Superconducting Magnets: Experimental Models," paper presented at the 1976 Applied Superconductivity Conference, Palo Alto, California, August 17-20, 1976.

45. Y. Iwasa, M. O. Hoenig, and D. B. Montgomery, "Cryostability of a Small Superconducting Coil Wound with Cabled Hollow Conductor," paper presented at the 1976 Applied Superconductivity Conference, Palo Alto, California, August 17-20, 1976.

BLANK PAGE

6. THE NEXT STEP (TNS) PROGRAM

M. Roberts, Manager

*S. E. Attenberger[1]
*J. K. Ballou[2]
E. S. Bettis[3] (EPR)
E. H. Bryant[4] (EPR)
J. S. Butts
*R. N. Cherdack[5]
Engineering Design Team[6]
C. A. Flanagan[6]
*P. N. Haubenreich[7]
*T. J. Huxford[4] (EPR)
G. A. Krist[6]
*C. G. Lawson[2] (EPR)
*J. W. Lue[2]
*F. B. Marcus[8]
*J. May[9]
*D. G. McAlees[8,10]
*H. E. McCoy[11]
*A. T. Mense[8]
*Y-K. M. Peng[8]
*J. A. Rome[8]
*R. T. Santoro[12]
*G. Schilling[13]
*J. L. Scott[11] (EPR)
*T. E. Shannon[4]
P. T. Spampinato[9]
*W.C.T. Stoddart[2,4]
*M. A. Uckan[8]
*J. S. Watson[14]
H. L. Watts[4] (EPR)
*F. W. Wiffen[11] (EPR)
*W. B. Wood[4]
*R. Wysor[4]
*H. T. Yeh[2]

In terms of the overall fusion design process, the FY 75-76 Experimental Power Reactor (EPR) study[1-9] represents the most extensive effort to date in advanced studies of early power reactors, though it is still only the present point on the evolutionary scale of design for the first fusion "reactor." The results of this study have been two-fold in nature. On the detailed technical level many issues have been investigated and more clearly appreciated; work is now under way to address the problems identified. On the broader programmatic level, the need for an achievable, high power density fusion plasma device which would be extrapolatable to an economically viable reactor has been keenly made clear.[10,11] The present EPR design does not satisfy the economic viability criterion, although it does fulfill the technical requirements (as determined by a preliminary design). The recognition of the pressing need for operation at higher power density has led to the development of The Next Step (TNS) program;[12] The Next Step after Tokamak Fusion Test Reactor (TFTR) is being pursued as an ignition device whose characteristics do extrapolate to an economically viable fusion reactor.[11]

*Part-time.

1. Computer Sciences Division.
2. Magnetics and Superconductivity Section.
3. Consultant.
4. UCC-ND Engineering.
5. Burns and Roe, Inc., Paramus, New Jersey.
6. Westinghouse Electric Company, Pittsburg, Pennsylvania.
7. Large Coil Program.
8. Plasma Theory Section.
9. Grumman Aerospace Corporation, Bethpage, New York.
10. Exxon Nuclear Co., Inc., Bellevue, Washington.
11. Metals and Ceramics Division.
12. Neutron Physics Division.
13. Plasma Heating and Fueling Section.
14. Chemical Technology Division.

6.1 EPR STUDY PRECEDING TNS

The principal activities in the EPR program fall into three major phases: a scoping study,[2] development of a reference design,[3] and evaluation of the Reference Design.[4-9]

The previous annual report described the first two phases and the initiation of reference design evaluation. In this report, the improvements to the Reference Design and the technical evaluation are summarized and the conclusions of the EPR study summarized.

6.1.1 Improvement of the Reference Design

The bases on which the Reference Design was established varied widely from explicit calculations to technical judgments. Consequently, the

major thrust of the work in FY 76 was to perform a technical evaluation of the Reference Design and to upgrade it where necessary. Figure 6.1 illustrates the Oak Ridge EPR design elevation view. Figure 6.2 presents a composite chart of each of the key preparatory steps before operation and the key events during an operating cycle. A tabulation of overall system parameters and their values for the EPR is shown in Table 6.1. During this period a number of technical issues were addressed, and, where possible, "solutions" were developed. That is to say, in a number of critical areas, those ideas which appeared to be feasible design concepts have been proposed and examined. In the current reference design, for example, the following items have been added to the original:

1) a fuller description of an ignited plasma;[5]
2) a new toroidal field (TF) magnet design more credible in terms of fabrication.[6] Additional analytic tools have been developed and used to define more closely the stability margin and the ac losses;
3) in-depth study of the ohmic heating (OH) and electromagnetic shielding systems driving the plasma current, protecting the TF coils, and reducing the energy requirements.[5,6] Critical questions have been identified;[9]
4) a new modular, maintainable, workable blanket design;[7]
5) establishment of the basis for the overall structural system;[8]
6) a first pass at the balance of the plant.[8]

6.1.2 Evaluation of the Reference Design

In addition to reemphasizing the importance of resolving the key technical issues, the conceptual development of some of the technical problems has identified some very difficult judgmental issues.

1) The benefit/cost for a low power, high cost design must be assessed.
2) The mechanical system is extremely complex. *Even though a case can be made for the successful execution of any one problem, the successful execution of all simultaneously seems doubtful.*
3) Of the required extrapolations in plasma physics parameters, it is the extrapolation with pulse time that is the greatest and hence the most uncertain.
4) Each of the component technologies is being pushed and extended significantly beyond present capabilities.

In each of these four issues, the risks, though clearly visible, are not quantifiable. Considerable work is needed if these issues are to be made more quantitatively balanced between gain and risk.

6.1.3 Principal Findings

On the basis of the technical evaluation, a number of key findings became clear; these findings are considered in this section. This consideration and an appreciation of the difficult judgmental issues raised in Sect. 6.1.2 led to an examination of the fundamental assumptions used in the study; this examination is made in Sect. 6.1.4. The principal findings impacting the technical program can be divided into three convenient categories.

Scientific

- In the area of scaling, continually improved models are available for performance prediction,[13] but significant additions to the experimental data base and improvements to the analysis are needed before confidence can be generated that, for example, the scaling relations are appropriate and profile effects have been properly considered.
- In the area of dynamics, detailed experiments are needed to provide hard information on start-up/burn (fueling)/shutdown for engineering criteria.
- Similarly, in impurity effects and plasma electromagnetics, experimental information

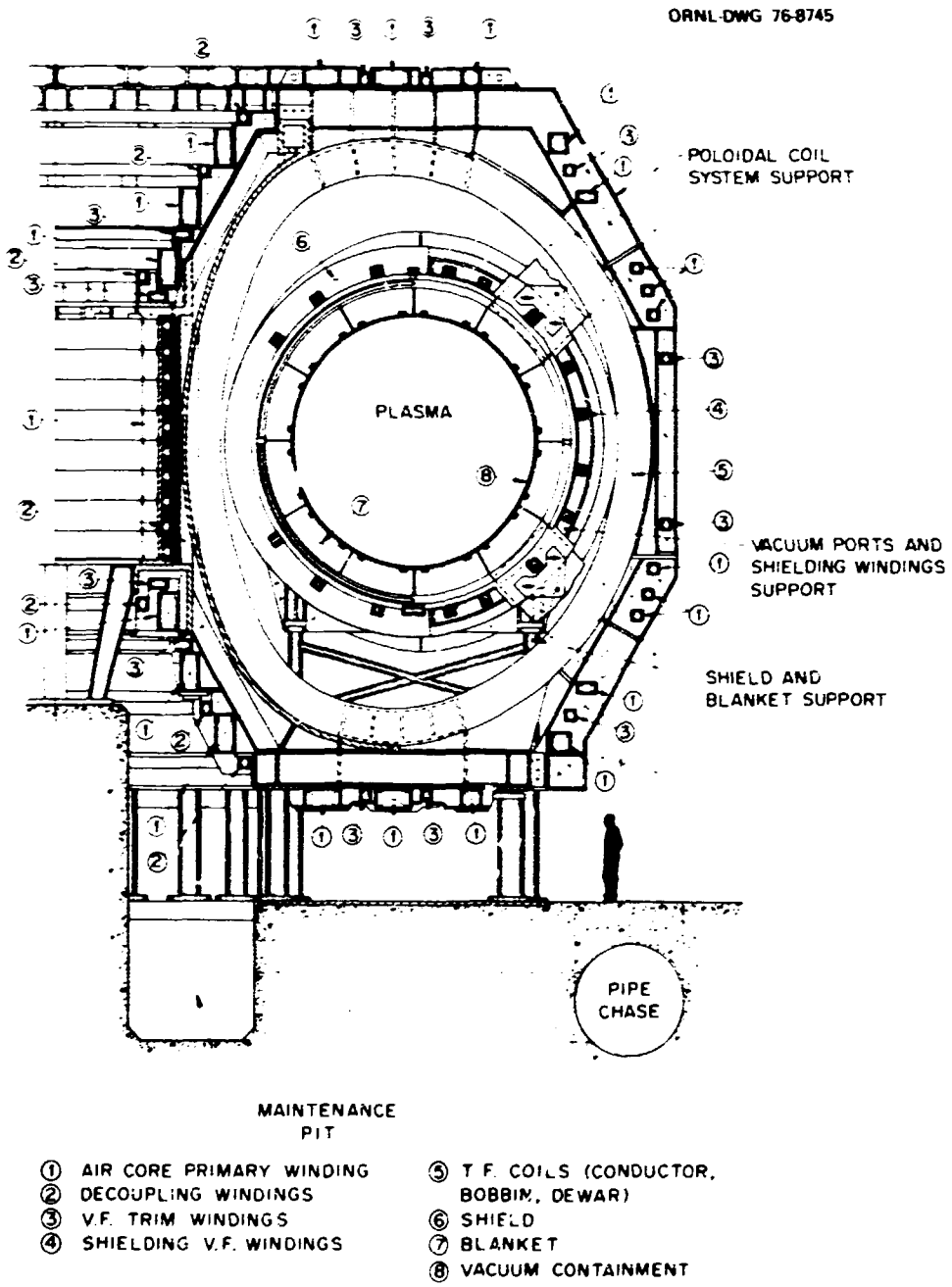

Fig. 6.1. Oak Ridge EPR design -- elevation view.

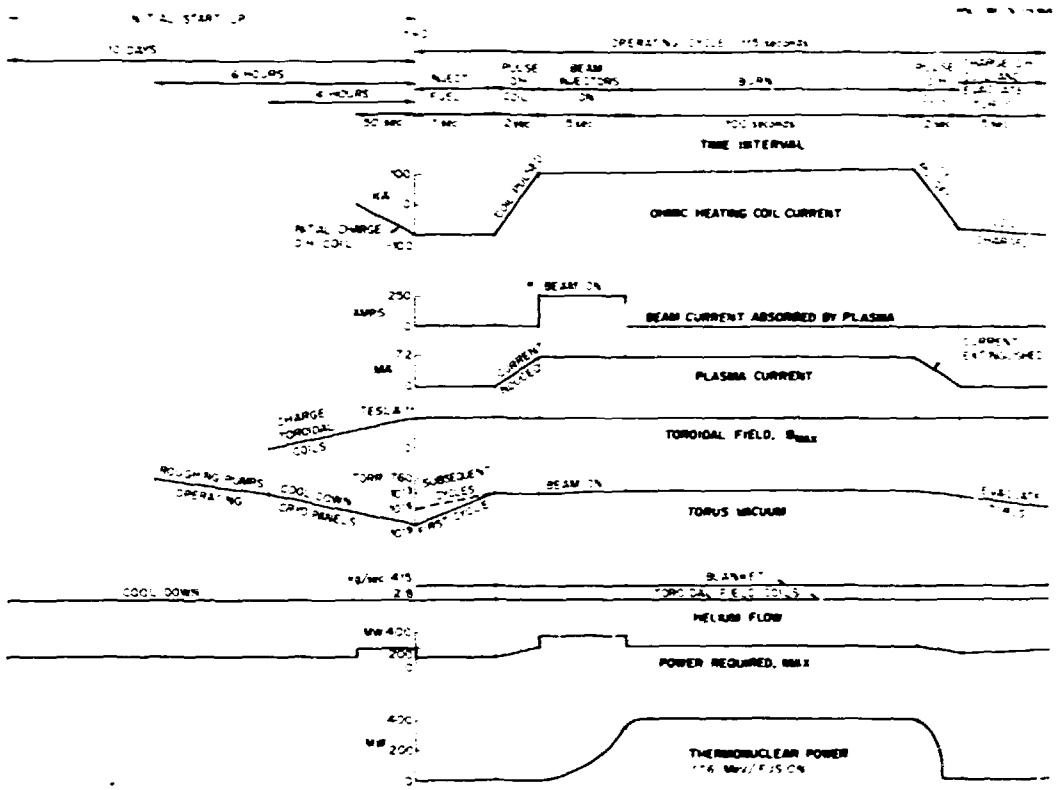

Fig. 6.2. EPR operating chart.

is sorely needed for guidance of design efforts.

Technological

- Demonstrations at the appropriate scale are required for each of the key technological components required in the EPR design: TF and poloidal field (PF) coils, tritium handling, heating techniques and hardware, etc.
- Nb_3Sn superconductor development must be emphasized and expanded if the critical technological flexibility of higher magnetic field is to be available for any next step.
- A dedicated PF coil design and development effort is required to address this crucial and newly appreciated area.
- Development of a nonconducting structural material capable of meeting the stringent thermal, mechanical, electrical, and nuclear requirements of the OH coil support structure is essential to the feasibility of a superconducting PF system.
- Energy storage, transfer, and control associated with the PF system require a dedicated, intensive effort to make this aspect feasible; cost reduction is a secondary objective here.

Table 6.1. Overall system parameters for the EPR

	Symbol	Value
A. General characteristics		
1. Requirements		
Device lifetime	t_L	10 years
Duty cycle	dc	87%
Availability – normal		80%
Thermonuclear power (ignition)	$P_o(th)$	410 MW
Net electric power	$P_o(e)$	~10 MW
2. Other features		
Plasma radius	a	2.25 m
Major radius	R_o	6.75 m
Aspect ratio	A	3.0
Plasma edge to winding distance	Δ	1.40 m
Plasma volume	V	675 m^3
Overall height	H	15 m
Overall diameter	D	23.3 m
B. Plasma parameters		
Burn time	t_B	100 sec
Current	I_p	7.2 MA
Confinement measure	$N_e\tau_E$	2.7×10^{20} sec m^{-3}
Plasma temperature		
Ion temperature	T_i	12.2 keV
Electron temperature	T_e	13 keV
Beta poloidal	β_p	1.9
Beta (total)	β	0.03
Safety factor	q	2.5
Electron density	N_e	7.4×10^{19} m^{-3}
Fuel ion density	N_i	7.0×10^{19} m^{-3}
Impurity level	Z_{eff}	1.34
Injected deuteron power	P_b	50 MW
Injected deuteron energy	E_b	200 keV
Particle confinement time	τ_p	9.6 sec
Energy confinement time	τ_E	3.7 sec
C. Electromagnetic parameters		
Maximum toroidal field	B_{max}	11 T
Toroidal field on axis	B_T	4.8 T
Number of toroidal coils	N_c	20
Magnetic field ripple at plasma edge	ΔB	2.2%
Conductor configuration		composite cable in a square aluminum conduit

Table 6.1. (continued)

	Symbol	Value
Superconductor		
in the high field region		Nb_3Sn in Cu-Sn matrix conductor
in the moderate and low field region		NbTi in Cu matrix conductor
Average poloidal field at plasma edge	B_p	0.64 T
Poloidal field coil core type		air
Poloidal coil volt-seconds	VS	165 Wb
D. Thermal		
Maximum power rating of blanket	P_R	800 MW
Blanket coolant		helium
Outlet temperature of blanket coolant	T_{out}	370°C
Blanket coolant pressure	P_{He}	70 atm
Shield coolant		borated water
Coil coolant (superconducting)		helium
E. Nuclear parameters		
Neutron flux on first wall (operating point)	P_w	0.55 MW/m^2
Neutron wall loading (design point)	P_w	1.07 MW/m^2
Neutron flux on first wall (operating point)	Φ_w	2.4×10^{19} $n/m^2/sec$
Neutron flux on first wall (design point)	Φ_w	4.7×10^{19} $n/m^2/sec$
Tritium breeding ratio (in one experimental module)	BR	1.15

- Plasma heating requirements demand an uncertain combination of ingenious plasma operating scenarios to make use of the available positive ion beam technology and creative negative ion source development for flexibility in the design.
- Exploitation of the indications of extended material lifetimes under irradiation is a fundamental necessity in the drive for economical systems in which replacement costs are a dominant factor in the plant economics.

Engineering

Given that a number of significant engineering issues have been addressed successfully (e.g., workable design solutions in the blanket, TF coil, and remote maintenance areas), the net result is still an extraordinarily complex device.

This complexity can be appreciated by considering the following four areas of design requirements:

- mechanical complexity of nested tori, wide temperature ranges, large structural loads on large elements, and intertwined coil sets,
- many operating pulses,
- high auxiliary power demands, and
- remote handling combined with high tritium inventory.

The key finding here is not this list of complexities but rather the appreciation of means of reducing the complexity.

- Increasing the aspect ratio relieves the first problem considerably.
- Lengthening the burn time relieves the second.
- Increasing the thermal power output reduces the impact of the third.
- Ingenuity and serious design can relieve the fourth.

The finding here, then, is a set of requirements for both engineering and plasma physics that can lead to an economically viable power plant.

6.1.4 Technical Considerations

Taking into account the key findings and judgmental issues, it is instructive to reexamine the underlying scientific and technological considerations that have led to the present situation.

Size and cost

The size of the EPR plasma and its blanket and shield determine the size of the superconducting coil which, in turn, is closely related to the overall cost. The plasma size is determined by the scaling laws used to specify the energy containment of the plasma. All of the EPR designs have used the so-called trapped ion mode scaling at densities of $\sim 0.7 \times 10^{20}$ m^{-3} to specify the energy containment time. This has led to large plasma sizes, which are necessary in order to attain an $N_e\tau_E$ near the ignition condition. This large plasma size, combined with the necessity for a blanket and shield between the plasma and the superconducting coils, has resulted in EPR superconducting coils roughly 7 m (horizontal) by 10 m (vertical) with a weight of several hundred tons each.

Low aspect ratio

The EPR designs are of low aspect ratio machines. Once an aspect ratio has been chosen — and low aspect ratios are favored in the present regimes of the models — the magnetic field in the plasma is determined by the maximum allowable field at the conductor. There is thus strong motivation to utilize the more expensive high field superconductors. However, the use of high field superconducting magnets in a low aspect ratio torus results in extreme asymmetric forces on the coils; these forces must be minimized by the fabrication of asymmetric coils. Unfortunately, the fabrication of such asymmetric coils is complicated by the fact that they must be of large size and in accord with the EPR designs. Simultaneously, the general design and assembly problems are made most difficult by the cramped nature of a low aspect ratio device.

High fusion power density

The fusion power density produced in a magnetic confinement system varies as β^2B^4; therefore, the attainment of high beta and high magnetic field has been emphasized in the EPR studies.

In the ORNL EPR studies, β_p has been limited to ~ 1. As a result, the attainable total beta in the EPR designs is $\lesssim 3\%$.

Elongation of the plasma may permit an increase in the attainable value of beta, but uncertainties exist about the equilibrium and stability behavior to be expected in such cases, and economic and engineering difficulties are associated with producing a high degree of elongation. The incentive for elongated plasmas is clear, but the actual advantage remains to be determined.

Although the fusion power varies as the fourth power of the magnetic field, the importance of achieving the highest possible value of beta follows from the difficulty of obtaining high magnetic fields. The strength of the magnetic field (B) which can be utilized in a magnetic confinement device is constrained by technology. There is a limit on the magnetic field for the two types of superconductor, NbTi and Nb_3Sn, which are available in commercial quantities. In addition, practical engineering considerations and economic

constraints may prevent the use of fields much in excess of 12 T at the surface of the superconducting coil.

Many of the difficulties perceived to exist in the technology and engineering areas result from the plasma physics scaling laws and beta relationships discussed above. If the power density and the aspect ratio could be increased, many of these problems would be less severe. The concept of flux conservation through intense neutral beam heating appears to have potential as a way to comply with both requirements.[10,14] The exploration of the implementation of this more attractive set of conditions forms the basis for the positive tone of the conclusions presented below.

6.1.5 Conclusions[15]

- EPR should produce a significant amount of power.

The step in the fusion program that encompasses thermonuclear power production at a high duty cycle will be large, difficult, and costly. Because this step appears to be inherently very expensive, it should be accompanied or characterized by production of an amount of power that represents a significant fraction of the output of a commercial power plant.

- The assumption and requirements used in the EPR study have resulted in a large device and the need for major technology extrapolations.

The inherent difficulty and associated cost follow directly from the need for a large device. The size is dictated by the plasma scaling assumptions used in the study and by the need for the blanket/shield to satisfy the requirement for continuous, high duty cycle operation at hundreds of thermal megawatts. The TF magnet size compatible with this system is itself very large and is a major extrapolation from current experience. Similarly, the neutral beam power requirements and OH system characteristics far exceed those of present devices.

- The current EPR device is uncomfortably large and the power output is uncomfortably small.

For a device of the size and complexity of the current EPR design, the cost appears to be in the range of $1-2 billion. The fusion power density depends on a number of variables and can potentially be improved by technical advances. Therefore, effort must first be directed toward developing improved performance in a device of reduced size.

- EPR, as presently conceived, is <u>not</u> the next logical step.

Because the magnitude of the EPR task is such a large increment beyond the present state of the art and the benefit is uncertain, the EPR is <u>not</u> the next logical step to take in the fusion program. Following the line of argument above, efforts are needed to conceive, develop, and demonstrate means of improving the fusion power density before an EPR is undertaken. These efforts are discussed in Sect. 6.2.

6.2 THE NEXT STEP

The outcome of the EPR study indicates that intermediate steps will be required to support development of an EPR.[10,16]

TNS at ORNL (supported by the Westinghouse Fusion Power Systems Department) has been initiated to develop the basis for a major experiment in the mid-1980's having two principal objectives: (1) achievement of a fusion reactor core, i.e., deuterium-tritium (D-T) ignition and burning, and (2) forcing function for reactor technology. The ORNL TNS program is based on the operation of high density, hot plasma using technologies being developed in the Division of Magnetic Fusion Energy (DMFE) plan. Long pulse length operation permitting burn dynamics to be studied is planned, whereas continuous, high duty cycle operation is deferred until the EPR phase of the fusion program. Preliminary calculations indicate a thermal power output greater than 1500 MW in

an $n = 2 \times 10^{20}$ m^{-3} plasma whose minor radii are 1.25 m (horizontal) by 2.0 m (vertical). Judging by these preliminary indications, TNS will have a benefit/cost considerably greater than the EPR design discussed here (four times output power in half size); furthermore, the extrapolation from TNS is to an economically viable fusion reactor. The technical basis for TNS appears verifiable in the next three to five years in the experimental and theoretical programs now under way: high beta in Oak Ridge Tokamak (ORMAK) Upgrade,[17] superconducting coil performance in the Large Coil Program (LCP),[18] and high power beams in the TFTR beam programs.[19]

6.2.1 Reexamination of the EPR Objectives and Basic Physics Extrapolation

Examination of the EPR objectives indicates that many of the objectives subordinate to the ultimate EPR goal of net electric power can be achieved in earlier, lesser facilities. Those objectives that can only be achieved in an EPR are related to the high duty cycle and availability of the plant and to the full energy conversion and tritium breeding in the blanket. With the renewed assignment of these most advanced goals to the EPR, satisfaction of the subordinate objectives can be achieved at a benefit/cost ratio and cost level seen to be acceptable.

The basic plasma engineering assumptions concerning minimum size and field for ignition play a dominant role in setting the overall size and difficulty of the EPR. Recent advances, both experimental and conceptual, have led to a rethinking of these basic assumptions.[16,15] These advances indicate that (1) it may be possible to achieve higher beta values than previously supposed and (2) operation at high density should provide improved performance. The key to improved benefit/cost for the next major fusion step is the assumed value of plasma density. Using a value of $n < 10^{20}$ m^{-3} resulted in both a plasma radius of >2 m (high cost) and a wall loading of <1 MW/m^2 (low benefit). In setting up the basis for the next tokamak step, use will be made of the benefits of high density plasma operation and close attention will be given to a better understanding of its achievement. "Making" $n > 10^{20}$ m^{-3} does improve the benefit/cost both for TNS and for reactors. Achieving this higher density of $n \sim 2 \times 10^{20}$ m^{-3} clearly requires additional information on plasma stability at high beta equilibria and on materials properties at higher wall loadings (~2-4 MW/m^2). More data on the scientific and technological basis for the postulated high density, high beta operation will be forthcoming from the next generation of large experiments and continued materials research.

6.2.2 Initiation of TNS Studies

April 1976 TNS nominal reference

On the basis of our previous EPR study, we established an initial set of basic machine parameters for the exploration of the TNS design space. These parameters, which would produce a reactor grade plasma, included the following: noncircular plasma radii of 1.0 m × 1.6 m, major radius of 4 m, magnetic field on axis of 4.5 T (using NbTi conductor with 8 T at the winding), TF coil bore of approximately 3 m × 5 m, fusion power output of 700 MW(t) and 100 MW of 200-keV neutral beam injection.

Explicit calculational simulations of plasma confinement using one-tenth trapped particle scaling indicated that the plasma horizontal radius must be increased to 1.25 m to achieve ignition for a 4.5-T magnetic field on axis. In addition, our exploration of this design point showed that approximately 0.6 m of device shielding was required to limit the average TF coil nuclear heating to acceptable values. These considerations resulted in an increase of the TF coil horizontal bore from 3 m to 4.5 m. An evaluation of impurity control and gas throughput concluded that an active control mechanism should be included in the nominal design point. A poloidal divertor was chosen as the primary technique because it typifies the possible complexity in design and cost, is compatible with a

high beta PF system, and fits inside elongated TF coils. Our evaluation of neutral beam, auxiliary heating options indicated that new injection approaches may be necessary. Above 200 keV, straightforward positive ion systems appear unattractive because of significantly reduced efficiency. However, alternate concepts such as direct recovery, negative ion sources, ripple injection, and innovative start-up scenarios exist and were judged worthy of future investigation for possible application to TNS.

Upgrading of planned major fusion devices

We completed an evaluation of the potential for upgrading various features (e.g., plasma size and shape, plasma current, toroidal field, pulse length, and neutral beam power) of existing and planned fusion experiments to determine the potential impact of these upgrades on the definition of TNS design objectives and to further clarify the role of TNS in the overall fusion power program. The fusion devices considered in this evaluation were PLT, PDX, Doublet III, ISX, ORMAK Upgrade, and TFTR.

The basic ground rule initially observed for determining what constitutes an upgrade is that only reasonable modifications, within the framework of existing experimental objectives and without construction of a totally new device, were considered. In addition, the upgrades considered were to have a minimum impact on the scheduled initial operation of these devices.

Examination of the non-D-T devices (all but TFTR) indicates that D-T operation cannot be factored into a simple upgrade of these units. The timely achievement of the established objectives of these machines is very important to the overall program, and the upgrading of selected features may be justifiable in individual cases that could provide special opportunities for specific physics or engineering studies, to the extent that the original experimental goals are not compromised.

The feasibility of upgrading TFTR was considered in much greater detail than the other devices because this device has a greater potential impact on the evolution of the TNS concept than any other. TFTR is scheduled to demonstrate D-T burning at reactor grade conditions and provide vital information in the areas of plasma confinement scaling and neutral beam injection. In view of the large investment which will be made in the TFTR facility, it is logical to consider ways to maximize the usefulness of the test complex to the overall fusion program.

Four TFTR upgrade scenarios were postulated, and design, cost, and schedule implications were evaluated for each case. The principal parameters which were upgraded were:

- toroidal field flat top duration,
- toroidal field on axis, and
- plasma minor radius.

Variation of these quantities resulted in significant changes to tokamak support systems such as power supplies and neutron beam injectors. An overall summary of the key features of the four upgrades is provided in Table 6.2. The net cost data were developed on a system-by-system basis by identifying required hardware changes and by scaling the appropriate baseline TFTR cost estimate of October 1975. Allowance for Engineering, Design, Inspection, and Administration (EDIA) and contingency has been provided; however, escalation was not considered. The resulting cost estimates range from $48.8 million for TFTR U-1 to $201 million for TFTR U-4.

An important conclusion which was reached was that none of the upgrades defined according to the original set of ground rules was likely to achieve ignition. However, if the modifications considered are coupled with successful innovations in plasma physics [i.e., high density ($\sim 4 \times 10^{20}$ m^{-3}), high beta ($\sim$15%), and $Z_{eff} \sim 1$], then current calculation models predict ignition. Furthermore, in view of our perception of the engineering requirements associated with an ignition experiment, this capability appears to require a new machine and either a new facility or a substantially upgraded existing (or planned) facility. A final consideration is that implementation of any of the upgrades would not eliminate the need for a main-line, reactor

Table 6.2. Summary of TFTR upgrade options

Option	Features	Availability	Net cost (with EDIA and contingency, M$ 1975)
TFTR U-1	Immediate implementation-delay baseline schedule. Increase toroidal field by 10% (to 5.7 T on axis), extend TF flat top from 1 to 4 sec.	1982-1983	48.8
TFTR U-2	Immediate implementation-delay baseline schedule. Increase vacuum vessel size to accommodate a plasma with a 1.1 m at R_0 = 2.8 m. Increase toroidal field by 10% (to 5.3 T on axis) and extend flat top from 1 to 4 sec.	1982-1983	134.2
TFTR U-3	Complete baseline experimental program in 1986, dismantle and modify device, facility, as in TFTR U-2 above.	1988-1989	152.5
TFTR U-4	Initiate new device and facility modifications in 1980, in parallel with baseline device completion. Complete baseline operation in 1986 and switch over shared equipment. Same device features as TFTR U-2.	1986-1988	201.0
TFTR II	Same scenario as TFTR U-4, except that TF bore is enlarged to reduce ripple and device is designed to achieve ignition (but not sustained burn).	1986-1988	200.0

technology-oriented machine in the mid-1980's to provide the data base for the design of an electric power producing device in the early 1990's. Because innovative advances in plasma physics could result in achievement of ignition by these upgrades, we recommend that effort be expended to pursue attainment of these innovations.

In the context of the upgrade study described in this report, a large new machine (designated TFTR-II because it is not really an upgrade) was considered as an alternative to TFTR U-4 (see Table 6.2). This machine would focus primarily on ignition plasma physics and presumably would correct the deficiencies of U-4 (larger TF bore, augmented cooling, shielding to handle ignition, and some impurity control) and use the existing (after completion of the baseline experimental program) TFTR facility. It appears that the maximum hardware savings which could be realized by using portions of the existing TFTR facility is about $90-95 million. This savings, if it could be achieved, would be obtained at the price of flexibility and interference with the baseline operation of TFTR. Regardless of when TFTR-II is initiated, its availability is tied to the baseline TFTR schedule, which currently calls for completion of D-T operations in 1986. At this point, facility and equipment modifications could be completed and common items of equipment switched over from TFTR to TFTR-II. Allowing for at least a year of non-D-T checkout and experimental operation, the earliest that initial D-T operation of TFTR-II could occur would be 1987-1988. It should be noted that this approach, starting with new facilities, is one of the TNS options under consideration (see Sect. 6.2.3).

The TFTR-II approach, which has only briefly been examined here, certainly merits additional study to develop fully its advantages and disadvantages, and it is recommended that consideration be given to performing such a study. We do feel, however, that there are a number of basic difficulties with this approach.

The applicability of baseline TFTR hardware (neutral beam lines, power supplies, etc.) must be substantiated and quantified.

- Overall program credibility requires that the baseline TFTR goals and schedule be achieved with minimum compromise.
- Early curtailment of baseline TFTR experiments will be difficult to justify, in view of the overall investment involved.
- The proximity of existing labs and offices to the TFTR site may not be compatible with ignition level D-T operations.

6.2.3 Discussion of the July 1976 TNS Updated Nominal Reference Point

Our first studies, from April through June 1976, resulted in an improved, self-consistent reference point which included the following parameters: noncircular plasma radius of 1.25 m × 2.0 m, major radius of 5.0 m, magnetic field on axis of 4.3 T, and a TF coil bore of 4.5 m × 7.3 m. The plasma density assumed was 2×10^{20} m^{-3} and the fusion power produced was 1900 MW(t). The neutral beam power required was 100 MW, with an accelerating voltage of 200 keV.

Physics evaluations

Our physics evaluations of this improved reference point indicated that the plasma characteristics were reactor-like and self-consistent. High beta operation was judged necessary for an economic reactor, and a plasma density of 2×10^{20} m^{-3} seemed sufficient for ignition. Achieving high beta operation appeared credible based on analytic investigations of the flux conserving tokamak (FCT) concept. Attainment of high density is supported by Alcator results, which indicate both high density and low Z_{eff} operation.

As shown in Fig. 6.3, the physics margin for "achievement" of ignition for this reference point is minimal for a field on axis of 4.3 T and is increased to more prudent values for fields of 5.0 T or 6.0 T. Figure 6.4 emphasizes the importance of effective impurity control, indicating that calculational simulations predict that ignition is not "achievable" for $Z_{eff} > 1.2$ in the particular model conditions assumed.

Additional physics margins may be included in this reference point by using a beam heating system with increased accelerating voltage. However, for energies >200 keV, the attractiveness of current positive ion technology decreases because of reduced neutralization efficiency, and positive beam systems may not be adequate. Therefore, the need for improved neutral beam technology or innovative start-up scenario increases in importance if operating flexibility is to be included in the design.

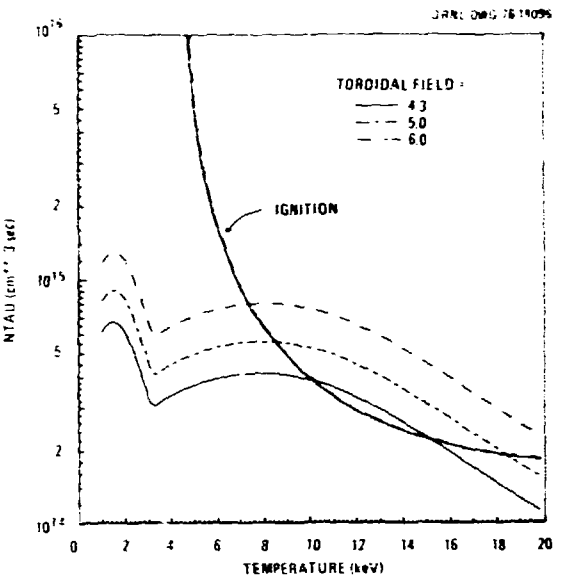

Fig. 6.3. $N\tau$ required for ignition and system $N\tau$ operating characteristics as a function of temperature and various field strengths.

For this reference point the poloidal divertor requirements were not completely specified. The coil current and position were compatible with an FCT PF system, and a scrape-off region was included in the TF coil bore. However, vacuum and gas handling considerations were not fully factored in, and mechanical and electrical evaluations were not completed.

Engineering studies

Our engineering studies of this updated reference point focused on the performance of trade studies to serve as the basis for initiating conceptual design studies. These trade studies can be categorized as "global" and "local." Global trade studies

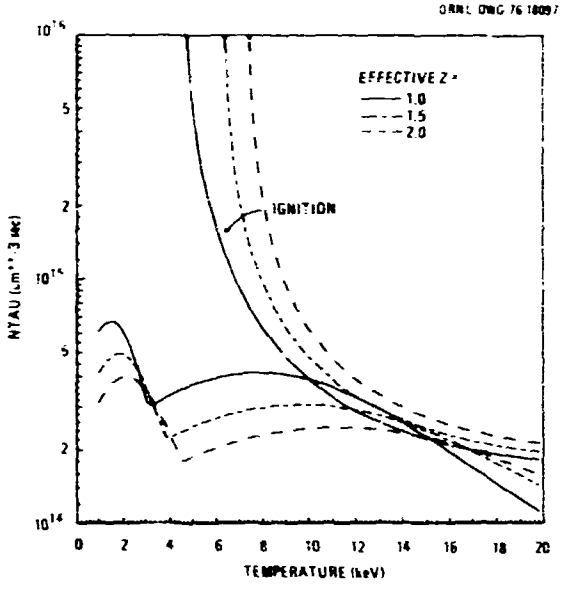

Fig. 6.4. Nτ required for ignition and system Nτ operating characteristics as a function of temperature and various impurity (iron) levels.

include an investigation of various machine configurations and an evaluation of the reference point sensitivity to various operating scenarios. Local trade studies consider system and component options relative to the reference design point.

Configuration trades. Five alternate approaches to the definition of TNS were examined on a common basis to develop data suitable for a comparison of respective costs, complexity, risk, and availability. Preliminary sizing studies were completed for each version of TNS, and emphasis was to be placed on model refinement and improvement. The versions of TNS which are under study consist of:

- TNS-1 – D-T fuel with copper TF coils,
- TNS-2 – H_2 fuel with NbTi superconducting TF coils (included for comparison with D-T case),
- TNS-3 – D-T fuel with NbTi superconducting TF coils,
- TNS-4 – D-T fuel with Nb_3Sn superconducting TF coils, and
- TNS-5 – D-T fuel with copper/NbTi (hybrid) TF coils.

A goal of this study was to determine the smallest device in each category and presumably the smallest cost possible, consistent with achieving ignition (according to a specific plasma model) and with meeting the engineering constraints. Sets of parameters were determined for four of these options (TNS-1 through TNS-4), and costing models were under development before this effort was generalized to consider a broader range of possible sizes along with technology options (see Sect. 6.2.4).

As might be expected, the water-cooled copper TF coil version of TNS was found to be the smallest device; however, the overall range of major radii was from 4 m for the copper version to 5 m for the reference point version (TNS-3). Therefore this comparison of four FCT TNS ignition options indicated a size variation in major radii of only ±10% about the midpoint radius.

Operating scenario trades. A complementary study was also performed on the relationship of pulse length, duty factor, and relative cost. The reference point (TNS-3) was selected and components sized for combinations of 8, 16, 32, and 62 sec and time intervals between pulses of 1, 2, 3, 5, and 10 min. The principal conclusions from this preliminary study are summarized in Fig. 6.5, which depicts the relative hardware costs associated with various pulse lengths and intervals. Time-sensitive hardware costs are judged to represent from 30 to 50% of total plant costs. From Fig. 6.5 we conclude that time-sensitive hardware costs increase by approximately 10% (total cost equivalent of 5%) for a pulse length increase from 10 sec to 30 sec. Therefore, our interim conclusion is that total cost is much more determined by the requirement to achieve ignition than by the requirement to sustain the burn.

System and component trades. Design trades were performed for system and component options for the interim reference point. Examples of these studies include secondary vacuum enclosure schemes and vacuum vessel materials choice.

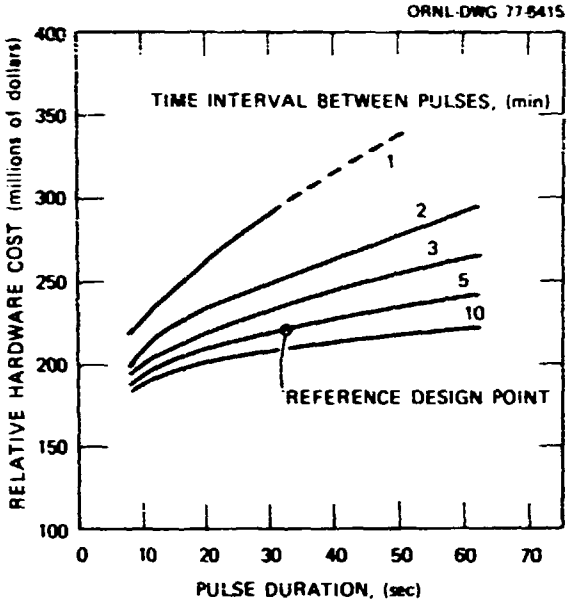

Fig. 6.5. Dependence of relative hardware costs for various systems on pulse duration and time interval between pulses, based on reference TNS-3 configuration of 6/30/76. Systems included are: field coil power, vacuum pumping, divertor, facility shielding, heat transport and rejection, refrigeration, fuel gas supply, and processing.

Four approaches to the vacuum system configuration were identified and design issues developed for analysis. Specific options consist of:

1) a primary toroidal high vacuum enclosure with individual vacuum dewars about the superconducting field coils. The cell atmosphere would be maintained slightly below ambient;
2) a primary toroidal high vacuum enclosure with common TF coil dewars;
3) a secondary vacuum enclosure outside the TF coils permitting reduced atmospheric loading on the primary toroidal vessel and the coil dewars;
4) evacuation of the entire test cell.

Thermal evaluation of the various enclosure options was completed and vacuum pumping requirements defined. A definitive recommendation was not made at this time pending further definition of a specific TF coil option and dewar design approach.

A comparison was made of four materials:

- AISI type 316 stainless steel,
- titanium alloys,
- aluminum alloys, and
- molybdenum alloy TZM.

The criteria used in the comparison were:

- mechanical-chemical properties,
- thermophysical properties,
- reliability,
- radiation and safety, and
- specific device factors.

The results of the evaluation favor type 316 stainless steel by a considerable margin.

Preliminary cost estimate

A scoping Plant and Capital Equipment (PACE) cost estimate was made supporting the preparation of a preliminary version of a short form Schedule 44 Construction Data Sheet.

Because the design features of the reference design point were not completely defined in many cases, many estimates had to be made as to appropriate sizes and ratings of the most cost-sensitive components. These estimates were made at the second level of the reference work breakdown structure (i.e. major subsystems) and based primarily on unit costs derived from the vendor quotation evaluations prepared for the TFTR conceptual design in October 1975.

Our scoping estimate indicated a cost (excluding engineering and contingency costs) in the range of $500 million. The tokamak system and tokamak support systems account for approximately half of the estimated costs and the peripheral systems (power supplies, neutral beam systems, etc.) account for the other half.

Conclusions

Three overall conclusions stand out from this study:

- ignition is costly and difficult,
- ignition is a cost and technology threshold to reactors, and

primary focus should be on large uncertain cost items (heating, fueling, impurity control).

The initial TNS studies of the April-June 1976 quarter resulted in the selection of an updated July 1976 reference design point for TNS. The subsequent, much larger effort in the July-September 1976 transition quarter was designed to support the selection of feasible technical goals for TNS. Operational trade studies of pulse length, downtime and frequency, considerations of materials, assembly techniques, and investigation of the July 1976 reference point made up much of the transition quarter's activity. The original objective of the transition quarter's activity was the definition of a comprehensive reference design based on the selection of the July 1976 design point. As a result of discussions between ORNL and DMFE, this objective was changed to be a more broadly based examination of alternative design routes to an ignition device. This broader study was aimed at identifying the range of technical benefits and risks and total cost to support recommendation of a design concept for continued reference design investigations for TNS.

6.2.4 Exploratory Studies to Support Conceptual Design Point Decision in Mid-FY 77

The intent of this phase of the TNS program is to come to a well conceived and supported starting point for reference design studies by mid-FY 77. Achievement of this design basis is being pursued in an integrated program consisting of four main parts.

1) We are specifically investigating the most critical scientific problems, especially impurity control and PF winding locations, as well as determining the sensitivity of plasma performance to variations in key parameters.
2) We are performing a trade study evaluation to support a plasma size and TF coil technology decision.
3) We are evaluating research and development (R&D) programs to identify available and required experimental support basis.
4) We will begin developing a comprehensive construction schedule and plan to establish proper sequencing of design tasks, R&D tasks, and construction elements to support the orderly preparation of a TNS device.

The findings in each of these four areas will be synthesized into the reference design decision process.

Our goal continues to be the definition of the best next tokamak step after TFTR, considering objectives, achievability, and reactor viability. Our primary objective for TNS is development of a fusion reactor core which can be extrapolated to an economically viable reactor plant. This objective requires achievement of ignition at a high power density that is efficiently developed ($\beta \sim$ 5-15%); however, this objective does not specify a particular path of implementation considering both physics and technology. The objectives of the TNS study are more immediate than a set of working drawings; the TNS design project is needed now to:

- initiate required R&D programs,
- focus experimental programs,
- order technology needs,
- emphasize needs for ideas leading to economically viable power plants,
- develop an appreciation for the schedule and its implications, and
- alert the system required to act on TNS.

More exploratory work is needed before a decision on a TNS reference design is made because implementation of a program estimated to cost in the range of $500 million (or more) is uncertain. Our effort during this period is aimed at reducing this uncertainty.

Physics evaluations

The continuing theoretical analysis and experimental results are supportive of basic TNS physics assumptions. A parameter sensitivity

study identifying ignition requirements as a function of operating parameters has been completed. An analytic investigation of radial profile effects indicates that the value of beta required for ignition and burning is lower by about one-third than previous estimates using radially averaged values. A calculational simulation of plasma heating using neutral beam injection and alpha heating indicates that fusion alpha particle heating in the central core region may considerably reduce (to values on the order of 150 keV) beam energy needed to achieve ignition. Magnetohydrodynamic (MHD) equilibrium and stability analyses have provided encouraging results to support attainment of high beta operation in a flux conserving manner.

Basic assumptions and experimental results. Two basic assumptions set the bases for our scientific work:

1) high density, high beta operation leads to ignition in smaller, less costly devices, and
2) high beta (>5%) is obtained in an FCT by rapid heating and is maintained.

The correctness of these assumptions is subject to some fundamental uncertainties in our present knowledge, namely: plasma diffusion at high temperature (low $\nu^* < 1$), impurity evolution and diffusion, and upper stability limits on beta. These issues form the direction for much of the future theoretical and experimental program. The present experimental results demonstrate operation at high density and favorable confinement and support the case for positive projections during the period of investigation of the fundamental uncertainties. ORMAK has demonstrated ion and electron heating by neutral beams and density increase due to gas puffing and injection. Scaling laws of $n\tau \sim n^2a^2$, $Z_{eff} \sim 1/n$ have been observed in ORMAK, Princeton Large Torus (PLT), T-10, Alcator, and Pulsator. Plasma densities much greater than 10^{20} m^{-3} have been observed in Alcator and Pulsator.

Performance prediction sensitivity. Continued work on understanding the sensitivity of the model predictions to variations in key parameters is required to determine the most flexible operating scenario. Additional experimental work is, of course, required to validate the basic model assumptions.

A parameter survey was completed to determine the sensitivity of the nominal reference point to variations in n_e, B_T, T_i, σ (elongation), Z_{eff}, and confinement time. Also, variations of the empirical scaling law were considered, as well as various coefficients in the trapped particle scaling relationships. In scaling from one device size to another, the product na is held fixed to allow for a constant $n\tau$ product and a constant beam penetration depth.

In each variation, a plot of ignition requirements and expected performance was developed as a function of the relevant parameters. In this manner, a graphic depiction of the potential working margin is developed for each major design parameter. An important part of this effort is the inclusion of key physics factors that impact a particular parameter variation.

We conclude from this study that sensitivities found in the predication of ignition are less accurate than the basic foundations of the model and, therefore, there is strong support for developing flexible operating conditions to account for known analytic predicative uncertainties. This study has documented the presently available data base which will be integrated with engineering trade studies to define the best next step.

MHD equilibria with transport modifications. Time-dependent modifications of MHD equilibria by a large but finite conductivity of the plasma are being studied to predict the access to high beta and the long-time plasma behavior after reaching high beta examination of steady-state, FCT equilibria with the pressure profile determined by energy balance requirements has been initiated. Energy transport calculational simulations incorporating the alpha heating from D-T reactions have been initiated to determine required beam heating profiles.

The one-dimensional, time-dependent ORNL transport code with uniform fueling, divertor boundary, and one-tenth trapped particle losses has been used to demonstrate TNS burning equilibrium. Assuming a spatially flat fueling, centrally peaked profiles of plasma density and temperature are derived self-consistently and indicate that ignition can be achieved at a beta of $\leq$10% rather than at the previous estimate of β = 15% using spatially averaged parameters.

A time-dependent, two-dimensional MHD equilibrium code has been coupled to the ORNL transport code to examine the physics of rapid heating in high density plasmas. A calculational simulation (100 MW at 120-keV beam injection into a 0.85-m radius tokamak) provided an independent demonstration of the existence of flux conservation, namely alpha profile remains fixed in a large, rapidly heated tokamak. While alpha profile remains fixed, other plasma parameter profiles (e.g., electron density) change markedly during the intense heating. While earlier calculations assumed that flux conservation was a constraint, this simulation shows it to be a self-consistent result of rapid heating.

We have coupled an optimized MHD FCT equilibrium with a simplified transport code to determine the required beam heating profiles. Peaked pressure profiles reveal low beta values for ignition (7%) and burn (8.5%) at a magnetic field on axis of 4.3 T. Heating to ignition may be achieved by 150-keV beam deposition with the contribution of alpha heating concentrated at the plasma center. Previous estimates without inclusion of the alpha heating indicated beam energies of at least 200 keV. This calculation was performed assuming ideal impurity conditions ($Z_{eff} \sim 1$).

Having discussed various transport implications of higher beta equilibria, the stability question will now be considered. At this stage of analysis of MHD stability there are still many uncertainties.

- Present estimates of ballooning instabilities are based on linear ideal MHD codes.
- Thus far, instabilities have been studied for a narrow range of equilibria.
- Stability limits can depend strongly on shape and profile effects.

In light of these concerns we are engaged in an extensive program of analysis.

- We are using our stability codes as well as studying results from elsewhere, both numerical and analytical.
- With our linear, ideal, initial value MHD stability code, a marginal stability point is found at $\beta \sim 5\%$.
- This value ($\beta \sim 5\%$) is near to ignition requirements, which have been reduced through inclusion of profile effects.

Conclusions. From our studies so far, having developed and used a wide variety of powerful tools, the following important conclusions emerge.

1) Sensitivity studies support need for flexibility in operating parameters.
2) Because of profile effects, a given fusion power level can be achieved at a $\beta \leq 10\%$ rather than $\beta \sim 15\%$ with spatially averaged parameters.
3) Flux conservation emerges as a self-consistent feature in our calculations.
4) Alpha heating lowers beam energy and beam power requirements to $\sim$150-keV levels.

In order to limit the set of distinctly different options satisfying our objectives to a reasonable size, we concluded that plasma size and TF coil technology are the most important characteristics to investigate in our initial trade studies. Plasma size is judged to be the most important characteristic because it directly translates into machine and plant size and cost. In addition to the quantifiables of device size and cost, plasma size is judged to be a key parameter in evaluating the flexibility of the system to achieve our objectives. TF coil technology is considered as one of our highest priority parameters because available options exhibit a discernible range of maximum magnetic field and a wide range of system complexities.

In addition, a choice of TF coil technology is needed as soon as practicable to provide timely input to our ongoing R&D programs.

Engineering evaluations

Our engineering evaluations are focused on trade studies to define a conceptual design point by mid-FY 77. We have completed all tasks established for our first quarter FY 77 work plan. We have developed the trade study framework, including:

- statement of TNS objectives,
- determination of design options,
- production of trade study logic and tools for cost and performance analysis,
- development of detailed ground rules, and
- initiation of trade studies.

Objectives. Our objectives of a fusion reactor design define TNS trade studies:

- achieve ignition and demonstrate burning dynamics,
- provide for potential design solutions for long pulse operation,
- extrapolate to a viable reactor, and
- be a technology forcing function.

When these technical objectives are coupled to the requirement for minimum time to commercialization, we find that the total number of major machines (and hence cost) between TFTR and Demo must be minimized.

Design options. Achievement of our objectives is most sensitive (i.e., cost, risk) to the choice of plasma size and TF coil technology. The versions of TNS under consideration include:

- TF coil technology — B_T-max
  - TNS-1 water-cooled copper — 12 T
  - TNS-3 superconducting NbTi — 8 T
  - TNS-4 superconducting Nb_3Sn — 12 T
  - TNS-5 hybrid-NbTi/copper — 8 T/12 T
- Plasma physics considerations
  - plasma size, minor radius — 1-2 m
  - B_T on axis — 4-6 T.

Consideration of the previous TNS-2 option (TNS-3 with hydrogen fuel) has been terminated because it is not consistent with our stated objective of ignition.

After being used to determine these highest priority choices (plasma size and TF coil type) the trade study methodology will permit sensitivity studies in other areas; for example: pulse length and duty cycle, location of PF windings, gas throughput-impurity control, and engineering design margin.

Trade study logic and tools. The TNS trade study logic (see Fig. 6.6 and Table 6.3) is aimed at developing information to support a plasma size and coil technology decision by mid-FY 77.

ORNL-DWG 77-249

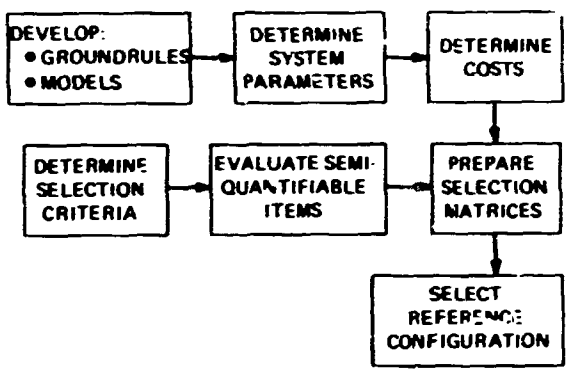

Fig. 6.6. TNS trade study logic.

Detailed system modeling is required to ensure that a firm engineering basis for technical decisions is factored into our trade study. The calculational model is a semiautomated design procedure coupling known relationships and engineering judgment. This procedure incorporates the following steps:

1) sizes vessel, coil, and shield systems,
2) sizes plasma/magnet support systems (neutral beams, vacuum, tritium, power supplies, and cooling),
3) sizes facility support systems,
4) represents major system interactions,

Table 6.3. Summary of ground rules and assumptions — TNS configuration trade studies

Operation	
Design basis facility lifetime	10 years
Total number of pulsing cycles	10^6
Pulse repetition period	300 sec
Pulse scenario	
Pulse OH	0-2 sec
Neutral beam injection	2-8 sec
Ignition excursion	8-16 sec
Burn	16-32 sec
Quench	32-42 sec
D-T operation envelope (design basis)	
Annual dose at site boundary	≤ 5 mrem
On-site restricted area annual dose	≤ 1 rem
On-site restricted area quarterly dose	≤ 600 mrem
On-site unrestricted area annual dose	≤ 100 mrem
Copper electrical insulation dose limit	10^{10} rads
Upper limits on number of D-T pulses	
Lifetime limit	Equivalent to 4000 full energy pulses
Annual limit	Equivalent to 1000 full energy pulses
Vacuum vessel	
Vessel material	AISI 316 SS
Construction	I-beam stiffened shells (w/o bellows)
Vessel cross section	Elliptical
Segmentation	Not factored into models
Wall thickness	Variable
Toroidal limiter	One or two tungsten segments (radiation cooled)
Diagnostic penetrations	Fixed number
Peak bulk wall temperature	400°C
Vessel coolant	Water
Toroidal field coils	
Number of coils	Variable
Conductor type	
TNS-1	Copper (H_2O-cooled)
TNS-3	NbTi (LHe-cooled)
TNS-4	Nb_3Sn (LHe-cooled)
TNS-5	Copper/NbTi (H_2O-LHe-cooled)
Coil shape	Constant tension "D"
Peak field at conductor	12 T — copper
	8 T — NbTi
	12 T — Nb_3Sn
Cooling mode	Single phase forced flow
Fault protection	Electrical provisions only

Table 6.3. (continued)

Poloidal field system	
Conductor material	Oxygen free high conductivity copper
Location	OH windings outside TF VF windings inside TF
OH flux swing	Variable
Conductor current limit	20 kA
Conductor current density limit	1.5 kA/cm^2
Conductor coolant	Forced flow water
Impurity control technique	Wall treatment (low sputtering liner, low-Z wall, etc.) Note: It is recognized that a magnetic divertor may be necessary. This will be examined in a parallel study.
Vacuum pumping	
Final pumping stage	Cryosorption pumps
Base pressure (prepulse)	1×10^{-8} torr
Outgassing surface area	Ten times smooth area of vessel
Tritium systems	
On-site/in-process T_2 inventory	Variable
Tritium storage	Uranium chip beds
Fuel recovery-recycling plant	Variable capacity (common approach)
Tritium cleanup systems	Variable capacity (common approach)
Fueling	Prefill: gaseous D-T Refueling: solid T and D-T pellets
Neutral beam injection lines	
Beam power, energy	Varies with plasma conditions
Single arm specifications	
Sources	Three 100-A positive ion
Dimensions	10.4 m long × 4 m wide × 6 m high
Number	Varies with plasma conditions
Vessel aperture per line	Duct 40 cm wide × 90 cm high
Duct shielding	As required by coil type
Heat dissipation systems	
Final facility heat sink	Mechanical draft evaporative cooling towers to atmosphere
Vacuum vessel coolant	Water – variable capacity
Shield coolant	Borated water – variable capacity
Buffer loop coolant	Water – variable capacity
Cryogenic refrigeration systems	Variable capacity
Facility air conditioning	Fixed base load, reactor cell air conditioning variable
Thermal loads	Variable – depending on option

Table 6.3. (continued)

Operational diagnostics	
Number, type, penetrations	Constant in all studies
Electrical systems	
Facility feed	Fixed utility constraints
Superconducting TF supplies	Line-driven rectifier supplies (except for hybrid)
Cu TF supplies	AC-MG storage-rectifier conversion
Neutral beam supplies	AC-MG storage-rectifier conversion
Poloidal field power supplies	AC-MG storage-rectifier conversion
Electrical loads	Variable — depending on option
Instrumentation and Control	Fixed for all options
Architectural and facility	
Site	500 m radius site boundary "free-standing"
Reactor cell	Reinforced ordinary concrete Fixed walls (~2.9 m), ceiling (~2.3 m), vertical height fixed Floor space, basement: variable
Electrical power system buildings	Variable
Balance of plant buildings	Fixed

5) checks for internal consistency (mechanical, structural, thermal, etc.), and
6) provides cost estimates for all work breakdown structure (WBS) and PACE items.

COAST, the TNS system code, models all major subsystems and computes costs; a summary of the COAST logic is presented in Fig. 6.7. An example of the level of detail incorporated into the COAST code is summarized in Fig. 6.8.

Engineering judgment is factored into our trade study methodology by interacting specific component designs with the computer model. Specific examples of areas of engineering judgment include clearances for assembly and access, facility interfaces and impact, and overall systems integration.

We conclude that this semiautomated methodology plus engineering judgment will permit quantitative comparisons of TNS options at a level consistent with the depth and breadth of our current knowledge.

Ground rules and assumptions. A critical consideration in the exploration of the parameter space for TNS is the development of ground rules and assumptions for the development of models which are internally consistent and, to the greatest extent possible, will not prejudice the outcome in an unfair manner.

We have attempted to identify a set of design assumptions which will yield representative model solutions and represent the key size and cost sensitivities which can bear on a final decision (see Table 6.3). No attempt is made in the present study to provide detailed design solutions or to represent optimum configurations, in view of the time and effort constraints which have been identified for the work.

In order to reduce the number of variables to a manageable level, engineering (and physics) judgment has been used to fix certain parameters for initial studies. This does not preclude the possibility of treating these items as variables in later cost/size sensitivity studies.

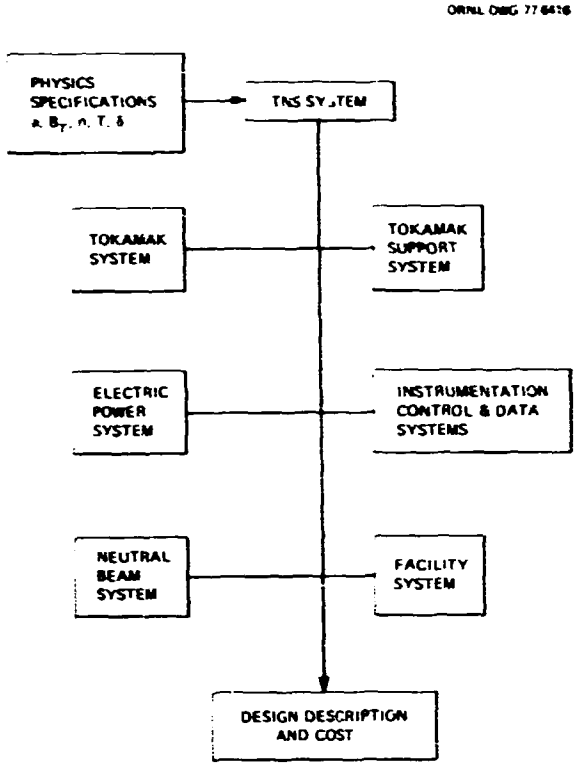

Fig. 6.7. TNS system code (COAST) logic summary.

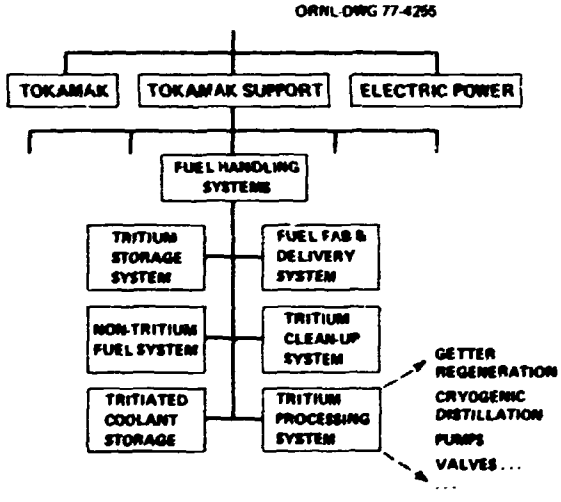

Fig. 6.8. Example of system detail included in COAST code.

It is anticipated that all of the ground rules will be the subject of continuing discussions and are subject to change as new information or modeling difficulties are encountered.

Our impurity and gas throughput control strategy brackets potential solutions. We have placed strong emphasis on materials selection, treatment, quality control, in situ cleaning, and bakeout. We have assumed passive wall treatment and plasma edge control for our trade studies. However, in conjunction with the trade studies, alternate concepts are under investigation: Magnetic divertors, gas blanket divertor, and various particle collection approaches. We judge that our choice for trade studies will not prejudice our selection process and as detailed design analysis is initiated, alternate concepts can readily be factored in if they are judged necessary.

We conclude that these common elements of all TNS options represent credible options and ensure a fair and unbiased technology evaluation and decision.

The following examples – vacuum vessel and shield cooling systems and OH coil power conditioning circuit – are illustrative of important subsystem design models. Our vacuum vessel and shield cooling systems, depicted in Fig. 6.9, use low pressure, low temperature water with an intermediate loop including energy storage facilities to buffer peak thermal loads. The OH coil power conditioning circuit, Fig. 6.10, provides fuel control start-up and full control shutdown at any time. These examples of realistic representations are indicative of the detail included in our model to ensure that size variations are appropriately scaled and the resulting cost impact determined.

Trade study initiation. A specific design layout has been prepared for each TNS option using the methodology and ground rules summarized above. These schematic representations are preliminary, self-consistent arrangements and do not depict optimized configurations. Figure 6.11 presents an example of the design layouts obtained from our trade study evaluation and, Table 6.4 summarizes the major characteristics of

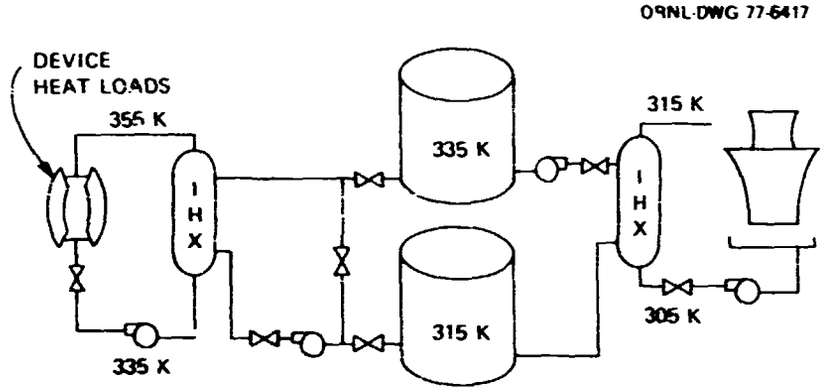

Fig. 6.9. Schematic of vacuum vessel and shield cooling systems.

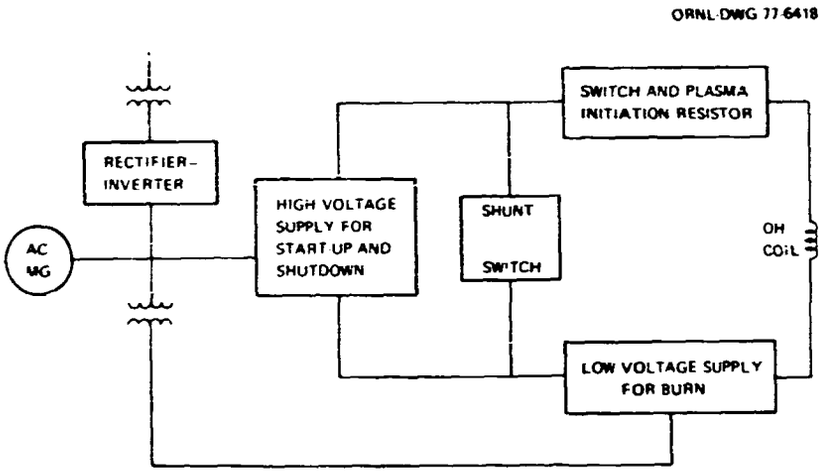

Fig. 6.10. Schematic of OH coil power conditioning circuit.

the TNS-3 options. Table 6.5 summarizes the TF coil assembly logic as an example of the major component modeling used to develop trade study data.

Preliminary results have been obtained from the COAST code; however, these results must be thoroughly checked to verify results, and cost models may require refinement. In addition, preliminary subsystem optimization must be completed, and after trends are determined the search strategy will be adjusted to seek minimum cost systems. As an example of the type of cost information available from the COAST code, Fig. 6.12 presents preliminary results from a study of relative cost versus the number of TF coils for the TNS-3 option.

Selection criteria. A rating system is being developed for TNS configuration selection. The major attributes to be considered follow.

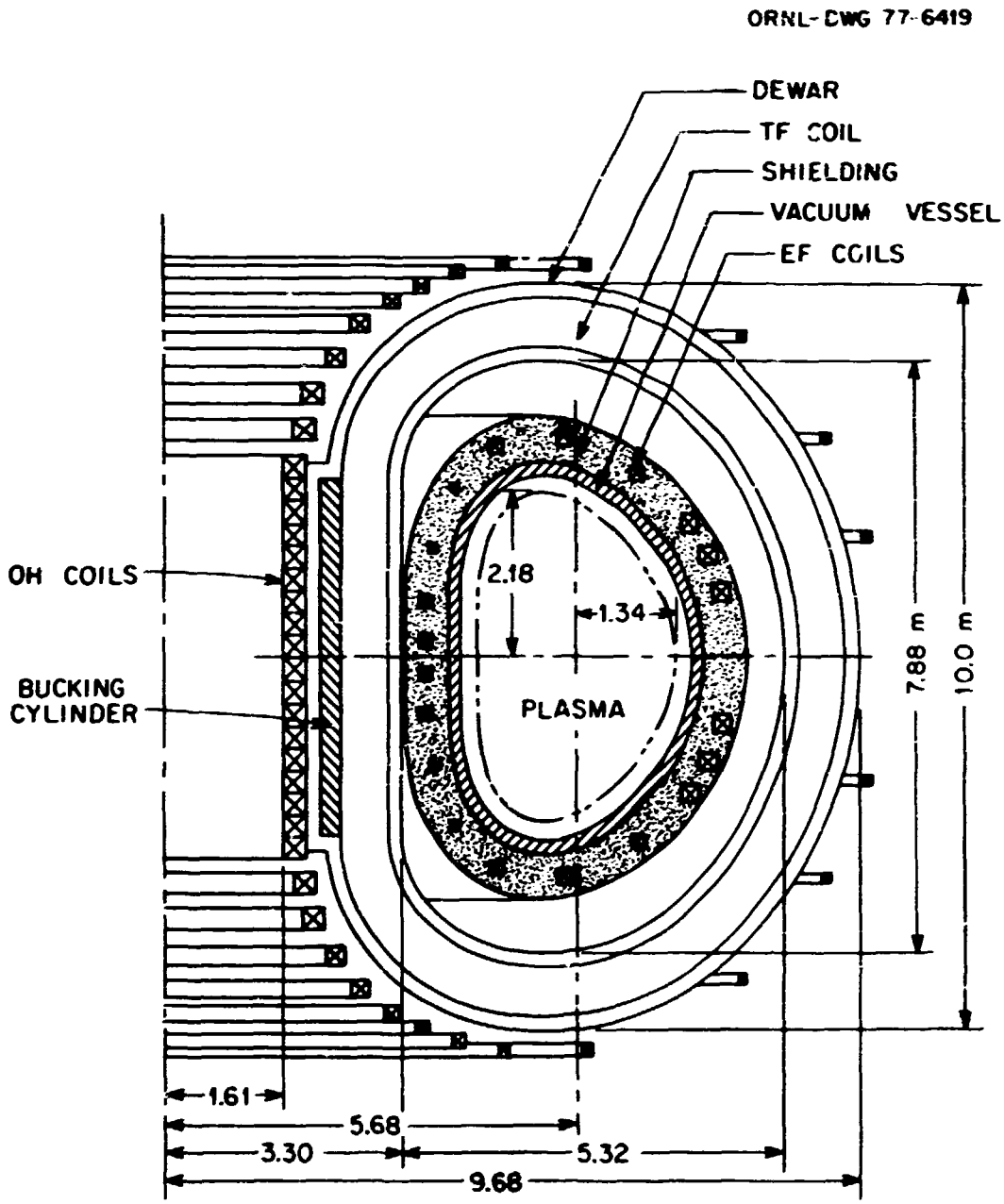

Fig. 6.11. Preliminary self-consistent (unoptimized) schematic arrangement of TNS-3.

Quantifiable	Semiquantifiable
capital cost	mechanical complexity
operation cost	technical risk
size	assembly/maintenance
performance	operational flexibility
schedule	cost/schedule risk
	reactor technology
	extrapolatability

This rating system is essential because our engineering and cost assessments provide only the quantifiable basis for a TNS recommendation.

Conclusions. Our engineering and design studies to date have led to the following conclusions.

1) Design options have been identified that bracket physics uncertainties.
2) Trade study models have been developed in detail with consistent physics and engineering rationale.
3) This tool is now operational for TNS option evaluation and selection.
4) Critical cost and schedule questions remain.

R&D needs assessment

An assessment of TNS research and development needs has been initiated. These needs are similar to EPR with some changes in timing and emphasis. The assessment is more extensive than the EPR activity, upon which it builds, in three ways - more specific, schedule oriented, and more inclusive. Initial R&D areas include:

- plasma heating - extension of positive ion beams to TNS service, initiation of negative ion beams or RF heating;
- impurity control and gas throughput handling - basic mechanisms;
- fueling - pellet acceleration criteria;
- superconducting coil technology - extensions to Nb$_3$Sn technology;
- PF system - windings and power supplies - mechanically feasible design and acceptable cost;
- remote maintenance - machine arrangement in actual design;
- tritium containment and pumping of gas mixtures;
- plasma physics design criteria in each area.

These topics currently under investigation at ORNL are discussed in the other sections of this report.

Development of a program plan

At ERDA-DMFE request we have initiated an effort to develop an overall TNS program plan. The objectives for this total assessment established by ERDA-DMFE included:

Table 6.4. TNS-3 option major characteristics

• TF coil system	NbTi, multifilamentary, pancake wound
• TF cooling	Liquid helium, supercritical, forced flow
• Centering force restraint	Bucking cylinder (noses in common dewar,
• Peak current density over winding slot	2500 A/cm^2
• Peak field at conductor	8 T
• A_s/A_c (area of structure/ area of conductor)	1.5

1) establishing the proper sequencing of design, R&D, and construction elements to support the orderly design and construction of TNS,
2) identification of all critical research, development, and demonstration tasks and programs necessary to support operation of TNS,
3) identification of the necessary schedule for TNS operation in 1986,
4) identification of modifications in the schedule of activities as a function of changes in scheduled operation, and
5) identification of the budget for each of the two preceding objectives and comparison with the current budget projection.

Table 6.5. Example of major component modeling - TF coil assembly logic

• Input	• TF coil type and number, plasma specifications.
• Determine	• Inner TF leg radial clearances (plasma liner, vessel, nuclear shielding, SF coils, thermal shielding, dewar, structure, assembly and expansion, nose ripple,.
	• Outer leg radial clearances (space for components, or NB access or ripple).
	• Radial build (ampere turns, ripple, conductor-structure areas).
	• Vertical bore constant tension D.
• Check	• To ensure that components fit.
• Iterate	• As needed for consistency.
• Calculate	• Material volumes and cost of all assembly elements.

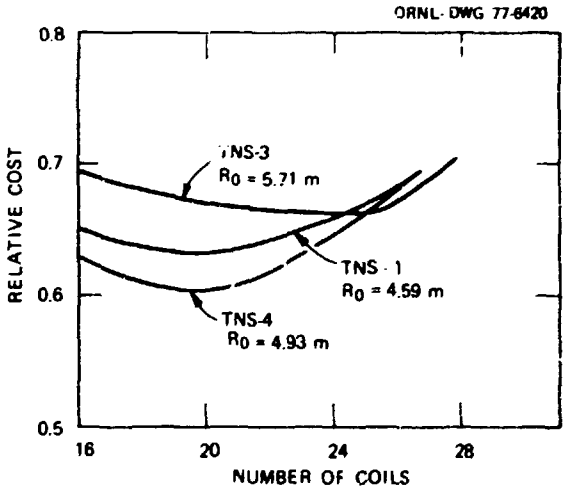

Fig. 6.12. Example of cost information available from COAST code -- relative cost vs number of TF coils.

The TNS concept used for the basis of this assessment is the July 1976 reference point including the four TF coil options. We are scheduled to complete a first draft of the program plan early next year.

6.2.5 Conclusions

The Oak Ridge TNS program is establishing a way to proceed toward the next step tokamak confinement device beyond TFTR. TNS is a device which leads to an economically viable fusion reactor and is being planned for mid-1980's operation. The Experimental Power Reactor study performed during FY 75 and FY 76 has led to an intermediate step and new design, TNS after TFTR, having a higher benefit/cost than EPR.

The TNS program, now in the early design stages, is focusing on providing bases for a conceptual design point decision by mid-FY 77 by:

- conducting a physics parameter study that provides theoretical framework,
- conducting an engineering trade study that develops quantitative comparisons,
- identifying specific R&D requirements that establish breadth of support needs and availability, and
- initiating a thorough consideration of an overall plan for the conduct of the TNS program.

1. P. N. Haubenreich (ed.), *Tokamak Experimental Power Reactor: Basic Considerations and Initiation of Studies at Oak Ridge*, ORNL/TM-4853, Oak Ridge National Laboratory, Oak Ridge, Tennessee (April 1975).
2. M. Roberts, *Oak Ridge Tokamak Experimental Power Reactor Study Scoping Report*, ORNL/TM-5038, Oak Ridge National Laboratory, Oak Ridge, Tennessee (1977).
3. M. Roberts and E. S. Bettis, *Oak Ridge Tokamak Experimental Power Reactor Study Reference Design*, ORNL/TM-5042, Oak Ridge National Laboratory, Oak Ridge, Tennessee (November 1975).
4. M. Roberts, *Oak Ridge Tokamak Experimental Power Reactor Study – 1976, Part 1: EPR Summary*, ORNL/TM-5572, Oak Ridge National Laboratory, Oak Ridge, Tennessee (1977).
5. D. G. McAlees and F. B. Marcus (eds.), *Oak Ridge Tokamak Experimental Power Reactor Study – 1976, Part 2: Plasma Engineering*, ORNL/TM-5573, Oak Ridge National Laboratory, Oak Ridge, Tennessee (November 1976).
6. J. W. Lue (ed.), *Oak Ridge Tokamak Experimental Power Reactor Study – 1976, Part 3: Magnet Systems*, ORNL/TM-5574, Oak Ridge National Laboratory, Oak Ridge, Tennessee (1977).
7. C. A. Flanagan (ed.), *Oak Ridge Tokamak Experimental Power Reactor Study – 1976, Part 4: Nuclear Engineering*, ORNL/TM-5575, Oak Ridge National Laboratory, Oak Ridge, Tennessee (1977).
8. T. E. Shannon and R. L. Reid (eds.), *Oak Ridge Tokamak Experimental Power Reactor Study – 1976, Part 5: Engineering*, ORNL/TM-5576, Oak Ridge National Laboratory, Oak Ridge, Tennessee (1977).
9. M. Roberts, *Oak Ridge Tokamak Experimental Power Reactor Study – 1976, Part 6: Research, Development, and Demonstration Needs*, ORNL/TM-5577, Oak Ridge National Laboratory, Oak Ridge, Tennessee (1977).
10. J. F. Clarke, *EPR and TNS*, ORNL/TM-5418, Oak Ridge National Laboratory, Oak Ridge, Tennessee (June 1976).
11. J. F. Clarke and D. G. McAlees, *High Beta Pre-Demonstration Fusion Devices*, ORNL/TM-5692, Oak Ridge National Laboratory, Oak Ridge, Tennessee (November 1976).
12. D. Steiner et al., *ORNL Fusion Power Demo Study: Interim Report*, ORNL/TM-5813, Oak Ridge National Laboratory, Oak Ridge, Tennessee (1977).
13. S. E. Attenberger et al., *Dynamics of Tokamak Plasma Experiments and Reactors*, ORNL/TM-5509, Oak Ridge National Laboratory, Oak Ridge, Tennessee (November 1976).
14. J. F. Clarke, *High Beta Flux Conserving Tokamaks*, ORNL/TM-5429, Oak Ridge National

Laboratory, Oak Ridge, Tennessee (June 1976).

15. D. G. McAlees, "The ORNL-EPR Study — Results and Implications," paper presented at the Winter Meeting of the American Society of Mechanical Engineers, New York, New York, December 5-10, 1976.
16. J. F. Clarke, *Suggestions for an Updated Fusion Power Program*, ORNL/TM-5280, Oak Ridge National Laboratory, Oak Ridge, Tennessee (February 1976).
17. L. A. Berry, *ORMAK Upgrade: A Proposed Tokamak Device for Plasma Heating and Stability Investigations*, ORNL/TM-5130, Oak Ridge National Laboratory, Oak Ridge, Tennessee (June 1976).
18. P. N. Haubenreich, W. C. Anderson, J. M. Luton, and P. B. Thompson, *Plan for the Large Coil Project*, ORNL/TM-5824, Oak Ridge National Laboratory, Oak Ridge, Tennessee (1977).
19. Plasma Heating Department of the Thermonuclear Division, *TFTR Neutral Beam Systems Conceptual Design*, ORNL/TM-5227, Oak Ridge National Laboratory, Oak Ridge, Tennessee (March 1976).

7. FUSION REACTOR TECHNOLOGY PROGRAM

D. Steiner, Program Manager

R. G. Alsmiller, Jr.[1]
B. R. Appleton[2]
J. Barish[3]
J. M. Barnes[3]
G. M. Begun[4]
J. T. Bell[4]
J. Bentley[5]
E. S. Bettis[6]
E. E. Bloom[5]
C. R. Brinkman[5]
R. E. Clausing[5]
S. D. Clinton[7]
R. J. Colchin[8]
S. Datz[4]
J. H. DeVan[5]
P. F. Dittner[4]
L. C. Emerson[5]
P. W. Fisher[7]
T. A. Gabriel[1]
M. L. Grossbeck[5]
L. Heatherly[5]
T. J. Hoffman[3]
J. A. Horak[5]
T. J. Huxford[6]
J. R. Keiser[5]
J. F. Land[4]
K. C. Liu[5]
D. L. Manning[5]
H. E. McCoy[5]
B. F. Maskewitz[1]
P. J. Maziasz[5]
A. T. Mense[9]
S. Overbury[4]
J. D. Redman[4]
R. L. Reid[6]
M. T. Robinson[2]
F. L. Rogers[7]
R. W. Roussin[1]
R. T. Santoro[1]
J. L. Scott[5]
J. E. Selle[5]
T. E. Shannon[6]
F. J. Smith[4]
J. O. Stiegler[5]
W.C.T. Stoddart[10]
J. B. Talbot[7]
D. K. Trubey[1]
J. S. Watson[7]
H. L. Watts[6]
W. M. Wells[6]
R. W. Werner[11]
C. W. White[2]
F. W. Wiffen[5]
M. L. Williams[1]
J. W. Woods[5]

1. Neutron Physics Division.
2. Solid State Division.
3. Computer Sciences Division.
4. Chemistry Division.
5. Metals and Ceramics Division.
6. Fusion Reactor Engineering Department, Experimental Engineering Division.
7. Chemical Technology Division.
8. Tokamak Experimental Section, Fusion Energy Division.
9. Plasma Theory Section, Fusion Energy Division.
10. Structural Analysis and Computer Methods Department, Engineering Analysis Division.
11. Visiting scientist, Lawrence Livermore Laboratory, California.

7.1 MATERIALS COMPATIBILITY STUDIES

7.1.1 Corrosion Studies of Two Austenitic Stainless Steels in Liquid Lithium[1]

J. F. Selle

Thermal convection loops were fabricated of types 304L and 321 stainless steel and operated with lithium for 3000 hr with a 600°C hot leg temperature and a 200°C ΔT. Tabular specimens were placed in the hot and cold legs so that mass transfer effects around the loop could be studied. Maximum corrosion rates of about 0.55 mils/year (3.7 mg/cm^2) were obtained for both loops. Weight losses from the hot leg specimen were due primarily to the solution of nickel and chromium from the stainless steel. In the cold leg, the

maximum deposition rate of chromium occurred at a temperature considerably above that for nickel. Metallography, electron microprobe analysis, weight change measurements, x-ray fluorescence analysis, x-ray diffraction, scanning electron microscopy, and magnetic susceptibility measurements were used to study the mass transfer around the loops.

7.1.2 Compatibility Tests in Static Lithium

J. E. Selle

Additions of various elements were made to lithium in static capsules for the purposes of identifying adverse effects of potential impurities in lithium, studying the possibility of inhibiting corrosion processes by in situ coating of test specimens with a diffusion barrier, and studying the effectiveness of potential impurity gettering elements. Tests were conducted in type 316 stainless steel capsules at 500, 600, and 700°C for times to 10,000 hr.

Stainless steel specimens gained weight following respective additions of silicon, manganese, cobalt, aluminum, and carbon. With the possible exception of carbon, all of the latter additions show potential for providing a diffusion barrier to inhibit the migration of alloying constituents from the stainless steel. Nitrogen has an adverse effect on corrosion by lithium under static conditions. Calcium and yttrium appear to be effective in removing nitrogen from lithium in static capsules.

7.1.3 The Reduction of Al_2O_3 in Niobium-Lithium Systems at 1000°C[2]

J. E. Selle J. H. DeVan

Various grades of Al_2O_3 were sealed inside capsules of Nb and Nb-1% Zr and exposed to liquid lithium for 3000 hr at 1000°C. Similar but unsealed capsules were tested under vacuum. Reduction of the Al_2O_3 occurred in the lithium treated capsules, but not in the vacuum treated capsules. Metallography and electron microprobe analysis showed reaction products in the form of compounds of niobium, aluminum, and zirconium. Lithium acted as a sink for oxygen.

7.1.4 Determination of Oxygen in Lithium

J. E. Strain J. H. DeVan

In 1969 the Metals and Ceramics Division of ORNL established a 14-MeV neutron activation analysis facility to determine oxygen in reactive metals, especially lithium and potassium. Using this facility, we conducted a cooperative study with R. M. Yonco and V. A. Maroni of Argonne National Laboratory (ANL) to measure the solubility of lithium oxide in liquid lithium. Aliquots of saturated lithium-oxygen solutions were drawn into thin-walled nickel capsules by the ANL workers, and the individual capsules were analyzed for total oxygen content at ORNL. A total of 28 solubility determinations were made, covering the temperature range 195-734°C.

7.1.5 The Corrosion Resistance of Type 316 Stainless Steel to Li_2BeF_4[3]

J. R. Keiser J. H. DeVan D. L. Manning

The corrosion rate of type 316 stainless steel in molten $LiF-BeF_2$ (66-34 mole %) has been measured in a thermal convection loop operating with a maximum temperature of 650°C and a ΔT of 160°C. The corrosion rate was correlated with the concentration of impurities in the salt and the fluoride ion oxidation potential as determined by an on-line volt-ammeter.

A corrosion rate of 5.6 mg/cm^2-yr was observed initially in the as-received salt. This rate decreased as reactions with initial salt impurities went to completion. Direct addition of beryllium metal to the salt further reduced the corrosion rate.

7.1.6 The Effects of Helium Impurities on Superalloys[4]

J. E. Selle

A review of the literature on the effects of helium impurities on superalloys at elevated temperatures was undertaken. The actual effects of these impurities vary depending on the alloy, composition of the gas atmosphere, and temperature. In general, treatment in helium produces significant but not catastrophic changes in the

structure and properties of these alloys. The effects of these treatments on the structure, creep, fatigue, and mechanical properties of the various alloys are reviewed and discussed. Suggestions for future work are presented.

7.2 MECHANICAL PROPERTIES OF STRUCTURAL MATERIALS

K. C. Liu C. R. Brinkman

This is a new program which was initiated at the beginning of the FY 76 transition quarter. The objective of this program is to identify materials engineering problem areas and needs as well as to assess the adequacy and the extent of validity in applying existing or proposed structural design rules and criteria to the design of power reactors by magnetic fusion energy (MFE). Specific and basic materials data needs will be defined and proposed for inclusion in a materials development and engineering test plan to provide essential information in support of MFE research and development effort.

The programmatic commitment has two specific goals in mind. They are to establish: (1) a set of unified structural design rules and guidelines that are acceptable to the MFE design community for interim design applications to major MFE systems and components, and (2) a set of comprehensive mechanical properties data of MFE structural materials for use in the implementation of the design rules and criteria.

To achieve the first goal, a coordinated effort is required in setting a national committee on structural design and materials engineering represented by various laboratories and industries that are conducting magnetic fusion research and development. Technical liaison with some MFE research laboratories has been initiated. A national committee for structural design of superconducting magnets comprised of working groups in such areas as physical and mechanical properties, design methods, design limits, fabrication and construction, nondestructive testing, safety, etc. was proposed at the workshop on Structural Analysis Needs for Superconducting Magnets held at Brookhaven National Laboratory (BNL) September 8-10, 1976. The proposal was generally accepted by the workshop participants.

Aside from the plasma physics problems, much of the long-term successful operation of the magnetic fusion reactor will depend heavily upon sound engineering judgment in design and selection of appropriate materials for the construction of the systems and components. During the past months, we have conducted a comprehensive review of the Experimental Power Reactor (EPR) Reference Designs by ORNL and ANL; a study of the counterpart by General Atomic Co. (GAC) will be conducted when the report becomes available. The effort will be extended to cover the designs of The Next Step (TNS) and demonstration plants. An analysis and assessment of the strengths and shortcomings of existing structural design codes and standards that are used in design of nuclear components for fission are being made on the basis of current information on the EPR designs. Presently, we are focusing our attention on the design of first-wall/blanket/shield systems.

On the basis of current information on the EPR Reference Designs, it has been illustrated that the thermal stresses induced by temperature gradients in the first wall and the radiation shield wall may cause serious problems[5] such that alteration of the designs or the selection of candidate materials may be required. A detailed study of these problems is currently under way.

7.3 NEUTRONICS

7.3.1 The Spatial Variation of the Damage Energy and Gas Production in the Experimental Volume of a Li(D,n) Neutron Radiation Damage Facility[6]

R. G. Alsmiller, Jr. J. Barish

Calculated results are presented of the variation with position in the experimental volume of a Li(D,n) neutron radiation damage facility of the damage energy and helium and hydrogen production in copper and in niobium when this volume is partially filled with experimental samples. The neutron nonelastic cross-section

data at the higher energies (≥15-20 MeV) needed to carry out the transport calculations were obtained from the intranuclear-cascade model of nuclear reactions.

7.3.2 Neutronics Calculations for the TFTR Neutral Beam Injectors[7]

R. T. Santoro R. G. Alsmiller, Jr.

Estimates, based entirely on one-dimensional transport calculations, of some of the effects of radiation on the operation and maintenance of the neutral beam injector for the Tokamak Fusion Test Reactor (TFTR) to be built at the Plasma Physics Laboratory of Princeton University are presented. Radiation effects due to 14-MeV neutrons produced by D-T reactions in the plasma and due to 2.6-MeV neutrons produced by D-D reactions in the calorimeter and in the charged-deuteron beam dump are considered. The results presented here are intended to indicate potential radiation problems rather than to be an accurate estimate of the magnitude of the actual radiation effects that will exist in the vicinity of the final injectors. This is particularly true since the results presented here are based on early injector design data, some of which are no longer applicable.

For 14-MeV neutrons, estimates are given of

1) the heating and activation of the toroidal field (TF) coils adjacent to the injector ports,
2) activation of the injector superstructure, and
3) heating in the cryopanel assemblies.

For 2.6-MeV neutrons, estimates are given of

1) activation of the calorimeter structure, and
2) dose rates in the vicinity of the charged-deuteron beam dump.

It is to be noted that no estimate is given here of the activation of the charged-deuteron bending magnet since at the time these calculations were performed no design for this magnet was available.

7.3.3 Neutronics and Photonics Calculations for the Tokamak Experimental Power Reactor[8]

R. T. Santoro V. C. Baker J. M. Barnes

The results of one-dimensional neutronic and photonic calculations that compare the nuclear performance of blanket and shield designs proposed for use in the Tokamak Experimental Power Reactor are presented. The nuclear analysis was carried out for both nonbreeding and tritium-breeding blanket modules to compare the spatial variations of the radiation flux and energy distributions, nuclear heating, radiation damage, and tritium breeding. Nonbreeding blanket modules that contain potassium plus 316 stainless steel or potassium only as the energy-absorbing medium and breeding blankets that use natural lithium as the fertile material were evaluated as a function of the first-wall cooling scheme.

7.4 RADIATION EFFECTS

7.4.1 Recent Progress in Bulk Radiation Effects Studies[9]

F. W. Wiffen J. O. Stiegler

A review of recent experiments that partially simulate fusion reactor structural materials irradiations has helped develop our understanding of effects that will be observed in fusion reactors. At the high fluences and elevated temperatures that will be characteristic of reactor operation, experimental data have shown that the high helium contents that result from (n,α) reactions will be important in determining the irradiation response. In particular, these high helium concentrations will result in more restrictive limits on reactor response than would be set based on results of fast spectrum fission reactor experiments. Low fluence, ambient temperature irradiations with 14-MeV neutrons have been compared to fission reactor irradiations on the basis of changes in several physical properties in a number of different materials. These comparisons suggest that

fission reactor neutrons provide an adequate simulation of the displacement damage component of fusion neutron irradiation, and that differences between the two types of irradiation can be understood. Since fission neutron irradiations do not usually produce the same amount of transmutation products as will fusion reactor service, all simulation experiments must be evaluated with awareness of this restriction.

7.4.2 Neutron-Irradiation Effects in Molybdenum and Molybdenum Alloys[10]

J. Bentley F. W. Wiffen

Molybdenum, Mo-0.5% Ti and TZM alloys have been irradiated in Experimental Breeder Reactor II (EBR-II) at temperatures of 698 to 1273 K to fluences of 2.5×10^{26} neutrons $\cdot$ m^{-2} (E > 0.1 MeV) or higher. The results of a transmission electron microscopy investigation of the irradiated specimens are reported. Microstructures generally coarsen with increasing irradiation temperature and there are no pronounced effects of alloying. The suppression of void formation in TZM observed at lower fluences ($\sim 10^{24}$ neutrons $\cdot$ m^{-2}) was not observed at the present higher fluences ($>10^{26}$ neutrons $\cdot$ m^{-2}) more typical of projected fusion reactor operation.

7.4.3 Swelling and Microstructural Changes in Type 316 Stainless Steel Irradiated Under Simulated Fusion Conditions[11]

P. J. Maziasz F. W. Wiffen E. E. Bloom

Tensile specimens of type 316 stainless steel were irradiated in the High Flux Isotope Reactor (HFIR) to displacement damage levels of 42-60 dpa (displacements/atom) and helium contents of 3000-4300 appm at temperatures from 380 to 680°C. The samples were irradiated in both the annealed condition (1 hr at 1050°C) and the 20% cold worked condition. The microstructures of these samples were examined by transmission electron microscopy (TEM). The results were compared with specimens of the same heat of steel irradiated in EBR-II to approximately the same conditions with the exception of helium content, which was ~15 appm. Swelling in annealed and cold worked samples with high helium content was approximately constant with temperature from 380 to 550°C and increased rapidly from 550 to 680°C. Swelling in cold worked samples was less than in the annealed samples for all temperatures except 680°C. Swelling was larger at all temperatures for samples containing large helium concentrations than for the same material with small helium concentrations, Recrystallization at 600°C destroyed the cold work swelling resistance. Cold work increased the cavity concentrations, decreased the cavity sizes, and reduced the swelling, compared with annealed material containing equivalent high helium concentrations. Swelling was greatly increased at irradiation temperatures above 600°C in both the annealed and cold work samples; the increase was due to the formation of very large cavities at the grain boundaries. Calculations to compare the amount of helium measured in the samples with the amount necessary to stabilize equilibrium bubbles have shown most of the cavities to be equilibrium helium bubbles.

7.4.4 Mechanisms of Ductility Loss in Fusion First-Wall Structural Materials[12]

F. W. Wiffen

The major irradiation-produced problem in metal structural components in the high-flux regions of fusion reactors will be loss of ductility. Available conceptual reactor designs and existing radiation effects data are combined to illustrate the mechanisms of ductility loss in materials and operating conditions of potential fusion interest. In the very large and complex fusion components, stresses will be imposed directly by coolant temperature gradients, imposed cyclically by the duty cycle of the reactor, and developed over long time periods by irradiation-produced swelling. Accommodation of these stresses will require some plastic deformation, although the required levels of ductility cannot yet be specified.

Several ductility reduction processes are possible, depending on the choice of structural material and the temperature-flux parameters of reactor operation. In some body-centered cubic (bcc) metals, the DBTT can be raised by irradiation to well above room temperature, and perhaps to the reactor operating temperature. Failures in this case are predominantly by a cleavage mode, with some component of grain boundary separation. In metals and loading conditions where failures are ductile and transgranular, elongation to fracture can be severely reduced, although the local ductility as measured by reduction in area at the fracture may be very high. The failure mode in this case occurs by the onset of plastic instability at yielding. All deformation is restricted to the necked region. Ductility is also reduced by the presence of insoluble gas in the grain boundaries. This allows grain separation to occur at stresses well below those required to deform the matrix. A general loss of ductility usually accompanies the lattice hardening resulting from irradiation-produced defects. This is of importance mainly as it relates to the other ductility loss mechanisms mentioned here.

Three types of behavior have been established in bcc metals with potential for fusion application.[13] In the case of molybdenum alloys, the DBTT can be raised to at least 550°C by neutron irradiation. While the ranges of irradiation and test conditions examined are too restricted to rule out molybdenum alloys for fusion use, the data do demonstrate the need for further testing to evaluate the ability of molybdenum structures to withstand the stresses generated during shutdown cycles of a reactor. Ductility loss by the onset of plastic instability is important under some conditions in niobium and tantalum alloys; where uniform elongation in irradiated samples has been measured as low as 0.1%. In service this could result in the situation in which any component overloaded to its yield stress will deform to fracture under constant or decreasing load. Under other irradiation and test conditions, niobium and tantalum alloys exhibit a general ductility loss while still retaining appreciable uniform elongation. Vanadium alloys exhibit a similar behavior. Ductility reductions are observed, but the uniform elongation remains adequate for structural application.

In austenitic stainless steels, the leading candidate material for first-generation fusion reactors, high helium generation rates promote grain boundary decohesion at low stresses. This intergranular failure mode will limit the application of type 316 stainless steel to temperatures below 600°C (Refs. 14 and 15). The importance of helium-enhanced intergranular failure in limiting the fusion application of other classes of alloys has not generally been established, although limited evidence suggests it is important in some other alloys.[16] Stainless steel irradiated under simulated fusion conditions at lower temperatures also shows reduced tensile ductilities, but the failure mode has not been established.

Proposed fusion reactor operating conditions will lead to severely reduced ductility of the reactor structural materials. Conditions have been identified where ductility limitations are set by the intergranular fracture mode, by the onset of plastic instability at yielding, and by the shift of the DBTT into the operating temperature range of the reactor. The available data establish that very careful reactor design will be required to keep stresses developed during operation compatible with the material properties and that future detailed experimentation will be required to define the temperature-fluence-strain-rate dependence of ductility reduction in proposed fields of reactor operating parameters.

7.4.5 The Use of ORR in Simulating Fusion Reactor Irradiations

J. A. Horak

The continuing evaluation of the facilities that can satisfy the criteria for simulation of fusion reactor irradiation conditions has focused

our attention on the unique advantages of the Oak Ridge Research Reactor (ORR) for the Radiation Effects Program. For an irradiation facility to be useful in the development of first wall materials it must:

1) produce dpa and helium at actual and accelerated rates (for a fusion reactor at 1 MW/m^2 these values are 13 dpa and 175 appm He per year for type 316 stainless steel);
2) allow active temperature and stress control during irradiation;
3) have the capability for in situ stress and strain measurement;
4) allow control of the irradiation environment; and
5) provide adequate experimental volume to accommodate large numbers of specimens.

An evaluation of the ORR against these criteria reveals the following facts.

1) It produces dpa and He at rates equivalent to real time up to ~2 MW/m^2 in alloys containing nickel.
2) Instrumentation is available for active control of irradiation temperature, stresses, and environments.
3) It is adaptable for conducting in situ measurements.
4) Large experimental volumes are available to accommodate the required test matrix.
5) The high duty factor results in high reactor availability.

The liabilities of the ORR as a simulation facility for fusion reactor irradiations are that it does not match the fusion reactor neutron energy spectrum and that it cannot produce relevant helium concentrations in materials that do not contain nickel. Because helium production in the ORR or any other thermal reactor proceeds by the two-step thermal neutron capture sequence

$^{58}Ni\ (n,\gamma)^{59}Ni$

$^{59}Ni\ (n,\alpha)^{56}Fe,$

the ratio of the thermal neutron flux to fast neutron flux must be periodically adjusted to match fusion reactor conditions. This neutron spectrum tailoring requires that fuel management, neutron absorbers, and/or neutron multipliers be used. In the ORR the thermal neutron flux can be increased by placing additional moderators between the fuel and the test specimens. This is usually accomplished by placing a beryllium sleeve around the experimental assembly and/or increasing the thickness of water between the fuel elements and the test specimens. The fast neutron flux can be increased while the thermal neutron flux is decreased, by placing a sleeve of aluminum containing from 5-15 at. % ^{235}U around the experimental assembly. In principle it is possible, without difficulty, to have any thermal and fast neutron fluxes desired over the range from about 1-6 × 10^{18} neutrons m^{-2} sec^{-1}.

The two initial fusion reactor materials irradiation experiments in the ORR will emphasize type 316 stainless steel but will include lesser amounts of modified stainless steels, PE-16, other nickel-base alloys, and developmental alloys. The specimens (loaded in 24 individually controllable positions in each experiment) will cover a range of irradiation temperatures from 250-650°C. Limited irradiation creep rate determinations will be accomplished with statically and dynamically pressurized tubes. Postirradiation examination of other samples will yield swelling, tensile, creep-rupture, and fatigue properties. Supporting examination will develop the irradiation effects on microstructure, fracture mode, and phase stability as functions of initial microstructure and irradiation parameters.

7.4.6 Irradiation Experiments in Progress

M. L. Grossbeck J. A. Horak P. J. Maziasz
F. W. Wiffen J. W. Woods

The lack of irradiation facilities that have the flux and spectrum of fusion reactors requires that all irradiations designed to evaluate the effect of fusion reactor operation on first-wall and structural materials must be accomplished using simulation techniques. In the ORNL irradiation effects program, the

emphasis is on simulation using fission reactors. The rate of the atom displacement component of fusion reactor irradiation can be achieved in a number of high flux fission reactors. The transmutation-produced helium is simulated in alloys containing nickel as discussed in Sect. 7.4.5.

The Radiation Effects Program makes continuous use of the six peripheral target positions at the outer zone of the HFIR flux trap region. In these experiments accelerated production of dpa and He, relative to fusion reactors, provides rapid simulation of fusion reactor exposures. Experiments in each position contain 10 or 11 tensile specimens with cylindrical geometry for irradiation at temperatures between 55 and 900°C. The six experiments currently under irradiation cover the temperature range 280-700°C and contain specimens of PE-16, type 316 stainless steel, and a titanium modified type 316 stainless steel. These will be evaluated for swelling, tensile properties, creep-rupture properties, phase stability, fracture mode, and microstructural effects. Irradiation of samples for postirradiation fatigue property measurements will begin with the next experiment.

Irradiation experiments in the EBR-II are used to reach high displacement damage levels on a large number of specimens. While the helium component of fusion reactor damage is not simulated in these irradiations, the partial simulation will set limits on the fusion reactor application of materials. Later experiments may further refine these limits. In EBR-II experiments, irradiation temperatures in the range of 370 to >1000°C can be achieved by passive control, either through gas gap control of heat flow or through the use of heat pipes. Two experiments are currently in the reactor, one each in row 7 and row 8. The range of temperatures in these two experiments is 400-800°C, and the maximum goal fluence is 2×10^{22} neutrons/cm^2 in the row 8 experiment and 4×10^{22} neutrons/cm^2 in the row 7 subassembly. Specimens of a number of alloys have been included and after irradiation will be evaluated for swelling, microstructural effects, and irradiation effects on mechanical properties. In addition, some pressurized tubes have been included to evaluate irradiation creep through measurement of tube swelling. Base metal and weld metal have been included, and samples preinjected with helium either by alpha implantation or tritium decay are included for evaluation of the effectiveness of preirradiation helium in simulating fusion reactor conditions. A limited number of type 316 stainless steel and Nimonic PE-16 samples are included to supplement the irradiations in the mixed spectrum thermal reactors. A greater emphasis is placed on the refractory metals in these experiments because the thermal reactor helium production in nickel-containing alloys does not apply in these materials. The refractory metals included are Nb, Nb-1 Zr, D-43, Mo, TZM, V-20 Ti, and V-10 Cr-5 Ti. Irradiation of the row 8 experiment will be completed early in 1977; the row 7 experiment will remain in the reactor until mid-1979.

7.4.7 Development of Fatigue Testing Capabilities

M. L. Grossbeck K. C. Liu

The pulsed operation of tokamak machines causes cyclic stresses in structural components. In addition to these cyclic stresses, irradiation will produce helium as well as displacement damage. It is, therefore, essential to conduct an experimental program to evaluate the effect of cyclic stresses on materials irradiated under simulated fusion reactor conditions.

Previous experiments on irradiated materials led to contradictory conclusions. The effect of cyclic loading appears to be very sensitive to temperature, environment, and other test parameters.

The importance assigned to the understanding of fatigue properties of structural materials in fusion reactors requires the development of fatigue testing equipment and a test program to develop an understanding of irradiation effects on fatigue properties. We have initiated

fatigue testing with the following goals:

1) development of equipment and techniques suitable for testing samples irradiated to high fluence levels in fission reactors. This requires testing in a hot cell;
2) determination of the effects of cyclic operation at various temperatures (with respect both to direction and magnitude). A sufficiently high fluence and helium content must be employed in order to clearly establish the effect of irradiation and make an unambiguous determination of its direction;
3) determination of the mechanisms of interaction of displacement damage and helium on the fatigue deformation and fracture processes. Before intelligent suggestions for improvement of fusion reactor first wall materials can be made, the mechanisms of failure must be understood; and
4) use of the results from the fatigue testing for development of improved alloys for fusion reactor service.

A servohydraulic fatigue testing system for a radiation hot cell has been designed and purchased. The system is undergoing assembly and preliminary testing. It is capable of simulating the stress conditions of typical tokamak duty cycles and can also be used to perform conventional stress-controlled and strain-controlled tests. The system will be capable of air, inert gas, or high vacuum environments in the temperature range of 25-700°C.

The constraints imposed on specimen size by the requirements of the irradiation experiment have necessitated the development of a new specimen geometry. A miniature hourglass type fatigue specimen has been tested. Appropriate redesign of reactor irradiation experiments to accommodate these specimens has been accomplished.

This facility will be the only high vacuum fatigue testing system in the United States capable of performing uniaxial tests on highly irradiated specimens.

7.4.8 Evaluation of Nickel Alloy Response to Simulated Fusion Reactor Irradiation

F. W. Wiffen

Among the alloys that have been considered as candidate structural materials for the first wall and other structural components in the high flux regions of a fusion reactor are a number of nickel-base alloys. Previous ORNL work on type 316 stainless steel showed that swelling under irradiation that closely simulates fusion reactor conditions can be quite different from swelling under fast reactor irradiation. The differences are due to the greater helium production rates under fusion reactor conditions and require that results from the Liquid-Metal Fast Breeder Reactor (LMFBR) programs be used with caution in the fusion program. Simulated fusion reactor conditions are, however, achieved in HFIR irradiations, and nickel-base alloys being investigated are PE-16 (typical of precipitation-strengthened nickel alloys) and Inconel 600 (typical of solid solution-strengthened nickel alloys). Both alloys are reported to be swelling resistant under limited ion bombardment conditions. The goals of these experiments are (1) to investigate swelling under conditions of concurrent displacement damage and transmutation helium production and (2) to examine tensile properties of these materials as a function of irradiation and test temperatures. Irradiation at temperatures from 300-700°C gave helium contents from 300-2000 appm and displacement levels of 4-9 dpa.

The results of swelling measurements for irradiations which produced 4-9 dpa and He levels of 360-1030 appm in PE-16, 630-1780 appm in Inconel 600 can be summarized as follows:

1) Inconel 600 swells throughout the temperature range of 300-700°C; PE-16 shows appreciable swelling only at T > 600°C.
2) Swelling values much larger than expected from fast reactor and ion bombardment results were found for several irradiation temperatures.
3) Densification in PE-16 is observed at low

irradiation temperatures.

4) Solution-annealed PE-16 exhibits little difference in swelling behavior from the solution-annealed and aged material.
5) Swelling of Inconel 600 is only weakly temperature-dependent between 300 and 600°C but increases at higher temperatures.
6) Swelling increases with increased helium content in the Inconel 600.
7) Cold work was not effective in suppressing swelling of Inconel 600.

Tensile property measurements on the same samples led to the following conclusions

1) Strength values are increased for irradiation at 300-400°C.
2) Strength values decreased below unirradiated values for irradiations at 600-700°C.
3) Elongation values are lowest at the temperature extremes, with values at 400 and 500°C greater than at 300 or 700°C.
4) Helium clearly determines the fracture mode at 700°C.

On the basis of these results a decision has been made to focus future efforts on the PE-16 alloy. New irradiation experiments will expand the matrix of irradiation conditions to higher and lower fluences. In addition to immersion density and tensile tests, examination by electron microscopy, fractography, and metallography will be used to identify irradiation effects mechanisms. When all results are available, they will be evaluated in the framework of fusion reactor conceptual designs that specify nickel-base alloys as structural materials. Limitations imposed on reactor design by property changes will be considered, and future experiments necessary to evaluate the potential of these alloys in fusion reactors will be designed.

7.5 RADIATION SHIELDING INFORMATION CENTER

B. F. Maskewitz R. W. Roussin D. K. Trubey

The Radiation Shielding Information Center (RSIC), established in 1962, serves the radiation transport and shielding community by collecting, organizing, processing, evaluating, packaging, and disseminating information related mainly to reactor and weapons radiation. The scope of this information includes the physics of interaction of radiation with matter, radiation production and transport, radiation detectors and measurements, engineering design techniques, shielding materials properties, computer codes useful in research and design, and nuclear data compilations. Originally established to support research related to fission, RSIC is now also being used to support fusion reactor technology. The major activities include (1) operating a computer-based information system and answering inquiries on radiation analysis; (2) collecting, testing, packaging, and distributing computer codes; and (3) those activities associated with evaluated and processed nuclear data libraries.

All of the RSIC services contribute to the fusion technology program, but perhaps most significant is the service offered through the MFE Evaluated Cross-Section Library and the MFE Processed Data Library.

Both data activities are of special importance because RSIC is responsible for the generation, packaging, and distribution of a general purpose neutron cross-section library to be used for radiation transport and neutronics studies by Division of Magnetic Fusion Energy contractors. The goal is to provide a multigroup cross-section library based on the best evaluated data available which can be applied to a wide range of problems. As the goal is achieved, a substantial savings results because each user avoids the cost of maintaining his own capability to generate cross sections for his particular applications.

During the last year a validation program for this 171-neutron, 36-gamma-ray group processed library was undertaken and completed with the cooperation of several MFE contractors throughout the country. A 36-material version has been announced for general release and designated DLC-41/VITAMIN-C. This is now being updated with 25 additional materials.

Some of the materials needed were not part of the current U.S. standard evaluated library, ENDF/B-IV, which was issued in 1974. The missing ones were acquired from the Livermore Evaluated Nuclear Data Library (LENDL) modified as necessary to conform to proper format, and processed. The next update of ENDF/B will not be made until 1978, although additional evaluated data important for MFE studies will be available soon. These will be added to the DMFE Evaluated Library and also processed into multigroup form as part of DLC-41/VITAMIN-C so that they are available in timely fashion for use by MFE contractors.

7.6 SURFACE STUDIES

7.6.1 Wall Conditioning Studies for ORMAK and ISX[17]

R. E. Clausing L. C. Emerson
R. J. Colchin L. Heatherly

Laboratory studies of various discharge cleaning techniques and the resulting surface trapping of hydrogen have been carried out in an attempt to explain conditions existing in the Oak Ridge Tokamak (ORMAK). Gold and stainless steel samples have been both directly and indirectly exposed to oxygen and hydrogen glow discharges. Samples exposed either directly or indirectly to oxygen discharges experienced a more rapid removal of carbon (hydrocarbons) than samples exposed in a simi. r manner to hydrogen discharges, and similar results have been obtained during discharge cleaning in ORMAK. Samples directly bombarded as the cathode of a glow discharge were more rapidly cleaned than those indirectly exposed, i.e., facing away from and not immersed in the discharge. The oxygen concentration was found to increase on the surfaces of those samples which were oxygen discharge cleaned. Similarly, an increase in the oxygen impurity in ORMAK discharges is sometimes noted after oxygen discharge cleaning; however, the hydrogen discharge cleaning cycle which always precedes the initiation of normal tokamak plasmas tends to mask this effect. The presence of impurities (CH_4 and H_2O) in the cleaning discharge influences the composition of the surface in equilibrium with the discharge; thus it is important to remove impurities (reaction products) as efficiently as possible during the cleaning operation.

Direct hydrogen ion bombardment of stainless steel surfaces and subsequent thermal desorption demonstrated that 20-50 monolayers of H_2 were present in the surface oxide layer. Similar bombardment of nickel and gold surfaces showed little hydrogen loading. Hydrogen desorption from oxidized stainless steel surfaces is significant at room temperature and increases rapidly with even a few degrees rise in temperature, thus suggesting that thermal desorption may be an important mechanism of hydrogen release from tokamak walls.

7.6.2 Surface Impurities and "Clean-Up" Techniques[18]

R. E. Clausing L. C. Emerson
R. J. Colchin L. Heatherly

The detrimental role played by impurities in thermonuclear devices is now well known. Experimental studies to identify those impurities residing on the liner, or first wall, of ORMAX have been carried out in the laboratory using Auger Electron (AES) and X-ray Photoelectron (XPS) spectroscopic techniques. Additionally, liner measurements have been made in situ using a small soft x-ray appearance potential spectrometer (SXAPS). Oxygen, iron, and carbon were found to be the major surface impurities and, as confirmed by plasma diagnostics, also the major plasma impurities. Glow discharge cleaning of gold and stainless steel surfaces has been studied using various gases and gas mixtures. Oxygen discharges are very effective and hydrogen moderately effective in removing carbon and hydrocarbon deposits from both types of surfaces. Other parameters involved in the contamination-decontamination process, such as pressure and temperature, have been studied using techniques to controllably contaminate surfaces with hydrocarbons.

7.6.3 Hydrogen Loading and Clean-Up of Tokamak Wall Materials during Glow Discharge Cleaning[19]

R. E. Clausing L. C. Emerson

Most of the impurities in the plasmas of today's tokamaks get into the plasma from the wall as the result of plasma-wall interactions. Recent experiments suggest that much of the hydrogen in the discharge may also come from the wall. During glow discharge cleaning, oxidized surfaces can be loaded with hydrogen equivalent to many monolayers. This hydrogen is weakly bonded and easily desorbed by a small increase in temperature. The results of experiments being carried out both in the Impurity Study Experiment (ISX) tokamak and in the laboratory concerning effects of ion energy, ion flux, and plasma impurity levels on both the surface composition and the hydrogen loading phenomena are described. Tokamak discharge characteristics will be correlated to wall conditioning in the next phase of ISX operations.

7.6.4 Surface Characterization: Hydrogen Profiling

D. D. Allred B. R. Appleton
G. J. Clark C. W. White

Ions and neutral atoms of hydrogen bombarding the interior surfaces of present-day fusion reactors initiate a series of complex reactions which adversely affect the plasma and materials properties of the first wall. Some of the bombarding hydrogen is reflected with loss of energy and/or change of charge back into the plasma, some penetrates the wall causing radiation damage, sputtering, desorption, gas bubble formation, and blistering; some becomes implanted, alters many of the above reactions, and causes chemical reactions or alterations of metallurgical properties. It is essential for evaluating most of these effects to know the concentrations and depth distributions of the hydrogen in the material. In anticipation of our need for such information in the current program, a technique was developed for determining the hydrogen concentration in solids and was tested on a variety of materials.

The technique exploits either of two resonant nuclear reactions for hydrogen, $^{1}H(^{19}F,\alpha\gamma)^{16}O$ or $^{1}H(^{15}N,\alpha\gamma)^{12}C$. Samples containing hydrogen are bombarded with energetic beams of either ^{19}F or ^{15}N obtained from the ORNL Tandem Van de Graaff accelerator. At the resonant energies [$E(^{19}F) = 16.44$ MeV, $E(^{15}N) = 6.38$ MeV], these ions interact with ^{1}H, giving off monoenergetic gamma rays. By varying the energy of the incident ion beam, the resonance can be made to occur at the surface or inside the solid as desired. The known or measured energy loss of the ions can be converted to depth, and the yield of gamma rays is proportional to the hydrogen concentration at that depth. In our initial experiments we profiled a variety of specimens ranging from control samples to test the depth resolution and sensitivity of the technique, to samples actually exposed to ORMAK, to a variety of insulators. The technique was easily sensitive to 0.1 at. % hydrogen, and more refined measurement techniques could improve this substantially. The ^{19}F reaction had a depth resolution ~75 Å near the surface and could probe to ~2500 Å before the next resonance interfered. The ^{15}N reaction, though down in yield, had comparable sensitivity, a depth resolution ~30 Å near the surface, and could probe to depths ~20,000 Å.

These preliminary results demonstrate the feasibility of this detection method for hydrogen and indicate that it has considerable potential for future applications. For example, a control sample and one that had been cleaned in a hydrogen discharge were given to us for analysis by the Surface Radiation Effects group of the Metals and Ceramics Division. Although equipment failure prevented us from obtaining a quantitative analysis of the samples, we easily detected differences in the surface concentrations of hydrogen in the two samples. Slight improvements in the experimental equipment (provisions for in situ discharge cleaning, heating, etc.) could be applied to determine the dynamic behavior (desorption, diffusion, etc.) of this and a number of other problems relevant to MFE. Similarly, studies of a number of

different kinds of quartz samples containing hydrogen seemed to show that hydrogen in crystalline quartz was quite mobile under beam irradiation, while in amorphous or highly disordered samples the hydrogen appeared to remain trapped. This could be an important line of study for a number of insulating materials being considered for use in fusion reactors. Because of the importance of hydrogen for understanding so many of the materials problems in MFE and because hydrogen is extremely difficult to detect by other methods, this promises to be a useful technique for future materials characterization.

7.6.5 Photon Emission Produced by Particle-Surface Collisions[20]

C. W. White N. H. Tolk

Visible, ultraviolet, and infrared optical emission results from low-energy (20 eV-10 keV) particle-surface collisions. Several distinct kinds of collision induced optical radiation are discussed which provide fundamental information on particle-solid collision processes. Line radiation arises from excited states of sputtered surface constituents and backscattered beam particles. This radiation uniquely identifies the quantum state of sputtered or reflected particles, provides a method for identifying neutral atoms sputtered from the surface, and serves as the basis for a sensitive surface analysis technique. Broadband radiation from the bulk of the solid is attributed to the transfer of projectile energy to the electrons in the solid. Continuum emission observed well in front of transition metal targets is believed to arise from excited atom clusters (diatomic, triatomic, etc.) ejected from the solid in the sputtering process. Application of sputtered atom optical radiation for surface and depth profile analysis is demonstrated for the case of submonolayer quantities of chromium on silicon and aluminum implanted in SiO_2.

7.6.6 Sputtering Calculations with the Discrete Ordinates Method

T. J. Hoffman H. L. Dodds M. T. Robinson

Sputtering of the first-wall material in a fusion device is partly caused by light ion (H and He) bombardment. Sigmund[21] had developed a Boltzmann transport equation model for the calculation of sputtering yields, but the technique he used to solve this equation, the moments method,[22] is only valid for infinite medium problems and, therefore, is not appropriate to sputtering by light ions.

The most widely used and highly developed method for numerical solution of the Boltzmann equation in finite regions is the discrete ordinates method.[23] Although the usual application of this method has been to neutron and gamma-ray shielding problems, many of the computational techniques that have been developed to accelerate convergence of these problems are applicable to sputtering problems. The current work is directed toward the adaptation of the discrete ordinates shielding code, ANISN,[24] to the calculation of sputtering yields by light ions.

Several modifications of ANISN are required to treat sputtering problems. A continuous slowing down term has been included to account for energy losses due to electronic interactions and small angle elastic scattering. Methods for treating the surface binding energy have also been incorporated into the ANISN calculations. The major development effort has been to process power approximations of Thomas-Fermi type and Born-Mayer type differential cross sections into multigroup cross-section sets for discrete ordinates computation.

Preliminary calculations with the modified program have been encouraging. Computation times are reasonable. Comparisons are being made with the analytical theory[21] and with experiment for heavy, rare gas ion (Ne, Ar, Kr, Xe) sputtering as a confirmation of the numerical technique. Applications to H and He sputtering will follow.

7.6.7 Hydrogen Recycle in Fusion Devices

S. Datz P. F. Dittner S. Overbury

A system has been constructed for the study of energy exchange, chemical reactivity, and chemical sputtering of first-wall materials with charge-exchanged hydrogen from the plasma. The initial study is on pyrolytic carbon interacting with 10-1000-eV beams of hydrogen and deuterium. The system – consisting of mass analyzed ion beam, heatable sample, mass filter, and electrostatic analyzer, all contained in a 10^{-10}-torr vacuum – has been completed. A low energy ion backscattering system for surface analysis has been developed and used to measure surface composition of high purity pyrolytic graphite. Significant concentrations of O and S are measured which decrease with Ar sputter cleaning and are reestablished, presumably by diffusion, upon heating to ~1500°C. The mass spectrometer system has been installed, and background pressures of CH_4 of $\sim 10^{-12}$ torr are found in the vacuum system. This should allow detection of $\sim 10^{-14}$ to 10^{-15}-torr CH_4 from chemical sputtering. A puzzling finding arose from a measurement in which carbon bombarded by a 10-keV proton beam was treated with an extraction solvent which dissolved the hydrocarbon component. Nuclear magnetic resonance (NMR) analysis indicated the presence of aromatic hydrocarbons, in spite of the fact that only CH_4 has been reported as the result of chemical sputtering.

For the low energy (<200-eV H^0) anticipated from the plasma, a considerable amount of reflection is anticipated. The electrostatic analyzer system has been employed for initial measurements of the energy spectra of H^+ and H^- backscattered from the carbon target and checked as a function of surface impurity composition for both surface conditions. A scheme has been devised (but not tested) for absolute determination of the neutral H^0 component in the reflected beam, which will allow a complete determination of the reflected energy spectrum which can then be compared with results of the MARLOWE computer program for this system.

7.7 SYSTEMS STUDIES

D. Steiner E. S. Bettis T. J. Huxford
H. E. McCoy A. T. Mense R. L. Reid
J. L. Scott T. E. Shannon W.C.T. Stoddart
H. L. Watts W. M. Wells R. W. Werner

The emphasis of the system studies during the past year has been directed to the Fusion Power Demonstration (Demo) Study.[25] The purpose of this study is to develop a plan for demonstrating, in this century, the commercial feasibility of fusion power based on the tokamak concept. In order to demonstrate commercial feasibility, the technical and economic feasibility of the tokamak concept for power generation must be clearly established through successful operation of demonstration facilities under practical utility conditions. A plan for demonstrating commercial feasibility must be based on technological directions, design approaches, and plasma characteristics which ensure the economic competitiveness of the tokamak concept. Not only must tokamak fusion power be perceived as a desirable goal, but also the cost and risk of achieving this goal must be viewed as acceptable. If commercial feasibility is to be realized in this century, the number of new technologies and facilities required for demonstration must be minimized. In the Demo Study, the application of current and near-term technologies has been emphasized. Such an approach should enhance the acceptability of the plan for demonstrating commercial feasibility without compromising the economic potential of fusion power systems.

The principal results of the Demo Study during the past year are as follows. We envision a commercial tokamak fusion power plant consisting of multiple (2-5) tokamak reactor units sharing a number of common elements. Two key shared elements would be the power supplies for driving the plasma current and the power supplies which provide the plasma auxiliary heating. Each reactor unit would produce about 500-1000 MW(e) of output power. The precise value of the electrical output of each unit would be determined both by plasma physics considerations and by cost optimization considerations.

The following points are noted with regard to the commercial tokamak fusion power plant.

1) The plasma characteristics required for the commercial units are essentially the same as those required for an ignition demonstration device. Thus, many of the components developed for ignition demonstration will be prototypical of components required for commercial power. This is important because it contributes to the possibility of minimizing the number of facilities required for demonstrating commercial feasibility.
2) The motivation for pursuing a power plant consisting of multiple reactor units with common elements is based on our cost studies, which show that the pulsed equipment required to initiate the plasma current and achieve plasma heating represents ~20% of the total plant costs. It appears that this pulsed equipment could be economically and conveniently shared among several units.
3) The plant cost studies indicate that neutron wall loadings in the vicinity of 2-4 MW/m^2 will result in nearly optimum plant costs. Moreover, we have reached the preliminary conclusion that a wall lifetime of five years and greater will not significantly impact plant availability. Therefore, it appears that integral wall loadings of ~10-20 MW-yr/m^2 should be acceptable for the structural material performance.

On the basis of these studies, the following plan is recommended for demonstrating, in this century, the commercial feasibility of fusion power based on the tokamak concept.

Commercial feasibility demonstration would involve three phases beyond the TFTR: (1) an ignition demonstration phase, (2) a power technology demonstration phase, and (3) a commercial prototype demonstration phase. The primary theme of the recommended plan is that a given site and facility should be developed to demonstrate sequentially the ignition, power technology, and commercial prototype phases. Thus, initially the program would be directed to the construction of an electromagnetic facility which would serve all phases of the demonstration program. During the first phase, a single tokamak unit would be constructed. The purpose of this first phase would be to examine ignition operation; it would not be concerned with power conversion and tritium breeding technology. In the second phase, power technology is the main goal; tritium breeding and power conversion components would be added to the basic facility. Following successful operation of this phase, additional tokamak power units would be added at the same site and tied into the common elements of the plant. During this phase, the facility would be demonstrating commercial prototype operation.

7.8 TRITIUM BEHAVIOR

G. M. Begun, J. T. Bell, S. D. Clinton, P. W. Fisher, J. F. Land, J. D. Redman, F. L. Rogers, F. J. Smith, J. B. Talbot, J. S. Watson

Cooperative and closely coordinated studies in the Chemical Technology and Chemistry Divisions are investigating tritium behavior and tritium processing techniques as an integral part of the Fusion Reactor Technology Program. Many of these studies are funded by the ERDA Division of Physical Research.

7.8.1 Vacuum Pumping Studies

Fusion reactors will require vacuum systems to remove leaking or diverted plasma during the reactor pulses (burns) and to remove unburned fuel and ash from the reactor between burns. Cryosorption pumps operating at 4.2 K could, in principle, meet all fusion reactor requirements in a single pump, but experimental results[26] have shown that vacuum pumps based on type 5A molecular sieve may not be able to pump hydrogen isotopes and helium on a single panel because condensed deuterium and tritium will block the adsorbent surface. This problem can be alleviated either by developing new cryosorption pumps

based on different adsorbents or by developing compound pumps employing separate panels for pumping hydrogen isotopes and for pumping helium. Cryosorption pumps at 4.2 K remain, perhaps, the only choice for helium pumping.

The pumping speed of hydrogen on an Excalibur Model 1106 cryosorption pump has been measured[26] as a function of pressure and loading at 4.2 K. The initial pumping speed shown in the upper curve on Fig. 7.1 is about 4.0 liters/sec/cm^2 from 10^{-8} to 10^{-4} torr where it begins to increase, becoming 5.6 liters/sec/cm^2 at 3×10^{-3} torr. However, after a short period of pumping in the range from 4×10^{-6} to 4×10^{-4} torr, the speed is reduced by the buildup of solid hydrogen. This is shown in the lower curve of Fig. 7.1. The minimum steady-state speed is found to be 1.9 liters/sec/cm^2 (less than half the initial pumping speed) at 10^{-5} torr. The pumping speed is also found to vary periodically with time for a constant loading rate near 10^{-5} torr. The speed decays from the initial high speed to the lower speed, where it levels out and appears to reach a steady state. However, after some time the pump undergoes rapid transition and reverts back to the initial high pumping speed. During this time there is a momentary pressure rise, and material condensed on the surface becomes adsorbed in the adsorbent. The rate at which the pump reduced the pressure in the test chamber after termination of the feed gas was dependent on both the previous pumping pressure and pump loading.

Pumping speeds of helium have also been measured.[27] The initial helium pumping speed was found to be 2.2 liters/sec/cm^2 from 10^{-8} to 3×10^{-5} torr. The speed, however, decreases with loading to a minimum near 0.3 liters/sec/cm^2. The pumping speed decreases monotonically with loading at feed rates below 6.3×10^{-6} torr-liters/sec/cm^2, but above this point it varies periodically with loading, undergoing rapid transitions to initial high pumping speeds

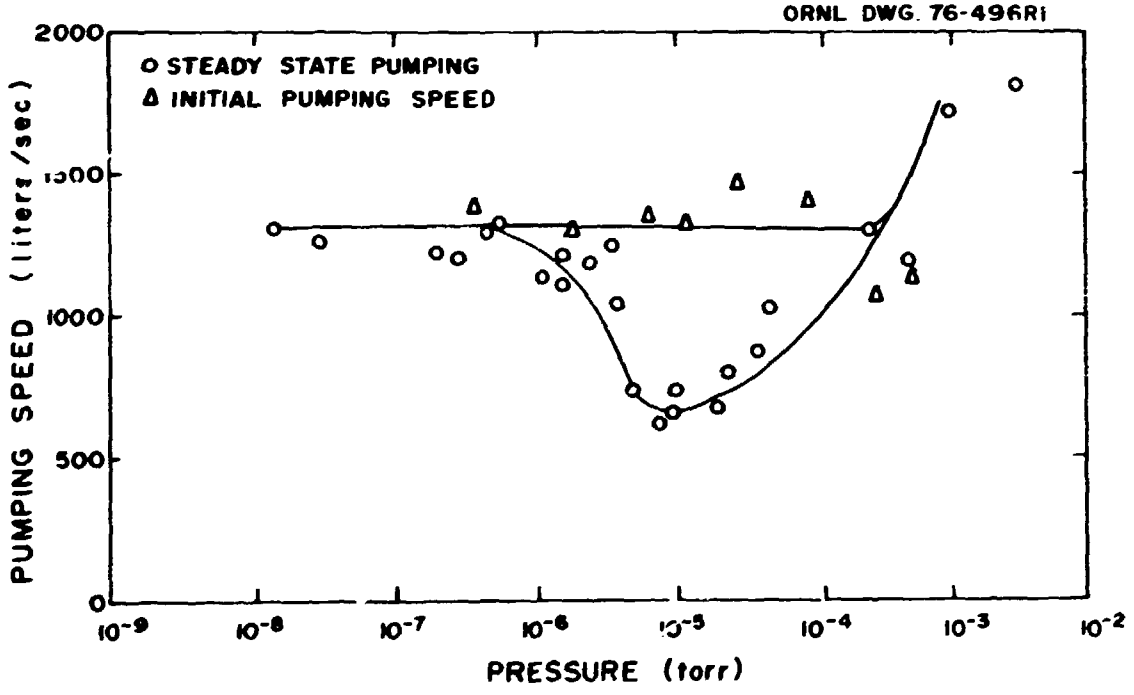

Fig. 7.1. Hydrogen pumping speed.

at the end of each cycle. Cycle lengths are related to loading rates, and minimum periods occurred at the highest achievable feed rates. These minimum cycle periods were approximately 1.7 torr-liter/gram adsorbent. Thermal runaway occurs at about 10^{-4} torr.

The experimental test stand has been modified to allow operation at higher temperatures (near 15 K). Measurement of deuterium and hydrogen pumping speeds at these temperatures is in progress. Studies of pump behavior for mixed gases and pulsed feed rates are also planned.

7.8.2 Tritium Sorption Studies*

Molten lithium appears to be the most promising blanket material for breeding tritium in fusion reactors. Three techniques are currently being considered for tritium recovery from liquid lithium: (1) extraction with a molten salt, (2) permeation through a niobium window, and (3) sorption on a hydrogen gettering metal. Tritium sorption from liquid metals has been studied in a batch contactor at 300-400°C, using metal sorbent samples of yttrium and zirconium. Recent results on tritium removal from relatively high purity lithium using an yttrium sorbent demonstrated the feasibility of such a blanket-recovery process system.

Twenty-one sorption runs were made at 300°C with the same yttrium metal sample (weight 3.45 g and geometric surface area 13.1 cm^2) and lithium containing 840 ppb tritium. The contacting time for each run ranged from 5 min to 90 hr. A lithium control sample was removed with each sorption run to confirm the initial concentration of tritium in the lithium. The results of these runs are shown in Fig. 7.2, in which the tritium concentration remaining in the lithium divided by the original concentration is plotted as a function of the contact time. Neglecting the first run, the tritium concentration can be reduced by a factor of two

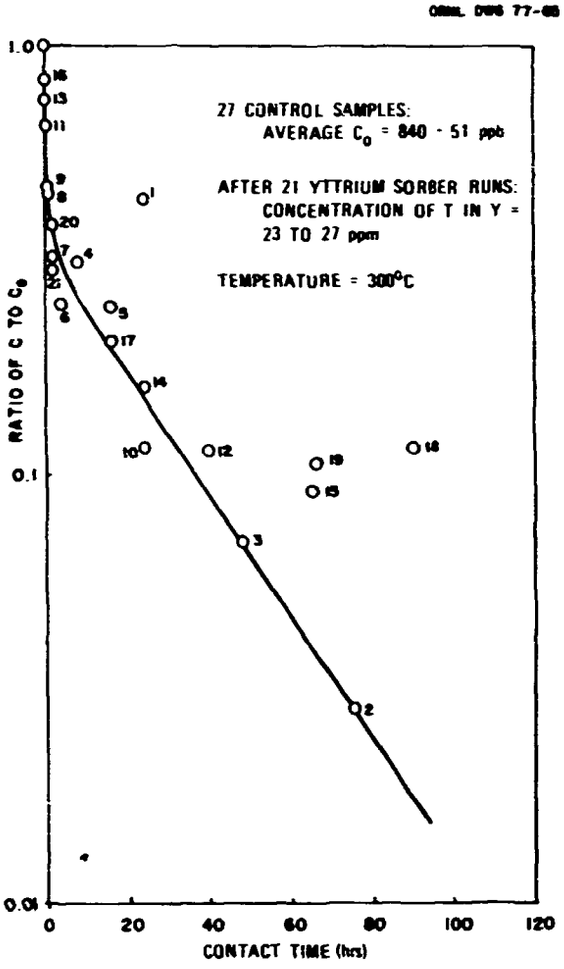

Fig. 7.2. Normalized tritium concentration in lithium vs contact time.

in 24 min; this corresponds to a mass transfer coefficient of 6×10^{-4} cm/sec. The controlling mass transfer resistance appears to be in the liquid film, and consequently the mass transfer rate could be increased perhaps by an order of magnitude with fused convection.

At the end of run 21, the yttrium metal sample was analyzed for tritium content by dissolving the metal in dilute hydrochloric acid. During the sorption experiments, the estimated tritium accumulation in the yttrium was 0.78 Ci. The tritium found during dissolution was 0.90 Ci (115 percent recovery).

*This work was funded by ERDA Division of Physical Research – Molecular Science.

7.8.3 Recovery of Tritium from Solid Blanket Materials*

Tritium release rates from irradiated aluminum and sintered aluminum product (SAP) containing small concentrations of lithium have been studied. Solid Li-Al alloy has been suggested as a potential tritium breeding material for fusion reactors, and SAP has been suggested as a blanket or structural material.[28] This study differs from current studies[29] of solid aluminum alloy blanket material at other laboratories because of the low (ppm) lithium concentration, the incorporation of oxygen within some of the samples (SAP), and the use of large (about 1-in.-long wafers) samples rather than powders.

A series of four runs was made to measure tritium release from irradiated SAP samples. The objective of the first run was to determine the temperature at which a significant tritium release rate was observed; this took place at about 250°C. The temperature of sample No. 7 was steadily increased to 450°C over a 30-hr period. The next run (sample No. 1) was to be made at a constant temperature of 400°C. There was difficulty in controlling the sample temperature, which decreased to 340°C after 10 hr and then increased to 420°C after 15 hr. The temperature controller was adjusted, and the 400°C experiment was repeated with sample No. 3. Finally, a sample (No. 2) was heated for a 450°C run. Figure 7.3 compares the percent tritium release of all four experiments.

Preliminary analysis of the data in Fig. 7.3 shows that the release rates follow the pattern expected for bulk diffusion in the solid. Solid diffusion is indicated because the slope of the curves at a constant temperature interval in Fig. 7.3 is approximately one-half. The diffusion coefficients at 400°C and 450°C are approximately 2×10^{-10} cm^2/sec and 8×10^{-10} cm^2/sec, respectively. The release rates observed by Wiswall and Wirsing[30] for Li-Al powder form did not follow a slope of one-half, and attempts to interpret their results were not successful. Powder samples probably do not follow this pattern because surface resistance to tritium release is more significant. Also, in their experiment, the sizes of the Li-Al, $LiAlO_2$, and Li_2SiO_3 particles were not known precisely (materials were crushed and screened) for determination of diffusion coefficients.

Experiments have been made heating an SAP sample (No. 5) to 450°C for about 100 hr and another (No. 6) to 500°C for about 30 hr. Analyses of the results are not complete. Three additional runs will be made at other temperatures of interest. The data will be analyzed to predict diffusion coefficients at the temperatures studied.

7.8.4 Materials Chemistry Related to Fusion Reactor Systems†

Tritium permeabilities of clean Incoloy 800, clean type 316 stainless steel, and tungsten-3.5% nickel-1.5% iron alloy were determined over the 500-1100 K range. The data can be expressed as DK = 6.77 exp(-19700/RT) for Incoloy 800, DK = 0.533 exp(-16260/RT) for type 316 stainless steel, and DK = 0.00788 exp(-14930/RT) for the ternary alloy. Permeation rates for tritium through Incoloy 800, type 316 stainless steel, and the ternary alloy were determined at various feed-gas pressures from 35-782 torr, with HT pressures from 1.5×10^{-4} to 33.1×10^{-4} torr (corresponding to T_2 pressures from 1.67×10^{-10} to 37.2×10^{-10} torr). With each material, the permeation rates were dependent on the square root of the tritium pressure.

Studies on the effects of in situ steam oxidation at 660°C to impede tritium permeation through Incoloy 800 were also continued. The formation of oxide layers by the oxidation with steam at partial pressures of 0.32, 0.70, and 0.94 atm for 150 days decreased permeability by factors of 250, 304, and 492, respectively. The

*This work was funded by ERDA Division of Physical Research — Molecular Science.

†This work was funded by ERDA Division of Physical Pesearch — Materials Science.

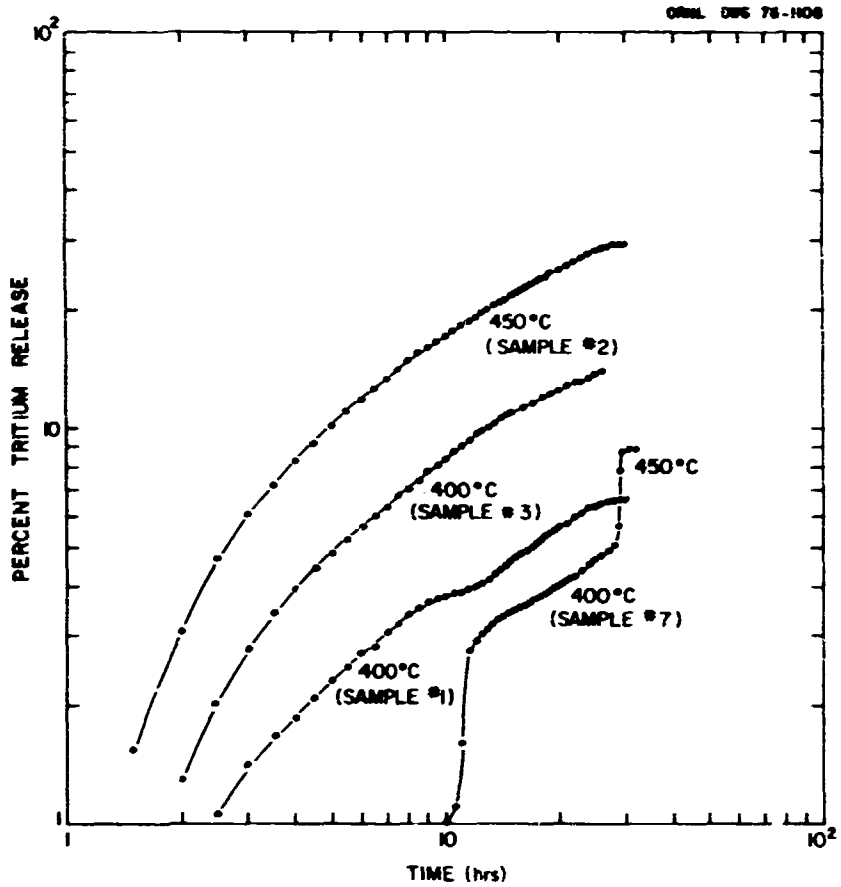

Fig. 7.3. Tritium release from solid Li-SAP alloy.

0.94-atm results are shown in Fig. 7.4. Calculations based on various fusion reactor designs indicate that permeation rates through the heat exchanger into the steam system must be 10^2 to 10^3 times less than the rates for the bare construction materials.

Severe thermal shock affected the physical character of the oxide layers such that the permeability increased to within a factor of ten of the clean Incoloy 800; however, the defects in the oxide in three experiments were annealed by continued oxidation at stable temperatures. Mild temperature cycles, ±20°C/30 min, did not affect the permeabilities. Ion microprobe techniques for the chemical analysis of the oxides on the permeation samples have been evaluated. These techniques give the oxygen profile through the oxide layer and the relative amounts of the different metals in the oxide layer. Such analyses have now become an integral part of the permeation studies.

The mutual solubilities of isotopic exchange of hydrogen and deuterium in lithium have been measured for the plateau region (two-phase coexistence region) at 700, 800, and 850°C. Both the total pressure and the individual partial pressures of H_2, HD, and D_2 have been determined as a function of the mole fraction LiH and LiD in

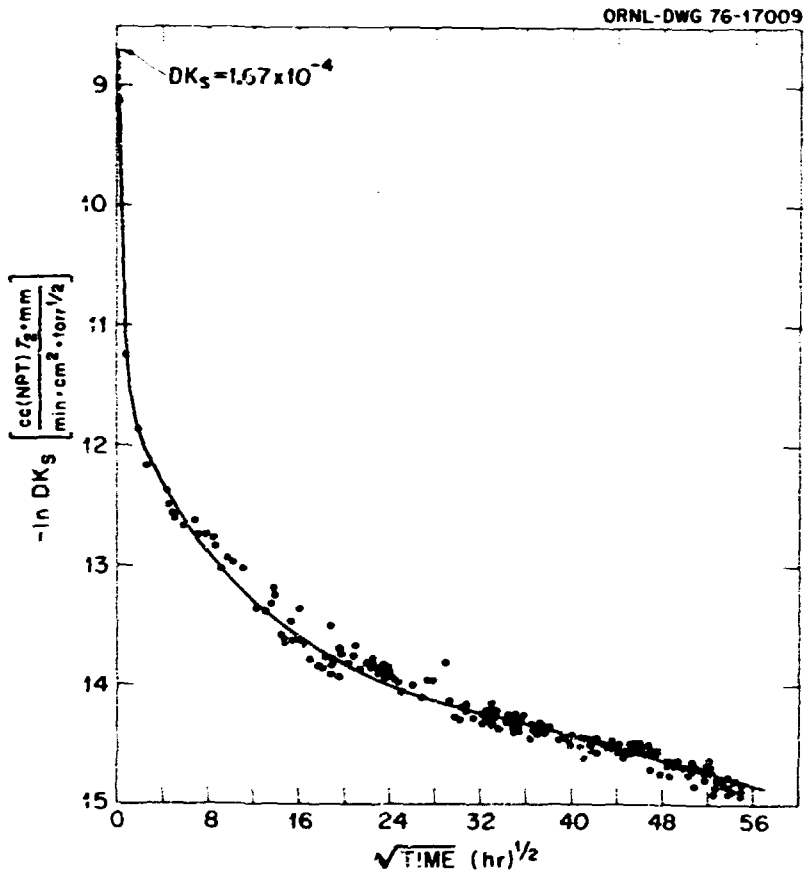

Fig. 7.4. Permeation of tritium through Incoloy 800 exposed to steam of 0.94 atm and temperature cycling between 640 and 660°C.

the liquid phases with varying hydrogen-to-deuterium ratios. The plateau boundaries of the two-phase region for the mixed hydrogen-deuterium-lithium system are identical to those for the single isotopes, and the boundaries are independent of the hydrogen-to-deuterium ratio. At 800°C the boundaries are given by the sum of mole fraction relationships, $N_{LiH} + N_{LiD} = 0.33$ and $N_{LiH} + N_{LiD} = 0.96$. The equilibrium pressures depended only on the relative amounts of isotopes present. The total pressure and the partial pressures of hydrogen and deuterium in the plateau region at 800°C may be expressed as

$$P^{1/2}_{total}\ (torr) = -3\ N_{LiH}/(N_{LiH} + N_{LiD}) + 15.9,$$

$$P^{1/2}_{H_2}\ (torr) = 12.9\ N_{LiH}/(N_{LiH} + N_{LiD}),\ \text{and}$$

$$P^{1/2}_{D_2}\ (torr) = 15.9\ N_{LiD}/(N_{LiH} + N_{LiD}).$$

Similar relationships are observed at 700 and 850°C. The equilibrium isotope effect, K, expressed by

$$P^{1/2}_{D_2}/P^{1/2}_{H_2} = K(N_{LiD}/N_{LiH})$$

is 1.28, 1.23, and 1.17 at 700, 800, and 850°C, respectively.

1. Abstract of ORNL/TM-5817, Oak Ridge National Laboratory, Oak Ridge, Tennessee (1976); also presented, in part, at the International Conference on Liquid Metal Technology in Energy Production, Champion, Pennsylvania, May 3-6, 1976.
2. Abstract of ORNL/TM-5828, Oak Ridge National Laboratory, Oak Ridge, Tennessee (in press).
3. Abstract of ORNL/TM-5782, Oak Ridge National Laboratory, Oak Ridge, Tennessee (in press).
4. Abstract of ORNL/TM-5812, Oak Ridge National Laboratory, Oak Ridge, Tennessee (in press).
5. A. P. Fraas and A. S. Thompson, *ORNL Demonstration Reactor Study: Fluid Flow, Heat Transfer, and Stress Analysis Consideration in the Design of Blankets for Full-scale Fusion Reactors*, ORNL/TM Report (Draft), Oak Ridge National Laboratory, Oak Ridge, Tennessee (September 30, 1976).
6. Abstract of ORNL/TM-5554, Oak Ridge National Laboratory, Oak Ridge, Tennessee (October 1976); to be published in Nucl. Technology.
7. ORNL/TM-5068, Oak Ridge National Laboratory, Oak Ridge, Tennessee (May 1976).
8. Abstract of ORNL/TM-5466, Oak Ridge National Laboratory, Oak Ridge, Tennessee (in press); submitted to Nucl. Technology.
9. Abstract of paper presented at the 2nd ANS Topical Meeting on the Technology of Controlled Nuclear Fusion, Richland, Washington, September 21-23, 1976; proceedings to be published.
10. Abstract of paper presented at the 2nd ANS Topical Meeting on the Technology of Controlled Nuclear Fusion, Richland, Washington, September 21-23, 1976; proceedings to be published.
11. Abstract of paper published in *Radiation Effects and Tritium Technology*, CONF-750989, p. I-259 (1976).
12. Summary of paper presented at the ANS 1976 Annual Meeting, Toronto, Canada, June 1976 [Trans. Am. Nucl. Soc. 23, 134 (1976)].
13. F. W. Wiffen, "The Tensile Properties of Fast Reactor Neutron Irradiated BCC Metals and Alloys," Nucl. Metall. 18, 176 (1973).
14. E. E. Bloom and F. W. Wiffen, "The Effects of Large Concentrations of Helium on the Mechanical Properties of Neutron-Irradiated Stainless Steel," J. Nucl. Mater. 58, 171 (1975).
15. E. E. Bloom, F. W. Wiffen, P. J. Maziasz, and J. O. Stiegler, "Temperature and Fluence Limits for a Type 316 Stainless Steel First Wall," submitted to Nucl. Technology (1976), see also E. E. Bloom, F. W. Wiffen, and P. J. Maziasz, Trans. Am. Nucl. Soc. 22, 128 (1975).
16. D. Kramer, K. R. Garr, A. G. Pard, and C. G. Rhodes, "A Survey of Helium Embrittlement of Various Alloy Types," *Irradiation Embrittlement and Creep in Fuel Cladding and Core Components*, p. 109, British Nuclear Energy Society, London, 1973.
17. Abstract of paper presented at the International Symposium on Plasma Wall Interaction, Julich, Federal Republic of Germany, October 18-22, 1976; proceedings to be published.
18. Abstract of paper presented at the International Conference on Surface Effects in Controlled Fusion Devices, San Francisco, California, February 16-20, 1976; to be published in J. Nucl. Mater. 63 (1976).
19. Abstract of paper presented at the Symposium on Molecular Processes at Solid Surfaces: Surface Chemical Problems in Controlled Thermonuclear Reactors, Montreal, Canada, May 29-June 2, 1977.
20. Abstract of paper presented at the International Conference on Surface Effects in Controlled Fusion Devices, San Francisco, California, February 16-20, 1976; to be published in J. Nucl. Mater. 63.
21. P. Sigmund, "Theory of Sputtering. I. Sputtering Yield of Amorphous and Polycrystalline Targets," Phys. Rev. 184, 383 (1969).

22. L. V. Spencer and U. Fano, "Calculation of Spatial Distributions by Polynomial Expansion," J. Res. Natl. Bur. Stand. 46, 446 (1951).

23. B. G. Carlson, *Solution of the Transport Equation by the S_n Method*, LA-1891, Los Alamos Scientific Laboratory, Los Alamos, New Mexico (1955).

24. W. W. Engle, Jr., *A User's Manual for ANISN, a One-Dimensional Discrete Ordinates Transport Code with Anisotropic Scattering*, K-1693, Computing Technology Center, Union Carbide Corporation (1967).

25. See D. Steiner et al., *ORNL Fusion Power Demonstration Study: Interim Report*, ORNL/TM-5813, Oak Ridge National Laboratory, Oak Ridge, Tennessee (March 1977).

26. P. W. Fisher and J. S. Watson, "Cryosorption Vacuum Pumping of Deuterium, Helium, and Hydrogen at 4.2°K for CTR Applications," paper presented at the American Nuclear Society Winter Meeting, Washington, D.C., November 1976; published in the proceedings of the Remote Systems Technology Section.

27. P. W. Fisher and J. S. Watson, "Cryosorption Pumping of Helium at 4.2°K by Type 5A Molecular Sieve," paper submitted to the Annual Meeting of the American Nuclear Society, New York, New York, June 12-17, 1977.

28. J. R. Powell et al., *Studies of Fusion Reactor Blankets with Minimum Inventory and with Tritium Breeding in Solid Lithium Components: A Preliminary Report*, BNL-18230, Brookhaven National Laboratory, Upton, New York (June 1973).

29. R. H. Wiswall and E. Wirsing, "Removal of Tritium from Solid CTR Blanket Material," paper presented at the American Nuclear Society Winter Meeting, Washington, D.C., November 1976.

30. R. H. Wiswall and E. Wirsing, *The Removal of Tritium from Solid CTR Blanket Materials: A Progress Report*, BNL-19766, Brookhaven National Laboratory, Upton, New York (February 1975).

8. LARGE COIL PROGRAM

P. N. Haubenreich, Manager

J. N. Luton[1]
L. W. Nelms[2]
P. B. Thompson[2]

8.1 OBJECTIVES AND PLAN

The Large Coil Program (LCP) was organized early in 1976 to accomplish the national fusion program objectives of fabricating, testing, and demonstrating the reliable operation of superconducting coils large enough to prove the design principles, materials, and fabrication techniques proposed for the toroidal magnet of a tokamak fusion reactor. The program will move as quickly as practicable into fabrication of several different large toroidal field (TF) coils in order to identify, to confront realistically, and to solve the spectrum of new and/or greater problems involved in design and fabrication of large superconducting tokamak magnets.

The long-range focus of the LCP at its inception was the Experimental Power Reactor (EPR) that was being considered. The focus later shifted to the needs of The Next Step (TNS). Preliminary studies to define TNS reference designs indicate that the TF coils must be superconducting, have an opening about 5 × 7 m, and produce a peak field of 8-12 T. Proposed designs for TNS reactor coils differ significantly in coolant conditions, conductor, and structural configuration; without fabrication and test results it is not certain which is best for TNS or even which are technically and economically feasible. Testing and extended operation of different coils in the LCP will permit a choice to be made so that detailed criteria can be prepared for full-scale TNS coils that are optimal from the standpoints of fabricability, performance, cost, and dependability.

Achievement of the broad objective of the LCP involves the following accomplishments:

- resolution of reactor magnet requirements,
- origination of coil concepts meeting these requirements,
- application of technology and engineering to produce detailed designs of test coils capable of proving the most promising concepts,
- fabrication of test coils of these designs,
- thorough testing of these coils,
- demonstration of reliable operation of coils and supporting systems under simulated reactor conditions, and
- recommendation of design criteria for TNS coils.

The general program outline shown in Fig. 8.1 was laid out to accomplish the LCP objective. The program is managed by an ORNL team with magnet technology, design engineering, project engineering, and management skills. The capabilities of U.S. industry will be utilized, and the results of research and development (R&D) in the Superconducting Magnet Development Program (SCMDP) will be disseminated by contracting for the conceptual design, detailed design, and fabrication of the large coils. Guidance, technical input, and evaluation are provided by ORNL, with reviews and approvals by the Division of Magnetic Fusion Energy (DMFE). The SCMDP performs the basic R&D and in addition performs coil design and developmental fabrication concurrently with the industrial work in the LCP. ORNL is responsible for designing and constructing a test facility and conducting the tests.

---

1. Magnetics and Superconductivity Section.
2. UCC-ND Engineering.

ORNL DWG 77-7330

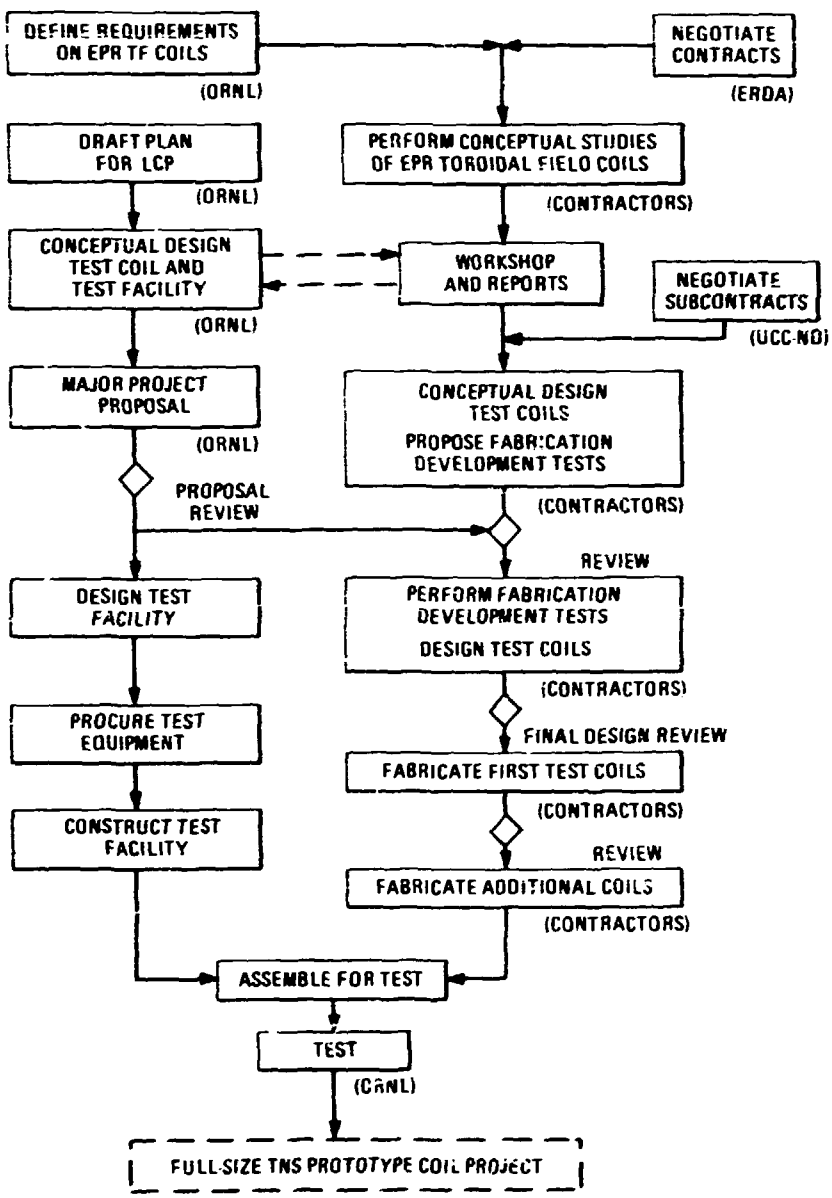

Fig. 8.1. Principal features of Large Coil Project strategy.

8.2 EPR TOROIDAL MAGNET STUDIES

An early activity of the LCP, which supplied input for selection of test coil design criteria, was the generation of concepts for the toroidal magnet of the EPR tokamak.

The LCP, in cooperation with the three EPR design teams at Argonne National Laboratory, General Atomic Company, and ORNL, extracted from the preliminary conceptual studies of the EPR tokamak the principal requirements placed on the magnet systems. The LCP staff reduced these requirements to a consistent set of guidelines, conceptual criteria, and design data. Contracts were then awarded to three industrial organizations [Westinghouse, Magnetic Corporation of America (MCA), and a team from General Electric (GE) and Intermagnetics General Corporation (IGC)] with experience and capability in superconducting magnets to produce conceptual designs of TF coils meeting these EPR requirements.

Each contractor was required to produce two concepts: one with a peak field of 8 T, the other with a peak field as high as practicable. An important consideration was the reliability of magnet system operation, which requires coils that are thermally stable and protected against disabling damage in any credible event. At the completion of the conceptual study, each contractor was required to describe his concepts, to identify major uncertainties, and to recommend R&D to minimize the uncertainties.

The principal features of the contractors' concepts are described in Tables 8.1 and 8.2. Each of the three contractors independently settled upon 12 T as the maximum practicable field. In the case of the MCA concept, this represented the upper limit on the applicability of niobium-titanium superconductor alloy. The other two concepts used Nb_3Sn, a material capable of superconductivity at higher temperatures and fields. The maximum practicable field for the EPR TF coils using Nb_3Sn was determined by the rapidly increasing amount of conductor and structural material (and hence cost and space) required to attain higher fields.

8.3 TEST COIL SIZE AND SHAPE

Ideally, test coils should be identical with those intended for reactor use. In view of the costs, however, it is a practical necessity to carry out the program of evaluating alternative concepts by testing smaller coils.

Analyses by ORNL and the EPR TF study contractors indicated that the test coil should be at least half size in order to reduce extrapolation uncertainties to an acceptable level. Conceptual studies of tokamak reactors generally find that the TF coils should be elongated in the vertical direction to fit the enclosed components in the most economical and practical manner; the coil shape favored on the basis of structural and fabrication considerations is a pure-tension D or some variation from it. The decision was therefore made that LCP test coils should have a shape approximating a pure-tension D with bore dimensions 2.5 × 3.5 m.

8.4 TEST CONDITIONS AND ARRANGEMENT

In order for the results of the LCP testing to be most directly applicable to TNS, it was decided that the coils and testing arrangement should duplicate TNS in:

- maximum field,
- average current density,
- conductor and winding, and
- heat flow geometry.

To the extent that is practical in a reasonable test arrangement involving only a few coils, the following TNS conditions should be approximated.

- coolant conditions,
- magnetic field distribution,
- pulsed fields,
- stresses and strains, and
- specific stored energy.

An important effect that will be encountered in superconducting magnets for the first time in TNS is the heating due to neutrons from the ignited plasma. LCP test coils will have embedded heaters to simulate this effect.

Table 8.1. Comparison of coil characteristics of contractors' EPR TF 8-T concepts

	GE-IGC	MCA	Westinghouse
Coil profile	Oval	D-shape	D-shape
Winding	Pancake	Layer (segmented)	Pancake (in plates)
Winding cross section shape	Rectangular	Trapezoid	Trapezoid
Current density over winding	1930 A/cm^2	2100 A/cm^2	2700 A/cm^2
Coil structure	Conductor core, coil case	Central structural skeleton, coil case	Pancake plates (segmented, bolted), spokes to dewar wall
Conductor material	Multifilament NbTi	Multifilament NbTi	Multifilament NbTi
Conductor form	Cable around stainless steel core inside Cu jacket	Cable around strip between Cu plates	Cable in rectangular channel
Current	10 kA	10.6 kA	10 kA
Heat transfer to helium	Pool-boiling on outside of conductor jacket	Pool-boiling around cable and plate	Forced convection to supercritical helium flowing through cable in channel
Helium inlet	4.2 K, 1 atm	4.2 K, 1 atm	4 K, 15 atm

Table 8.2. Comparison of conductor characteristics of contractors' EPR TF 12-T concepts

	GE-IGC	MCA	Westinghouse
Coil profile	Oval	D-shape	D-shape
Winding	Layer	Layer (segmented)	Pancake (in plates)
Winding cross section shape	Rectangular	Trapezoid	Trapezoid
Current density over winding	2100 A/cm^2	~4500 A/cm^2	2100 A/cm^2
Coil structure	Conductor jacket, coil case	Central structural skeleton, coil case	Pancake plates (segmented, bolted), spokes to dewar wall.
Conductor material	Multifilament Nb_3Sn	Multifilament NbTi	Multifilament Nb_3Sn
Conductor form	Compacted cable between Cu channels in stainless steel jacket	Cable around strip between Cu plates	Cable in rectangular channel
Current	15 kA	10 kA	10 kA
Heat transfer to helium	Forced convection to supercritical helium in channels beside conductor	Pool-boiling around braid and plates	Forced convection to supercritical helium flowing through cable in channel
Helium inlet	<6 K	2.5 K	4.5 K, 8 atm

The first test coils will be operable at a peak field of 8 T. This value was chosen on the basis of TNS studies and available magnet technology. (The LCP test facility will be capable of modification to permit testing of coils up to 12 T.)

Several different testing arrangements were proposed for the LCP. A methodical comparison was made of the various possibilities, using a set of detailed criteria for evaluation of relative benefits, risks, and costs. The chosen arrangement is a compact torus of six coils in which the peak field is reached in a single coil when it operates at design current while each of the other five operates at 0.8 of the ampere turns in the test coil. After consideration of the relative benefits of a fitted dewar and single vacuum tank, it was decided to locate the torus in a single large vessel.

8.5 TEST COIL SPECIFICATIONS

A detailed technical specification was prepared for inclusion in a Request for Proposal which could be sent to industrial firms interested in performing design and fabrication for a test coil. The specification was designed to ensure that a coil from any supplier would interface properly with the test facility and with the other coils, would reliably perform to certain standards while in the given environment, would not be damaged when subjected to particular fault simulations, and would be scalable to larger sizes and higher fields.

The darkened areas of Fig. 8.2 indicate areas which were specified precisely to ensure that the coil would fit other structures. Dashed lines do not define the actual coil boundaries, but the envelope within which the coil must lie. The specification also constrained coil weight (40 tons), current (10-15 kA) and refrigeration required so that the ratings of the test facility's cranes, power supplies, and liquid helium system would not be exceeded.

The performance characteristics required of the first LCP coil and the parameters describing their environment are listed in Table 8.3. They were derived from an analysis of the TNS conceptual designs and LCP testing scenarios.

In addition to operating reliably at design conditions, the test coil would be required to survive certain extended test environments. In this regime the coil need not be capable of recovering to the superconducting state if driven normal, but must suffer no permanent damage as a result of the test. The extended conditions included a doubling of artificial heat inputs, a 50% increase in the applied pulse field magnitude and rate, and nine different sets of currents in the six coils of the toroidal array which cover fault conditions and possible overcurrent testing of partial arrays.

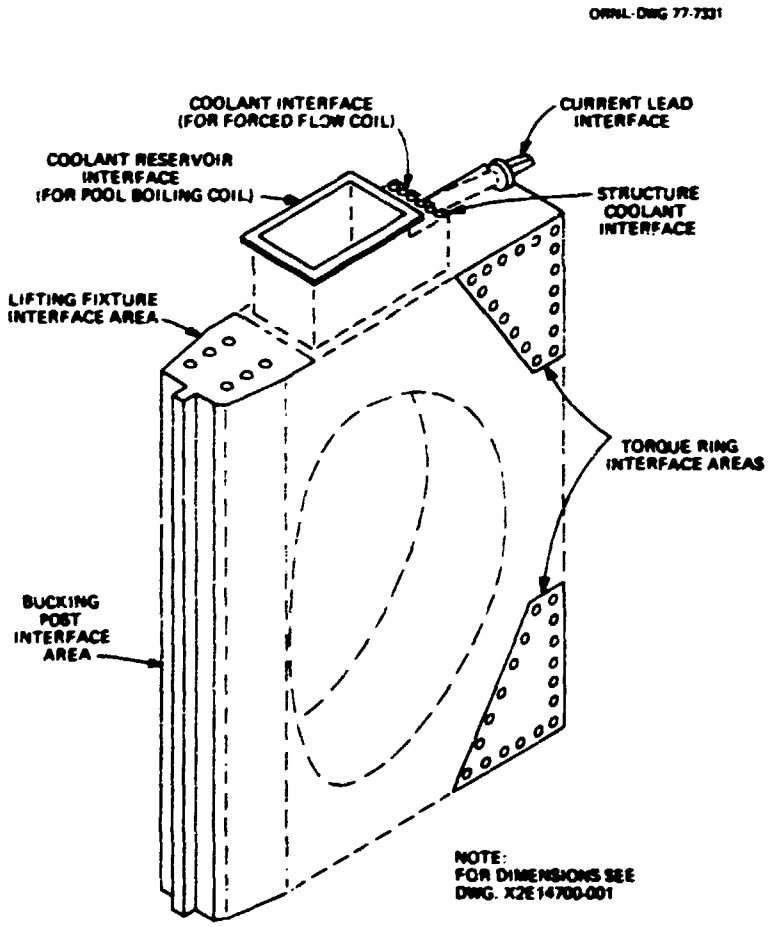

Fig. 8.2. Interface features.

Table 8.3. Selected LCP test coil requirements

Maximum field at the windings	8 T (when in standard array)
Design current	10-15 kA
Stability	(a) recover from all credible events (b) recover from a half-turn normal zone
Design life	10 years, including cycles: 50 thermal; 500 charging; 20 charging in each of the 9 alternative mode conditions; 3 million field pulses; 3 million heating pulses
Cool-down time	120 hr
Warm-up time	60 hr
Superconductor	NbTi or Nb_3Sn
Internal heaters	as required to simulate neutron heating and initiate normal zones

PART III. MANAGEMENT SERVICES SECTION

ABSTRACT

(Chapter 9)

9. MANAGEMENT SERVICES SECTION

In 1976, a new section was formed which incorporated the existing financial, administrative, purchasing, library, safety, and engineering services functions. Several new functions were added, including management information systems, reports office, coordinator for foreign exchange, personnel recruiting, and technology commercialization. The Management Services Section is responsible for providing timely and relevant information to support the operation, control, and management functions of the Division.

This organizational change was required to respond to the increasing requirements associated with an expanding program. It is the continuing goal of the Management Services Section to reduce the paperwork required of the section heads and program managers, to provide better and more timely information, and to reduce the time span between program needs and resolutions. During the year each group made progress toward the overall goal. Highlights of this progress are described, and emphasis is placed on those activities which were not performed in the past or have some unique new features.

9. MANAGEMENT SERVICES SECTION

O. B. Morgan, Acting Section Head

S. K. Adkins
D. R. Alford
A. B. Barnette
D. P. Brooks
J. L. Burke
C. J. Chamberlain
C. H. Cox
R. S. Edwards
J. C. Ezell
R. L. Hill
H. W. Jernigan
R. P. Jernigan
M. N. Johnson
J. A. Kelman
M. G. Kincaid
J. K. Lovin
R. E. Marcus*
G. D. Matlock
C. R. Nook[1]
B. L. Pope
P. N. Rader[2]
E. T. Rogers*
E. M. Ruckart
W. K. Russell
C. M. Sekula
B. L. Straine
D. Y. Ware
E. L. Watkin
M. S. Weasner
E. E. Webster[1]
E. R. Wells
C. Whitmire, Jr.
R. C. Wood

9.1 INTRODUCTION

One of the organizational changes in the Fusion Energy Division (FED) this year has been the formation of a Management Services Section. This section will incorporate essential financial, administrative, and project activities required to provide timely and relevant information to support the operation, control, and management functions of the Division. Management Services personnel work closely with the Division staff to meet commitments and to ensure that all relevant information is communicated to the appropriate research sections. The present organization of the section is shown in the FED organizational chart (Fig. 9.1).

The rapid growth of the Fusion Energy Program at ORNL, indicated by activity (Table 9.1) and by total funding (Fig. 9.2), requires reinforcement as well as advancement in the essential financial, administrative, and project information required to manage the Division's programs, sections, and projects.

The activities shown in Fig. 9.1 include the traditional administrative and financial services, purchasing, safety, quality assurance, library, and engineering services activities that have been provided in the past as staff functions. These activities continue to be essential to the program, and in many areas they have been reinforced by adding new staff members or facilities. Simultaneously, several new activities have been added, or formally recognized, within the Division to respond to the increased obligations and needs corresponding to the expanding program goals. These additions include the Reports Office, a Management Information System, a coordinator for Foreign Exchange and Personnel Recruiting, and a Technology Commercialization Officer.

Highlights of the activities of the Management Services Section follow.

9.2 PURCHASING, EXPEDITING, AND CONTROL

In 1975 the Procurement Office processed 1725 requisitions for materials, capital equipment, and miscellaneous services, representing a dollar volume of over $8 million. The Purchasing, Expediting, and Control activity has added staff members and a new computerized procurement module (computer program) developed by

---

*Part-time.

1. Information Division.
2. Finance and Materials Division.

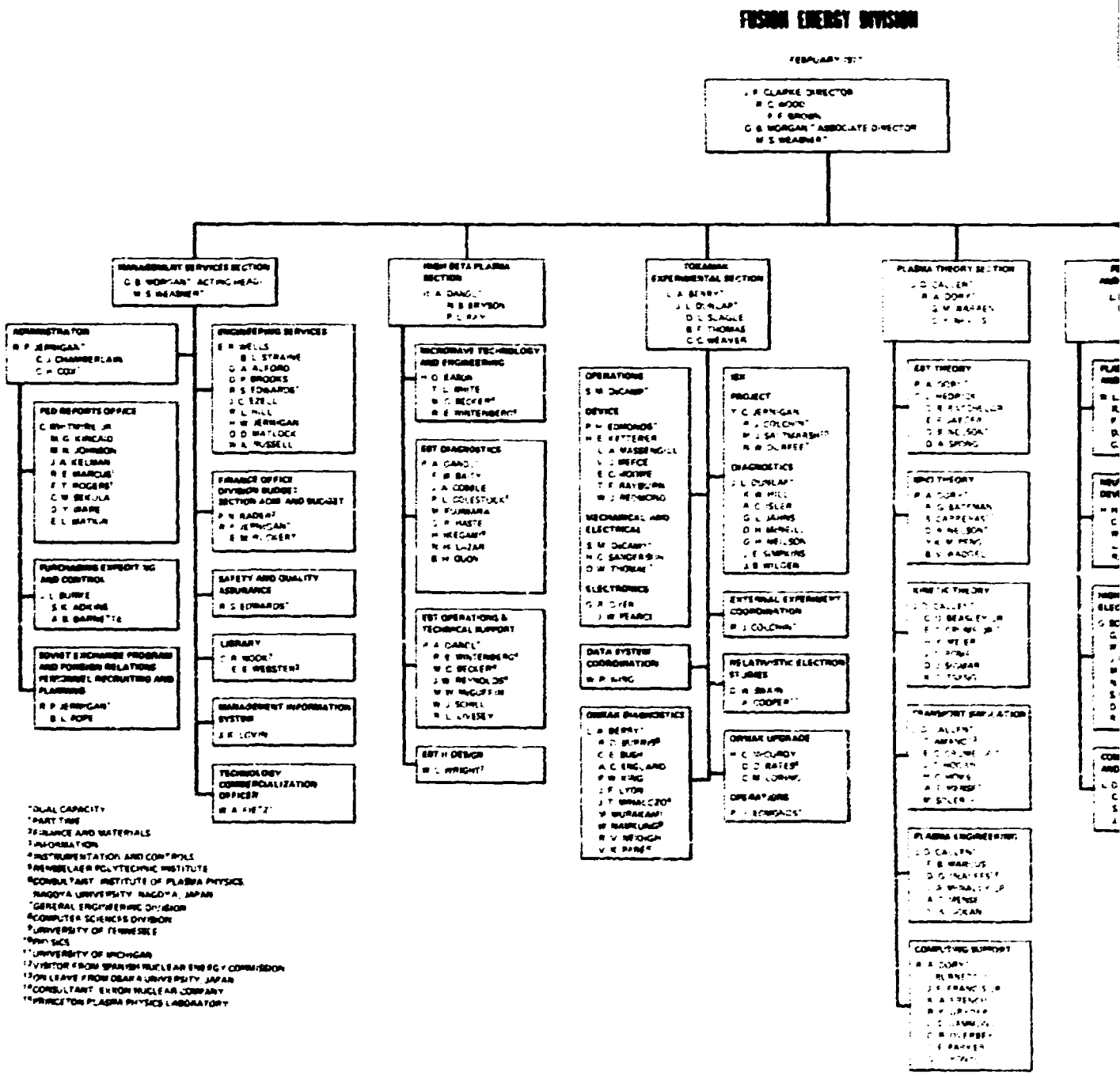

*DUAL CAPACITY
†PART TIME
‡ENGINEERING AND MATERIALS
§INFORMATION
¶INSTRUMENTATION AND CONTROLS
#RENSSELAER POLYTECHNIC INSTITUTE
@CONSULTANT, INSTITUTE OF PLASMA PHYSICS, NAGOYA UNIVERSITY, NAGOYA, JAPAN
^GENERAL ENGINEERING DIVISION
&COMPUTER SCIENCES DIVISION
$UNIVERSITY OF TENNESSEE
%PHYSICS
**UNIVERSITY OF MICHIGAN
††VISITOR FROM SPANISH NUCLEAR ENERGY COMMISSION
‡‡ON LEAVE FROM OSAKA UNIVERSITY, JAPAN
§§CONSULTANT, EXXON NUCLEAR COMPANY
¶¶PRINCETON PLASMA PHYSICS LABORATORY

Fig. 9.1. Fusion Energy Division organizational chart.

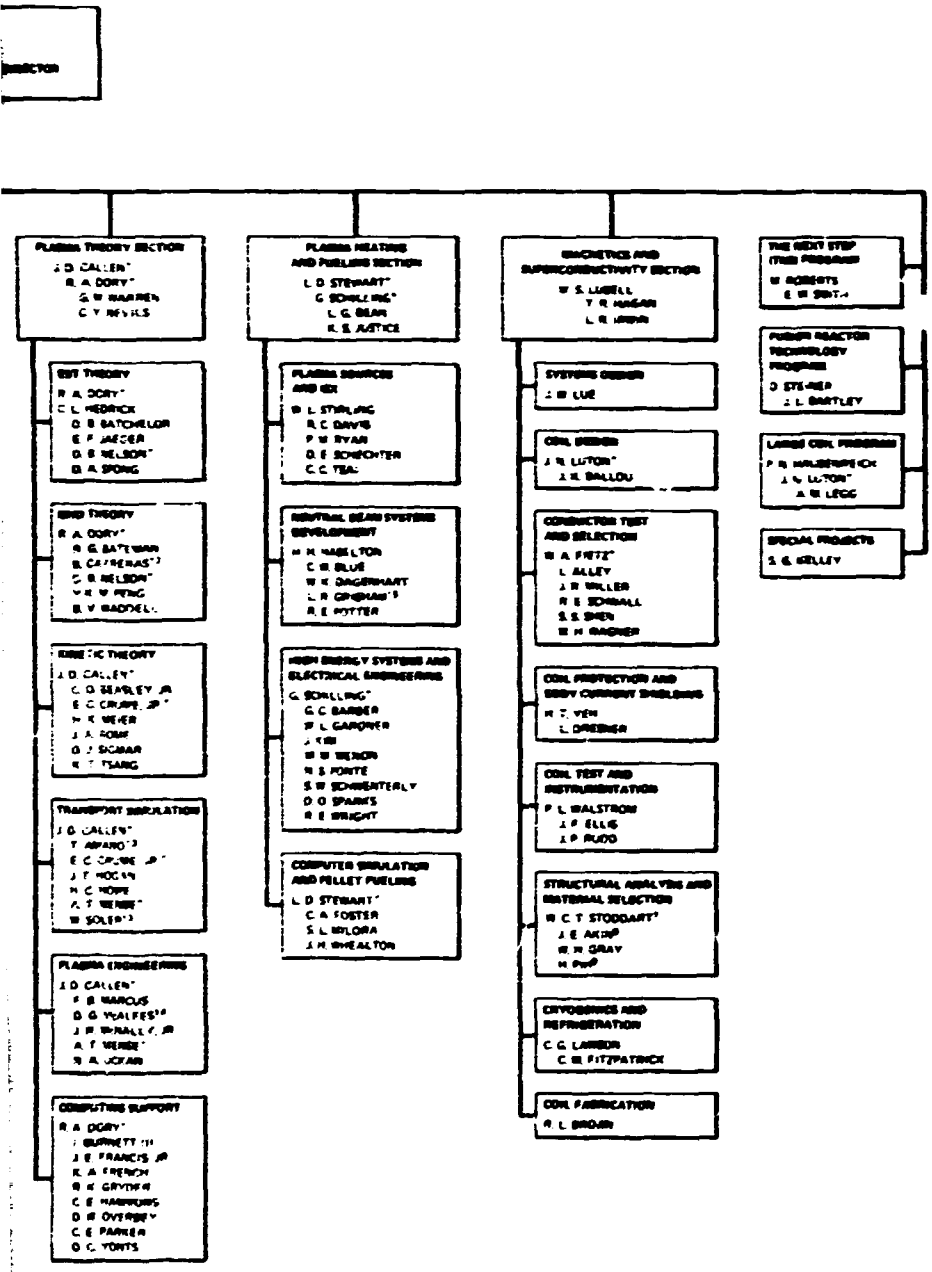
PLASMA THEORY SECTION
J. D. CALLEN*
R. A. DORY*
S. W. HARRIES
C. Y. REYES
PLASMA HEATING AND FUELING SECTION
L. D. STEWART*
G. SCHILLING*
L. G. BEAR
K. S. JUSTICE
KINETICS AND SUPERCONDUCTIVITY SECTION
W. S. LUSELL
T. R. HAGAR
L. R. [illegible]
THE NEXT STEP (TNS) PROGRAM
W. ROBERTS
E. W. SWIFT
FUSION REACTOR TECHNOLOGY PROGRAM
D. STEINER
J. L. BARTLEY
LARGE COIL PROGRAM
P. R. MALENFANT
J. V. LUTON*
A. W. LEGG
SPECIAL PROJECTS
S. G. KELLEY
TNS THEORY
R. A. DORY*
C. L. HEDRICK
D. B. BATCHELOR
E. F. JAEGER
D. B. NELSON*
B. A. SPONG
RFP THEORY
R. A. DORY*
R. G. BATEMAN
B. CATHEY*
D. B. NELSON*
W. W. PING
B. V. WADDELL
KINETIC THEORY
J. D. CALLEN*
C. O. BEASLEY, JR.
E. C. CRUME, JR.*
H. R. WEIER
J. A. ROME
D. J. SIGMAR
R. T. TSANG
TRANSPORT SIMULATION
J. D. CALLEN*
T. ARPARO*
E. C. CRUME, JR.*
J. F. HOCKS
H. C. HOPE
A. T. WEIER*
W. SOLER*
PLASMA ENGINEERING
J. D. CALLEN*
F. B. MARCUS
D. G. VEALFES*
J. F. WALLY, JR.
A. T. WEIER*
R. A. JOHAN
COMPUTING SUPPORT
R. A. DORY*
J. BURNETT*
J. E. FRANCIS, JR.
R. A. FRENCH
R. K. GRYTHE
C. E. HARRIS
D. R. OVERBY*
C. E. PARKER
D. C. YONTS
PLASMA SOURCES AND RFP
W. L. STIRLING
R. C. DAVIS
P. W. RYAN
D. E. SCHECHTER
C. C. TSAI
NEUTRAL BEAM SYSTEMS DEVELOPMENT
W. R. HAMILTON
C. R. BLUE
W. K. DAGENHART
L. R. GRIMMAS*
R. E. POTTER
HIGH ENERGY SYSTEMS AND ELECTRICAL ENGINEERING
G. SCHILLING*
G. C. BARBER
P. L. GARDNER
J. KIM
W. W. WENON
N. S. PORTE
S. W. SCHWENTERLY
D. O. SPARKS
R. E. WRIGHT
COMPUTER SIMULATION AND PELLET FUELING
L. D. STEWART*
C. A. FOSTER
S. L. MILORA
J. R. WHEATON
SYSTEMS DESIGN
J. W. LUE
COIL DESIGN
J. V. LUTON*
J. H. BALLOU
CONDUCTOR TEST AND SELECTION
W. A. FIETZ*
L. ALLEY
J. R. MILLER
R. E. SCHMALL
S. S. SHEN
W. H. WAGNER
COIL PROTECTION AND EDDY CURRENT SHIELDING
H. T. YEH
L. GREENER
COIL TEST AND INSTRUMENTATION
P. L. WALSTROM
J. P. ELLIS
J. P. RUDD
STRUCTURAL ANALYSIS AND MATERIAL SELECTION
W. C. T. STODDART*
J. E. AKIN*
W. N. GRAY
H. Pu*
CRYOGENICS AND REFRIGERATION
C. G. LAWSON
C. W. FITZPATRICK
COIL FABRICATION
R. L. BROWN

2

BLANK PAGE

Table 9.1. FED activity funding

Activity	Dollars in thousands FY 76 Actual	FY 77 Funding as of Feb. 1977	FY 77 Expected funding	FY 78 Presidential Budget
Confinement systems – closed confinement systems – research operations	5,190	6,800	7,800	9,650
Confinement systems – closed confinement systems – major device fabrication	3,100	5,500	5,500	6,950
Development and technolcgy – magnetic systems	3,400	5,475	5,575	9,400
Development and technology -- plasma engineering	5,291	6,250	6,725	6,150
Development and technology – materials	1,040	1,590	1,590	2,045
Development and technology – fusion systems engineering	1,405	2,140	2,390	2,920
Applied plasma physics -- fusion plasma theory	1,910	2,075	2,075	2,200
Applied plasma physics – experimental plasma research	640	870	870	920
Applied plasma physics – national CTR computer network	50	75	225	275
Total ORNL funding	$22,026	$30,775	$32,750	$40,510

the recently created Management Information System (MIS).

The procurement module is a computer-based system which provides obligated cost and status information on all vendor procurement actions. Data for each order include identification numbers, delivery date, cost, account number, vendor, requestor, and status. The module runs on-line and is easy to use because it prompts the user on the required action. An individual can use the module to determine the current status of an order. A project manager can quickly determine the amount of funds committed to outside procurement for the project or a specific task. The Procurement Officer can list orders due (or overdue) by a given date so that critical items can be expedited. The Division Director can quickly determine the total funds obligated for outside procurement, including an estimate of when the charges will occur.

9.3 ENGINEERING SERVICES, SAFETY, AND QUALITY ASSURANCE

9.3.1 Engineering Services

The Engineering Services personnel continue to be responsible for or helping to coordinate all of the engineering services of the Division that are not specific to a project or experiment. The group is also responsible for building and maintaining facilities and equipment, which include approximately $40 million of general program equipment. Basically this group provides those functions necessary for the smooth operation

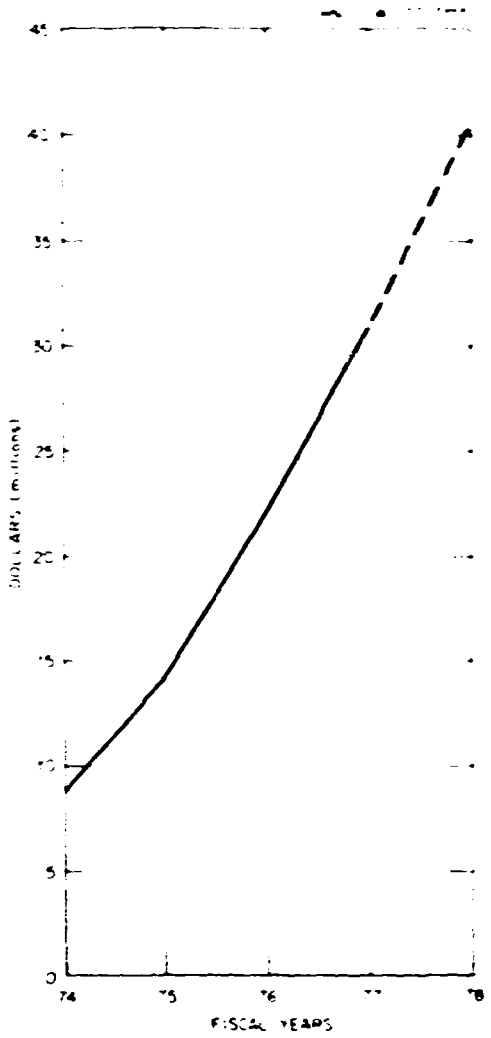

Fig. 9.2. FED funding projection.

of all Division work, including coordination of machine-shop work, maintenance craft work, inventory and storage of equipment and materials, and development of plans and job scopes of new projects which are needed to improve operations or provide new space for facilities.

During the past year nine expense type construction projects were completed using CPFF contractors. Seven new projects were started and are in various stages of completion. These projects provide improved distribution of utilities, repair of motor generator sets, renovation of rest rooms, improvement of lunch room and eating facilities, removal of obsolete experiments and contaminated areas, relocation of equipment, and rearrangement of the cyclotron area.

Three large GPP projects were completed by contractors.

1) A new building was completed on a fixed price contract to provide space for 36 engineering personnel.
2) New office space was provided for 30 additional people in Building 9204-1.
3) Three new laboratories were completed in Building 9204-1.

Preliminary design and cost estimates were prepared to support requests for future GPP funds. These projects include:

1) additional office and laboratory space in Building 9201-2,
2) supporting facilities for the Impurity Study Experiment (ISX) and the Oak Ridge Tokamak (ORMAK) Upgrade, and
3) cooling water system (phase II) to support superconducting magnet experiments.

In a continuing program of improving working conditions and providing adequate facilities, studies and cost estimates have been made on the electrical distribution system, building ventilation system, office and laboratory space available, and utility requirements. GPP, GPE, and line item funding have been requested to implement those areas which cannot be funded from expense funds. A $10 million line item request has been submitted for FY 79 to upgrade some of the major facilities required for the Fusion Energy Program. Efforts to increase the services from the ORNL overhead account require documentation of needs and costs associated with these services.

In addition, the Engineering Services group has:

1) scheduled and coordinated 93,600 hours of machine-shop work,
2) been responsible for maintaining buildings and utilities,

3) coordinated office moves, telephone requirements, and procurement of office furniture,
4) corrected OSHA violations, and
5) conducted an energy conservation program.

9.3.2 Safety

A safety program which includes both safety and fire inspections and six formal training sessions for all FED personnel has continued at the Division and section level. An extensive defensive driver training program was also conducted.

9.3.3 Quality Assurance

A top level quality assurance (QA) program is operated by this group and is being requested by the Energy Research and Development Administration (ERDA) for use as a model of a viable research and development QA approach by other groups in fusion energy work under ERDA. Quality assurance is a part of every job, whether it is shop work, field assembly, or engineering. This program has proven to be effective in providing more reliable experimental equipment at a reduced cost.

9.4 FINANCE OFFICE

The Finance Officer provides assistance to the section heads and project managers in preparing budgets and determining the financial position of the projects and the Division. Throughout the year costs are compared to budgets and projections are made of the year-end budget status. Plans have been made to meet the increasing demands for additional financial planning and controls associated with growing projects. The Finance Office will expand to provide the section heads and program managers with financial assistants who will handle two or three sections or programs with the goal of being able to handle most of the routine financial and administrative work. This should increase the effectiveness and efficiency of the section heads and program and project managers and permit logical program and project decisions to be made based on the correct information.

A study has been completed on how the Division is using work orders to maintain cost control. The result was a new procedure for utilizing work orders consistently throughout the Division. The new procedure is directed towards providing data on the type of expense incurred as well as on cost.

Considerable financial work has also been done in preparation for changing from the previous accounting system used at ORNL to a uniform accounting system. The problems created by this changeover are still being resolved. New methods were established to assist in accounting for an overall budget of operating and capital funds of approximately $35 million in the Fusion Energy Program.

9.5 MANAGEMENT INFORMATION SYSTEM

The Management Information System activity was started in September 1976 and is another key addition for the FED goal of providing section, program, or project managers with timely and relevant information for their review. This system will also indicate potential problem areas which require attention and will provide detailed backup information for problem areas upon request. Another goal is to reduce the effort and time required to assemble and maintain the data.

The first step was to determine what could be done in terms of improving the information process on functions related to planning and controlling budgets and schedules. A survey was made of the management staff's requirements, especially those which were not being adequately satisfied by existing data. A list of feasible concepts was developed which could be implemented to provide better information. The result of the survey was to set as the first major goal the ability to make budget projections based on current costs and obligations. This capability requires that several sources of information on costs and obligations be readily accessible. The approach being taken is to develop a separate module (computer program) for each major source. This is advantageous because individual modules are usable before the entire capability is operational. It also gives management the option

of reviewing each step before making a commitment to the next step. If the decision is not to continue, each module already developed can still provide a useful function.

The first activity developed was the currently operational procurement module,[1] which provides obligated cost and status information on all vendor procurement actions. Classes were given on using the procurement module, and after a one-hour class secretaries were able to get information on procurement obligations. Also the data base is now maintained by a clerk with no previous computer experience. An improved version of the module, which allows the user more flexibility in specifying the grouping of orders which are of interest, is almost ready for production. The major improvement is that it uses data directly from the financial systems to determine when payments are made and adds to the data base any orders which were not entered at the initiation of the procurement request. This eliminates a large portion of the manual effort required to maintain the data base. A draft of a revised user's manual for the improved module was completed, and a more comprehensive manual for data base maintenance and programmers is under way. A major benefit of the procurement module will be realized when it provides the obligated procurement cost to the end-of-year budget projection module.

Preliminary work has begun on other modules to provide cost-to-date information and non-division labor performance and cost information.

Assistance was provided to Project Engineering in assembling the capabilities required for a Project Performance Measurement System (PPMS). Documentation on several Program Evaluation and Review Techniques (PERT) computer programs was reviewed and two have been requested from the National Aeronautics and Space Administration. Using a work breakdown structure, the PPMS and PERT models can be supported by the MIS being developed. This will give a project manager visibility of the entire integrated schedule and cost and project the impact of a "what if" situation.

9.6 ADMINISTRATOR'S OFFICE

This office provides a variety of services required to keep the Division functioning in an efficient and effective manner. Some highlights follow.

9.6.1 Personnel Recruiting

Over 100 applicants for positions were interviewed in 1976. Of those interviewed and offered positions, 34 accepted. Major hiring was to provide scientific staff for the beam program, ELMO Bumpy Torus (EBT), ISX, and [illegible] operations and to staff the Reports Office. The Administrator's Office was also used to coordinate the U.S.S.R. and Spanish exchanges; three Spanish scientists are now working in the Division and a fourth is expected during CY 77.

9.6.2 Visitors

Visits were arranged for approximately 1200 visitors including 175 noncitizens.

9.6.3 Subcontracts

Calendar year 1976 was the first year involving a major industrial participation in ORNL's fusion effort. Interaction with industry through subcontracts totaled approximately $2.3 million, distributed among 14 subcontractors. Westinghouse [participating in The Next Step (TNS) studies] and Varian Associates (developing microwave sources) were the largest of the subcontractors. Greater participation is expected in CY 77 and CY 78, particularly in the Large Coil Program (LCP) and TNS.

9.6.4 FED Reports Office

A critical element in any rapidly progressing and expanding international program is the published material which characterizes the work being done. This material must be made available in a timely and understandable manner. The FED Reports Office provides a documentation service which includes editorial review and coordinating typing, drafting, photography, and

reproduction. During 1976, 57 numbered reports, 99 journal articles, and 135 abstracts and meeting papers were published.

9.6.5 Administrative Guidelines

The rapid growth of the Fusion Energy Division created a need for administrative guidelines. These guidelines were prepared in the early part of CY 76 to cover administrative situations unique to the Fusion Energy Division. The Administrative Guidelines are used as a supplement to the Nuclear Division Office Guide, the ORNL Style Guide, and the Standard Practice Procedures Manual. Fourteen sections have been completed, and more will be added as the need arises.

9.7 TECHNOLOGY COMMERCIALIZATION OFFICER

A new position was created with the responsibility of ensuring that technology developed by the Fusion Energy Program is transferred to commercial organizations. During the past year this goal was accomplished using several different methods. First, subcontracts were awarded to commercial firms to support the LCP and the TNS projects. In addition, industrial subcontracts were awarded for high technology items such as superconducting materials, a liquid helium refrigerator, power supplies, and beam cryopanels. On-site support was obtained from several firms having commercial interest. Finally, a very important method of technology dissemination is via technical reports, journal articles, scientific talks, and the Division's Annual Information Meeting. These external program involvements are expected to continue to grow in 1977 with a continued theme of including interested commercial industries in the program when possible.

9.8 FED LIBRARY

The FED library maintains a specialized collection of books and scientific journals in plasma physics and fusion technology. It also receives reports from the world's plasma physics laboratories which reflect current research in these specialized fields.

An expanding and important service provided by the library is automated literature searching. Offered are retrieval services through ERDA RECON, Lockheed's DIALOG, SDC's ORBIT, *New York Times'* Information Bank, and EPRI. In addition a vast number of data bases are available which are particularly appropriate to the Fusion Energy Division (Nuclear Science, ERDA Energy Data Base, Physics Abstracts, etc.).

---

1. J. K. Lovin and B. A. Clark, *Procurement Module for a MIS: User's Manual*, ORNL/TM-5693, Oak Ridge National Laboratory, Oak Ridge, Tennessee (December 1976).

PUBLICATIONS, PAPERS, AND REPORTS

Books and Journal Articles

I. Alvarez, C. Cisneros, C. F. Barnett, and J. A. Ray, "Negative-Ion Formation From Dissociative Collisions of H_2^+, H_3^+, and HD_2^+ in H_2, He, and Xe," Phys. Rev. A 14, 602 (1976).

J. L. Anderson, R. S. Booth, R. J. Colchin, R. V. Miskell, and J. M. Bailey, "Feedback Control for Plasma Equilibrium in ORMAK," Nucl. Fusion 16, 629-638 (1976).

D. B. Batchelor, "Parametric Resonance of Systems with Time-varying Dissipation," Appl. Phys. Lett. 29(5), 280-281 (1976).

C. O. Beasley, Jr., D. Z. Lominadze, A. B. Mikhailovsky, "Excitation of Short Wavelength Alfven Oscillations by High-Energy Ions in Tokamaks," Fiziky Plasmy 2, 170 (1976).

J. D. Callen, "Flux-Conserving-Tokamak (FCT) Equilibria as a Natural Consequence of High Power Neutral Beam Heating," Comments on Plasma Physics and Controlled Fusion 2(5), 159-166 (1976).

P. J. Catto, K. T. Tsang, J. D. Callen, W. M. Tang, "Resonant Electron Effects on Trapped Electron Instabilities," Phys. Fluids 19, 1596 (1976).

C. Cisneros, I. Alvarez, C. F. Barnett, and J. A. Ray, "Angular Distributions and Total Cross Sections for D^- Formation from Interaction of D^+ and D^0 with Cesium," Phys. Rev. A 14, 76 (1976).

C. Cisneros, I. Alvarez, C. F. Barnett, and J. A. Ray, "Differential Scattering and Total Cross Sections of Hydrogen and Deuterium Atoms in Nitrogen," Phys. Rev. A 14, 84 (1976).

C. Cisneros, I. Alvarez, C. F. Barnett, J. A. Ray, and A. Russek, "Angular Distributions and Total Cross Sections for D^- Formation from Interaction of D_2^+ with Cesium," Phys. Rev. A 14, 88 (1976).

J. F. Clarke, S. P. Hirshman, and D. J. Sigmar, "Neoclassical Transport Theory of a Multispecies Plasma in the Low Collision Frequency Regime," Phys. Fluids 19(5), 656 (May 1976).

R. E. Clausing, L. C. Emerson, L. Heatherly, R. J. Colchin, and J. C. Twichell, "Measurement and Modification of First-Wall Surface Composition in the Oak Ridge Tokamak (ORMAK)," J. Vac. Sci. Technol. 13, 437 (1976).

L. Dresner, "Propagation of Normal Zones in Composite Superconductors," Cryogenics 16, 675 (1976).

D. S. Easton and R. E. Schwall, "Performance of Multifilamentary Nb_3Sn under Mechanical Load," Appl. Phys. Lett. 29, 319 (1976).

J. T. Hogan, "Multifluid Tokamak Transport Models," Methods in Computational Physics 16, 131 (1976) (Review Paper).

H. C. Howe, L. A. Berry, and J. D. Callen, "Neutral Beam Injection," Physics News in 1976, pp. 67-68 (1976).

R. C. Isler, "Profiles and Polarizations of the Balmer-α Line from High-Temperature Hydrogen Atoms in Strong Magnetic Fields," Phys. Rev. A 14, 1015-1019 (1976).

R. C. Isler and L. E. Murray, "Optical Spectroscopy of Homonuclear Ion-Atom. $Ne^+ + Ne$," Phys. Rev. A 13, 2087 (1976).

G. L. Jahns, "Comments on 'Trapped Particle Instability,'" Phys. Fluids 19, 1432 (1976).

M. S. Lubell, "Superconductivity and Magnet Technology," *Proc. Symposium on Energy Sources for the Future*, ed. by J. L. Duggan and R. J. Cloutier, CONF-750733, Oak Ridge Associated Universities, Oak Ridge, Tennessee (1976).

W. M. Manheimer, E. Ott, K. R. Chu, J. P. Boris, and J. D. Callen, "Mode-Coupling Stabilization of the Dissipative Trapped-Electron Instability," Nucl. Fusion 16, 203 (1976).

J. R. McNally, Jr., "Mirrors: Past and Future," Physics Today, p. 15 (August 1976).

J. R. McNally, Jr. and R. D. Sharp, "Advanced Fuels for Inertial Confinement," Nucl. Fusion 16, 868-870 (1976).

D. N. McNeill, "A Ruby Filter for Stray Light Reduction in Scattering Experiments," Appl. Opt. 15, 573 (1976).

M. Murakami, J. D. Callen, and L. A. Berry, "Some Observations on Maximum Densities in Tokamak Experiments," Nucl. Fusion 16, 347-368 (1976).

Y-K. M. Peng, "Lagrangian Density for Collisional Plasma," J. Plasma Phys. 15, 165-174 (1976).

R. A. Phaneuf and R. H. McKnight, "Charge Transfer Collisions of N^{3+} with Atomic and Molecular Hydrogen," Bull. Am. Phys. Soc. 21(10), 1266 (1976).

J. A. Rome, D. G. McAlees, J. D. Callen, and R. H. Fowler, "Particle-Orbit Loss Regions and Their Effects on Neutral-Injection Heating in Axisymmetric Tokamaks," Nucl. Fusion 16, 55 (1976).

D. Steiner, "Fusion as An Energy Option," Review, Oak Ridge National Laboratory, Vol. 9, No. 2 (Spring 1976).

D. Steiner, "Materials Requirements for Fusion Power," *Critical Materials Problems in Energy Production*, ed. by Charles Stein, Academic Press, New York (1976).

D. Steiner, "Power by Fusion," *Knoxville News-Sentinel*, February 22, 1976.

W. M. Tang, C. S. Liu, M. N. Rosenbluth, P. J. Catto, and J. D. Callen, "Finite-Beta and Resonant-Electron Effects on Trapped-Electron Instabilities," Nucl. Fusion 16, 191-202 (1976).

K. T. Tsang and J. D. Callen, "Smooth Transition of Neoclassical Diffusion from the Banana to Pfirsch-Schlüter," Phys. Fluids 19, 667 (1976).

K. T. Tsang and E. A. Frieman, "Toroidal Plasma Rotation in Axisymmetric and Slightly Nonaxisymmetric Systems," Phys. Fluids 19, 747 (1976).

S. B. Woo, S. P. Hong, and J. H. Whealton, "Semi-Empirical Joint Ion-Neutral Speed Distributions in a Weakly Ionized Gas in Electric Fields," J. Phys. B 9, 2553 (1976).

Papers Presented at Scientific and Technical Meetings

American Physical Society Topical Conference on Diagnostics of High Temperature Plasmas, Knoxville, Tennessee, January 7-10, 1976 [proceedings published in Bull. Am. Phys. Soc. 21(5), 1976].

D. N. McNeill and R. A. Dandl, "Thomson Scattering Determination of Electron Temperature in ELMO Bumpy Torus (EBT)," p. 849 in proceedings.

W. R. Wing, "Computerized Data Acquisition and Analysis."

American Physical Society Meeting, New York, New York, February 2-5, 1976.

R. A. Dory, "The ELMO Bumpy Torus."

American Physical Society Meeting, Chicago, Illinois, February 7-10, 1976.

G. L. Johns, "Tokamak Plasma Dynamics as Deduced from Soft X-Ray Observations."

American Physical Society Topical Conference on Atomic Processes in High Temperature Plasmas, Knoxville, Tennessee, February 16-18, 1976.

K. W. Hill, "Bragg Crystal Spectrometers for Tokamak Impurity Studies."

R. C. Isler, "An Observation of the Reaction $H^{O} + O^{8+} + H^{+} + (O^{7+})$ During Neutral Beam Injection into ORMAK."

International Conference on Surface Effects in Controlled Fusion Devices, San Francisco, California, February 16-20, 1976.

R. J. Colchin and T. C. Jernigan, "ISX – A Tokamak for Surface and Impurities Studies."

R. J. Colchin et al., "ISX – Surface Interaction Studies."

J. T. Hogan and H. C. Howe, "An Impurity Beam-Trapping Instability in Tokamaks."

Tennessee State University, Nashville, Tennessee, March 18, 1976.

F. B. Marcus, "Nuclear Fusion."

Electric Power Research Institute Workshop on Switch Requirements and Research and Development for Fusion Applications, Palo Alto, California, March 24-26, 1976.

R. B. Easter, N. S. Ponte, M. Roberts, and G. Schilling, "Neutral Beam Injection and Ohmic Heating Switch for a Tokamak Experimental Power Reactor."

International Conference on the Computation of Magnetic Fields, Oxford, United Kingdom, March 31-*April* 2, 1976.

K. H. Carpenter and H. T. Yeh, "A Perturbation Expansion with Separated Time Dependence for Eddy Current Calculations."

Institute of Electrical and Electronics Engineers, Inc., Southeastern Conference, Williamsburg, Virginia, April 4-6, 1976.

A. Y. Broverman, R. B. Easter, J. F. Harris, R. E. Hill, J. M. Bailey, F. M. Heck, and J. E. Wolf, "Ohmic Heating System for ORMAK Upgrade."

International Conference on Metallurgical Coatings, San Francisco, California, April 5-8, 1976.

J. E. Simpkins, "A Coating Application for Fusion Research."

Annual Meeting on Theoretical Aspects of Controlled Thermonuclear Research (Project Sherwood), Madison, Wisconsin, April 7-9, 1976.

C. O. Beasley, Jr., H. K. Meier, W. I. van Rij, T. Uckan, and J. E. McCune, "Numerical Study of Drift-Kinetic Evolution of Collisional Plasmas in Tori."

P. J. Catto, K. T. Tsang, and J. D. Callen, "Collisional Effects on Trapped Electron Instabilities."

J. F. Clarke, Y-K. M. Peng, R. A. Dory, and D. J. Sigmar, "Flux Conserving High Beta Toroidal Equilibria."

E. C. Crume and K. T. Tsang, "Pfirsch-Schlüter Transport in Multiple Ion Species Plasmas."

C. L. Hedrick, D. B. Nelson, L. W. Owen, and G. E. Guest, "Theoretical Interpretation of Stability and Transport in E3T."

H. R. Hicks, J. W. Wooten, and G. Bateman, "Nonlinear Ideal MHD Evolution: Verification."

H. C. Howe, J. D. Callen, and L. A. Berry, "High Power Neutral Beam Injection in Tokamaks."

G. D. Kerbel, "Pellet Plasma Interaction Theory."

D. B. Nelson, "Effect of Hot Electrons on Localized MHD Instabilities."

Y-K. M. Peng and R. A. Dory, "High Beta Accessibility in a Cylindrical Tokamak."

G. O. Spies and D. B. Nelson, "Stability of the ELMO Bumpy Torus."

D. A. Spong, E. F. Jaeger, C. L. Hedrick, and E. G. Harris, "Neoclassical Transport in the EBT Device."

K. T. Tsang, N. A. Uckan, and J. D. Callen, "Magnetic Field Ripple Effects in Circular and Non-circular Tokamaks."

Radiation Shielding Information Center Seminar, Workshop on Radiation Energy Spectra, Institute for Energy Analysis, Oak Ridge, Tennessee, April 12, 1976.

M. Roberts, "There is Fusion in Your Future."

Workshop on Impurity Production and Transport Models, Kurchatov Institute, Moscow, U.S.S.R., April 12-13, 1976.

E. C. Crume, "Modeling of Tokamak Discharges in the Presence of Impurities."

E. C. Crume, "Pfirsch-Schlüter Regime Impurity Calculations."

J. T. Hogan, "Neutral Beam Calculations: Effects of Impurities and Compression."

J. T. Hogan, "Survey of the Status of International Work with Tokamak Transport Codes."

D. J. Sigmar and J. T. Hogan, "Alcator Scaling from Neoclassical and Neutral Hydrogen Transport."

Southeastern Symposium on Systems Theory, Knoxville, Tennessee, April 26-27, 1976.

R. B. Easter and J. M. Bailey, "Ohmic Heating System for an Experimental Power Reactor."

American Physical Society Meeting, Washington, D.C., April 26-29, 1976.

J. D. Callen, K. T. Tsang, and N. A. Uckan, "Fast Ion Losses in Tokamaks Due to Magnetic Field Ripples."

M. Murakami, "Plasma Confinement in ORMAK."

Second European Conference on Computational Physics, Garching, Federal Republic of Germany, April 27-30, 1976.

R. A. Dory and Y-K. M. Peng, "High Beta Equilibria in Beam Heated Tokamak Plasmas."

R. A. Dory and Y-K. M. Peng, "MHD Equilibria for High Pressure Tokamak."

J. T. Hogan, "Computation of Transport and Neutral Beam Heating in Tokamaks."

ERDA Ad Hoc Panel Meeting on Ion Layers, Washington, D.C., May 4-6, 1976.

J. R. McNally, Jr., "Advanced Fusion Fuels Prospects for Magnetic and Inertial Confinement."

J. R. McNally, Jr., "The Advanced Fusion Fuel, DD: Overview, Advantages, Prospects, and Problems."

Cornell University, Ithaca, New York, May 12, 1976.

J. R. McNally, Jr., "Advanced Fusion Fuels Prospects for Magnetic and Inertial Confinement."

1976 *Institute of Electrical and Electronics Engineers, Inc., International Conference on Plasma Science, Austin, Texas, May 24-26, 1975.*

S. E. Attenberger and D. G. McAlees, "Sputtering and Impurity Control Effects on D-T Plasma Operation."

G. D. Kerbel, D. G. McAlees, and D. J. Strickler, "The Pellet-Plasma Interaction Associated with Fueling."

D. G. McAlees, S. E. Attenberger, G. D. Kerbel, F. B. Marcus, Y-K. M. Peng, and N. A. Uckan, "Plasma Engineering Features in the ORNL EPR."

Y-K. M. Peng, J. R. Moore, D. J. Strickler, and F. B. Marcus, "Poloidal Field System Considerations for Future Tokamaks."

N. A. Uckan, K. T. Tsang, and J. D. Callen, "The Effect of Magnetic Field Ripple on Energy Confinement and Energetic Particle Loss in Tokamaks."

H. T. Yeh and J. W. Lue, "The Interaction and Protection of Superconducting Pulsed Coils and Toroidal Coils in Large Tokamak Devices."

Annual Meeting of the American Nuclear Society, Toronto, Ontario, Canada, June 13-18, 1976.

K T. Tsang, N. A. Uckan, and J. D. Callen, "Neoclassical Ion Confinement in an Elliptic Tokamak Reactor."

Institute of Electrical and Electronics Engineers, Inc., International Symposium on Electrical Insulation, Montreal, Quebec, Canada, June 14-16, 1976.

S. W. Schwenterly, M. M. Menon, R. H. Kernohan, and H. M. Long, "AC Dielectric Performance of Liquid Helium Impregnated Multi-Layer Plastic Film Insulation."

Massachusetts Institute of Technology Short Course on Fusion Technology, Cambridge, Massachusetts, June 14-16, 1976.

D. G. McAlees, "Tokamak Reactor Technology Notes for Fusion Reactors Course."

Joint MMM-Intermag Conference, Pittsburgh, Pennsylvania, June 15-18, 1976.

K. H. Carpenter and H. T. Yeh, "Eddy Current Calculations for Thin Cylinders of Finite Length with Driving Fields of Ramp Time Dependence."

Fifth International Conference on Atomic Physics, Berkeley, California, July 1976.

C. F. Barnett, "Role of Impurities in Magnetically Confined High Temperature Plasmas."

FPCC Meeting, Princeton Plasma Physics Laboratory, Princeton, New Jersey, July 1976.

J. F. Clarke, "Fusion Physics Status at ORNL."

Oak Ridge Associated Universities Symposium on Energy Sources of the Future, Oak Ridge, Tennessee, July 9, 1976.

J. R. McNally, Jr., "Some Fusion Perspectives."

Atomic Industrial Forum Fusion Committee, Princeton, New Jersey, July 28, 1976.

D. G. McAlees, "TNS Plasma Engineering Studies."

Applied Superconductivity Conference, Palo Alto, California, August 17-20, 1976.

J. E. Akin and A. Moazed, "Finite Element Calculation of Stress Induced Heating of Superconductors."

G. W. Donaldson and S. K. Penny, "Trapping Fields in Tape-Wound Cylindrical Superconducting Magnets."

L. Dresner, "Stability-Optimized, Force-Cooled, Multifilamentary Superconductors."

W. A. Fietz, "High Current Superconductors for Tokamak Toroidal Field Coils."

W. H. Gray and J. K. Ballou, "A Computer Program to Calculate Composite Conductor Losses in Pulsed Poloidal Coil Systems."

D. M. Kroeger, D. S. Easton, and A. Moazed, "Stress Induced Heating in Commercial Conductors and Its Possible Influence on Magnet Performance."

J. W. Lue and J. M. Luton, "Toroidal Field Coil System of the Oak Ridge EPR Reference Design."

J. R. Miller, J. W. Lue, and L. Dresner, "Investigation of Stability of Composite Superconductors in Typical Coil Configurations."

J. R. Miller and S. S. Shen, "Experimental Simulation of Pulsed Field Losses in Tokamak Toroidal Field Coils."

R. E. Schwall, "ORPUS 1 – A Pulsed Superconducting Solenoid."

S. S. Shen and H. T. Yeh, "Pulse Loss and Voltage Measurements on Superconducting Magnets."

Seminar presented at Princeton, New Jersey, August 20, 1976.

F. B. Marcus, "Plasma Start-Up in Tokamaks."

Third Symposium and Workshop on Plasma Heating in Toroidal Devices, International School of Plasma Physics, Varenna, Italy, September 6-17, 1976.

L. A. Berry et al., "Neutral Beam Injection Experiments on ORMAK."

O. B. Morgan, "The Development and Application of Neutral Injection Heating for ORMAK."

O. B. Morgan et al., "The Development of Neutral Injection Heating for Large Tokamaks and Reactors at ORNL."

1976 *Erice School on Tokamak Reactors for Breakeven, Sicily, Italy, September 20-October 1, 1976.*

J. F. Clarke, "Philosophy and Physics of Predemonstration Fusion Devices."

J. F. Clarke, "Predemonstration Fusion Devices: Research and Development Needs."

J. F. Clarke and D. G. McAlees, "Predemonstration Fusion Devices."

D. G. McAlees, "Characteristics of a Predemonstration Fusion Device."

American Nuclear Society Second Topical Meeting on the Technology of Controlled Nuclear Fusion, Richland, Washington, September 21-23, 1976.

S. E. Attenberger and D. G. McAlees, "Operation and Control of High Density Tokamak Reactors."

J. K. Ballou and W. H. Gray, "An Estimate of Thermoelastic Heat Production from Superconducting Composites in Pulsed Poloidal Coil Systems."

J. D. Callen, "Plasma Heating."

W. W. Haselton, M. B. Baer, W. K. Dagenhart, H. Eubank, L. R. Grisham, R. L. Johnson, D. E. Schechter, W. L. Stirling, and C. C. Tsai, "The ORNL/PPPL Neutral Beam System for PLT."

J. Kim et al., "The PLT and TFTR Neutral Beam Systems."

D. G. McAlees, N. A. Uckan, E. S. Bettis, P. B. Burn, C. L. Hedrick, D. B. Nelson, R. T. Santoro, H. L. Watts, H. T. Yeh, L. M. Lidsky, D. A. Ehst, A. Pant, J. S. Herring, D. L. Kaplan, and R. E. Potok, "The ELMO Bumpy Torus Reactor."

M. Roberts, "Oak Ridge EPR and TNS Studies."

M. Roberts, "Results and Conclusions from the ORNL Tokamak Experimental Power Reactor Conceptual Studies."

G. Schilling, D. D. Cannon, R. L. Johnson, and J. Kim, "A Multi-Megawatt Neutral Beam Injection System for TFTR."

W.C.T. Stoddart, T. E. Shannon, and J. W. Lue, "Mechanical Consideration of the TF Coil System for Tokamak Reactors."

Sixth International Conference on Plasma Physics and Controlled Nuclear Fusion Research, Berchtesgaden, Federal Republic of Germany, October 6-13, 1976 (proceedings published as IAEA-CN-35).

S. E. Attenberger, J. D. Callen, E. C. Crume, R. H. Fowler, H. C. Howe, G. D. Kerbel, D. G. McAlees, and J. A. Rome, "Plasma Modeling of Large Tokamaks."

L. A. Berry, "Summarization of Neutral Injection and Confinement Studies of ORMAK, TFR, and T-11."

L. A. Berry et al., "Confinement and Neutral Beam Injection Studies in ORMAK."

J. D. Callen, J. F. Clarke, R. A. Dory, F. B. Marcus, J. R. Moore, Y-K. M. Peng, D. J. Sigmar, D. J. Strickler, K. T. Tsang, and N. A. Uckan, "Tokamak Plasma Magnetics."

R. A. Dandl, J. A. Cobble, H. O. Eason, G. R. Haste, H. Ikegami, N. H. Lazar, and D. H. McNeill, "Experimental Observations in the ELMO Bumpy Torus (EBT)."

C. L. Hedrick, R. A. Dandl, J. A. Cobble, R. A. Dory, H. O. Eason, E. G. Harris, G. R. Haste, H. Ikegami, E. F. Jaeger, N. H. Lazar, D. H. McNeill, D. G. McAlees, D. B. Nelson, L. W. Owen, D. A. Spong, and N. A. Uckan, "Transport and Scaling in the ELMO Bumpy Torus (EBT)."

C. L. Hedrick, R. A. Dory, E. G. Harris, E. F. Jaeger, D. G. McAlees, D. B. Nelson, L. W. Owen, D. A. Spong, and N. A. Uckan, "Theoretical Calculations of Transport and Scaling in the ELMO Bumpy Torus (EBT)."

J. R. McNally, Jr., "Advanced Fusion Fuels Prospects for Magnetic and Inertial Confinement."

ORMAK Group, "Confinement Studies in ORMAK."

ORMAK Group, "Neutral Beam Injection Studies in ORMAK."

Y-K. M. Peng, G. Bateman, H. R. Hicks, J. W. Wooten, and R. A. Dory, "Effect of Large Beta-Poloidal on MHD Instabilities."

M. Roberts, W. M. Stacey, and C. C. Baker, "Results for Tokamak Experimental Power Reactor and Demonstration Plant Reactor Systems Studies."

L. D. Stewart, W. L. Stirling, G. Schilling, G. Barber, W. K. Dagenhart, R. C. Davis, L. R. Grisham, H. H. Haselton, J. Kim, N. S. Ponte, P. M. Ryan, D. E. Schechter, C. C. Tsai, J. H. Whealton, R. E. Wright et al., "Neutral Beam Injector Research and Development Work in the USA."

W. M-W. Tang, J. C. Adam, B. I. Cohen, E. A. Frieman, G. Rewoldt, P. H. Rutherford, J. A. Krommes, M. N. Rosenbluth, D. W. Ross, P. J. Catto, K. T. Tsang, and J. D. Callen, "Linear and Nonlinear Theory of Trapped-Particle Instabilities."

R. B. White, D. A. Monticello, M. N. Rosenbluth, and B. V. Waddell, "Nonlinear Tearing Modes in Tokamaks."

Instrument Society of America International Conference and Exhibit, Houston, Texas, October 10-14, 1976.

P. L. Walstrom, "Controlled Thermonuclear Reactors."

P. L. Walstrom, "Cryogenic Instrumentation Needs in the Controlled Thermonuclear Research Program."

International Symposium on Plasma Wall Interaction, Kernforschungsanlage, Julich, Federal Republic of Germany, October 18-22, 1976.

J. D. Callen, E. C. Crume, H. C. Howe, G. G. Kelley, A. T. Mense, E. M. Oblow, and K. T. Tsang, "Modeling the Edge of a Tokamak Plasma."

J. D. Callen, H. C. Howe, and K. T. Tsang, "A 'New' Model for Transport in Tokamaks."

R. E. Clausing, L. C. Emerson, L. Heatherly, and R. J. Colchin, "Wall Conditioning Studies for ORMAK and ISX."

R. J. Colchin, R. E. Clausing, L. C. Emerson, L. Heatherly, and R. C. Isler, "Surface and Impurity Studies in ORMAK and ISX."

J. T. Hogan, "Models for Impurity Production and Transport in Tokamaks."

Advisory Group Meeting on Atomic and Molecular Data for Fusion, Culham Laboratory, Abingdon, Oxfordshire, England, November 1-5, 1976.

C. F. Barnett, "Controlled Fusion Atomic Data Center."

J. T. Hogan, "Atomic and Molecular Data Needs, Priorities, and Accuracies for CTR Beam Injection."

Fusion Energy Corporation, Princeton, New Jersey, November 4, 1976.

J. R. McNally, Jr., "Advanced Fusion Fuels for Magnetic and Inertial Confinement."

Chattanooga Engineers Club, Chattanooga, Tennessee, November 8, 1976.

M. Roberts, "Fusion Energy Division ORNL Broadly Based, Aggressive Fusion Program Will Be Providing a Viable Energy Alternative for the Future."

M. Roberts, "TNS Program."

ASM Conference on the Manufacture of Superconducting Materials, Port Chester, New York, November 8-10, 1976.

W. A. Fietz, "Superconductors for National Laboratories."

FPCC Meeting, General Atomic Company, San Diego, California, November 12, 1976.

J. F. Clarke, "TNS Design Effort, Based Upon Two Year EPR Study, Addressing Direct Route To Economically Viable Fusion Reactors."

American Nuclear Society 1976 International Conference on World Energy – A Status Report, Washington, D.C., November 14-19, 1976.

D. G. McAlees, N. A. Uckan, E. S. Bettis, P. B. Burn, C. L. Hedrick, R. T. Santoro, H. L. Watts, H. T. Yeh, L. M. Lidsky, D. A. Ehst, J. S. Herring, D. L. Kaplan, A. Pant, and R. E. Potok, "The ELMO Bumpy Torus Reactor Study."

Annual Meeting of the Division of Plasma Physics, American Physical Society, San Francisco, California, November 15-19, 1976 [proceedings published in Bull. Am. Phys. Soc. 21(9), 1976].

R. Aghevli, "Kinetic Theory of Magnetized Plasmas, Inhomogeneous in Density and Temperature, in the Presence of a High-Frequency Electric Field," p. 1151.

S. E. Attenberger, F. B. Marcus, D. G. McAlees, "High Density Tokamak Reactors," p. 1194.

F. W. Baity and B. H. Quon, "Ion Charge-Exchange Measurements on ELMO Bumpy Torus (EBT)," p. 1118.

D. B. Batchelor, "Theory of Microwave Propagation and Absorption in the ELMO Bumpy Torus," p. 1070.

G. Bateman, H. R. Hicks, Y-K. M. Peng, "Effect of High Beta-Poloidal on Toroidal MHD Instabilities," p. 1089.

C. O. Beasley, Jr., E. C. Crume, J. E. McCune, H. K. Meier, and W. I. van Rij, "Local Neoclassical Equilibrium of a Fully Kinetic Plasma," p. 1115.

L. A. Berry, M. Murakami, J. F. Lyon, and H. C. Howe, "The Role of Neutral Beam Injection in the Electron Confinement in ORMAK."

C. E. Bush and J. F. Lyon, "Spatial Origin of the Energy Flux to the ORMAK Liner."

J. D. Callen, H. C. Howe, and K. T. Tsang, "A 'New' Model for Transport in Tokamaks," p. 1085.

P. J. Catto, "An Improved Gyro-Kinetic Description," p. 1189.

J. F. Clarke, "Revisiting the Equilibrium of High Beta Axisymmetric Plasmas."

A. Cooper, F. B. Marcus, D. W. Swain, S. E. Attenberger, and T. Kammash, "Runaway Production in Reactor-Sized Tokamaks," p. 1051.

E. C. Crume, C. O. Beasley, Jr., J. E. McCune, H. K. Meier, and W. I. van Rij, "Ion-Impurity Equilibrium and Transport in Tokamaks," p. 1115.

W. K. Dagenhart, J. E. Francis, H. H. Haselton, R. W. Napier, J. W. Reynolds, and R. E. Wright, "Computer Data Acquisition and Computer Assisted Control for Neutral Beam Lines at the ORNL Medium Energy Test Facility."

R. A. Dory and Y-K. M. Peng, "High-Beta (FCT) Tokamak Equilibria: I. Approach," p. 1034.

J. L. Dunlap, J. H. Harris, and V. K. Pare, "Internal Mode Structures in ORMAK."

O. C. Eldridge and W. Namkung, "Electron Cyclotron Heating in Tokamaks," p. 1172.

A. C. England, R. H. Fowler, H. C. Howe, J. T. Mihalczo, and J. A. Rome, "Neutron Time Benavior due to Deuterium Neutral Beam Injection into a Hydrogen Plasma," p. 1072.

C. A. Foster, P. H. Edmonds, A. C. England, J. T. Mihalczo, and M. Murakami, "The Evolution of Plasma Profiles Due to Cold Gas Injection – Experimental Observations."

R. H. Fowler, D. J. Beckett, J. T. Hogan, Y-K. M. Peng, and J. A. Rome, "Neutral Beam Penetration in Large, Dense, Impure Tokamaks," p. 1119.

W. Gambill, H. H. Haselton, S. L. Milora, J. Kim, C. C. Queen, and W. L. Stirling, "Neutral Beam Targets and Beam Stops."

Y. Goren, N. T. Gladd, R. C. Davidson, and D. B. Batchelor, "Lower-Hybrid-Drift Mode in Screw and Reversed-Field Pinches," p. 1056.

L. R. Grisham, W. L. Stirling, and C. C. Tsai, "Effect of Shaped Extraction Apertures on Ion Beam Optics."

H. H. Haselton, L. R. Grisham, C. C. Tsai, D. E. Schechter, and W. L. Stirling, Optimization of Injected Neutral Beam System for PLT."

C. L. Hedrick and E. F. Jaeger, "Kinetic Transport Model for the ELMO Bumpy Torus," p. 1070.

H. R. Hicks, R. G. Bateman, and D. N. Clark, "Effect of Toroidicity on MHD Instabilities," p. 1080.

J. T. Hogan, "Classical Diffusion in Tokamaks at High-β_θ," p. 1098.

J. T. Hogan, "Models for Impurity Production and Transport in Tokamaks," p. 1125.

H. C. Howe, "Evidence for a Density Pinch in Tokamaks," p. 1170.

R. C. Isler, R. V. Neidigh, and R. A. Phaneuf, "Extreme Ultraviolet Radiation from ORMAK."

E. F. Jaeger, C. L. Hedrick, D. A. Spong, and D. B. Batchelor, "One Dimensional Transport Simulation for the ELMO Bumpy Torus," p. 1069.

G. L. Jahns and J. D. Callen, "Direct Experimental Measurement of Heat Transport in ORMAK," p. 1117.

G. D. Kerbel, S. L. Milora, and D. J. Strickler, "Pellet-Plasma Interaction Theory," p. 1050.

J. Kim, R. J. Colchin, C. A. Foster, R. J. Turnbull, and S. Milora, "Solid Hydrogen Pellet Injection into ORMAK."

J. Kim and R. C. Davis, "Enhancement of Atomic Hydrogen Ion Fraction in DuoPIGatron Ion Source by Means of Predissociation."

N. H. Lazar, E. F. Jaeger, H. W. Moos, and E. S. Warden, "Study of the Neutral Hydrogen Spatial Distribution in EBT," p. 1070.

J. F. Lyon, "Interpretation of Tokamak Injection Results."

F. B. Marcus and S. E. Attenberger, "Plasma Start-up in Tokamaks," p. 1125.

D. G. McAlees, N. A. Uckan, and L. M. Lidsky, "The ELMO Bumpy Torus Reactor (EBTR) Feasibility Study," p. 1070.

R. W. McGaffey, J. F. Lyon, and G. H. Neilson, "Interpretation of Charge-Exchange Measurements: Neutral Density and Ion Toroidal Drift Velocity."

J. R. McNally, Jr. and R. D. Sharp, "Advanced Fusion Fuel Symbiosis," p. 1163.

D. H. McNeill, "'Continuum' Background Light in a Low Density Thomson Scattering Experiment," p. 1117.

H. K. Meier, C. O. Beasley, Jr., J. E. McCune, and W. I. van Rij, "Thermal Relaxation Times Computed with a New Version of the Collisional Plasma Model," p. 1045.

A. T. Mense, "Transport Model for Tokamaks with Divertors," p. 1100.

S. L. Milora, C. A. Foster, and G. D. Kerbel, "A Survey of Possible Pellet Injection Techniques for Refueling Tokamak Reactors," p. 1052.

J. K. Munro, Jr. and J. T. Hogan, "Models Used in the Oak Ridge Tokamak Transport Code," p. 1119.

M. Murakami, P. H. Edmonds, C. A. Foster, P. W. King, and D. L. Shaeffer, "Scaling Experiments with Cold Gas Injection in ORMAK."

W. Namkung and H. C. Howe, "Electron Cyclotron Resonance Heatings (Profile) in Tokamaks and Numerical Simulations in ISX."

R. V. Neidigh and D. J. Sigmar, "Plasma Rotation Revisited," p. 1044.

G. H. Neilson, J. F. Lyon, H. C. Howe, and H. E. Ketterer, "Ion Power Balance and Temperature Scaling for Neutral Beam Injection in ORMAK."

D. B. Nelson and G. O. Spies, "MHD Analysis of Large Scale Instabilities in ELMO Bumpy Torus," p. 1069.

L. W. Owen, C. L. Hedrick, and J. F. Roberts, "Single Particle Containment in Present and Future EBT Designs," p. 1070.

V. K. Paré, J. H. Harris, and J. L. Dunlap, "System for Frequency-Domain Analysis of Oscillatory Diagnostic Signals."

Y-K. M. Peng and R. A. Dory, "High Beta (FCT) Tokamak Equilibria: II. Results," p. 1034.

J. A. Rome and Y-K. M. Peng, "Particle Orbits in High-β D-Shaped Flux Conserving Tokamaks," p. 1100.

P. M. Ryan and J. Kim, "An On-Line Optical Diagnostic for Neutral Beam Injectors."

G. Schilling, J. Kim, and J. H. Whealton, "Beam Optics of a Two-Stage DuoPIGatron Ion Source," p. 1065.

S. W. Schwenterly, W. K. Dagenhart, H. H. Haselton, R. L. Johnson, G. Schilling, and W. L. Stirling, "Cryopumps for Neutral Beam Injection Systems."

R. D. Sharp and J. R. McNally, Jr., "Excitation-Heating of Pellet Fuels to Ignition," p. 1194.

D. J. Sigmar and J. T. Hogan, "Classical $n-\tau$ Scaling for High Density Tokamaks," p. 1125.

D. A. Spong, E. G. Harris, and C. L. Hedrick, "Neoclassical Ion Transport Coefficients for the ELMO Bumpy Torus Device," p. 1069.

W. L. Stirling, K. N. Leung, and C. C. Tsai, "Magnetic Multipole Plasma Source for Ion Extraction."

C. C. Tsai, H. H. Haselton, D. E. Schechter, and W. L. Stirling, "20 cm DuoPIGatron Ion Source."

K. T. Tsang and J. D. Callen, "Asymptotic Behavior of Trapped Electron Instability in the Large $k_\theta \rho_i$ Limit," p. 1197.

K. T. Tsang, G. Vahala, J. D. Callen, and P. J. Catto, "Turbulence Theory of Trapped Electron Instability," p. 1111.

N. A. Uckan, C. L. Hedrick, E. F. Jaeger, D. B. Nelson, L. W. Owen, J. F. Roberts, and D. A. Spong, "Plasma Physics Constraints Imposed on the ELMO Bumpy Torus Reactor (EBTR) Study," p. 1070.

N. A. Uckan, K. T. Tsang, and J. D. Callen, "Magnetic Field Ripple Effects in Arbitrary Cross Section Tokamaks," p. 1197.

T. Uckan and C. O. Beasley, Jr., "Comparison of Model Distribution Functions with Collisional Plasma Model (CPM) Results," p. 1045.

G. Vahala, I. Vahala, J. H. Harris, B. V. Waddell, and G. Bateman, "Relation Between Magnetic Loop Signals and Internal Mode Structure in Tokamaks," p. 1149.

W. I. van Rij, C. O. Beasley, Jr., R. W. McGaffey, and H. K. Meier, "DKES - A Modular Computer Program for Solving a Toroidal-System Drift-Kinetic Equation," p. 1045.

B. V. Waddell, H. R. Hicks, G. L. Jahns, and J. D. Callen, "Comparison of Tearing Mode Theory with ORMAK Data," p. 1149.

B. V. Waddell, H. R. Hicks, G. L. Jahns, and J. D. Callen, "Interpretation of Tokamak Sawtooth Oscillations."

E. S. Marmar, H. W. Moos, and M. H. Lazar, "Spatially Resolved Impurity Distributions in EBT," p. 1071.

J. H. Whealton, J. C. Whitson, and E. F. Jaeger, "Optics of Ions Extracted from a Plasma," p. 1066.

J. B. Wilgen, J. F. Lyon, and G. H. Neilson, "Interpretation of Charge-Exchange Measurements: $T_i(r)$."

W. R. Wing, "Some Thoughts on the Structure and Organization of Data Systems for Pulsed Experiments."

S. J. Zweben, D. W. Swain, H. H. Fleischmann, and H. E. Knoepfel, "Confinement of High Energy Plasmas in ORMAK."

Workshop on the Use of XUV and X-ray Radiometry in Plasma Diagnostics 5 eV *to* 10 keV, *National Bureau of Standards, Gaithersburg, Maryland, November* 29-30, 1976.

R. C. Isler, "Spectroscopic Observations from 15 A to 150 A Based on the Intensities of O VI, VII, and VIII Lines."

Division of Electron and Atomic Physics Meeting, Lincoln, Nebraska, December 1976 [proceedings published in Bull. Am. Phys. Soc. 21(10) 1976].

R. A. Phaneuf and R. H. McKnight, "Charge Transfer Collisions of N^{3+} with Atomic and Molecular Hydrogen."

Second International Conference on Submillimeter Waves and Their Application, San Juan, Puerto Rico, December 1976.

D. P. Hutchinson and K. L. Vander Sluis, "Characteristics of a 38 mm Waveguide CH_3I and CH_3F Submillimeter Wave Laser Oscillator."

D. P. Hutchinson and K. L. Vander Sluis, "Design of a High Power Submillimeter Oscillator-Amplifier System."

Winter Annual Meeting of the American Society of Mechanical Engineers, New York, New York, December 5, 1976.

D. G. McAlees, "ORNL EPR Study – Results and Implications."

Technical Society of Knoxville, Knoxville, Tennessee, December 6 *and* 13, 1976.

J. F. Clarke, M. Roberts, and D. Steiner, "Presentation on the Development of a Viable Fusion Power Plant."

Reports

ORNL Reports

Author(s)	Title	Number
P. B. Thompson	Procedures for Parametric Studies of Costs of Superconducting Toroidal Test Assemblies	ORNL/TM-4821
R. T. Santoro, E. S. Bettis, D. G. McAlees, H. L. Watts, M. L. Williams	Neutronic Scoping Studies for the Tokamak Experimental Power Reactor	ORNL/TM-5035
L. A. Berry	ORMAK Upgrade Proposal: A Proposed Tokamak Device for Plasma Heating and Stability Investigations	ORNL/TM-5130

G. Schilling	TFTR Neutral Beam Systems Conceptual Design	ORNL/TM-5227
Y-K. M. Peng, R. A. Dory, D. B. Nelson, R. O. Sayer	Magnetohydrodynamic Equilibria and Local Stability of Axisymmetric Tokamak Plasmas	ORNL/TM-5267
J. F. Clarke	Suggestions for an Updated Fusion Power Program	ORNL/TM-5280
H. M. Long, R. H. Kernohan, M. M. Menon, S. W. Schwenterly	Cryogenic Power Transmission Technology — Cryogenic Dielectrics, Twelfth Quarterly Report	ORNL/TM-5302
H. K. Meier, W. I. van Rij, C. O. Beasley, Jr., J. E. McCune	The Collisional Plasma Model: A Velocity Space Orthogonal-Function Representation for the Distribution Function of a Collisional Plasma	ORNL/TM-5314
H. K. Meier, W. I. van Rij, C. O. Beasley, Jr.	Techniques for Computing the Numerical Values of the Matrix Elements of the Collision Operator in the Collisional Plasma Model	ORNL/TM-5315
W. I. van Rij, H. K. Meier, C. O. Beasley, Jr., J. E. McCune	Kinetic Equations for the Collisional Plasma Model	ORNL/TM-5316
C. O. Beasley, Jr., H. K. Meier, W. I. van Rij, J. E. McCune	Numerical Study of Drift-Kinetic Evolutions of Collisional Plasmas in Tori	ORNL/TM-5317
W. H. Gray, C. T. Sun	Theoretical and Experimental Determination of Mechanical Properties of Superconducting Composite Wire	ORNL/TM-5331
W. E. Deeds, C. V. Dodd	A Two-Dimensional Relaxation Program for Systems with Inhomogeneous Permeability	ORNL/TM-5333
J. T. Hogan, M. C. Howe	An Impurity Beam-Trapping Instability in Tokamaks	ORNL/TM-5361
K. T. Tsang, E. C. Crume	Temperature Screening Effect in Two-Ion Species Pfirsch-Schlüter Transport	ORNL/TM-5366
Magnetics and Superconductivity Section	Letter Report for the Superconducting Magnet Development Program, December 1, 1975 to March 1, 1976	ORNL/TM-5394
Magnetics and Superconductivity Section	Program for Development of Toroidal Superconducting Magnets for Fusion Research (Revision of ORNL/TM-5109)	ORNL/TM-5401
J. F. Clarke	EPR and TNS	ORNL/TM-5418
A. C. England, O. C. Eldridge, F. B. Marcus, J. C. Sprott, W. Namkung, J. B. Wilgen	High Power Electron Cyclotron Heating in ISX and ORMAK Upgrade at ORNL	ORNL/TM-5425
J. F. Clarke	High Beta Flux-Conserving Tokamaks	ORNL/TM-5429
N. A. Uckan, K. T. Tsang, J. D. Callen	Effects of the Poloidal Variation of the Magnetic Field Ripple on Enhanced Heat Transport in Tokamaks	ORNL/TM-5438

R. A. Dandl, R. A. Dory, H. O. Eason, E. G. Harris, G. R. Haste, C. L. Hedrick, H. Ikegami, E. F. Jaeger, N. H. Lazar, J. N. Luton, D. G. McAlees, D. H. McNeill, D. A. Spong, N. A. Uckan	The ELMO Bumpy Torus Program	ORNL/TM-5451
J. D. Callen, G. L. Jahns	Experimental Measurement of Electron Heat Diffusivity	ORNL/TM-5481
R. H. Fowler, J. D. Callen, J. A. Rome, J. Smith	FIFPC, A Fast Ion Fokker-Planck Code	ORNL/TM-5487
S. W. Schwenterly	Cryogenic Power Transmission Technology – Cryogenic Dielectrics	ORNL/TM-5498
S. E. Attenberger, F. B. Marcus, D. G. McAlees	Dynamics of Tokamak Plasma Experiments and Reactors	ORNL/TM-5509
H. T. Yeh, J. W. Lue	The Interaction and Protection of Superconducting Poloidal Field Coils and Toroidal Field Coils in a Tokamak Experimental Power Reactor	ORNL/TM-5542
L. Dresner	Propagation of Normal Zones in Composite Superconductors	ORNL/TM-5543
R. A. Dory, Y-K. M. Peng	High Pressure, Flux-Conserving Tokamak Equilibria	ORNL/TM-5555
D. G. McAlees, F. B. Marcus, S. E. Attenberger, R. N. Cherdack, G. D. Kerbel, J. R. McNally, Jr., Y-K. M. Peng, G. Schilling, D. J. Strickler, N. A. Uckan	Plasma Engineering in a Deuterium-Tritium Fueled Tokamak	ORNL/TM-5573
J. W. Lue, J. K. Ballou, R. L. Brown, R. Easter, C. G. Lawson, W.C.T. Stoddart, H. T. Yeh	Magnet Systems – Oak Ridge Tokamak Experimental Power Reactor Study 1976	ORNL/TM-5574
C. A. Flanagan, E. S. Bettis, H. L. Watts, J. T. Huxford, R. T. Santoro, J. L. Scott, J. S. Watson, S. D. Clinton, R. N. Cherdack	*Nuclear Engineering*	ORNL/TM-5575
M. Roberts, D. G. McAlees, J. W. Lue, C. A. Flanagan, T. E. Shannon	Research, Development, and Demonstration Needs – Oak Ridge Tokamak Experimental Power Reactor Study 1976	ORNL/TM-5577
P. L. Walstrom	Cryogenic Instrumentation Needs in the Controlled Thermonuclear Research Program	ORNL/TM-5596

J. F. Clarke, D. J. Sigmar	Global Properties of High Pressure Flux Conserving Tokamak Equilibria	ORNL/TM-5599
N. A. Uckan, T. Uckan, J. R. Moore	Calculation of Magnetic Field Ripple Effects in Circular and Noncircular Tokamaks	ORNL/TM-5603
S. W. Schwenterly, H. M. Long, M. M. Menon, R. H. Kernohan	Cryogenic Power Transmission Technology – Cryogenic Dielectrics	ORNL/TM-5608
K. T. Tsang	Banana Drift Diffusion in a Tokamak Magnetic Field with Ripples	ORNL/TM-5630
C. J. Long	Structural Materials for Large Superconducting Magnets for Tokamaks	ORNL/TM-5632
J. K. Ballou, W. H. Gray, J. R. Miller, R. E. Schwall, S. S. Shen, H. T. Yeh	Papers on AC Losses and Pulsed Coils Submitted to the Applied Superconductivity Conference, August 17-20, 1976	ORNL/TM-5635
J. E. Akin, D. S. Easton, W. A. Fietz, D. M. Kroeger, J. W. Lue, J. N. Luton, A. Moazed	Papers on Conductors and Toroidal Field Design Submitted to the Applied Superconductivity Conference, August 17-20, 1976	ORNL/TM-5636
L. Dresner, J. W. Lue, J. R. Miller	Papers on Stability Submitted to the Applied Superconductivity Conference, August 17-20, 1976	ORNL/TM-5637
K. H. Carpenter, H. T. Yeh	Papers on Eddy Current Calculations	ORNL/TM-5652
D. S. Easton, R. E. Schwall	Performance of Multifilamentary Nb_3Sn Mechanical Load	ORNL/TM-5653
K. J. Froelich, C. M. Fitzpatrick	Lap Shear Strength of Selected Adhesives (Epoxy, Varnish, B-Stage Glass Cloth) in Liquid Nitrogen and at Room Temperature	ORNL/TM-5658
J. K. Ballou, W. H. Gray	An Estimate of Thermoelastic Heat Production from Superconducting Composites in Pulsed Poloidal Coil Systems	ORNL/TM-5661
W. L. Stirling, P. M. Ryan, C. C. Tsai	15 cm DuoPIGatron Ion Source	ORNL/TM-5662
D. G. McAlees, N. A. Uckan, E. S. Bettis, C. L. Hedrick, E. F. Jaeger, D. B. Nelson, L. W. Owen, J. F. Roberts, R. T. Santoro, D. A. Spong, H. L. Watts, H. T. Yeh	The ELMO Bumpy Torus (EBT) Reference Design	ORNL/TM-5669
J. F. Clarke, D. G. McAlees	High Beta Predemonstration Fusion Devices (Philosophy, Characteristics and R&D Requirements)	ORNL/TM-5692
J. K. Lovin, B. A. Clark	Procurement Module for a MIS: User's Manual	ORNL/TM-5693
J. C. Whitson, J. H. Whealton	A Fast Exponential Calculation for the IBM 370-195 at the Oak Ridge Gaseous Diffusion Plant	ORNL/TM-5719

Other Reports

Author(s)	Title	Number
C. F. Barnett (co-author)	Report of Subcommittee on Energy-Related Atomic and Molecular Science, National Academy of Sciences (1976)	
C. F. Barnett, W. L. Wiese, (eds.)	Atomic Data for Fusion	Vol. 2, Nos. 1-6 (1976)
C. O. Beasley, Jr., D. G. Lominadze, A. B. Mikhailovsky	Unstable Alfvén Waves in Two Component Tokamaks	Soviet Institute of Atomic Energy Report IAE-2615
J. D. Callen, J. F. Clarke, R. A. Dory, F. B. Marcus, J. R. Moore, Y-K. M. Peng, D. J. Sigmar, D. J. Strickler, K. T. Tsang, N. A. Uckan	Tokamak Plasma Magnetics	IAEA-DN-351 BIO, 1976
Tokamak Experimental Section	Report of the Ad Hoc Panel on rf Heating in Tokamaks	ERDA-76/115, Washington, D.C. July 1976

DISTRIBUTION LIST

ORNL-5275
Dist. Category UC-20

INTERNAL DISTRIBUTION

1. R. G. Alsmiller, Jr.
2. W. C. Anderson
3. E. R. Appleton
4. S. E. Attenberger
5. F. W. Baity
6. J. K. Ballou
7. G. C. Barber
8. C. F. Barnett
9. D. B. Batchelor
10. R. G. Bateman
11. C. D. Beasley, Jr.
12. M. Bender
13-14. L. A. Berry
15. E. S. Bettis
16. C. W. Blue
17. C. J. Borkowski
18. G. R. Bright
19. R. L. Brown
20. E. H. Bryant
21. P. B. Burn
22. C. E. Bush
23. W. D. Cain
24-25. J. D. Callen
26. D. D. Cannon
27. H. P. Carter
28. J. M. Case
29-128. J. F. Clarke
129. R. E. Clausing
130. S. D. Clinton
131. J. A. Cobble
132. R. J. Colchin
133. P. L. Colestock
134. E. C. Crume
135. F. L. Culler
136. W. K. Dagenhart
137-138. R. A. Dandl
139. S. Datz
140. R. C. Davis
141. J. H. DeVan
142. R. A. Dory
143. L. Dresner
144. J. L. Dunlap
145. H. O. Eason
146. R. B. Easter
147. P. H. Edmonds
148. J. F. Ellis
149. L. C. Emerson
150. A. C. England
151. G. Fee
152. W. A. Fietz
153. P. Fisher
154. M. J. Fortenbery
155. C. A. Foster
156. A. P. Fraas
157. W. Fulkerson
158. T. A. Gabriel
159. W. L. Gardner
160. W. H. Gray
161. M. L. Grossbeck
162. H. H. Haselton
163. G. R. Haste
164-165. P. N. Haubenreich
166. C. L. Hedrick, Jr.
167. R. F. Hibbs
168. K. W. Hill
169. J. T. Hogan
170. H. C. Howe, Jr.
171. J. Horak
172. T. J. Huxford
173. R. C. Isler
174. E. F. Jaeger
175. G. L. Jahns
176. T. C. Jernigan
177. R. B. Johnson
178. W. D. Jones
179. O. L. Keller
180. G. G. Kelley
181. H. E. Ketterer
182. J. Kim
183. P. W. King
184. J. P. Kois
185. G. Krist
186. C. G. Lawson
187. N. H. Lazar
188. R. S. Livingston
189. C. J. Long

190. H. M. Long
191. J. K. Lovin
192-193. M. S. Lubell
194. J. W. Lue
195. J. N. Luton, Jr.
196. J. F. Lyon
197. F. C. Maienschein
198. T. L. Mann
199. F. B. Marcus
200. J. B. Marshall
201. B. F. Maskewitz
202. J. May
203. P. J. Maziasz
204. W. McAfee
205. H. C. McCurdy
206. H. E. McCoy
207. H. F. McDuffie
208. J. R. McGuffey
209. J. R. McNally, Jr.
210. D. McNeill
211. H. K. Meier
212. M. M. Menon
213. A. T. Mense
214. J. T. Mihalczo
215. J. R. Miller
216. S. L. Milora
217. R. V. Miskell
218-219. O. B. Morgan
220. M. Murakami
221. W. Namkung
222. A. Navarro
223. R. V. Neidigh
224. G. H. Neilson
225. L. W. Nelms
226. D. B. Nelson
227. V. K. Paré
228. Y-K. M. Peng
229. H. Pih
230. N. S. Ponte
231. H. Postma
232. R. L. Reid
233. B. H. Quon
234-235. M. Roberts
236. M. T. Robinson
237. J. A. Rome
238. M. W. Rosenthal
239. P. M. Ryan
240. M. J. Saltmarsh
241. R. T. Santoro
242. D. E. Schechter
243-244. G. Schilling
245. R. E. Schwall
246. S. W. Schwenterly
247. J. L. Scott
248. J. E. Selle
249. T. E. Shannon
250. S. S. Shen
251. D. J. Sigmar
252. J. E. Simpkins
253. A. H. Snell
254. P. Spampinato
255-256. D. Steiner
257. P. H. Stelson
258. W. L. Stirling
259. W.C.T. Stoddart
260. D. W. Swain
261. P. B. Thompson
262. C. C. Tsai
263. K. T. Tsang
264. N. A. Uckan
265. K. L. Vander Sluis
266. B. V. Waddell
267. P. L. Walstrom
268. J. S. Watson
269. H. L. Watt
270. J. R. Weir
271. E. R. Wells
272. R. Werner
273. J. H. Whealton
274. J. C. White
275. T. L. White
276. F. W. Wiffen
277. J. L. Wiloen
278. M. K. Wilkinson
279. W. R. Wing
280. W. Wood
281. R. E. Wright
282. W. J. Yaggi
283. H. T. Yeh
284. A. Zucker
285. Biology Division Library
286-287. Central Research Library
288. Laboratory Shift Supervisor
289-298. Laboratory Records Department

299. Laboratory Records, ORNL - RC
300. ORNL Document Reference Section
301. ORNL Patent Office
302. ORNL - Y-12 Technical Library
303-305. Fusion Energy Division Reports Office
306-315. Fusion Energy Division Library

EXTERNAL DISTRIBUTION

316. E. Adam, Airco, 100 Mountain Avenue, Murray Hill, NJ 07974
317. Y. Aiyama, Electrotechnical Laboratory, 5-4-1 Mukodai-cho, Tanashi-City, Tokyo, Japan
318. J. L. Anderson, LASL Fusion Program, Los Alamos Scientific Laboratory, P.O. Box 1663, Los Alamos, NM 87545
319. D. J. Anthony, General Electric Co., Building 7, Room 467, 1 River Road, Schenectady, NY 12345
320. V. D. Arp, National Bureau of Standards, Boulder, CO 80302
321. P. L. Auer, Laboratory of Plasma Studies, Cornell University, 312 Upson Hall, Ithaca, NY 14853
322. D. M. Axelrod, Consulting Engineer, Advanced Engineering Department, United Engineers and Constructors, Inc., 30 South 17th Street, Philadelphia, PA 19101
323. C. C. Baker, General Atomic Co., San Diego, CA 92138
324. D. Baldwin, L-388, Lawrence Livermore Laboratory, P.O. Box 808, Livermore, CA 94550
325. J. Baublitz, Division of Magnetic Fusion Energy, Energy Research and Development Administration, Washington, DC 20545
326. J. Beal, Division of Magnetic Fusion Energy, Energy Research and Development Administration, Washington, DC 20545
327. G. Bekefi, Massachusetts Institute of Technology, Room 20A-112, Cambridge, MA 02139
328. R. A. Blanken, Office of Confinement Systems, Division of Magnetic Fusion Energy, Mail Code G-234, Energy Research and Development Administration, Washington, DC 20545
329. S. L. Bogart, Division of Magnetic Fusion Energy, Energy Research and Development Administration, Washington, DC 20545
330. G. Bogner, Forschungslaboratorien, Siemens Aktienge Sellshaft, Postfach 325, D9520 Erlanger 2, Federal Republic of Germany
331. R. W. Boom, 513 Engineering Research Building, University of Wisconsin, Madison, WI 53706
332. C. M. Braams, FOM-Instituut Voor Plasma-Fysica, Rijnhuizen, Jutphaas, The Netherlands
333. W. B. Briggs, McDonnell-Douglas Astronautics Company-East, St. Louis, MO 63166
334. G. Bronca, Department du Synchrotron Saturne, CEN/Saclay, F91190, Gif-sur-Yvette, France
335. B. Brunelli, Director, Laboratorio Ionizzati, Casella Postale No. 65, Frascati (Rome), Italy
336. S. J. Buchsbaum, Research Communications Principles Division, Bell Telephone Laboratories, Inc., Murray Hill, NJ 67971
337. A. M. Budker, Nuclear Physics Institute, Siberian Academy of Sciences, Novosibirsk 90, U.S.S.R.
338. O. Buneman, Stanford Electronics Laboratories, Stanford, CA 94305
339. R. W. Bussard, 462 Santa Cecelia, Solana Beach, CA 92075
340. P. Caldirola, Laboratorio di Fisica del Plasma ed Elettronica Quantistica del C.N.R., Via Celoria, 16, 20133 Milano, Italy
341. Centre de Recherches en Physique des Plasmas, 21 Avenue des Bains, 1007 Lausanne, Switzerland

352. C. T. Chang, Physics Department, Research Establishment Risø – Danish AEC, Raskilde, Denmark, DK
353. R. M. Churchill, Burns and Roe Inc., 283 Highway 17, Paramus, NJ 07652
354. A. Clark, National Bureau of Standards, Boulder, CO 80302
355. D. L. Coffey, American Magnetics Inc., P.O. Box R, Oak Ridge, TN 37830
356. F. E. Coffman, Division of Magnetic Fusion Energy, Energy Research and Development Administration, Washington, DC 20545
357. M. Cohen, Division of Magnetic Fusion Energy, Energy Research and Development Administration, Washington, DC 20545
358. H. Coles, NASA Lewis Research Laboratory, Cleveland, OH 44108
359. R. W. Conn, Department of Nuclear Engineering, University of Wisconsin, Madison, WI 53706
360. H. Conrads, Kernforschungsanlage Jülich GmbH (KFA), P.O. Box 1913, 5170 Jülich 1, Federal Republic of Germany
361. T. Consoli, Centre d'Etudes Nucleaires de Grenoble, Avenue des Martyrs-38-Grenoble, France
362. J. G. Cordey, Culham Laboratory, United Kingdom Atomic Energy Authority, Abingdon, Oxon, OX14 3DB, United Kingdom
363. D. M. Cornish, Lawrence Livermore Laboratory, P.O. Box 808, Livermore, CA 94550
364. E. M. Cramer, Southern California Edison Co., 601 West Fifth Street, Los Angeles, CA 90017
365. E. C. Creutz, Assistant Director for Research, National Science Foundation, Washington, DC 20550
366. W. S. Cullingford, Development and Technology, Division of Magnetic Fusion Energy, Mail Code G-234, Energy Research and Development Administration, Washington, DC 20545
367. M. D'Agostino, Grumman Aerospace Corporation, Bethpage, NY 11714
368. E. Dalder, Division of Magnetic Fusion Energy, Energy Research and Development Administration, Washington, DC 20545
369. J. E. Darby, Jr., CTR Program, 0208, Argonne National Laboratory, 9700 South Cass Avenue, Argonne, IL 60439
360. R. C. Davidson, Division of Magnetic Fusion Energy, Mail Code G-234, Energy Research and Development Administration, Washington, DC 20545
361. M. A. Davies, Office of Confinement Systems, Division of Magnetic Fusion Energy, Mail Code G-234, Energy Research and Development Administration, Washington, DC 20545
362. S. O. Dean, Assistant Director, Office of Confinement Systems, Division of Magnetic Fusion Energy, Mail Code G-234, Energy Research and Development Administration, Washington, DC 20545
363. J. F. Decker, Division of Magnetic Fusion Energy, Energy Research and Development Administration, Washington, DC 20545
364. Department of Nuclear Engineering Sciences, 202 Nuclear Science Center, University of Florida, Gainesville, FL 32611
365. R. W. Derby, Magnetics Engineering Associates, 247 Third Street, Cambridge, MA 02141
366. H. Desportes, STIPE, CEN/Saclay, F91190, Gif-sur-Yvette, France
367. D. A. Dingee, Manager, Fusion Programs, Battelle-Northwest, Battelle Boulevard, Richland, WA 99352
368. Director, Research & Technical Support Division, Energy Research and Development Administration, Oak Ridge Operations, Oak Ridge, TN 37830
369. Director, Technical Library, Defense Atomic Support Agency, Sandia Base, Albuquerque, NM 87115

370. G. W. Donaldson, School of Electrical Engineering, University of New South Wales, P.O. Box 1, Kensington, New South Wales 2033, Australia
371. W. E. Drummond, Department of Physics, University of Texas, Austin, TX 78712
372. A. M. Dupas, Documentation S.I.G.N., Département de la Physique du Plasma et de la Fusion Controlée, Association EURATOM-CEA sur la Fusion, Centre d'Etudes Nucleaires, Cedex No. 85 – Centre du Tri, 38041 Cedex, Grenoble, France
373. T. Edelbaum, Charles Stark Draper Laboratories, 75 Cambridge Parkway, Cambridge, MA 02142
374. O. C. Eldridge, Department of Physics, The University of Tennessee, Knoxville, TN 37916
375. H. P. Eubank, Plasma Physics Laboratory, Princeton University, P.O. Box 451, Princeton, NJ 08540
376. R. W. Fast, Manager, Experimental Facilities, National Accelerator Laboratory, P.O. Box 500, Batavia, IL 60510
377. A. Favale, Grumman Aerospace Corp., Bethpage, NY 11714
378. S. Fernbach, Lawrence Livermore Laboratory, P.O. Box 808, Livermore, CA 94550
379. J. J. Ferrante, General Electric Co., Schenectady, NY 12345
380. F. Fickett, National Bureau of Standards, Boulder, CO 80302
381. J. File, Princeton University, Plasma Physics Laboratory, Princeton, NJ 08540
382. C. Finfgeld, Division of Magnetic Fusion Energy, Energy Research and Development Administration, Washington, DC 20545
383. E. von Fischer, Bechtel Corp., P.O. Box 3965, San Francisco, CA 94119
384. C. A. Flanagan, Westinghouse Electric Corp., Fusion Power Systems, P.O. Box 10864, Pittsburgh, PA 15236
385. H. K. Forsen, Exxon Nuclear Company, 777 106th Avenue, N.E., Bellevue, WA 98004
386. T. K. Fowler, Lawrence Livermore Laboratory, P.O. Box 808, Livermore, CA 94551
387. J. W. French, Westinghouse Electric Corp., Fusion Power Systems, P.O. Box 10864, Pittsburgh, PA 15236
388. J. P. Friedberg, Los Alamos Scientific Laboratory, Los Alamos, NM 87544
389. H. P. Furth, Plasma Physics Laboratory, Princeton University, P.O. Box 451, Princeton, NJ 08540
390. Y. Furuto, Chief of Superconducting Group, Central Research Laboratory, Furukawa Electric Co., Ltd., 9-15, 2-Chome, Futaba, Shinagawa-ku, Tokyo 141, Japan
391. W. F. Gauster, c/o H. Kirchmayr, Director, Institut für Experimentalphysik, der Technischen Hochschule in Wien, A-1040 Vienna, Karlsplatz 13, Austria
392. A. Gibson, Deputy Manager, JET Design Group, Culham Laboratory, UKAEA Research Group, Abingdon, Oxfordshire, OX14 3DB, United Kingdom
393. G. Gibson, Westinghouse Electric Corp., Fusion Power Systems, P.O. Box 10864, Pittsburgh, PA 15236
394. G. von Gierke, Institute for Plasma Physics, 8046 Garching bei München, Federal Republic of Germany
395. F. C. Gilbert, Division of Military Applications, Energy Research and Development Administration, Washington, DC 20545
396. W. S. Gilbert, Lawrence Berkeley Laboratory, University of California, Berkeley, CA 94120
397. B. Gore, Pacific Northwest Laboratories, Battelle Boulevard, P.O. Box 999, Richland, WA 99352
398. M. B. Gottlieb, Princeton University, P.O. Box 451, Princeton, NJ 08540
399. W. C. Gough, Electric Power Research Institute, P.O. Box 10412, Palo Alto, CA 94304

400. R. W. Gould, Professor of Electrical Engineering and Physics, Building 116-81, California Institute of Technology, Pasadena, CA 91109
401. N. Grace, Division of Magnetic Fusion Energy, Mail Code G-234, Energy Research and Development Administration, Washington, DC 20545
402. H. Grad, Courant Institute, New York University, 251 Mercer Street, New York, NY 10012
403. S. Gralnick, Plasma Physics Laboratory, Princeton University, P.O. Box 451, Princeton, NJ 08540
404. E. Gregory, Airco Inc., Murray Hill, NJ 07974
405. H. R. Griem, Department of Physics, University of Maryland, College Park, MD 20742
406. R. A. Gross, Department of Mechanical Engineering, Columbia University, New York, NY 10027
407. G. E. Guest, General Atomic Company, P.O. Box 81608, San Diego, CA 92138
408. I. Gverdsiteli, Physico-Technical Institute, Georgian Academy of Sciences, Sukhumi, U.S.S.R.
409. D. S. Hackley, General Dynamics, Convair Division, P.O. Box 80847, San Diego, CA 92138
410. O. Hagena, Kernforschungszentrum Karlsruhe, Postfach 3640, 7500 Karlsruhe 1, Federal Republic of Germany
411. A. M. Hamende, International Centre for Theoretical Physics, Trieste, Italy
412. R. Hancox, UKAEA, Culham Laboratory, Culham, Abingdon, Oxfordshire, United Kingdom
413. C. Kofoed-Hansen, Risø Laboratories, Atomic Energy Commission of Denmark, Raskilde, Denmark
414. R. Harder, General Atomic Co., San Diego, CA 92138
415. B. G. Harris, Department of Physics, University of Tennessee, Knoxville, TN 37916
416. W. V. Hassenzahl, Los Alamos Scientific Laboratory, P.O. Box 1663, Los Alamos, NM 87544
417. A. F. Haught, United Technologies Research Center, 400 Main Street, East Hartford, CT 06108
418. W. Heinz, Gesellschaft für Kernforschung, Institut für Experimental Kernphysik, 75 Karlsruhe, Postfach 3640, Federal Republic of Germany
419. C. D. Henning, Division of Magnetic Fusion Energy, Mail Code G-234, Energy Research and Development Administration, Washington, DC 20545
420. G. K. Hess, Division of Magnetic Fusion Energy, Mail Code G-234, Energy Research and Development Administration, Washington, DC 20545
421. R. L. Hirsch, Deputy Manager, Science and Technology Department, Exxon Nuclear Corp., Room 4330, 1251 Avenue of Americas, New York, NY 10020
422. T. Hiraoka, Japan Atomic Energy Research Institute, Tokai, Ibaraki, Japan
423. M. O. Hoenig, Massachusetts Institute of Technology, National Magnet Laboratory, 170 Albany Street, Cambridge, MA 02139
424. T. Hsu, Office of Confinement Systems, Division of Magnetic Fusion Energy, Mail Code G-234, Energy Research and Development Administration, Washington, DC 20545
425. P. Hubert, Service de Recherches sur la Fusion Controlée, Centre d'Etudes Nucleaires, Fontenay-aux-Roses (Seine), France
426. H. Hurwitz, Jr., General Electric Co., P.O. Box 1088, Schenectady, NY 12301
427. K. Husimi, Institute for Plasma Physics, Nagoya University, Nagoya, Japan
428. S. Ihara, Energy Division, Electrotechnical Laboratory, 5-4-1 Mukodai-cho, Tanashi-City, Tokyo, Japan
429. H. Ikegami, Plasma Physics Division, Institute of Plasma Physics, Nagoya University, Nagoya 464, Japan
430. Institute for Energy Analysis, P.O. Box 117, Oak Ridge, TN 37830
431. M. Iwamoto, Central Research Laboratory, Mitsubishi Electric Corp., 80 Nakano, Minamishimizu, Amagasaki, Hyogo Prefecture, Japan 660
432. V. E. Ivanov, Physical-Technical Institute of the Ukranian Academy of Sciences, Sukhumi, U.S.S.R.

433. V. O. Jensen, Physics Department, Research Establishment Risø – Danish AEC, Raskilde, Denmark
434. C. K. Jones, Manager, Cryogenic Research Laboratory, Westinghouse Electric Corp., Research and Development Center, Pittsburgh, PA 15235
435. N. E. Johnson, Mechanics Research Inc., Oak Ridge, TN 37830
436. J. Junker, Max Planck Institut für Plasmaphysik, Abteilung E2, 8046 Garching bei München, Federal Republic of Germany
437. T. Kasahara, Hitachi Works, 3-1-1 Saiwai-cho, Hitachi-shi, Ibaraki-ken 317, Japan
438. G. D. Kerbel, Lawrence Livermore Laboratory, University of California, P.O. Box 808, Livermore, CA 94551
439. D. W. Kerst, University of Wisconsin, Sterling Hall, Madison, WI 53706
440. K. K. Kim, Department of Electrical Engineering, University of Illinois, Urbana, IL 61801
441. E. E. Kintner, Director, Division of Magnetic Fusion Energy, Mail Code G-234, Energy Research and Development Administration, Washington, DC 20545
442. D. Klein, Westinghouse Electric Corp., Fusion Power Systems, P.O. Box 10864, Pittsburgh, PA 15236
443. A. Knobloch, Institut für Plasmaphysik, Abteilung Technik, 8046 Garching bei München, Federal Republic of Germany
444. H. E. Knoepfel, Laboratorio Gas Ionizzati, Associazione Euratom-CNEN, Casella Postale N. 65, Frascati (Roma), Italy
445. A. A. Koch, Brown, Boveri & Co., Itenhard 29, CH-5620 Bremgarten, CH-8050 Zurich, Bade, Switzerland
446. A. C. Kolb, President, Maxwell Laboratories, Inc., 9244 Balboa Avenue, San Diego, CA 92123
447. E. Komar, D. V. Efremov Scientific Research Institute for Electrophysical Equipment, Leningrad, U.S.S.R.
448. P. Komarek, Institut für Experimental Kernphysik, 75 Karlsruhe, Postfach 3640, Federal Republic of Germany
449. R. Kostoff, Division of Magnetic Fusion Energy, Energy Research and Development Administration, Washington, DC 20545
450. L. M. Kovrizhnikh, Lebedev Institute of Physics, Academy of Sciences of the U.S.S.R., Leninsky Prospect 53. Moscow, U.S.S.R.
451. K. Koyama, Electrotechnical Laboratory, 5-4-1 Mukodai-cho, Tanashi-City, Tokyo, Japan
452. N. A. Krall, Science Applications, Inc., P.O. Box 2354, 1200 Prospect Street, La Jolla, CA 92037
453. G. Kulcinski, Nuclear Engineering Department, University of Wisconsin, Madison, WI 53706
454. D. Kummer, Materials and Process, McDonnell Douglas, P.O. Box 516, St. Louis, MO 63166
455. K. Kuroda, Hitachi, Ltd., Central Research Laboratory, 1-280, Higa Shiko Igakubo, Kokubunji, Tokyo 185, Japan
456. H. L. Laquer, Los Alamos Scientific Laboratory, P.O. Box 1663, Los Alamos, NM 87544
457. C. Laverick, 543 Hampshire Lane, Boling Brook, IL 60439
458. E. Lehnert, Royal Institute of Technology, Stockholm 70, Sweden
459. R. Lengye, Bibliothek, Max Planck Institut für Plasmaphysik, 8046 Garching bei München, Federal Republic of Germany
460. L. L. Lengyel, Max Planck Institut für Plasmaphysik, Abteilung E2, 8046 Garching bei München, Federal Republic of Germany

461. L. M. Lidsky, Department of Nuclear Engineering, Massachusetts Institute of Technology, Cambridge, MA 02139
462. M. Lotker, Advanced Energy Conversion Research, Northeastern Utilities Service Co., P.O. Box 270, Hartford, CT 06101
463. N. J. Lubin, Department of Mechanical and Aerospace Science, River Campus Station, University of Rochester, Rochester, NY 14627
464. D. R. MacFarlane, Mechanical and Structural Engineering, Commonwealth Edison Co., P.O. Box 767, Chicago, IL 60690
465. O. P. Manley, Division of Magnetic Fusion Energy, Mail Code G-234, Energy Research and Development Administration, Washington, DC 20545
466. V. A. Maroni, CTR Program, 208 W115, Argonne National Laboratory, 9700 South Cass Avenue, Argonne, IL 60439
467. A. Martinelli, DSS SEDAP, B.P. No. 2, CEN/Saclay. F91190, Gif-sur-Yvette, France
468. R. Mason, Division of Magnetic Fusion Energy, Energy Research and Development Administration, Washington, DC 20545
469. C. E. Max, Lawrence Livermore Laboratory, University of California, P.O. Box 808, Livermore, CA 94551
470. D. G. McAlees, Research and Technology Center, Exxon Nuclear Co., Inc., 2955 George Washington Way, Richland, WA 99352
471. D. M. Meade, Plasma Physics Laboratory, Princeton University, P.O. Box 451, Princeton, NJ 08540
472. C. Mercier, Service de Recherches sur la Fusion Controlée, Centre d'Etudes Nucleaires, Fontenay-aux-Roses (Seine), France.
473. G. Miley, Department of Nuclear and Electrical Engineering, University of Illinois at Urbana-Champaign, 214 Nuclear Engineering Laboratory, Urbana, IL 61801
474. B. Miller, Division of Controlled Thermonuclear Research, Energy Research and Development Administration, Washington, DC 20545
475. R. Mills, Princeton Plasma Physics Laboratory, Princeton University, P.O. Box 451, Princeton, NJ 08540
476. B. Montgomery, National Magnet Laboratory, Massachusetts Institute of Technology, 170 Albany Street, N.W. 14, Cambridge, MA 02139
477. F. Moon, Department of Theoretical and Applied Mechanics, Cornell University, Ithaca, NY 14850
478. K. Moses, Division of Magnetic Fusion Energy, Energy Research and Development Administration, Washington, DC 20545
479. M. R. Murphy, Development and Technology, Division of Magnetic Fusion Energy, Mail Code G-234, Energy Research and Development Administration, Washington, DC 20545
480. J. O. Neff, Division of Magnetic Fusion Energy, Energy Research and Development Administration, Washington, DC 20545
481. M. Nozawa, Japan Atomic Energy Research Institute, Tokai Research Establishment, Tokai-mura, Naka-gun, Ibaraki-ken, Japan
482. C. Oberly, Aero Propulsion Laboratory, Power Distribution Branch, Wright-Patterson Air Force Base, OH 45433
483. T. Ogasawara, Department of Physics, College of Science and Engineering, Nihon University, Kanda-Surugadi, Chiyoda-ku, Tokyo, Japan
484. H. Ogiwara, Toshiba Research and Development Center, 1 Komukai Tsohibacho, Saiwai-ku, Kawasaki-City, Kanagawa 210, Japan

485. T. Ohkawa, General Atomic Co., P.O. Box 81608, San Diego, CA 92112
486. D. Palumbo, Directorate General for Research and Training, EURATOM, 51 Rue Belliard, Brussels 5, Belgium
487. J. Parain, CEN/Saclay, B.P. No. 2, F91190 Gif-sur-Yvette, France
488. P. B. Parks, General Atomic Co., P.O. Box 81608, San Diego, CA 92138
489. L. D. Pearlstein, L-388, Lawrence Livermore Laboratory, P.O. Box 808, Livermore, CA 94550
490. R. S. Pease, United Kingdom Atomic Energy Authority, Culham Laboratory, Culham, Abingdon, Oxon, United Kingdom
491. D. Pfirsch, Institute for Plasma Physics, 8046 Garching bei München, Federal Republic of Germany
492. P. A. Politzer, Department of Nuclear Engineering, Massachusetts Institute of Technology, Cambridge, MA 02139
493. R. F. Post, University of California, Lawrence Livermore Laboratory, P.O. Box 808, Livermore, CA 94551
494. J. Powell, Brookhaven National Laboratory, Upton, Long Island, NY 11973
495. F. Prevot, Chef du Service du Confinement des Plasmas, CEA, B. P. No. 6, 92260 Fontenay-aux-Roses, France
496. R. E. Price, Division of Magnetic Fusion Energy, Mail Code G-234, Energy Research and Development Administration, Washington, DC 20545
497. J. R. Purcell, General Atomic Co., P.O. Box 81608, San Diego, CA 92138
498. M. S. Rabinovich, P. N. Lebedev Institute of Physics of the U.S.S.R. Academy of Sciences, Moscow, U.S.S.R.
499. P. Reardon, Princeton Plasma Physics Laboratory, Princeton University, P.O. Box 451, Princeton, NJ 08540
500. R. P. Reed, National Bureau of Standards, Boulder, CO 80302
501. Research Information Center, Institute of Plasma Physics, Nagoya University, Nagoya, Japan
502. F. L. Ribe, Los Alamos Scientific Laboratory, P.O. Box 1663, Los Alamos, NM 87544
503. W. Riedmuller, Max Planck Institut für Plasmaphysik, Abteilung E2, 8046 Garching bei München, Federal Republic of Germany
504. J. D. Rogers, Q-26, Los Alamos Scientific Laboratory, P.O. Box 1663, Los Alamos, NM 87544
505. A. Rogister, Institute for Plasma Physics, KFA, Postfach 1913, D-5170, Jülich 1, Federal Republic of Germany
506. D. J. Rose, Department of Nuclear Engineering, Massachusetts Institute of Technology, Cambridge, MA 02139
507. M. N. Rosenbluth, Institute for Advanced Study, Princeton, NJ 08540
508. C. H. Rosner, Intermagnetics General Corp., Charles Industrial Park, New Karner Road, Guilderland, NY 12084
509. P. H. Rutherford, Princeton Plasma Physics Laboratory, Princeton University, P.O. Box 451, Princeton, NJ 08540
510. G. Sacerdoti, Laboratorio Nazionali, Ces. Postale 70, 00044 Frascati, Italy
511. P. Sager, General Atomic Co., San Diego, CA 92112
512. S. St. Lorant, Stanford Linear Accelerator Center, Sand Hill Road, Palo Alto, CA 94304
513. M. Salvat, Max Planck Institut für Plasmaphysik, Abteilung E2, 8046 Garching bei München, Federal Republic of Germany
514. W. B. Sampson, Brookhaven National Laboratory, Upton, Long Island, NY 11973
515. Y. Sawada, Manager of Advanced Engineering Group, Heavy Apparatus Engineering Laboratory, Tokyo Shibaura Electric Co., Ltd. 4, 2-Chome, Suehiro-cho, Tsurumi-ku, Yokahama, Japan

516. G. Sawyer, Los Alamos Scientific Laboratory, Los Alamos, NM 87544
517. A. Schlüter, Institute for Plasma Physics, 8046 Garching bei München, Federal Republic of Germany
518. L. C. Schmid, Pacific Northwest Laboratories, Battelle Boulevard, P.O. Box 999, Richland, WA 99352
519. G. Schmidt, Plasma Physics Laboratory, Princeton University, P.O. Box 451, Princeton, NJ 08540
520. J. Schmidt, Plasma Physics Laboratory, Princeton University, P.O. Box 451, Princeton, NJ 08540
521. K. Schmitter, Max Planck Institut für Plasmaphysik, 8046 Garching bei München, Federal Republic of Germany
522. F. R. Scott, Electric Power Research Institute, P.O. Box 10412, Palo Alto, CA 94304
523. T. Sekiguchi, University of Tokyo and IPP Nagoya, Tokyo, Japan
524. V. D. Shafranov, I. V. Kurchatov Institute of Atomic Energy, 46 Ulitsa Kurchatova, P.O. Box 3402, Moscow, U.S.S.R.
525. Z. Shapiro, Executive Assistant to the General Manager, Breeder Reactor Division, Westinghouse Electric Corp., P.O. Box 355, Pittsburgh, PA 15230
526. S. Shimamoto, Japan Atomic Energy Research Institute, Tokai Research Establishment, Tokai-mura, Naka-gun, Ibaraki-ken, Japan
527. G. Siegel, Tennessee Valley Authority, 1360 Commerce Union Bank Building, Chattanooga, TN 37401
528. A. Simon, Department of Mechanical and Aerospace Sciences, University of Rochester, Rochester, NY 14627
529. L. D. Smullin, Massachusetts Institute of Technology, Cambridge, MA 02139
530. M. Spadoni, Laboratori Nazionali, Cas. Postale 70, 00044 Frascati, Italy
531. J. C. Sprott, Department of Physics, University of Wisconsin, Madison, WI 53706
532. W. M. Stacey, CTR Program, 208 WIIS, Argonne National Laboratory, 9700 South Cass Avenue, Argonne, Illinois 60439
533. Z.J.J. Stekly, Magnetic Corporation of America, 179 Bear Hill Road, Waltham, MA 02154
534. L. D. Stewart, Plasma Physics Laboratory, Princeton University, P.O. Box 451, Princeton, NJ 08540
535. T. H. Stix, Plasma Physics Laboratory, Princeton University, P.O. Box 451, Princeton, NJ 08540
536. B. P. Strauss, Fermi National Accelerator Laboratory, P.O. Box 500, Batavia, IL 60510
537. D. Sweetman, United Kingdom Atomic Energy Authority, Culham Laboratory, Culham, Abingdon, Oxon, United Kingdom
538. K. Tachikawa, Chief of Electric Materials Laboratory, National Research Institute for Metals, 3-12, 2-Chome, Nakameguro, Meguru-ku, Tokyo, Japan
539. K. Takayama, Institute of Plasma Physics, Nagoya University, Nagoya, Japan
540. C. E. Taylor, Lawrence Livermore Laboratory, P.O. Box 808, L-384, Livermore, CA 94551
541. J. B. Taylor, United Kingdom Atomic Energy Authority, Culham Laboratory, Culham, Abingdon, Oxon, United Kingdom
542. C. E. Thomas, Department of Nuclear Engineering, Massachusetts Institute of Technology, Cambridge, MA 02139
543. R. Thomas, General Atomic Co., P.O. Box 81608, San Diego, CA 92138
544. K. Thomassen, Controlled Thermonuclear Research Division, Mail Stop 640, P.O. Box 1663, Los Alamos, NM 87544

545. A. Trivelpiece, Department of Physics and Astronomy, University of Maryland, College Park, MD 20742
546. M. Trocheris, Service de Recherches sur la Fusion Controlée, Centre d'Etudes Nucleaires, Fontenay-aux-Roses (Seine), France
547. R. J. Turnbull, 5621 Charlotte Way, Apartment 14, Livermore, CA 94550
548. B. Twining, Division of Magnetic Fusion Energy, Energy Research and Development Administration, Washington, DC 20545
549. C. T. Uchida, Nuclear Engineering Department, University of Tokyo, Tokyo, Japan
550. G. Vahala, Physics Department, College of William and Mary, Williamsburg, VA 23185
551. T. C. Varljen, Westinghouse Electric Corp., Fusion Power Systems, P.O. Box 10864, Pittsburgh, PA 09864
552. C. von Keszycki, Grumman Aerospace Corp., Research Center, Building 26, Bethpage, NY 11714
553. S. Waddle, Energy Research and Development Administration, Oak Ridge Operations, P.O. Box E, Oak Ridge, TN 37830
554. F. Waelbroeck, Institute for Plasma Physics, KFA Jülich, Federal Republic of Germany
555. C. Walters, Technology Division, Building R25, Rutherford Laboratory, Chilton, Didcot, Oxfordshire, OX110QX, United Kingdom
556. S. T. Wang, Argonne National Laboratory, 9700 South Cass Avenue, Argonne, IL 60439
557. J. P. Waszczak, Manager, Energy Programs, General Dynamics, Convair Division, P.O. Box 80847, San Diego, CA 92138
558. C. N. Watson-Munro, University of Sydney, Wills Plasma Project, Sydney, Australia
559. A. M. Weinberg, Institute for Energy Analysis, P.O. Box 117, Oak Ridge, TN 37830
560. J. M. Williams, Division of Magnetic Fusion Energy, Mail Code G-234, Energy Research and Development Administration, Washington, DC 20545
561. J. W. Willis, Office of Confinement Systems, Division of Magnetic Fusion Energy, Mail Code G-234, Energy Research and Development Administration, Washington, DC 20545
562. C. E. Winters, Washington Representative, Union Carbide Corp., 1730 Pennsylvania Avenue, N.W., Washington, DC 20006
563. S. L. Wipf, Q-26, Los Alamos Scientific Research Laboratory, P.O. Box 1663, Los Alamos, NM 87544
564. W. W. Withee, Director, Energy Systems, General Dynamics, Convair Division, P.O. Box 80847, San Diego, CA 92138
565. J. Wong, Supercon, Inc., 9 Erie Drive, Natick, MA 01760
566. J. T. Woo, Massachusetts Institute of Technology, Room 38-176, Cambridge, MA 02139
567. H. H. Woodson, Chairman, Department of Electrical Engineering, The University of Texas at Austin, Austin, TX 78712
568. K. Yamamoto, Director, Japan Atomic Energy Research Institute, 1-1-13 Shinbashi, Minato-ku, Tokyo, Japan
569. K. Yasukochi, Department of Physics, College of Science and Engineering, Nihon University, Kanada-Surugadai, Chiyoda-ku, Tokyo, Japan
570. S. Yoshikawa, Institute of Advanced Studies, Princeton University, Princeton, NJ 08540
571. J. L. Young, Westinghouse Electric Corp., P.O. Box 10864, Pittsburgh, PA 15236
572. E. J. Ziurys, Division of Magnetic Fusion Energy, Mail Code G-234, Energy Research and Development Administration, Washington, DC 20545
573. K. Zwilski, Division of Magnetic Fusion Energy, Energy Research and Development Administration, Washington, DC 20545

574-765. Given distribution as shown in TID-4500, Controlled Thermonuclear Processes (25 copies NTIS)

US GOVERNMENT PRINTING OFFICE: 1977 748-189/66